Mantle-melt and mantle-fluid interactions in suprasubduction zones : evidence from the Troodos Massif, Cyprus.

Freeman, Jonathan

Mantle-melt and mantle-fluid interactions in suprasubduction zones: Evidence from the Troodos Massif, Cyprus.

by

Jonathan Freeman BSc. (Hons)
University of St. Andrews.

A thesis submitted in partial fulfilment of the requirements for the degree of Doctor of Philosophy

Department of Geological Sciences,
University of Durham.
December 1996

ABSTRACT

The Troodos Massif exposes an intact section of harzburgitic mantle from its contact with crustal lithologies to a depth of approximately 3 km, where it is faulted out against a mass of heavily fractured and serpentinised peridotites: the serpentinite diapir. The harzburgites are host to several generations of pyroxenitic and dunitic intrusives, many of which have features suggestive of a reaction relationship with the enclosing harzburgites such as resorbed harzburgite xenoliths and marginal dunites.

Mineral chemistry and whole-rock data suggest that the harzburgites in the Troodos sequence are residues from up to 30% fractional partial melting in the spinel stability field. The serpentinite diapir exposes lherzolitic lithologies which can be modelled by 10 to 15% fractional partial melting in the spinel stability field. In both cases, the starting composition for the melt modelling was a fertile MORB mantle source.

Deviations from the compositions expected to result from simple fractional partial melting are found in several situations in the mantle section and suggest that melts/fluids interacted with the mantle during and after the partial melting event. Three main situations are identified: i) enrichments in mineral chemistry and whole-rock parameters in specific parts of the *background* harzburgite section; ii) mineral chemistry enrichments around pyroxenites and iii) the clinopyroxene crystals in the Troodos harzburgites which have LREE/HREE ratios higher than those that could be produced by simple fractional melting models.

In the *background* harzburgites, mineral chemistries were enriched at the top of the sequence (*Anomaly 1*) and in a layer towards the base of the sequence (*Anomaly 2*). Pyroxenites also enriched their wallrocks and two trends were identified on the basis of spinel compositions. The Type I trend is of Cr-Fe-Ti enrichment and is similar to the mineral chemistry variations in the *Anomaly 1* harzburgites. The melt involved is inferred to be tholeiitic. The Type II trend is of Mg-Al enrichment and is similar to the mineral chemistry variations in the *Anomaly 2* harzburgites. The melt involved is inferred to be boninitic. The fact that the lower pillow lavas (LPL) have tholeiitic chemistries and the upper pillow lavas (UPL) boninitic chemistries suggests a link between the melt which crystallised the pyroxenites and the pillow lava sequence.

The clinopyroxene trace element patterns from the *background* harzburgites suggest that the LREE, Nd, Sr and Zr are enriched in these minerals compared to the expected values for fractional melting. The enriched component was modelled from the clinopyroxene data and is similar in trace element pattern to the enriched component in the UPL. This suggests that the addition of the subduction component that has been proposed to explain the UPL chemistries was probably added to the mantle both during and after the melting event which produced the UPL.

ACKNOWLEDGEMENTS

Firstly, I'd like to thank my Dad for being endlessly patient for the last four years, providing moral support during the fieldwork and keeping me financially afloat.

Thanks to my supervisors for all their help: Julian Pearce, who allowed me to get on with my own thing; Donny Hutton, who provided much appreciated encouragement during my first field season; and Bob Thompson, who was always on hand for advice about numerous geochemical matters. This PhD was funded by NERC studentship GT92147G.

Graham Pearson gave me many useful comments about the Mineral Chemistry Chapter and random nuggets of geochemical wisdom over the last year or so. Thanks also to Steve Edwards for the afternoon on the rocks in Cyprus, stimulating discussions on mantle textures and the top advice about thesis layouts (know what I mean !?!).

Where would we be without Ron Hardy? Ron has been an absolute star for the past four years. Thanks for letting me calibrate the XRF in unusual ways, for the dubious advice about analytical errors (its all to do with the square root of 2 apparently) and entertaining discussions on Fablon and other interesting subjects. Ron and Julie made me an excellent set of polished thin section, mostly at very short notice, and thanks to Dave Asberry for road maps, financial advice (!?) and electrical repairs. Chris Ottley and the Durham ICP-MS saved the day by finally producing some whole-rock data for me at the eleventh hour. Andrew Peckett, Christine Peirce and Neil Goulty all provided advice on various mathematical problems and George Ruth kept our office computer under control.

I am also grateful for all the help I received from the Cyprus Geological Survey while I was out doing my fieldwork. Thanks to Costas Xenophontos for the guided tour, the Mapping Department for lending me aerial photos and the secretaries for allowing me to use the library at odd hours. The Xenophontos family at Troodos Camping looked after me for two summers.

During the course of my research I was fortunate to spend a considerable amount of time at Edinburgh University using various bits of machinery. I'd like to thank Peter Hill and Stuart Kearns at the Electron Probe Unit who allowed me to have a pretty much free run on the machine with out which I could never have obtained most of the vital data in this thesis. Richard Hinton and Jon Craven kept me on the straight and narrow during my ion probe sessions and tolerated me turning the lab into my bedroom on several occasions. In

particular, I'd like to thank Richard who kept the ion probe running at all hours of the day and night far beyond the call of duty. Nick Odling lent me his magic heating stage in a failed attempt to make beads to analyse by laser ablation. I'd also like to thank all the postgrads and staff at Edinburgh who showed an interest in my research and made me realise that, at least in some departments, your research ability is measured by the work you do rather than the length of time you spend in the coffee room.

I also spent a fair amount of time at the NERC ICP-MS facility trying to coax data out of solutions with seemingly nothing in them. Thanks to Kym Jarvis, Julian Wills and Bridget Gibson for help operating Bertha and my Aunty Joan and Uncle Bernard for providing me with a bed and a large variety of cakes.

Thanks to all the members of UCBC for managing to distract me long enough to make sure that I made it almost to the end of my fourth year. Thanks to Billy Beveridge for the Hatfield Cup coaching, Robin, the Maroon and Tom for endless rowing chat, and Bill Parker and the lads from St. Leonards for the glorious outings in the VIII (just how many lengths was that winning margin at York!!). Thanks also to the members of the Karakoram'95 expedition for a memorable experience, to Tony Johnson for his encouragement and the Royal Geographical Society, the Durham University Expeditions Committee and all the trust funds for providing the cash.

My approach to the analytical work in this thesis was heavily influenced by the experience I gained while working at the British Geological Survey. Thanks to all the original chemimetrisists, Rod, Dee, Bob, Effie and Tricky, for the Christmas parties, fieldwork in glamorous locations and statistical chat.

Cheers to all the unfortunates who have shared an office with me over the past four years, Andy Kerr, Kate, the two Sarahs, John Bole and Robin. Thanks to Mike and Mark for getting me started on the Karakoram idea, and Steve, Andy and Nilpf for the nights out, and Parky (or should I say Professor Sruttucks?!?) for his long-distance email advice on mantle melting, KDs and other sundry geochemical titbits.

CONTENTS

CHAPTER 3
MICROSTRUCTURE

CHAPTER 4
MINERAL CHEMISTRY

CHAPTER 5
WHOLE-ROCK GEOCHEMISTRY

CHAPTER 6
CONCLUSIONS

REFERENCES

APPENDIX A
ANALYTICAL TECHNIQUES

APPENDIX B

SECONDARY ION MASS SPECTROMETRY ANALYSIS OF SPINEL

APPENDIX C

EQUATIONS

APPENDIX D

GEOCHEMICAL DATA SET

CHAPTER 1
INTRODUCTION

1.1 AIM OF THE PROJECT

Subduction zones are one of the most complex magma-forming environments, with several possible sources including the mantle wedge, the subducted slab and the base of the overlying crust. Numerous geochemical studies of subduction zone volcanics have attempted to characterise these end-member sources and assess their relative contributions to the erupted melts. However, the compositions of the erupted magmas are usually modified by high level processes, such as fractional crystallisation, and are often the pooled products of an extended partial melting period. This means that the original partial melting and metasomatic processes are difficult to resolve.

Recent drilling of the Izu-Bonin arc by the Ocean Drilling Programme has sampled residual peridotites produced by partial melting in the subduction zone. Parkinson *et al.* (1992) have shown that the geochemistry of these lithologies records partial melting and melt/fluid interaction processes from the start of subduction to the present day. Unfortunately, the field relationships between the different lithologies are not sampled by drilling, so the precise relationships between the different rock types and the geochemical processes responsible for their formation are impossible to prove.

The Troodos Massif is one of the world's best-studied ophiolites and is generally accepted to be of supra-subduction zone type. The mantle sequence of the Troodos Massif has a similar lithology to the samples collected from the Izu-Bonin arc by the Ocean Drilling Programme, and is exposed well enough to allow the spatial relationships of the various veins, pods and dykes in the mantle to be ascertained and sampled in detail. The aim of this thesis is to use the geochemistry of the mantle lithologies to document the relative age, nature and extent of the partial melting and various fluid-melt-mantle interaction processes in the Troodos supra-subduction zone mantle.

1.2 GEOGRAPHICAL SETTING AND REGIONAL GEOLOGY

The island of Cyprus is located in the north-eastern corner of the Mediterranean Sea, approximately 100 km west of Syria (Figure 1.1).

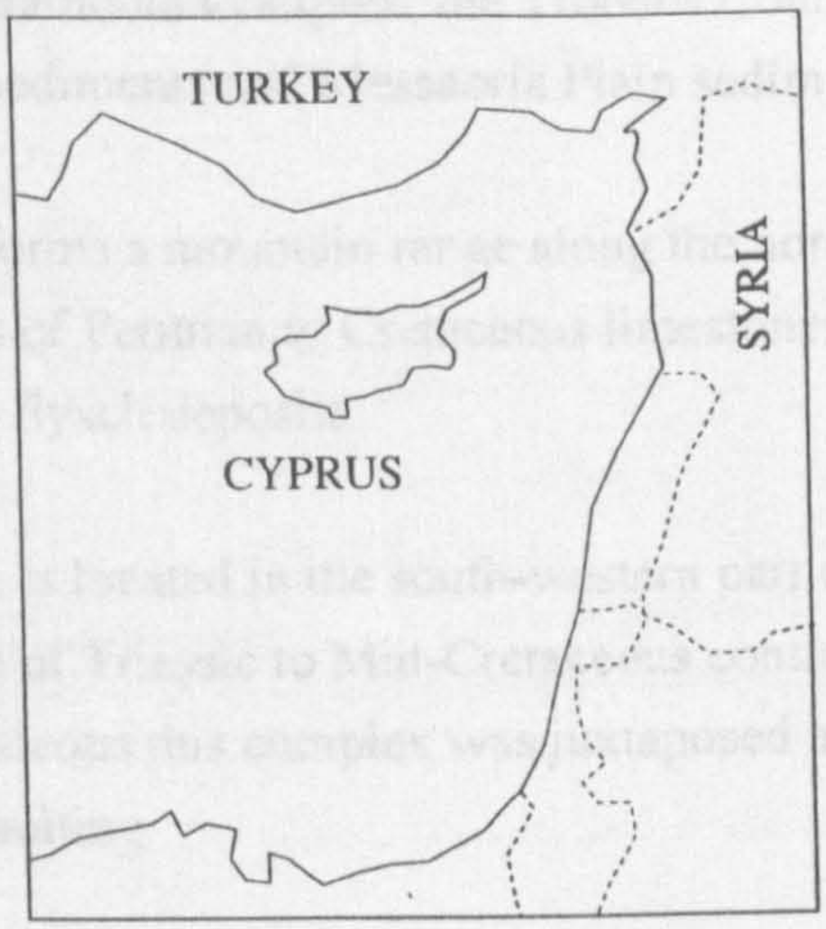

Figure 1.1 The location of the island of Cyprus.

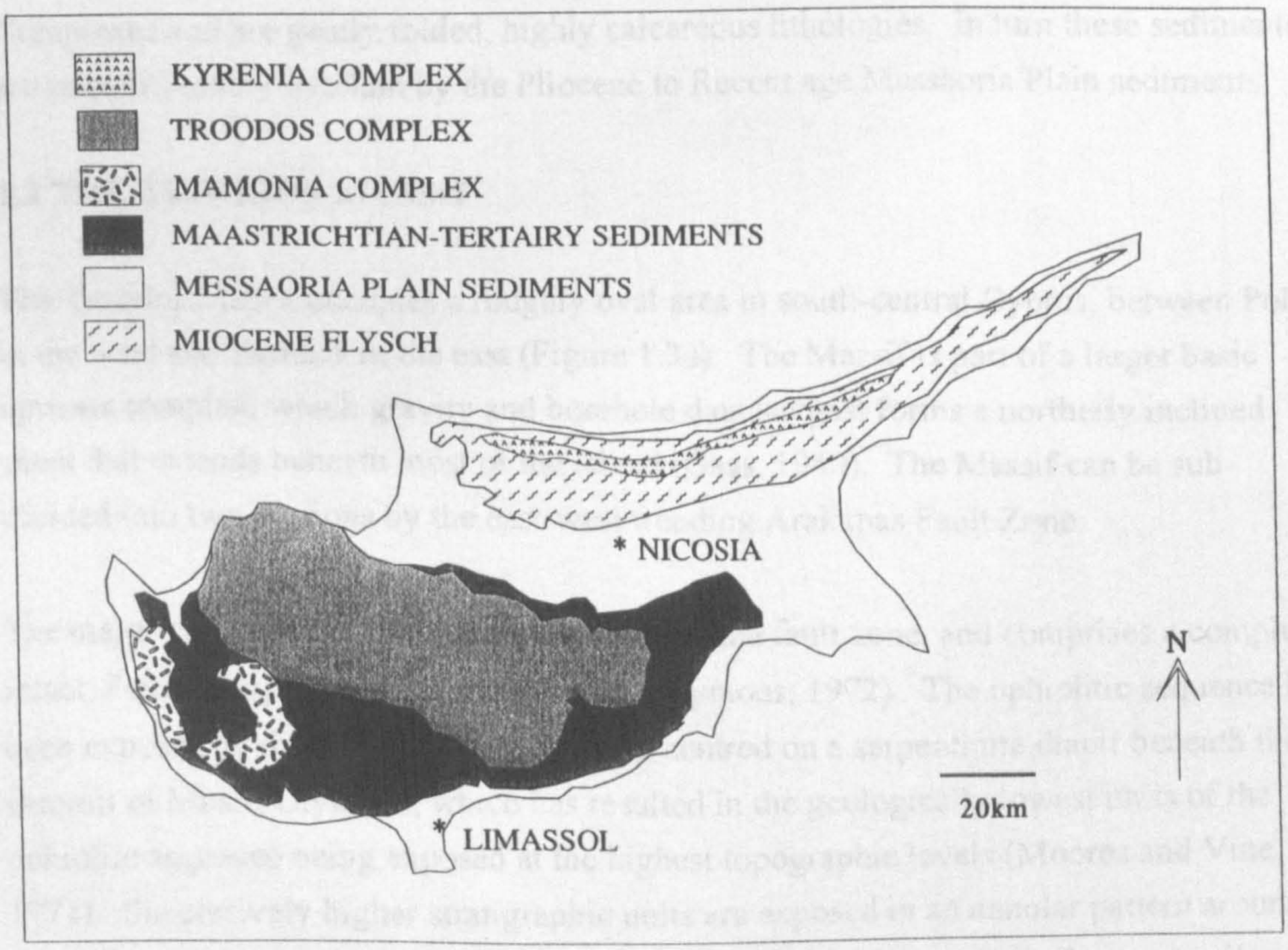

Figure 1.2 The main geological units exposed on Cyprus (redrawn from Malpas *et al.* 1990 and references therein).

The geology of Cyprus can be divided into six main geological units (Figure 1.2): the Kyrenia Complex, the Mamonia Complex, the Troodos Complex, Miocene flysch, Maastrichtian-Tertairy sediments and Messaoria Plain sediments.

The Kyrenia Complex forms a mountain range along the northern coast of Cyprus. It consists of thrust blocks of Permian to Cretaceous limestones and basic volcanics which are flanked by Miocene flysch deposits.

The Mamonia Complex is located in the south-western part of Cyprus and consists of an allochthonous sequence of Triassic to Mid-Cretaceous continental margin sediments. During the Upper Cretaceous this complex was juxtaposed against the Troodos Massif by large-scale strike-slip faulting.

The Troodos Massif is an Upper Cretaceous ophiolite and forms the mountainous terrain in south-central Cyprus.

Maastrichtian-Tertiary sediments unconformably overlie the Mamonia and Troodos Complexes and are gently folded, highly calcareous lithologies. In turn these sediments are unconformably overlain by the Pliocene to Recent age Messaoria Plain sediments.

1.3 THE TROODOS MASSIF

The Troodos Massif occupies a roughly oval area in south-central Cyprus, between Polis in the west and Larnaca in the east (Figure 1.3a). The Massif is part of a larger basic igneous complex, which gravity and borehole data suggest forms a northerly inclined sheet that extends beneath most of the island (Gass, 1980). The Massif can be sub-divided into two portions by the east-west trending Arakapas Fault Zone.

The major part of the Massif lies to the north of the fault zone, and comprises a complete, intact, Penrose-type ophiolite sequence (Anonymous, 1972). The ophiolitic sequence has been exposed by differential Tertiary uplift, centred on a serpentinite diapir beneath the summit of Mount Olympus, which has resulted in the geologically lowest units of the ophiolite sequence being exposed at the highest topographic levels (Moores and Vine, 1971). Successively higher stratigraphic units are exposed in an annular pattern around the central mantle outcrop (Figure 1.3b). South of the Arakapas Fault Zone a smaller, heavily faulted, ophiolitic sequence is exposed in the Limassol Forest area (Figure 1.3c). The Limassol Forest Complex also preserves a Penrose-type ophiolite stratigraphy; however, extensive deformation by predominantly east-west trending shear zones heavily disrupts the sequence.

A

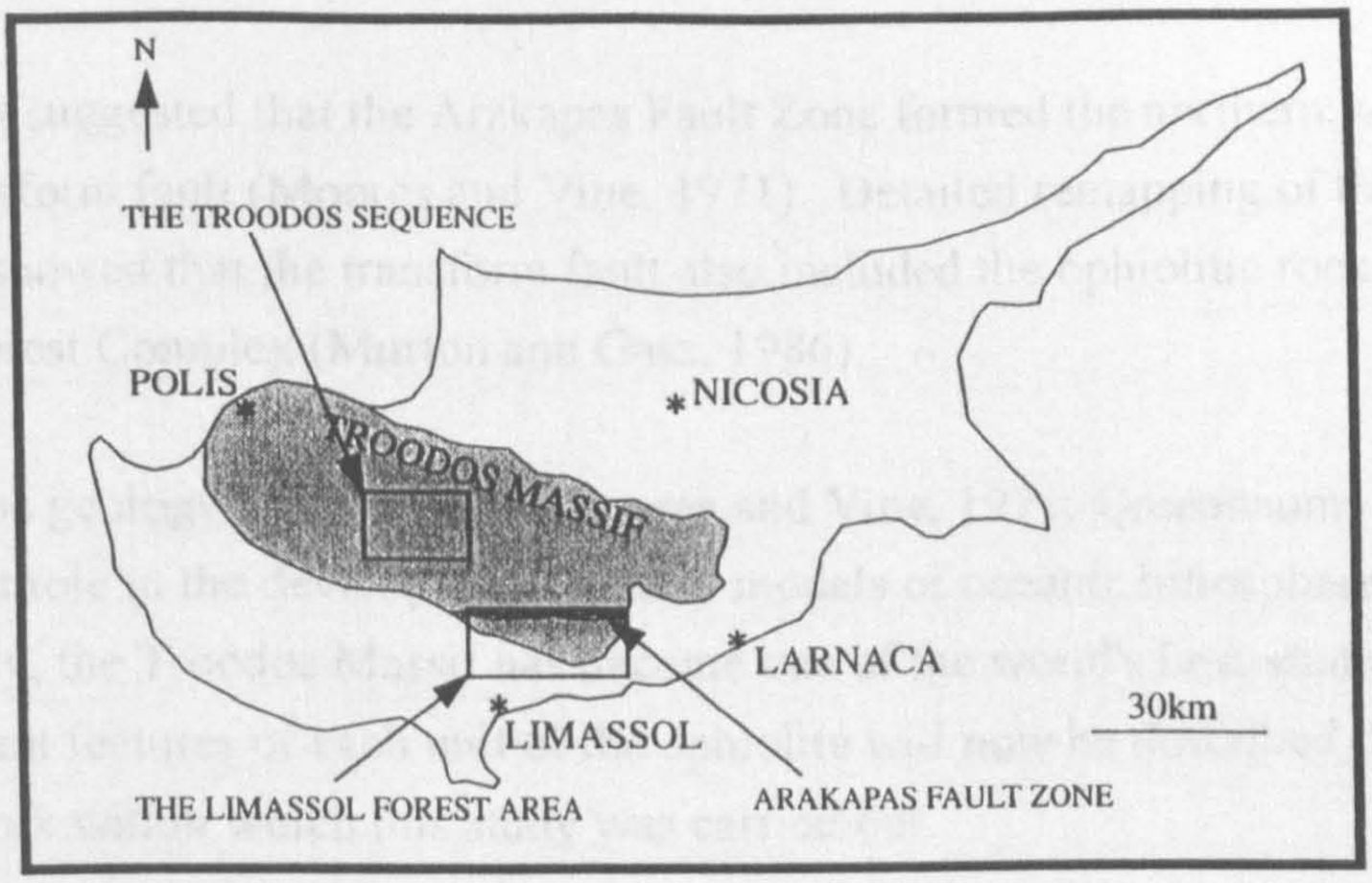

B

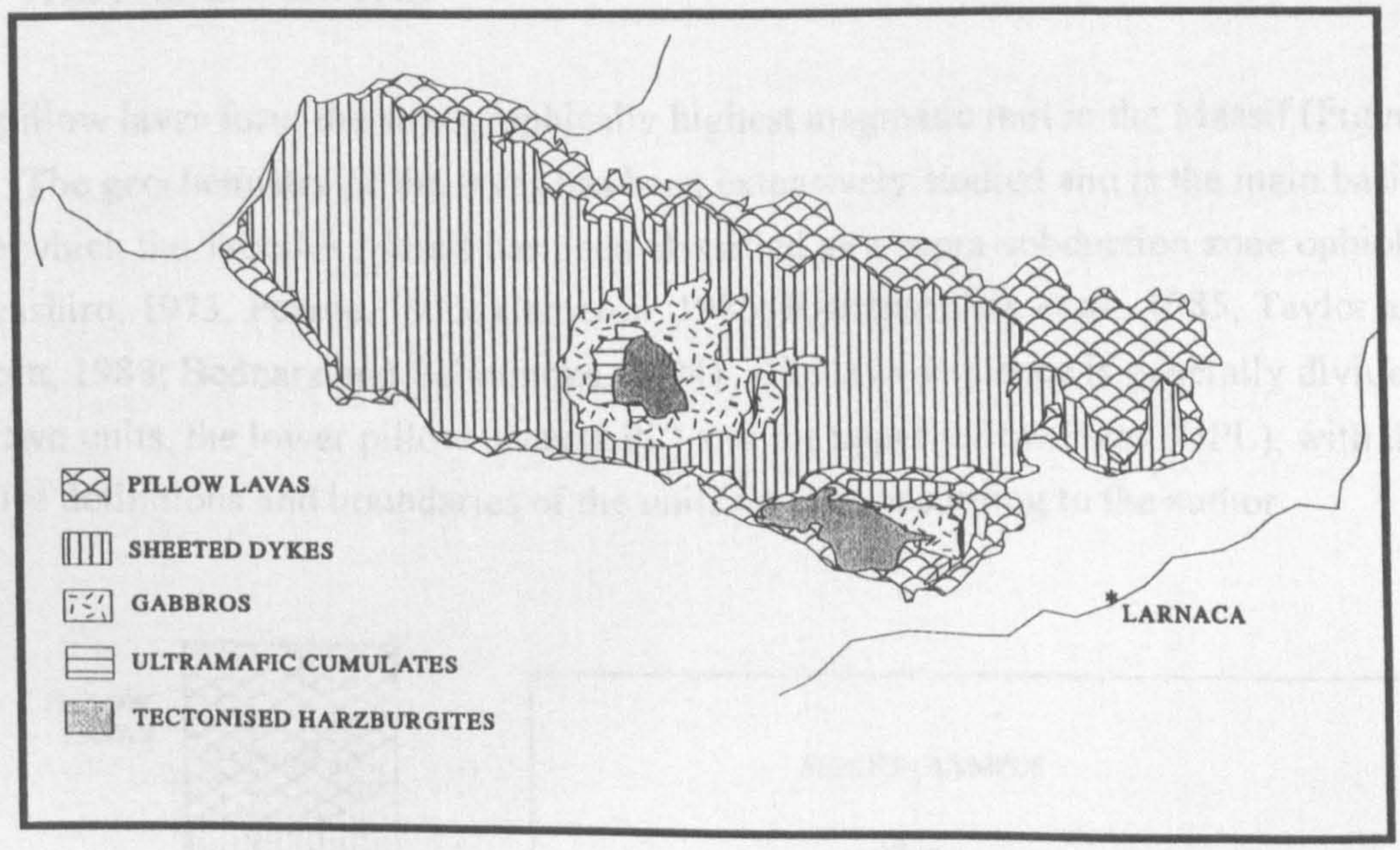

C

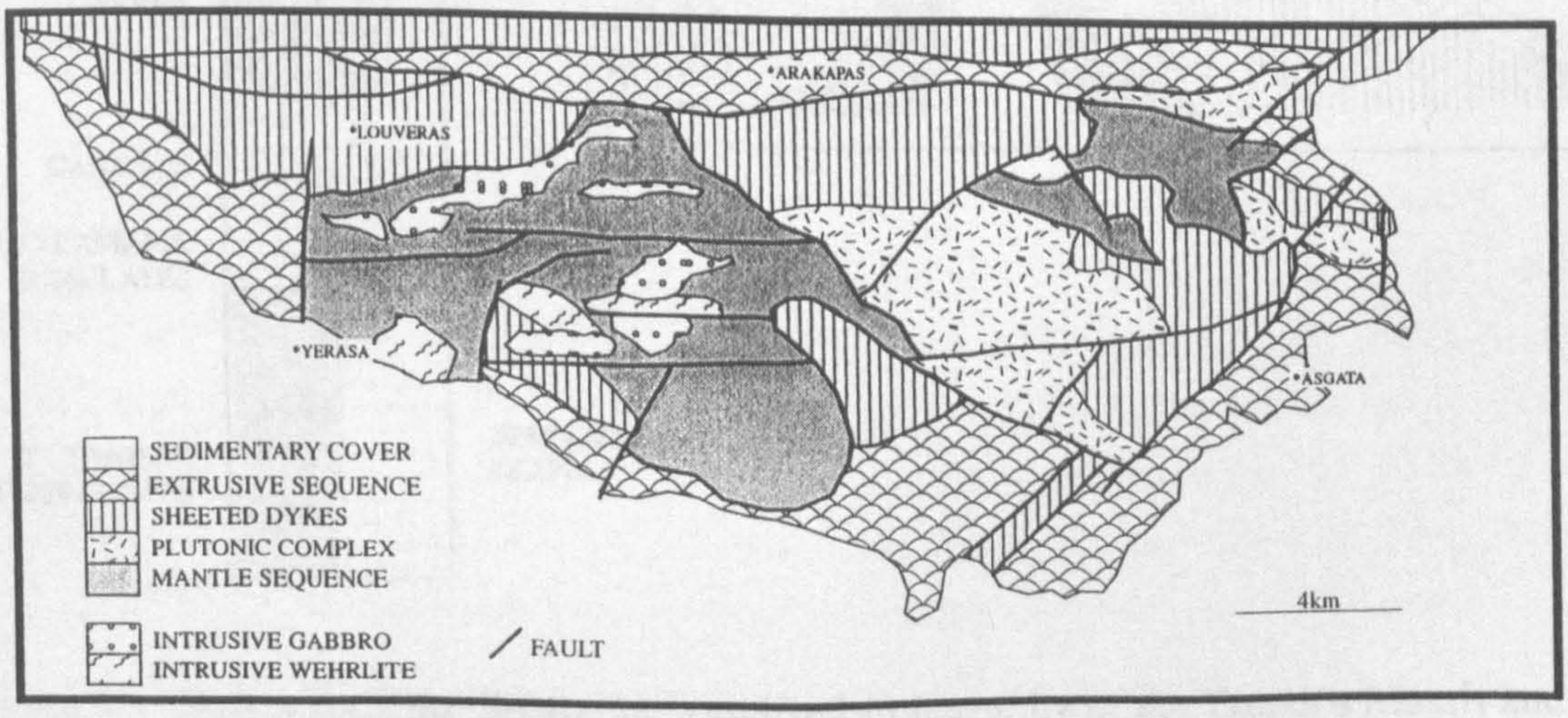

Figure 1.3. A. Location of the Troodos Massif, the Troodos sequence and the Limassol Forest area; B. The outcrop pattern in the Troodos Massif (Malpas *et al.* 1990 and references therein); C. Geological map of the Limassol Forest (Murton 1986).

Early studies suggested that the Arakapas Fault Zone formed the northern wall of an oceanic transform fault (Moores and Vine, 1971). Detailed remapping of the Limassol Forest area showed that the transform fault also included the ophiolitic rocks of the Limassol Forest Complex (Murton and Gass, 1986).

Studies of the geology of the Massif (Moores and Vine, 1971; Greenbaum, 1972) played an important role in the development of early models of oceanic lithosphere formation. Subsequently, the Troodos Massif has become one of the world's best-studied ophiolites and the salient features of each unit of the ophiolite will now be described, in order to set the framework within which this study was carried out.

1.3.1 THE PILLOW LAVAS

The pillow lavas form the stratigraphically highest magmatic unit in the Massif (Figure 1.4). The geochemistry of the lavas has been extensively studied and is the main basis upon which the Troodos Massif has been classified as a supra-subduction zone ophiolite (Miyashiro, 1973; Pearce, 1975; Cameron, 1985; Rautenschlein *et al.*, 1985; Taylor and Nesbitt, 1988; Bednarz and Schmincke, 1994). The lava sequence is generally divided into two units, the lower pillow lavas (LPL) and the upper pillow lavas (UPL), with the precise definitions and boundaries of the units varying according to the author.

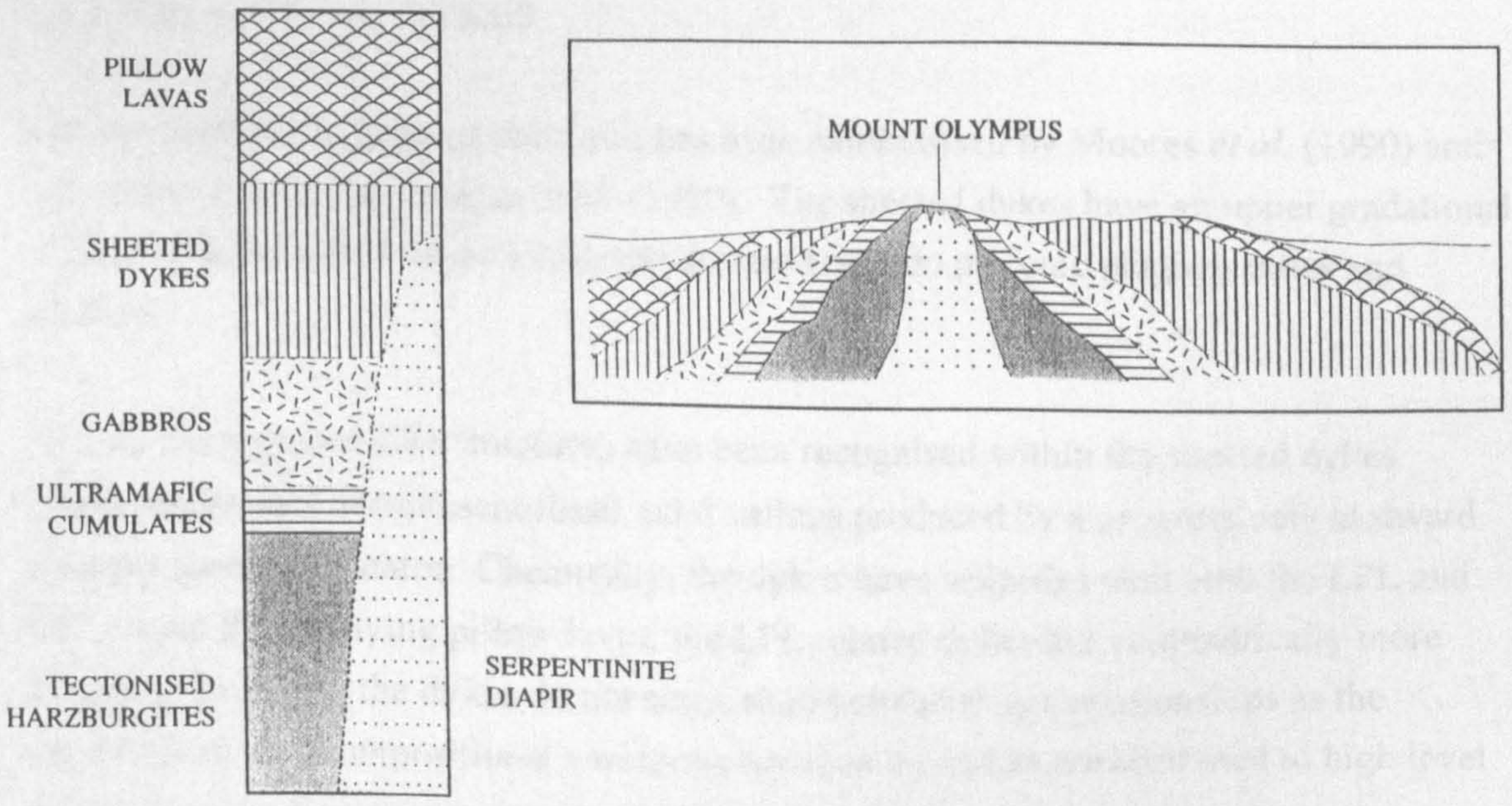

Figure 1.4 Sketch sections illustrating a stylised stratigraphy of the Troodos Massif and a vertically exaggerated section drawn N-S through the Massif (redrawn from Malpas *et al.* 1990 and references therein).

The LPL are in transitional contact with the underlying sheeted dykes and are a low-Ti series of basaltic andesites, which are separated from the overlying UPL unit by a metamorphic discontinuity. They are generally thought to be an island arc suite, erupted at a minor spreading axis in a marginal sea above a subduction zone (Gass, 1980).

The UPL are significantly less altered than the LPL and are, in general, a thinner sequence of lavas. The UPL are generally divided into 3 groups on the basis of their trace element chemistry (e.g. Kostopoulos and Murton, 1992). Group I has island-arc tholeiite characteristics and outcrops mostly in the north of the Massif. Group II is transitional in nature between island-arc tholeiites and boninite series volcanics, and outcrops mostly in the south and west. Group III lavas have the trace element characteristics of boninite series volcanics and outcrop mainly in the south. Although there is a general younging from groups I to III, the group II and III lavas are often interbedded.

Most authors describe a pattern of increasing LREE and LILE enrichment upwards through the UPL sequence (e.g. Cameron, 1985), and attribute the variations in the lava geochemistry to three main sources: a variable depleted mantle, a LILE-rich subduction-related fluid and a HFSE-rich silicate melt. Some authors (Bednarz and Schminke, 1994) have also suggested that the lower crust may melt and form a source component for the older lavas.

1.3.2 THE SHEETED DYKES

The structure of the sheeted dyke unit has been summarised by Moores *et al.* (1990) and their geochemistry by Baragar *et al.* (1990). The sheeted dykes have an upper gradational contact with the pillow lavas and grade downwards into plutonic plagiogranites and gabbros.

At least three graben-like structures have been recognised within the sheeted dykes. These are thought to represent fossil axial valleys produced by a progressively eastward jumping spreading centre. Chemically, the dykes have affinities with both the LPL and UPL. Like the overlying pillow lavas, the LPL related dykes are volumetrically more abundant, however, the dykes do not show such consistent age relationships as the overlying lavas. Compositional variations between the dykes are attributed to high level crystal fractionation processes in both open and closed systems.

1.3.3 THE PLUTONIC SERIES

The sheeted dykes grade downwards into a sequence of fine-grained gabbroic, tonalitic and trondhjemitic intrusives which, in turn, overlie ultramafic cumulates. The cumulates display phase layering and a mineral lamination produced by crystal settling. Early models for the formation of the cumulate sequence proposed a single, steady state magma chamber (Greenbaum, 1972), although a multiple magma chamber model, with magma bodies waxing and waning over time, is now more widely accepted (Gass, 1980).

The mineral chemistry of the cumulate sequence is fairly well known, both from field studies and from the borehole CY-4 drilled by the Cyprus Crustal Study Project (Malpas *et al.*, 1990, and references therein). These studies propose that the cumulate sequence can be divided into an early suite of deformed cumulates which were subsequently intruded by a suite of later plutons. In the CY-4 core, the earlier cumulate sequence consists of a high-Ti gabbroic and gabbro-norite series which is intruded by a lower-Ti series of gabbro-norites and websterites. It is possible that these two series are the plutonic equivalent of the UPL and LPL. However, field evidence suggests that both magma series were present at the same time (Malpas, 1990).

Parental magmas of the plutonic series have been calculated from mineral chemistry data by Hébert and Laurent (1990), who suggest that they would have had Mg# of approximately 75 and high Al_2O_3/TiO_2 and CaO/TiO_2 ratios. Furthermore, the appearance of calcic plagioclase and amphibole in the crystallisation series suggests that high water pressures prevailed during crystallisation. These characteristics are consistent with the plutonic series having affinities with arc-type sequences, which agrees with the geochemical evidence from the pillow lava series.

1.3.4 THE MANTLE SEQUENCE

A harzburgitic mantle section forms the base on to which the overlying cumulates were precipitated. Tectonised harzburgites form approximately 90% of the total outcrop within the mantle sequence, and enclose dunite, chromitite and pyroxenitic bodies which become more abundant as the contact with the overlying cumulates is approached. A foliation in the harzburgites is defined by the alignment of orthopyroxene and spinel crystals, and is enhanced by segregation of olivine and pyroxene into centimetre wide bands. It is generally accepted that the harzburgites represent depleted mantle, from which basaltic or picritic melts have been extracted to form the overlying crustal sequence (Gass, 1980).

Two separate mantle sections are exposed in the Troodos Massif. The first is located in the centre of the massif in the area surrounding Mount Olympus (Figure 1.3). This outcrop exposes a stratigraphically intact section of mantle from its uppermost contact with crustal dunites to a depth of approximately 3 km, where it is faulted against heavily fractured and serpentinised peridotites termed the serpentinite diapir by Wilson (1959). This mantle section has been examined in detail and the study area is illustrated in Figure 1.5. This mantle section is referred to as the 'Troodos sequence' in this thesis. The second mantle outcrop is located in the Limassol Forest Complex to the south of the Arakapas Fault Zone (Figure 1.3c). This mantle sequence has been heavily disrupted by east-west trending shear zones and the original stratigraphy of the mantle tectonites is almost impossible to determine. Study of this mantle section is further compounded by complete serpentinisation which obscures textural and lithological variations within the peridotites.

1.4 THESIS DEFINITIONS

This thesis is primarily concerned with the geochemical evolution of the Troodos sequence harzburgites. To facilitate description of the harzburgites they have been sub-divided into several groups, based on both outcrop and mineral chemistry criteria. The initial sub-divisions of the Troodos harzburgites were made on the basis of outcrop characterisitics. Some of these harzburgite types were then further sub-divided on the basis of mineral chemistry data. This section gives an overview of the sub-divisions used in this thesis.

Harzburgites which were collected > 5 m away from dunites, veins or minor intrusions are termed *background* harzburgites. These samples are intended to represent the geochemical background of the Troodos mantle section, on to which geochemical variations produced by the injection of minor intrusions may have been superimposed. Any *background* harzburgites which outcrop within 500 m (measured vertically through the sequence) of the crustal dunite-harzburgite contact (see Fieldwork Chapter) are described as '*top-of-the-sequence*' harzburgites.

The *background* harzburgites have been further sub-divided on the basis of $Cr\#_{spn}$ data. The variations in *background* harzburgite $Cr\#_{spn}$ data are illustrated as a map contoured in 10 $Cr\#_{spn}$ units in Figure 1.6, this data is described and discussed in more detail in Chapter 4. The $Cr\#_{spn}$ data defines large domains, orientated parallel to the harzburgite-dunite contact, in which $Cr\#_{spn}$ decreases with increasing depth in the mantle sequence. Notable exceptions to this trend are found in the south-west of the study area (around 8650,6525), where unusually low $Cr\#_{spn}$ values occur in a section of harzburgite

enclosed by a tongue of dunite at the top of the mantle section, and in the centre of the study area (around 8875,6650) where a layer of low $Cr\#_{spn}$ is perched in an area of higher $Cr\#_{spn}$. The *background* harzburgites outcropping in these areas are termed the *Anomaly 1* and *Anomaly 2* harzburgites respectively in this thesis (see Figure 1.6).

On the basis of outcrop characteristics two other harzburgite types have been defined. Firstly, harzburgite samples which were collected from between the orthopyroxene banding mentioned above (section 1.3.4) are treated as an individual group and termed 'banded harzburgites'. The pyroxene banding is described in detail in the Fieldwork Chapter. Secondly, samples from xenolithic harzburgite fragments outcropping in the base of the crustal dunites (see Fieldwork Chapter) are plotted as a separate group and labelled harzburgite *xenoliths*.

Dunites exposed in the Troodos mantle section can be divided into two groups on the basis of their stratigraphic position with respect to the harzburgites. Firstly, crustal dunites are defined as those which stratigraphically overlie the harzburgites. The contact between the two lithologies is a sharp, mappable boundary as shown in Figure 1.5. The base of the crustal dunites is characterised by the presence of a spinel foliation which is oriented parallel to the pyroxene foliation in the underlying harzburgites. This foliation decreases in strength vertically upwards through the crustal dunites.

The second group of dunites form minor intrusions within the harzburgite sequence and are termed the mantle dunites. These dunites have been sub-divided on the basis of their structural attitude with respect to the harzburgite foliation into the following groups:

(i) dunites which form bodies parallel to the foliation;
(ii) dunites which form the wallrocks to chromitite bodies;
(iii) dunites associated with orthopyroxenites;
(iv) dunites which cross-cut the harzburgite foliation;
(v) dunites with interdigitating contacts against the harzburgites.

A more detailed description of the mantle dunites is given in the Fieldwork Chapter.

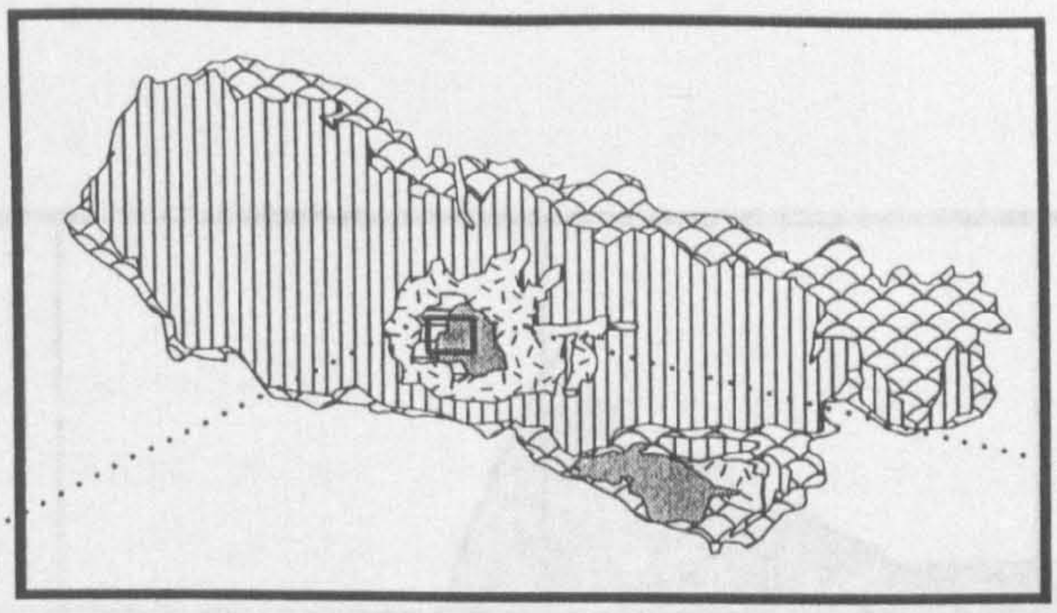

Figure 1.5 The location of the study area in the Troodos Massif.

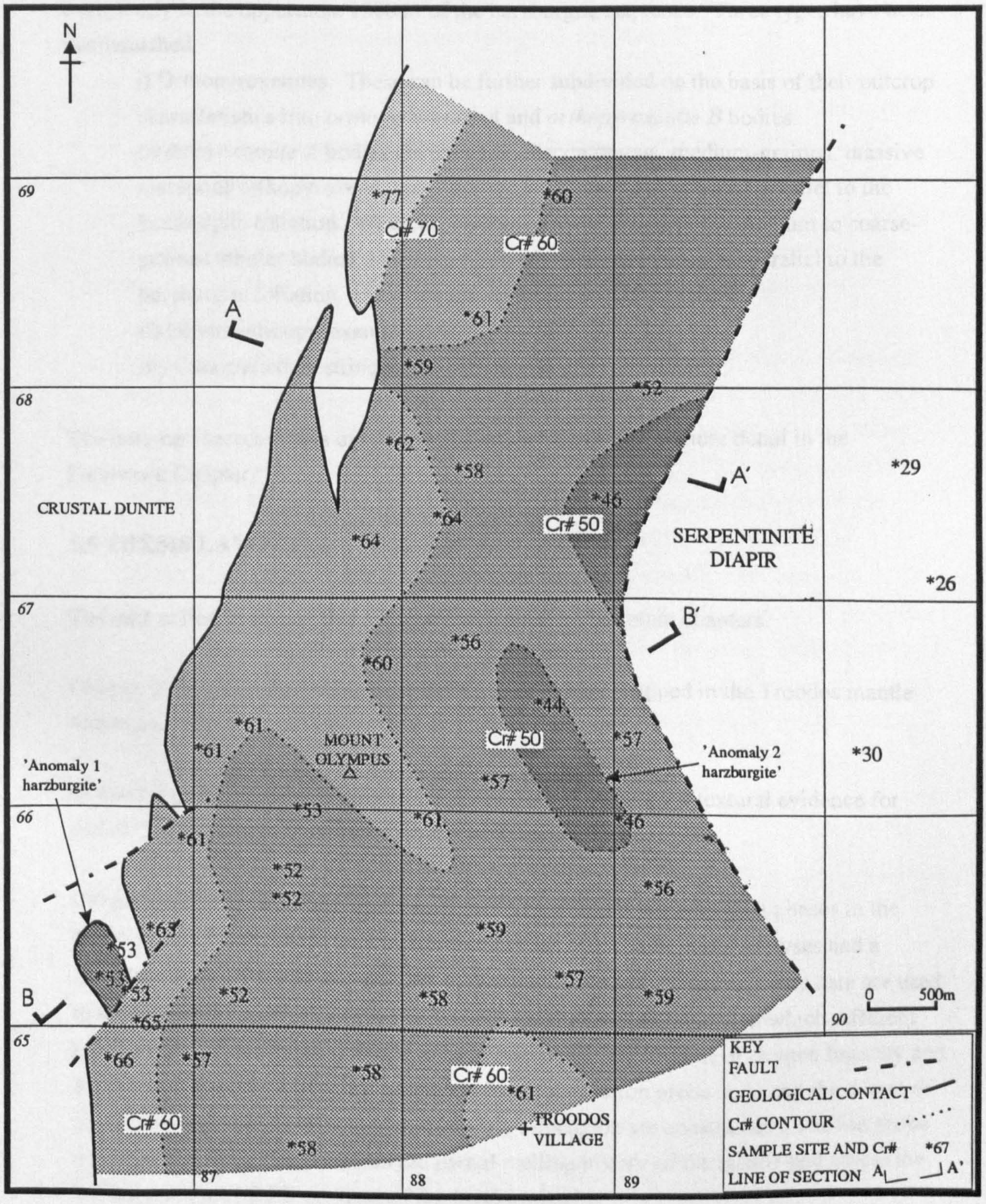

Figure 1.6 A map illustrating the variation of $Cr\#_{spn}$ in the *background* harzburgites with the locations of the *Anomaly 1* and *2* harzburgites labelled.

The harzburgites also enclose a variety of pyroxenitic pods and veins which are found exclusively in the uppermost 1500 m of the harzburgite sequence. Three types have been distinguished.

i) Orthopyroxenites. These can be further subdivided on the basis of their outcrop characteristics into *orthopyroxenite A* and *orthopyroxenite B* bodies. *Orthopyroxenite A* bodies are irregular, discontinuous, medium-grained, massive masses of orthopyroxene, usually 5 to 15 cm thick and oriented parallel to the harzburgite foliation. Whereas, *orthopyroxenite B* bodies are medium to coarse-grained tabular bodies, 1 to 2 cm thick which are also oriented parallel to the harzburgite foliation.

ii) Olivine-clinopyroxenite veins.

iii) Clinopyroxene stringers.

The outcrop characteristics of these intrusions are described in more detail in the Fieldwork Chapter.

1.5 THESIS LAYOUT

The data collected during this study are presented in four main chapters.

Chapter 2 describes the lithological variations that were mapped in the Troodos mantle sequence.

Chapter 3 describes the microstructure of the peridotites and the textural evidence for partial melting and melt-mantle interaction is documented.

Chapter 4 presents the mineral chemistry data for the four main mineral phases in the Troodos peridotites, based on a comprehensive set of electron probe analyses and a smaller number of ion probe analyses of clinopyroxene. The electron probe data are used to sub-divide the harzburgites in the Troodos sequence into domains in which different geochemical processes are thought to have operated. Calculations of oxygen fugacity and equilibrium melt chemistry are also made from the electron probe data, and the extent of partial melting and the effects of melt-mantle interaction are constrained. The ion probe data are used to further constrain the partial melting history of the mantle and assess the variations in the LREE contents of the harzburgites.

During this project an attempt was made to obtain trace element data from spinels by secondary ion mass spectrometry. Unfortunately, several analytical problems remained outstanding at the time of writing which meant that the data were not of sufficient quality

to be used in petrogenetic discussions. Therefore, the data collected, a description of the analytical technique, and a discussion of the analytical problems still to be resolved, have been presented separately from the main data set in Appendix B.

Chapter 5 presents the whole-rock geochemistry of the Troodos peridotites. The data are used to examine the chemical effects of serpentinisation. In the case of the Limassol Forest peridotites the serpentinisation process is shown to be non-isochemical. This evidence is then used to asses which elements were the least mobile during the alteration process in the Troodos sequence harzburgites. These elements are then used to further constrain the partial melting and melt interaction history of the mantle sequence.

Chapter 6 draws together the evidence from each of the previous chapters and discusses the conclusions of the thesis. The data from the Troodos Massif are used to assess several of the recent models for melt evolution in the mantle, including the Navon and Stolper (1987) chromatographic column model and the Keleman *et al.* (1992) model of mantle-melt interaction. The geochemistry of the mantle sequence, its relationship with the overlying crustal sequence and the implications for the geodynamic setting of the Troodos Massif are discussed. Finally, a model for the geochemical development of the Troodos mantle section is presented. In order to familiarise the reader with the processes involved and to set an overall framework for the thesis a flow diagram which is presented as the conclusion to Chapter 6 is reproduced here as Figure 1.7. The diagram summaries a possible geochemical evolution of the Troodos mantle sequence based on the results of this thesis.

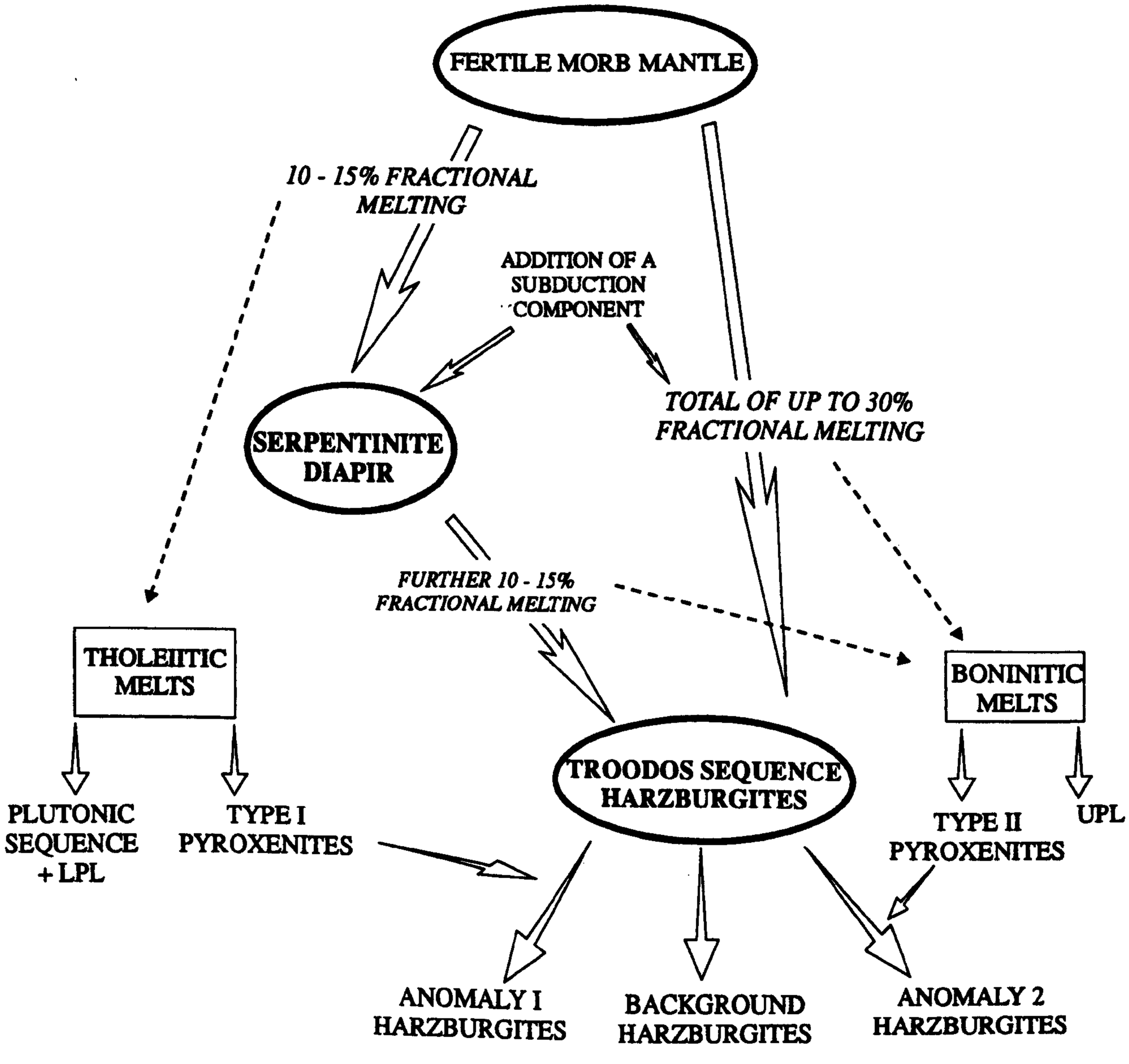

Figure 1.7 Flow diagram summarising a possible evolution of the Troodos Massif mantle section.

CHAPTER 2
FIELD RELATIONS

2.1 INTRODUCTION

This chapter describes the mantle lithologies exposed in the Troodos Massif, Cyprus. The intact Troodos sequence is described in most detail, with emphasis placed on the ultramafic pods and dykes which are enclosed by the harzburgite tectonites. The study area is located around Mount Olympus, the highest point on the island, and is illustrated in Figure 2.1. Exposure is generally very good, with the deeply incised northeast-southwest trending stream sections in the southwest of the study area providing particularly good exposure.

As described in the previous chapter, the Troodos sequence exposes a section of mantle from its uppermost contact with crustal dunites to a depth of approximately 3 km, where it is faulted against heavily fractured and serpentinised peridotites termed the serpentinite diapir by Wilson (1959). The sample localities of the peridotites studied in this thesis are illustrated in Figure 2.2.

The second mantle exposure, located in the Limassol Forest Complex, has not been studied in the same detail as the Troodos sequence because intense deformation associated with east-west trending shear zones, and complete serpentinisation, obscures textural and lithological variations within the peridotites. Exposure in the Limassol Forest is much worse than in the Troodos sequence, which further compounds the problems posed by the tectonic disruption of the sequence.

2.1.1 PREVIOUS WORK

The first comprehensive description of the Troodos Massif was published by the Cyprus Geological Survey (Wilson, 1959) and included a compilation of geological maps of the central part of the Massif. The main lithological divisions and a downwards increase in basicity were recognised. Of particular relevance to this study, was the identification of olivine-pyroxene banding in the harzburgites (termed enstatite-olivinite by Wilson, 1959), in which a foliation is defined by the alignment of pyroxene and spinel crystals. Wilson (1959) suggested that the banding formed by selective removal of enstatite by SiO_2 undersaturated vapours, which eventually produced dunitic lithologies. The Massif was interpreted as a layered complex, similar to the Skaergaard complex, in which the

harzburgites, layered peridotites and gabbros formed a differentiated series that had subsequently been intruded by the dunite. The pillow lavas and sheeted dykes were taken as evidence for the complex being intruded in a submarine, tensional environment.

A link between the stratigraphy of the Troodos Massif and oceanic lithosphere was made by Moores and Vine (1971), Greenbaum (1972) and Gass and Smewing (1973). In this model, the harzburgite was interpreted as a residuum from which the melt that crystallised the overlying crustal sequence had been extracted. These papers provide little extra field data from the mantle lithologies. Menzies and Allen (1974) described the mantle section in some detail and noted the presence of orthopyroxenite veins, which were interpreted as the products of the last dregs of melt to be extracted from the mantle.

The structure of the mantle sequence was studied by George (1978), who recognised that the deformation affecting the harzburgites extended into the dunites at the base of the cumulate sequence. A second pyroxene foliation was also identified in a few outcrops and attributed to a mild, late-stage deformation event. The co-existence of two spinel fabrics was stressed by Bartholomew (1993), who found that the fabrics were much more widely distributed than the second pyroxene fabric identified by George (1978). Bartholomew (1993) envisaged the two fabrics being formed contemporaneously, as the result of interaction between adjacent diapiric uprise centres. Bartholomew (1993) also remapped the dunite-harzburgite contact as a much simpler, planar contact than previous authors had proposed.

In general, the Limassol Forest Complex has received much less attention than the Troodos sequence. Moores and Vine (1971) interpreted the Arakapas Fault Belt as a possible transform fault. However, it was not until the area was the subject of postgraduate studies at the Open University in the 1980s that the structure and petrology of the Limassol Forest Complex were elucidated in detail (Murton and Gass, 1986; Murton, 1986; MacLeod, 1990). Other than the presence of numerous east-west shear zones, the main difference between the two mantle exposures is the presence of late, transform-related wehrlite and gabbro bodies which intrude the mantle peridotites. Petrographically, the mantle peridotites are similar to those exposed in the Troodos sequence and have been interpreted (Murton, 1986) as having a similar upper mantle origin.

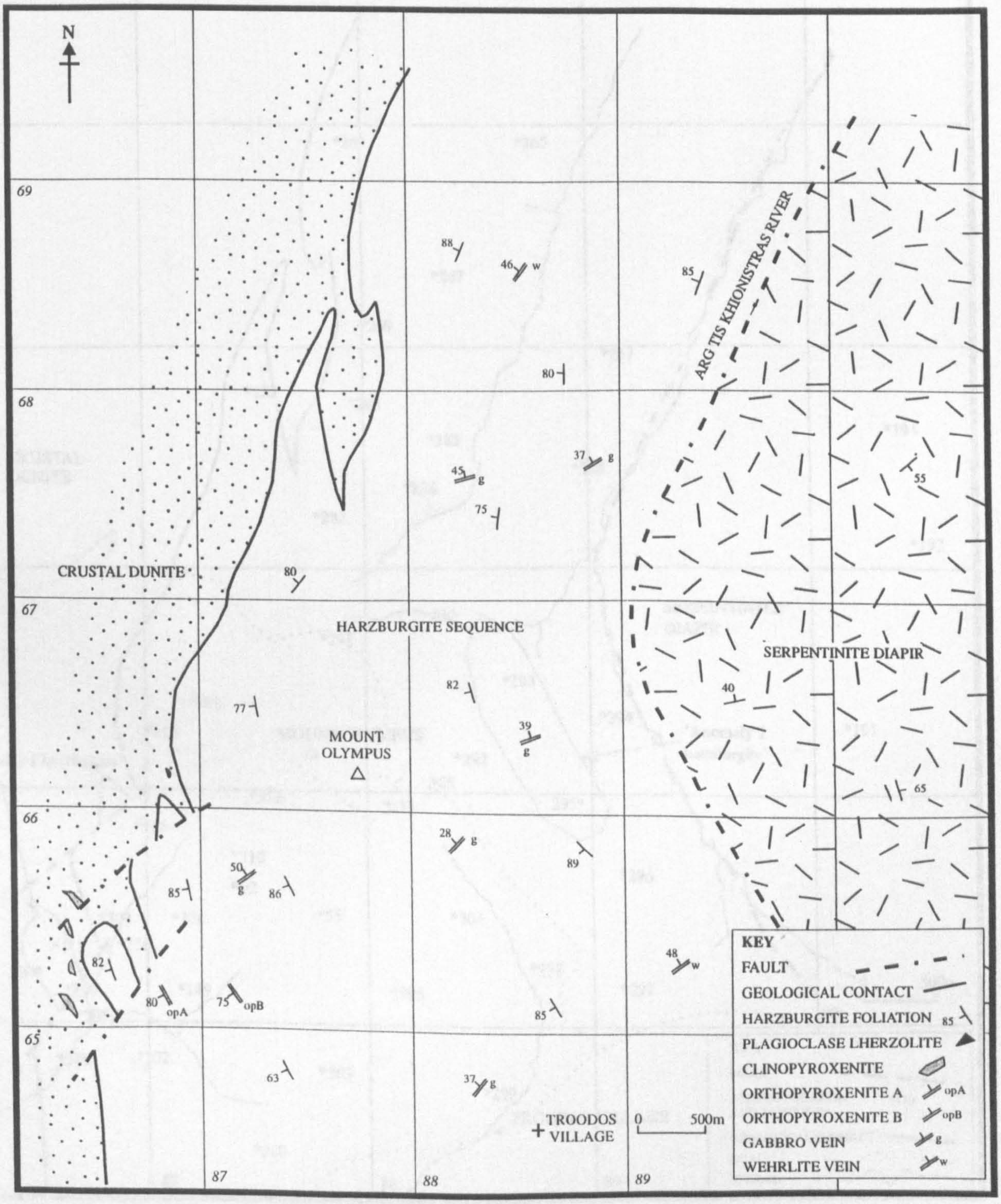

Figure 2.1 The study area with the attitude of the harzburgite foliation and minor intrusion.

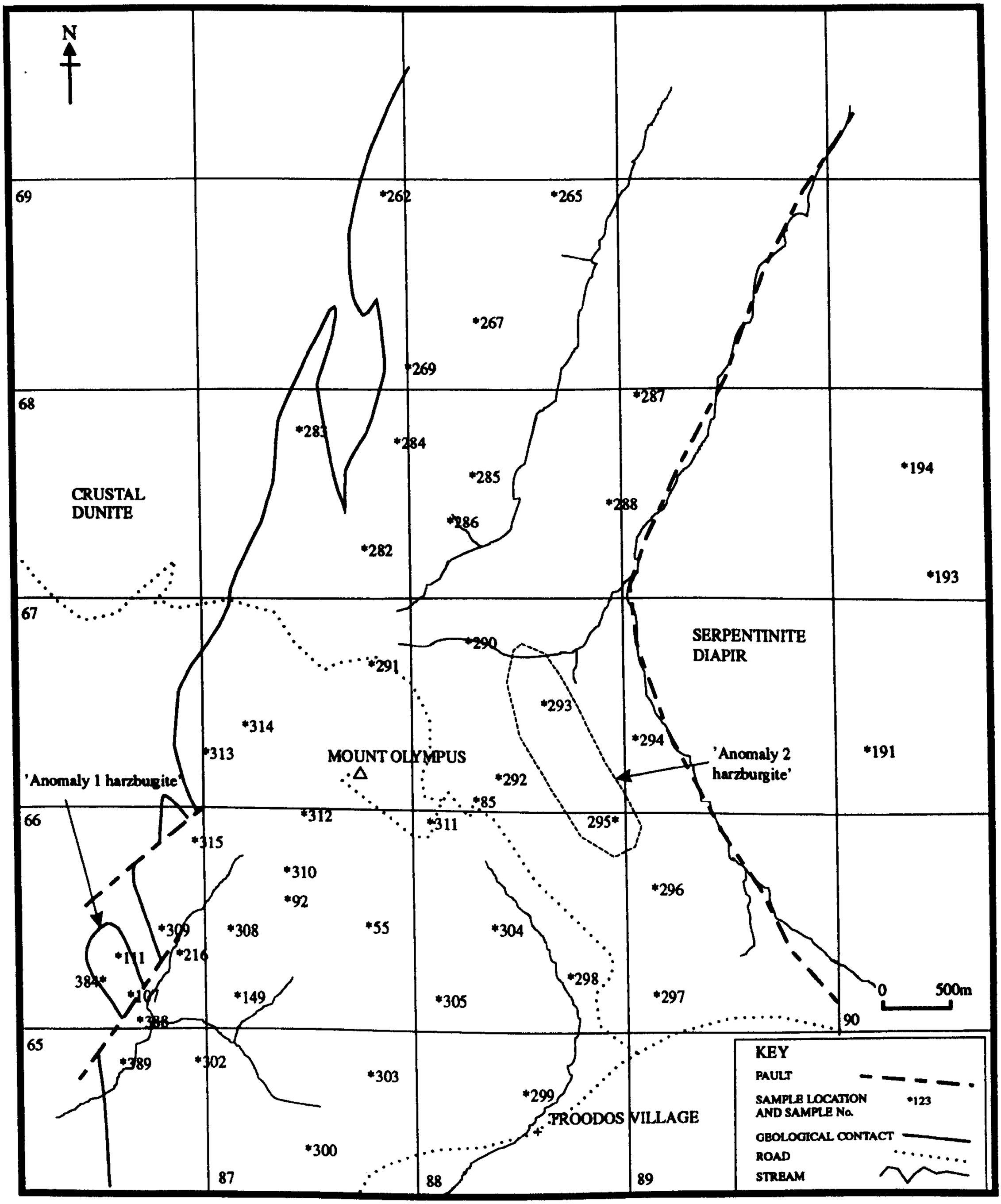

Figure 2.2A *Background* harzburgite sample locations.

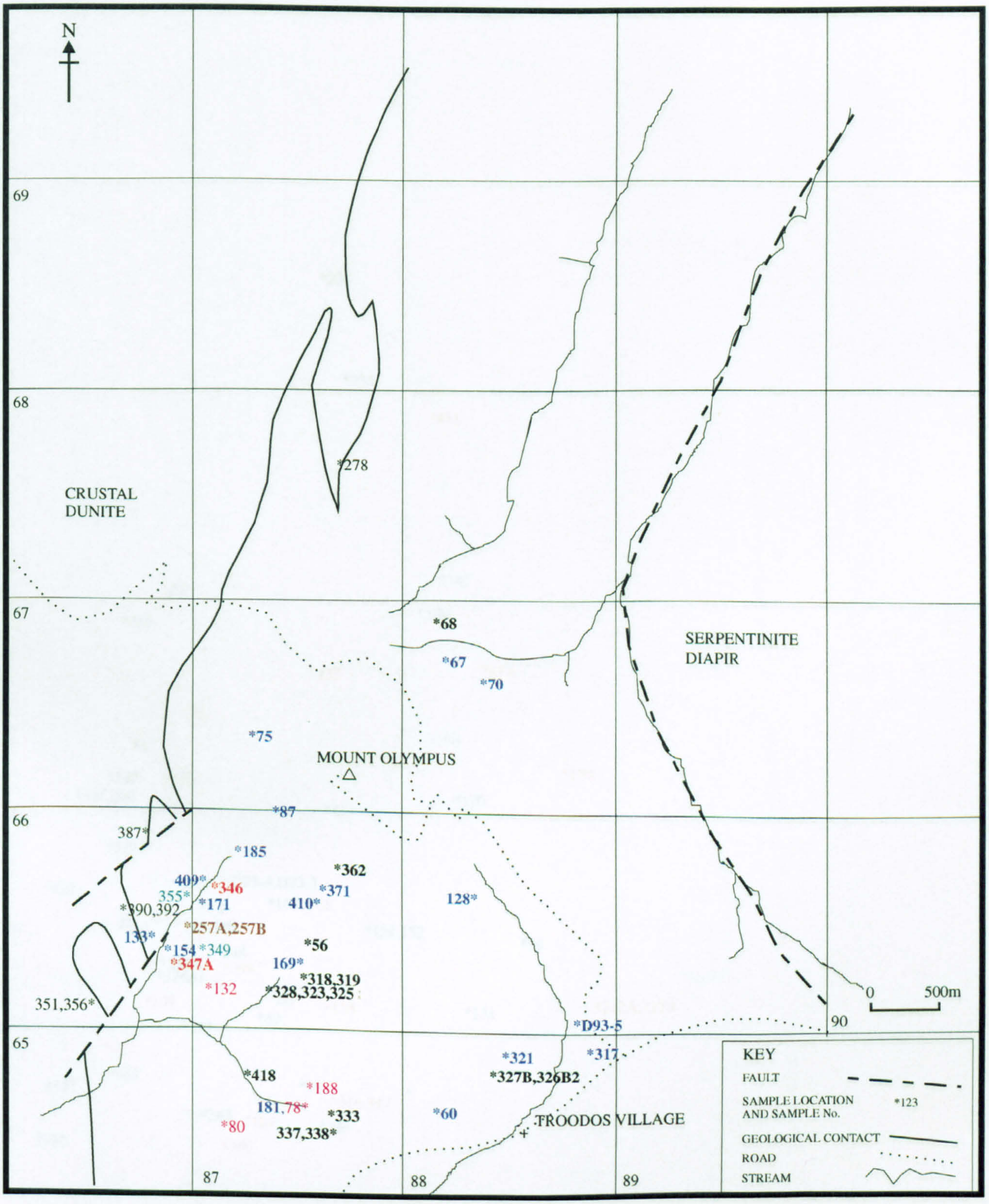

Figure 2.2B Harzburgite sample locations, key to sample types as follows:

*123 = Harzburgite xenoliths

***123 = Wallrock A harzburgites**

***123 = Wallrock B harzburgites**

***123 = Banded harzburgites**

***123 = Harzburgites adjacent to dunites**

*123 = Harzburgites adjacent to chromite occurences

*123 = Harzburgites with interdigitating contacts against dunites

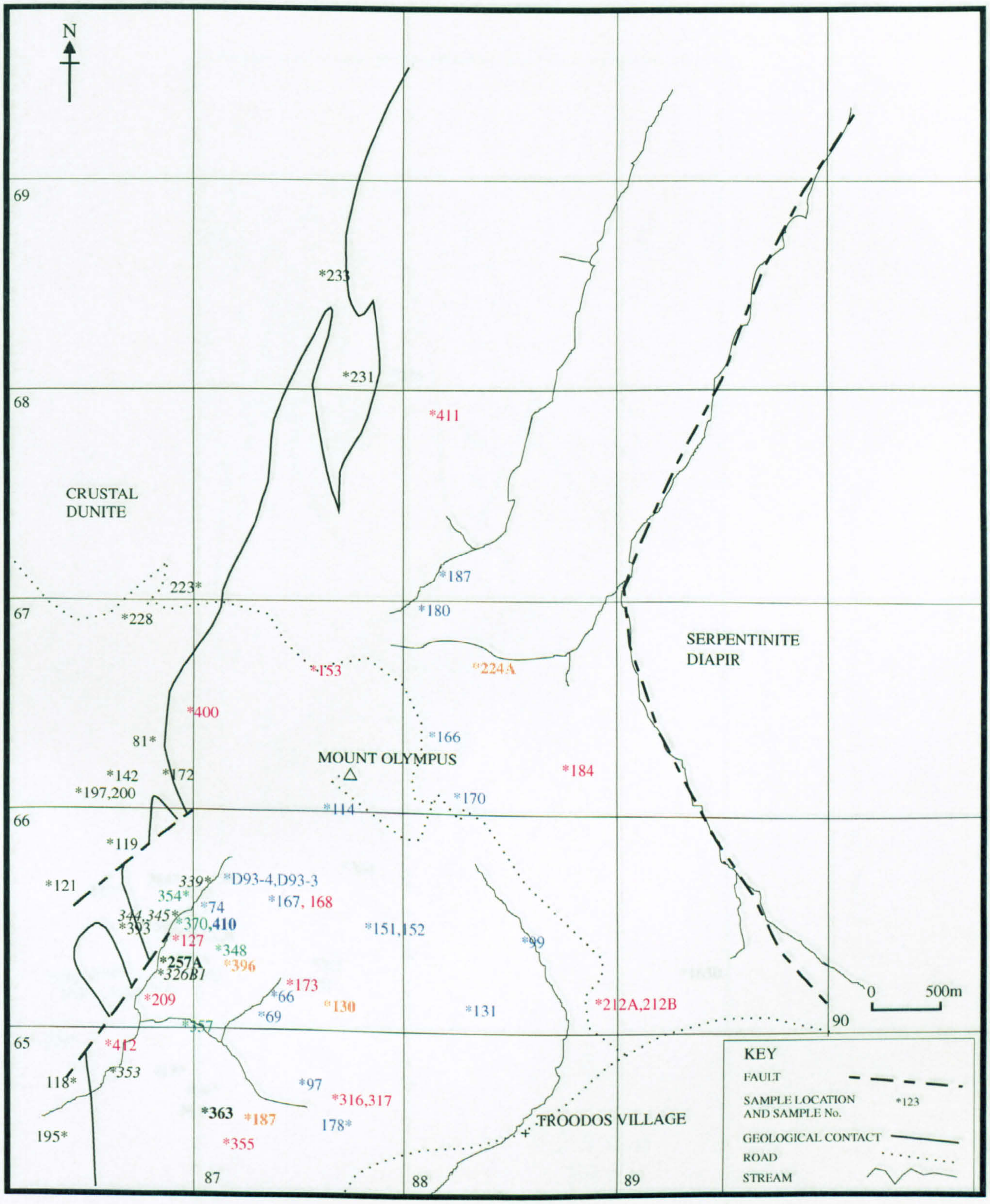

Figure 2.2C Dunite sample locations; key to sample types as follows:

*123 = Crustal dunite

*123 = Interdigitating dunites

***123 = Wallrock to Orthopyroxenite A**

***123 = Dunite folded about foliation**

*123 = Dunite parallel to the foliation

*123 = Dunite cross-cutting the foliation

**123 = Wallrock to Orthopyroxenite B*

*123 = Dunite wallrocks in chromitite occurences

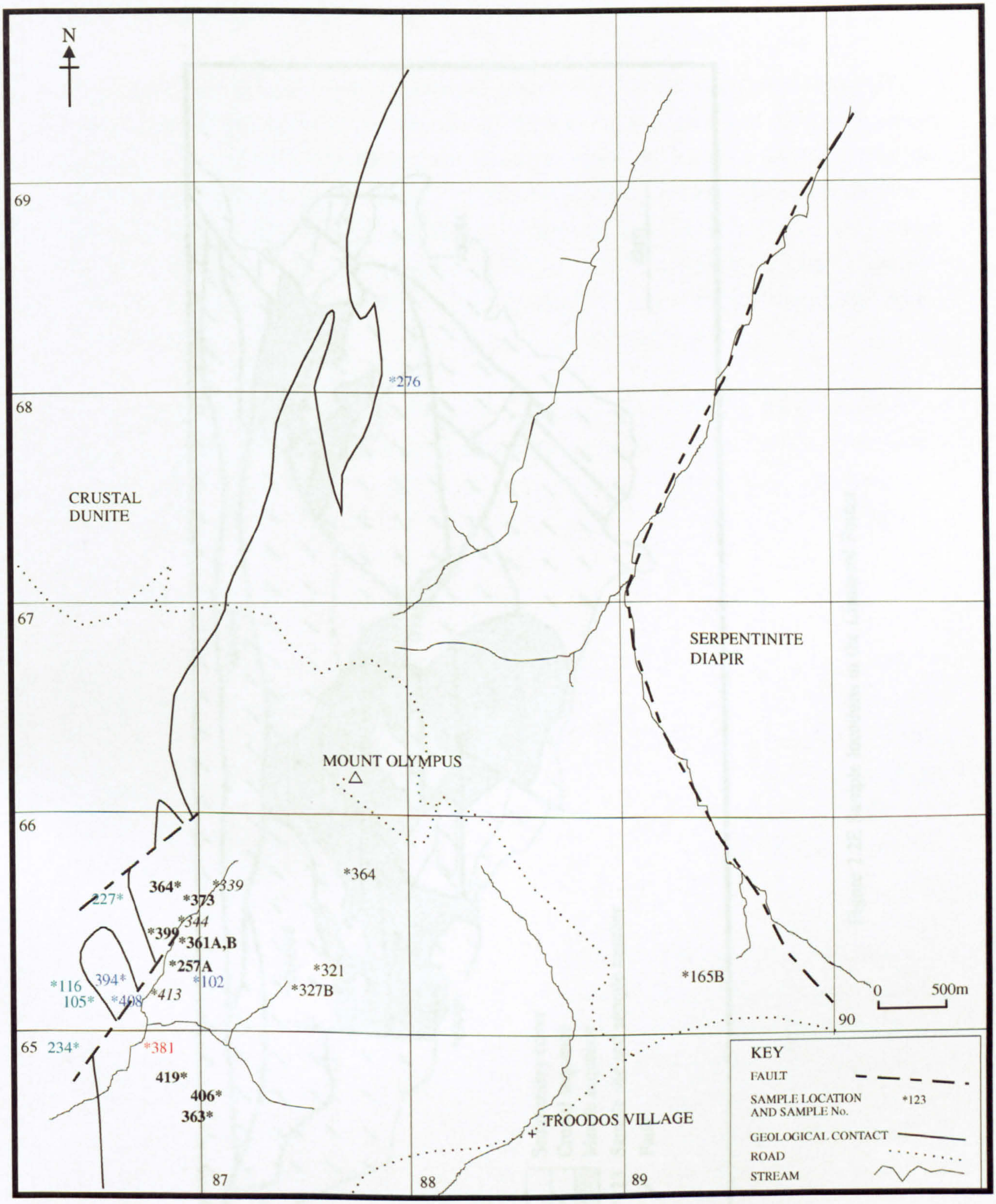

Figure 2.2D Pyroxenite sample locations; key to sample types as follows:

*123 = Harzburgite band

***123 = Orthopyroxenite A**

**123 = Orthopyroxenite B*

*123 = Olivine-clinopyroxenite

*123 = Clinopyroxenite in crustal dunite

*123 = Clinopyroxenite stringer

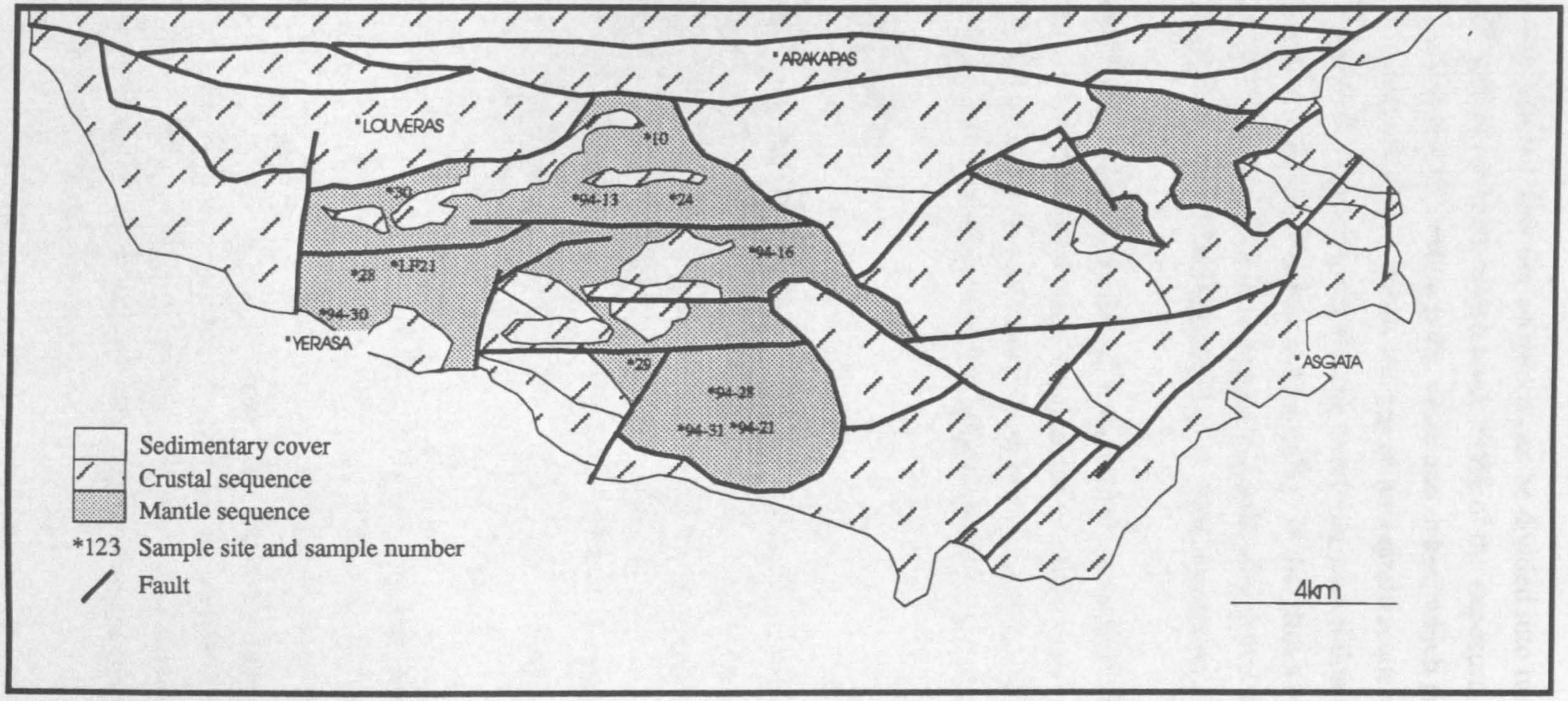

Figure 2.2E Sample locations in the Limassol Forest.

2.2 THE TROODOS SEQUENCE

The mantle section of the Troodos sequence can be divided into two components; (i) pervasively foliated peridotites, which form >95% of the exposure, and (ii) a wide variety of ultramafic, mafic and chromitite pods, veins and dykes, which are enclosed within the peridotites. For purpose of this thesis, the top of the mantle sequence has been taken as the contact between the harzburgites and the overlying crustal dunites (Figure 2.1), which has been mapped in detail by Bartholomew (1993). In this thesis the term crustal dunite is applied to all the dunite which outcrops stratigraphically above the harzburgites. The harzburgite-crustal dunite contact is described in detail in section 2.2.6.

Accurate topographic maps of the Troodos area are not available. For the purposes of this study, outcrops were located using a combination of the original 1:6360 field sheets of the Cyprus Survey and aerial photographs lent by the Cyprus Survey. Detailed lithogical observations were then made on large scale sketches of individual outcrops.

2.2.1 HARZBURGITES

Tectonised harzburgites form the bulk of the mantle sequence (>90%) and are easily recognised in outcrop by their rough, orange-brown weathering surfaces. Fresh surfaces are green-black in colour, with a granular texture. The harzburgites are generally medium to coarse-grained, except in the uppermost 50 m of the section where they become finer-grained. Modal compositions show considerable variation due to the heterogeneous distribution of orthopyroxene, and lie in the range of approximately 75-80% olivine, 10-25% orthopyroxene, < 3% spinel and < 3% clinopyroxene.

A pervasive foliation in the harzburgites is defined by the alignment of orthopyroxene and spinel crystals. The foliation dips steeply westwards throughout the mapped area and varies in strike from NW-SE to NE-SW, as shown in Figure 2.1. Bartholomew (1993) recorded a second spinel fabric oblique to the main orthopyroxene-spinel foliation, but this was not observed during this study. However, a second pyroxene foliation was observed, which consistently cuts the primary foliation at an acute angle (Plate 2.1a), and is found throughout the harzburgite sequence. Whether this fabric is the same as that identified by George (1978) is not clear.

Plate 2.1

a) Harzburgite showing two pyroxene fabrics; the main fabric is oriented vertically in the photograph and the second fabric is parallel to the pen.

b) Typical banded harzburgite exposure; the orthopyroxene bands are the dark brown weathering features in the centre of the photograph.

c) Finely banded harzburgite (the bands weathering slightly proud of the surface in this example) from the top of the harzburgite sequence.

A.

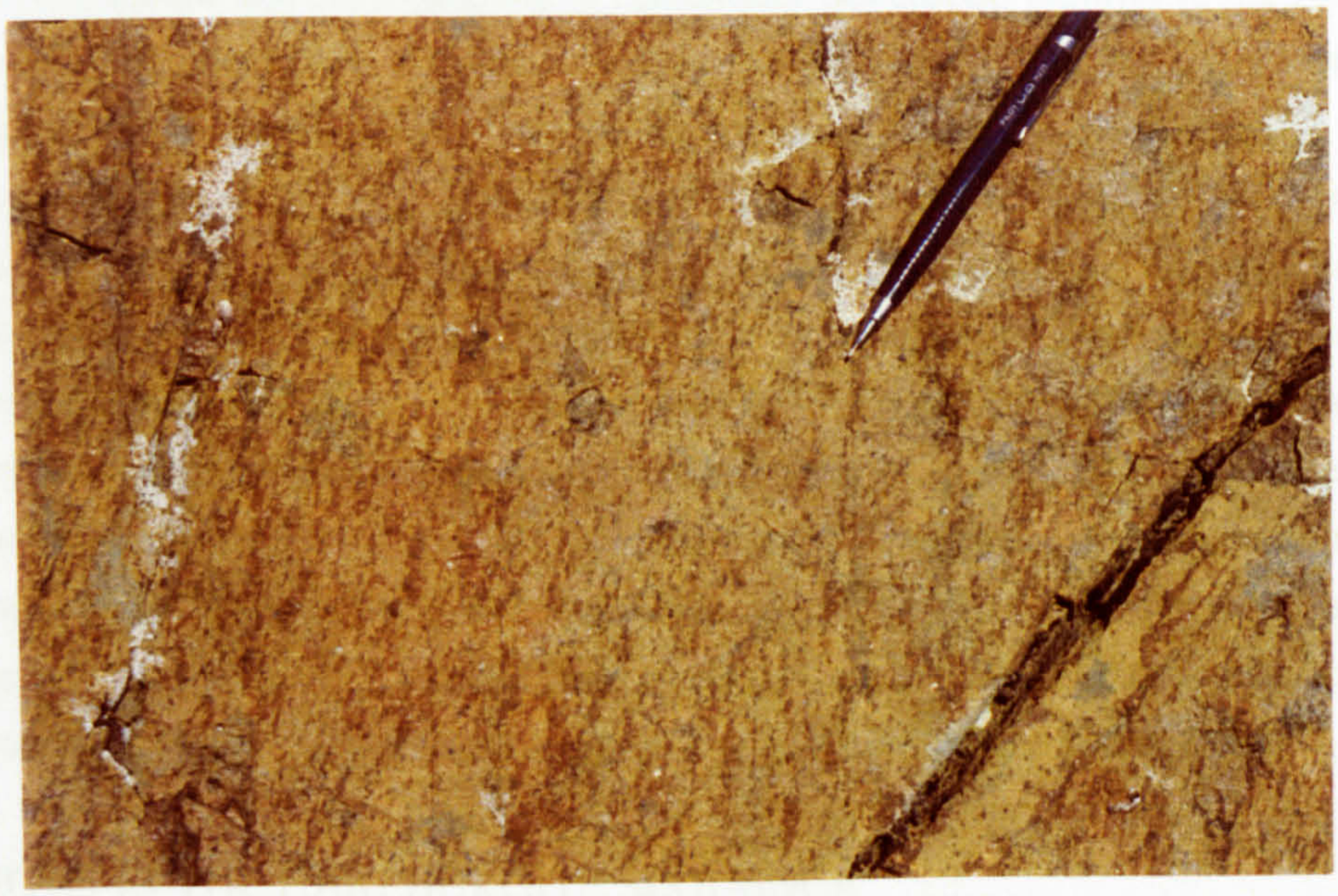

B.

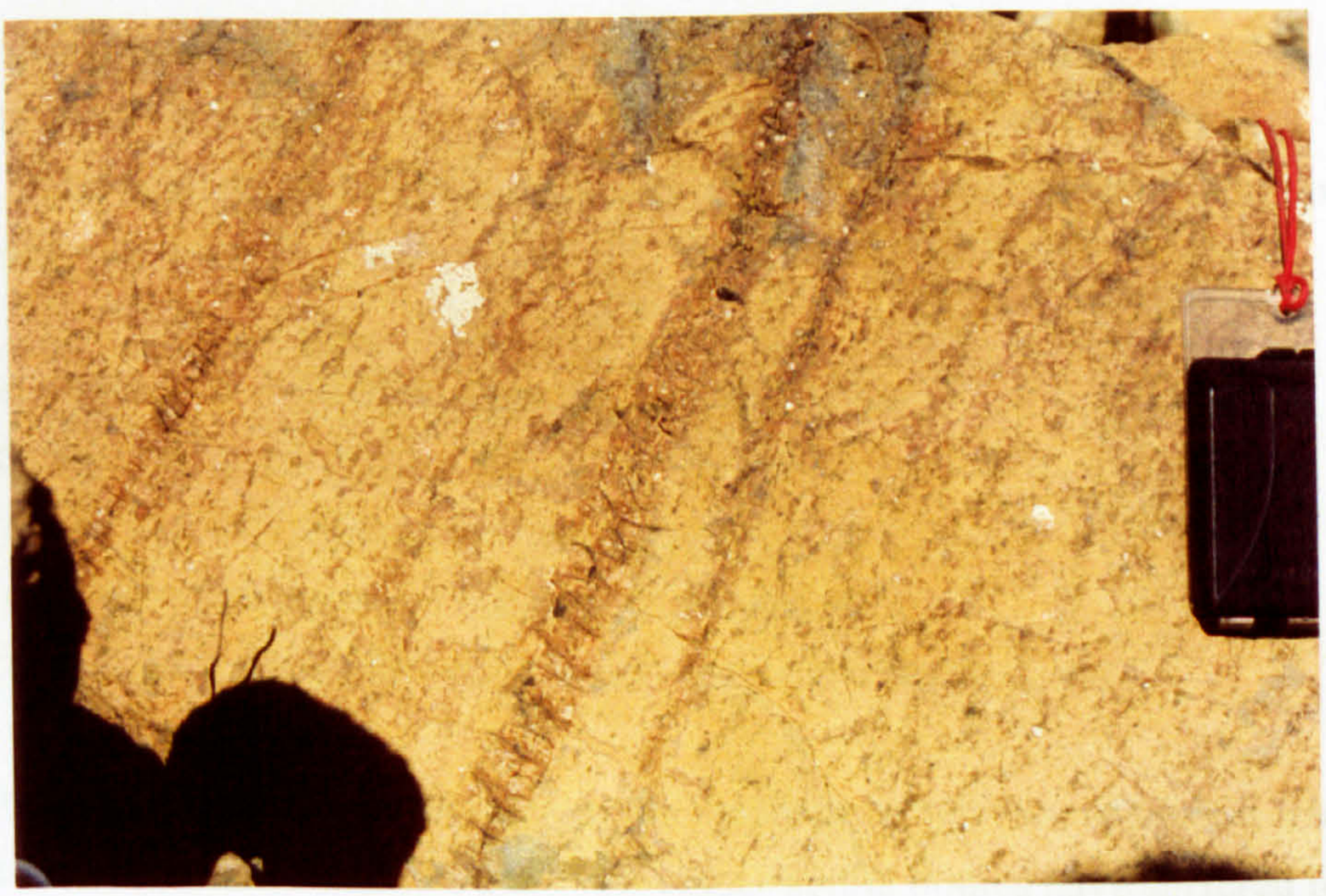

C.

Throughout the mantle section a banding is commonly developed parallel to the foliation by variations in the proportions of orthopyroxene and olivine (Plate 2.1b). The bands occur in irregularly spaced zones one to two metres wide (measured perpendicular to the strike of the foliation), separated by areas of massive, foliated harzburgite. The bands are laterally persistent on an outcrop scale, but cannot be traced between outcrops. Band width varies from the width of a single crystal up to a maximum of three centimetres wide, the average width being approximately one cm. At the base of the *in situ* mantle sequence, where the banding is most strongly developed, the enclosing harzburgite becomes more olivine-rich adjacent to bands and the orthopyroxene crystals within the bands are coarser-grained than those in the enclosing harzburgite. In the uppermost 20 m of the sequence, where the harzburgites become finer-grained, the pyroxene banding is developed on a much finer scale than it was deeper in the sequence (Plate 2.1c).

2.2.2 DUNITES IN THE HARZBURGITE SEQUENCE

The harzburgite sequence is host to a variety of dunite bodies which become progressively more abundant as the contact with the overlying crustal sequence is approached. The dunites can be characterised by the attitude and nature of their contacts with the harzburgites into five main types:

(i) dunites which form bodies parallel to the foliation;
(ii) dunites which form the wallrocks to chromitite bodies;
(iii) dunites associated with orthopyroxenites;
(iv) dunites which cross-cut the harzburgite foliation;
(v) dunites with interdigitating contacts against the harzburgites.

Cross-cutting relationships between these dunite types have not been observed. However, on the basis of the amount of deformation individual dunite bodies have suffered relative to the host harzburgites, foliation-parallel, chromitite wallrock dunites and dunites associated with orthopyroxenites are thought to be the oldest dunites, and the cross-cutting dunites and those with interdigitating contacts the youngest.

Plate 2.2

a) Thin dunite bodies oriented parallel to the harzburgite foliation.

b) Sample of an *orthopyroxenite A* body (labelled P), showing a marginal dunite facies (D) against the host harzburgite (H).

c) A sheet of dunite which cross-cuts the harzburgite foliation (the harzburgite foliation is parallel to the pen in the photograph).

A.

B.

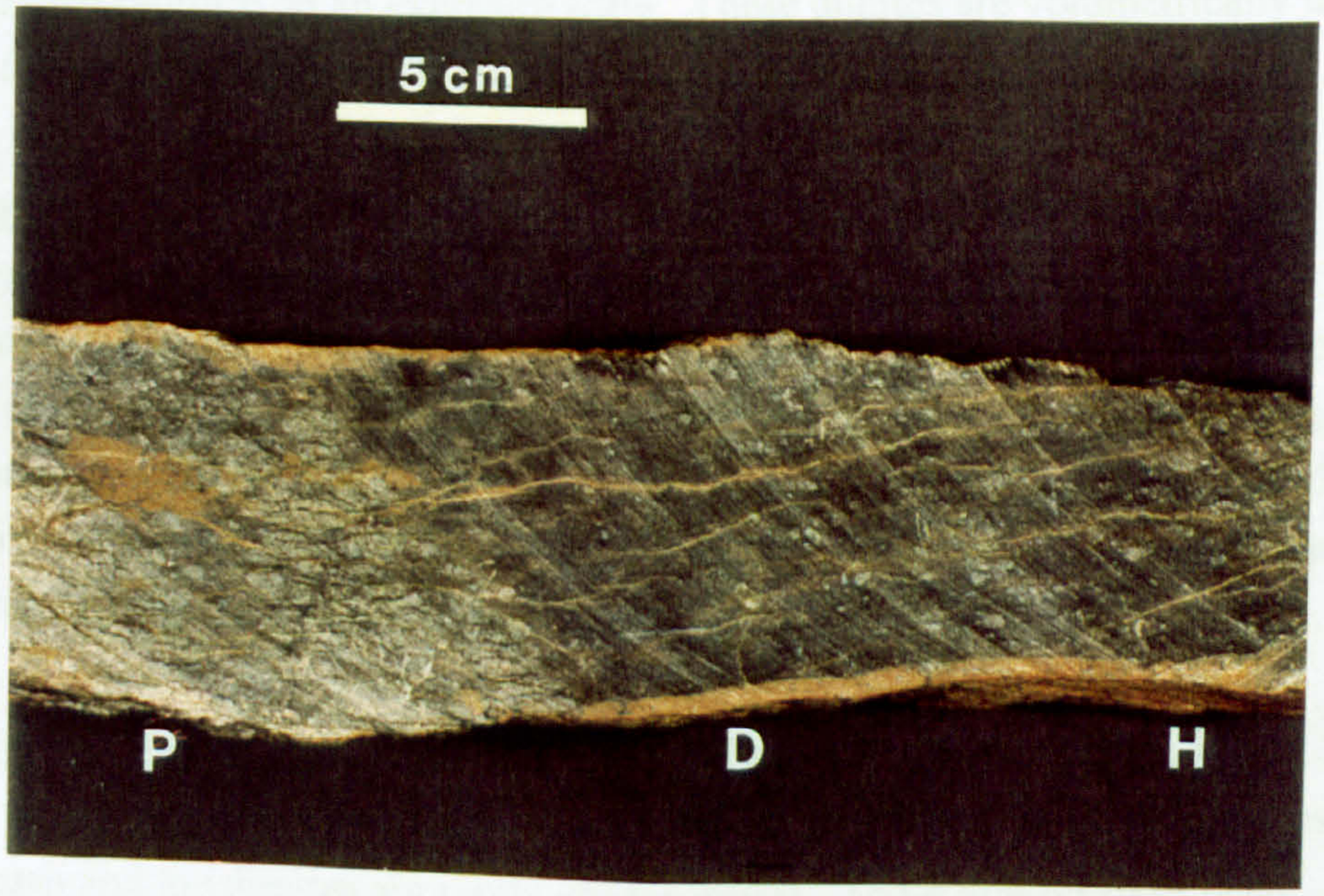

C.

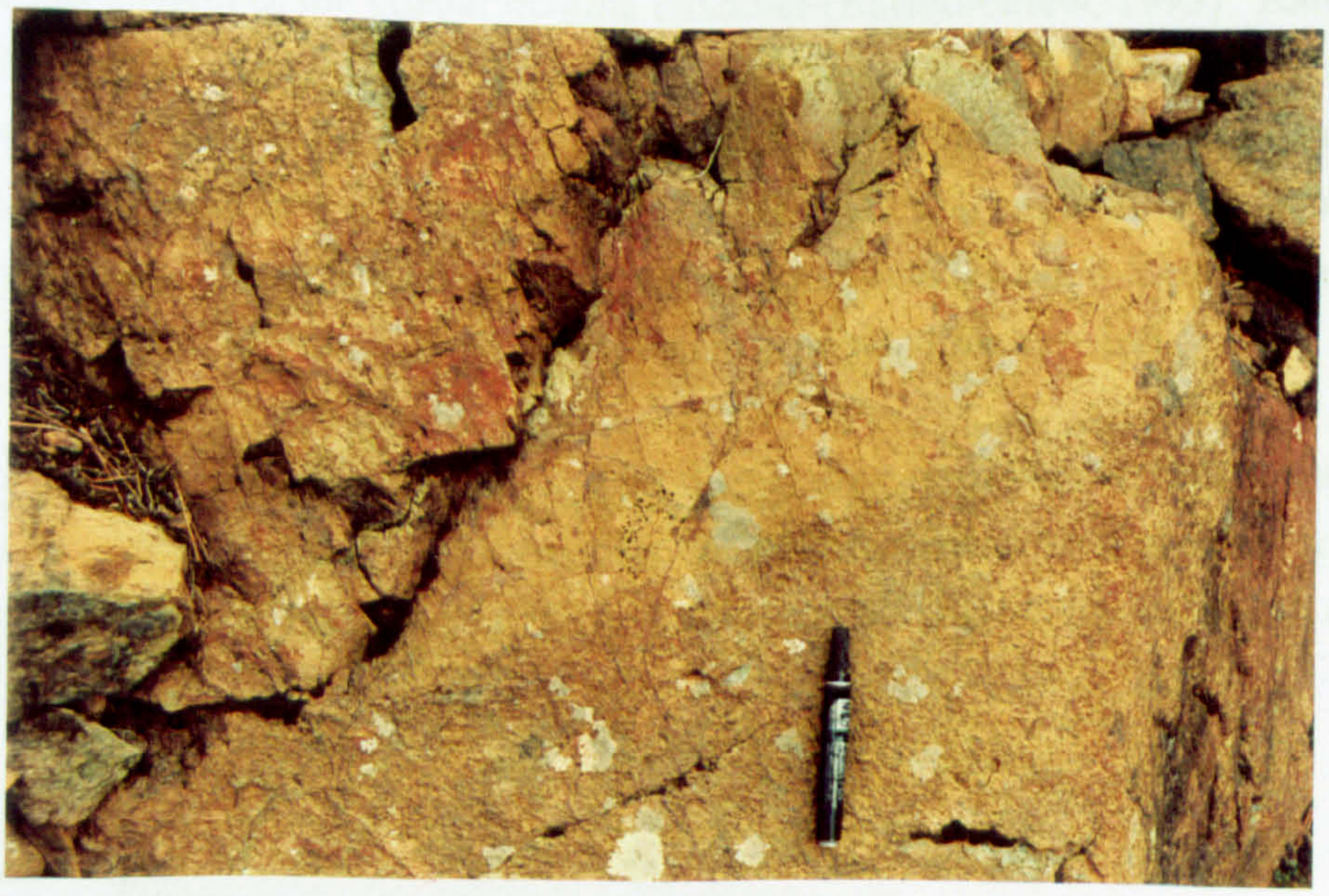

Foliation parallel dunites (Plate 2.2a) are found throughout the sequence and are generally continuous on an exposure scale, but cannot be traced between exposures. At the base of the section they are typically 1 to 2 cm wide bodies, which form sharply-defined bands within the harzburgite. Higher in the sequence, these dunites are thicker and often contain trains of chromites oriented parallel to the foliation. These chromitite stringers are always separated from the harzburgite by 1 to 2 cm of dunite. These dunites maybe transitional to the wallrock dunites of the large chromitite bodies.

Wallrock dunites surround the chromitite bodies and are equivalent to the dunite pods of other authors (Greenbaum, 1977). These dunites are generally in sharp contact with the enclosing harzburgites and the enclosed chromitite. They are most common in the uppermost 1400 m of the sequence, where they form elongate bodies with long axes aligned parallel to the harzburgite foliation. Pods range in size from < 2 m in length up to a maximum of approximately 200 m; the smallest pods can be seen to be completely enclosed by harzburgite on an exposure scale. These dunites are volumetrically the most abundant form of dunite.

Dunites associated with orthopyroxenites (Plates 2.2b) occur as a marginal facies between orthopyroxenite bodies and the enclosing harzburgites. Two different types of orthopyroxenite bodies have been identified (described in detail below), and the outcrop character of the marginal dunites are the same for both types. These dunites range from a few millimetres to 10 cm thick and have irregular, but sharp, contacts against both the orthopyroxenites and the harzburgite. The orthopyroxenites and associated dunites are always oriented parallel to the harzburgite foliation.

Dunites which cross-cut the foliation (Plate 2.2c) generally form inclined sheets, 2 to 150 cm thick, in the uppermost 1 km of the section. Contacts against the harzburgites are always sharp and the dunites are rarely chromiferous. These dunites have been interpreted as feeders to the crustal magma chamber (Bartholomew, 1993). Rarely, these dunites are disharmonically folded about the harzburgite foliation (Plate 2.3a), in which case the contacts against the harzburgites are diffuse due to mechanical mixing of the dunite and harzburgite along the sheet margins. The fact that some of these dunites are affected by the mantle deformation, while others form parallel sided, undeformed bodies, suggests that dunite formation took place over an extended time period.

Dunites with interdigitating contacts against the harzburgites (Plate 2.3b) are usually large bodies (< 50 m maximum dimension), which are oriented parallel to the foliation on a large scale. On an exposure scale, these dunites cross-cut the foliation due to the

complex, interdigitating nature of their contacts with the host harzburgite. Contacts with the harzburgites are always sharp, and the margins of these dunites usually contain ragged harzburgite xenoliths and clots of orthopyroxene crystals. The pyroxene foliation in the xenoliths is always oriented parallel to the foliation in the adjacent harzburgite. These dunites often contain pea-sized spinel grains, which are also aligned in trains parallel to the harzburgite foliation.

2.2.3 CHROMITITES

The Troodos mantle sequence is host to numerous chromite bodies which range in size from thin layers and schlieren to large podiform bodies, within which the former mines of Kannoures and Hadji Pavlou are located (Figure 2.3). In all cases, the chromitites are hosted by dunite and are orientated parallel to the harzburgite foliation. The former chromite mines are no longer accessible, so sampling of these bodies has been restricted to the surrounding spoil heaps.

Detailed descriptions of the chromite deposits are given by Greenbaum (1977) who had access to the sub-surface exposures in the mines. Greenbaum (1977) stressed the relationship between chromite concentrations and dunites, and noted the wide variety of chromite textures, which show a complete gradation from unaltered cumulate textures to deposits in which schlieren structures predominate. Detailed mapping showed that there was no geographical relationship between the composition or texture of the chromite bodies and their position in the mantle sequence. A primarily magmatic origin was proposed, with extensive post-crystallisation deformation producing a tectonic overprint of schlieren structures and bringing the chromite concentrations into parallelism with the harzburgite foliation. However, the recognition of a wide variety of hydrous silicate inclusions within the chromite grains has led McElduff and Stumpfl (1990; 1991) to conclude that a fluid phase might have played an important role in triggering chromite crystallisation.

Plate 2.3

a) Folded dunite sheet; note the parallelism between the harzburgite foliation and the fold axes (dashed lines on the photograph). The edge of the sheet has been highlighted in pen on the photograph.

b) Contact of an interdigitating dunite (bottom half of the photograph) and host harzburgite; note the coarse spinel (black flecks on the photograph located to the right of the lens cap) and orthopyroxene clots with a foliation parallel to that in the host harzburgite.

c) *Orthopyroxenite A* bodies (brown weathering bodies ribbed with black serpentinite veins in the centre of the photograph) aligned parallel to the harzburgite foliation and boudinaged along the foliation (the foliation is parallel to the hammer shaft in the photograph).

A.

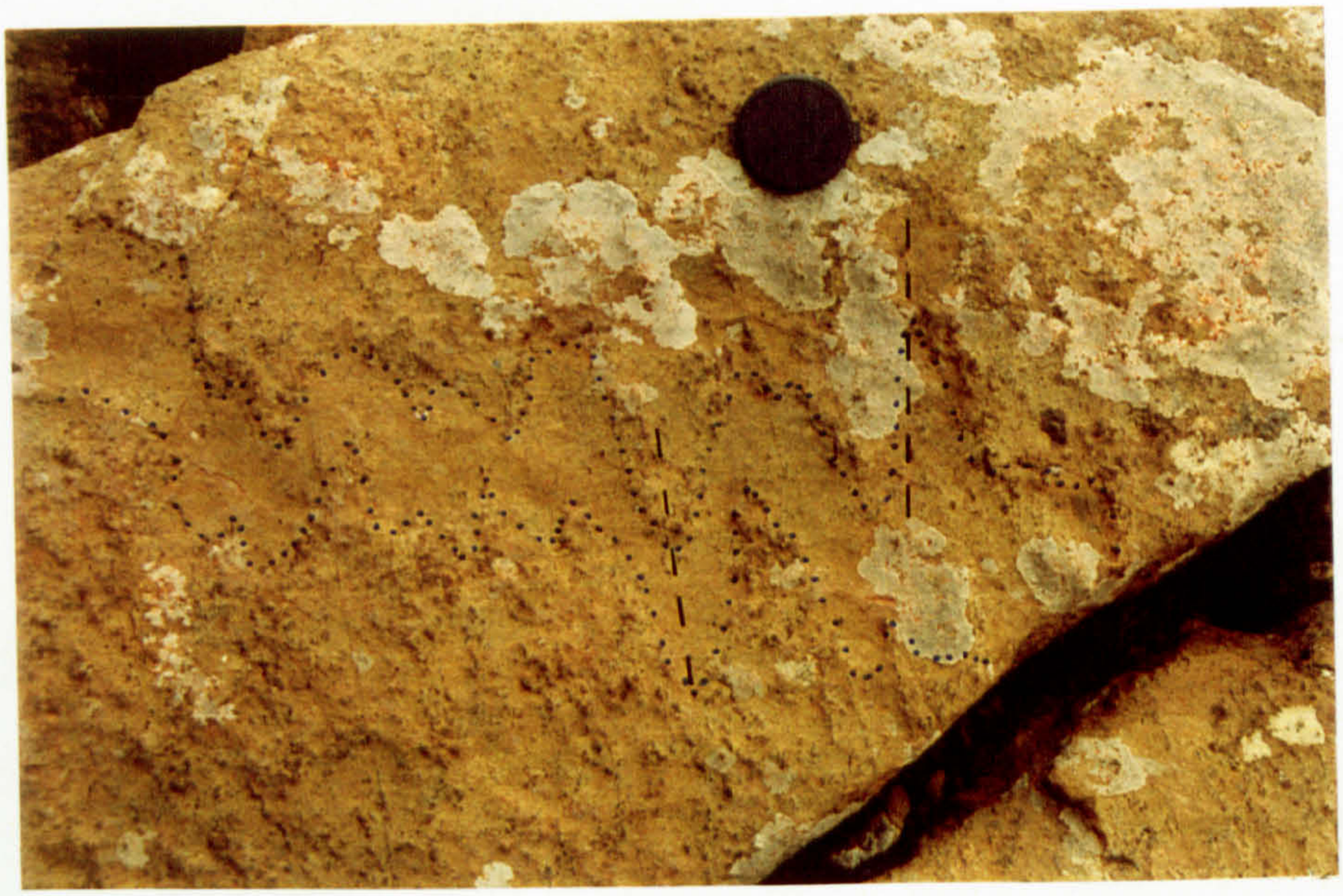

B.

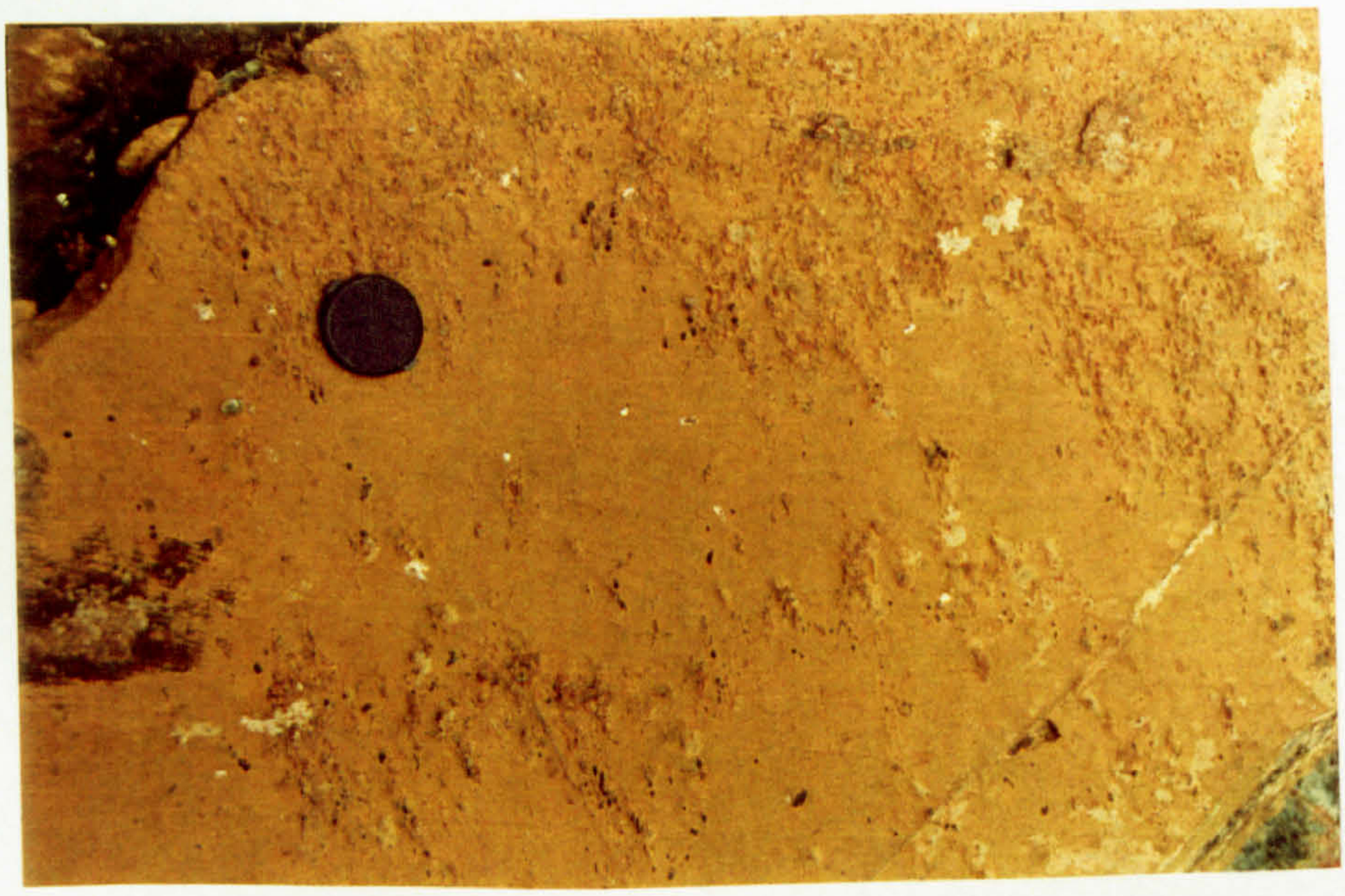

C.

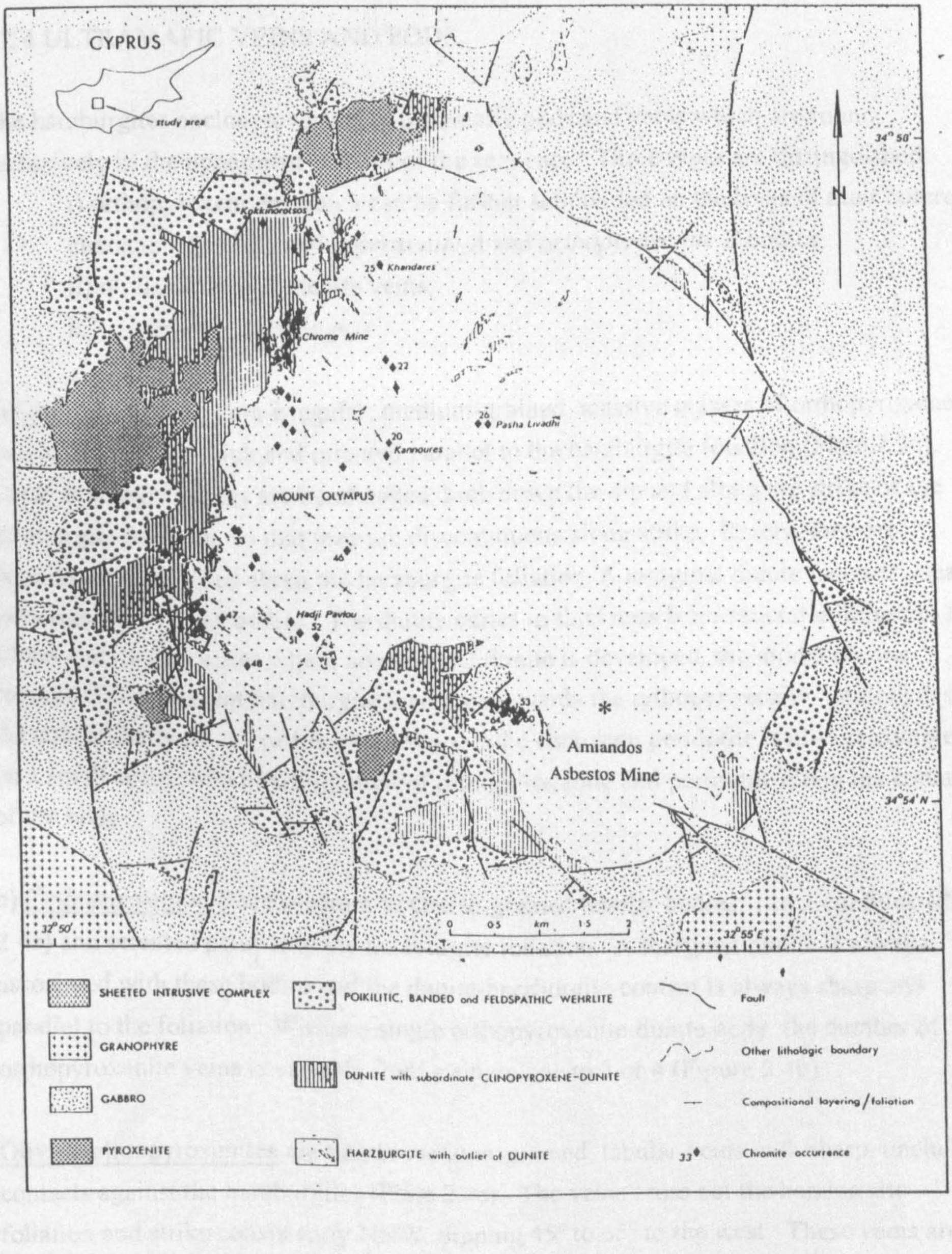

Figure 2.3 Geological sketch map of the Mount Olympus area reproduced from Greenbaum (1977) showing the position of the chromite mines and other chromite occurrences.

In this thesis chromitites will be classified according to the nature of the host body into:

(i) chromitites in the podiform dunites located in the uppermost parts of the harzburgite sequence;

(ii) chromitites forming layers or schlieren in the crustal dunites.

2.2.4 ULTRAMAFIC VEINS AND PODS

The harzburgites enclose a variety of ultramafic pods and veins which are found exclusively in the uppermost 1500 m of the sequence. Three types are distinguished:

i) orthopyroxenites, which can be further subdivided on the basis of their outcrop characteristics into *orthopyroxenite A* and *orthopyroxenite B* bodies;

ii) olivine-clinopyroxenite veins;

iii) clinopyroxene stringers.

a) *Orthopyroxenite A* are irregular, medium-grained, massive masses of orthopyroxene, usually 5 to 15 cm thick and oriented parallel to the harzburgite foliation (Plate 2.3c). These orthopyroxenites are boudinaged, both down the dip and along the strike of the harzburgite foliation, so that they are discontinuous along strike. Rarely, they are asymmetrically folded about the harzburgite foliation. A marginal dunite facies is usually associated with these bodies. The dunite varies in thickness from several millimetres to 10 cm and, in exposures where no marginal dunite is developed, the modal olivine content of the adjacent harzburgite increases towards the orthopyroxenite. In both cases, the contact between the orthopyroxenite and the enclosing peridotite is always complex on a small scale, with interdigitation of orthopyroxenite and peridotite along the contacts of the body.

b) *Orthopyroxenite B* are medium to coarse-grained tabular bodies, 1 to 2 cm thick (Plate 2.4a) and oriented parallel to the harzburgite foliation. A marginal dunite is always associated with these bodies and the dunite-harzburgite contact is always sharp and parallel to the foliation. Within a single orthopyroxenite-dunite body, the number of orthopyroxenite veins is variable from a single one to 3 or 4 (Figure 2.4b).

Olivine-clinopyroxenites are fine to medium-grained, tabular veins with sharp, unchilled contacts against the harzburgites (Plate 2.4c). The veins cross cut the harzburgite foliation and strike consistently NNW, dipping 45° to 65° to the west. These veins are never associated with a marginal dunite and are only found close to the harzburgite-crustal dunite contact.

Plate 2.4

a) *Orthopyroxenite B* body containing a single orthopyroxenite vein; note the marginal dunite with sharp contacts against the enclosing harzburgites.

b) Outcrop of an *orthopyroxenite B* body displaying multiple orthopyroxenite veins (located centre-right in the photograph) and a marginal dunite facies against the host harzburgite.

c) An olivine-clinopyroxenite vein.

A.

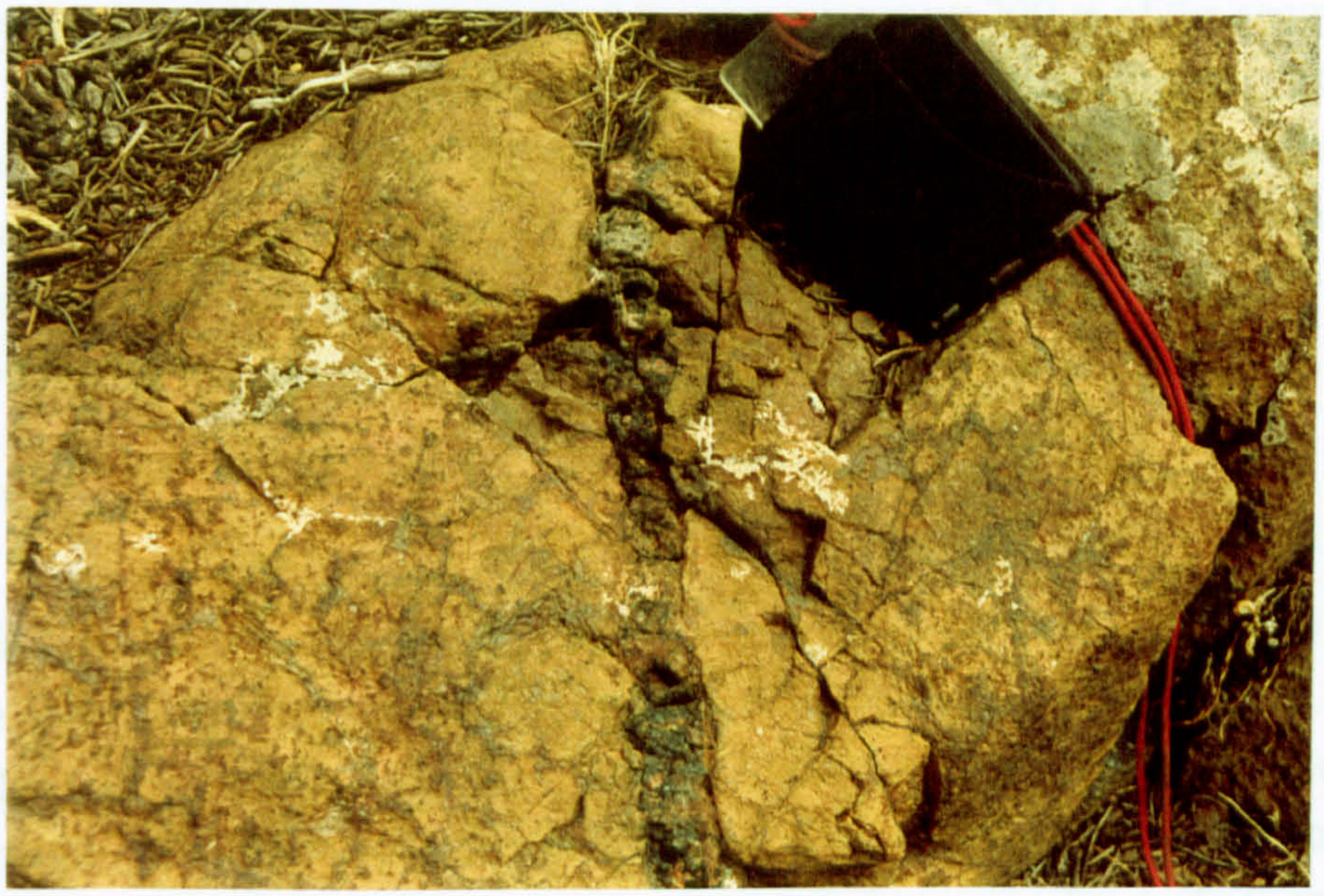

B.

C.

Clinopyroxene stringers are rare and only found in the uppermost 200 m of the sequence (Plate 2.5a). The stringers consist of irregular, planar masses of coarse to pegmatitic clinopyroxene crystals surrounded by dunite. The stringers vary from < 10 cm in length up to 1.5 m, rarely display branching morphologies and are irregularly oriented with respect to the harzburgite foliation. The clinopyroxenites are the least abundant pyroxenites in the mantle sequence.

2.2.5 LATE VEINS

Tabular wehrlite and gabbro veins, from 1 to 15 cm thick, cross-cut the harzburgite at all depths in the mantle sequence. Neither lithology have chilled margins. The veins become thicker and more abundant towards the top of the harzburgite sequence. Both vein types trend approximately northeast-southwest and dip between 30° and 50° towards the north (Figure 2.1). At depth in the sequence, the veins are generally medium to coarse-grained, often displaying comb textures indicative of magmatic crystallisation from the walls of the vein. In the mantle-crust transition zone, grain sizes become pegmatitic, and the largest gabbro veins often show several generations of intrusion. These gabbros grade into small, irregularly shaped, gabbro bodies up to 5 m in maximum dimension. Commonly a network of thin gabbro veins intruded around joint blocks of dunite are found at the margins of these bodies (Plate 2.5b)

2.2.6 THE MANTLE-CUMULATE TRANSITION ZONE

At the top of the mantle section the harzburgites are in contact with cumulate dunites, pyroxenites and gabbros via a sequence of deformed dunites which were termed the 'transitional dunite' by Bartholomew (1993). The deformed dunites are identified in the field by the alignment of spinel crystals and stringers parallel to the harzburgite foliation. The contact between the harzburgite and dunites was initially thought to be complex, resulting from folding of the dunite into the harzburgite (Wilson, 1959; Greenbaum, 1972). Remapping of the contact by Bartholomew (1993) showed it is simpler than originally proposed, defining a sub-vertically dipping plane with only minor embayments of dunite.

A.

B.

In this thesis, the term 'crustal dunite' is applied to all the dunite that outcrops stratigraphically above the uppermost harzburgites and includes both the undeformed cumulate dunites and transitional dunite of Bartholomew (1993). The contact between the crustal dunite and the harzburgites is marked by zone 0.5 to 1m thick in which the crustal dunite intrudes around joint blocks of harzburgite. Occasionally these joint blocks become separated from the underlying harzburgite to form xenoliths within the base of the crustal dunite. The xenoliths are always aligned with their long axes, and pyroxene foliation, parallel to the foliation in the underlying harzburgites. Contacts between the two lithologies are always sharp and the margins of the xenoliths are usually rounded and resorbed in appearance, suggesting that corrosion of the harzburgite has occurred (Plate 2.6a).

The lowermost crustal dunites also contain a variety of pyroxene and plagioclase-rich lithologies which are strongly layered, and oriented parallel to the harzburgite foliation. Clinopyroxenites occur as elongate, pod-shaped bodies. At the margin of these bodies, coarse-grained clinopyroxenes poikilitically enclose olivine (Plate 2.6b), and grade inwards into strongly layered, coarse to pegmatite clinopyroxene-dunite masses. The clinopyroxenite pods are up to 20m in maximum dimension and outcrop exclusively in the southwest of the study area (Figure 2.1).

A plagioclase lherzolite unit, consisting of elongate plagioclase crystals surrounded by clinopyroxene in a matrix of olivine, occurs to the west of Mount Olympus (Figure 2.1). Menzies and Allen (1974) suggested that the plagioclase lherzolite represents a section of primary aluminous mantle. However, subsequent workers (George 1978; Bartholomew 1993) have shown that the plagioclase lherzolite is separated from the harzburgites by a dunite layer, and suggest that they have a cumulate origin. Re-examination of the outcrop during this study confirmed George (1978) and Bartholomew's (1993) findings.

2.2.7 SERPENTINISATION

Serpentinisation affects all the rocks comprising the mantle sequence. The degree of serpentinisation ranges from 10 to 70 %. Olivine is the most susceptible to alteration, followed by orthopyroxene, spinel and clinopyroxene. Weathering of the serpentine minerals gives the ultramafic rocks their characteristic orange-brown weathering colour.

Plate 2.6

a) A resorbed harzburgite xenolith in the base of the crustal dunites; note the parallelism between the foliation in the xenolith (vertical in the photograph) and the foliation in the harzburgite located top left in the photograph.

b) Poikilitic clinopyroxene on the margin of a massive clinopyroxenite body located within the crustal dunites.

c) Typical exposure of a heavily serpentinised Limassol Forest harzburgite.

A.

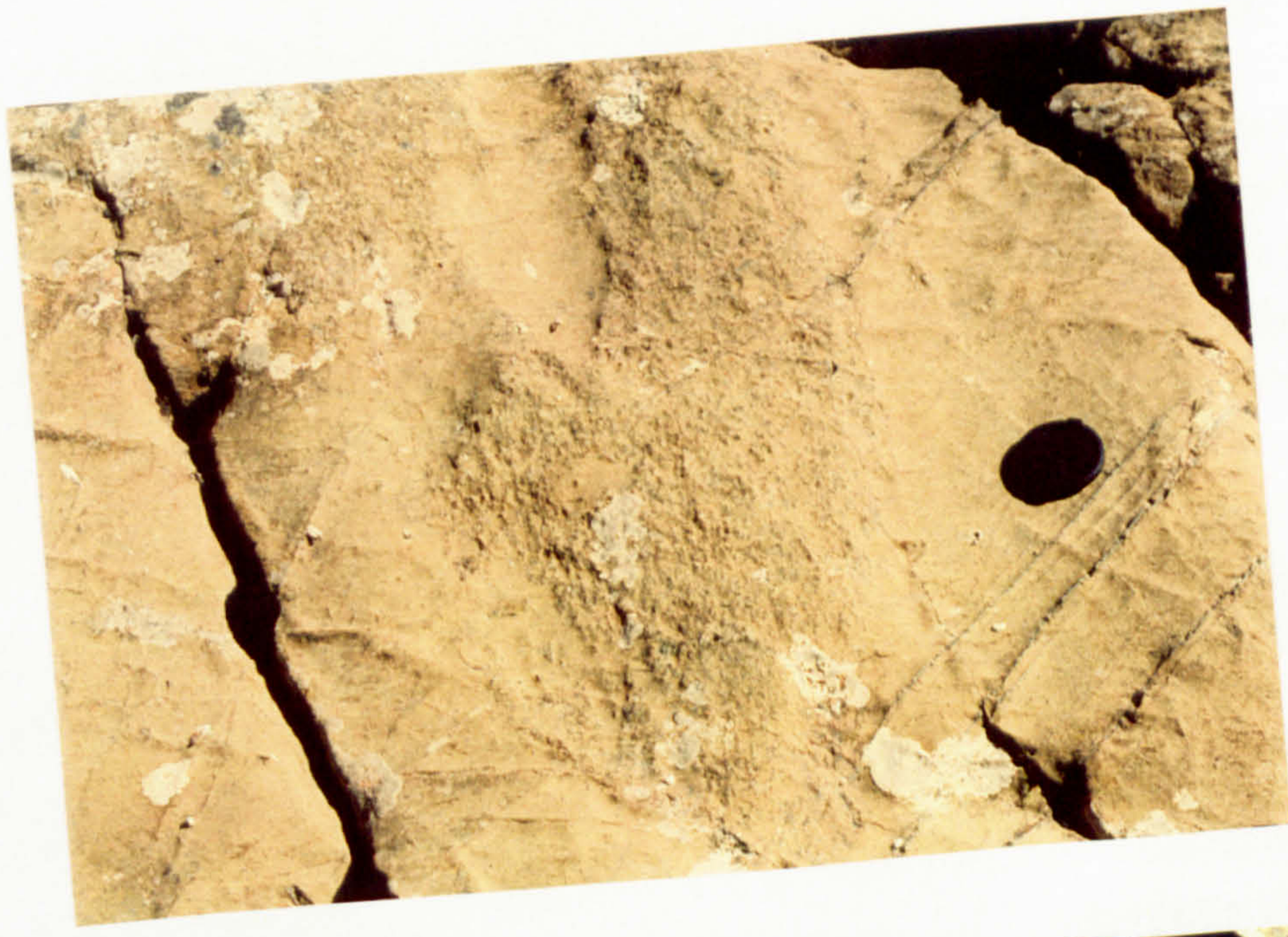

B.

C.

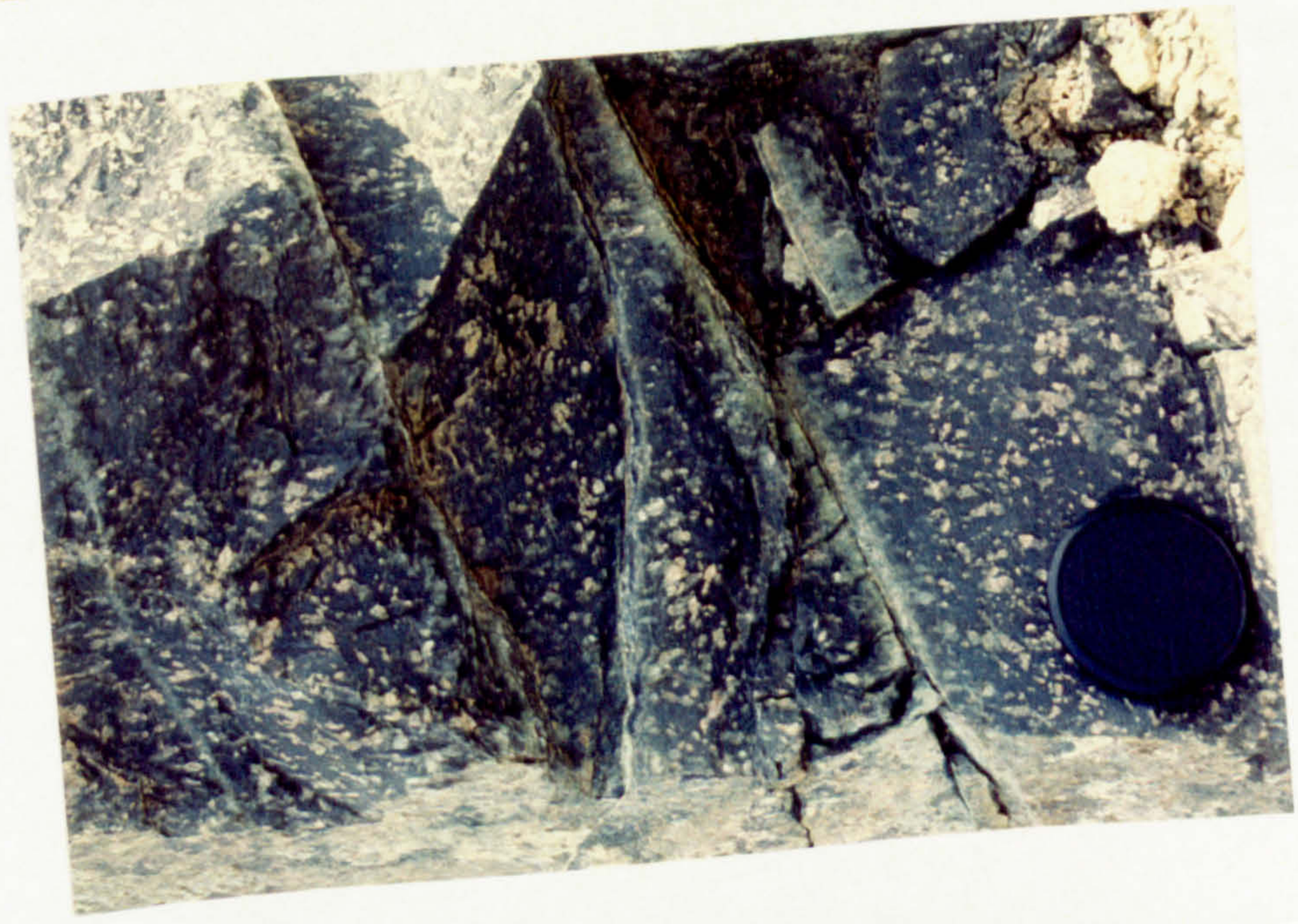

2.2.8 THE SERPENTINITE DIAPIR

The serpentinite diapir is defined as the area of heavily shattered and serpentinised peridotites to the east of the Troodos sequence (Figure 2.1). The contact between the two peridotite masses is faulted and marked by the deeply eroded Arg Tis Khionistras River valley. Exposure within the serpentinite diapir area is poor and the harzburgite foliation has a random orientation, in contrast to the regular pattern of the intact sequence to the west

The peridotites in the diapir have lherzolitic compositions with 5 to 10 % medium-grained clinopyroxene, although the poor exposure precludes the identification of any regional differences in composition throughout the diapir. A network of thin, discontinuous chrysotile and picrolite veins cross-cut the peridotites, and are most common in the south of the area around the old Aminandos asbestos mine (Figure 2.3). No consistent order of emplacement of the veins is recognisable, and both types show multiple crystallisation episodes within single veins. Crystal growth within the veins is usually perpendicular to the walls, suggesting the most of the veins formed in normally dilational fractures.

Because of the intense fracturing, deep weathering and concomitant poor exposure in the serpentinite diapir area, the study of this area has been restricted to regional sampling for comparative purposes with the *in situ* mantle sequence to the west.

2.3 THE LIMASSOL FOREST

The Limassol Forest complex is separated from the Troodos Massif by the east-west trending Arakapas Fault Belt (Chapter 1, Figure 1.3), which has been interpreted as an oceanic transform fault (Moores and Vine, 1971; Murton and Gass, 1986). Oceanic crust to the south of the fault belt is thought to have been generated at an 'Anti-Troodos' ridge axis (Murton and Gass, 1986). Serpentinite shear zones disrupt the mantle sequence exposed in the Limassol Forest and exposure is poor. This study of the Limassol Forest mantle has, therefore, been restricted to regional sampling for comparative purposes with the Troodos harzburgites.

Serpentinisation is more intense in the Limassol Forest area than in the Troodos Massif, and it is rare that the ultramafics of the Limassol Forest are less than 99% serpentinised. This gives the rocks a characteristic black colour with a splintery, concoidal fracture

(Plate 2.6c). Thin anastomosing chrysotile veins pervasively cross-cut the mantle rocks, and orthopyroxene crystals are often brecciated with chrysotile fibres filling the fractures.

2.4 SUMMARY

The Troodos Massif exposes a 3 km thick harzburgitic mantle section with an upper contact against crustal dunites and a lower, fault defined contact against the serpentinite diapir. The harzburgites are host to several generations of pyroxenitic and dunitic intrusions. The harzburgites, and some of the intrusions, have been subjected to intense deformation which has created a strong mineral foliation in the harzburgite, and rotated the intrusions into parallelism with this foliation. Later intrusions cross-cut this mantle fabric. The contact between the harzburgites and the overlying dunites is a complex zone in which dunites intrude the uppermost harzburgites and a variety of clinopyroxenitic and plagioclase-rich lithologies are developed.

The Limassol Forest mantle exposures are upto 100 % serpentinised and regional faulting has disrupted the original stratigraphy of the mantle sequence.

CHAPTER 3
MICROSTRUCTURE

3.1 INTRODUCTION

This chapter describes the microstructure of the mantle lithologies exposed in the Troodos Massif. The principal aim of this chapter is to try to establish whether petrographic variations in the harzburgites can be used to identify mantle melting and mantle-melt interaction processes in the Troodos Massif. The location and morphology of any minerals related to melt infiltration will then be used to establish the relative chronology of mantle-melt interaction and mantle deformation.

The subdivisions of the harzburgites outlined in Chapter 1 are used in this chapter and are repeated in brief below. Because some of these sub-divisions are erected on the basis of $Cr\#_{spn}$ variations, the key diagram illustrating the $Cr\#_{spn}$ data is reproduced here as Figure 3.1.

Harzburgites which were collected > 5 m away from dunites, veins or minor intrusions are termed *background* harzburgites. These samples are intended to represent the geochemical background of the Troodos mantle section, on to which geochemical variations produced by the injection of minor intrusions may have been superimposed. Any *background* harzburgites which outcrop within 500 m (measured vertically through the sequence) of the crustal dunite-harzburgite contact (see Fieldwork Chapter) are termed '*top-of-the-sequence*' harzburgites.

The *background* harzburgites have been further sub-divided on the basis of $Cr\#_{spn}$ data (Figure 3.1). The $Cr\#_{spn}$ data defines large domains, orientated parallel to the harzburgite-dunite contact, in which $Cr\#_{spn}$ decreases with increasing depth in the mantle sequence. Notable exceptions to this trend are found in the south-west of the study area (around 8650,6525), where unusually low $Cr\#_{spn}$ values occur in a section of harzburgite enclosed by a tongue of dunite at the top of the mantle section, and in the centre of the study area (around 8875,6650) where a layer of low $Cr\#_{spn}$ is perched in an area of higher $Cr\#_{spn}$. The *background* harzburgites outcropping in these areas are termed the *Anomaly 1* and *Anomaly 2* harzburgites respectively in this thesis (see Figure 3.1).

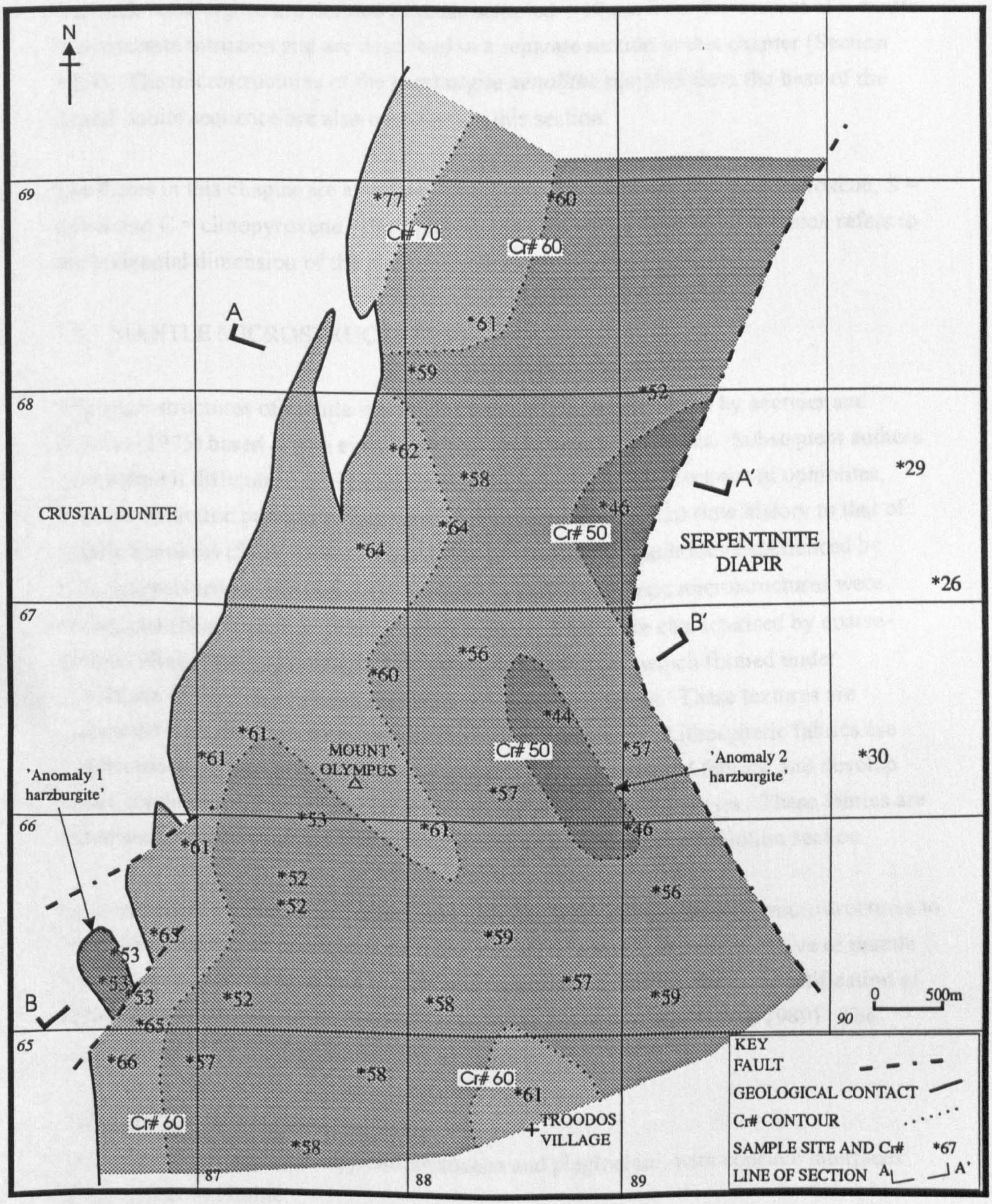

Figure 3.1 A map illustrating the variation of $Cr\#_{spn}$ in the *background* harzburgites.

Wallrock harzburgites are defined as those sampled < 10 cm from the contact of a dunite or pyroxenite intrusion and are described in a separate section in this chapter (Section 3.2.4). The microstructures of the harzburgite *xenoliths* sampled from the base of the crustal dunite sequence are also described in this section.

The Plates in this chapter are annotated as follows: Ol = olivine, O = orthopyroxene, S = spinel and C = clinopyroxene. Each plate is labelled with a field of view which refers to the horizontal dimension of the photomicrograph.

3.1.1 MANTLE MICROSTRUCTURES

The microstructures of mantle lithologies were originally classified by Mercier and Nicolas (1975) based on the examination of upper mantle xenoliths. Subsequent authors have found it difficult to apply this classification to the mantle sections of ophiolites, because ophiolitic peridotites have suffered a distinctly different flow history to that of mantle xenoliths (Suhr, 1993). To account for the unique conditions experienced by ophiolite peridotites, the terms asthenospheric and lithospheric microstructures were introduced (Nicolas *et al.*, 1980). Asthenospheric fabrics are characterised by coarse-grained olivine microstructures, with strong lattice fabrics, which formed under conditions of very high temperature and low deviatoric stress. These textures are associated with the spreading period of ophiolite peridotites. Lithospheric fabrics are characterised by fine-grained olivine neoblasts with unrecovered fabrics, and develop under conditions of lower temperatures and higher deviatoric stresses. These fabrics are associated with detachment and subsequent emplacement of the ophiolitic section.

In more recent studies, the emphasis has changed from using peridotite microstructures to infer the deformation conditions, to using them to identify textures indicative of mantle processes, such as melting and mantle-melt reaction. A scheme for the identification of residual and melt-related textures has been proposed by Nicolas (1986, 1989). The proposed textures can be summarised as follows.

Textures indicative of melt formation:

i) interstitial minerals, usually clinopyroxene and plagioclase, with concave interfaces with respect to olivine;

ii) continuity between diffuse plagioclase-clinopyroxene segregations and indigenous dykes;

iii) depletion halos around clinopyroxene/plagioclase;

iv) the regular distribution of melt products on a massif scale.

Textures indicative of melt impregnation:
i) interstitial clinopyroxene and plagioclase with poikilitic habits, clinopyroxene sometimes showing growth twins;
ii) heterogeneous development of irregular patches of lherzolite/wehrlite/troctolite, typically restricted to 1 km below the MOHO;
iii) textures that mimic cumulates with corrosion of olivine producing euhedral faces and recrystallisation of spinel to euhedral shapes.

This classification is primarily based on the textures of individual minerals. However, as other authors have pointed out (Suhr, 1993; Edwards and Malpas 1996), particular mineral associations and intergrowth textures may be more powerful fingerprints of mantle processes.
Other textures identified as indicative of mantle processes are:
i) resorption of orthopyroxene by olivine producing embayed orthopyroxene margins - partial melting (Girardeau and Lagabrille, 1992);
ii) association of orthopyroxene, clinopyroxene and spinel in clusters of coarse grains - partial melting (Smith, 1977);
iii) undeformed trails of clinopyroxene grains - melt interaction (Suhr, 1993);
iv) spinel-clinopyroxene intergrowths (with or without minor orthopyroxene) showing identical optical extinction of separate clinopyroxene crystals - melt interaction (Suhr, 1993).

In the following descriptions emphasis will be placed on differentiating textures associated with partial melting from those associated with mantle-melt interaction. All microstructural observations were made in thin sections cut perpendicular to the harzburgite foliation and, where it was visible, parallel to the mineral stretching lineation.

3.1.2 PREVIOUS WORK

The harzburgites of the Troodos Massif were originally described the Wilson (1959) who noted the "irregular interstitial, or apparent relics, of orthopyroxene". Menzies and Allen (1974) identified the harzburgites as a residuum of partial fusion and interpreted the diopside content of the harzburgites as the product of a "residual pore fluid". George (1978) published the first comprehensive fabric analysis of the Troodos Massif and recognised a second, younger, generation of orthopyroxene and clinopyroxene in harzburgite samples within 20 m of the crustal dunite-harzburgite contact. These crystals were thought to be related in some way to the intrusion of the overlying cumulate

sequence. George (1978) also recognised that the mantle deformation occurred under conditions of low deviatoric stress at temperatures above the peridotite solidus. Bartholomew (1993) reanalysed the Troodos mantle section and recognised the co-existence of two ductile mantle fabrics. Both of these fabrics were related to ductile flow in the asthenosphere and developed by interaction between separate diapiric uprise centres.

3.2 THE TROODOS SEQUENCE

Textures throughout the Troodos sequence are coarse-grained asthenospheric (in the terminology of Nicolas, 1989), with a foliation defined by the alignment of spinel and orthopyroxene porphyroclasts. Overprinting by lower temperature lithospheric strain has not been observed. This is consistent with the absence of any outcrop evidence for any detachment faulting.

The peridotites sampled from the Troodos sequence have a common set of microstructures. Olivine has the highest modal abundance in the peridotites and is the load-bearing phase. Olivine in the matrix is always coarse-grained, and a second generation of finer-grained olivine neoblasts is often associated with the embayed margins of orthopyroxene crystals. Serpentinisation of olivine is a ubiquitous feature of the peridotites and destroys the details of grain boundaries in all samples. Most olivine in the peridotites is assumed to be residual. However, as discussed in the following chapter, the mineral chemistry data suggests that many of the *background* harzburgites have NiO_{ol} contents which are too low to be residual, and must have been affected by melt infiltration. The presence of the finer-grained olivine neoblasts may reflect this process, although the fact that the adjacent orthopyroxene is embayed is usually attributed to the incongruent melting of orthopyroxene (see below).

Orthopyroxene is present as isolated crystals and in crystal aggregates along with clinopyroxene and spinel (Plate 3.1a). In both situations, orthopyroxene crystals often display strained extinction and, more rarely, kink-bands. Within the orthopyroxene aggregates, orthopyroxene-orthopyroxene contacts vary from smooth and interpenetrating to curvilinear and well-recovered. Embaying of orthopyroxene grain boundaries by fine-grained olivine neoblasts is common throughout the Massif (Plate 3.1b). Lamellar and bleb exsolution of clinopyroxene is shown by approximately 25% of orthopyroxene crystals. The deformed nature of the orthopyroxene crystals suggests that most are residual grains from the partial melting event. This interpretation is consistent with the mineral chemistry data presented in the forthcoming chapter, which shows that the

orthopyroxene compositions fall on proposed partial melting trends. Resorption of grain margins and formation of neoblastic olivine is also consistent with incongruent melting of orthopyroxene (Girardeau and Lagabrille, 1992).

Clinopyroxene is present throughout the sequence, although only one or two grains per thin section may be present in the most depleted harzburgites. Clinopyroxene grain sizes are coarse in the serpentinite diapir and generally fine-grained in the *background* harzburgites. Spinel is also present as a minor phase, with porphyroclastic grains being volumetrically the most abundant textural type. Typical textures of each chemical division are described below and used to elucidate the origin of clinopyroxene and spinel in the Troodos peridotites.

3.2.1 *BACKGROUND* HARZBURGITES

The *background* harzburgites display textural and modal variations from the base to the top of the sequence. These textural and modal variations mirror mineral chemistry variations that are described in the following chapter. Modal proportions vary between approximately 75 to 80% olivine, 10 to 25% orthopyroxene, trace to 3% clinopyroxene and trace to 3% spinel. *Background* harzburgites at the base of the section typically have relatively high modal clinopyroxene (approximately 2 to 3 %), whereas samples from the uppermost parts of the section (i.e. the *top-of-the-sequence* harzburgites) only have one or two grains of clinopyroxene per thin section. Between these two extremes there is a gradual decrease in modal clinopyroxene upwards through the section. Six different textural types of clinopyroxene have been identified in the basal harzburgites.

Type 1. Medium to fine-grained, anhedral clinopyroxene crystals around the margins of orthopyroxene grains (Plate 3.1c). Crystals in this position either have equant shapes, or composite morphologies consisting of curvilinear contacts against the adjacent orthopyroxene and concave, interstitial contacts against the matrix olivine grains. A small proportion of these crystals display growth twins. The crystals in this position that have growth twins or the interstitial morphology are interpreted as having crystallised from a melt. The origin of the equant grains is equivocal. They may be either residual crystals or products of granule exsolution from orthopyroxene (Nicolas, 1989). A residual origin is preferred for the medium-grained crystals which are much coarser than the bleb clinopyroxene exsolution in orthopyroxene. The finer-grained crystals may result from either exsolution or partial melting.

Plate 3.1

a) Typical orthopyroxene aggregate in a Troodos harzburgite with associated irregular spinels and clinopyroxene. The field of view is 5 mm wide.

b) Olivine deeply embaying the margin of a porphyroclastic orthopyroxene in a Troodos harzburgite. The field of view is 2.5 mm wide.

c) Type 1 clinopyroxene (light yellow birefringence colour) located on the margin of an orthopyroxene aggregate in a Troodos harzburgite. The field of view is 1 mm wide.

d) Type 2 clinopyroxene (the light green coloured grains), consisting of 2 optically continuous crystal, which probably form 1 single grain in 3 dimensions, located in an interstitial position within an orthopyroxene aggregate in a Troodos harzburgite. The field of view is 1 mm wide.

A.

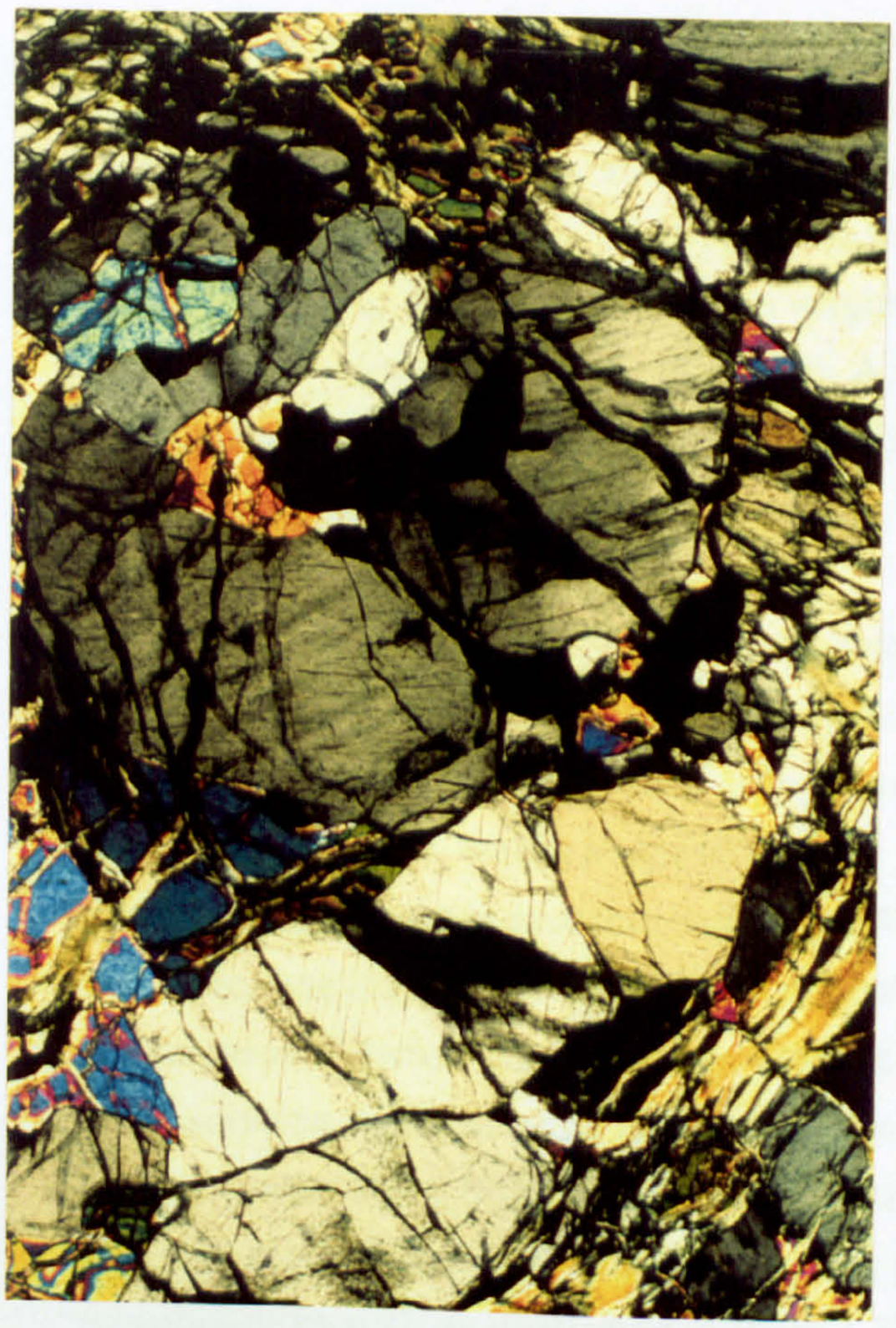

B.

C.

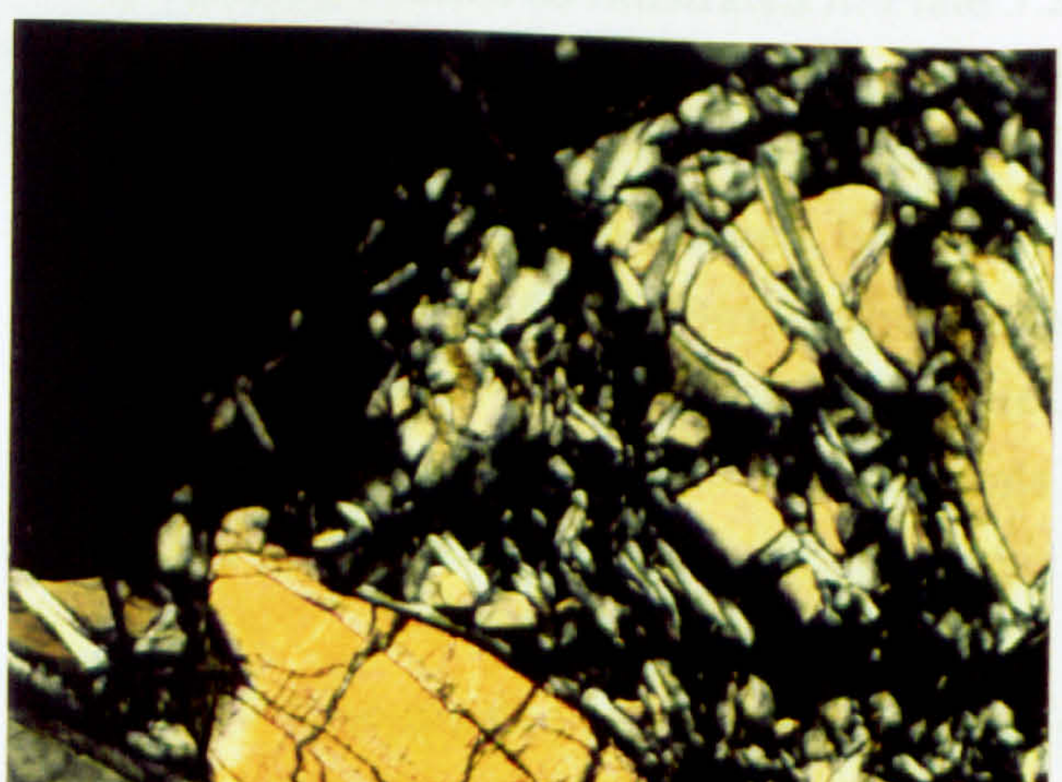

D.

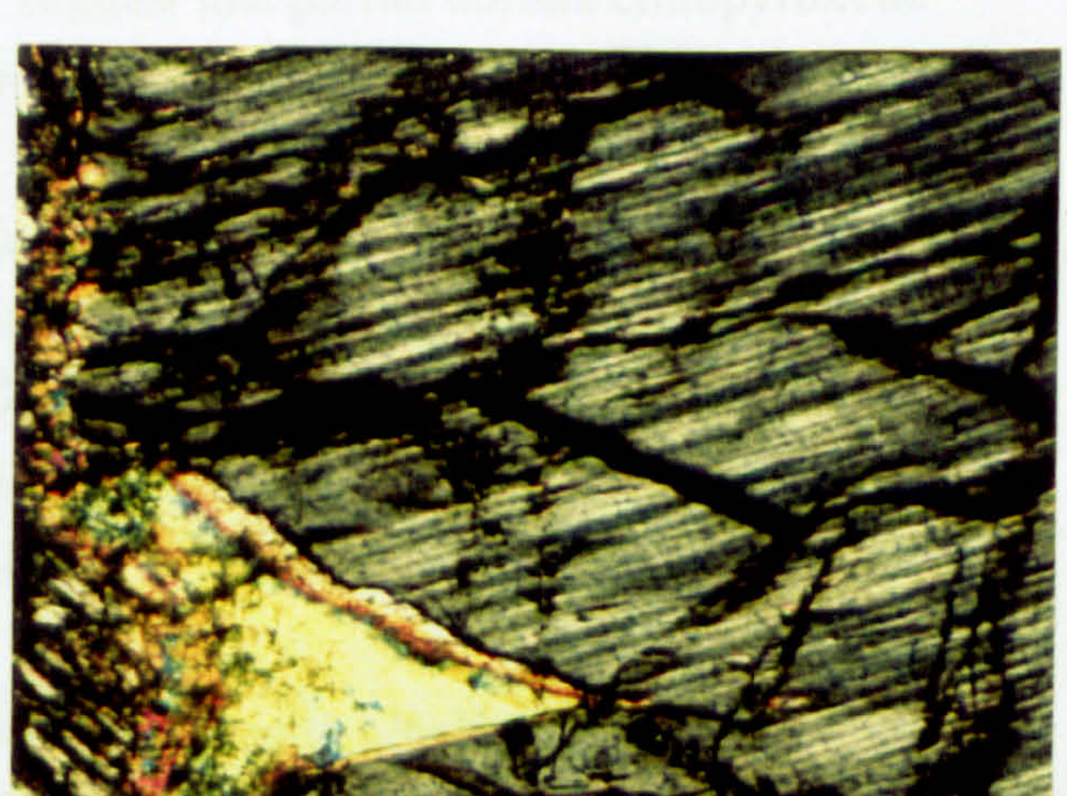

Type 2. Medium to fine-grained clinopyroxene crystals interstitial in orthopyroxene aggregates (Plate 3.1d). These occur as either single anhedral grains or several separate clinopyroxene grains within the same orthopyroxene aggregate, all of which have identical optical orientation. This suggests that they all form part of the same crystal in three dimensions, in which case a melt origin is inferred. However, the origin of the single anhedral grains is again equivocal. A residual origin is preferred for the medium-grained crystals and the finer-grained crystals may result from either granule exsolution or be residual from the partial melting event.

Type 3. Partial coronas of clinopyroxene around orthopyroxene grains (Plate 3.2a). These crystals are always preferentially located along the 001 faces of orthopyroxene grains. As the photomicrograph shows, these develop after the orthopyroxene grains have been embayed, which suggests that the coronas formed after the partial melting event. A melt origin is possible, with the orthopyroxene providing a substrate for clinopyroxene crystallisation. However, features characteristic of melt crystallisation, such as growth twins, have not been observed in these clinopyroxenes. Instead, an origin via exsolution from the associated orthopyroxene is proposed. The preferential location of the coronas along 001 faces would be consistent with an exsolution process. Rare, complex clinopyroxene crystals comprising part corona, part poikilitic and part interstitial morphologies such as illustrated in Plate 3.2b suggest that partial corona clinopyroxene crystals can be overgrown by melt crystallisation.

Type 4. Medium to fine-grained, isolated, anhedral clinopyroxene crystals in the olivine matrix. Morphologically these grains are usually unremarkable, however these grains occasionally have embayed margins (Plate 3.2c). The absence of magmatic features such as growth twins suggests that most crystals in this position are residual. The embayed nature of some of these grains supports this origin.

Type 5. Fine-grained clinopyroxene crystals intergrown with blebby spinel grains (Plate 3.2d). These are usually located within the olivine matrix and the clinopyroxene often occurs as several separate grains within the same intergrowth, all of which have identical optical orientation. In two cases, growth twins have been observed in these clinopyroxene crystals. Like the Type 1 and 2 clinopyroxenes, the optical continuity between grains and the presence of growth twins, suggests that these intergrowths crystallised from a melt. The same conclusion was reached by Edwards and Malpas (1996) and Suhr (1993) for similar intergrowths in Hess Deep and Bay of Islands peridotites respectively. The occurrence of these intergrowths in such diverse tectonic settings underlines the importance of melt infiltration in peridotite evolution.

Plate 3.2

a) Type 3 clinopyroxene (bright blue birefringence colour) forming a partial corona on an embayed orthopyroxene crystal in a Troodos harzburgite. The field of view is 0.5 mm wide.

b) Type 3 clinopyroxene (very irregularly shaped, yellow coloured crystal) forming a partial corona to the orthopyroxene crystal (located on the right hand edge of the photomicrograph) and overgrowing to form an interstitial morphology to the matrix olivine (located on the left hand side of the photomicrograph) in a Troodos harzburgite. The field of view is 1 mm wide.

c) Type 4 clinopyroxene, isolated and embayed crystal in the olivine matrix in a Troodos harzburgite. The field of view is 1 mm wide.

d) Type 5 clinopyroxene intergrown with spinel in a Troodos harzburgite. The field of view is 1 mm wide.

A.

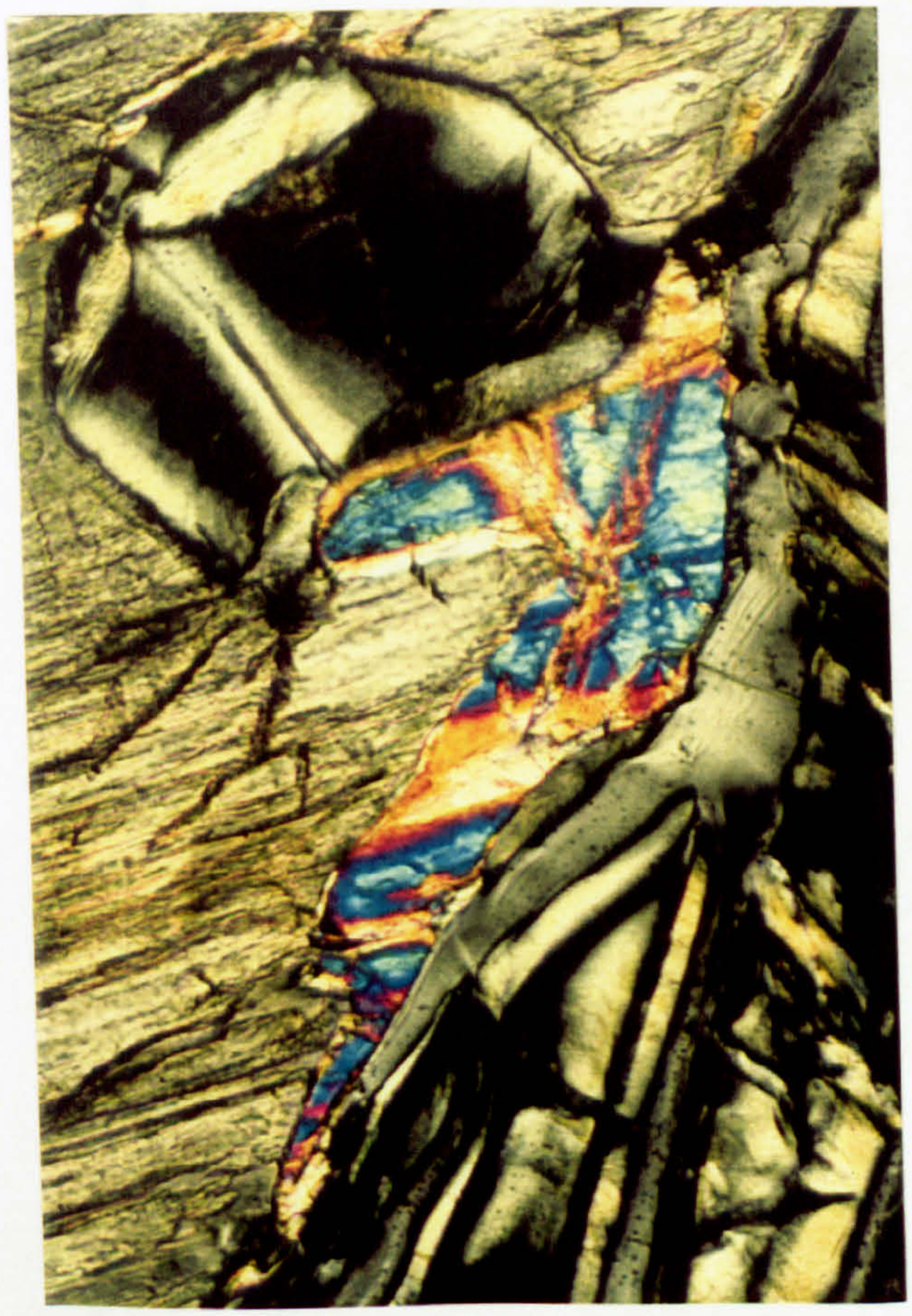

B.

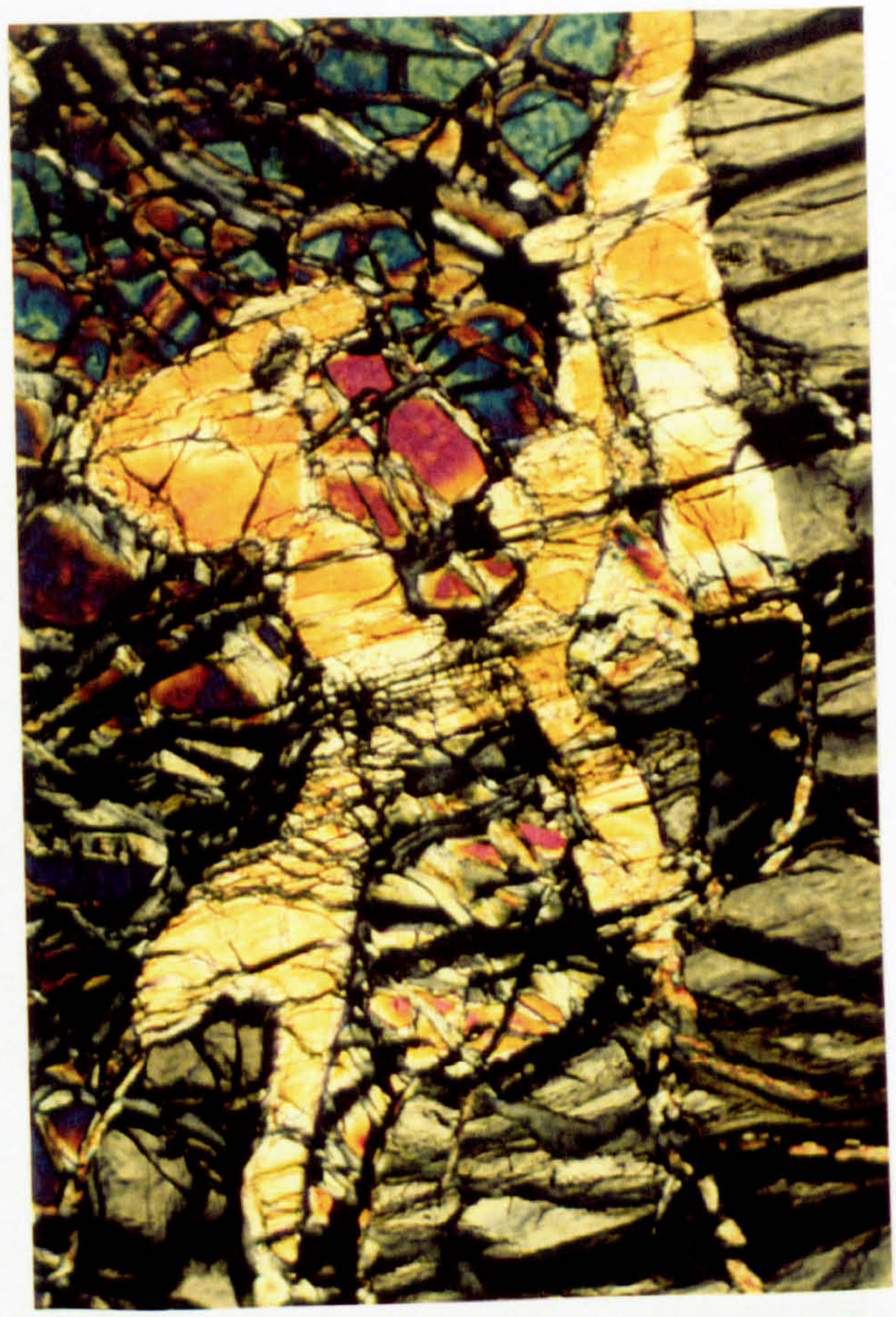

C.

D.

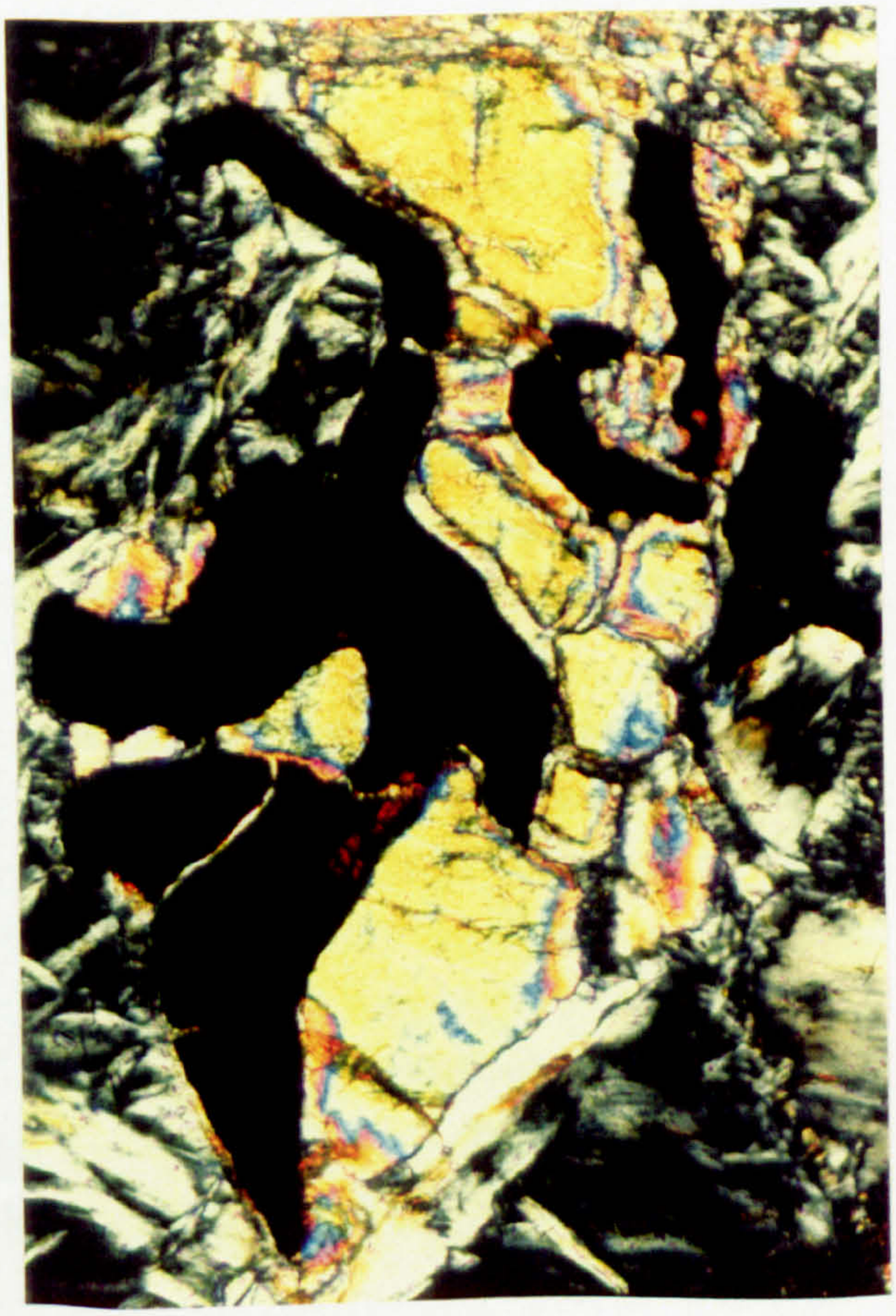

Type 6. Fine-grained, anhedral clinopyroxene crystals on the margins of porphyroclastic spinel grains. These crystals usually display growth twins and are therefore interpreted as melt products.

Of these textural varieties, Types 1, 2 and 5 are the most common in the basal harzburgites. With decreasing depth in the sequence, the fine-grained clinopyroxene-spinel intergrowths (Type 5) and partial coronas (Type 3) become less common, and are completely absent from the *top-of-the-sequence* samples. In the *top-of-the-sequence* samples, clinopyroxene is present mostly as anhedral crystals, often displaying growth twins, located on the margins of orthopyroxene aggregates and porphyroblastic spinel grains. These crystals are interpreted as melt-related.

Spinel textures also show a base to top zonation in the mantle sequence. *Background* harzburgites are characterised by bimodal spinel grain sizes throughout the section. Coarse spinel grains are typically porphyroclastic and are found throughout the section (Plate 3.3a). These grains display pull-apart deformation producing finer grain sizes, and define the foliation along with orthopyroxene. Rarely, coarse to medium-grained spinels are located within orthopyroxene-clinopyroxene-spinel aggregates. The spinel typically occupies a central position in the aggregate, with arms of spinel radiating outwards from the central spinel grain between the pyroxene crystals (Plate 3.3b). Both of these textural varieties are interpreted as residual. In particular, the orthopyroxene-clinopyroxene-spinel aggregates are similar to those described by Smith (1977), who attributed their formation to the breakdown of garnet during decompression and partial melting.

At all depths, the porphyroclastic grains often have rounded grain edges or hook-shaped growths on crystal edges. This suggests that spinel dissolution and regrowth occurred throughout the harzburgite evolution. In one remarkable sample from a *background* harzburgite collected immediately to the south of the *Anomaly 2* harzburgites, a euhedral spinel grain has a fringe of fine-grained vermicular spinel and clinopyroxene (Plate 3.3c).

The fine-grained spinel population varies in texture with depth in the sequence. Harzburgites from the base of the sequence have fine-grained spinel in intergrowths with clinopyroxene, as described above (e.g. Plate 3.3b). In the *top-of-the-sequence* harzburgites however, fine-grained spinel is present as subhedral to euhedral grains which are interstitial to the matrix olivine (Plate 3.3d). Occasionally these grains form partial chain textures. Another characteristic of the *top-of-the-sequence* samples is the occasional occurrence of coarse, anhedral, poikilitic spinel grains, which enclose fine-grained olivine oikicrysts. These are generally located along the foliation from non-

poikilitic spinel porphyroclasts, and are interpreted as fragments of pulled-apart spinel porphyroclasts which have undergone a phase of overgrowth, during which olivine was enclosed in the spinel crystal.

In addition to these fine-grained spinel types, most samples contain some fine-grained, anhedral spinel grains which are always preferentially located close to, or within, the orthopyroxene aggregates. A very small proportion of the spinel population (approximately one or two grains in every three or four samples) occurs with one of two distinctive textures. Either, as very fine wormy grains along the contacts between orthopyroxene and olivine crystals, or as fine to medium-grained spinel embayed by fine orthopyroxene crystals. In the best developed examples of the wormy spinel type, the spinel grains form partial coronas around resorbed orthopyroxene grains. Both of these textural types are more commonly found in the orthopyroxenite bodies and are illustrated and described in more detail in Section 3.2.3. The significance of these textures will be discussed below.

The spinel-clinopyroxene intergrowths in the harzburgite at the base of the section have already been interpreted as melt-related (see above). The euhedral morphology and interstitial location of the fine-grained spinel population in the *top-of-the-sequence* harzburgites, suggests that they are also melt-related. The presence of melt in the *top-of-the-sequence* harzburgites is supported by the poikilitic character of some of the coarse spinel grains. The difference in texture of the fine-grained spinel between the top and the bottom of the sequence is notable, considering an origin via melt infiltration is preferred for both textural types. Possible reasons for the textural variation are discussed below.

The textural variations recorded in the *background* harzburgites are summarised in Table 3.1.

	Base of sequence	Top of sequence
Clinopyroxene	modal % decreases from the base to the top of sequence	
	wide textural variety	mostly anhedral grains with growth twins
Spinel	coarse porphyroclastic grains throughout	
	fine spinel in intergrowths with pyroxenes	fine spinel, sub-euhedral and interstitial to olivine

Table 3.1 Summary of the main modal and textural variations in the *background* harzburgites.

Plate 3.3

a) Typical porphyroclastic spinel in a Troodos harzburgite. The field of view is 10 mm wide.

b) Spinel-orthopyroxene-clinopyroxene aggregate with centrally located spinel grain displaying radiating 'arms' of spinel between the associated silicates in a Troodos harzburgite. The field of view is 2.5 mm wide.

c) Euhedral spinel with fringing overgrowth of fine-grained vermicular spinel and clinopyroxene in a Troodos harzburgite. The field of view is 5 mm wide.

d) Interstitial, fine-grained, subhedral spinel in a *top-of-the-sequence* harzburgite, note the location of the spinel interstitial to the matrix olivine. The field of view is 5 mm wide.

A.

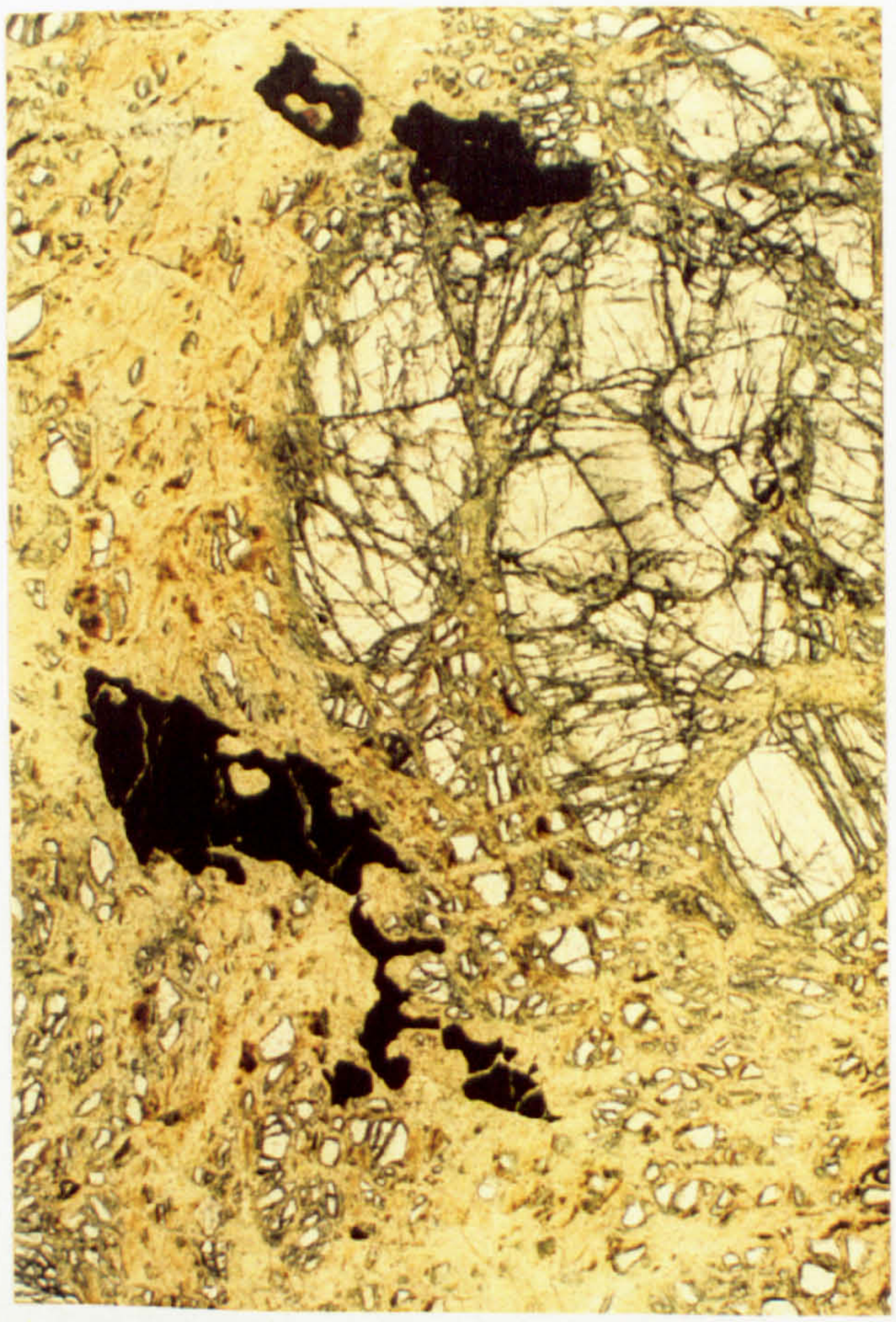

B.

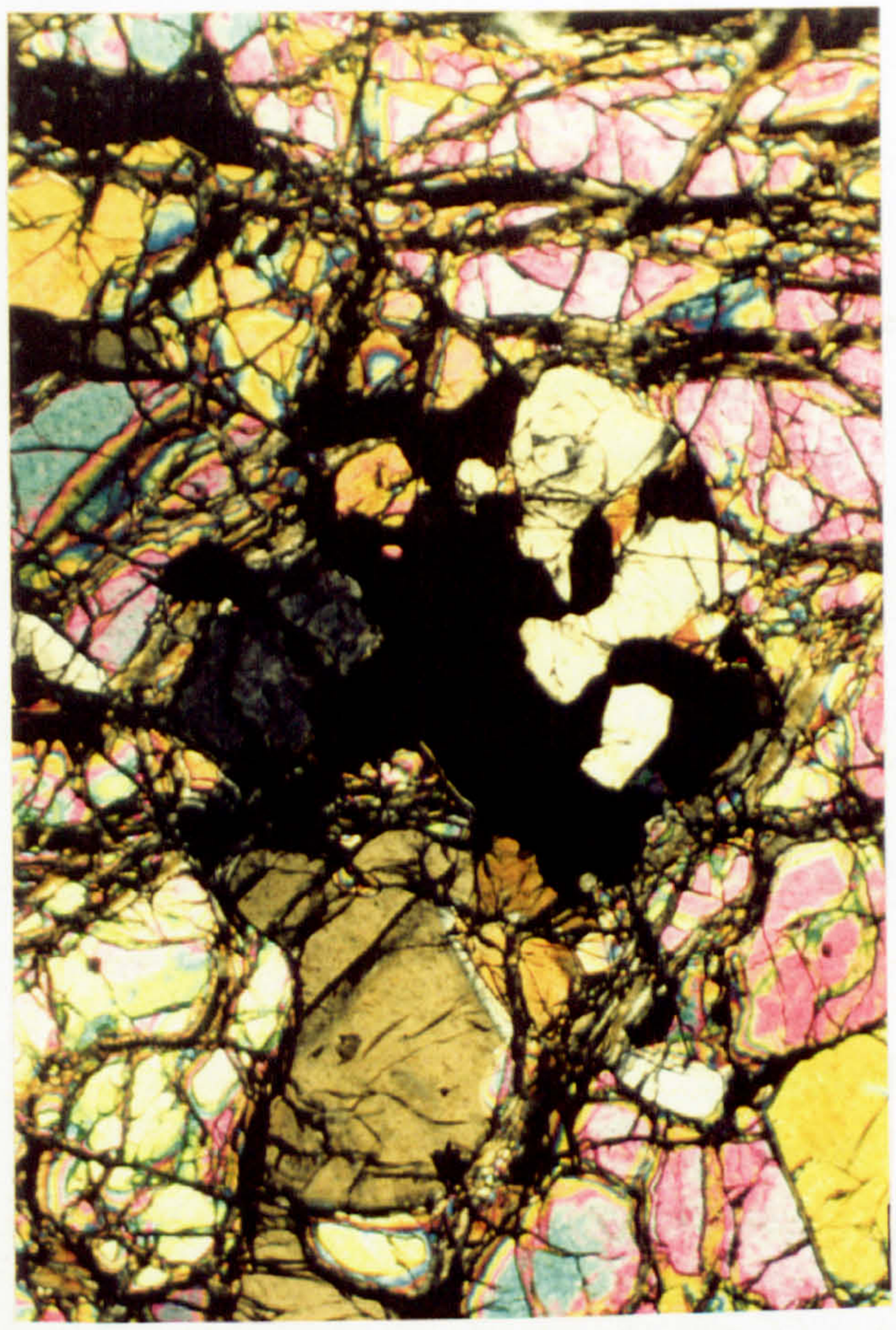

C.

D.

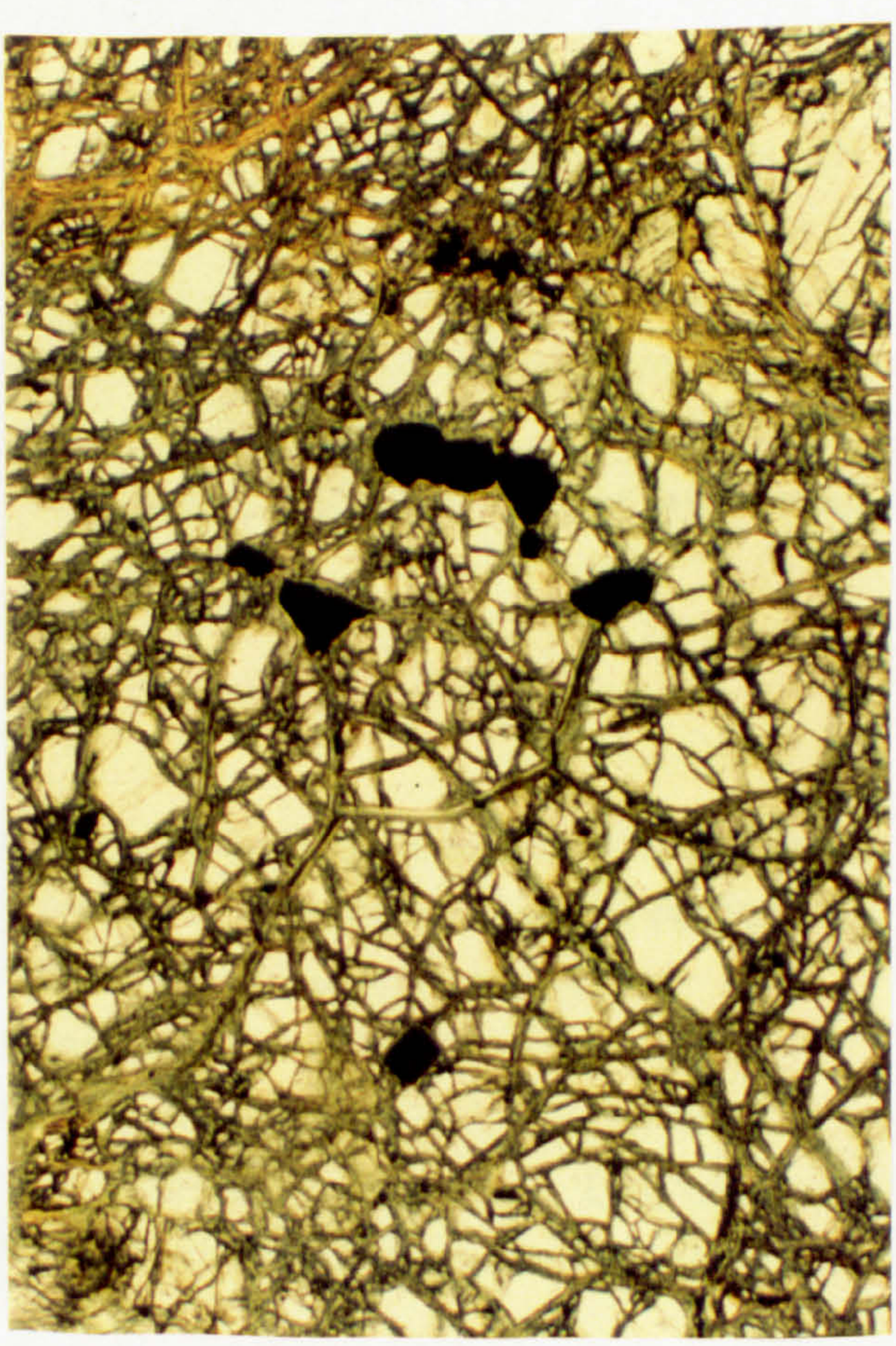

3.2.1.1 *ANOMALY 1* HARZBURGITES

Anomaly 1 harzburgites combine the textural characteristics of the *top-of-the-sequence* harzburgites with relatively high, but variable, modal clinopyroxene contents (approximately 0.5 to 3 %). Clinopyroxene textures are the most distinctive feature of the *Anomaly 1* harzburgites, with coarse, anhedral grains that poikilitically enclose olivine (Plate 3.4a) being unique to these samples. The coarse, poikilitic grains generally form trails parallel to foliation. Individual clinopyroxene crystals are undeformed and often have growth twins. Another distinctive feature of these crystals is abundant red-brown coloured iron staining of the clinopyroxene grains and possible fine spinel exsolution along cleavages. Clinopyroxene also commonly occurs as anhedral crystals located on the margins of orthopyroxene, and as interstitial crystals within orthopyroxene aggregates. Fine-grained clinopyroxene crystals intergrown with blebby spinel grains (the Type 5 clinopyroxene described above) are occasionally found in these samples.

The poikilitic texture of clinopyroxene in the *Anomaly 1* harzburgites, and the presence of growth twins, supports an origin via melt crystallisation. The fact that these crystals are located in trails parallel to foliation, and that the individual crystals are undeformed, indicates that crystallisation took place under conditions of directed stress (Girardeau and Lagabrielle, 1992).

Spinel in the *Anomaly 1* harzburgites has a similar range of textures as spinel in the *top-of-the-sequence* harzburgites, namely coarse porphyroclastic grains and fine euhedral crystals in the olivine matrix. As noted above, there is also a small proportion of blebby spinel intergrown with clinopyroxene similar to that found at the base of the sequence. Again a melt origin is inferred for the fine-grained spinel population. The occurrence of both fine euhedral grains and intergrowths is significant, and is discussed in more detail below.

3.2.1.2 *ANOMALY 2* HARZBURGITES

Anomaly 2 harzburgites are characterised by the abundance of vermicular spinel-silicate intergrowths (Plate 3.4b), which are usually located in the pressure shadows of pyroxene crystals. The intergrown silicate is usually, but not exclusively, clinopyroxene. Orthopyroxene and olivine also occur in the intergrowths. A cluster of fine, equant, subhedral spinel grains also occurs in one of the *Anomaly 2* samples and may be equivalent to the fine-grained spinel in the *top-of-the-sequence* samples. Clinopyroxene (approximately 1.5%) is present either as anhedral grains on the edge of orthopyroxene

clusters, which have concave interstitial contacts against the matrix olivine (similar to the Type 1 clinopyroxene described above), or as intergrowths with spinel.

There are three possible processes which could produce the vermicular intergrowths: partial melting, melt infiltration or exsolution. The high proportion of spinel in these intergrowths means that exsolution is unlikely to be responsible for their formation. The absence of these intergrowth textures from other *background* harzburgites also suggests that partial melting is unlikely to be responsible for their formation. It is inferred, therefore, that an origin via melt interaction is the most likely explanation. This is supported by the mineral chemistry evidence for melt reaction in the *Anomaly 2* harzburgites. The fact that the intergrowths are preferentially located in the orthopyroxene pressure-shadows suggests that melt infiltration occurred during the mantle deformation.

3.2.1.3 INTERPRETATION OF *BACKGROUND* HARZBURGITE PETROGRAPHY

As discussed in the following chapter, there are two main processes which control harzburgite mineral chemistry in the Troodos sequence: partial melting and reaction between the peridotites and melts. The mineral chemistry data presented in the next chapter suggest that the degree of partial melting increases upwards through the section, and that reaction with melts has been most significant in the *Anomaly 1* and *2* harzburgites. There are three significant petrographic variations from the base to the top of the Troodos mantle sequence: an up-section decrease in the modal proportion of clinopyroxene, an up-section decrease in the textural variety of clinopyroxene and a change in the texture of the fine-grained spinel population.

As pointed out in several studies (Bonatti and Michael, 1989; Dick *et al.*, 1984; Kostopoulos, 1991), the progressive evolution towards more mafic mineral compositions in peridotites during partial melting, is accompanied by changes in the modal proportions of the peridotites. In particular, the modal proportion of clinopyroxene decreases in residues during melting, until it disappears at between 15-30% (Bonatti and Michael, 1989) or up to 42% (Kostopoulos, 1991) partial melting, depending on starting mineralogy and type of melting process. The mineral chemistry data from the *background* harzburgites suggest that the degree of partial melting increases upwards through the section and, as described above, the modal proportion of clinopyroxene decreases upwards through the sequence. A first order interpretation of the changes in modal composition in the Troodos mantle section would be that the modal clinopyroxene content of the *background* harzburgites reflects the degree of partial melting.

A.

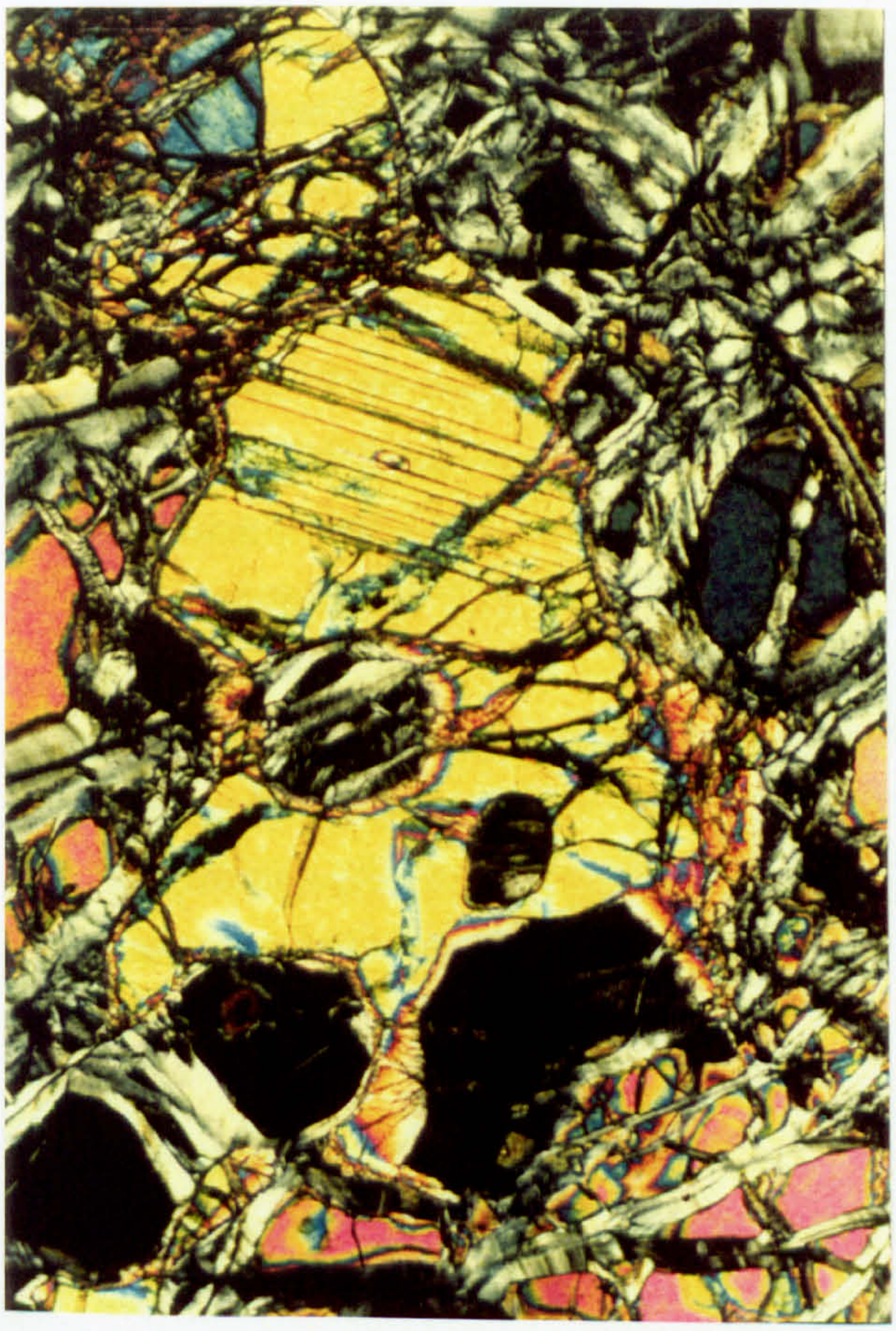

B.

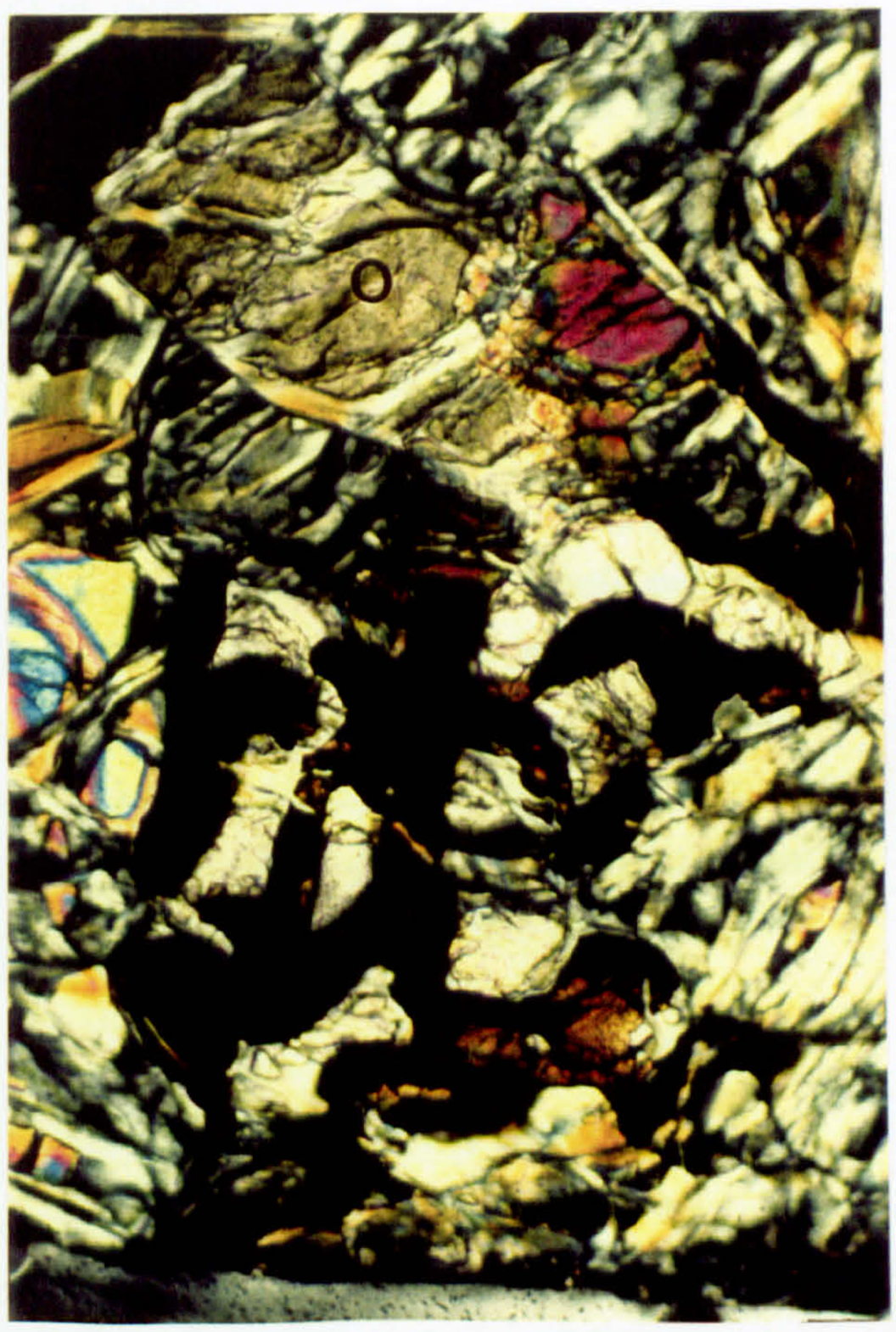

C.

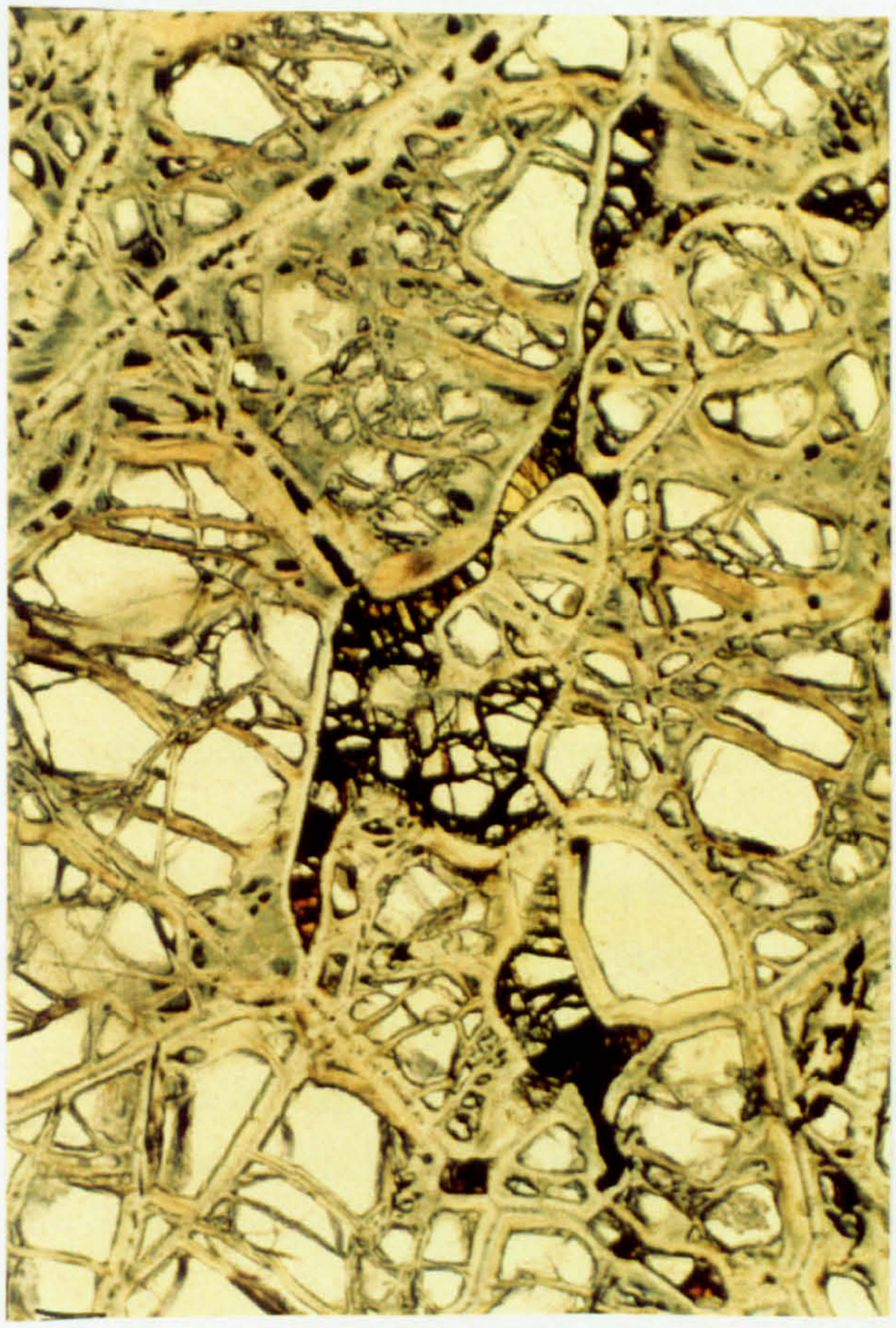

D.

As noted above, the *background* harzburgites at the base of the mantle section can also be distinguished from the *top-of-the-sequence* harzburgites by the greater textural variety of clinopyroxene. A significant, and variable, proportion of the clinopyroxene in the harzburgites at the base of the section has characteristics of melt-related crystals, such as growth twins and optical continuity between separate grains within the orthopyroxene aggregates. This suggests that, although the mineral chemistry data are consistent with these samples lying on partial melting trends (see Chapter 4), interaction with melt has also been a significant process during the evolution of these harzburgites. This supports the conclusions of Elthon (1992), who proposed that reaction with melts would produce mineral chemistry trends which mimic partial melting trends. However, the occurrence of the *Anomaly 2* harzburgites near the base of the section, which also have melt-related textures but which, in terms of mineral chemistry (see Figure 3.1 and Chapter 4), are compositionally more enriched than the adjacent *background* harzburgites, suggests that interaction between melts and peridotites was not a simple process in this part of the mantle section.

It is instructive to consider the ways in which melt might have reacted with the *background* harzburgites. Two end-member types of mantle-melt reaction can be considered. Firstly, if the melt infiltrates into the peridotite, is trapped and then crystallises, the melt should be recognisable as a distinctive mineral assemblage or texture. Secondly, if the melt flushes through the peridotite, reacting with the host minerals but not directly precipitating any new crystals, the resulting peridotite will not necessarily develop any distinctive mineral assemblages or texture. In both cases, the mineral chemistry of the peridotite will indicate that interaction with melt has occurred. A third scenario can be envisaged, in which textures characteristic of melt involvement can be produced at the same time as residual mineral chemistries are preserved. In this case, a percentage of the melt produced *in situ* by partial melting might remain in the source (Bottinga and Allègre, 1978; Rabinowicz *et al.*, 1986). Cooling of the peridotite below the solidus at any time during the partial melting event will crystallise the interstitial melt, producing textures indicative of the presence of melt but without enriching the minerals major element chemistries.

Therefore, a possible explanation for the relative abundance of melt-related clinopyroxene textures at the base of the sequence, might be that the last dregs of partial melt were not extracted from these peridotites and crystallised *in situ*. Theoretical studies show that partial melts in peridotites will be produced where the four harzburgite mineral phases are in contact (Maaløe, 1981), a condition which is most likely to be met within orthopyroxene-clinopyroxene-spinel aggregates. The location of most of the

clinopyroxene in these *background* harzburgites within the orthopyroxene aggregates is consistent with these studies, and with a local origin for the parental melt.

The fact that the incompatible element concentrations in the Troodos clinopyroxenes can not be modelled by a simple fractional melting process is discussed in the following chapter. A model of post-partial melting enrichment by fertile melts (a model conceptually similar to the open system melting model of Johnson and Dick, 1992) is proposed to explain the variations in clinopyroxene chemistry. The clinopyroxene trace element data suggest that clinopyroxene crystallised from a Nd-Sr-Zr-LREE-rich melt. Given the depleted nature of the Troodos harzburgites, this melt is unlikely to represent the last dregs of partial melt to be extracted.

These facts, together with the abundance of melt-related clinopyroxene in the base of the sequence, could be reconciled in two ways. Firstly, if the clinopyroxene does represent melt produced *in situ*, the Nd-Sr-Zr-LREE concentrations should be low because the source is depleted. The enrichments in these elements could have been produced via exchange with a fertile melt from deeper in the melting column which did not itself directly crystallise any new clinopyroxene. Secondly, if the clinopyroxene was directly crystallised from fertile transient melts, the hypothesis of decreasing amounts of partial melting with depth to explain the variations in mineral parameters could be erroneous, and might be better explained by melt-interaction mirroring partial melting trends (Elthon, 1992). These possibilities will be discussed in more detail in the Conclusions Chapter.

The mineral chemistry enrichments in the *Anomaly 2* harzburgites coincide with the appearance of vermicular spinel intergrowths which are not found in the other *background* harzburgites. This suggests that the melt which interacted with these harzburgites was not the same as that in the adjacent *background* harzburgites. This agrees with the mineral chemistry data, which indicate that the melt was relatively fertile and possibly from deeper in the mantle sequence. The location of the intergrowths in the orthopyroxene pressure shadows is consistent with melt interaction occurring during the mantle deformation event.

The gradual decrease in the textural variety of clinopyroxene upwards through the section is probably another reflection of the increase in the degree of partial melting upwards through the section. As partial melting progresses, the modal proportion of clinopyroxene decreases (Bonatti and Michael, 1989), and hence the number of residual grains will decrease. Orthopyroxene will also become more mafic (Bonatti and Michael,

1989) and will, therefore, be less able to exsolve clinopyroxene. This would reduce the potential for clinopyroxene to occur as partial coronas on orthopyroxene, or as exsolved granules around orthopyroxene crystals, in the *top-of-the-sequence* harzburgites because the orthopyroxene in these harzburgites would be undersaturated with respect to its clinopyroxene solid-solution component.

An increase in partial melting upwards through the sequence might also explain the variation in the texture of the fine-grained spinel population, from spinel-clinopyroxene intergrowths at the base of the section to euhedral spinel at the top. Both textural types have been interpreted as products of melt interaction (see above). The reason that melt only produces euhedral spinel at the top of the section might be that the *top-of-the-sequence* harzburgites are the residues of greater degrees of partial melting. This would mean that, prior to melt interaction, the *top-of-the-sequence* harzburgites were more undersaturated with respect to clinopyroxene than the harzburgites at the base of the section. The *top-of-the-sequence* harzburgites would, therefore, be capable of absorbing more clinopyroxene from the melt before crystallising free clinopyroxene in intergrowths with spinel (e.g. work by Suhr and Robinson, 1994; Edwards and Malpas, 1996). This would leave spinel crystallising alone as interstitial, euhedral grains.

Anomaly 1 harzburgites have both fine-grained euhedral and intergrown spinel. These harzburgites also have a relatively high percentage of clinopyroxene with textures characteristic of melt crystallisation (i.e. poikilitic habit and growth twins). The high clinopyroxene contents suggest that a relatively large amount of melt has reacted with these harzburgites, which is consistent with the mineral chemistry data illustrated in Figure 3.1 and described in detail in Chapter 4. This would support the suggestion that the spinel-clinopyroxene intergrowths only crystallise when a certain degree of clinopyroxene saturation has been exceeded in the host harzburgite.

The nature and location of the minerals thought to be formed by melt interaction also allows a rough chronology to be established for the mantle deformation and melt infiltration events. It is generally agreed that the mantle is deforming during melting (Nicolas, 1989). Minerals related to melt infiltration in the *Anomaly 1* harzburgites are located in trails parallel to the foliation and are internally undeformed, implying that crystallisation occurred under conditions of directed stress. The melt-related minerals in the *Anomaly 2* harzburgites are located in the pressure shadows of the orthopyroxene, which suggests that melt infiltration occurred during the mantle deformation. It is possible, therefore, that the melt infiltration event in the *Anomaly 2* harzburgites was an older event than that in the *Anomaly 1* harzburgites.

3.2.2 DUNITES

The mineral chemistry data described in the following chapter suggests that the two main dunite-forming processes in the Troodos Massif are magmatic crystallisation and reaction between melts and peridotite. The petrography of the dunites was examined with the aim of establishing whether these processes produced characteristic textures.

The simple mineralogy of dunites means that the range of textures they record is much narrower than that in the harzburgites. Olivine grain sizes vary from medium to coarse-grained in all the dunites. Olivine is always anhedral and serpentinisation has destroyed crystal contacts in all samples. Spinel is typically fine to medium-grained, although rare coarse grains have been found. In most samples the alignment of spinel grains defines a foliation.

With the exception of the dunites that have interdigitating contacts against the harzburgites, spinels from the other dunites in the mantle section, including the marginal dunites associated with pyroxenites, are always subhedral to euhedral, and interstitial to olivine. Spinel aggregates sometimes form partial chain textures parallel to the harzburgite foliation and, rarely, the euhedral crystals develop rounded morphologies which suggests a period of dissolution after crystallisation. Occasionally, these dunites contain rounded, anhedral orthopyroxene crystals with finer grain sizes than those in the *background* harzburgites. These are interpreted as xenocrysts from the wallrock harzburgites. The textures of these dunites are consistent with crystallisation from a magma under conditions of directed stress.

Spinel in crustal dunites is fine-grained, euhedral and interstitial to olivine. Crustal dunites sampled close to the contact with the underlying harzburgites have a foliation, defined by the alignment of spinel crystals parallel to the harzburgite foliation. The characteristic feature of the crustal dunites is the presence of fine-grained, interstitial clinopyroxene (Plate 3.4c). There is a gradation between these fine-grained crystals and medium-grained clinopyroxene with poikilitic habits similar to those in the *Anomaly 1* harzburgites. These textures are also typical of magmatic cumulates, an interpretation which is consistent with the mineral chemistry variations in the crustal dunites described in the previous chapter.

Dunites with interdigitating contacts against the harzburgites have several unique petrographic features. Spinel is typically bimodal in grain size, occurring as coarse-grained, pulled-apart, porphyroclastic grains and fine, euhedral grains. The fine-grained

spinel forms only a very minor proportion of the total spinel content of these dunites. The porphyroclasts differ from those in the harzburgites only by having more rounded morphologies. In some samples, the porphyroclasts have numerous anhedral, twinned clinopyroxene crystals growing on their margins. The porphyroclastic spinel is typically associated with irregular, discontinuous bands of orthopyroxene, and individual porphyroclast fragments often contain high concentrations of olivine oikicrysts. Both the orthopyroxene bands and porphyroclastic spinel are aligned parallel to the harzburgite foliation. The orthopyroxene has similar morphologies to that in the *background* harzburgites and the bands have a variable clinopyroxene content. Rarely, very deeply embayed orthopyroxene crystals (Plate 3.4d) are also present as isolated grains in the olivine-rich parts of these dunites. Clinopyroxene is present as interstitial grains in the orthopyroxene bands and anhedral grains on the edge of orthopyroxene grains. Magmatic features such as poikilitic textures and optical continuity between interstitial grains are common. Clinopyroxene is also present as fine-grained, interstitial crystals in the olivine-rich areas of these dunites.

3.2.2.1 INTERPRETATION OF DUNITE PETROGRAPHY

The data suggest that dunite textures reflect the two proposed dunite-forming processes of magmatic crystallisation and melt-peridotite reaction. Magmatic spinel textures are most common and, notably, are found in the marginal dunites around orthopyroxenite bodies. The mineral chemistry data from the dunites is generally ambiguous (see Chapter 4), with some dunites having high TiO_{2spn} contents consistent with magmatic crystallisation but most having spinel compositions similar to the *background* harzburgites. As pointed out by several authors (George, 1978; Ceuleener and Rabinowicz, 1992; Nicolas, 1989), extensive melt-peridotite interaction can produce magmatic textures in the resulting lithologies. The presence of magmatic spinel textures in these dunites might, therefore, be misleading.

The textures of the spinel in the interdigitating dunites are thought to be inherited from the enclosing harzburgites during melt-peridotite reaction. The presence of the orthopyroxene bands in these dunites is also thought to be a result of this process. Both the orthopyroxene and porphyroclastic spinel would be restite grains in this interpretation. The rounding of spinel porphyroclast margins and their poikilitic morphology, suggest that dissolution and regrowth of spinel has occurred during the formation of these dunites. The availability of existing spinel grains as nuclei for neoblastic spinel possibly explains the relative absence of fine, euhedral spinel in these samples compared to the other mantle dunites. This evidence supports the field evidence and mineral chemistry data for

the formation of these dunites by reaction between melts and harzburgites. The relative abundance of magmatic clinopyroxene in these samples suggests that the melt involved was relatively fertile. There is however, surprisingly little textural evidence for the breakdown of orthopyroxene, other than the isolated embayed crystals.

3.2.3 PETROGRAPHY OF THE PYROXENITES

As described in the Fieldwork Chapter, there are three types of pyroxenite in the Troodos Massif: orthopyroxenites, clinopyroxenites and olivine-clinopyroxenites. The orthopyroxenites can be divided into three types on the basis of outcrop characteristics: *orthopyroxenite A*, *orthopyroxenite B* and pyroxene bands in the harzburgite. In terms of their mineral chemistries (see Chapter 4), the *orthopyroxenite A* bodies and pyroxene bands display trends of both Cr-Fe-Ti and Al-Mg enrichment in spinels, whereas the *orthopyroxenite B* bodies display the Al-Mg enrichment trend exclusively. Clinopyroxenites form massive bodies in the lowermost crustal dunites and olivine-clinopyroxenites form tabular veins located in the top of the harzburgite sequence.

The main aims of the petrological study were to determine whether the different outcrop or mineral chemistry divisions of the pyroxenites were associated with a characteristic petrography, and to see if there was any textural evidence for mantle-melt interaction during pyroxenite formation.

3.2.3.1 *ORTHOPYROXENITE A*

As a group, the *orthopyroxenite A* samples have a wide range of modal proportions. Orthopyroxene contents fall between approximately 75 and 95%, olivine between 2 and 20%, clinopyroxene up to 4% and spinel up to 2%. No petrographic differences were found between the Type I and II *orthopyroxenite A* samples.

The *orthopyroxenite A* intrusions consist of a mass of medium to coarse-grained, equigranular, anhedral orthopyroxene crystals. Orthopyroxene-orthopyroxene crystal contacts are always well recovered and curvilinear. Internal deformation of orthopyroxene is common, with crystals displaying strained extinction and kink-bands. *Orthopyroxenite A* thin-sections can be divided into orthopyroxene-rich patches which are separated by olivine-rich areas. The contacts between the two are marked by deep embaying of orthopyroxene by the olivine (Plate 3.5a). In the olivine-rich areas, grain sizes are fine to medium.

Clinopyroxene in the *orthopyroxenite A* samples is always located in the orthopyroxene-rich patches. Grain sizes are fine to medium and crystals are typically interstitial to the orthopyroxene. Growth twins are common and some clinopyroxene crystals have undulose extinction. In the clinopyroxene-rich samples, the clinopyroxene typically forms medium-grained, anhedral crystals, usually interstitial and often with undulose extinction.

Spinel grain size and texture vary with position in thin-section. Within the orthopyroxene-rich areas grain sizes are typically medium to coarse-grained, and the crystals have porphyroclastic morphologies. These crystals are usually oriented parallel to the contacts of the orthopyroxenite. The margins of these crystals are often embayed by fine-grained orthopyroxene and olivine crystals (Plate 3.5b). Rarely, spinel porphyroclasts are overgrown with rims of vermicular spinel intergrown with pyroxene, usually orthopyroxene. These are similar to those described in the *background* harzburgites (Section 3.2.1) and illustrated in Plate 3.3c. These textures suggest that a reaction relationship existed between the orthopyroxene and spinel.

Spinel is also located around the margins of the olivine-rich areas. In this position the spinel is always fine-grained, anhedral and irregular in shape. These crystals are always associated with fine-grained orthopyroxene, against which they have complex, interpenetrating contacts (Plate 3.5c). Fine-grained, irregular, wormy spinel grains also occur along the contacts of the orthopyroxene-rich and olivine-rich areas (Plate 3.5d). In extreme cases, wormy spinel grains can form partial coronas around orthopyroxene crystals which have rounded, resorbed morphologies. It is possible that the fine, anhedral grains and the worm-shaped grains are related, and the relationship of both with orthopyroxene again suggests that a reaction relationship existed between olivine, orthopyroxene and spinel.

Typically, individual thin-sections have predominately coarse, porphyroclastic spinel or fine, irregular spinel grains. It is uncommon for both types to be found together in a single section, although this may be due to the modal variability of the *orthopyroxenite A* samples on a thin-section scale. There does not appear to be any correlation between the predominant textural variety of spinel in a sample, and the mineral composition divisions into Type I and II pyroxenites.

In one unique sample, spinel crystals are coarse, equant and subhedral to euhedral in both the orthopyroxenite and adjacent marginal dunite. This pyroxenite also has a margin of fine-grained orthopyroxene against the contact with the dunite which may represent either

a chilled contact against the dunite, or recrystallisation of the dyke margin during deformation. None of the other *orthopyroxenite A* samples display any change in grain size towards their contacts.

3.2.3.2 *ORTHOPYROXENITE B*

Orthopyroxenite B intrusions are coarser-grained than the *orthopyroxenite A* samples and modal clinopyroxene contents are much lower. Modal proportions are variable, typically lying between approximately 80 and 95% orthopyroxene, 5 and 15% olivine, up to 2% spinel and trace clinopyroxene.

The segregation into olivine-rich and orthopyroxene-rich areas is not as strongly developed in the *orthopyroxenite B* samples, although occasionally the same inter-crystal relationships are developed as displayed by the *orthopyroxenite A* samples, with well-recovered orthopyroxene-orthopyroxene contacts and olivine embaying along orthopyroxene crystal edges.

Spinel mostly forms coarse, porphyroclastic grains with heavily embayed margins. Olivine is the most common embaying silicate. In contrast to the *orthopyroxenite A* samples, only a very small proportion of the spinel in the *orthopyroxenite B* samples occurs as fine-grained, irregular, wormy grains along the contacts of orthopyroxene and olivine crystals.

3.2.3.3 ORTHOPYROXENE BANDS IN HARZBURGITE

Orthopyroxene bands have the greatest variation in modal clinopyroxene content of all the orthopyroxenite bodies. Modal mineralogies vary between approximately 70 to 90% orthopyroxene, 10 to 25% olivine, up to 5% clinopyroxene and up to 2% spinel. Orthopyroxene-orthopyroxene contacts are, in general, slightly less recovered than in the *orthopyroxenite A* and *B* bodies, and orthopyroxene grain sizes within bands are much less uniform.

The distribution of clinopyroxene in these samples is extremely heterogeneous. In one thin section containing two bands, the modal clinopyroxene content varies between 5% in one band to trace amounts in the other. In the clinopyroxene-rich band, the clinopyroxene crystals are medium to coarse-grained and anhedral. In clinopyroxene-poor band the clinopyroxene is fine-grained and interstitial to orthopyroxene. Growth twins and undulose extinction are common in both.

Plate 3.5

a) Part of an *orthopyroxenite A* intrusion displaying an orthopyroxene-rich area (left hand side of the photomicrograph) with straight, well-recovered inter-crystal contacts which is embayed by olivine. The field of view is 10 mm wide.

b) Irregularly shaped spinel with deeply embayed contacts against orthopyroxene from an *orthopyroxenite A* intrusion. The field of view is 2.5 mm wide.

c) and d) Examples of irregular, wormy spinel grains in *orthopyroxenite A* intrusions.

c) Shows spinel forming a partial corona separating a heavily embayed orthopyroxene (white birefringence colour) from olivine. The field of view is 2.5 mm wide.

d) Spinel located on the edge of an olivine-rich area with associated orthopyroxene. The field of view is 2.5 mm wide.

A.

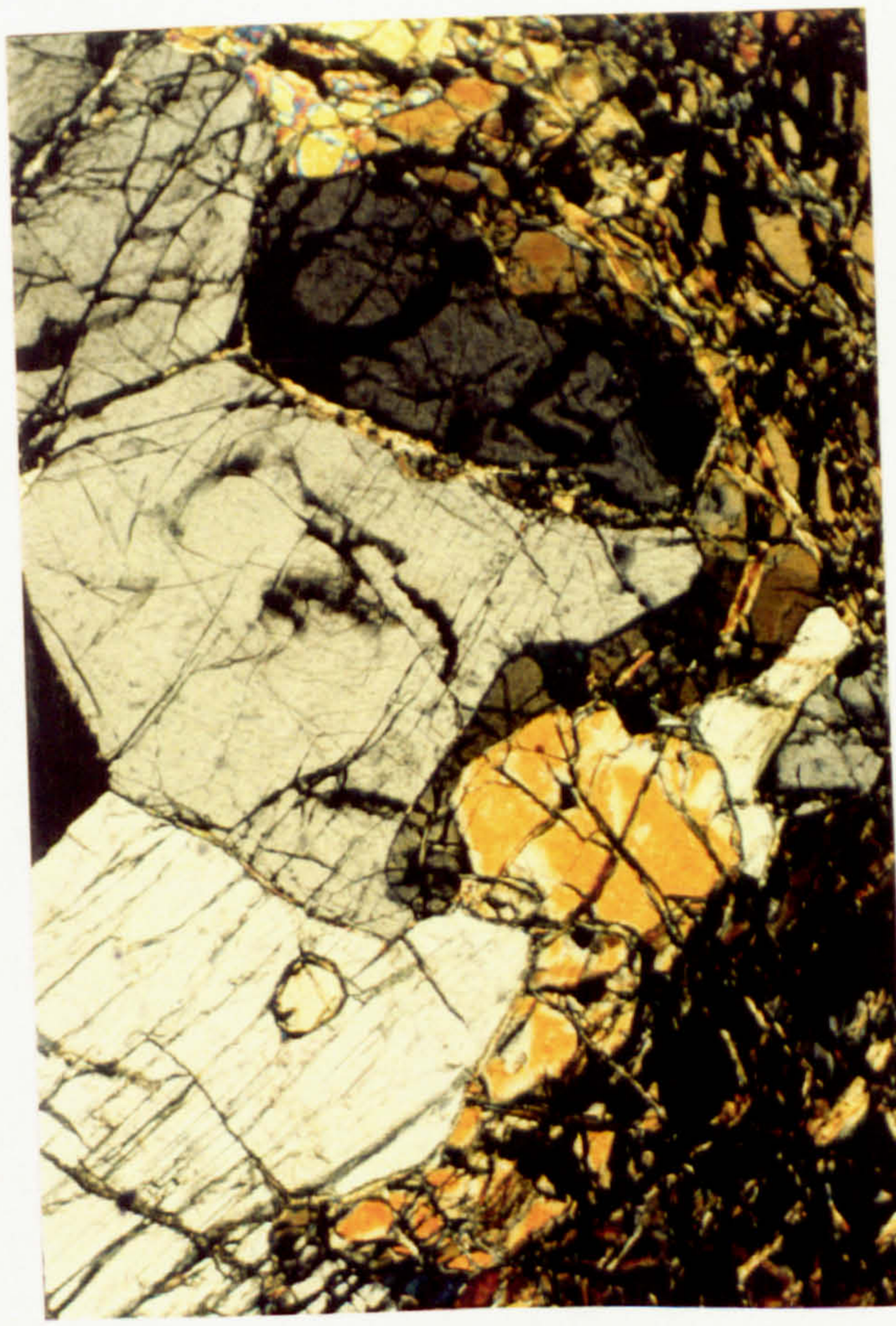

B.

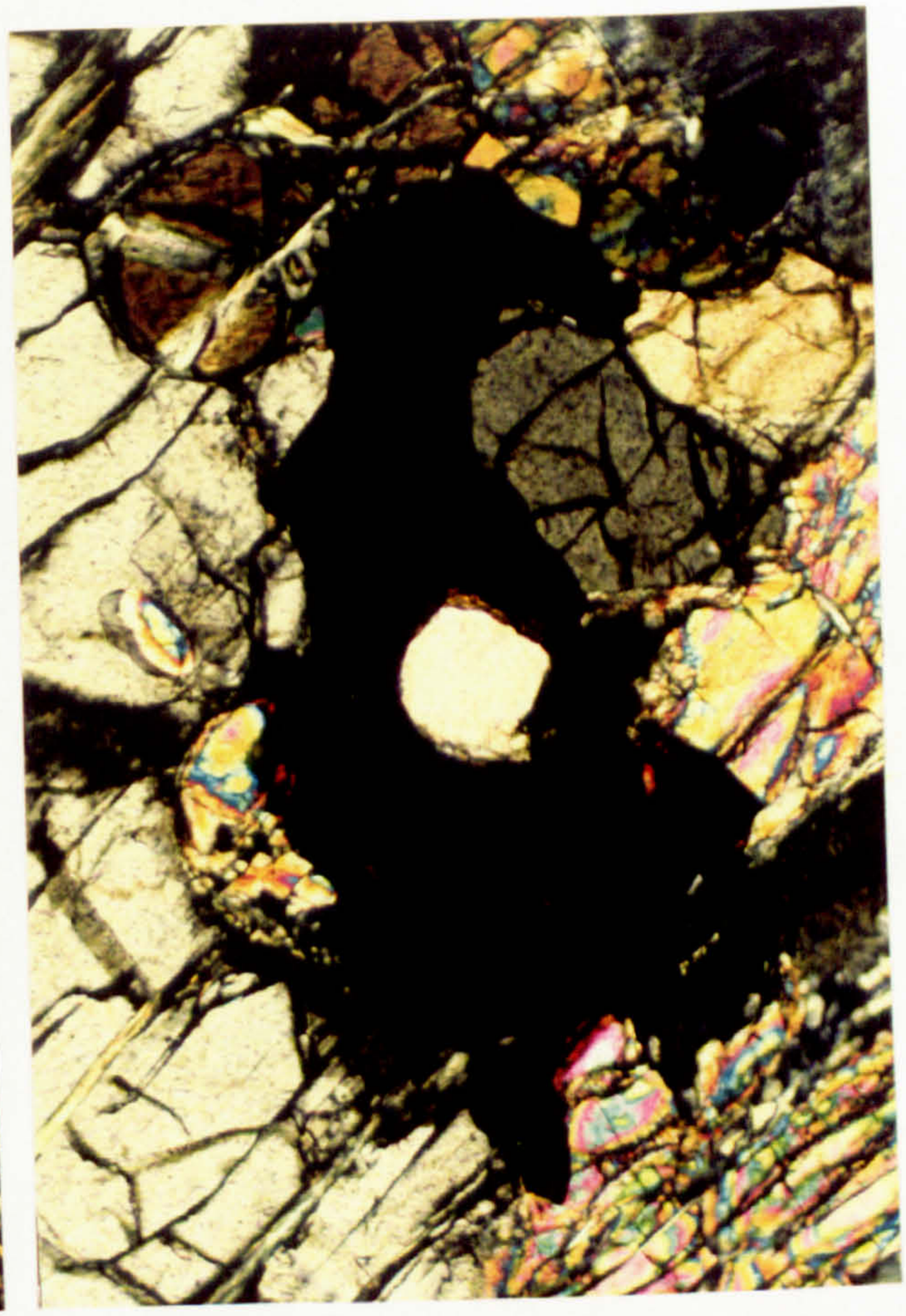

C.

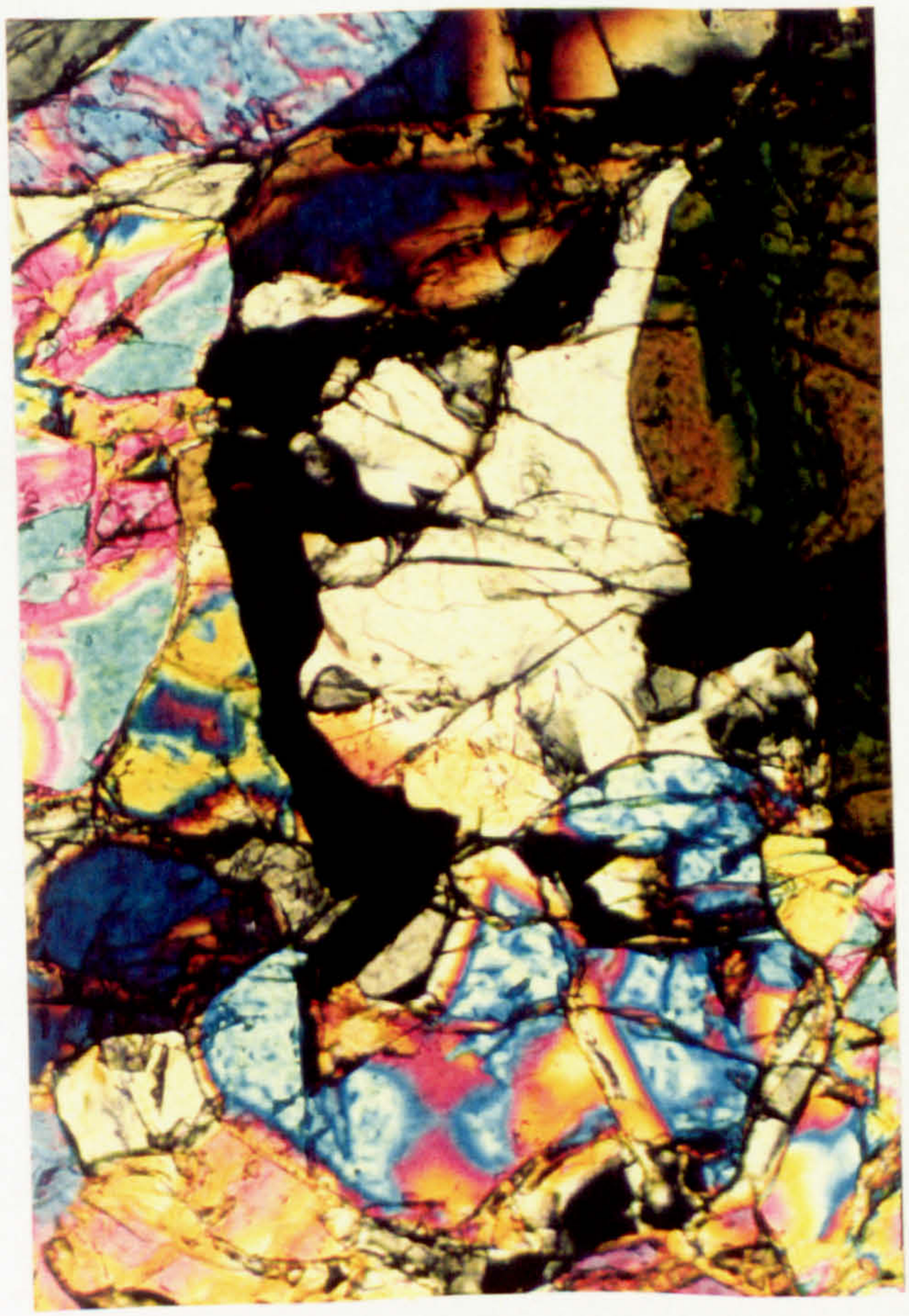

D.

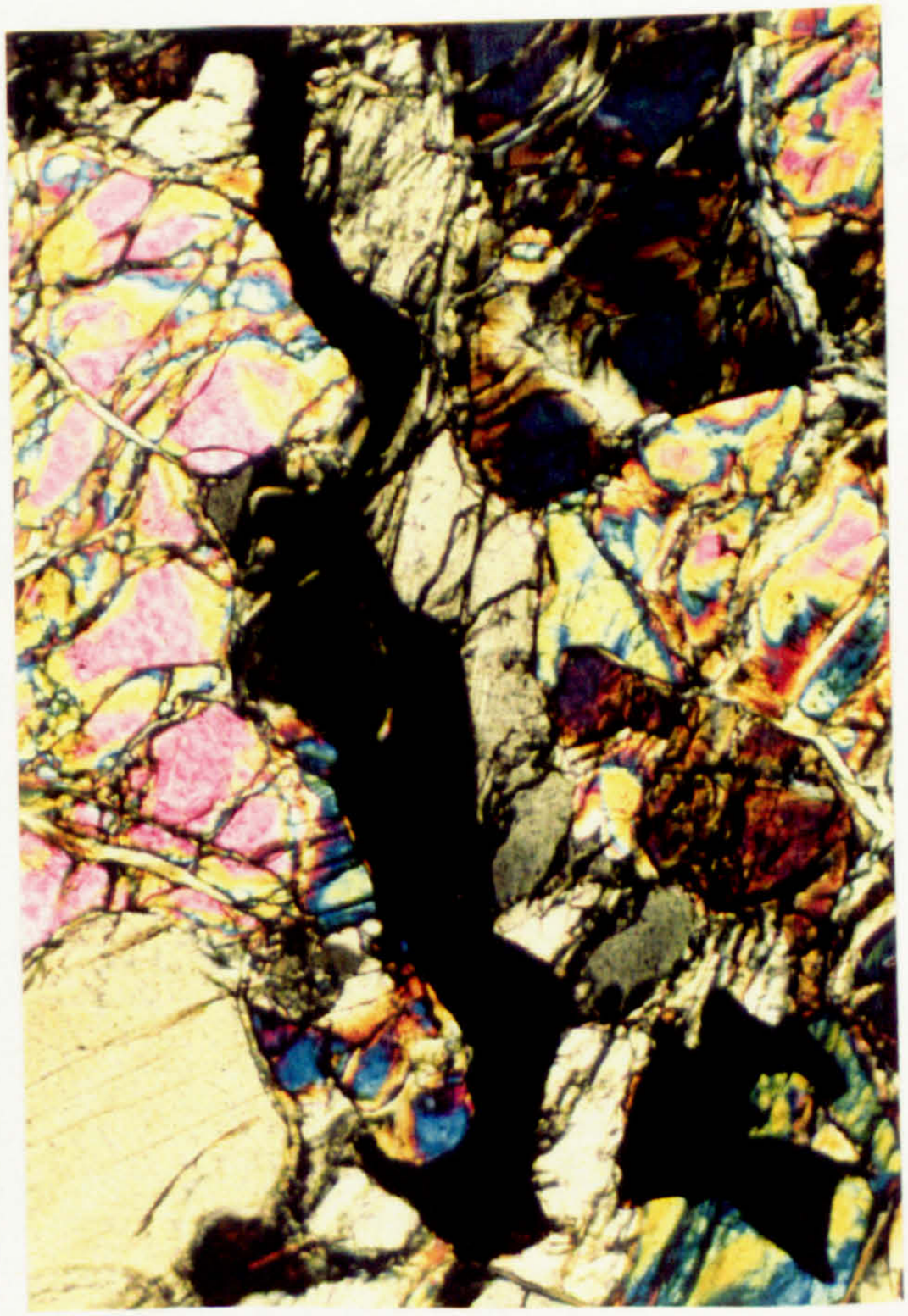

Spinel textures are variable and, in general, similar to those described from the *orthopyroxenite A* bodies. Fine-grained, irregular, wormy spinel grains located along the contacts of orthopyroxene and olivine grains are common and form crystals up to 1 mm in length; much larger than those in the *orthopyroxenite A* samples. Spinel also occurs as coarse, porphyroclastic crystals. Vermicular intergrowths of spinel and clinopyroxene or orthopyroxene, similar to those described from the base of the *background* harzburgites, are also found. In a similar way to the *orthopyroxenite A* samples, the spinel in any particular pyroxene band sample is predominantly either fine and wormy or coarse and porphyroclastic.

Contacts between the bands and enclosing harzburgite are irregular and sharp in thin-section. The adjacent harzburgite is generally dunitic and often contains orthopyroxene crystals which are very heavily embayed by olivine. Notably, the sample with the highest proportion of wormy spinel along orthopyroxene-olivine contacts also has the largest number of blebby spinel-orthopyroxene intergrowths in the adjacent harzburgite. These intergrowths will be described in more detail in Section 3.2.4.1.

3.2.3.4 CLINOPYROXENITES

Clinopyroxenites are typically coarse-grained and consist of a mass of interlocking plates of anhedral clinopyroxene (Plate 3.6a). Modal proportions vary between approximately 80 to 85% clinopyroxene, 15 to 20% olivine and trace orthopyroxene and spinel. There is no alignment of the clinopyroxene crystals, crystals are internally undeformed and occasionally poikilitically enclose olivine. Lamellar and bled exsolution of orthopyroxene is common. Crystal contacts are usually consertal, although curvilinear contacts are rarely found. Orthopyroxene forms partial coronas to clinopyroxene and spinel is typically fine grained and euhedral, except when poikilitically enclosed in clinopyroxene where the spinel crystals have rounded morphologies.

3.2.3.5 OLIVINE-CLINOPYROXENITES

Olivine-clinopyroxenites are generally fine to medium-grained and equigranular, with no strong shape or alignment fabrics (Plate 3.6b). Modal proportions are highly variable on a thin-section scale and fall between approximately 10 to 80% olivine, 20 to 90% clinopyroxene with trace spinel and orthopyroxene. Clinopyroxene occurs as ragged, interstitial crystals, often displaying growth twins and minor orthopyroxene exsolution lamellae. The coarser grains poikilitically enclose olivine crystals. Spinel is equant and subhedral to euhedral.

3.2.3.6 INTERPRETATION OF PYROXENITE PETROGRAPHY

The clinopyroxenites display several textural features consistent with an origin via crystallisation from a melt; namely consertal contacts between crystals, poikilitic habits and growth twins. The orientation of clinopyroxenites parallel to the harzburgite foliation suggests that they crystallised under conditions of directed stress during the mantle deformation. The unrecovered, consertal crystal contacts indicate that the intrusions were not subjected to any significant post-intrusion annealing, and therefore, were probably intruded at a late stage of the deformation event. This conclusion is supported by the absence of crystal lattice deformation.

The clinopyroxene in olivine-clinopyroxenites has similar morphologies to that in the clinopyroxenites, which suggests that they also have an origin from melt crystallisation. This is consistent with the occurrence of the olivine-clinopyroxenites as tabular veins and the habit of spinel in this lithology which is similar to that in the crustal dunites. The orientation of the olivine-clinopyroxenites suggests that they were not controlled by the mantle deformation and are, therefore, younger than the clinopyroxenites.

In contrast, the orthopyroxenites display abundant evidence for internal deformation of the constituent orthopyroxene crystals which, along with the field evidence for boudinage of the orthopyroxenites along the mantle foliation, suggests that they suffered more mantle deformation than the clinopyroxenites. They are, therefore, probably older than the clinopyroxenites. Crystal contacts are generally well recovered which indicates that the orthopyroxenites also experienced a longer period of recrystallisation than the clinopyroxenites. This is also consistent with the orthopyroxenites being the older intrusions. A magmatic origin for the orthopyroxenites is supported by the presence of growth twins in the interstitial clinopyroxene. The fact that the clinopyroxene is usually deformed suggests that the clinopyroxene crystallised prior to the mantle deformation, and is not a product of later melt percolation as is the case in the *Anomaly 1* harzburgites.

Spinel textures in the orthopyroxenites can be divided into the porphyroclastic type and the fine-grained anhedral type. The porphyroclastic spinel may result from deformation of originally euhedral magmatic crystals. However, orthopyroxenites probably reacted as fairly rigid blocks within the deforming harzburgite, with strain partitioning around them. If this was the case, it is unlikely that originally euhedral, magmatic spinel crystals could be subjected to enough strain to develop porphyroclastic morphologies. Alternatively, the porphyroclastic spinel might be inherited from the host harzburgite during

orthopyroxenite formation. This hypothesis would be consistent with the arguments developed in the forthcoming chapter for reaction between the host harzburgites and the incoming orthopyroxenite melt. The heavily embayed nature of the edges of the porphyroclastic grains suggests that they were out of equilibrium with the orthopyroxenite melt.

The fine-grained, anhedral spinel in orthopyroxenites characteristically forms wormy grains along olivine-orthopyroxene contacts and irregular grains associated with fine-grained orthopyroxene. Notably, both of these textural types are located on the edges of the olivine-rich areas. In the case of the wormy spinel, a reaction between olivine and orthopyroxene to produce spinel is suggested by the textural relationships of the minerals. The origin of the other fine-grained spinels is more ambiguous. One possibility is that they represent a more complete stage of the resorption of the porphyroclastic spinel, which is only preserved as coarse grains in the orthopyroxene-rich patches. Alternatively, they could be reaction products representing a stage further in the process that formed the wormy spinel. Whichever is the case, the textural evidence suggests that mantle-melt reaction was as significant a process during orthopyroxenite formation, as was direct crystallisation from a melt. The greater abundance of the fine-grained spinel in *orthopyroxenite A* bodies, and the predominance of porphyroclastic spinel in *orthopyroxenite B* bodies, suggests that the process of melt reaction was more important in the formation of *orthopyroxenite A* bodies.

The orthopyroxene bands in the harzburgite have similar textures to those in the *orthopyroxenite A* bodies. This supports Nicolas (1989) suggestion that pyroxenite banding is formed by rotation of orthopyroxenite intrusions into parallelism with the mantle fabric during mantle deformation. Edwards (1990) and Edwards and Malpas (1995) suggest that mechanical mixing and melt impregnation by orthopyroxenites might be an important mechanism in controlling the orthopyroxene contents of harzburgites and dunites in the Bay of Islands Ophiolite. The textural similarities between the pyroxene bands and orthopyroxenites in the Troodos mantle sequence suggests that a similar process of mechanical mixing during the mantle deformation event may have operated in the Troodos Massif. This hypothesis would also explain the rare occurrence of textures such as spinel coronas on orthopyroxene in the *background* harzburgites (Section 3.2.1), which might have been inherited from pyroxenites that are now intimately mixed with the harzburgite.

Plate 3.6

a) Typical clinopyroxenite intrusion displaying consertal textures, twinning and interstitial morphologies. The field of view is 10 mm wide.

b) Olivine-clinopyroxenite intrusion showing typical equigranular texture. The field of view is 5 mm wide.

c) and d) Spinel textures in pyroxenite wallrocks.

c) Blebby spinel associated with fine-grained orthopyroxene crystals. The field of view is 5 mm wide.

d) Irregular spinel fragments located within an orthopyroxene crystal. The field of view is 5 mm wide.

A.

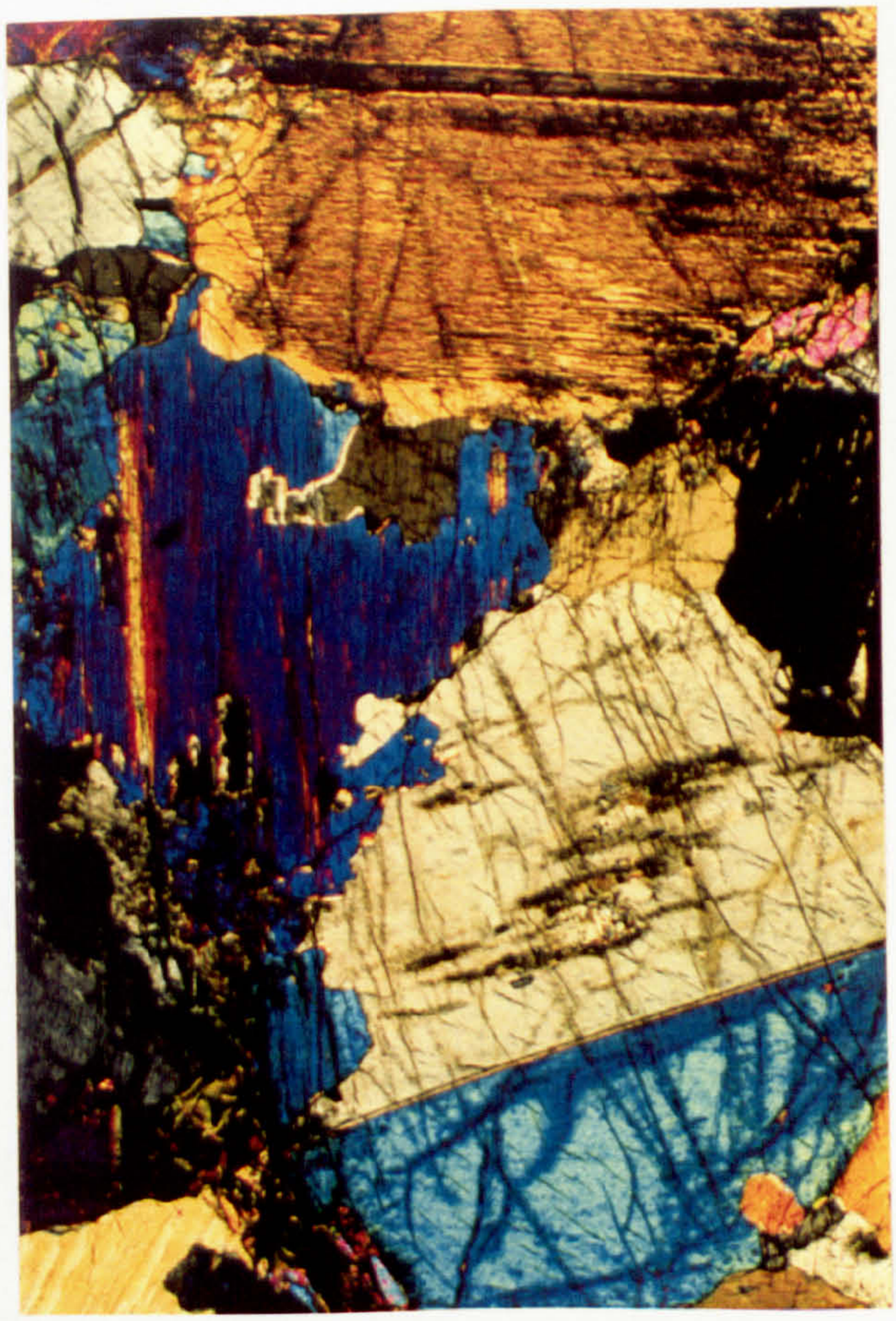

B.

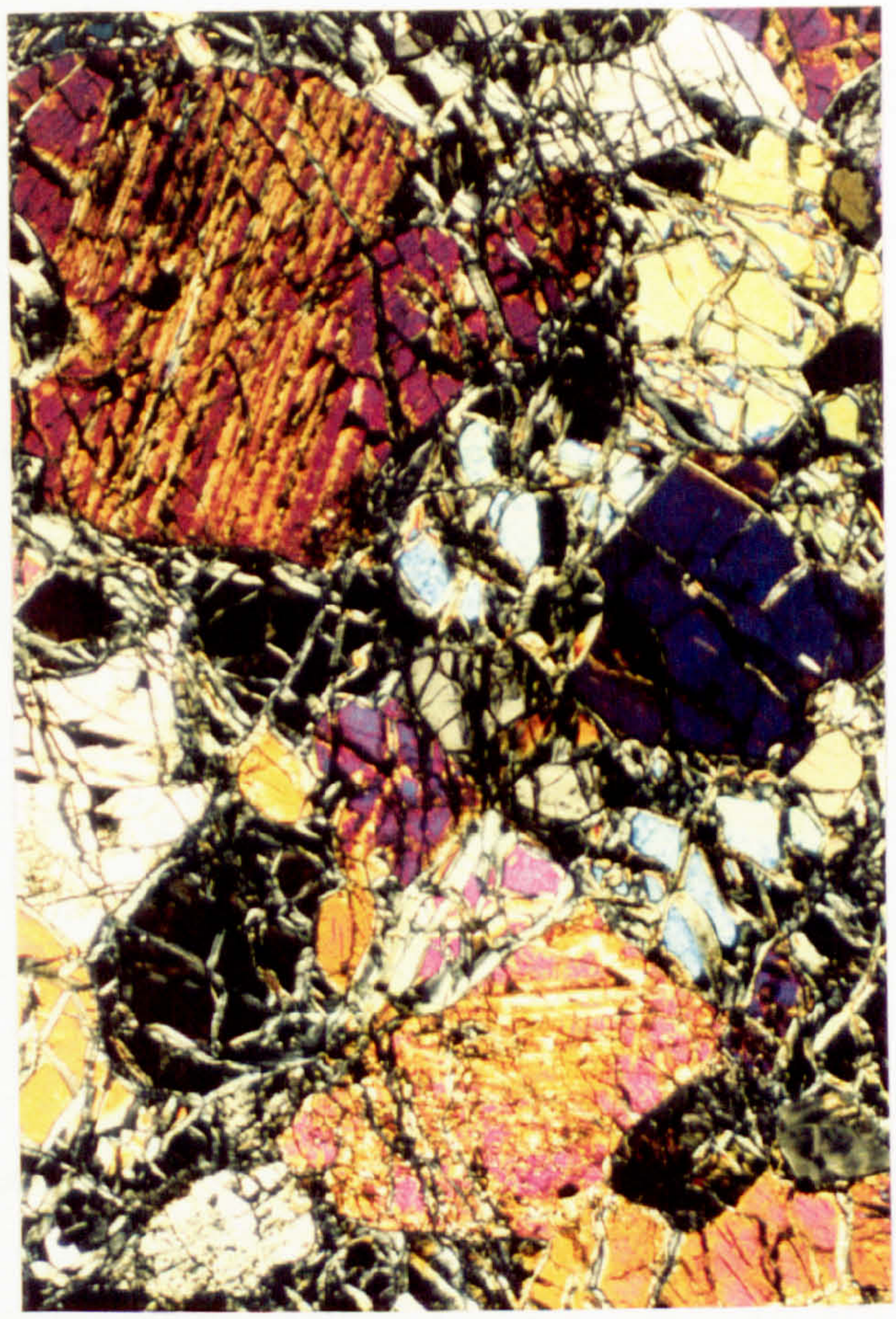

C.

D.

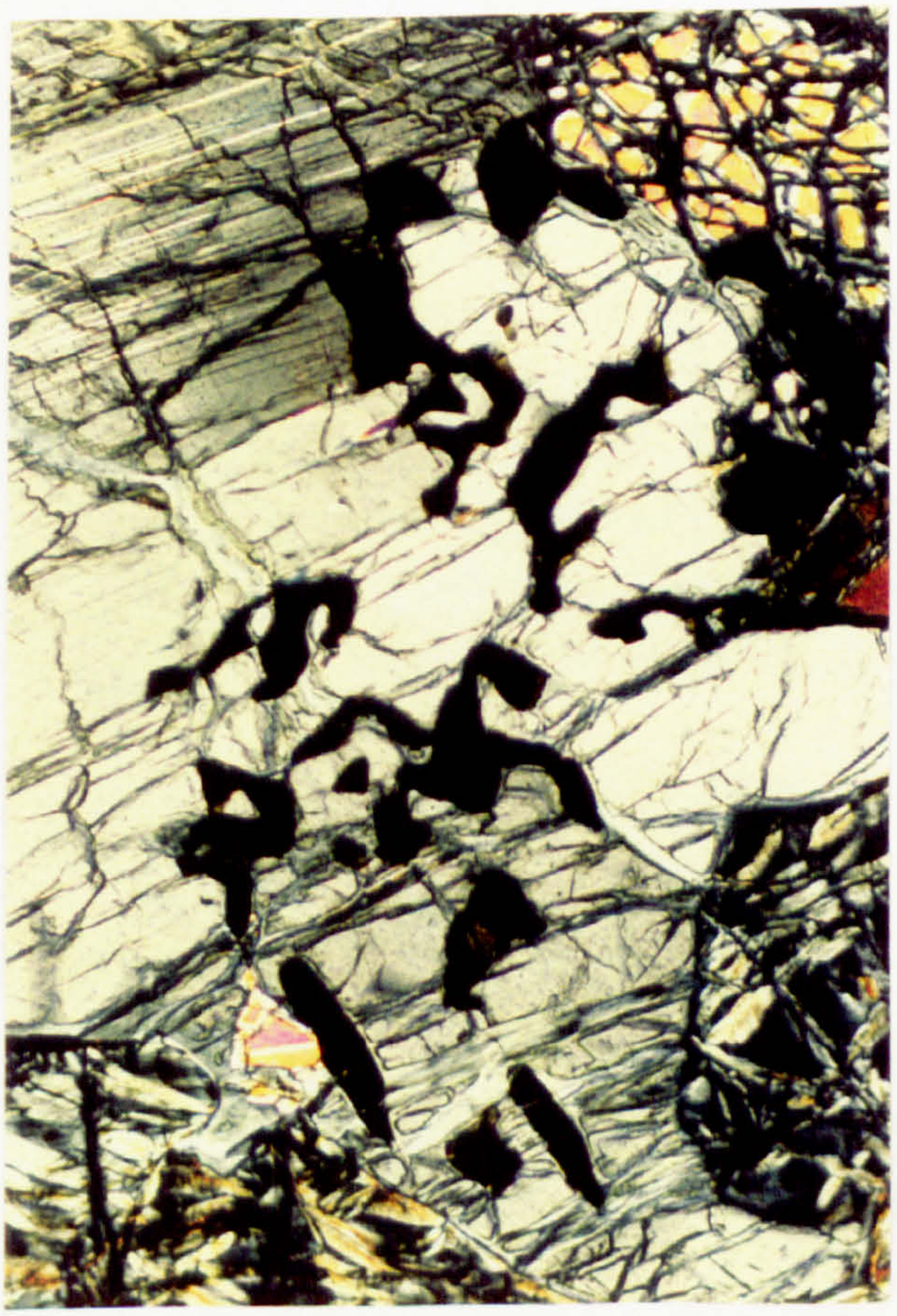

3.2.4 PETROGRAPHY OF WALLROCK HARZBURGITES

In this section, the petrography of wallrock harzburgites around pyroxenite intrusions and dunite bodies is described. The petrography of these harzburgites is compared with the *background* harzburgites to establish whether the formation of the pyroxenites produced any textural changes in the wallrocks. The petrology of the harzburgite *xenoliths* collected from the dunite tongue which separates the *Anomaly 1* harzburgites from the underlying *background* harzburgite sequence will also be described in this section.

3.2.4.1 PYROXENITE WALLROCKS

The banded harzburgites (harzburgites sampled from between the pyroxene banding) have textures with similarities to both the *background* harzburgites and the pyroxenite bands. As a group they are characterised by widely variable modal orthopyroxene contents between approximately 10 and 40%. In several samples, orthopyroxene forms large aggregates in which orthopyroxene-orthopyroxene contacts are curvilinear and well recovered, similar to those in the pyroxene bands. The edges of the aggregates are embayed by olivine. Clinopyroxene contents are generally less than 1% and spinel less than 2%.

Spinel textures range from porphyroclastic, which form only a small proportion of the total spinel population compared to the *background* harzburgites, to fine, wormy grains along orthopyroxene-olivine contacts. Medium-grained, blebby spinel grains which are always located close to the margins of orthopyroxene aggregates, and are intergrown with fine orthopyroxene, are also a common feature of these samples (Plate 3.6c). In half the banded harzburgite samples studied, a unique texture consisting of numerous, fine-grained, irregular spinel crystals within single medium to coarse-grained orthopyroxene crystals was found (Plate 3.6d). Sometimes the intergrowths are located in orthopyroxene pressure shadows but, more often, they show no preferred location in thin-section.

Like the banded harzburgites, the harzburgites sampled close to the orthopyroxenites often show textures similar to both the *background* harzburgites and the adjacent pyroxenite. *Orthopyroxenite A* wallrocks have spinel porphyroclasts with embayed margins and fine-grained blebby spinel associated with fine-grained orthopyroxene. In traverses away from *orthopyroxenite A* bodies the modal abundance of clinopyroxene decreases from approximately 2.5% at the marginal dunite-harzburgite contact, to 1.5% at 15 cm from the pyroxenite. The clinopyroxene crystals are always interstitial and usually

isolated within the olivine matrix rather than being associated with orthopyroxene aggregates.

Orthopyroxenite B bodies wallrocks also show a decrease in modal clinopyroxene away from the contacts; in the traverse studied the sample at the marginal dunite-harzburgite contained approximately 0.5% clinopyroxene, whereas at 15 cm from the contact only a trace of clinopyroxene was observed. Spinel is mostly porphyroclastic with less embayed margins than in the *orthopyroxenite A* wallrocks.

Only one sample was taken adjacent (approximately 10 cm from the contact) to an olivine-clinopyroxenite vein in this study. The petrology of the sample is very similar to that of the *top-of-the-sequence* harzburgites, which is not surprising considering that the sample was taken from within 100 m of the crustal dunite-harzburgite contact. The most important features of the section are the fine-grained euhedral morphology of spinel grains which are interstitial to both olivine and orthopyroxene, and the very low modal clinopyroxene content (less than 0.5%). Also, several orthopyroxene grains with apparently interstitial morphologies are present within the matrix olivine. The olivine which surrounds these crystals is medium to coarse-grained and the orthopyroxene crystals have undulose extinction.

3.2.4.2 DUNITE WALLROCKS

Harzburgites sampled from the contacts of dunite bodies are generally indistinguishable from the *background* harzburgites. In a few cases, the matrix olivine coarsens slightly towards the dunite and deeply embayed orthopyroxene crystals are more common than in the *background* harzburgites.

However, harzburgite samples collected from the contacts of the interdigitating dunites do have a relatively coherent set of textural characteristics. The spinel in these samples is typically entirely porphyroclastic and defines a strong foliation. The porphyroclasts are pulled apart along the foliation to a greater extent than in the *background* harzburgite samples. The individual porphyroclast fragments have knobbly, rounded morphologies similar to those described from the interdigitating dunites. Heavily embayed fragments of strained orthopyroxene are common in the olivine matrix. Clinopyroxene contents are low, usually less than 1%, and the crystals are always located on the margins of the orthopyroxene aggregates. The clinopyroxene crystals typically have interstitial morphologies against the matrix olivine.

3.2.4.3 HARZBURGITE XENOLITHS

Harzburgite *xenoliths* sampled from the dunite tongue share common outcrop characteristics of rounded, embayed margins against the enclosing dunite (see Fieldwork Chapter for more details), but mineralogically span a wide range of compositions from dunitic-harzburgite to wehrlitic. Orthopyroxene abundances vary from approximately 5 to 20% and crystals are usually embayed by olivine. The lowest orthopyroxene contents are found in the samples with the highest clinopyroxene contents, which vary up to a maximum of 10%. Clinopyroxene is medium-grained and forms aggregates, weakly aligned along the foliation, within which the clinopyroxene-clinopyroxene contacts are consertal. Some clinopyroxene crystals poikilitically enclose olivine. Spinel textures are relatively simple, mostly fine to medium-grained, equant, anhedral to subhedral, isolated grains. Porphyroclastic crystals are not present in these samples.

3.2.4.4 INTERPRETATION OF WALLROCK PETROGRAPHY

As a group the distinguishing feature of the wallrock peridotites is that they commonly display textures of both the *background* harzburgites and the adjacent pyroxenite or dunite. In particular, the occurrence in the banded harzburgites of the wormy spinel type along the edge of orthopyroxene crystals, and the unusual blebby spinel located within orthopyroxene crystals, suggests that the pyroxene banding in the harzburgite might indicate areas of mantle-melt reaction. In a similar way, the orthopyroxenite wallrocks have spinel textures similar to those in the adjacent orthopyroxenite, suggesting that either chemical exchange or mechanical mixing between the pyroxenite and surrounding harzburgite has occurred.

Only the wallrocks of the interdigitating dunites have comparable textures to those of the adjacent dunite which is consistent with evidence from mineral chemistry data (Chapter 4) that these dunites were formed by melt-peridotite reaction. Notably, the spinel pull-apart fragments define an unusually strong foliation in these samples, suggesting that their formation was contemporaneous with the mantle deformation and indicating perhaps, that formation of the dunites allowed strain to be focused into the reaction zone.

3.2.5 THE SERPENTINITE DIAPIR

In the serpentinite diapir, the peridotites are lherzolitic in composition and are usually slightly coarser-grained than in the *background* harzburgites. Modal proportions vary between 65-75% olivine, 10-15% orthopyroxene, up to 10% clinopyroxene and up to 2%

spinel. The most distinctive feature of these samples is the presence of clinopyroxene crystals which have a similar range of morphologies to orthopyroxene crystals in the *background* harzburgites. Clinopyroxene often occurs in aggregates of coarse crystals, some of which are deformed (bent cleavage planes and strained extinction) and some of which have lamellar orthopyroxene exsolution (Plate 3.7a). No growth twins have been observed in this clinopyroxene. Coarse clinopyroxene is also present as isolated grains in the olivine matrix which, along with the orthopyroxene aggregates, clinopyroxene aggregates and porphyroclastic spinel, define the foliation. Crystal margins of both the clinopyroxene and orthopyroxene are usually embayed, any neoblastic olivine which might have been associated with these grains having been destroyed by serpentinisation. Clinopyroxene, orthopyroxene and spinel often occur together in aggregates (Plate 3.7b). A small proportion of clinopyroxene in the serpentinite diapir samples also forms fine-grained intergrowths with blebby spinel, similar to those described from the *background* harzburgites. An important difference between the intergrowths in the base of the *background* harzburgite section and those in the serpentinite diapir, is the fact that the clinopyroxene grains in the serpentinite diapir intergrowths are always deformed.

Spinel textures in the serpentinite diapir samples are characterised by their restricted range of morphologies compared to the *background* harzburgites, and by the fact that spinel is almost always located close to pyroxene crystals. Grain sizes are always fine to medium-grained and coarse spinel porphyroclasts are almost completely absent from these samples. The most common, and volumetrically most important, spinel type in these samples is fine to medium-grained, anhedral spinel which is always closely associated with pyroxene crystals, usually clinopyroxene (Plate 3.7c). These crystals vary in morphology from wormy shapes, located along the edges of pyroxene crystals, to more equant shapes on the edge of pyroxene crystals. More rarely, spinel occurs as medium-grained intergrowths with clinopyroxene or as medium to coarse grains within pyroxene aggregates.

3.2.5.1 INTERPRETATION OF SERPENTINITE DIAPIR PETROGRAPHY

The textures of the clinopyroxene in the serpentinite diapir samples are consistent with the crystals being residual from the partial melting event. The deformed crystal lattices, embayed margins, location within crystal aggregates and absence of magmatic twins support this hypothesis. The occasional appearance of spinel-clinopyroxene intergrowths suggest, by analogy with similar textures in the basal *background* harzburgites, that some melt was trapped in these samples. The deformed nature of the clinopyroxene in the intergrowths indicates that the melt was trapped before the end of the deformation event.

Plate 3.7

a) Coarse, deformed clinopyroxene crystal from the serpentinite diapir showing orthopyroxene exsolution. The field of view is 5 mm wide.

b) Spinel-orthopyroxene-clinopyroxene aggregate from the serpentinite diapir, orthopyroxene is labelled O and clinopyroxene C. The field of view is 2.5 mm wide.

c) Typical spinel textures in the serpentinite diapir. The field of view is 5 mm wide.

d) Example of overprinting lithospheric deformation in a Limassol Forest peridotite. Note the neoblastic olivine forming asymmetric pressure shadows around orthopyroxene. The field of view is 5 mm wide.

A.

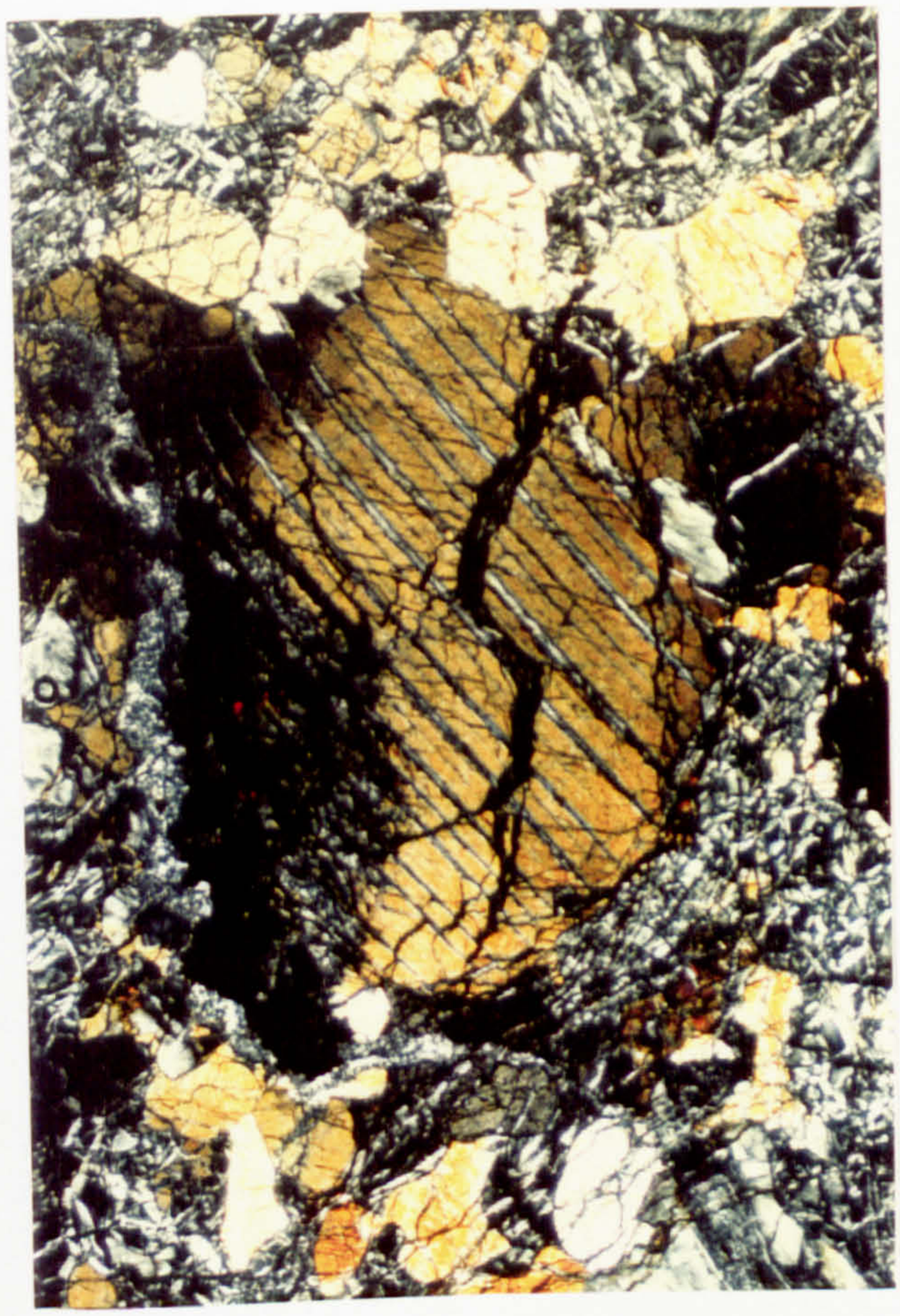

B.

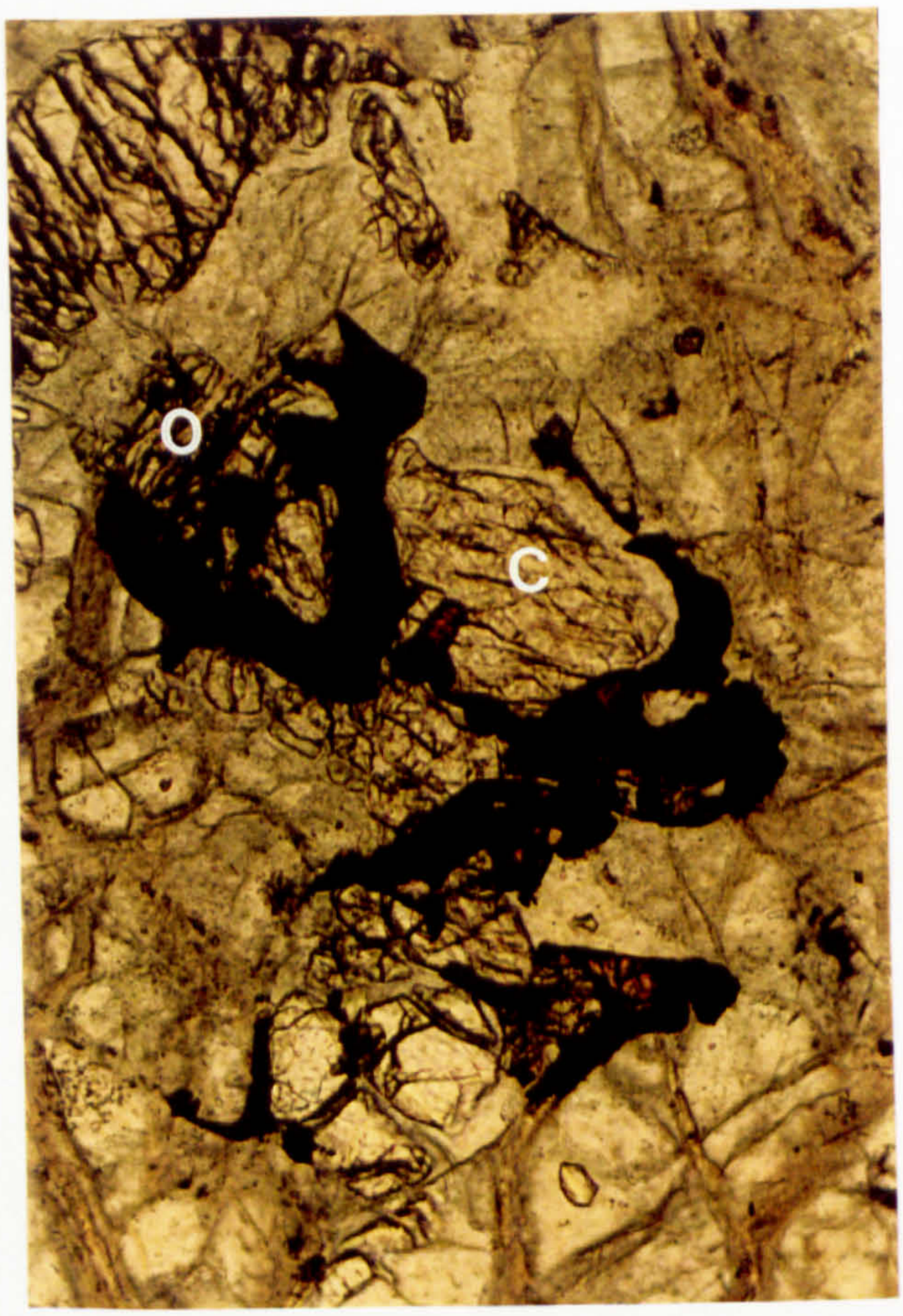

C.

D.

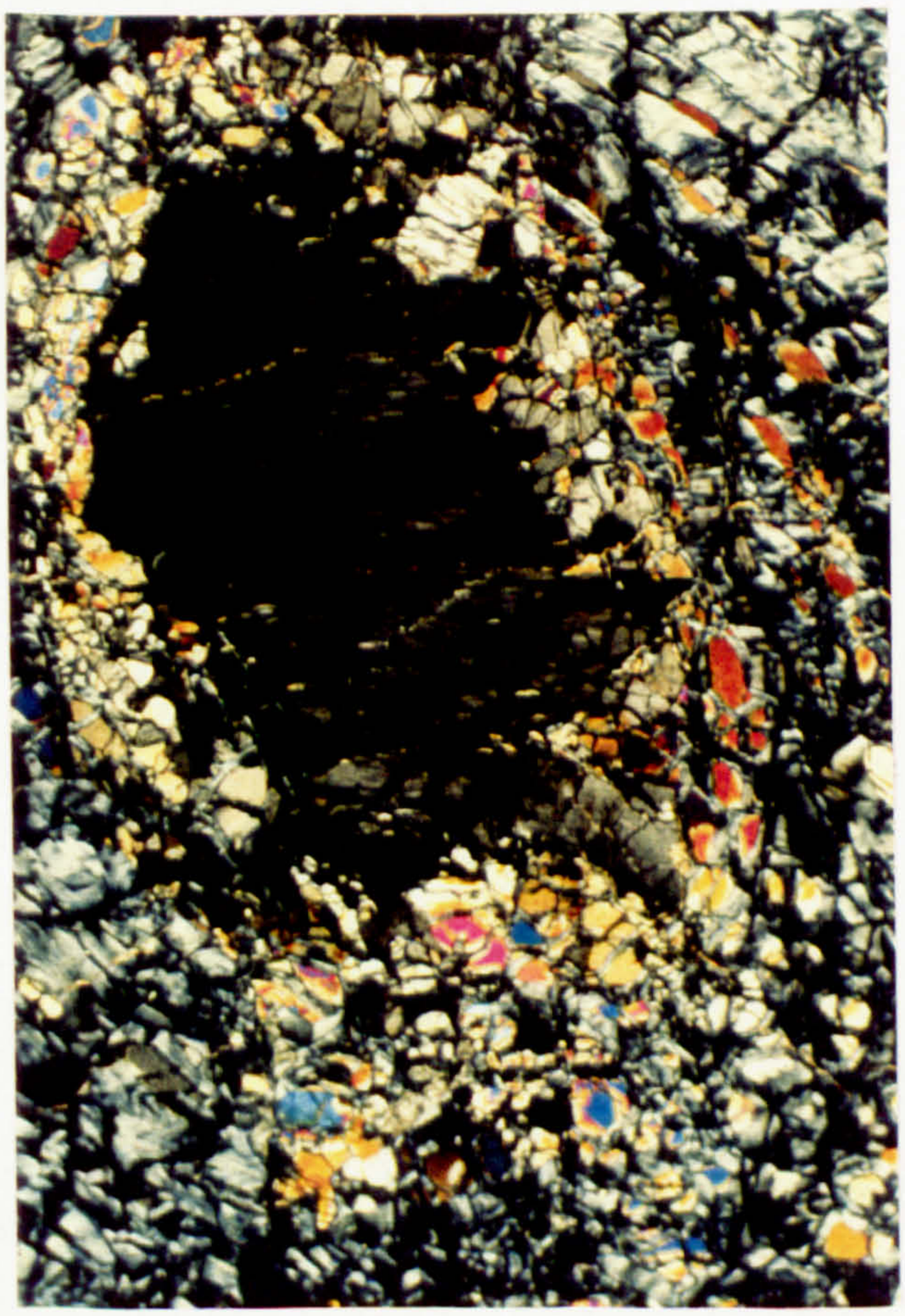

Spinel textures in the serpentinite diapir samples are distinctly different from those in the *background* harzburgites. Notably, spinel porphyroclasts, which are the volumetrically most important type of spinel in the *background* harzburgites, are absent from the serpentinite diapir samples. This suggests that porphyroclasts develop as partial melting increases during asthenospheric deformation. Possibly, the porphyroclasts form by mechanical and chemical aggregation of the fine-grained spinel. This mechanism would be consistent with the occasional appearance of olivine oikicrysts in the porphyroclastic spinel.

3.3 THE LIMASSOL FOREST

The primary mineralogies in most of the Limassol Forest peridotites sampled are almost entirely destroyed by serpentinisation. However, in a few samples, original textures and minerals are partially preserved. In general, the modal proportions and textures of the Limassol Forest samples are similar to those described from the *background* harzburgites at the base of the sequence, and coarse asthenospheric textures are the most common. Orthopyroxene is porphyroclastic and defines the foliation along with porphyroclastic, pulled-apart spinel grains. Clinopyroxene is present as anhedral grains around the edge of orthopyroxene aggregates, as partial coronas to orthopyroxene grains and rarely as intergrowths with fine-grained spinel.

In one sample, the asthenospheric texture has a weak lithospheric overprint (Plate 3.7d). Matrix olivine grains are recrystallised into fine-grained neoblasts and neoblasts also crystallise in the pressure shadows of orthopyroxene porphyroclasts. Orthopyroxene aggregates are pulled apart and individual grains develop equant morphologies with recrystallised margins. Asymmetric pressure shadows containing fine-grained clinopyroxene and neoblastic olivine are developed around orthopyroxene and suggest that a dextral sense of shear prevailed during deformation.

3.3.1 INTERPRETATION OF LIMASSOL FOREST PETROGRAPHY

The similarity between the petrography of the Limassol Forest harzburgites and the *background* harzburgites in the Troodos sequence suggests that they were affected by a similar range of processes.

The presence of lithospheric textures is consistent with the proposed tectonic setting of the Limassol Forest complex in a transform zone (Murton and Gass, 1986), where

shallow level, lower temperature deformation of the uppermost mantle would be expected.

3.4 SERPENTINISATION

Background harzburgites are between 10 and 60% serpentinised and there is no apparent correlation between position in the sequence and degree of serpentinisation. The degree of serpentinisation increases up to 80% in the serpentinite diapir and the Limassol Forest peridotites are between 90 and 99% serpentinised.

In each location the susceptibility of the constituent minerals to serpentinisation varies as follows: olivine > orthopyroxene >> clinopyroxene > spinel. The most common texture is the replacement of olivine by mesh textured serpentine (Plate 3.8a), which probably consists mostly of lizardite (Wicks and Whittaker, 1977; Maltman, 1978). Orthopyroxene crystals usually develop thin serpentine rims during alteration and, in more extreme cases, talc and serpentine fringes develop (Plate 3.8b). In the Limassol Forest samples, orthopyroxene crystals are usually completely altered to featureless plates of serpentine, probably lizardite (Wicks and Whittaker, 1977). Clinopyroxene crystals are usually only slightly altered along cracks, even in the most highly altered Limassol Forest samples. Spinel is the phase most resistant to alteration and develops very thin magnetite rims.

Vein serpentine (Plate 3.8c) is only developed in the serpentinite diapir and Limassol Forest areas. In both locations sinuous, anastomosing picrolite, chrysotile and talc veins cross-cut each other with no consistent age relationships.

Plate 3.8

a) Mesh textured serpentine replacing olivine in a Troodos harzburgite. The field of view is 1 mm wide.

b) Talc and serpentine fringes on an orthopyroxene crystal in a Troodos harzburgite. The field of view is 5 mm wide.

c) Vein serpentine (high birefringence colours) in the serpentinite diapir. The field of view is 2.5 mm wide.

A.

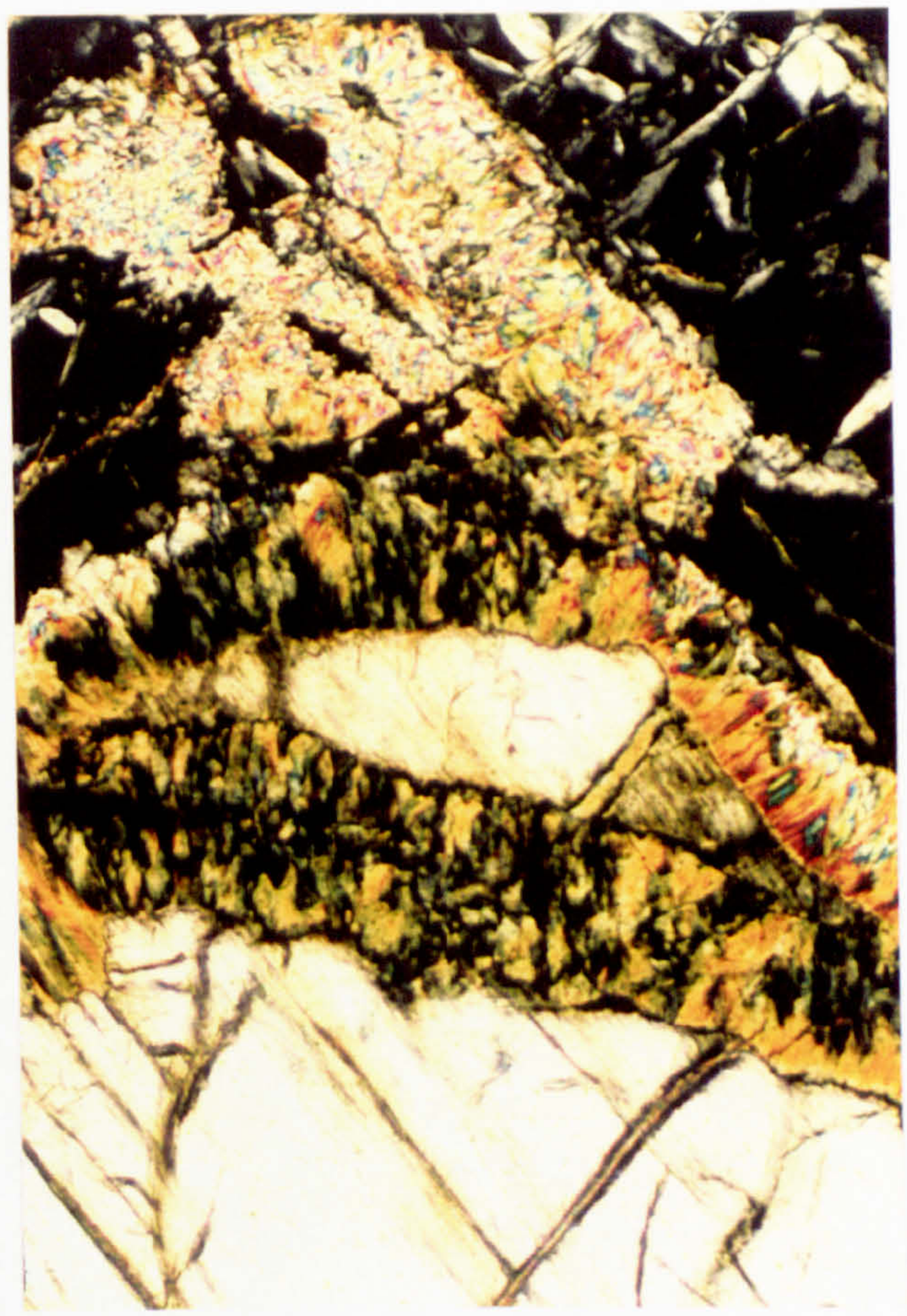

B.

C.

3.5 SUMMARY

In the previous chapter the variety of minor intrusions in the mantle sequence and their preferential location towards the top of the sequence was noted. In the field the harzburgites were observed to be fairly homogeneous in appearance with the exception of finer scaled banding being developed at the top of the sequence.

In this chapter the *background* harzburgites have been shown to be much more variable in their modal mineralogy and microstructures than the field evidence suggested. Most significantly these variations occur in a systematic pattern, showing both a vertical decrease in the modal proportion and textural variety of clinopyroxene from the base of the mantle sequence to the top, and a correlation between microstructure and mineral chemistry in the case of the *Anomaly 1* and *2* harzburgites. Furthermore, it has been possible in many cases to discriminate between a melt crystallisation or reaction origin for an individual crystal, and a residual origin from the partial melting event. The data collected support previously proposed criteria for melt related crystals, such as the presence of growth twins. Moreover, new melt related textures, such as wormy spinel located between olivine and orthopyroxene grains, have also been identified.

In the *background* harzburgites the modal clinopyroxene content and the variety of clinopyroxene textures decrease from the base to the top of the sequence. This is consistent with the proposed increase in the degree of melting upwards through the section illustrated by the $Cr\#_{spn}$ data in Figure 3.1 and discussed in greater detail in the following chapter. Spinel textures also show a base to top variation. Three basic processes were proposed to explain the textural variation of clinopyroxene and spinel: partial melting, melt impregnation/reaction and, for clinopyroxene only , exsolution from orthopyroxene. The criteria used to distinguishing these textural types are summarised in Table 3.2.

Anomaly 1 and *2* harzburgites are *background* harzburgite sub-types identified on the basis of their mineral chemistries as discussed at the start of this chapter (see Figure 3.1, Section 3.1). In thin section, the *Anomaly 1* harzburgites are characterised by a high modal abundance of poikilitic clinopyroxene and the *Anomaly 2* harzburgites by numerous spinel-pyroxene intergrowths. These textures are attributed to the influence of melt interaction.

	Mantle melting	Melt-mantle reaction
Orthopyroxene	Embayed margins	Delicate, undeformed morphologies Embayed margins
Clinopyroxene	Embayed margins Anhedral, ragged grains in orthopyroxene aggregates	Growth twins Interstitial, optically continuous grains in orthopyroxene aggregates Poikilitic habits
	Exsolution origin preferred for fine grains and partial coronas located on 001 faces	
Spinel	Coarse, porphyroclastic grains	Hook-shaped terminations on porphyroclasts Fine, sub-euhedral grains interstitial to olivine Intergrowths with pyroxenes

Table 3.2. Summary of textural types related to mantle melting and mantle-melt reaction.

Spinel is the only petrographically useful mineral in dunites, because serpentinisation has largely destroyed the olivine textures. With the exception of the dunites with interdigitating contacts against the harzburgites, spinel in dunites is sub-euhedral and interstitial, consistent with an origin via crystallisation from a melt. In the interdigitating dunites, spinel occurs as rounded porphyroclasts and fine, euhedral, interstitial grains. The porphyroclasts are interpreted as xenocrysts from the adjacent harzburgite, and the bimodal association of the porphyroclasts and euhedral spinel supports the hypothesis that these dunites form partly by mantle-melt reaction and partly by melt crystallisation.

The pyroxenites also have textures indicative of crystallisation from a melt such as consertal contacts, poikilitic habits and growth twins. The occurrence of wormy spinel textures located at orthopyroxene-spinel contacts, particularly in the *orthopyroxenite A* bodies, shows that melt-mantle reaction was also an important process in these bodies. This hypothesis is supported by the fact that the wallrock harzburgites have textural features inherited from both the *background* harzburgites and the adjacent pyroxenites.

CHAPTER 4
MINERAL CHEMISTRY

4.1 INTRODUCTION

This chapter describes the mineral chemistry of olivines, pyroxenes and spinels from the Troodos and Limassol Forest mantle sequences. The data will be used to assess the partial melting history of the two mantle sequences and the effects of mantle-melt interaction.

In the first part of the chapter, major and minor element data obtained by electron probe are discussed. After testing the data for their susceptibility to sub-solidus alteration, the mineral compositions are used to constrain the possible tectonic origins of the two mantle exposures. The data from the Troodos sequence are then presented as a contour map and stratigraphic sections, which illustrate how mineral chemistries vary with position in the mantle. These data are also plotted as a series of bivariate plots in order to examine the partial melting and reaction history of the mantle. The origin of pyroxenites, dunites and chromitites in the Troodos mantle sequence is examined, and the effects of their formation on the chemistry of the surrounding mantle discussed.

In the second part of the chapter, clinopyroxene trace element data collected by secondary ion mass spectrometry are presented. The data are used to further constrain melting models for the Troodos peridotites and determine the nature and extent of mantle-melt interaction. During this project spinels were analysed for the first time on the Edinburgh University ion probe in an attempt to characterise their trace element chemistry. At the time of writing several analytical problems with these analyses were still unresolved, in particular with the lowest abundance elements which are difficult analyse by other techniques, such as Ga and Y. Therefore, the data collected are not presented in this chapter. The analytical problems which were encountered are described in detail in a separate appendix (Appendix B), for the information of anyone attempting similar analyses in the future.

In the chapter samples are classified by lithology with the following distinctions being made.

a) *Background* harzburgites are samples from the *in situ* Troodos mantle section collected > 5 m away from dunites, veins or minor intrusions, and are intended to represent the geochemical background of the mantle section. The samples from the Limassol Forest

were all collected away from minor intrusions and also represent the geochemical background.

b) Samples described as '*top-of-the-sequence*' are *background* harzburgites collected within 500 m of the main dunite-harzburgite contact (measured vertically through the sequence).

c) Harzburgite *xenoliths* are samples from the xenolithic harzburgite fragments outcropping in the base of the crustal dunites (see Fieldwork Chapter).

d) Harzburgites described as 'between bands' were collected from between the orthopyroxenitic banding described in the Fieldwork Chapter.

e) Samples described as adjacent to dunites or minor intrusions, were sampled either at the contact or, if this was not accessible, within 10 cm of the contact.

f) Dunites in the harzburgite sequence are differentiated on the basis of their structural setting (a full description is given at the start of the section on dunite mineral chemistry and in the Fieldwork Chapter).

g) Crustal dunites are those which structurally overlie the harzburgites and are synonymous with those termed "transition zone" lithologies by other workers (Nicolas and Prinzhofer, 1983).

4.1.1 PREVIOUS WORK

There is little published data on the mineral chemistry of the Troodos peridotites. Menzies and Allen (1974) noted that the harzburgites had homogeneous mineralogies, and magnesian olivine and orthopyroxene. Greenbaum (1977) analysed spinel from the harzburgites and chromitites, by XRF and electron probe, and found that "the Troodos samples follow a pronounced trend of reciprocal Cr-Al substitution typical of the Alpine variation". No systematic variation between the chromitite deposits was found and he concluded that they had formed by magmatic gravitational segregation. Dick and Bullen (1984) used Greenbaum's data to classify the Troodos Massif as a type III peridotite, related to arc formation on oceanic crust.

Some trace element concentrations in clinopyroxene from the serpentinite diapir have been determined by Batanova *et al.* (1994). REE patterns exhibit LREE enrichment, coupled with strongly depleted MREE and HREE values corresponding to the most depleted end of the abyssal peridotite spectrum. Batanova *et al.* (1994) attribute the LREE enrichment to the influence of a "subduction zone component", and used the presence of positive Ti and Zr anomalies in harzburgite clinopyroxene to suggest that, in the harzburgites, the clinopyroxene had formed by exsolution from orthopyroxene.

No mineral chemistry data from the Limassol Forest area have been published, although a comprehensive study of chromitites in the adjacent, and probably closely related, Akapnou Forest complex has been described by Georgiou and Xenophontos (1980), who favour their formation as cumulates from primary melts.

4.1.2 ANALYTICAL METHODS

Mineral compositions were determined at the Electron Probe Unit, Edinburgh University. Approximately 1500 points were analysed and the details of the probe configuration, operating procedures and error estimates are given in Appendix A. Fe^{2+} and Fe^{2+} in spinel were calculated by stoichiometry using an on-line programme in the electron probe software. A subset of samples was analysed by secondary ion probe mass spectrometry at Edinburgh to determine the trace element content of clinopyroxene. The operating conditions of the ion probe and error estimates are presented in Appendix A.

The data presented below are the averages of at least three analyses per mineral per sample. Only values for core analyses are used in the discussion of mantle melting and reaction to avoid the effects of subsolidus changes (see below). With the exception of orthopyroxenes, all analyses were made with the electron beam in spot mode. For orthopyroxene analyses, the beam was rastered over 30 μm square areas in order to integrate the effects of fine-scale clinopyroxene exsolution. Clinopyroxene crystals were examined optically, and with the electron probe in backscatter mode, and no evidence for orthopyroxene exsolution was observed.

The graphs in this chapter are annotated with 2σ error bars and dashed lines labelled dl, which indicate the value of the detection limit for the particular element under consideration. For several mineral parameters (e.g. $Cr\#_{spn}$), the errors are smaller in size than the points on the graph. In these cases, the error bars have been omitted for clarity, and the error can be assumed to be less than the size of the points on the graph.

4.2 MINERAL ZONING

Numerous studies have described core-to-rim zonations in mantle minerals. These zonations have been interpreted as the result of subsolidus exchange between adjacent minerals, in response to falling temperature and pressure (Quick 1981a), or the result of hydrothermal alteration (Kimball, 1990). Spinel, in particular, is sensitive to exchange reactions, displaying increasing Cr/Al (Cr#) and decreasing Mg/Fe^{2+} (Mg#) values from core to rim during hydrothermal alteration (Kimball, 1990), and decreasing Cr# and Mg#

from core to rim during down-temperature sub-solidus exchange (Conquéré and Fabriès, 1984; Quick, 1981a; Ozawa and Takahashi 1995). These studies also show that, within a single sample, core compositions are constant and correlate with $Mg\#_{Ol}$, which suggests that subsolidus processes are not pervasive on a grain scale. The effects of subsolidus re-equilibration are usually greatest in the least abundant mineral phases (Ozawa, 1994), while minerals with the greatest modal abundance will be buffered closest to magmatic compositions.

To investigate whether subsolidus exchange has affected mineral compositions in the Troodos samples, a subset of 23 samples (harzburgites and dunites) was analysed for core and rim compositions. Olivine is always heavily serpentinised and it was therefore, impossible to analyse olivine rims. However, olivine has the greatest modal abundance in the Troodos samples and thus, except in the immediate vicinity of other mineral species, olivine compositions should be close to magmatic (Conquéré and Fabriès, 1984; Ozawa, 1994). Clinopyroxene is always fine to very fine-grained which also precludes the study of core-rim variations. Therefore, only zoning data for orthopyroxene and spinel are presented.

Core-rim values are compared in Figure 4.1. Spinel Cr# and TiO_2 contents are uniform between the cores and rims of grains, whereas the Mg# of cores are usually higher than Mg# for rims. The $Fe^{2+/3+}$ ratio varies from core to rim only at values greater than 10, where cores show higher values than rims. The orthopyroxenes analysed show a 1:1 relationship between core and rim analyses which suggests that this phase is not zoned.

In the light of the possible subsolidus processes described above, and the data obtained from the Troodos spinels and orthopyroxenes, the following conclusions were reached regarding the mineral chemistry parameters most applicable for use in examining magmatic processes:

Olivine - has the highest modal abundance and is therefore least likely to be affected by subsolidus processes. Only isolated, matrix crystals were analysed in order to avoid any possible exchange effects around spinel grains.

Orthopyroxene - no zoning was found in the Troodos samples and therefore orthopyroxene is assumed to be relatively unaffected by subsolidus exchange.

Spinel - the Troodos data shows that the core and rim analyses lie close to a 1:1 line and the grains are therefore homogeneous and assumed to have primary compositions.

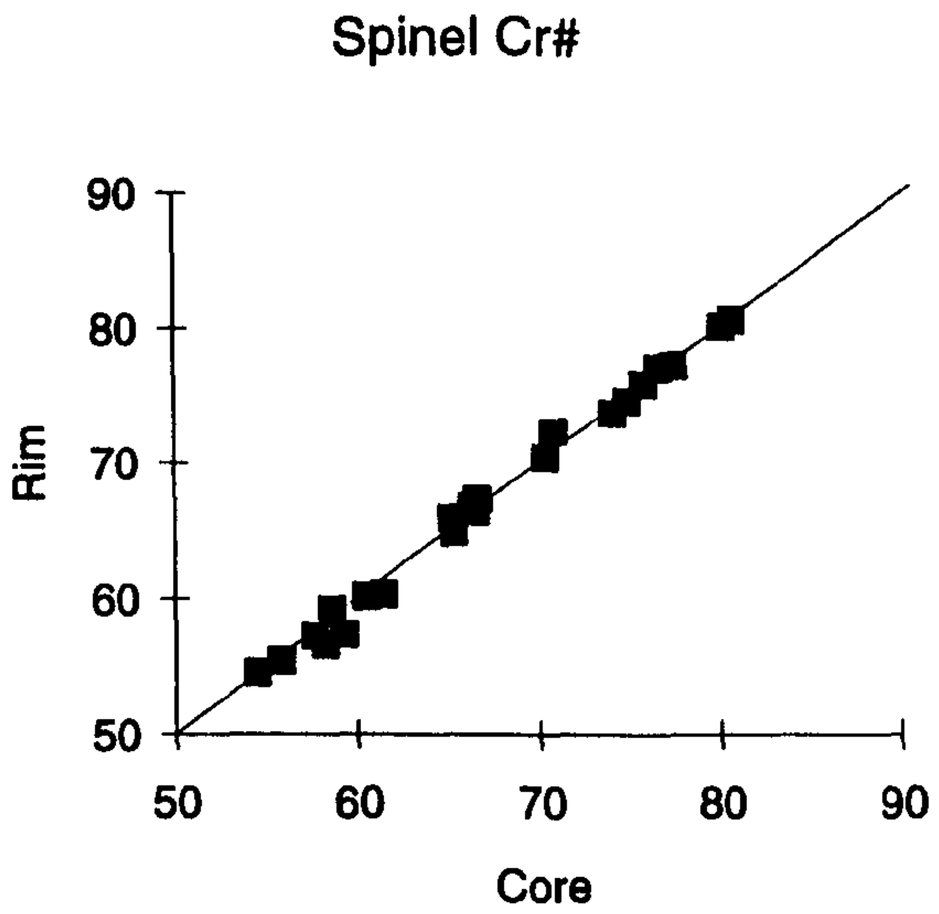

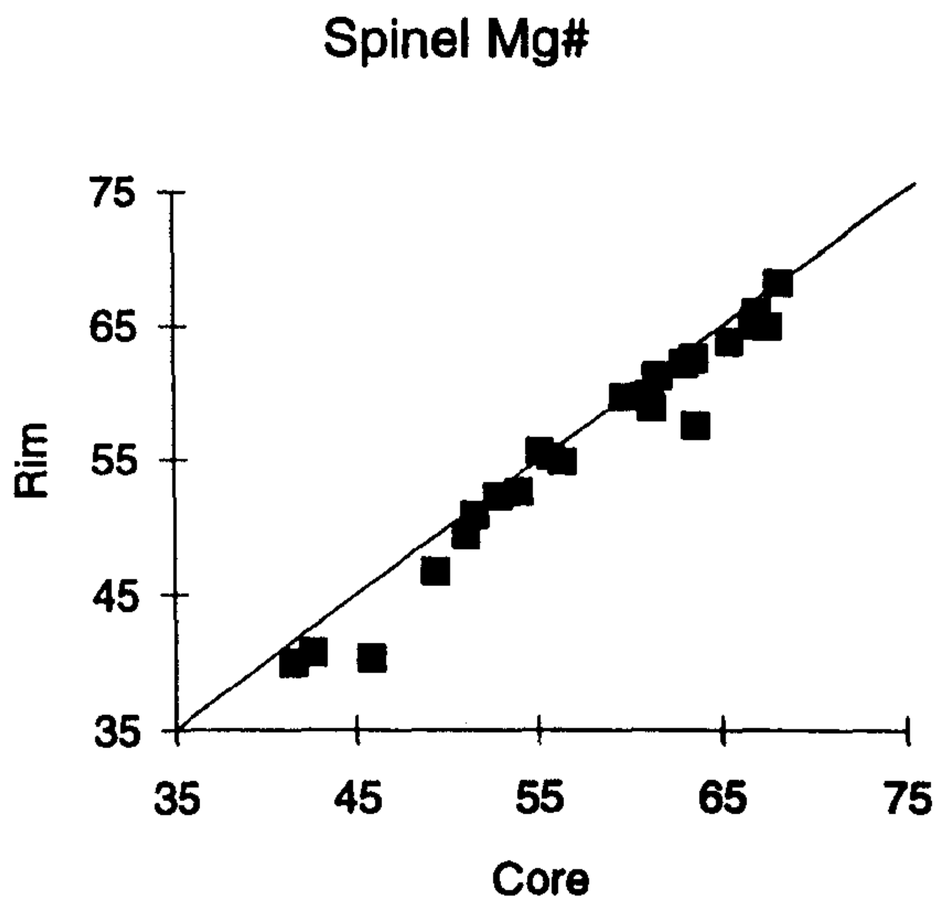

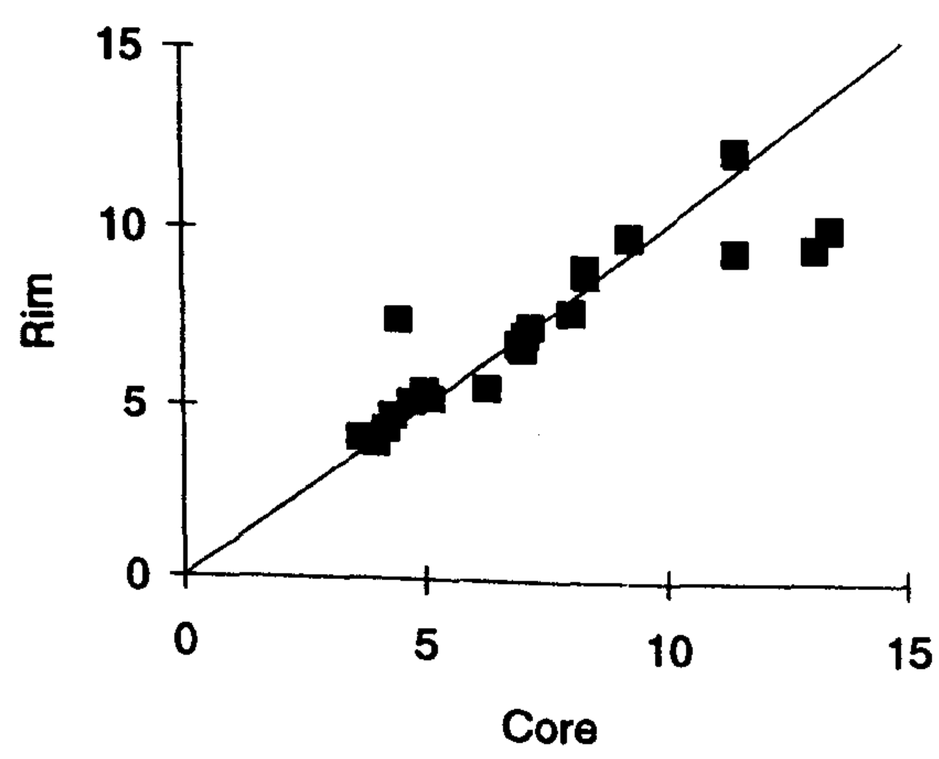

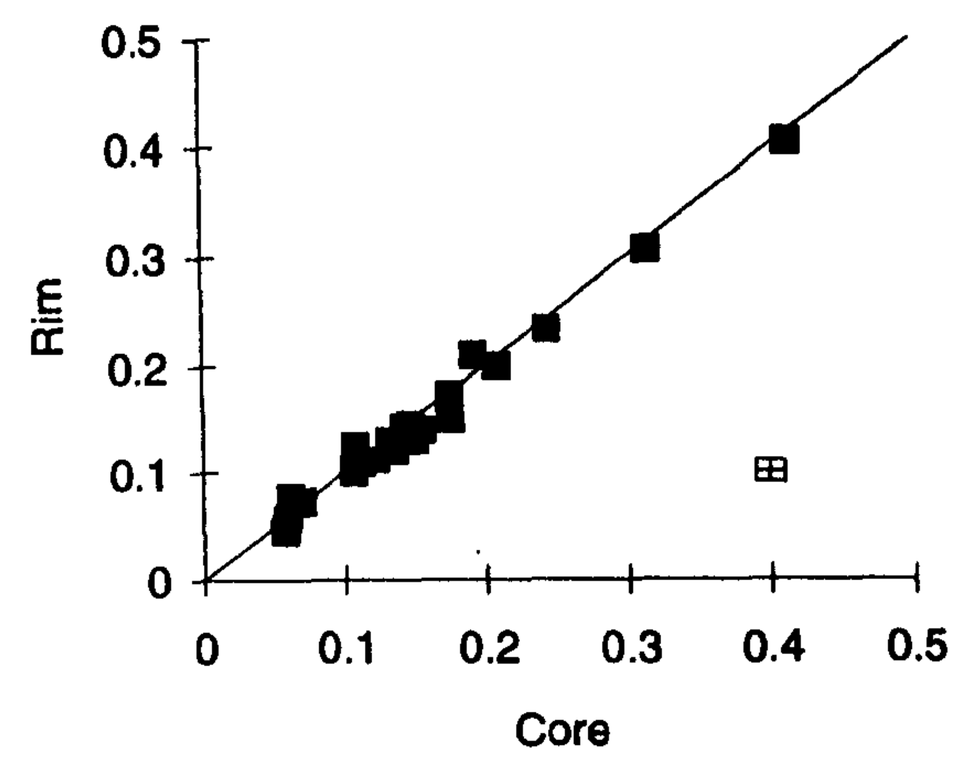

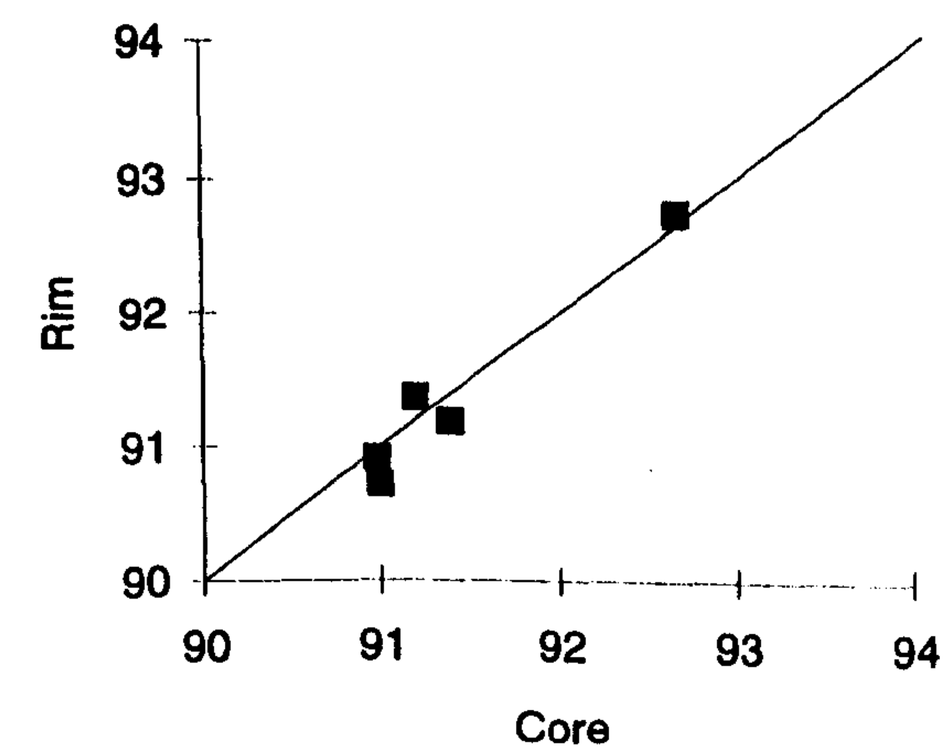

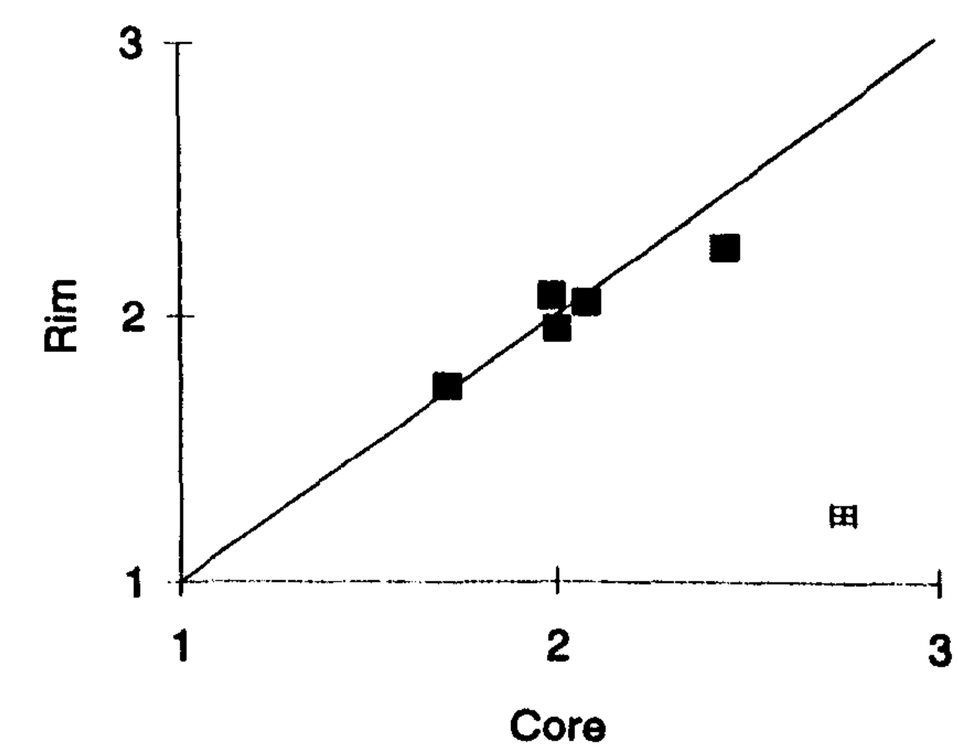

Figure 4.1 Comparison of core and rim values for various mineral parameters in orthopyroxene and spinel.

Clinopyroxene - the fine grain size of this phase means that it is the most susceptible to exchange processes, and that homogeneity on a grain scale will be more easily attained by both magmatic and subsolidus processes. The absence of zoning in orthopyroxene and spinel however, suggests that subsolidus processes were not significant in the Troodos peridotites and the clinopyroxene compositions are therefore assumed to be close to magmatic.

The Troodos data presented above suggest that subsolidus exchange has not been significant in the Troodos peridotites, perhaps because they cooled quickly through the blocking temperatures of the exchange reactions. However, as a precaution, all the analyses presented below were made from the cores of crystals.

4.3 MINERAL CHEMISTRY

The main compositional variations found in this study are outlined below. Representative mineral analyses are given in Table 4.1. The full electron probe data set is presented in Appendix D.

4.3.1 OLIVINE

Olivines are refractory with Mg# ranging from 89.2 to 94.0. *Background* harzburgites (91.0±0.4) and harzburgite *xenoliths* (91.0±1.0) have the highest average Mg#, and pyroxenites (90.2±0.6) the lowest. The greatest range of Mg# is in the dunites (89.3 to 94.0). Nickel contents vary from 0.04 to 0.50 wt% NiO. Pyroxenites (0.37±0.08) and harzburgite *xenoliths* (0.345±.06) have the highest nickel contents and crustal dunites (0.16±0.11) the lowest.

4.3.2 SPINEL

There is a wide variation in spinel chemistry, with Cr# for harzburgite spinels varying from 21.5 to 77.2, the lowest values being from the serpentinite diapir and the higher ones from the top of the *in situ* mantle sequence. Spinels in dunites have the highest Cr#'s, with values ranging between 47.9 and 81.0. Spinels in pyroxenites range between Cr# 35.4 and 75.0. Chromitites have the most limited range of compositions, from Cr# 65.5 to 74.0. Of the minor elements, Ti contents vary between 0.04 and 0.42 wt% TiO_2, the highest values being associated with crustal dunites (0.26±0.01). V contents range from 0.11 to 0.49 wt%. Most lithologies have average V_2O_3 contents of about 0.23 wt%, the exception being spinels from chromitites which have much lower V contents (0.15±0.04

wt%). $Fe^{2+/3+}$ ratios range from 1.75 to 17.61; pyroxenites associated with dunites (9.57 ±3.45) and *background* harzburgites (9.07±3.73) have the highest average values, and crustal dunites (4.57±1.48) and chromitites (5.23±1.64) the lowest

4.3.3 ORTHOPYROXENE

Orthopyroxene compositions are enstatitic with Mg# values ranging from 89.8 to 92.0. Al_2O_3 contents vary from 0.89 to 4.4 wt%, TiO_2 contents from 0.01 to 0.09 wt % and CaO contents from 0.89 to 2.75 wt%. In harzburgite samples, the highest TiO_2 and Al_2O_3 concentrations are found in the serpentinite diapir samples, whereas the harzburgites at the *top-of-the-sequence* show high TiO_2 and low Al_2O_3 contents. Pyroxenites have a range of TiO_2, Al_2O_3 and Cr_2O_3 contents similar to that of the harzburgites but are slightly less Mg-rich (Mg# 89.8 to 91.9).

4.3.4 CLINOPYROXENE

Clinopyroxene has correspondingly high Mg# and wollastonite contents ranging from 51.5 to 36.7. Harzburgite clinopyroxene ranges from Mg# 92.3 to 94.6, pyroxenites from 90.3 to 93.6 and interstitial clinopyroxene in dunites (see Microstructure Chapter) from 92.0 to 94.9. TiO_2 contents range from 0.03 to 0.23 wt% with the highest values being found in the pyroxentites (0.07±0.03), crustal dunites (0.09±0.06) and the serpentinite diapir area (0.17±0.03). Na_2O and Al_2O_3 contents are also highest in the serpentinite diapir (0.28±0.07 and 4.22±0.62 respectively). Samples from the *top-of-the-sequence* have the lowest Al_2O_3 (1.99±0.69).

4.3.5 MINERAL INTERGROWTHS

In addition to isolated crystals of spinel and clinopyroxene in the Troodos peridotites, a small proportion of these phases also occur as fine-grained intergrowths, the petrology of which are described in more detail in the Microstructure Chapter. Previous studies have interpreted this texture as the product of either incongruent melting of orthopyroxene (Dick and Bullen, 1984) or crystallisation from an infiltrating melt (Edwards and Malpas, 1996). To investigate the origins of these intergrowths, clinopyroxene and spinel grains present both as intergrowths and isolated crystals were analysed in a subset of 10 samples. The compositions of intergrown grains and isolated crystals are compared in Figure 4.2.

sample	28	111	191	195	262	295	323	257a	344	400	065a
lithology	harzburgite	harzburgite	harzburgite	dunite	harzburgite	harzburgite	harzburgite	pyxite A	pyxite B	dunite	chromitite
location	lim.for	anomaly 1	serp diapir	crustal	bckgrd	anomaly 2	between bands			x fol	
Olivine											
SiO2	40.24	40.43		40.27	40.08	40.53	40.46			40.06	
MgO	50.23	49.74		50.02	49.65	50.45	49.83			49.53	
FeOt	9.22	8.90		8.46	8.98	7.97	8.99			9.41	
Al2O3	bd	0.02		0.01	0.01	0.01	0.06			0.01	
CaO	0.05	0.05		0.13	0.03	0.05	0.02			0.03	
Na2O	0.02	bd		bd	0.03	bd	bd			bd	
NiO	0.30	0.44		0.25	0.28	0.23	0.29			0.40	
TiO2	0.02	bd		0.02	0.01	0.02	0.01			bd	
Cr2O3	bd	0.02		0.02	bd	bd	0.02			bd	
V2O5	bd	bd		bd	bd	bd	bd			0.004	
MnO	0.13	0.12		0.14	0.14	0.15	0.14			0.15	
ZnO	0.03	bd		0.02	bd	0.04	bd			0.02	
Total	100.27	99.74		99.33	99.23	99.45	99.84			99.63	
Mg#	90.7	90.9		91.3	90.8	91.9	90.7			90.4	
Spinel											
SiO2	0.03	0.03	0.03	0.03	0.04	0.02	0.04	0.08	0.03	0.04	0.03
MgO	13.29	12.49	16.73	12.87	9.47	13.94	14.55	14.01	14.44	12.73	13.75
FeO	14.83	16.88	12.55	15.66	19.04	14.85	14.46	14.50	14.34	16.21	12.35
Fe2O3	2.58	2.33	2.26	5.32	1.64	2.15	1.87	2.71	1.10	1.70	2.89
Al2O3	20.95	25.61	40.90	23.31	11.46	29.93	31.14	25.68	29.00	25.78	11.78
CaO	0.02	bd	bd	bd	bd	bd	bd	bd	bd	bd	bd
Na2O	bd	bd	bd	bd	0.029	0.018	0.024	bd	0.025	bd	0.000
NiO	0.10	0.11	0.19	0.07	0.05	0.06	0.10	0.10	0.12	0.10	0.02
TiO2	0.07	0.10	0.12	0.28	0.04	0.09	0.06	0.05	0.08	0.06	0.14
Cr2O3	48.07	42.63	26.43	41.42	57.91	37.53	37.46	42.97	40.05	42.82	57.67
V2O5	0.28	0.23	0.14	0.18	0.39	0.21	0.21	0.18	0.20	0.27	0.12
MnO	0.25	0.27	0.17	0.31	0.33	0.25	0.21	0.25	0.20	0.38	0.25
ZnO	0.131	0.237	0.199	0.157	0.215	0.312	0.278	0.127	0.110	0.284	0.083
Total	100.56	100.92	99.62	99.62	100.64	99.36	100.39	100.67	99.71	100.38	99.06
Cr#	60.6	52.8	30.2	54.4	77.2	45.7	44.7	52.9	47.8	52.7	76.7
Mg#	61.5	56.9	70.4	59.4	47.0	62.6	64.2	63.3	64.0	58.3	66.5
Fe2+/Fe3+	5.7	7.3	5.6	2.9	11.6	6.9	7.8	5.4	14.4	10.6	4.8
Orthopyroxene											
SiO2	56.19	55.75	54.51		56.40	55.81	55.21	55.561	55.07		
MgO	34.14	33.40	33.00		33.60	34.11	33.07	33.98	32.97		
FeOt	5.81	5.70	5.92		5.66	5.23	5.79	5.70	5.73		
Al2O3	1.61	2.15	3.61		0.89	2.30	2.90	2.11	2.64		
CaO	1.64	1.47	1.02		1.66	0.90	1.79	1.440	1.52		
Na2O	0.02	bd	0.02		0.02	0.02	bd	0.02	0.02		
NiO	0.05	0.12	0.09		0.08	0.06	0.09	0.08	0.13		
TiO2	0.02	0.036	0.087		bd	0.053	0.033	0.019	0.040		
Cr2O3	0.14	0.13	0.16		0.15	0.13	0.15	0.14	0.03		
V2O5	0.62	0.66	0.68		0.52	0.67	0.87	0.73	0.78		
MnO	bd	bd	bd		bd	bd	bd	bd	0.13		
ZnO	bd	bd	bd		0.03	0.03	bd	bd	bd		
Total	100.27	99.42	99.12		99.03	99.34	99.94	99.80	99.07		
Mg#	90.9	90.5	90.8		91.4	92.0	90.6	91.4	91.1		
En	89.4	88.4	88.5		88.9	89.2	87.7	88.9	88.4		
Fs	8.9	9.3	9.0		8.4	7.8	9.1	8.4	8.6		
Wo	1.7	2.3	2.6		2.7	3.0	3.1	2.7	2.9		
Clinopyroxene											
SiO2	52.23	52.66	51.66	51.43	53.06	52.32	51.69	52.12	52.42		
MgO	17.46	17.57	16.76	17.28	17.66	17.14	17.49	18.14	17.06		
FeOt	2.49	2.45	2.32	2.25	1.99	2.06	2.31	2.50	2.18		
Al2O3	2.06	2.44	4.03	3.01	0.94	2.53	2.78	2.82	2.85		
CaO	23.24	23.20	23.20	23.29	23.23	22.90	23.04	22.41	23.40		
Na2O	bd	0.03	0.30	0.16	0.72	0.21	0.02	0.03	0.12		
NiO	0.07	0.07	0.06	0.03	0.05	0.04	0.03	0.07	0.07		
TiO2	0.04	0.06	0.21	0.23	0.02	0.09	0.07	0.05	0.06		
Cr2O3	0.10	0.08	0.09	0.08	0.08	0.08	0.10	0.07	0.04		
V2O5	0.98	0.93	1.07	1.27	0.59	0.98	0.95	1.23	1.04		
MnO	0.03	bd	bd	0.04	0.03	0.03	0.04	bd	0.08		
ZnO	bd	bd	bd	.03	bd	bd	bd	bd	bd		
Total	98.71	99.55	99.72	99.08	98.40	98.39	98.52	99.48	99.33		
Mg#	92.6	92.8	92.8	93.2	94.1	93.7	93.1	92.8	93.3		
En	49.1	49.3	48.2	49.0	49.8	49.3	49.5	50.9	48.6		
Fs	3.9	3.8	3.7	3.6	3.1	3.3	3.6	3.9	3.5		
Wo	47.0	46.8	48.0	47.4	47.1	47.4	46.9	45.2	47.9		

The following compositional parameters are in mol.%: Mg# = 100Mg/(Mg+Fe), Cr# = 100Cr/(Cr+Al), En = 100Mg/(Mg+Fe+Ca), Fs = 100Fe/(Mg+Fe+Ca), Wo = 100Ca/(Mg+Fe+Ca). bd = below detection limit. Abbreviations: lim.for = Limassol Forest, serp diapir = serpentinite diapir, bckgrd = *background* harzburgite, x fol = cross-cutting harzburgite foliation, pyxite = orthopyroxenite.

Table 4.1 Representative mineral analyses.

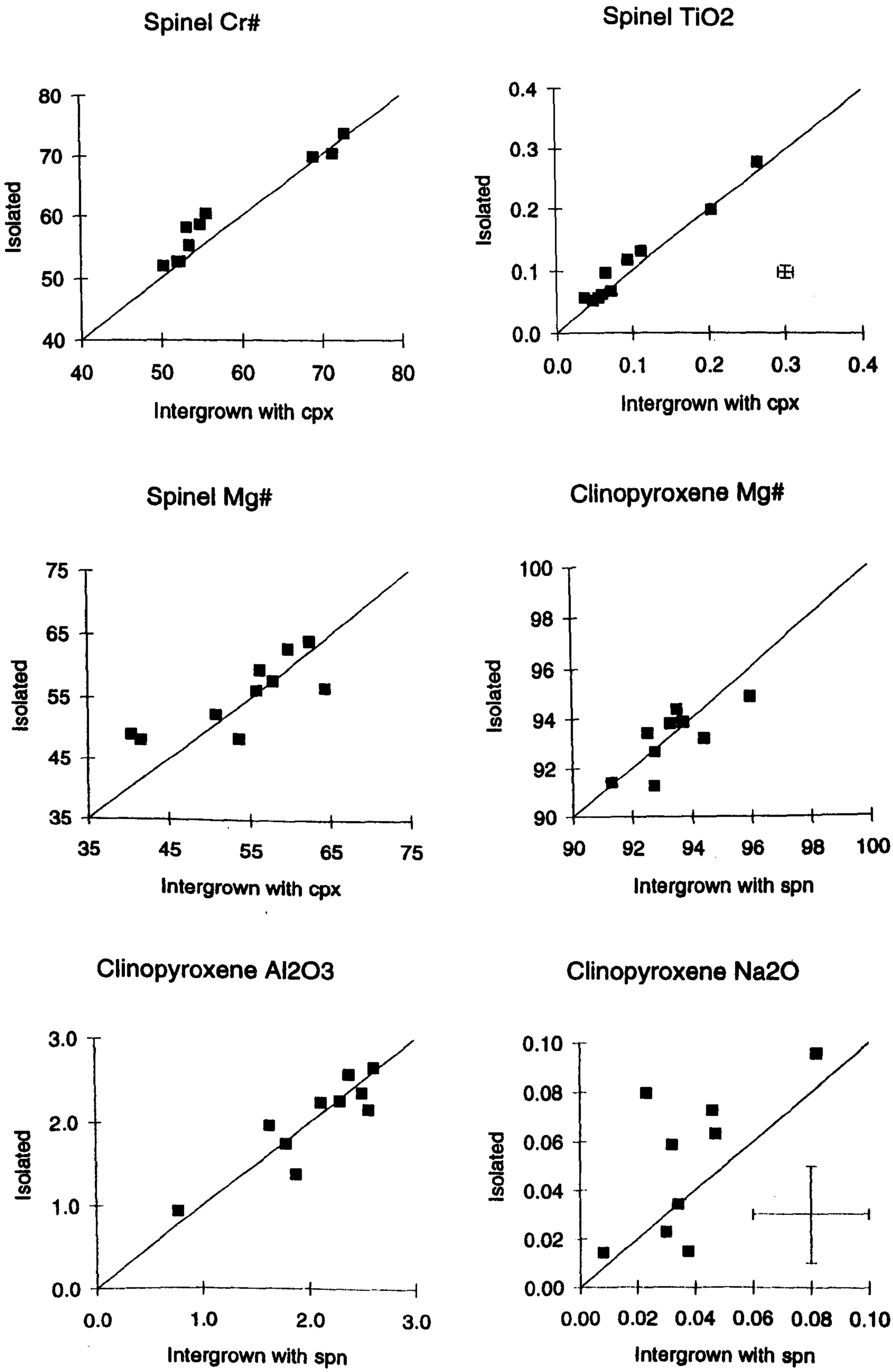

Figure 4.2 Graphs comparing the compositions of spinel and clinopyroxene crystals isolated in the olivine matrix and those spinel and clinopyroxene crystals occurring as intergrown grains.

Despite the considerable scatter in the data, most elements lie close to the 1:1 line. The similarity in compositions between the two textural types is not surprising considering their fine grain size, which would allow rapid re-equilibration and homogenisation of compositions during both sub-solidus processes and reaction with melts.

The mineral chemistry data are therefore equivocal. However, as pointed out by Keleman *et al* (1990), Varvalfy *et al.* (1996) and Edwards and Malpas (1996), mantle-melt interaction can involve pyroxene dissolution at the same time as re-fertilisation of mineral chemistries. It is likely therefore, that the intergrowths are indicators of mantle-melt interaction, whether by direct crystallisation from the melt or by melt-induced pyroxene dissolution. The delicate, undeformed nature of the intergrowths suggests that whichever process produced the intergrowths, it occurred after the main asthenospheric deformation. Moreover, the homogeneous mineral compositions in the Troodos samples indicates that equilibrium was reached on a thin section scale during mantle-melt interaction.

4.4 MINERALOGICAL EVIDENCE FOR THE PALAEOTECTONIC SETTING OF THE CYPRIOT PERIDOTITE MASSIFS

Studies of mantle peridotites have shown that mineral compositions vary systematically with geotectonic setting (Michael and Bonatti, 1985; Bonatti and Michael, 1989). These authors have shown that the Mg# of silicates and Cr# of spinels increase, and the Al, Na and Ti contents of pyroxenes decrease in the order pre-oceanic → passive margin → mature ocean ridge → subduction zone peridotite. These compositional changes correlate with changes in modal abundances, which show an increase in modal olivine, rapid decrease in clinopyroxene (disappearing at 15-30% melt depending on the starting composition and the nature of the partial melting process) and decrease in orthopyroxene, in the order pre-oceanic → subduction zone peridotite (Bonatti and Michael, 1989).

Bonatti and Michael (1989) suggest that these variations are primarily a result of variable degrees of partial melting, which increases from pre-oceanic rifts to subduction zones. This agrees with the concept of subduction zone peridotites experiencing a second stage of fluid induced melting (Dick and Bullen, 1984; Parkinson *et al.*, 1992) beyond that which produced abyssal peridotites. The fact that these natural trends have been reproduced by melting experiments (Mysen and Kushiro, 1977; Jaques and Green, 1980), supports the hypothesis that partial melting is the primary control on mineral composition.

Recently, it has been proposed that some of the modal variations in abyssal peridotites may also result from mantle-melt interaction, with olivine, in particular, increasing in modal abundance as a result (Kinzler *et al.*, 1993). Similarly, Keleman *et al.* (1992) have suggested that the orthopyroxene content of subcontinental and subduction zone peridotites is also controlled by mantle-melt interaction. As pointed out by Dick and Natland (1996), these two processes may be related, with olivine or orthopyroxene crystallising depending on whether or not the mantle is melting at the same time as the melt interaction occurs.

Pyroxene and spinel data for *background*, serpentinite diapir and Limassol Forest samples are presented in Figure 4.3 (olivine data are not considered in this section because serpentinisation has completely destroyed this phase in the serpentinite diapir and Limassol Forest samples). Also plotted are data for plagioclase-free abyssal peridotites from the SW Indian and American-Antarctic Ridges (Dick, 1989), and ODP Leg 125 supra-subduction zone peridotites from the Izu-Bonin forearc (Ishii *et al.*, 1992). On all projections in Figure 4.3, the serpentinite diapir data plot in the abyssal peridotite field, whereas the *background* and Limassol Forest samples plot in the field defined by the supra-subduction zone peridotites. As pointed out above, these compositional variations could be interpreted as a product of variations in the degree of melting or a result of mantle-melt interaction. In the Troodos case, a melting origin is preferred because it explains the regional distribution of the mineral chemistry variations more readily than an interaction model. The spread of data, particularly on Figure 4.3a, suggests that the Cyprus samples record a wide range of partial melting, from 10-25% in the serpentinite diapir to ~30% in the *background* samples (Bonatti and Michael, 1989).

The *background* sample data confirm Dick and Bullen's (1984) conclusion, based on spinel chemistry, that the Troodos Massif is subduction zone-related. This palaeotectonic setting is also supported by the geochemistry of Troodos lavas (Miyashiro, 1973; Pearce 1975). The Limassol Forest samples are similar in composition to the *background* samples which agrees with Michael and Bonatti's (1985) suggestion that fracture zone peridotites are generally representative of other peridotites from the same geographic area.

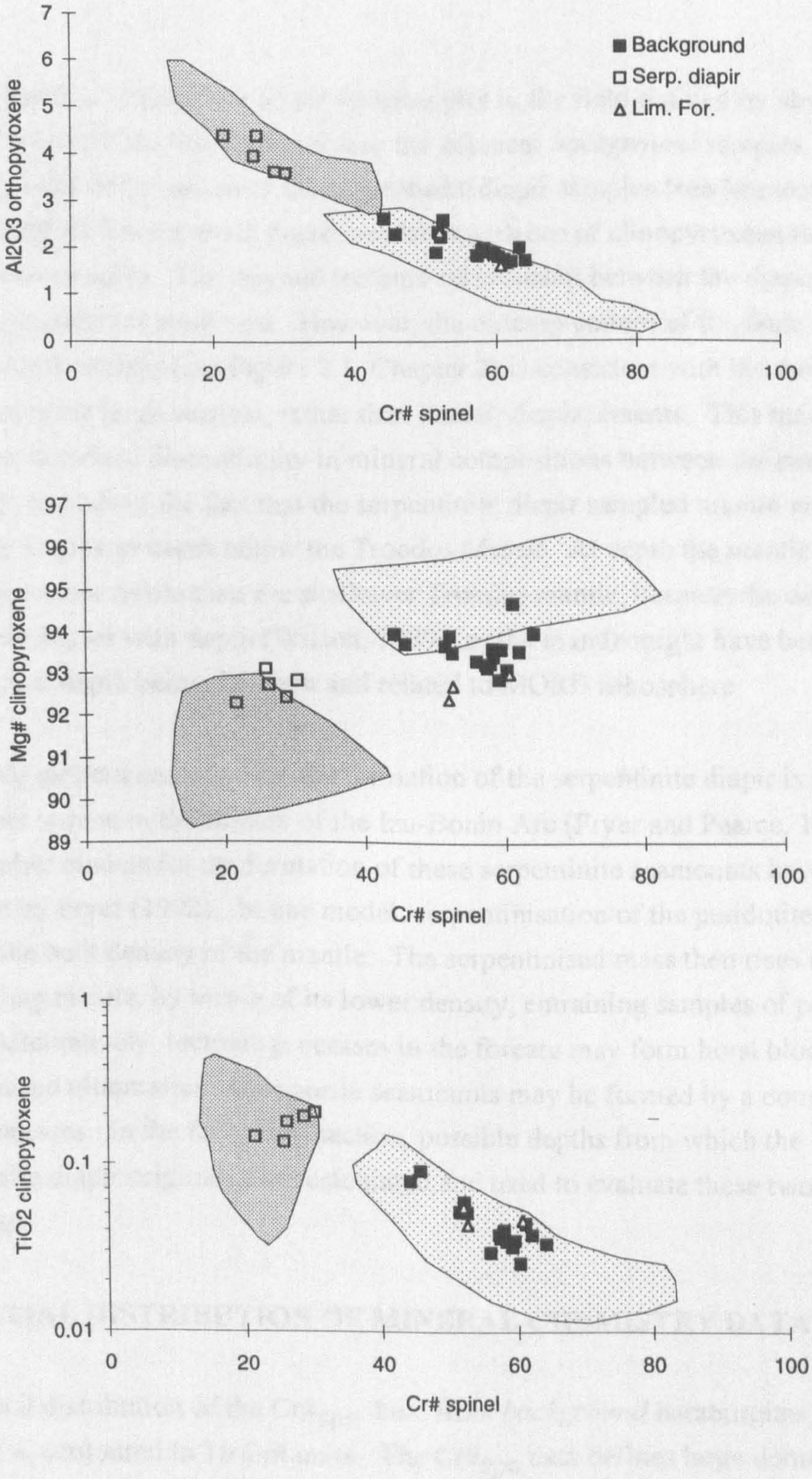

Figure 4.3 Plots showing the variations in orthopyroxene, clinopyroxene and spinel chemistries in the Troodos harzburgites compared to peridotites from other tectonic settings. Heavily shaded area indicates the composition of abyssal peridotites (data from Dick, 1989) and the lightly shaded area indicates the composition of forearc peridotites (data from Ishii *et al.* 1992). Background = *backgroumd* harzburgite values, Serp. diapir = serpentinite diapir values and Lim. For. = Limassol Forest harzburgite data.

The fact that the serpentinite diapir samples plot in the field defined by abyssal peridotites suggests that they are less depleted than the adjacent *background* samples. This agrees with the modal composition of the serpentinite diapir samples (see Microstructure Chapter), which have a much higher modal abundance of clinopyroxene than the *background* samples. The original tectonic relationship between the diapir and *in situ* Troodos sequence is equivocal. However, the outcrop pattern of the fault separating the two peridotite masses (see Figure 2.1, Chapter 2) is consistent with the fault accommodating large vertical, rather than lateral, displacements. This makes it most likely that the sharp discontinuity in mineral compositions between the two peridotite masses, is a result of the fact that the serpentinite diapir sampled mantle which was originally at greater depth below the Troodos Massif. At depth the mantle might have either been more fertile than the shallower Troodos mantle, because the degree of partial melting decreases with depth (Wilson, 1989), or the mantle might have been layered, with the source at depth being different and related to MORB lithosphere.

A possible modern analogue for the formation of the serpentinite diapir is the serpentinite seamounts terrane in the forearc of the Izu-Bonin Arc (Fryer and Pearce, 1992). Two end-member models for the formation of these serpentinite seamounts have been proposed by Fryer (1992). In one model, serpentinisation of the peridotites at depth reduces the bulk density of the mantle. The serpentinised mass then rises through the surrounding mantle, by virtue of its lower density, entraining samples of peridotite from depth. Alternatively, tectonic processes in the forearc may form horst blocks of serpentinised ultramafics. Composite seamounts may be formed by a combination of these processes. In the following section, possible depths from which the Troodos serpentinite diapir originated are calculated and used to evaluate these two end-member processes.

4.5 SPATIAL DISTRIBUTION OF MINERAL CHEMISTRY DATA

The spatial distribution of the $Cr\#_{spn}$ data, from *background* harzburgites, is shown in Figure 4.4, contoured in 10 Cr# units. The $Cr\#_{spn}$ data defines large domains, oriented parallel to the harzburgite-dunite contact, in which $Cr\#_{spn}$ decreases with increasing depth in the mantle sequence. Notable exceptions to this trend are found in the south-west of the study area (around 8650,6525), where unusually low $Cr\#_{spn}$ values occur in a section of harzburgite enclosed by a tongue of dunite at the top of the mantle section, and in the centre of the study area (around 8875,6650) where a layer of low $Cr\#_{spn}$ is perched

in an area of higher $Cr\#_{spn}$. These anomalies are referred to as *Anomaly 1* and *Anomaly 2* respectively in the following text.

To illustrate the variations in mineral chemistry with depth, cross-sections have been drawn along the lines marked A-A' and B-B' on Figure 4.4. The sections were constructed by projecting samples near the section lines into their approximate structural positions on the lines, and calculating their depths below the dunite by assuming that the compositional banding in the harzburgites represents a palaeo-horizontal (Nicolas, 1989). Field evidence (this study and Bartholomew, 1993), suggests that the *background* harzburgite sequence has not been significantly disrupted by faulting and therefore, no attempt has been made to apply any corrections for fault displacements. It is possible that some of the data spread on the sections is the result of minor faulting. However, the coherent trends of the mineral chemistry parameters with depth supports the field evidence for the absence of large-scale faulting in the sequence.

Sections showing the variations in several mineral parameters are presented in Figures 4.5 and 4.6. Section A-A' intersects a large dunite body around (8775,6800) which has been interpreted by Bartholomew (1993) as a large sub-Moho magma chamber. Section B-B' intersects the areas of anomalous $Cr\#_{spn}$ harzburgite identified on the $Cr\#_{spn}$ map (*Anomalies 1 and 2*). Also plotted on section B-B' are the compositions of harzburgite *xenoliths* (see Fieldwork Chapter) found within the tongue of dunite which encloses the *Anomaly 1* harzburgites, and the composition of the crustal dunites overlying the harzburgite sequence.

Section A-A' (Figure 4.5) shows a uniform decrease in $Cr\#_{spn}$ and increase in Ti_{spn} with depth. $Mg\#_{ol}$ values below the dunite show a progressive decrease in depth, mirroring the $Cr\#_{spn}$ variation, whereas the $Mg\#_{ol}$ values in the uppermost harzburgite on this section have lower values than would be anticipated from the below-dunite trend. Na_{cpx} contents are at the detection limit of the electron probe throughout the section. Linear trends in $Cr\#_{spn}$ and $Mg\#_{ol}$ are typical for mantle peridotites, and most likely reflect variations in the degree of melting (Dick and Bullen, 1984; Michael and Bonatti, 1985; Suhr and Robinson, 1994). The decreases in $Cr\#_{spn}$ and $Mg\#_{ol}$ are consistent with a decrease in the degree of melting with increasing depth in the sequence (Bonatti and Michael, 1989). The trend to lower $Mg\#_{ol}$ values at the top of the sequence does not fit the partial melting trend and is discussed further below.

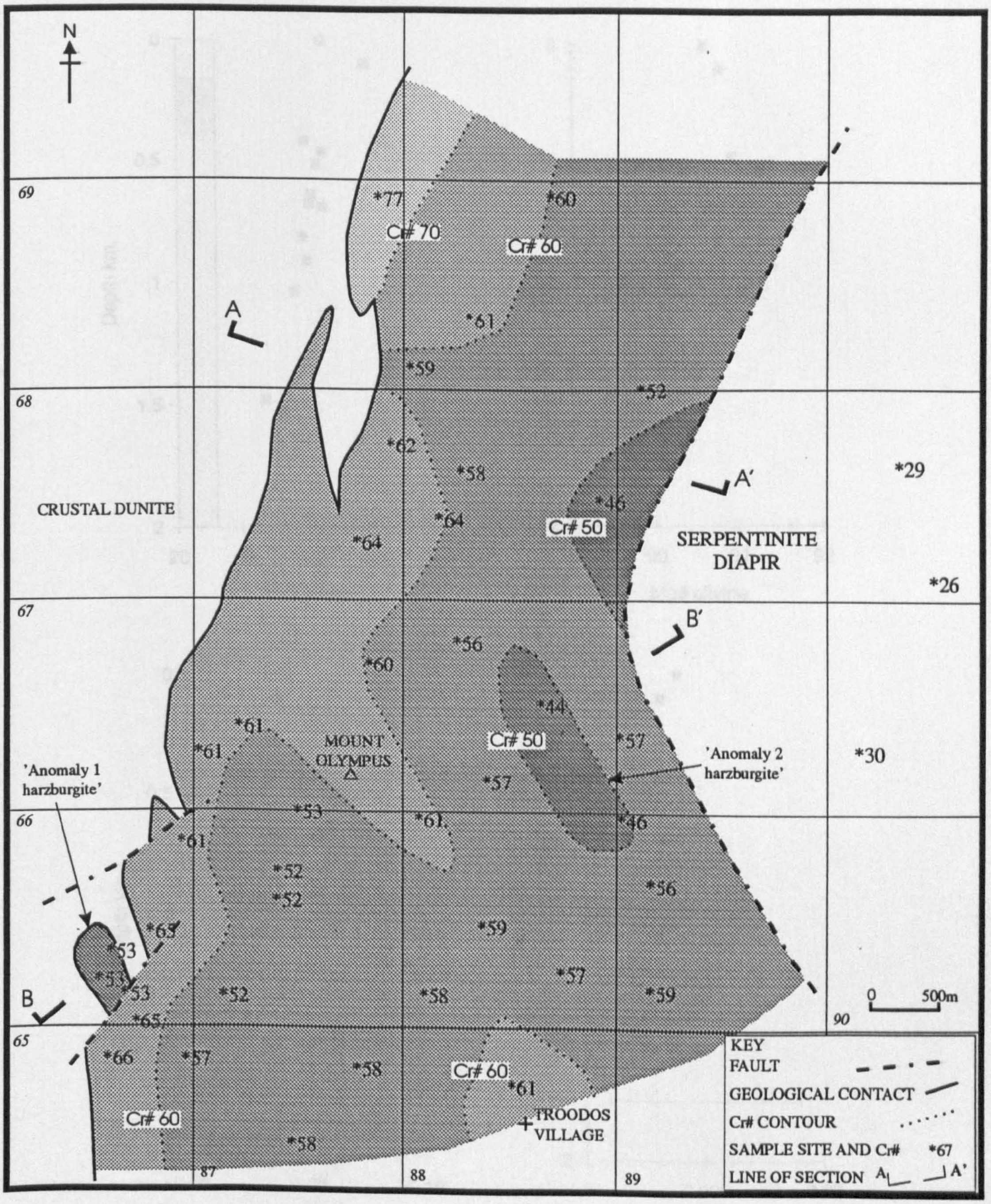

Figure 4.4 A map illustrating the variation of $Cr\#_{spn}$ in the *background* harzburgites.

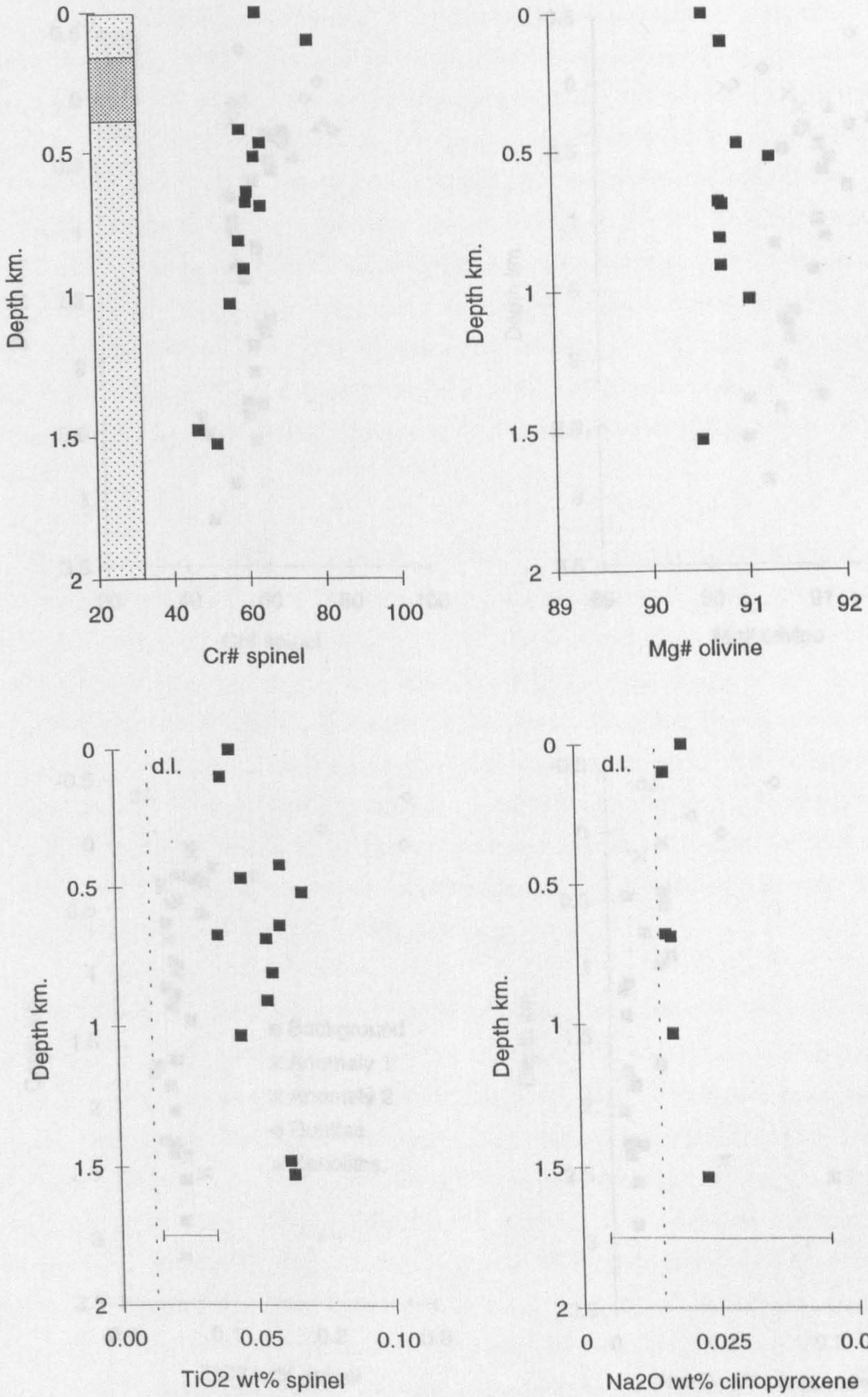

Figure 4.5 The variation of selected mineral parameters with depth in the mantle sequence along the line of section A-A' (see Figure 4.4). Sketch section on the $Cr\#_{spn}$ graph shows harzburgite as light shading and dunite as heavy shading.

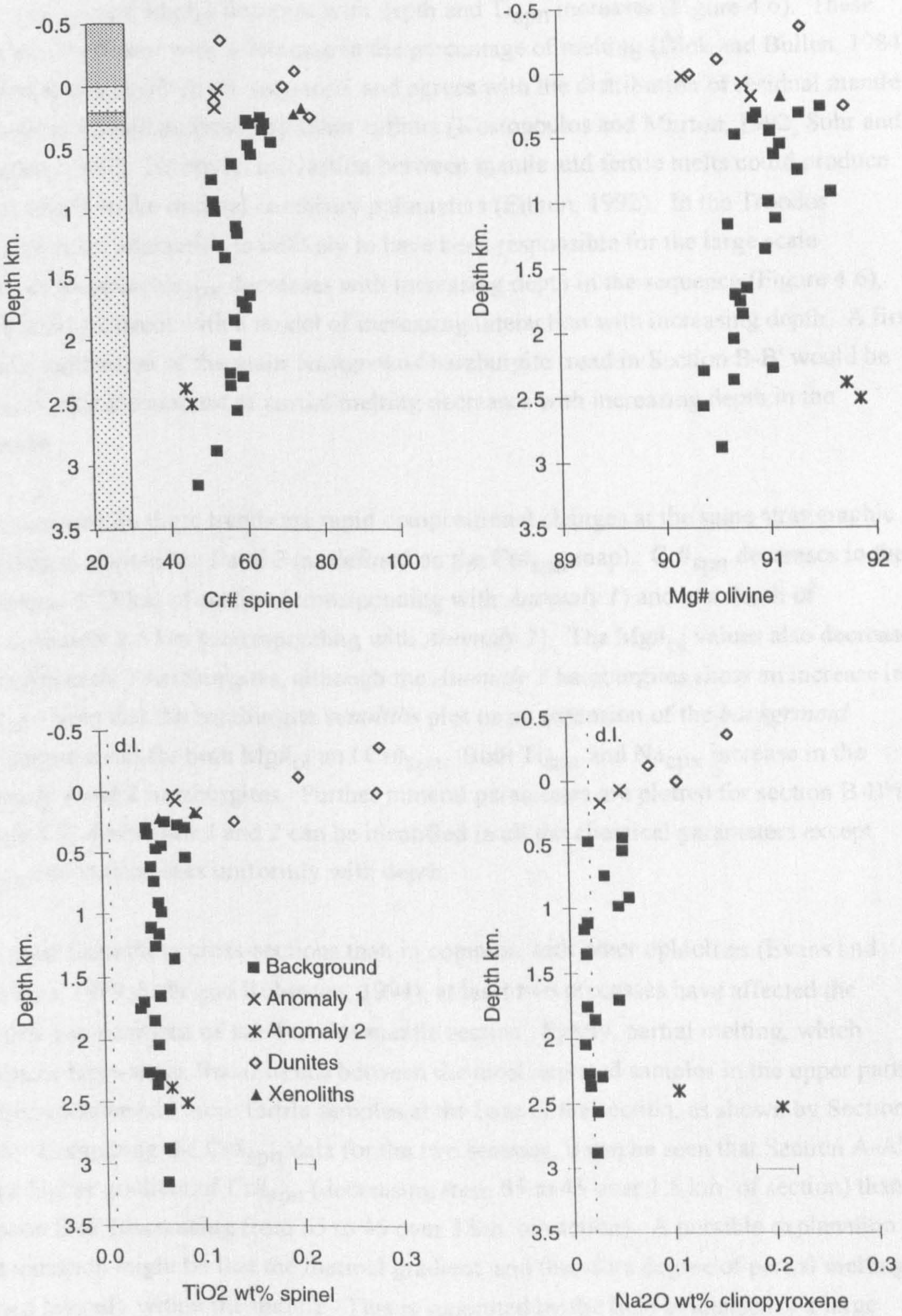

Figure 4.6 The variation of selected mineral parameters with depth in the mantle sequence along the line of section B-B' (see Figure 4.4). Sketch section on the $Cr\#_{spn}$ graph shows harzburgite as light shading and dunite as heavy shading.

Section B-B' shows broadly similar compositional changes with depth to those in section A-A'. $Cr\#_{spn}$ and $Mg\#_{ol}$ decrease with depth and Ti_{spn} increases (Figure 4.6). These trends are consistent with a decrease in the percentage of melting (Dick and Bullen, 1984) with increasing depth in the sequence, and agrees with the distribution of residual mantle in the upper mantle proposed by other authors (Kostopoulos and Murton, 1992; Suhr and Robinson, 1994). However, interaction between mantle and fertile melts could produce similar trends in the mineral chemistry parameters (Elthon, 1992). In the Troodos sequence, melt interaction is unlikely to have been responsible for the large scale variations because Na_{cpx} decreases with increasing depth in the sequence (Figure 4.6), which is inconsistent with a model of increasing interaction with increasing depth. A first order interpretation of the main *background* harzburgite trend in Section B-B' would be therefore, that the amount of partial melting decreases with increasing depth in the sequence.

Superimposed on these trends are rapid compositional changes at the same stratigraphic positions as *Anomalies 1* and *2* (as defined on the $Cr\#_{spn}$ map). $Cr\#_{spn}$ decreases in the uppermost 0.25 km of section (corresponding with *Anomaly 1*) and at a depth of approximately 2.5 km (corresponding with *Anomaly 2*). The $Mg\#_{ol}$ values also decrease in the *Anomaly 1* harzburgites, although the *Anomaly 2* harzburgites show an increase in $Mg\#_{ol}$. Note that the harzburgite *xenoliths* plot on an extension of the *background* harzburgite trend for both $Mg\#_{ol}$ and $Cr\#_{spn}$. Both Ti_{spn} and Na_{cpx} increase in the *Anomaly 1* and *2* harzburgites. Further mineral parameters are plotted for section B-B' in Figure 4.7; *Anomalies 1* and *2* can be identified in all the chemical parameters except Fe_{cpx} which decreases uniformly with depth.

It is clear from these cross-sections that, in common with other ophiolites (Evans and Hawkins, 1989; Suhr and Robinson, 1994), at least two processes have affected the mineral compositions of the Troodos mantle section. Firstly, partial melting, which produces large-scale, linear trends between the most depleted samples in the upper parts of the sequence and more fertile samples at the base of the section, as shown by Section A-A'. Comparing the $Cr\#_{spn}$ data for the two sections, it can be seen that Section A-A' has a higher gradient of $Cr\#_{spn}$ (decreasing from 65 to 45 over 1.5 km. of section) than Section B-B' (decreasing from 65 to 45 over 3 km. of section). A possible explanation for this variation might be that the thermal gradient, and therefore degree of partial melting, varied laterally within the mantle. This is supported by the field evidence for a large dunitic magma chamber at the top of Section A-A' (Bartholomew, 1993), which suggests that the magma supply was greater at the top of Section A-A' than B-B'.

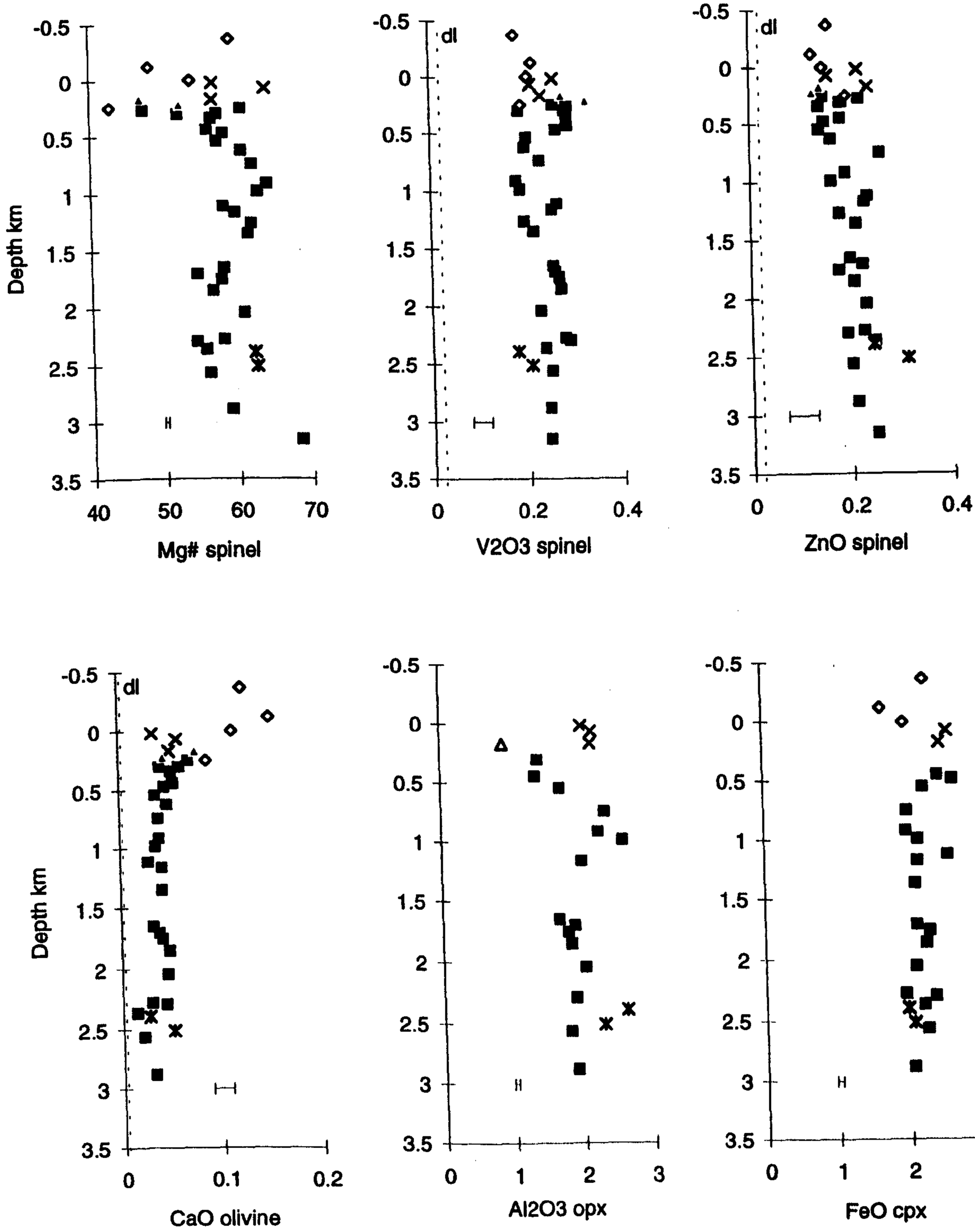

Figure 4.7 The variation of mineral parameters with depth in the sequence along the line of section B-B' (see Figure 4.4). Symbols the same as for Figure 4.6.

Superimposed upon the partial melting trend are local enrichments in incompatible elements, shown by *Anomalies 1* and *2* in Section B-B'. *Anomaly 1* harzburgites are intermediate in composition between the depleted harzburgites, typical of the uppermost parts of the section, and the overlying dunites. This relationship suggests that the *Anomaly 1* harzburgites have been refertilised by interaction with the melt which subsequently crystallised to form the overlying cumulate sequence. The existence of percolating melts is supported by the petrology of the overlying dunites in which clinopyroxene is interstitial to olivine and spinel, and in places poikilitically encloses these phases (see Microstructure Chapter). As described in the Fieldwork chapter, the poikilitic clinopyroxene grades into massive clinopyroxenites which are elongated parallel to the harzburgite foliation. This means that the infiltration event must have occurred before, or during, the asthenospheric deformation of the mantle. Furthermore, the outcrop of massive clinopyroxenites in the crustal dunites is geographically restricted to a horizon stratigraphically above the *Anomaly 1* harzburgites (see Figure 2.1, Chapter 2).

The mantle cross-sections presented in Figures 4.6 and 4.7 show that these melts added Al, Fe, Na and Ti to the *Anomaly 1* harzburgites. The $Cr\#_{spn}$ map shows that the enrichments are not laterally continuous along the dunite-harzburgite contact, which suggests that melt percolation through the Troodos mantle sequence was focused into a zone approximately 200 to 300 m wide.

Anomaly 2 harzburgites also show enrichments in Ti, Na and Al, which suggests that melt impregnation was not restricted to the uppermost harzburgites. Moreover, it is notable that the *Anomaly 2* harzburgites are located stratigraphically below the *Anomaly 1* harzburgites, and within the possible zone of melt percolation. The *Anomaly 2* data also show a sharp increase in $Mg\#_{ol}$, opposite to the trend shown by *Anomaly 1* harzburgites. Possible explanations for this reversal might be:

a) *Anomaly 2* represents an area of abnormally high melting which was selectively refertilised by an Fe-poor melt.

b) The melt which added Ti and Na was Mg- rather than Fe- rich.

The formation of the *Anomaly 2* harzburgites is discussed further below.

The compositions of the harzburgite *xenoliths* (sampled from the dunite enclosed the *Anomaly 1* harzburgites) are plotted on Figures 4.6 and 4.7, and show that these harzburgites have minor element (Ti_{spn}, Ca_{ol}) contents similar to the *Anomaly 1* harzburgites. However, *xenolith* $Cr\#_{spn}$ and $Mg\#_{ol}$ lie on an extension of the *background* harzburgite trend. The embayed nature of the *xenolith*-dunite contacts (see

the Fieldwork Chapter) implies that reaction between the two lithologies took place during dunite formation. The $Cr\#_{spn}$ and $Mg\#_{ol}$ values of the *xenoliths* may therefore, have been buffered towards those of the original *top-of-the-sequence* harzburgites, from which the *xenoliths* were formed.

For all the mineral parameters other than $Mg\#_{ol}$, the crustal dunite samples plot on trends consistent with cumulate processes (increasing incompatible contents with height in the sequence). However, the $Mg\#_{ol}$ data show a sharp discontinuity between the dunite tongue and the overlying dunites. Furthermore, the overlying dunites trend towards more magnesian compositions with increasing height in the sequence; the reverse of a typical cumulate trend. At least two possible explanations exist for this behaviour:

a) Oxygen fugacity increased with height (and therefore percentage of crystallisation) in the dunite magma chamber stabilising Fe^{3+} and therefore increasing the Mg# of crystallising olivines. As discussed below, the V_{spn} content of the crustal dunites and fO_2 values calculated from the probe data (see Section 4.6.3), support the hypothesis of oxidising conditions in the magma chamber. The oxidising conditions could result from the presence of hydrous fluids which would be consistent with the proposed supra-subduction zone origin of the Troodos Ophiolite (Gass, 1980).

b) The magma chamber was an open system which allowed the behaviour of the trace and major elements to become decoupled (O'Hara and Matthews, 1981).

The data is insufficient to draw firm conclusions. Mineral chemistry data from dunites in the Leka ophiolite, discussed in Nicolas (1989), show similar trends for $Mg\#_{ol}$. These trends were interpreted as the result of episodes of magma chamber replenishment with primitive melt. Browning (1984) also identified reversed cycles in the Oman ophiolite, which he attributed to open system processes in the magma chamber. However, late-stage intercumulus processes were the preferred explanation for major and trace element decoupling in the Oman cumulates.

As noted above, the $Mg\#_{ol}$ data at the top of Section B-B' also trend towards lower values. This trend is comparable to that in the *Anomaly 1* harzburgites and suggests that the harzburgites at the top of Section B-B' have also been affected by melt infiltration. However, the absence of any enrichment trends in the other mineral chemistry parameters in these samples, indicates that melt infiltration was probably a relatively minor process in these harzburgites.

4.5.1 DEPTH OF ORIGIN OF THE SERPENTINITE DIAPIR

As noted above, the primary control on mantle mineral chemistries is partial melting, which decreases systematically with depth in the sequence, producing apparent linear trends in chemical parameters. The $Cr\#_{spn}$ values from *background* harzburgites in Section A-A' and the lower part of Section B-B' show this trend particularly well (Figures 4.6 and 4.7). By fitting a regression line to this data it is possible to calculate the rate of change of $Cr\#_{spn}$ with depth and therefore, to estimate the depth of origin of a sample if its $Cr\#_{spn}$ is known (assuming that the sample has not been affected by melt infiltration).

A regression line calculated for the *background* harzburgite data in Section B-B' (excluding the *Anomaly 1* and *2* harzburgites) is illustrated in Figure 4.8 (Section B-B' was chosen because the $Cr\#_{spn}$ gradient in Section A-A' may be abnormally high as discussed above). The results obtained when the equation of the line is used to calculate the depth of the serpentinite diapir samples are summarised in Table 4.2, and sample locations in the diapir area are illustrated in Figure 4.9.

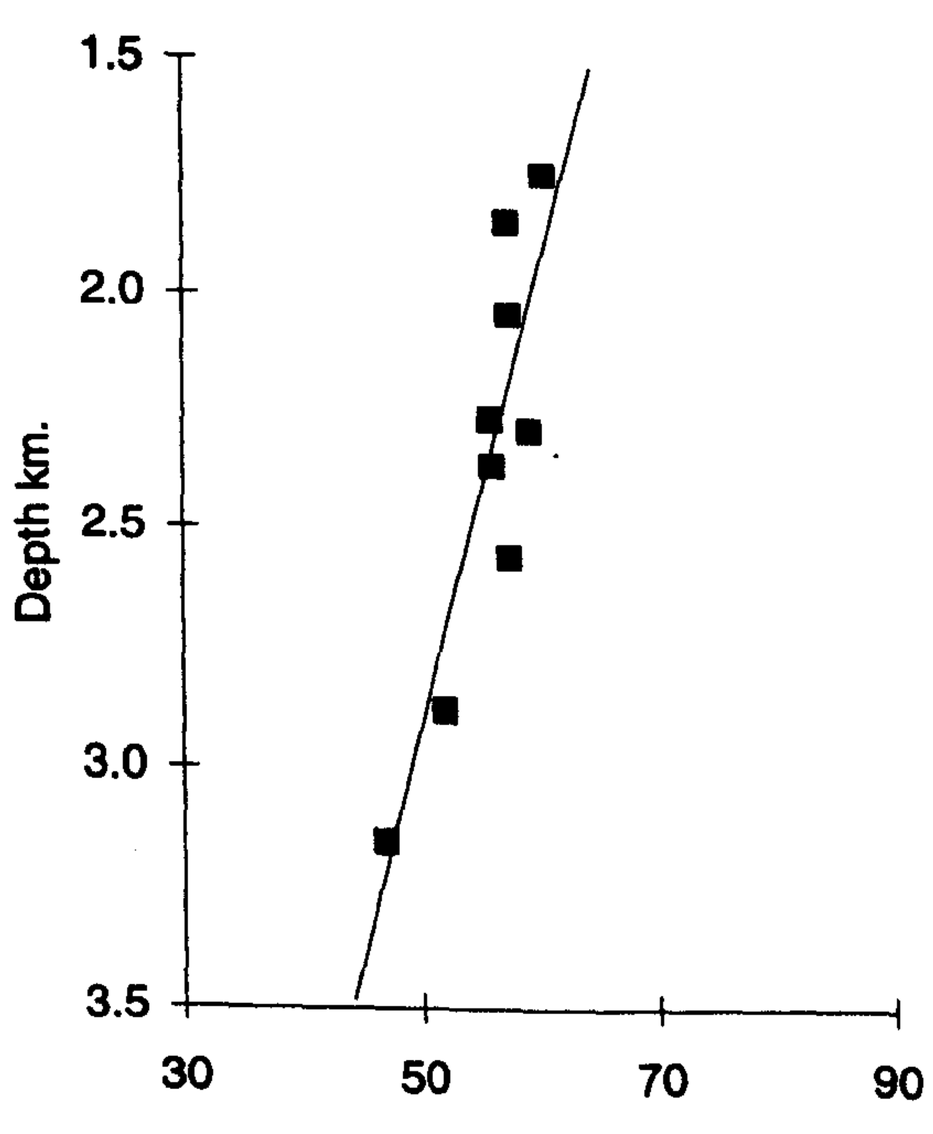

Figure 4.8 The variation in $Cr\#_{spn}$ with depth in the sequence along the line of section B-B' (see Figure 4.4) and the best fit line for the data; the equation of the regression line is $y = -0.10x + 7.79$.

Sample	Cr#spn	Calc. Depth (km)	Sample	Cr#spn	Calc. Depth (km)
191	30.2	4.8	256	28.7	5.0
193	26.2	5.2	251	21.5	5.7
194	26.8	5.2	255	25.7	5.3

Table 4.2. Calculated depths below the main harzburgite-dunite contact for samples from the serpentinite diapir.

Considering that the potential errors in these calculations are quite large (estimated to be $\pm$ 0.3 km.), it is notable that, despite the wide geographical distribution of the samples, the calculated depths are all reasonably similar.

If the density instability model (described in Section 4.4, Fryer, 1992), for serpentinite diapir formation was applicable to the Troodos serpentinite diapir, peridotites from a large range of depths would be entrained in the ascending mass. However, the calculated depth data suggest that a relatively uniform stratigraphic depth is exposed. This data is therefore, more consistent with a block faulting model (Fryer, 1992), in which the serpentinite would act as a coherent mass.

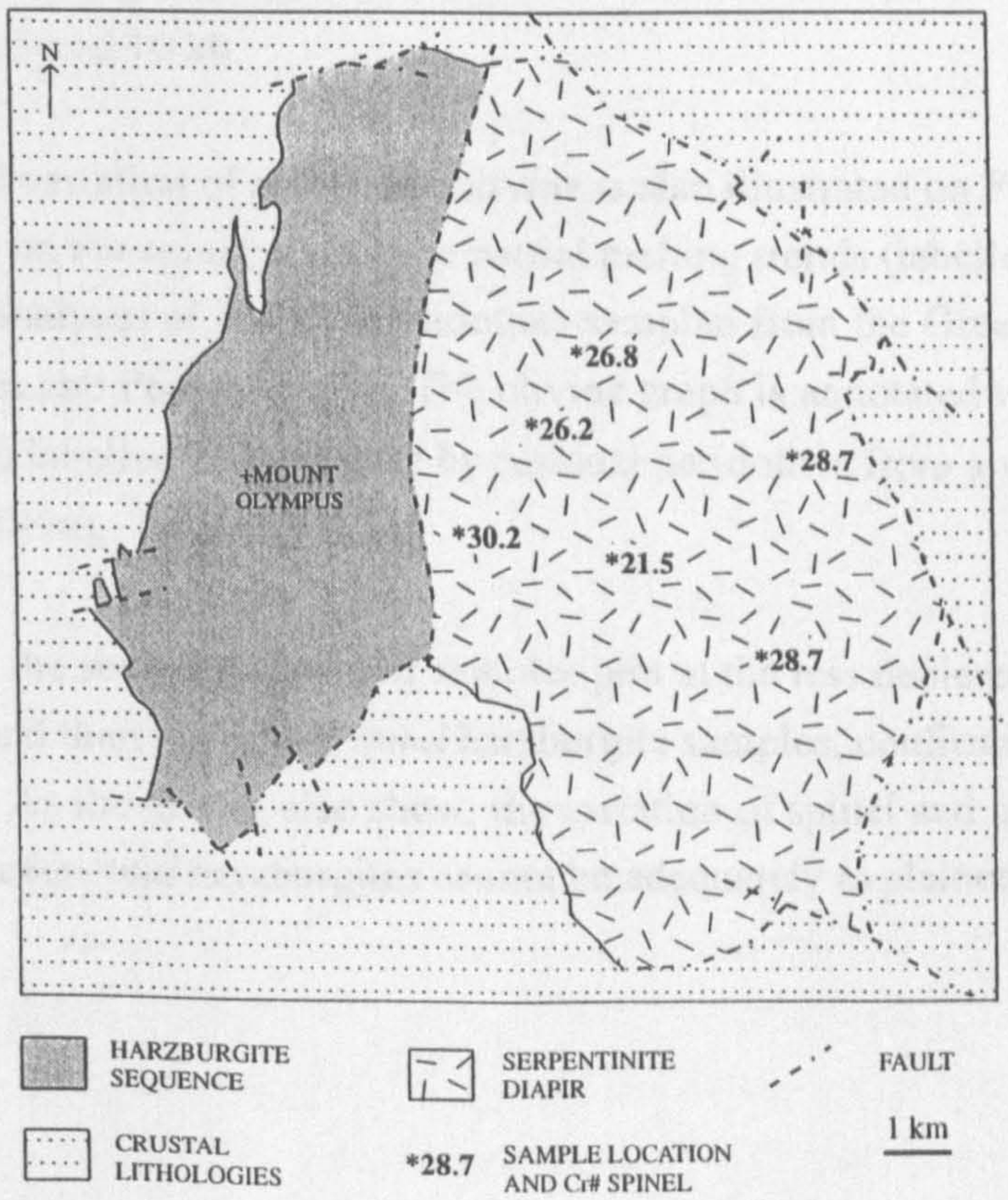

Figure 4.9 The sample locations in the serpentinite diapir.

4.6 MINERAL CHEMICAL EVOLUTION OF THE *BACKGROUND* HARZBURGITES

The mineral chemistry cross-sections through the Troodos mantle sequence suggest that at least two processes have affected the mantle: partial melting and reaction with melts. In this section, these processes are examined in more detail using bivariate plots of mineral chemical parameters. Samples are differentiated in the same way as the previous section, with *Anomaly 1* and *2*, and *top-of-the-sequence* (labelled top seq on the graphs) harzburgites plotted separately from the other *background* harzburgites.

4.6.1 PARTIAL MELTING TRENDS

Figure 4.10 shows the $Mg\#_{ol}$ - $Cr\#_{spn}$ variation in the Troodos samples, with the composition of abyssal (Dick, 1989) and forearc (Ishii *et al.*, 1992) peridotites for comparison. The data define a coherent array of increasing $Mg\#_{ol}$ and $Cr\#_{spn}$ which is typical of mantle peridotites, and most likely reflects varying degrees of partial melting (Dick and Bullen, 1984; Michael and Bonatti, 1985; Arai, 1990). This variation has been reproduced experimentally (Jacques and Green, 1980; Mysen and Kushiro, 1977) and the experimental results are shown with the Troodos data on Figure 4.10b. The data suggest that the Troodos harzburgites might have experienced 10 to 25% partial melting at pressures between 5 and 10 kb.

The compositional variation of spinel and olivine is also illustrated on Figures 4.11 and 4.12. Also shown on the spinel graphs are partial melting trends (labelled PM) constructed from analyses of residual peridotites sampled from the Greek Tethyan Ophiolites (Rassios and Pearce, 1995). The olivine graph is annotated with a partial melting trend (also labelled PM) defined by residual peridotites from a variety of tectonic settings (Ozawa, 1994).

On all the graphs, the serpentinite diapir samples plot at the less depleted end of the partial melting trend than the *background* harzburgite samples, confirming their more fertile chemistry. As the graphs also show, the variation of spinel and olivine chemistry in the Troodos *background* harzburgites cannot be adequately explained by partial melting alone.

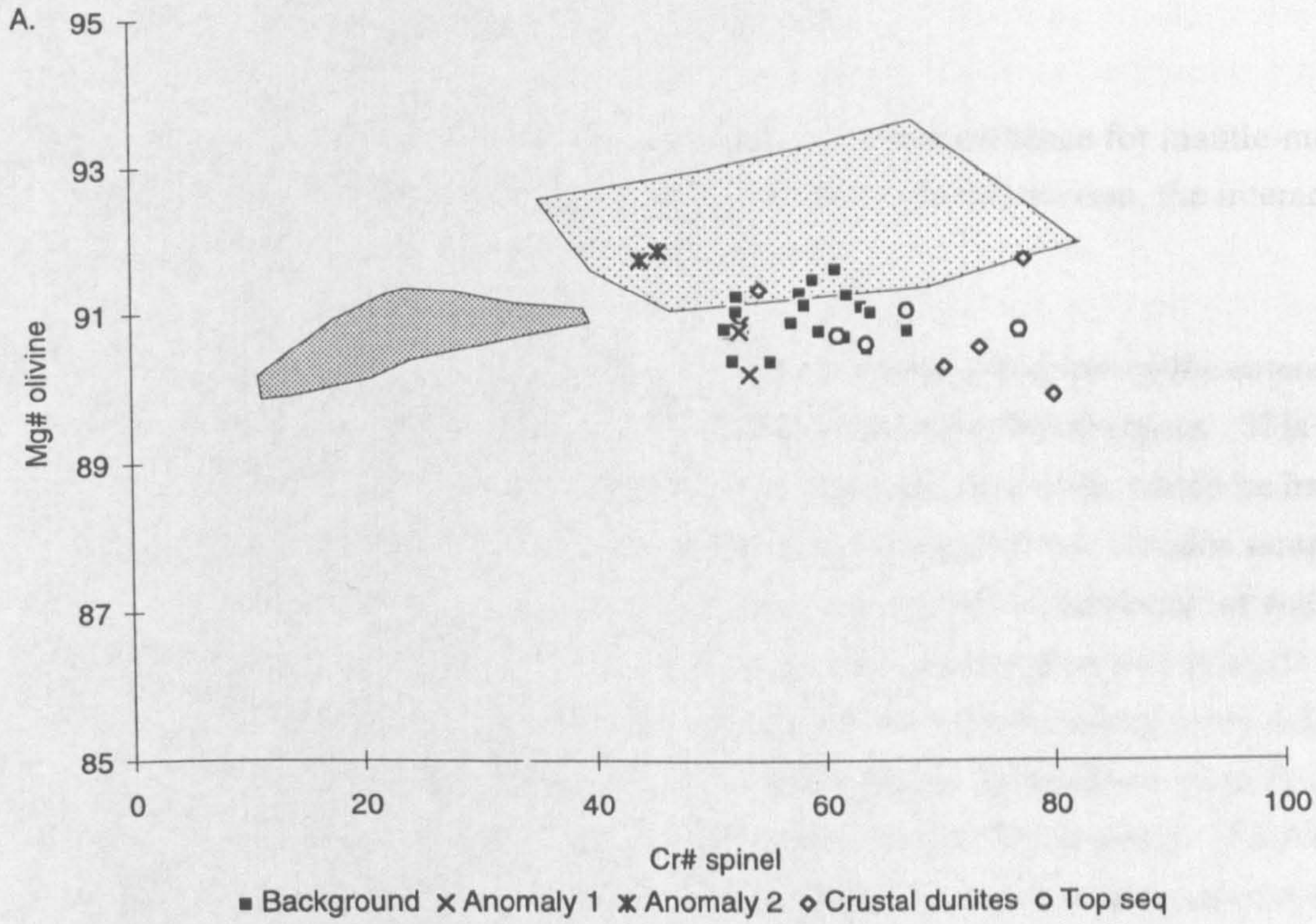

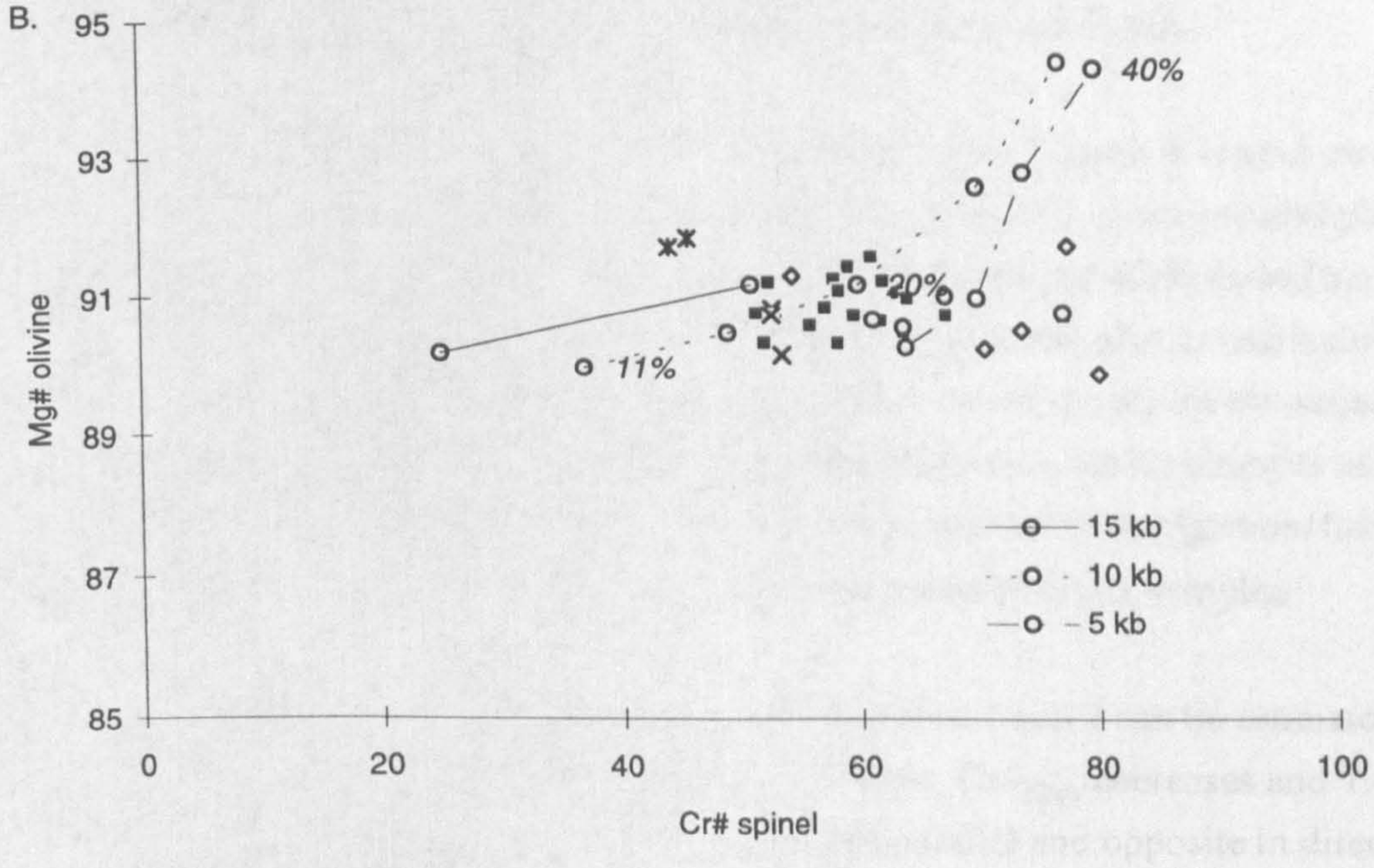

Figure 4.10 Graphs illustrating the $Mg\#_{ol}$-$Cr\#_{spn}$ variation in the Troodos peridotites, a) compared to abyssal peridotites (heavy shading; data from Dick, 1989) and forearc peridotites (light shading; data from Ishii *et al.* 1992), b) compared to experimentally determined variations (from Jacques and Green, 1980, starting composition = Tinaquillo Lherzolite) in residual olivine and spinel compositions during equilibrium partial melting, figures in italics indicate the % of partial melt.

4.6.2 MANTLE-MELT INTERACTION TRENDS

The mantle cross-sections described above provide strong evidence for mantle-melt interaction at various positions in the mantle sequence. In this section, the interaction trends are considered in more detail.

On the $Mg\#_{ol}$ - $Cr\#_{spn}$ graph (Figure 4.10a), the *Anomaly 1* and *top-of-the-sequence* samples plot towards lower $Mg\#_{ol}$ than the other *background* harzburgites. This trend is equivalent to that found by Ozawa (1994) in the Miyamori ophiolite, which he interpreted as a result of melt infiltration. A similar origin is envisaged for the Troodos samples, which agrees with the proposed reaction between the uppermost harzburgites and melts, illustrated in the cross-sections above. The *Anomaly 2* harzburgites however, do not follow this trend and plot at the least depleted end of the partial melting array defined by the other *background* harzburgites. This is consistent with the evidence from the mineral cross-sections for the Troodos mantle becoming less depleted with depth. However, the enrichments in incompatible elements in the *Anomaly 2* samples, compared to the adjacent harzburgites on the cross-sections, show that a decrease in the degree of melting cannot be the sole explanation for the chemistry of these harzburgites.

The $Cr\#_{spn}$-TiO_{2spn} variation in the Troodos harzburgites (Figure 4.11a) shows that, when considered as groups, the *top-of-the-sequence* and harzburgite *xenoliths* plot as en echelon arrays, towards progressively higher TiO_2, between the *background* harzburgites and the crustal dunites. The *Anomaly 1* and *2* harzburgites also plot as two tightly defined groups. The *Anomaly 1* harzburgites plot on an extension of the *top-of-the-sequence* sample arrays, and within the compositional range defined by the harzburgite *xenoliths*. The *Anomaly 2* harzburgites plot at the least depleted end of the *background* harzburgite array, between the *background* samples and the serpentinite diapir samples.

Expected interaction trends for samples from *Anomalies 1* and *2* can be estimated from the cross-sections described above. In both anomalies, $Cr\#_{spn}$ decreases and TiO_{2spn} increases resulting in an interaction vector oriented parallel and opposite in direction to the melting trend (illustrated as a dashed line labelled IT1 on Figure 4.11a). This orientation agrees with Elthons (1992) proposal that refertilisation of upper mantle peridotites by transient melts produces compositional trends which mirror partial melting trends. The fact that the *Anomaly 1* and *2* samples plot on the least depleted end of the harzburgite array could be interpreted as a result of either, a low degree of partial melting or a high degree of melt interaction. For the *Anomaly 1* harzburgites, melt interaction is the preferred explanation because of the complimentary variation of other mineral

parameters and their location in the sequence. *Anomaly 2* harzburgites show similar displacements from the inferred partial melting trends in the cross-sections as the *Anomaly 1* harzburgites, and therefore, their position on the $Cr\#_{spn}$-TiO_2 graph is also interpreted as a result of mantle-melt interaction.

However, as noted above, the *Anomaly 1* and *2* harzburgites plot in slightly different positions on the $Cr\#_{spn}$-TiO_{2spn} projection. The cross-sections described above provide strong evidence that the *Anomaly 1* harzburgites reacted with melts which eventually crystallised as the crustal dunites. These facts, along with the position of the crustal dunites on the $Cr\#_{spn}$-TiO_{2spn} graph, suggest that there maybe a second interaction vector (illustrated as a dashed line labelled IT2 on Figure 4.11a) describing reaction between *background* harzburgites and melts crystallising as the crustal dunites. A second reaction vector, in the direction labelled IT2, would also be consistent with the compositional variation of the *top-of-the-sequence* and *xenolith* samples, explaining their position as en echelon arrays between the *background* harzburgites and the crustal dunites. In this scenario, the arrays would represent progressively greater amounts of melt reaction. The spread of the *top-of-the-sequence* and *xenolith* samples perpendicular to the IT2 vector and parallel to the IT1 vector could be a result of different degrees of partial melting, different degrees of interaction or additional reaction with melts along IT1.

Implicit in the hypothesis that there are two reaction trends in the harzburgites, is that there were at least two different reacting melts. The melt for IT2 has already been associated with that which crystallised the crustal dunites. The IT1 vector displaces the *Anomaly 2* harzburgites back along the partial melting trend towards the serpentinite diapir samples. The melt associated with IT2 could therefore be interpreted as a fertile melt from deeper in the mantle section. The possibility that a variety of melt compositions were available to react with the mantle harzburgites is supported by the wide range of lava compositions found at the top of the Troodos crustal sequence (Cameron, 1985; Rautenschlein *et al.*, 1985; Bednarz and Schmincke, 1994).

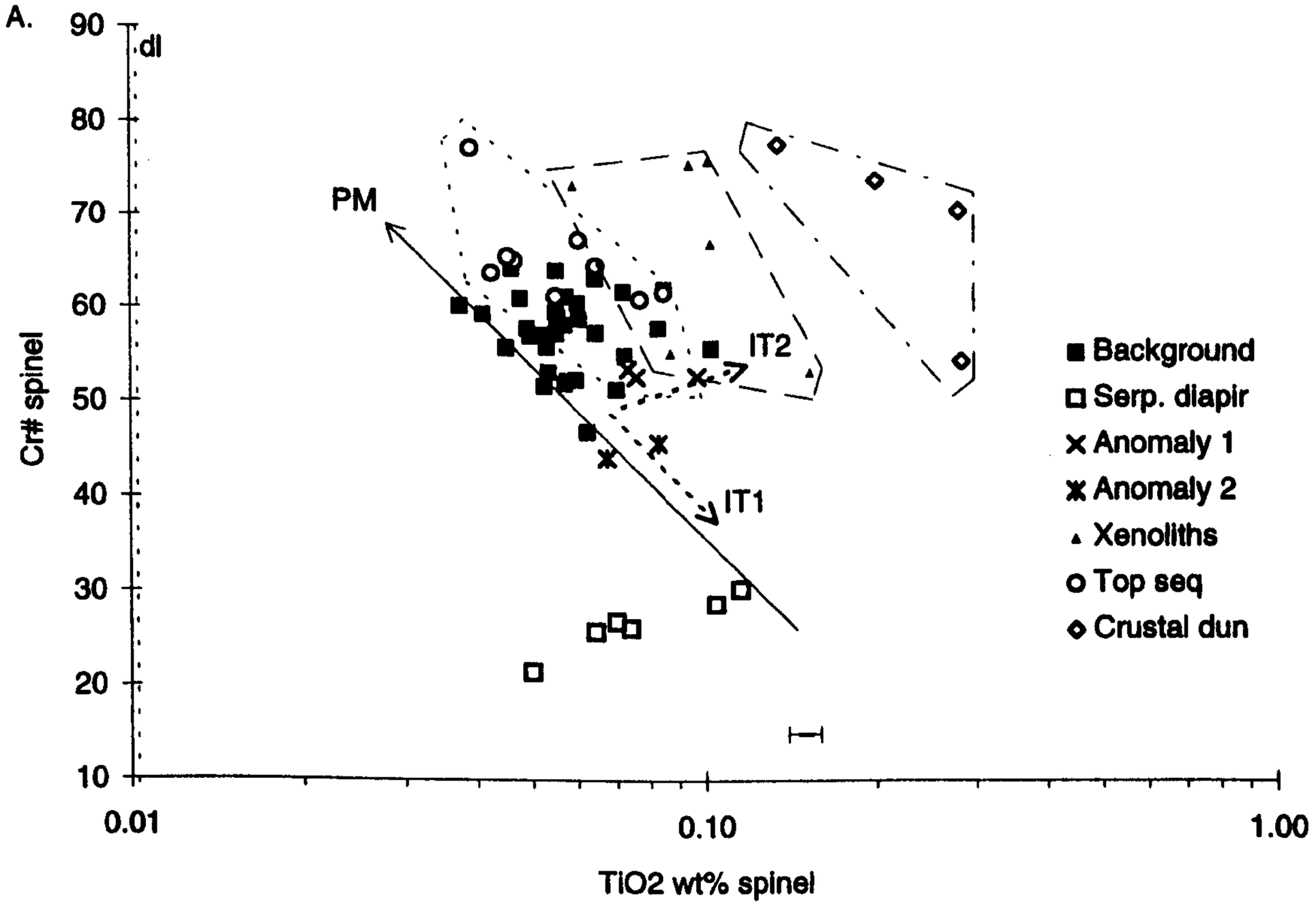

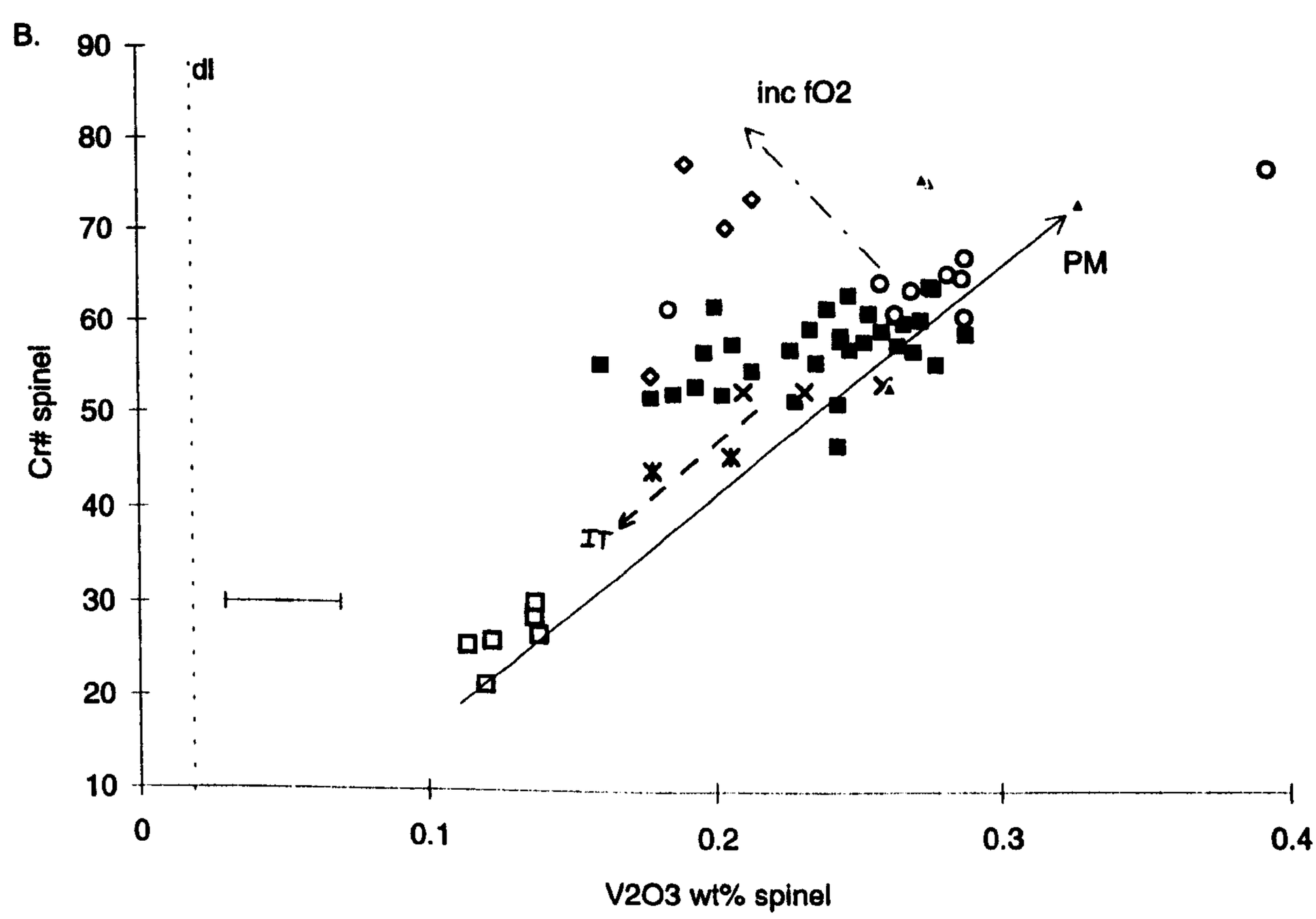

Figure 4.11 a) Graph illustrating the $Cr\#_{spn}$-TiO_{2spn} variation in the Troodos peridotites. b) Graph illustrating the $Cr\#_{spn}$-V_2O_{3spn} variation in the Troodos peridotites.

The serpentinite diapir samples also show considerable variation in Ti_{spn} content on this graph, forming an array oriented parallel, but opposite in direction, to the proposed IT2 trend. A possible explanation for the compositional variation of these samples might be that they have also reacted with an IT2 melt. However, the starting peridotite composition in this case would have to have an unrealistically low Ti_{spn} content. Unfortunately, dense faulting and heavy serpentinisation makes it impossible to ascertain the original spatial relationships between these samples, so a more detailed explanation of this Ti_{spn} variation cannot be given with the available data.

The importance of the $Cr\#_{spn}$-V_2O_{3spn} projection (Figure 4.11b) as a potential discriminant between spinels crystallising from magmas under different oxygen fugacity conditions has been discussed by Rassios and Pearce (1995), and is tentatively applied here to the Troodos mantle spinels.

The theoretical basis underlying the control of fO_2 on V_{spn} is as follows (Rassios and Pearce, 1995). In oxidised magmas, such as those generated above subduction zones, V will be present in the 4+ or 5+ state, in which form it cannot be readily accommodated in the spinel lattice. Oxidised magmas should therefore crystallise low-V spinels, independent of the initial V content of the magma. In reducing conditions, V^{3+} will be stable and is more easily accommodated in the spinel lattice. Reduced magmas, such as those generated at mid-ocean ridges, have the potential therefore, to crystallise high V spinel. However, the actual V content of spinels crystallising from low fO_2 magmas will be dependant on the V content of the magma.

The fact that boninites have low V contents (e.g. 35 - 45 ppm., Wilson, 1989) and crystallise from oxidised magmas, and N-MORB has higher V contents (e.g. 250 - 270 ppm, Wilson, 1989) and crystallise from reduced magmas supports this argument. The theoretical vector (Rassios and Pearce, 1995) for spinel crystallisation from an oxidising magma is shown on Figure 4.11b.

During mantle melting, the V distribution coefficient will also depend on the oxygen fugacity conditions. Experimentally determined partition coefficients between clinopyroxene and melt for varying fO_2 have been summarised by Pearce and Parkinson (1993). When oxidising conditions prevail during melting, the clinopyroxene-melt distribution coefficient is <0.2, whereas in reducing conditions the coefficient is close to 1. Therefore, in oxidised melting zones, such as subduction zones, V will be removed from the source more rapidly than in reducing conditions, such as those at mid-ocean ridges.

During mantle-melt reaction the same argument will apply, with oxidising conditions stabilising the less compatible $V^{4+/5+}$ and therefore, crystallising low-V spinel. Similarly, reducing conditions favour high V spinel formation, as long as the reacting melt has a high V content.

Expected interaction trends for samples from *Anomalies 1* and *2* can again be estimated from the cross-sections described above. In both cases, $Cr\#_{spn}$ and V_2O_{3spn} decrease, resulting in an interaction vector oriented parallel and opposite in direction to the melting trend (dashed line labelled IT on Figure 4.11b). Again this trend mimics the melting trend, and further supports Elthons (1992) proposal that peridotites refertilised by melts display compositional trends which mirror partial melting trends. The IT trend suggests that interaction in the Troodos mantle section involved coupled substitution of Al and Cr, thereby lowering the $Cr\#_{spn}$ at the same time as generating low-V_{spn} values. At least two mechanisms for generating low-V_{spn} are possible, either removal of V from existing spinels by the reacting melt, or crystallisation of new, low V spinel. The petrographic evidence for spinel dissolution and crystallisation is presented in the next chapter.

On the $Cr\#_{spn}$-V_2O_{3spn} graph, the *Anomaly 1* harzburgites plot at the least depleted end of the *background* harzburgite array, and within the compositional range defined by the harzburgite *xenoliths*. The *Anomaly 2* harzburgites again plot on the PM trend, between the *background* and serpentinite diapir samples. The *top-of-the-sequence* harzburgites plot almost entirely at the most depleted end of the partial melting trend, with the *xenolith* samples again plotting at intermediate positions between the *top-of-the-sequence* samples and the crustal dunites.

Clearly, the relative positions of the *Anomaly 1* and *2* harzburgites on the $Cr\#_{spn}$-V_2O_{3spn} projection mirror those on the $Cr\#_{spn}$-TiO_{2spn} plot. The *xenoliths* again plot at intermediate positions between the partial melting trend and the crustal dunites, providing further evidence for reaction between the melts which crystallised the crustal sequence and the uppermost parts of the mantle section. Note that, on this projection, the *top-of-the-sequence* samples plot at the most depleted end of the partial melting trend. This supports the evidence from the mineral chemistry cross-sections that the degree of depletion increases upwards through the mantle section.

Comparing the positions of the *top-of-the-sequence* samples on the $Cr\#_{spn}$-V_2O_{3spn} and $Cr\#_{spn}$-TiO_{2spn} plots suggests that mantle interaction has added Ti to these samples at the same time as leaving V contents at their residual values. However, the *Anomaly 1* and

2 samples appear to have had Ti added at the same time as low V contents were generated. As pointed out by Rassios and Pearce (1995), one way to decouple the behaviour of Ti and V is to crystallise spinel under oxidising conditions which would generate spinel high in Ti and low in V. This suggests that mantle-melt reaction in the Troodos sequence involved oxidised melts.

Note that the $Cr\#_{spn}$-V_2O_{3spn} plot also shows that the crustal dunites plot along the theoretical trend for spinel crystallisation under oxidising conditions. This supports the proposal that melts may have oxidised the mantle sequence and is consistent with the proposed supra-subduction palaeotectonic origin of the Troodos Ophiolite (e.g. Pearce, 1975). The implications of the crustal dunite trend is discussed in more detail in Section 4.8. A summary of the variations in spinel chemistry in each of the harzburgite sub-types is presented in Table 4.3.

The variations in olivine chemistry are illustrated in Figure 4.12a. Like the spinel data, the olivine compositions of the *xenolith* and *top-of-the-sequence* samples plot off the partial melting trend (labelled PM and defined by Ozawa (1994) from olivine analyses from peridotites from various tectonic settings). Figure 4.12a is annotated with an olivine crystallisation trend (labelled XT) defined by the Troodos crustal dunites, which matches the trend defined by Ozawa (1994) for the crystallisation and removal of olivine during wehrlite intrusion in the Miyamori Ophiolite. The *xenolith* and *top-of-the-sequence* samples plot at intermediate positions between this crystallisation trend and the partial melting trend. The *Anomaly 1* samples define a broad trend between the *background* harzburgites on the partial melting trend and the most evolved crustal dunites. These relationships lend further support to the conclusion drawn from the spinel data, that the *xenolith*, *top-of-the-sequence* and *Anomaly 1* compositions can be described in terms of interaction between the *background* harzburgites and melts crystallising the crustal sequence.

Unfortunately, serpentinisation has destroyed all the primary olivine in the serpentinite diapir samples. However, comparison with peridotites from other ophiolites that have similar $Cr\#_{spn}$ (Suhr and Robinson, 1994), suggests that the serpentinite diapir olivines would have compositions of approximately Mg# 90 and NiO 0.4 wt%, and would therefore, plot at the least depleted end of the partial melting trend.

Sample	Cr# spinel	Ti spinel	V spinel	Process
Background	increases base to top of the section	low	increases base to top of the section	partial melting
Anomaly 1	low	high	low	melt reaction
Anomaly 2	low	high	low	melt reaction
Xenoliths	low	high	low	melt reaction
Top-of-the-sequence	high	high	high	minor melt reaction

Table 4.3. Summary of spinel chemistries in the Troodos sequence, high and low refer to the values of the mineral parameters compared to the geographically nearest *background* harzburgite value.

Olivines from *Anomaly 2* harzburgites plot at the least evolved end of the XT trend. In terms of olivine composition therefore, the *Anomaly 2* harzburgites are not intermediate between the *background* harzburgites and the serpentinite diapir samples. The low Ni content of *Anomaly 2* olivine indicates that they cannot be simple melting residues. Of the two possible explanations of the *Anomaly 2* mineral chemistry outlined in the previous section (either abnormally high melting and reaction with an Fe-poor melt, or addition of Ti and Na by a melt which was Mg-rather than Fe-rich), interaction with a magnesian melt would be more consistent with the olivine data, because the high melting model would generate olivine with high Ni contents.

The *background* harzburgite data also plot in a distinctly different pattern on the NiO_{ol}-Mg# graph, compared to their distribution on the graphs of spinel data. Three groups can be distinguished:
i) along the melting array;
ii) along the olivine crystallisation line;
iii) at positions intermediate between these two trends.

As discussed above, refertilisation of peridotites can produce trends similar to partial melting (Elthon, 1992) and it can therefore, be difficult to distinguish between the two processes. The NiO_{ol}-Mg# graph suggests that olivine composition may be a useful discriminant, with low Ni values indicating melt interaction. Moreover, the importance of olivine crystallisation during peridotite-melt interaction, has been stressed in several studies (Keleman *et al*, 1990; Edwards and Malpas, 1996; Zhou *et al*, 1996). The Troodos *background* harzburgite data suggest that olivine crystallisation has influenced the composition of a significant proportion of the mantle sequence.

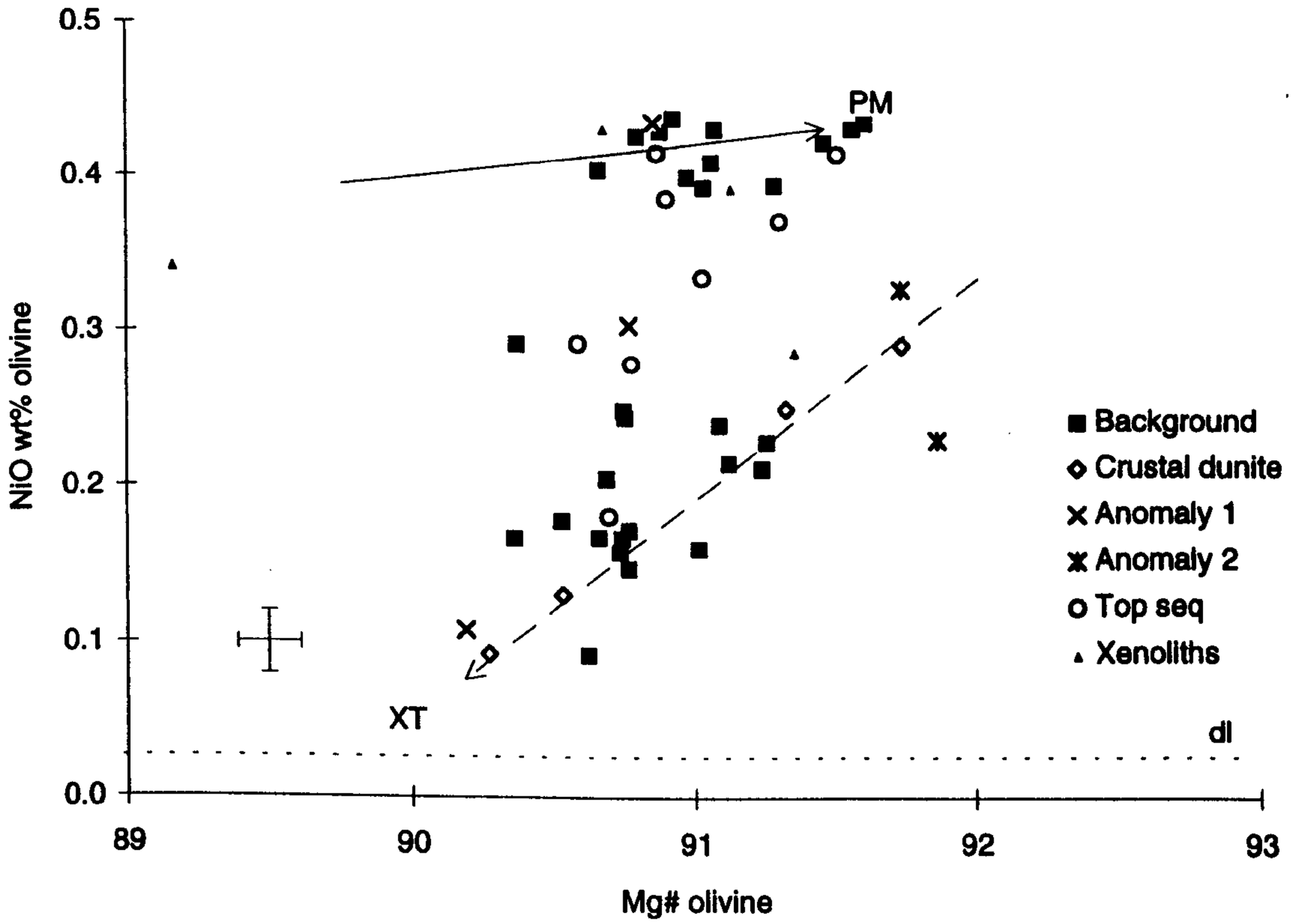

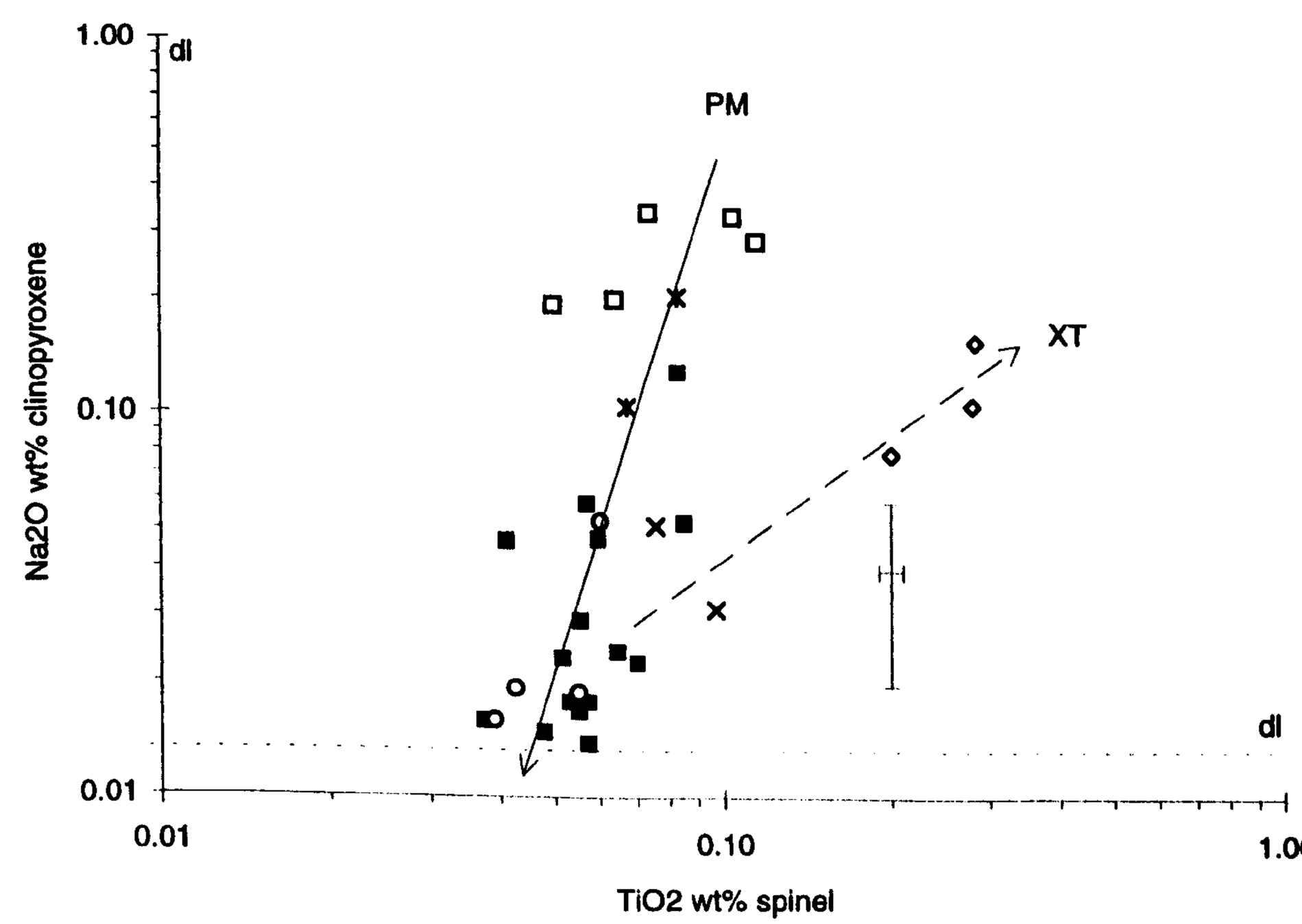

Figure 4.12 a) Graph illustrating the NiO_{ol}-$Mg\#_{ol}$ variation in the Troodos peridotites. b) Graph illustrating the Na_2O_{cpx}-TiO_{2spn} variation in the Troodos peridotites.

Figure 4.12b shows the Na_2O_{cpx}-TiO_{2spn} variation in the Troodos samples. The graph is annotated with partial melting and crystallisation trends determined in the same way as on the NiO_{ol}-$Mg\#_{ol}$ plot. On the Na_2O_{cpx}-TiO_{2spn} projection, the *Anomaly 1* and 2 harzburgites are clearly delineated. The *Anomaly 1* harzburgites again plot between the *background* samples and the crustal sequence dunites. The *Anomaly 2* harzburgites again plot on the partial melting trend, between the *background* harzburgites and the serpentinite diapir samples. These relationships once more support the conclusions drawn above, that the *Anomaly 1* harzburgites have interacted with melt which eventually crystallised the crustal dunites, and that the *Anomaly 2* harzburgites have compositions controlled by reaction with melts that drove their compositions back along the partial melting vector (Elthon, 1992).

In terms of the graphs discussed in this section, the melts interacting with the *Anomaly 1* and *2* harzburgites can be qualitatively described. Both melts were probably aluminous (interaction resulting in coupled Al-Cr substitution in spinel which lowered the Cr#) and Ti-rich. Compared to the *Anomaly 2* melt, the melt reacting with the *Anomaly 1* harzburgites was probably poorer in Na, which would account for their less pronounced deviation from *background* harzburgite concentrations in terms of Na_{cpx}. It is possible that the melts in both locations were related and that reaction with the *Anomaly 2* harzburgites removed most of the Na from the melt before it percolated further up the sequence and reacted with the *Anomaly 1* harzburgites. The *Anomaly 1* melt also crystallised more Fe-rich olivine than the *Anomaly 2* melt and therefore probably had a lower Mg#.

4.6.3 OXYGEN FUGACITY

The possible effects of oxygen fugacity on spinel composition have been discussed above in relation to the V content of spinel. The fO_2 conditions under which olivine-pyroxene-spinel assemblages last equilibrated can be determined by oxygen thermobarometry (Wood *et al.*, 1990; Ballhaus *et al.*, 1990). This technique uses the ferrous and ferric iron contents of the peridotite phases, analysed by electron probe, to calculate fO_2 using the equilibrium (Mattioli and Wood, 1986;1988):

$$\underset{\text{olivine}}{6Fe_2SiO_4} + O_2 = \underset{\text{pyroxene}}{3Fe_2Si_2O_6} + \underset{\text{spinel}}{2Fe_3O_4}$$

Potentially, the errors in this technique are quite large (estimated to be equivalent to 4.5 log units of fO_2 by Wood and Virgo, 1989) because the electron probe calculates ferric

iron in spinel by stoichiometry, which produces precise but inaccurate results. This can be overcome by using secondary spinel standards with accurately known ferric-ferrous ratios determined by Mössbauer spectrometry (Wood and Virgo, 1989), to correct the electron probe data. Unfortunately, these standards were not available during this study. However, the errors in ferric iron when determined by electron probe are essentially a linear function of Al_2O_3 concentration (Wood and Virgo, 1989), which is relatively low in the Troodos chrome spinels. The errors in the Troodos data should therefore be at a minimum, and are estimated to be between 10 and 15%.

The equilibrium equation has been parameterised for ease of calculation by Wood *et al.* (1990) and is reproduced in Appendix C. Ballhaus *et al.* (1990) emphasise the model dependency of mantle fO_2 calculations and present an alternative formulation of the equation (also reproduced in Appendix C), which they calibrate over a wider range of Cr_{spn} than the Wood *et al.* (1990) barometer. Oxygen fugacity values for the Troodos samples have been calculated using both equations, for a standard pressure of 15 kb. Temperatures were calculated using the Ca-in-orthopyroxene method of Brey and Kohler (1990, reproduced in Appendix C), because the rastered orthopyroxene analyses allowed accurate determination of Ca_{opx} despite the clinopyroxene exsolution. Calculated temperatures range between 1030 and 1190 ^oC ($\pm$ 40 ^oC) for the *background* harzburgites. There is no apparent systematic variation of calculated temperature with position in the sequence, probably because the exposed mantle section is too thin to show any significant vertical temperature gradients, and because the calculations are not sufficiently precise to show small-scale temperature fluctuations.

Notably, the temperatures recorded by the Ca_{opx} geothermometer are significantly higher that the blocking temperatures of sub-solidus exchange reactions between peridotite minerals (e.g. olivine-spinel exchange reactions have blocking temperatures of approximately 600°C, Ozawa, 1983). This fact is consistent with the mineral zoning data presented in Section 4.2, which suggested that the Troodos peridotites cooled quickly and did not experience a protracted period of sub-solidus re-equilibration.

The calculated fO_2 values for the Troodos harzburgites are illustrated in Figure 4.13. The graphs confirm that the calculated fO_2 values are strongly model dependant (Ballhaus *et al.*, 1990). The Wood *et al.* (1990) equation produces fO_2 values of -1.9 to -3.7 (average -2.7) relative to FMQ for the *background* harzburgites, whereas, the Ballhaus *et al.* (1990) formulation gives fO_2 in the range 0.11 to -1.4 (average -0.6). Both these authors found a strong correlation between tectonic setting of the peridotites analysed and the calculated fO_2 values which are summarised in Table 4.4.

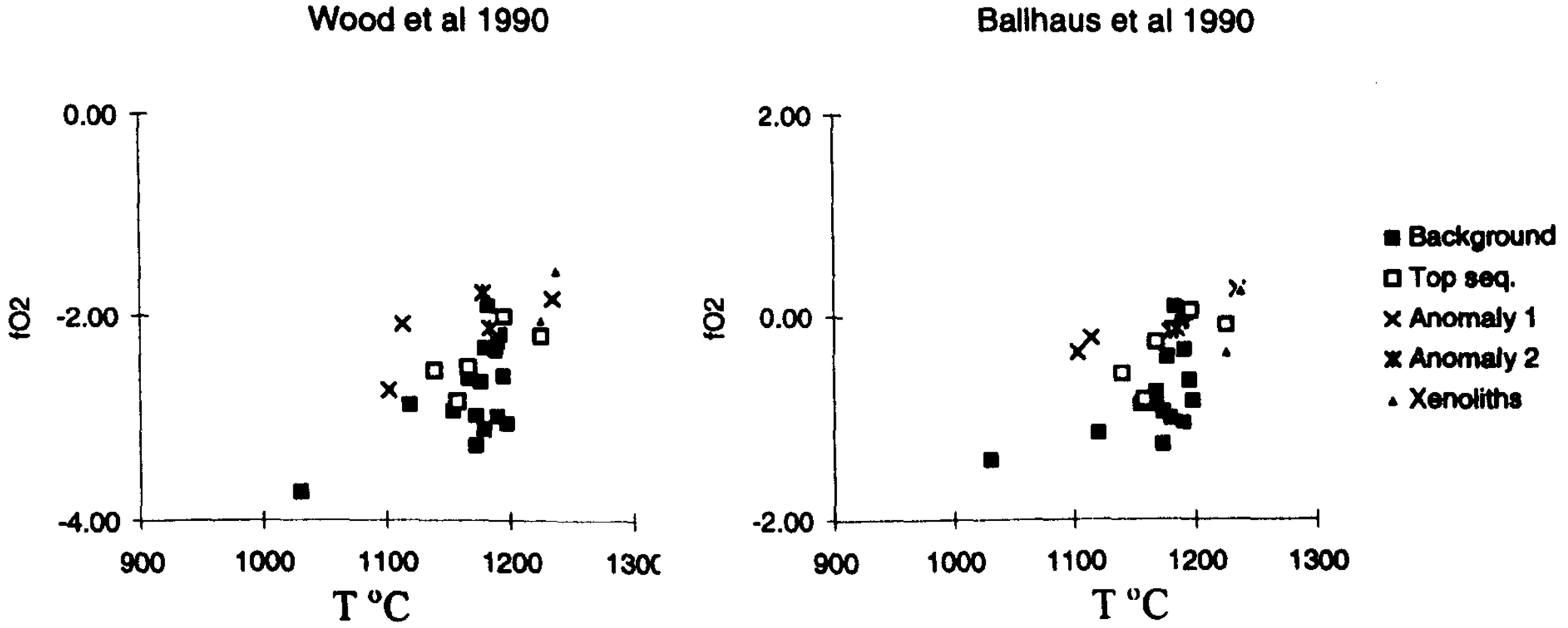

Figure 4.13 A comparison between fO_2 values calculated using the Wood *et al.* (1990) and Ballhaus *et al.* (1990) methods.

Both studies quoted in Table 4.4 confirm the consensus view (Wood and Virgo, 1989; Mattioli *et al.*, 1989), that mantle peridotites with evidence of LREE or LIL metasomatism have the most oxidised fO_2 values. The highest values in all these studies are always recorded in supra-subduction zone samples, and the high fO_2 conditions are attributed to the presence of a hydrous phase during metasomatism. Given the compositional similarities between the Troodos samples and the forearc peridotites noted above (which have fO_2 of -1 to +3.5 log units, Parkinson (1993) - calculated using the Wood *et al.* 1990 equation), the reduced fO_2 values of Troodos samples are surprising, and closer to the range of values found in MORB peridotites. However, because of the possibility of large systematic errors in this data (Wood and Virgo, 1989), this comparison should be treated with caution.

	MORB source peridotites	Metasomatised peridotites	Subduction related peridotites
Ballhaus *et al.* (1990)	0 to -2	0 to +2	+1 to +3
Wood *et al.* (1990)	0 to -2.5	0 to +1.5	> +1

Table 4.4. Summary of mantle fO_2 conditions.

Regardless of what the true fO_2 values are for the Troodos samples however, the data set should be internally consistent because of the high precision of the electron probe (Wood and Virgo, 1989). Therefore, comparisons of harzburgites from different positions in the Troodos sequence should be valid.

Both graphs in Figure 4.13 show that the samples already noted as having a melt interaction component (i.e. the *Anomaly 1* and *2* harzburgites, *top-of-the-sequence* and *xenolith* samples), plot on the more oxidised side of the Troodos *background* harzburgite array. This indicates that the mantle-melt interaction in the Troodos mantle might be associated with oxidising conditions and, by analogy with previous studies (Wood and Virgo, 1989; Mattioli *et al.*, 1989; Wood *et al.*, 1990; Ballhaus *et al.*, 1990), the presence of a hydrous phase. This supports the conclusion drawn above from the $Cr\#_{spn}$-V_{spn} data, that the reacting melts were oxidising and favoured the formation of low V spinel during melt interaction.

To test the hypothesis that V_{spn} contents are controlled by fO_2 (see section 4.o.2) the spinel data from *background* harzburgites and crustal dunites have been plotted against fO_2 on Figure 4.14. The crustal dunites display a coherent trend of decreasing V_{spn} with increasing fO_2, which confirms the theoretical trend of $Cr\#_{spn}$-V_{spn} variation during crystallisation under oxidising conditions (see Figure 4.11) proposed by Rassios and Pearce (1995). The *xenoliths*, *top-of-the-sequence* and *Anomaly 1* and *2* harzburgites are offset towards higher fO_2, than the majority of the *background* harzburgites. However, only the *xenoliths* and *Anomaly 1* and *2* harzburgites trend towards lower V_{spn} concentrations. This data is broadly consistent with the model of V leaching under oxidising conditions, although the trends are rather weak.

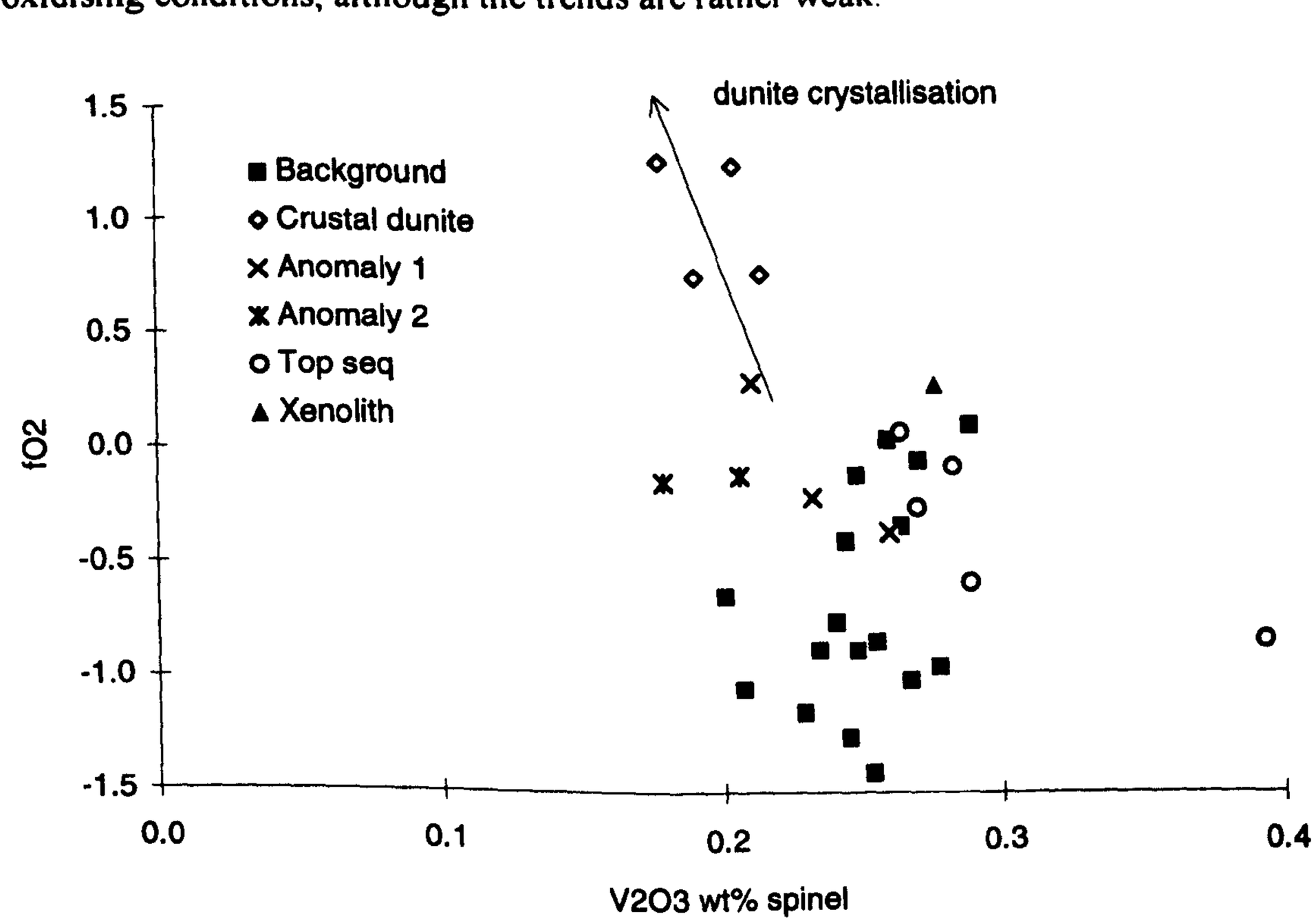

Figure 4.14 Graph showing the variation between calculated fO_2 values (using the Ballhaus *et al.* model) and V_2O_{3spn} for the Troodos harzburgites.

4.6.4 COMPOSITION OF MELTS IN EQUILIBRIUM WITH THE *BACKGROUND* HARZBURGITES

Roeder and Emslie (1970) have derived the following distribution coefficient, which enables the Mg# of the last melt that was in equilibrium with a peridotite to be calculated, if the olivine composition is known (a K_D of 0.3 was used for the calculation):

$$K_D = \frac{X_{FeO}^{Ol}}{X_{FeO}^{liq}} \frac{X_{MgO}^{liq}}{X_{MgO}^{Ol}}$$

Applying this formula to the *background* harzburgites produces Mg#'s of the melt ranging from 73.2 to 76.4 (average 75.1±0.7). This compares with Mg# values of 60-70 for primitive MORB, and 70-75 for island-arc basalts and boninites (Wilson, 1989). This data supports the conclusions drawn from the compositions of spinel, olivine and pyroxene in the *background* harzburgites, that the Troodos sequence has affinities with supra-subduction zone mantle.

The *Anomaly 1* harzburgites have calculated equilibrium melts with Mg# between 73.4 and 74.9 (average 74.3±0.8), which lie at the lower end of the *background* harzburgite values as would be expected from the graphs discussed above. The crustal dunites give Mg# values between 73.6 and 76.9 (average 75.12±1.6 - the large standard deviation reflects the influence of fractional crystallisation on the composition of these samples), which are similar to the values calculated for the *Anomaly 1* and other *background* harzburgite samples. However, the *Anomaly 2* harzburgites have calculated equilibrium melts with Mg# 76.9 to 77.2 (average 77.1±0.2) which are significantly more magnesian than the melts calculated for the *Anomaly 1* harzburgites. This supports the suggestion made above, that the melt reacting with the *Anomaly 2* harzburgites had a lower Fe content than the *Anomaly 1* melt.

4.7 DUNITES AND CHROMITITES IN THE MANTLE SECTION

In this section, the mineral chemistry of dunites and chromitites is described and their origin discussed. The formation of the Troodos chromitite bodies is considered with the formation of dunite because the chromitites are always surrounded by a dunitic wallrock. This is a common relationship in ophiolite chromitite bodies, and has lead to a consensus view in previous studies, that there is an intimate relationship between dunite and chromitite formation (e.g. Zhou *et al.*, 1996).

Petrogenetic theories for the origin of ophiolitic dunite bodies have been widely discussed in the literature, and can be broadly divided into those advocating igneous processes (melt-peridotite reaction and/or fractional crystallisation) and those supporting aqueous metasomatism. The igneous theories can be further sub-divided into those involving crystallisation from a melts passing through the mantle (e.g. Suhr and Robinson, 1994), and those which regard dunite as the residue from extensive partial melting (e.g. Dick and Sinton, 1979; Arai, 1994). Several authors have emphasised the role of melt-mantle reaction during magma transport through the mantle, during which dunite may be formed (Quick, 1981b; Keleman, 1990a; Quick and Gregory, 1995; Edwards and Malpas, 1996; Zhou *et al.*, 1996). The draining of melt from the mantle into fractures to form dunites with essentially residual wallrocks, has also been proposed (Takahashi, 1992). These studies suggest that dunites may have complex origins, and detailed studies of individual dunites (Quick, 1981b; Takahashi, 1992) have shown that several processes may operate during the formation of a single dunite body. The aqueous metasomatic theory has received little support in the recent literature and requires pyroxene in peridotites to be replaced by olivine during subsolidus reaction with aqueous fluids (Dungan and Avé Lallement, 1977).

As mentioned previously, Greenbaum (1977) described the mineral chemistry of many of the Troodos chromitite deposits, and interpreted them as magmatic cumulates. McElduff and Stumpfl (1990; 1991) describe complex suites of hydrous silicate inclusions in spinels from the podiform chromite bodies, and from schlieren within the crustal dunites. These authors suggested that the inclusions attested to the influence of a fluid phase during chromite crystallisation.

In the Fieldwork Chapter, the variety of structural attitudes between the dunite bodies and harzburgite foliation, and the variety of contact relationships with the host harzburgites, has been described. This classification is used to differentiate the dunites in this section and can be summarised as follows:

(i) dunites which are parallel to the foliation (labelled II foliation on the graphs);
(ii) dunites which form the wallrocks to chromitite bodies (labelled wallrock);
(iii) dunites associated with pyroxenites (labelled dun assoc pyx);
(iv) dunites which cross-cut the harzburgite foliation (labelled x foliation);
(v) dunites with interdigitating contacts against the harzburgites (labelled interdigitating);
(vi) crustal dunites.

Chromitites are classified according to the nature of the host body into:

(i) chromitites forming the podiform chromite deposits in the uppermost harzburgites;

(ii) chromitites forming layers or schlieren in the crustal dunites.

4.7.1 COMPOSITION OF DUNITES

The composition of olivine and spinel from various dunite bodies is illustrated in Figure 4.15. Olivine in the dunites has a similar range of compositions as the olivine in the *background* harzburgites. In general, there is no apparent correlation between the structural attitude of a dunite and its position on the Ni_{ol}-$Mg\#_{ol}$ graph (Figure 4.15a). However, the foliation parallel dunites do plot exclusively towards lower Ni_{ol} than the *background* harzburgites and within the field of compositions expected for cumulate lithologies (Figure 4.15a).

Spinels in dunites however, have a much greater range of compositions than harzburgite spinel, particularly in terms of Ti_{spn} (Figure 4.15b). On the $Cr\#_{spn}$-$Mg\#_{spn}$ graph (Figure 4.15c), the dunites plot on the *background* harzburgite trend and on an extension of this trend towards higher Cr#'s and lower Mg#'s. The dunites which plot towards lower $Mg\#_{spn}$ are the crustal dunites and most of the foliation parallel dunites. The same trend has been noted in abyssal dunites (Dick and Bullen, 1984) and interpreted as a fractional crystallisation trend (Dick and Bullen, 1984). On the $Cr\#_{spn}$-Ti_{spn} graph (Figure 4.15b), the crustal dunites and foliation parallel dunites define a trend towards higher Ti_{spn}, which has also been shown to be a crystallisation trend in the previous section.

Dunites which cross-cut the harzburgite foliation have the largest range of spinel compositions, spanning the range defined by the *background* harzburgites and the crustal dunites. Spinel in dunites which have interdigitating contacts against the harzburgites, span a similar, but slightly more restricted, range of compositions. On the $Cr\#_{spn}$-$Mg\#_{spn}$ graph the dunites associated with pyroxenite bodies plot predominantly along the *background* harzburgite trend, and are displaced from this trend towards lower $Mg\#_{spn}$. These dunites also have a large range of Ti_{spn} values.

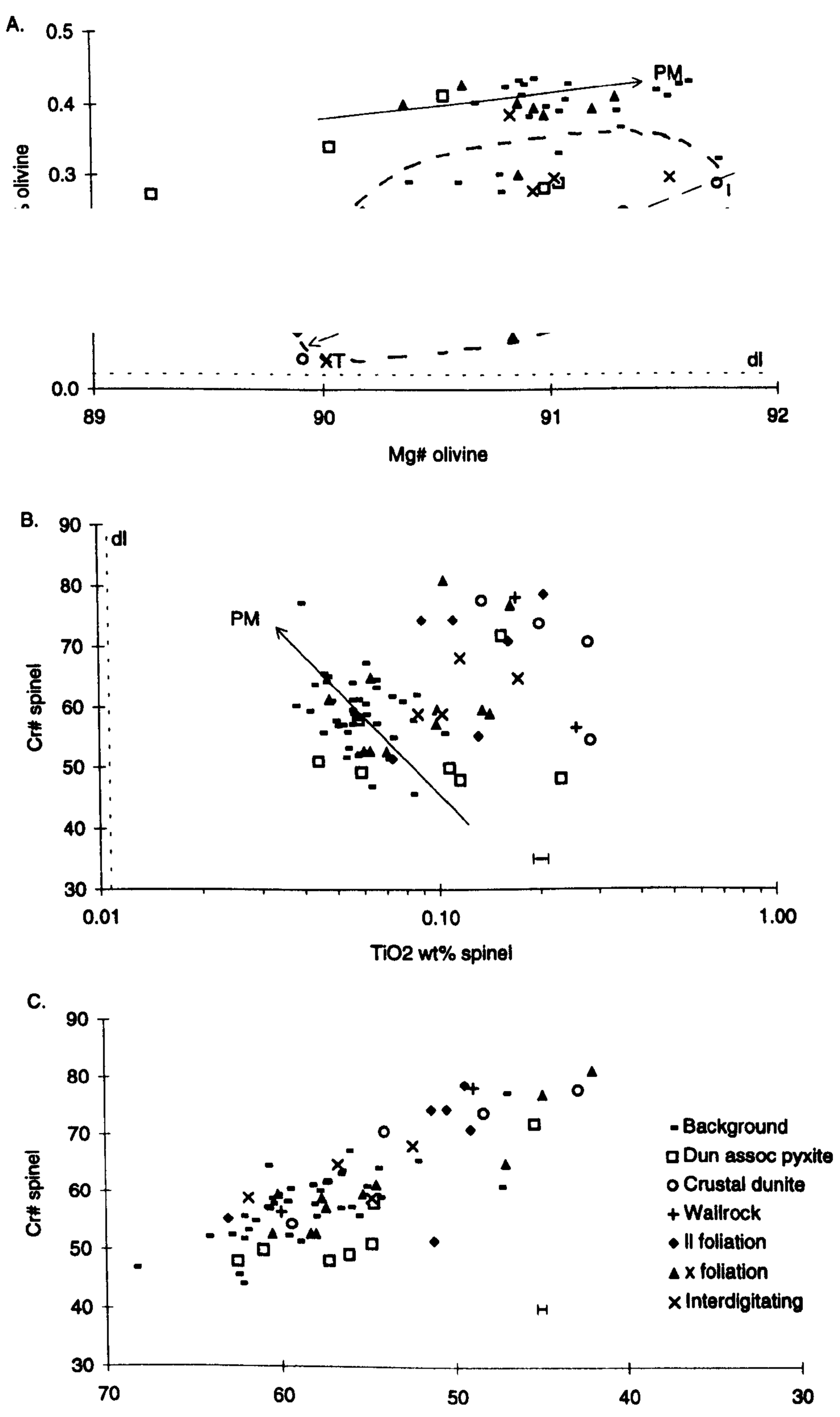

Figure 4.15 Graphs illustrating the variations in mineral chemistries of the Troodos dunites. Also illustrated for comparison are the data from the *background* harzburgites. PM = partial melting trend defined by the *background* harzburgites, XT = fractional crystallisation trend defined by the crustal dunites. Area outlined in dashed line on graph A indicates possible range of cumulate chemistries.

4.7.2 COMPOSITION OF CHROMITITES

The composition of spinel in chromitite bodies is summarised in Figure 4.16 (olivine compositions are not available for the chromitites because this phase is 100% serpentinised in these samples). Chromitites from the podiform bodies have a restricted range of compositions, with higher $Cr\#_{spn}$, Ti_{spn} and Mg_{spn} than the *background* harzburgites. The V_{spn} content of the podiform bodies is low and similar to the crustal dunites. No correlation has been found between spinel chemistry and the location, or texture, of chromitites. Chromitites in the crustal dunites have a much greater range of spinel compositions, showing a spread of values from those similar to the podiform bodies to those similar to the most evolved crustal dunites.

4.7.3 THE EFFECTS OF DUNITE FORMATION ON HARZBURGITE CHEMISTRY

Figure 4.17 illustrates the composition of harzburgites sampled adjacent to the various dunite bodies. Spinel compositions show no distinct correlation between the nature of the adjacent dunite and the Ti_{spn} content in the harzburgite, with most values falling within the range defined by the *background* harzburgites. Olivine compositions in harzburgites sampled adjacent to the podiform chromitites and dunites which cross-cut the foliation, plot on the partial melting trend, whereas, harzburgites sampled adjacent to foliation parallel dunites plot on the olivine fractionation trend.

4.7.4 THE ORIGIN OF DUNITES AND CHROMITITES

The major element variation of spinels in the dunite bodies (Figure 4.15b) can be broadly divided into those with compositions similar to the *background* harzburgites, and those which have lower Mg#'s and higher Cr#'s. The samples with lower Mg#'s and higher Cr#'s also have higher Ti_{spn} contents than the *background* harzburgites, and these features are interpreted as characteristics of magmatic cumulates. As pointed out by Keleman (1990), strictly residual dunites should have more depleted chemistries than their host harzburgites, hence the $Cr\#_{spn}$-Ti_{spn} variation in the Troodos dunites rules out this mode of formation.

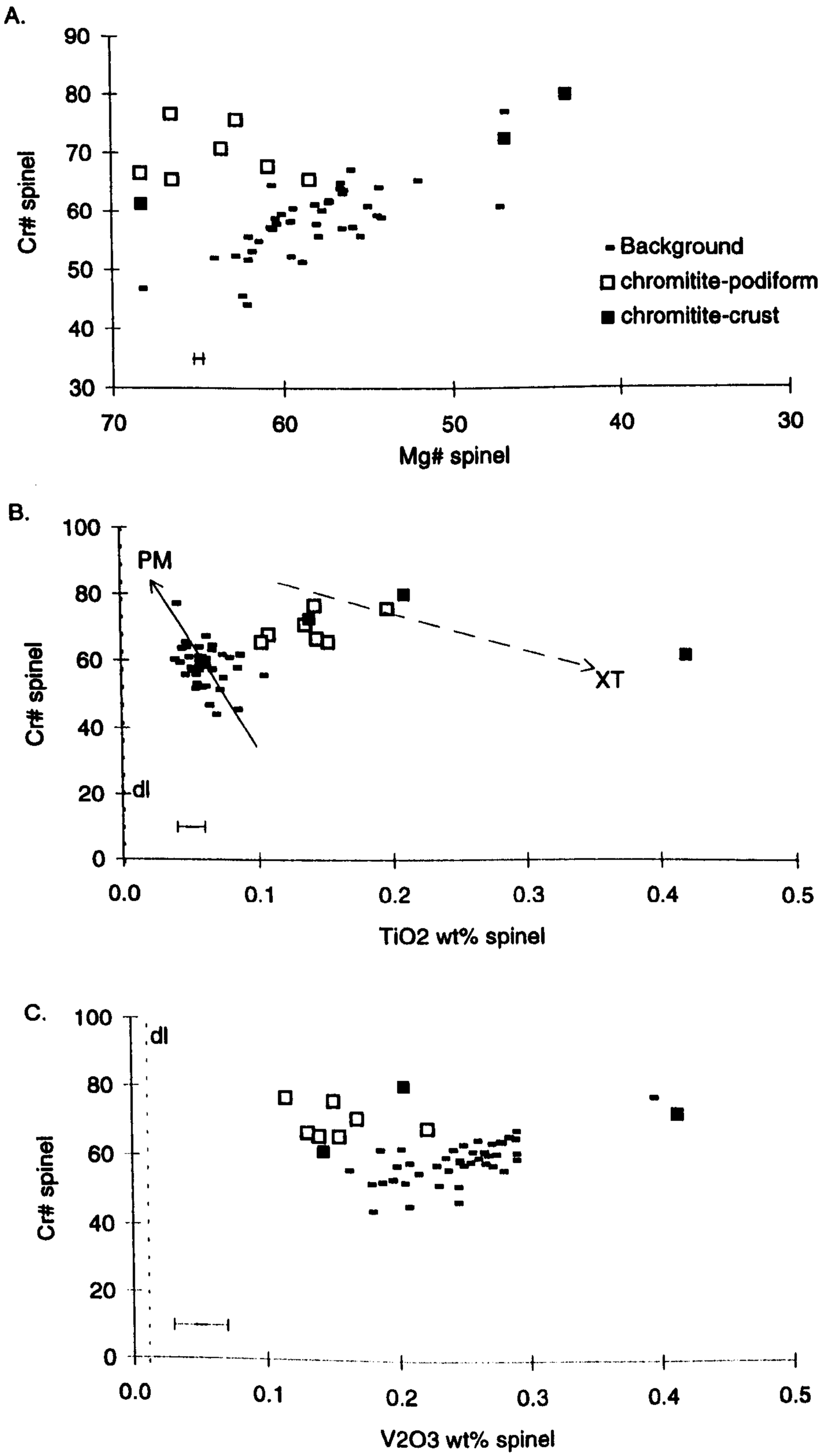

Figure 4.16 Graphs illustrating the compositional variation of spinel from the Troodos chromitite bodies. Also illustrated for comparison are the data from the *background* harzburgites.

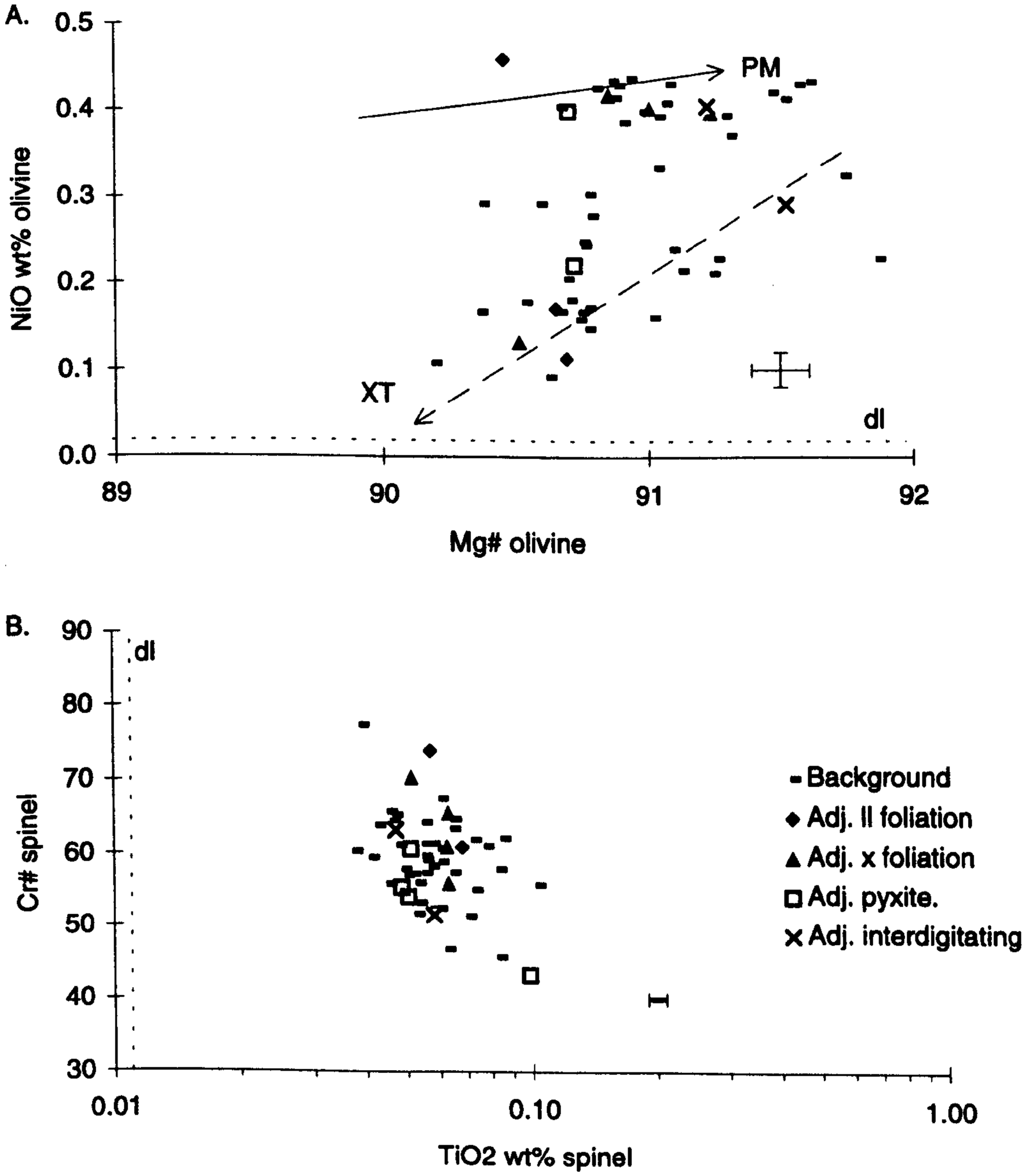

Figure 4.17 Graphs illustrating the variation of olivine and spinel chemistries in the wallrocks adjacent to various Troodos dunites. Also illustrated for comparison are the data from the *background* harzburgites.

The interdigitating dunites also have high Ti_{spn} contents, but $Cr\#_{spn}$ and $Mg\#_{spn}$ similar to the *background* harzburgites. These characteristics would be consistent with the proposed mechanism of dunite formation by reaction between transient melts or fluids and the harzburgites (e.g. Quick and Gregory, 1995). During this process, major elements will be buffered towards the composition of the harzburgite, and the incompatible elements (i.e. Ti_{spn}) will be enriched by the melt. The relatively low Ti_{spn} content of the harzburgites adjacent to the interdigitating dunites is consistent with extraction of incompatible elements from the wallrocks of these dunites. Furthermore,

the contact relations between the interdigitating dunites and the enclosing harzburgites, particularly the corroded harzburgite xenoliths along the periphery of the dunite, are also consistent with reaction between the dunite and harzburgite. Note that similar xenoliths are found at the base of the crustal dunite section, which indicates that the crustal dunites are probably composite bodies formed partly by reaction, but in the main by fractional crystallisation. A similar origin is envisaged for the dunites which cross-cut foliation and also show a broad range of compositions.

The data from the Troodos dunites suggests therefore, that crystallisation from primitive melts and reaction between melts and harzburgites are the two main dunite forming processes in this ophiolite. As the data from the crustal dunites shows, both crystallisation and reaction can occur during the formation of an individual dunite, as emphasised by Quick (1981b). The harzburgite mineral compositions are, in general, not significantly affected by dunite formation on the rather coarse scale of sampling adopted during this project. However, it is possible that detailed traverses away from dunites (particularly those with interdigitating contacts) might show chemical gradients in the incompatible elements, as has been shown by Quick (1981b) in the Trinity ophiolite.

The narrow compositional range of the podiform chromitites is consistent with an origin as either residues of extensive partial melting, or the earliest cumulates from a melt. The elevated Ti_{spn} contents of the podiform chromitites and their textures (Greenbaum, 1977; McElduff and Stumpfl, 1990; 1991) support the cumulate hypothesis. Furthermore, the fact that the podiform bodies have low V contents suggests that the melt crystallised under oxidising conditions (see Section 4.6.2). This would be consistent with McElduff and Stumpfl's (1990; 1991) proposal that a fluid phase influenced chromite crystallisation, and agrees with the suggestion made by Rassios and Pearce (1995), that the chromitite bodies in the Greek ophiolites crystallised in high fO_2 conditions.

The chromitites in the crustal dunites span a wide range of compositions. The range of values is consistent with crystallisation from the same evolving melt which crystallised the crustal dunites. The fact that the most primitive crustal chromitites have similar compositions to the podiform bodies suggests a genetic link between them. The podiform chromitites might represent crystallisation within the magma conduits which were supplying melt to the crustal dunite magma chamber. Augé (1987) presents an equation which relates the Al_2O_3 content of a spinel to that in the parental melt, based on experimental equilibration of spinel with basaltic melt:

$$Al_2O_3\ \text{spinel} = 0.035\ (Al_2O_3\ \text{melt})^{2.42} \qquad \text{values in wt\%}$$

Applying this equation to the Troodos podiform chromitites produces melt Al_2O_3 values of 11.07 to 13.33 wt%. These values are comparable to the Al_2O_3 contents of glass samples from the boninitic lavas in the overlying crustal sequence (Laurent, 1990, and references therein). Roberts (1992) emphasised the link between chromitite formation and a high degree of depletion of the enclosing mantle sequence, favoured by one or more melting episodes in a hydrous environment. The Troodos chromitite data support this hypothesis and provide further evidence for a supra-subduction zone origin for the ophiolite.

4.8 PYROXENITES IN THE MANTLE SEQUENCE

Mantle sequence pyroxenites can be divided into two main lithological types: orthopyroxenites and clinopyroxenites. The orthopyroxenite bodies can be characterised by their outcrop relationships (see Fieldwork Chapter), and are either:

a. Massive, medium-grained bodies which are discontinuous along strike. Usually 5 to 15 cm thick, oriented parallel to the harzburgite foliation and show evidence of deformation such as boudinage, and rarely, isoclinal folding around the harzburgite foliation. These orthopyroxenites are often associated with a marginal dunite which is in sharp contact with the host harzburgite. These pyroxenites are termed *orthopyroxenite A*;

b. Medium to coarse-grained, tabular, bodies generally less than 1 cm thick and oriented parallel to foliation. Always associated with a marginal dunite which is in sharp contact with the host harzburgite. These pyroxenites are termed *orthopyroxenite B*.

Olivine-clinopyroxenites are fine to medium-grained tabular bodies. They cross-cut the harzburgite foliation, do not have marginal dunites and are only found close to the harzburgite-crustal dunite contact.

Clinopyroxenites in the harzburgite sequence occur as stringers of coarse to pegmatitic clinopyroxene crystals, which are always surrounded by dunite and are located exclusively in the uppermost 200m of the sequence (see Fieldwork Chapter). The clinopyroxenites are the least abundant pyroxenites in the mantle sequence. Clinopyroxenites also outcrop as massive, layered bodies at the base of the crustal dunites; the composition of these bodies is also described in this section.

The absence of chilled margins against the enclosing dunite or harzburgite, and the apparent lack of any exposure-scale modal variation in the host harzburgites surrounding the intrusion, are common features of all the pyroxenites. These pyroxenites are distinct from the pyroxene banding in the harzburgites which have a grain size equivalent to that in the enclosing harzburgite, gradational contacts with the harzburgite and define the harzburgite foliation along with the grain-shape-alignment of pyroxene crystals. They are labelled pyroxene bands in the following section.

4.8.1 THE COMPOSITION OF THE PYROXENITES

The pyroxenites' mineral chemistry variation is illustrated in Figure 4.18.

The range in compositions of the orthopyroxenites is greater than the *background* harzburgites, and can be divided into two sub-types on the basis of spinel composition (Figure 4.18 a and b). Type I orthopyroxenites contain Cr, Fe and Ti-rich spinels, whereas Type II orthopyroxenites have Al-Mg-rich spinels. This classification parallels that proposed by Varfalvy *et al.* (1996) for pyroxenites from the Bay of Islands ophiolite, and the trends are equivalent to those defined by Edwards and Malpas (1996) in harzburgites from the Hess Deep.

Clinopyroxene, orthopyroxene and olivine compositions (Figure 4.18c,d and e) in Type I pyroxenites all show trends towards more Fe-rich compositions (i.e. lower Mg#). This Fe enrichment occurs for weakly increasing Na contents in clinopyroxene and weakly decreasing Ni contents in olivine. In orthopyroxenes, the Fe enrichment occurs with a strong Al depletion. Type II pyroxenites are characterised by much weaker trends towards Fe-rich compositions along with an Al enrichment in orthopyroxene, a Ni enrichment in olivine and strong Na enrichment in clinopyroxene.

In terms of outcrop characteristics, *orthopyroxenite B* samples always fall on the Type II trend whereas, *orthopyroxenite A* and the harzburgite pyroxene bands fall on both Type I and II trends. One of the olivine-clinopyroxenite samples shows extreme Fe_{spn} enrichment and plots apart from the main Type I trend (Figure 4.18a). However, in terms of clinopyroxene, orthopyroxene and olivine compositions, the olivine-clinopyroxenites define the high Cr-Ti-Fe end-member of the Type I pyroxenite trend.

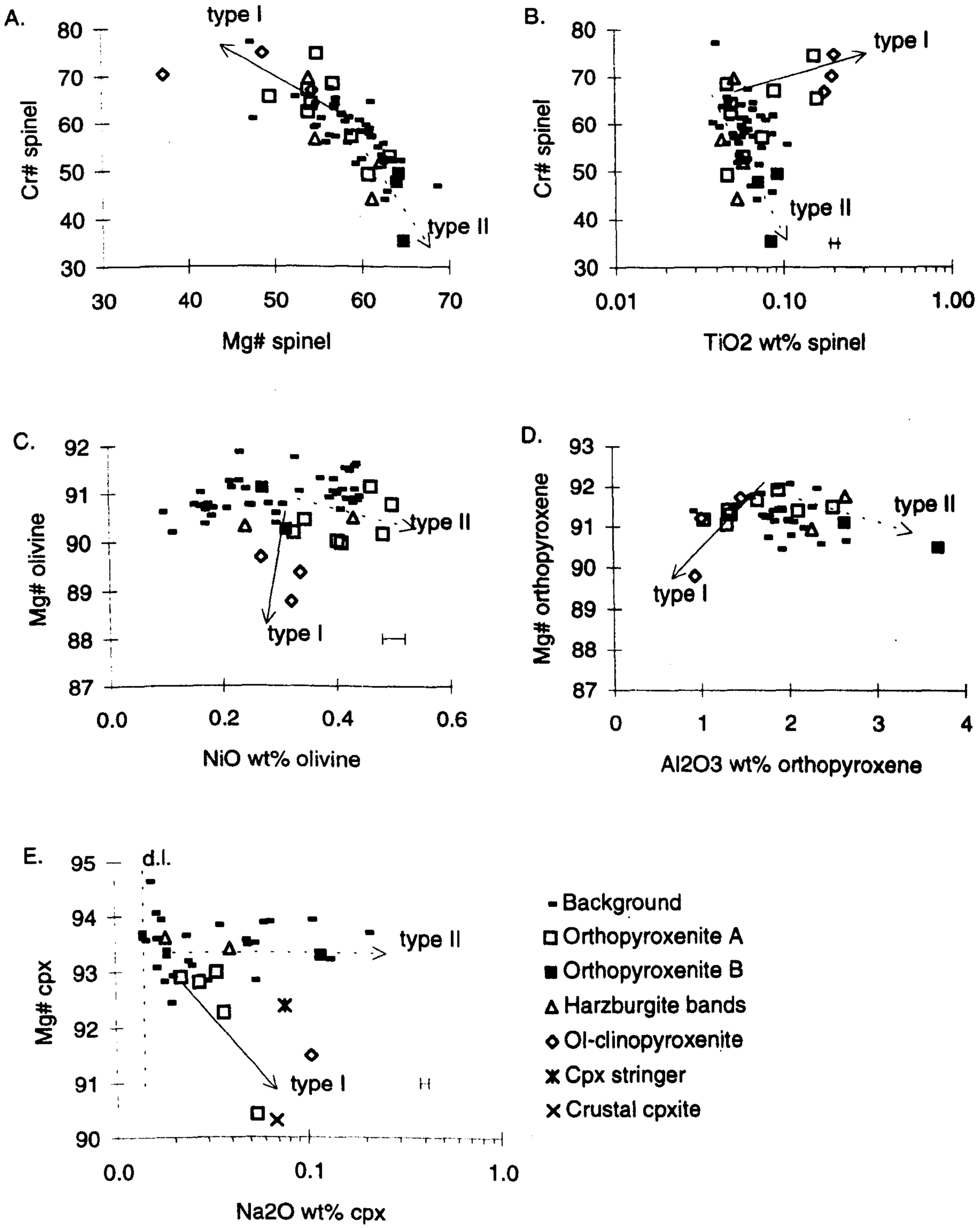

Figure 4.18 Plots illustrating the variations in mineral chemistries in the Troodos pyroxenites. Also illustrated for comparison are the data from the *background* harzburgites.

The clinopyroxene compositions of a clinopyroxenite stringer and a massive clinopyroxenite from the crustal dunites are also illustrated on Figure 4.18e. Both clinopyroxenites plot on the Type I trend, the massive clinopyroxenite having a significantly more Fe-rich composition than the stringer.

4.8.2 THE EFFECTS OF PYROXENITE FORMATION ON HARZBURGITE CHEMISTRY

The compositions of wallrock harzburgites, sampled at the harzburgite-pyroxenite contacts (or if the pyroxenite was surrounded by a marginal dunite at the harzburgite-dunite contact), are illustrated in Figure 4.19. *Wallrock A* samples are those sampled adjacent to *orthopyroxenite A* bodies and *wallrock B* samples are those sampled adjacent to *orthopyroxenite B* bodies. Samples were also taken from between the pyroxene bands in the harzburgite and are labelled 'banded harzburgite'.

As Figure 4.19 shows, there is a weak correlation between the composition of wallrock harzburgites and the type of pyroxenite with which they are in contact. In general, the wallrock harzburgites are displaced along the same vectors as their associated pyroxenites. This correlation is particularly noticeable for the olivine-clinopyroxenite wallrock sample, and the clinopyroxene compositions of *wallrocks A* and *B*. Banded harzburgites plot along both Type I and II vectors, mirroring the position of the pyroxene bands.

4.8.3 THE ORIGIN OF PYROXENITES IN THE TROODOS MANTLE SECTION

The origin of pyroxenite bodies in the mantle section of ophiolites has been widely discussed in the literature. An orthopyroxenite from Troodos was analysed by Menzies and Allen (1974), who interpreted its moderately fertile chemistry, compared to the enclosing harzburgites, as a result of crystallisation from melts produced during the final stages of harzburgite fusion. Jaques and Chappell (1980) described orthopyroxenites from the mantle section of the Papuan Ultramafic Belt, which are also slightly less depleted than their host harzburgites. These orthopyroxenites were also thought to represent melts produced during the final stages of melting, and were correlated with tonalite intrusives in the cumulate sequence. The chemistry of the tonalites suggested that their parent magmas were melts from a severely depleted mantle source located close to a subduction zone.

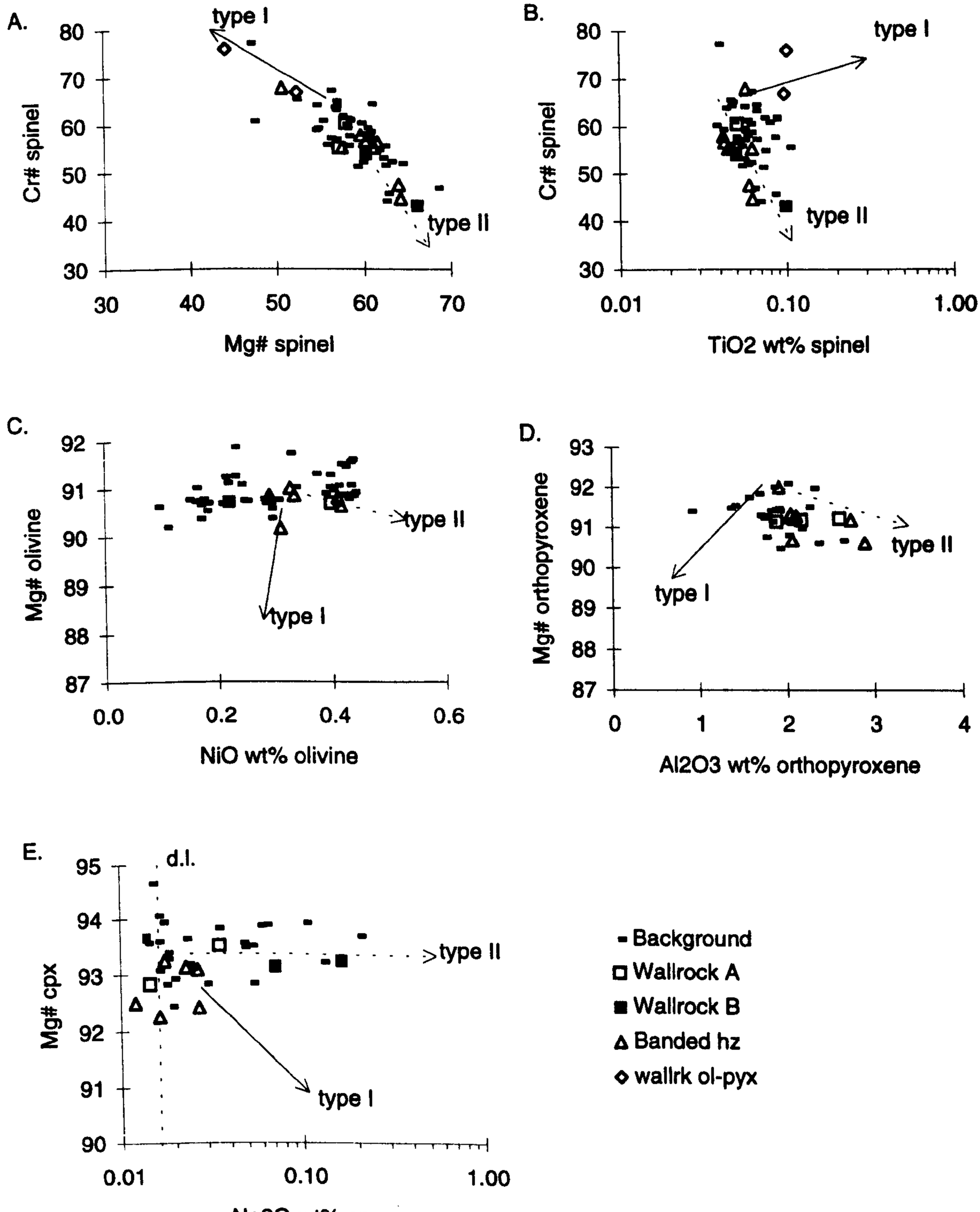

Figure 4.19 Plots illustrating the variations in mineral chemistries in the harzburgite wallrocks adjacent to the Troodos pyroxenites. Also illustrated for comparison are the data from the *background* harzburgites.

Pyroxenites are also important components in the mantle sections of the Bay of Islands ophiolite, and have been described from the Lewis Hill Massif by Edwards (1990; 1995) and Edwards and Malpas (1995), and from the North Arm Mountain Massif by Varfalvy *et al.* (1996). As mentioned above, Varfalvy *et al.* (1996) subdivided the pyroxenites on the basis of spinel composition into a suite exhibiting Cr-Fe-Ti enrichment (Type I), and one of Mg-Al enrichment (Type II). Reaction relationships between the pyroxenites and the harzburgites were important in modifying the chemistries of both lithologies. The primary melts which crystallised the pyroxenites were inferred to have boninitic chemistries.

The mineral chemistry of the orthopyroxenites analysed in this study are similar to those described from the Papuan and Bay of Islands ophiolites. In particular, the Type I and II pyroxenites defined by Varfalvy *et al.* (1996) in the Bay of Islands ophiolite, can be identified in the Troodos pyroxenites. Troodos olivine-clinopyroxenites are Type I (low-Al suite) pyroxenites whereas, *orthopyroxenite B* samples are Type II (high-Al suite) according to the definition of Varfalvy *et al.* (1996). *Orthopyroxenite A* samples plot on both Type I and II trends.

The mineral chemistry parameters illustrated in Figure 4.18 show that the variation in Type II pyroxenites generally mirrors the partial melting trend. However, the mineralogy of the these pyroxenites, and the high Na_{cpx} values, precludes an origin as partial melting residues. Similarly, the elevated Ti_{spn} contents and low $Mg\#_{cpx}$ of the Type I pyroxenites, and their bulk mineralogy, are also inconsistent with an origin as melting residues. The wide range of major element compositions of the pyroxenites also make a purely metasomatic origin unlikely, because this process would buffer major element values towards those in the host harzburgite (Keleman, 1990). These facts suggest that the pyroxenites crystallisation from a melt. The same conclusion was by Varfalvy *et al.* (1996) in the Bay of Islands ophiolite. Furthermore, the enrichment of the wallrock harzburgites in incompatible elements (the *orthopyroxenite B* wallrocks in Na_{cpx} and olivine-clinopyroxenite wallrocks in Ti_{spn}), shows that the pyroxenites cannot have been extracted from the adjacent harzburgites, and supports their origin as intruded, more fertile, melts. Unfortunately, no wallrock data was obtained for the clinopyroxenite stringers, and their low Na_{cpx} contents are unequivocal in determining whether they represent locally produced melts.

The Mg# of melts in equilibrium with the pyroxenites have been calculated (see Section 4.6.4). The melts have high Mg# values, between 70.4 and 76.6, with no significant difference between the Type I (average Mg# 73.4$\pm$1.4) and II (average Mg# 74.0$\pm$1.2)

pyroxenites. Melts with such high Mg# values are characteristic of subduction-related basalts (Wilson, 1989), which are usually interpreted as second stage melts from a depleted source (Pearce *et al.*, 1992). The mineral chemistry of the Type I pyroxenites also suggests that the melts associated with these pyroxenites were Cr-Fe- and Ti-rich, and poor in Al, Ni and Na. Type II melts would have been rich in Mg, Al and Na, but poor in Ti.

The silicate minerals in Type I pyroxenites show a trend towards lower Mg# values and notably, the clinopyroxene-bearing pyroxenites form the most evolved end-member of this trend. The same variations in the Bay of Islands pyroxenites were interpreted by Varfalvy *et al.* (1996) as a crystal fractionation trend. Mineral chemistry data for the lower-most Troodos ultramafic cumulates (Malpas *et al.*, 1990, and references therein) are illustrated in Figure 4.20, along with the *background* harzburgite values and the pyroxenite Type I and II trends. The graphs show that the Type I variation is similar to the trend for the ultramafic cumulates, which supports the suggestion that the Type I trend is, at least partly, the result of crystal fractionation. Furthermore, the fact that the crustal cumulates plot on an extension of the Type I trend suggests that the melts which crystallised the pyroxenites and the cumulates were probably related.

Considering the overwhelming evidence for a supra-subduction zone location of the Troodos Massif, from lava geochemistry (Pearce, 1975) and mantle mineralogy (Dick and Bullen, 1984; this study), the existence of intrusives with boninitic affinities in the mantle sequence is not surprising. The relationship between the Type I and II pyroxenites is equivocal. The vein morphologies of the olivine-clinopyroxenites (Type I), which cross-cut the foliation and are undeformed, indicate that they crystallised from melt percolating through the mantle at a late stage. The fact that deformed *orthopyroxenite A* bodies also plot on the Type I trend, suggests that the Type I melt was supplied to the mantle over a long period of time. The Type II melts crystallised *orthopyroxenite A* and *B* bodies, which are both parallel to the foliation, and were presumably only intruded into the mantle sequence at a relatively early stage of its evolution. These relationships are summarised in Table 4.5.

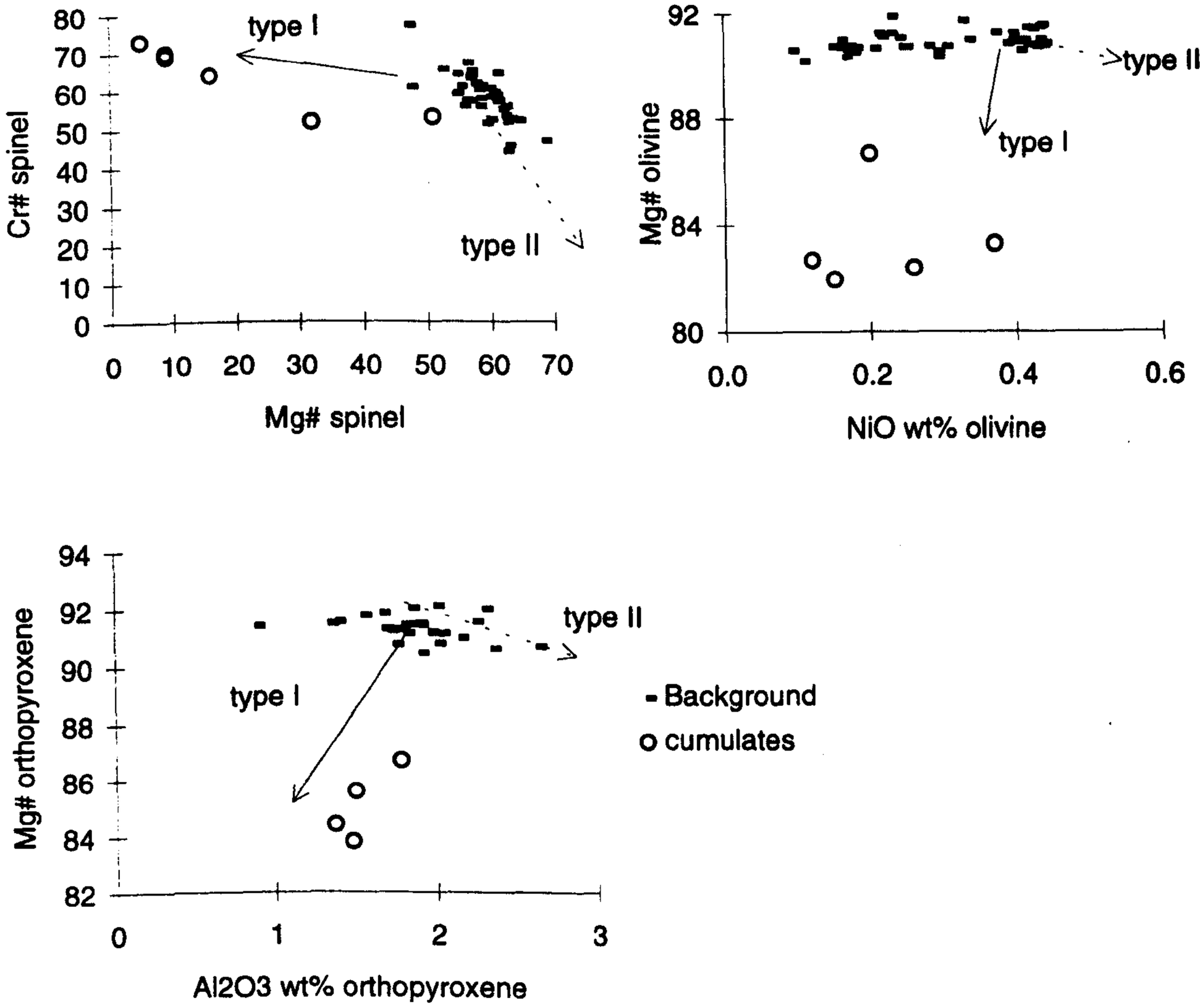

Figure 4.20 Plots illustrating the mineral variations defined by the Type I and II pyroxenites and the mineral compositions in the ultramafic cumulates from the Troodos crustal sequence.

Pyroxenite	Attitude	Spinel	Marginal dunite	Type
Orthopyroxenite A	foliation parallel	Al-Mg and Cr-Fe-Ti rich	yes	I and II
Orthopyroxenite B	foliation parallel	Al-Mg rich	yes	II
Ol-clinopyroxenite	cross-cuts foliation	Cr-Fe-Ti rich	no	I
Clinopyroxenite	irregular orientation	Cr-Fe-Ti rich	yes	I

Table 4.5. Summary of pyroxenite relationships.

The relationship between the composition of pyroxenites and their corresponding wallrocks implies that the chemistry of the wallrock harzburgites has been modified by reaction with the pyroxenite melts. The presence of marginal dunites around the pyroxenites suggests that reaction between the melt and the host harzburgite involved dissolution of orthopyroxene and crystallisation of olivine. The sharp contacts between pyroxenites, marginal dunites and wallrock harzburgites, and the apparent absence of any exposure-scale modal variations in the host harzburgites place constraints the reaction process. The sharp contacts, particularly between the marginal dunite and harzburgites, preclude the reaction process occurring by percolation and crystallisation of the pyroxenite magma into the harzburgites, which would presumably result in gradational contacts. Instead a similar process as that proposed by Keleman *et al.* (1992) for reaction zones in the Trinity peridotite, where phase saturation in the migrating magma was important in switching the crystallisation of individual phases on or off, is envisaged.

The fact that orthopyroxene was apparently dissolved by the melt-mantle reaction suggests that the melt was, at least initially, undersaturated with orthopyroxene. This is surprising considering that marginal dunite bodies are characteristic of orthopyroxenite intrusions, which presumably were crystallised from melts which were oversaturated with respect to orthopyroxene and not olivine.

The consequences of mantle-melt interaction have been investigated by Keleman (1990) and Keleman *et al.* (1990), who used experimental and phase diagram constraints to suggest that melt-mantle reaction will crystallise dunite with Mg# buffered close to that of the host harzburgite, and produce liquids which become Fe-enriched. The trend of Type I pyroxenites towards more Fe-rich compositions agrees with the Keleman model for melt evolution during reaction. However, the dunite data discussed in the previous section show that the marginal dunites have a wide range of chemistries, suggesting that both reaction between melts and mantle and direct crystallisation from a melt has occurred.

Furthermore, the Type I pyroxenite trend towards higher Ti_{spn} values, parallels that noted in the *Anomaly 1* harzburgites, harzburgite *xenoliths* and *top-of-the-sequence* harzburgites in Section 4.6 (labelled IT2 in Figure 4.11). Also, the Type II pyroxenites have mineral chemistries that mirror the partial melting trend, which is similar to variations described in the *Anomaly 2* harzburgites. The nature and extent of reaction between the pyroxenite melt and the host harzburgites is discussed further in the Conclusions Chapter.

Pyroxene bands in the harzburgite have a range of compositions similar to the enclosing harzburgite. The banded harzburgites, sampled from between the pyroxene bands, also have a similar range of compositions to the other *background* harzburgites. These data are consistent with the model proposed by Dick and Sinton (1979) for formation of the pyroxene bands through mechanical accumulation of pyroxene grains by pressure-solution creep during asthenospheric deformation. In this scenario the pyroxene bands and adjacent harzburgite should have similar mineral chemistries as is the case in the Troodos samples.

4.9 SUMMARY OF THE ELECTRON PROBE DATA

In this section, the mineral chemistry data presented so far are summarised, before the trace element chemistry of Troodos clinopyroxene is described in the following part of this chapter. The most important conclusion to be drawn from the electron probe data is that both partial melting processes, and reaction with melts, have significantly affected the composition of the Troodos mantle sequence. Partial melting depletes minerals in the magmaphile elements (Michael and Bonatti, 1985; Bonatti and Michael, 1989), and increases upwards through the harzburgite sequence. Reaction with melts has been shown to occur in several locations in the sequence: at the top of the mantle section (*Anomaly 1* harzburgites, harzburgite *xenoliths* and *top-of-the-sequence* harzburgites), within well defined layers in the mantle sequence (*Anomaly 2*), adjacent to pyroxenites and possibly adjacent to some dunites.

Analysis of the *background* harzburgite data allowed two reaction vectors to be defined with respect to $Cr\#_{spn}$-Ti_{spn} variation. One vector is oriented towards increasing $Cr\#_{spn}$ and Ti_{spn} (which was labelled IT2, Figure 4.11a) and accounts for the variation in samples from the top of the mantle section. The second is oriented parallel, and opposite in direction, to the partial melting trend (which was labelled IT1, Figure 4.11a), and accounts for the variation in the *Anomaly 2* harzburgites. Vectors with identical orientation were also identified in the mineral chemical variation of the pyroxenites. Type I pyroxenites match the IT2 trend and Type II pyroxenites the IT1 trend. Significantly, the end-member of the Type I pyroxenite trend is olivine-clinopyroxenite which is found exclusively in the uppermost harzburgites. It is likely, therefore, that the olivine-clinopyroxenites are the crystallised products of the melt which enriched the *Anomaly 1* harzburgites, harzburgite *xenoliths* and *top-of-the-sequence* harzburgites. Similarly, the Type II pyroxenites might represent a product of the melt which caused the enrichment of the *Anomaly 2* harzburgites. The Type II pyroxenites are generally more

deformed and, therefore, probably older than the Type I pyroxenites. The composition of the *Anomaly 2* harzburgites might, therefore, reflect mechanical mixing of a Type II pyroxenite and residual harzburgite during deformation. The *Anomaly 1* harzburgites, harzburgite *xenoliths* and *top-of-the-sequence* harzburgites are more likely to have been enriched by intergranular migration of melts at the top of the sequence, which occasionally coalesced to form the olivine-clinopyroxenite veins.

4.10 CLINOPYROXENE TRACE ELEMENT GEOCHEMISTRY

The trace element content of clinopyroxenes has been determined by secondary ion mass spectrometry at the University of Edinburgh. In accordance with the depleted mineral chemistry of the Troodos harzburgites described above, the incompatible trace element contents of clinopyroxenes are very low. Because of this, the standard analytical procedure had to be modified in order to improve the detection limit for the Rare Earth Elements (REE). Detection limits were in the order of 5 ppb for the LREE, 30 ppb for the HREE and 5 to 20 ppb for the other trace elements analysed. Instrumental precision is estimated to be better than 15% for the REE and 10% for the other trace elements. Details of the analytical procedure are given in Appendix A. The full clinopyroxene data set is listed in Appendix D and a selection of representative analyses is presented in Table 4.6.

sample	LF21	262	191	195	293	257a	344
lithology	harzburgite	harzburgite	harzburgite	dunite	harzburgite	opyxite A	opyxite B
location	lim.for	background	serp diapir	crustal	anomaly 2		
Sc	59.43	46.00	62.15	68.73	55.30	55.74	72.53
Ti	191.05	24.67	871.81	1042.12	312.83	144.79	294.36
V	186.65	132.31	178.03	174.93	157.28	144.79	200.61
Sr	0.331	0.708	0.438	1.969	0.433	0.244	7.482
Zr	0.175	0.062	0.611	1.688	0.092	0.104	0.222
Nb	0.166	0.088	0.139	0.235	0.131	0.170	0.167
Ba	0.076	0.091	3.396	0.683	0.022	0.062	1.599
Y	1.277	0.103	6.173	9.101	1.904	0.787	1.210
La	0.003	0.004	0.007	0.035	0.004	0.001	0.002
Ce	0.007	0.004	0.013	0.109	0.005	0.002	0.004
Pr	0.004	0.001	0.006	0.042	0.001	0.001	0.001
Nd	0.015	0.006	0.121	0.586	0.008	0.002	0.011
Sm	0.006	0.002	0.189	0.486	0.005	0.002	0.012
Eu	0.006	0.001	0.098	0.226	0.005	0.001	b.d.
Gd	0.071	b.d.	0.584	1.128	0.046	0.024	0.046
Tb	0.015	0.001	0.144	0.201	0.017	0.007	0.013
Dy	0.203	0.009	1.009	1.795	0.306	0.083	0.153
Yb	0.609	0.191	0.925	1.440	0.591	0.277	0.382

Table 4.6. Summary of representative clinopyroxene trace element analyses. All data in ppm. Abbreviations: lim.for = Limassol Forest; serp diapir = serpentinite diapir; bd = below detection limit.

4.10.1 INTRODUCTION

Clinopyroxene is the mantle mineral most commonly analysed for its trace element content because it is considered to be the main repository for the incompatible trace elements (Johnson *et al.*, 1990). However, recent studies have shown that, in clinopyroxene-poor peridotites, orthopyroxene may contain a significant proportion of the whole-rock trace element budget (Rampone *et al.*, 1991). If this is the case, it may not be appropriate to use clinopyroxene trace element contents to interpret whole-rock trace element patterns (McDonough *et al.*, 1992; Ayers, 1993).

In order to establish whether or not clinopyroxene is the predominant host for trace elements in the Troodos harzburgites, the three primary silicate phases were analysed in one *background* harzburgite, sample No.188. As discussed in greater detail below, the REE content of the Troodos clinopyroxene is uniformly low and in many cases close to the detection limit of the ion probe. For the olivine and orthopyroxene grains analysed in sample No.188, the REE were always below the detection limit of the ion probe. Therefore, it is assumed that, of the primary silicates, clinopyroxene is the repository for the REE in the Troodos samples. The data for the other trace elements are summarised in Table 4.7, together with whole-rock values determined by ICP-MS.

	Clinopyroxene	Orthopyroxene	Olivine	Spinel	Whole-rock
Modal %	0.4	15.7	82.4	0.8	
Sc	69.97	28.73	7.70	-	4.94
Ti	50.35	30.33	1.44	281.5*	8.63
V	115.23	66.38	9.39	2522.8*	12.12
Sr	1.60	0.082	0.297	-	0.104
Zr	0.095	0.053	0.122	-	0.027
Nb	0.131	0.013	bd	-	0.004
Y	0.271	0.042	0.018	-	0.018
Ba	0.288	bd	0.014	-	0.068

Table 4.7 Comparison of mineral concentrations and whole-rock abundances for selected trace elements from Troodos *background* harzburgite sample No.188. Modal proportions were calculated from electron probe and whole-rock data; * = electron probe data. All data in ppm.

Also presented in Table 4.7 are modal abundances which were calculated using the Solver function on Microsoft Excel. The modal abundances were calculated by writing a mass balance equation for each element, which related the electron probe data for each of the four main phases to the whole-rock data. The equations had the following form:

$$\text{Calculated } WR_i = (\text{Olivine}_i * \%\text{Olivine}) + (\text{Orthopyroxene}_i * \%\text{Orthopyroxene}) + (\text{Clinopyroxene}_i * \%\text{Clinopyroxene}) + (\text{Spinel}_i * \%\text{Spinel})$$

where Calculated WR_i is the calculated whole-rock content of element i derived from the mass-balance equation, Olivine_i is the concentration of element i in olivine and %Olivine is the modal proportion of olivine, etc.

Residuals can then be calculated by subtracting the measured whole-rock abundance of element i from the calculated whole-rock abundance of element i. To calculate the sum of the squares of the residuals, each residual value for each element under consideration is squared and then summed. For example, for elements i, j and k:

$$\text{Calculated } WR_i - \text{Measured } WR_i = \text{Residual}_i \rightarrow (\text{Residual}_i)^2$$
$$\text{Calculated } WR_j - \text{Measured } WR_j = \text{Residual}_j \rightarrow (\text{Residual}_j)^2$$
$$\text{Calculated } WR_k - \text{Measured } WR_k = \text{Residual}_k \rightarrow (\text{Residual}_k)^2$$

$$\overline{\qquad\qquad\qquad}$$

Sum of the squares of the residuals

The Solver function then manipulates the modal proportions of the minerals in each mass-balance equation with the aim of minimising the sum of the squares of the residuals. This calculation was carried out using XRF whole-rock data for the major elements and Cr, V and Ni.

The accuracy of the calculated modal abundances can be assessed by back-calculating whole-rock data, using the electron probe analyses and the calculated modal abundances. The back-calculated whole-rock values and measured whole-rock values are presented in Table 4.8. As the data show, the Solver programme models the major elements quite well, but the calculated whole-rock trace element data are significantly in error. There may be several reasons for this. Firstly, if the trace elements are concentrated in minor phases, or surface films, which are not taken into account in the mass balance calculations (Suzuki, 1987; Bodinier *et al.*, 1996), the measured whole-rock abundances will be higher than those predicted by the calculation. Also, the ion probe was operating close to the

detection limit for the olivine analyses, which means that the analytical errors are potentially high. This could result in a large over- or under-estimation of the calculated whole-rock abundance of an element, because the high modal proportion of olivine will result in the analytical errors being magnified. Furthermore, the whole-rock analyses comprise both the primary silicate portion of the rock and the secondary serpentinite minerals. If any of the elements are mobile during the alteration process, the calculated data, based on the primary silicate data, will be unable to model the measured data. The effects of serpentinisation on whole-rock chemistry are considered in more detail in Chapter 5.

With these considerations in mind, the mineral trace element data for the four phases analysed in the *background* harzburgite sample are compared in Figure 4.21.

	Measured whole-rock	Calculated whole-rock		Measured whole-rock	Calculated whole-rock
MgO	46.53	46.71	Sc	4.94	11.12
Al_2O_3	0.30	0.26	Ti	8.63	7.79
SiO_2	42.40	42.41	V	12.12	26.30
CaO	0.32	0.31	Sr	0.10	0.26
Cr_2O_3	0.31	0.58	Zr	0.03	0.11
MnO	0.13	0.16	Nb	0.01	0.003
Fe_2O_3	9.33	8.44	Y	0.02	0.02
NiO	0.26	0.36	Ba	0.07	0.01

Table 4.8 Comparison of calculated and measured whole-rock analyses, major elements (in wt%) analysed by XRF and trace elements (in ppm) by ICP-MS for sample No.188.

Figure 4.21a shows the relative abundances of the trace elements measured in each phase. The graph suggests that clinopyroxene is the major inventory for most trace elements except for Ti and V, which have a high abundance in spinel. In Figure 4.21b, the data are adjusted using the calculated modal abundances to reflect the modal proportion of each mineral phase in sample No.188. Because of the large errors inherent in the modal calculation, and the low abundances, the data in this graph are only used to discuss the relative differences between the modally adjusted data and the absolute abundances of the trace elements.

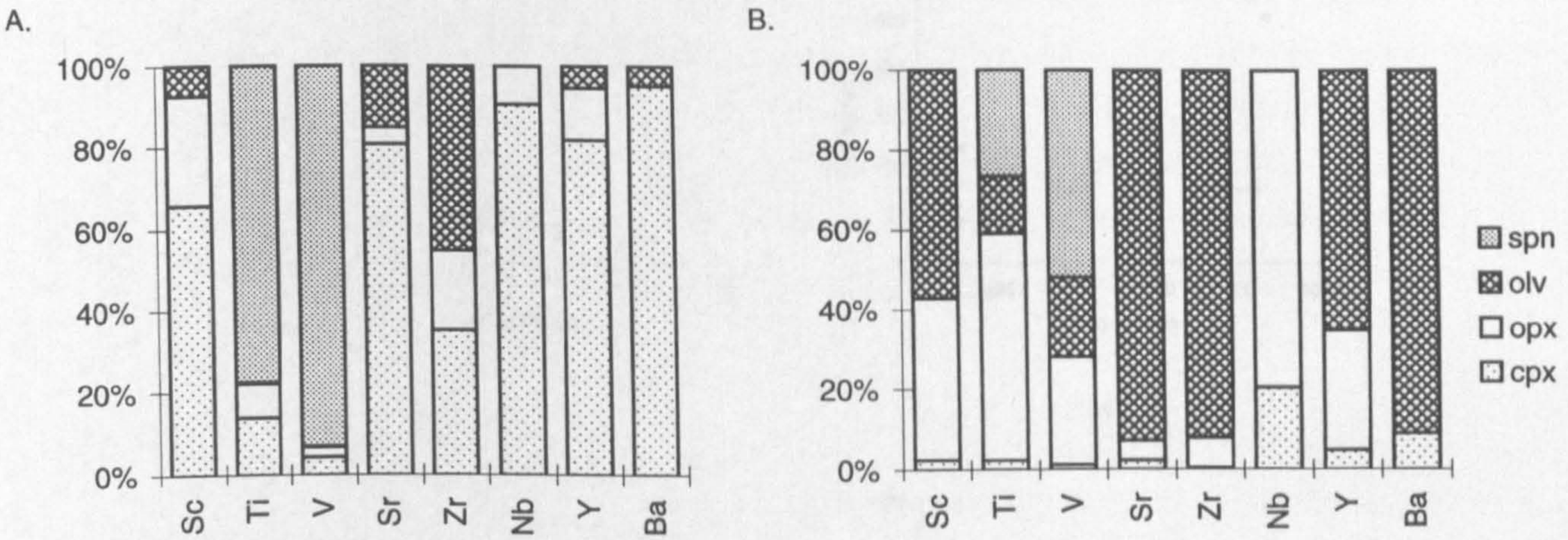

Figure 4.21 Bar charts illustrating the relative contribution each mineral makes to the whole-rock abundances of selected elements: a) relative abundances; b) adjusted for modal proportions.

As Figure 4.41b shows, despite the fact that olivine generally has the lowest trace element concentrations of the phases analysed, the contribution of olivine to the whole-rock abundance of certain trace elements might be quite large because olivine has a high modal abundance. Similarly, the contribution of Sc, Ti and Nb from orthopyroxene to the whole-rock abundance seems higher than that from clinopyroxene because of the difference in the modal abundances of the two phases. It must be stressed again that the errors inherent in the calculations used in this section are large and the data can, at best, only be treated qualitatively. However, the Troodos data do seem to support the arguments of McDonough *et al.* (1992) and Ayers (1993) that as the degree of depletion of a peridotite increases, the trace element contents of clinopyroxene become less good proxies for whole-rock values. Clinopyroxene trace element contents may not, therefore, be good proxies for whole-rock values in very depleted Troodos peridotites.

As a test of this hypothesis, whole-rock trace element abundances, analysed by ICP-MS, are compared with the clinopyroxene trace element data for the *backgroumd* harzburgites in Figure 4.22. Only the Zr, Y, Yb and Ti data show a positive correlation between whole-rock and clinopyroxene concentrations. There are no apparent correlations between whole-rock and clinopyroxene trace element contents for Ce, Sr and Ba. A first order interpretation of these data is that the Zr, Y, Yb and Ti contents of clinopyroxene would be good proxies for the whole-rock data, whereas Ce, Sr and Ba would not. This hypothesis is clearly contradictory to that made from the silicate trace element analyses made from *backgroumd* harzburgite sample No.188 described above.

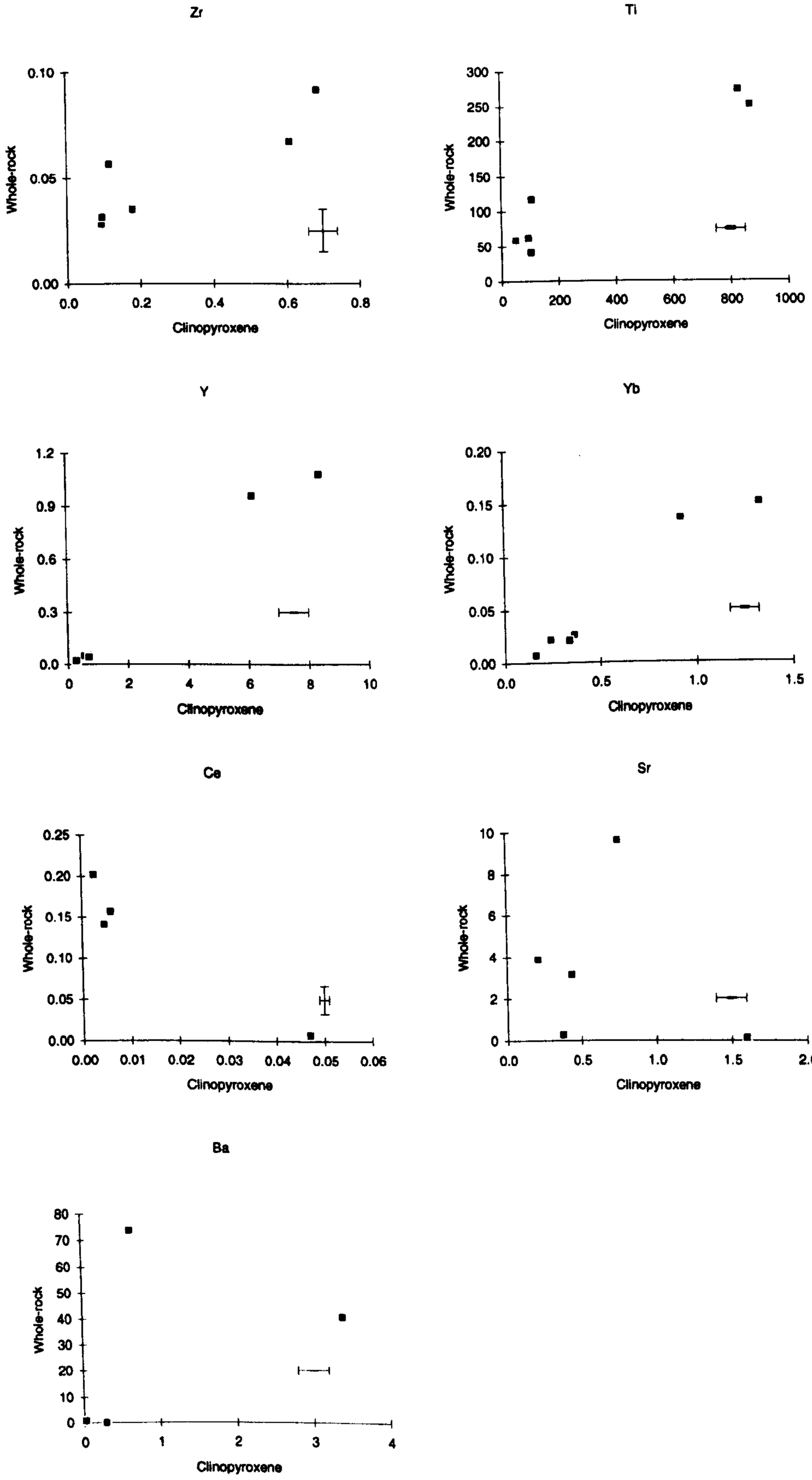

Figure 4.22 Graphs comparing the whole-rock and clinopyroxene trace element data for the Troodos harzburgites; all data in ppm.

In detail, it can be seen that the best fit lines for the Ti and Zr data do not pass through the origin of the whole-rock vs clinopyroxene graphs. The fact that at trace element contents of zero in clinopyroxene, these elements would still have a measurable whole-rock concentration, suggests that other mineral phases contribute to the whole-rock abundances of Ti and Zr. This agrees with the trace element data presented above for the *background* harzburgite No.188. It can be seen from Table 4.7 that spinel will have a significant contribution to the whole-rock Ti budget.

The Ce, Sr and Ba data show a bimodal distribution on Figure 4.22, with one sample plotting at high clinopyroxene values but low whole-rock concentrations. Coincidentally, this is also *background* harzburgite sample No.188, for which the trace element data for each of the main silicate phases was presented above. One possible explanation for this might be that serpentinisation has redistributed these elements and therefore affected their whole-rock values.

With these data in mind, no attempt will be made in this thesis to extrapolate trace element data from clinopyroxene to whole-rock values. Where enrichments or depletions of elements are discussed they will refer to enrichments and depletions in the specific clinopyroxene under discussion, rather than to any inferred whole-rock concentrations.

4.10.2 TRACE ELEMENT GEOCHEMISTRY OF TROODOS HARZBURGITE CLINOPYROXENE

Chondrite-normalised REE plots for clinopyroxene from the Troodos and Limassol Forest harzburgite samples are presented in Figure 4.23, (normalising values are from Anders and Grevesse, 1989). Also shown for comparison are patterns from non-hotspot, abyssal peridotite clinopyroxene, sampled from the American-Antarctic and Southwest Indian Ridges (Johnson *et al.*, 1990).

Background harzburgites (Figure 4.23a) have steeply sloping HREE-MREE patterns with flat MREE-LREE. All *background* samples show a slight upward inflection in La relative to Ce, and HREE contents are all less than the most depleted abyssal peridotite. (Ce/Yb)n values range between 0.002 and 0.009, compared with ratios of 0.002 to 0.05 in the abyssal peridotites. Notably, the most depleted harzburgite (i.e. highest $Cr\#_{spn}$) has the lowest concentration of the HREE and steepest-sloping HREE-MREE patterns.

Patterns for other *background* harzburgites are shown in Figure 4.23b. Sample 293 is an *Anomaly 2* harzburgite, sample 188 was collected from the area of the Hadji Pavlou

chrome mine, and sample LF21 from the Limassol Forest. The *Anomaly 2* harzburgite and the Limassol Forest sample have similar patterns to the other *backgroumd* harzburgites, although the HREE contents are slightly higher. However, the sample from the chrome mine has a much flatter REE pattern with a (Ce/Yb)n ratio of 0.078.

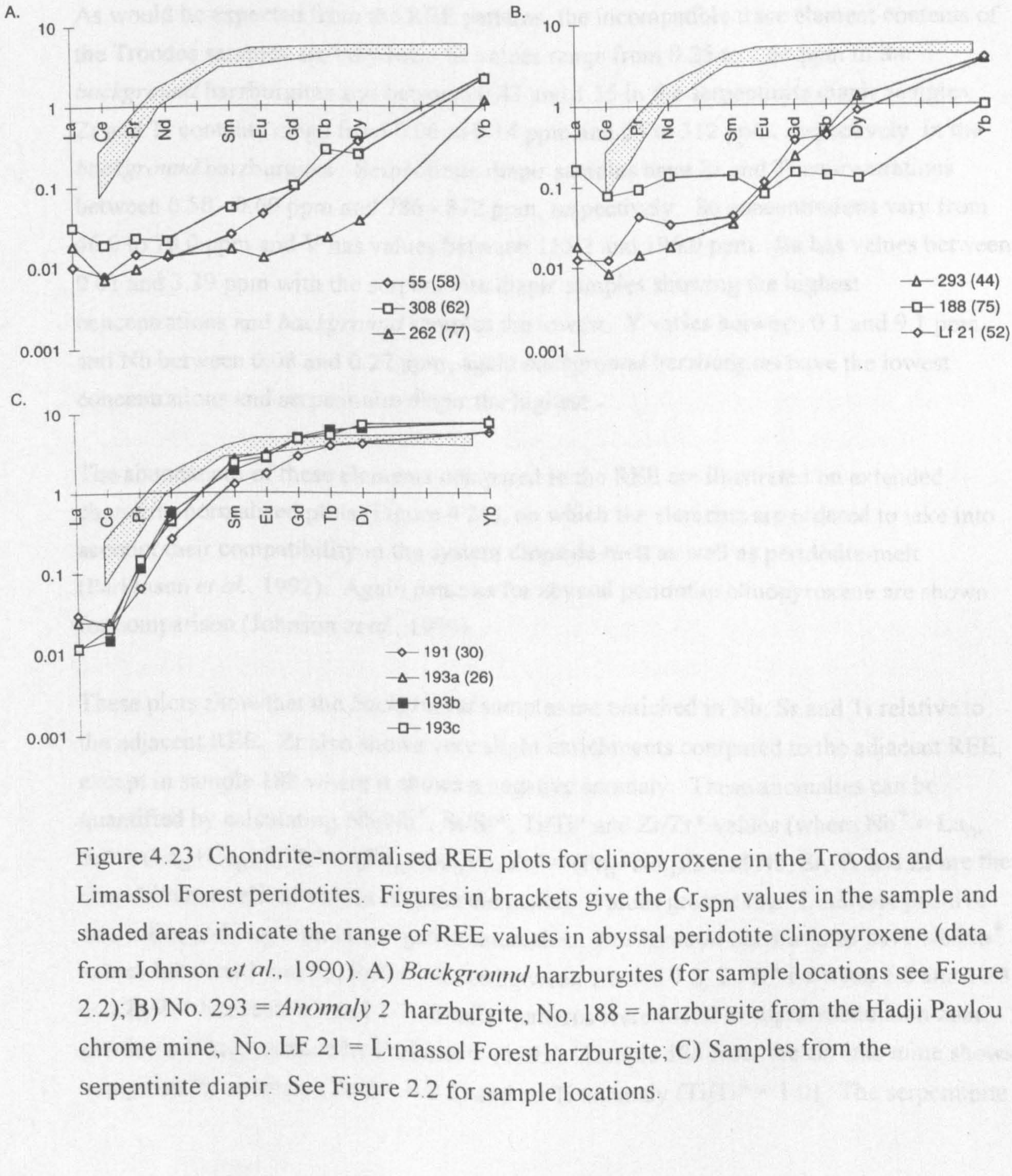

Figure 4.23 Chondrite-normalised REE plots for clinopyroxene in the Troodos and Limassol Forest peridotites. Figures in brackets give the Cr_{spn} values in the sample and shaded areas indicate the range of REE values in abyssal peridotite clinopyroxene (data from Johnson *et al.*, 1990). A) *Backgroumd* harzburgites (for sample locations see Figure 2.2); B) No. 293 = *Anomaly 2* harzburgite, No. 188 = harzburgite from the Hadji Pavlou chrome mine, No. LF 21 = Limassol Forest harzburgite; C) Samples from the serpentinite diapir. See Figure 2.2 for sample locations.

Samples from the serpentinite diapir (Figure 4.23c) have MREE-HREE profiles and abundances that are similar the abyssal peridotites, but with slightly steeper MREE-LREE profiles. Several analyses were made on one of the samples (numbered 193 on the Figure) to check for intra- and inter-crystal variations. The analyses labelled 193a and 193c are from the cores of 2 different grains, and analysis 193b is a rim analysis corresponding to core analysis 193c. The similarity of the patterns demonstrates the homogeneity of REE contents on a thin-section scale and the absence of any core-rim zoning.

As would be expected from the REE patterns, the incompatible trace element contents of the Troodos samples are very low. Sr values range from 0.25 to 1.61 ppm in the *background* harzburgites and between 0.43 and 1.35 in the serpentinite diapir samples. Zr and Ti contents range from 0.06 to 0.14 ppm and 24 to 312 ppm, respectively, in the *background* harzburgites. Serpentinite diapir samples have Zr and Ti concentrations between 0.58 - 0.69 ppm and 786 - 872 ppm, respectively. Sc concentrations vary from 46.0 to 70.0 ppm and V has values between 115.2 and 196.0 ppm. Ba has values between 0.01 and 3.39 ppm with the serpentinite diapir samples showing the highest concentrations and *background* samples the lowest. Y varies between 0.1 and 9.1 ppm and Nb between 0.08 and 0.27 ppm; again *background* harzburgites have the lowest concentrations and serpentinite diapir the highest.

The abundances of these elements compared to the REE are illustrated on extended chondrite-normalised plots (Figure 4.24), on which the elements are ordered to take into account their compatibility in the system diopside-melt as well as peridotite-melt (Parkinson *et al.*, 1992). Again patterns for abyssal peridotite clinopyroxene are shown for comparison (Johnson *et al.*, 1990).

These plots show that the *background* samples are enriched in Nb, Sr and Ti relative to the adjacent REE. Zr also shows very slight enrichments compared to the adjacent REE, except in sample 188 where it shows a negative anomaly. These anomalies can be quantified by calculating Nb/Nb^*, Sr/Sr*, Ti/Ti* and Zr/Zr* values (where $Nb^* = La_n$, $Sr^* = (La_n+Ce_n)/2$, $Ti^* = (Eu_n+Gd_n)/2$, $Zr^* = (Pr_n+Nd_n)/2$ and Nb, Sr, Ti and Zr are the chondrite normalised values of these elements). Values greater than 1 indicate positive anomalies and less than one negative anomalies. *Background* harzburgites have Nb/Nb^* values between 3 and 53, Sr/Sr* values between 1.6 and 7.2, Ti/Ti* between 1.8 and 10.3 and Zr/Zr* between 1.3 and 1.7. Similar patterns were found in supra-subduction zone peridotite clinopyroxene by Parkinson (1993). Sample 188 from the chrome mine shows a negative Zr anomaly (Zr/Zr* = 0.2) and no Ti anomaly (Ti/Ti* = 1.0). The serpentinite

diapir samples also show large positive Nd and Sr anomalies (Nb/Nb* 19 to 56, Sr/Sr* 2.3 to 10.9), but negative Zr (Zr/Zr* 0.5 to 0.9) and Ti (Ti/Ti* 0.5 to 0.9) anomalies.

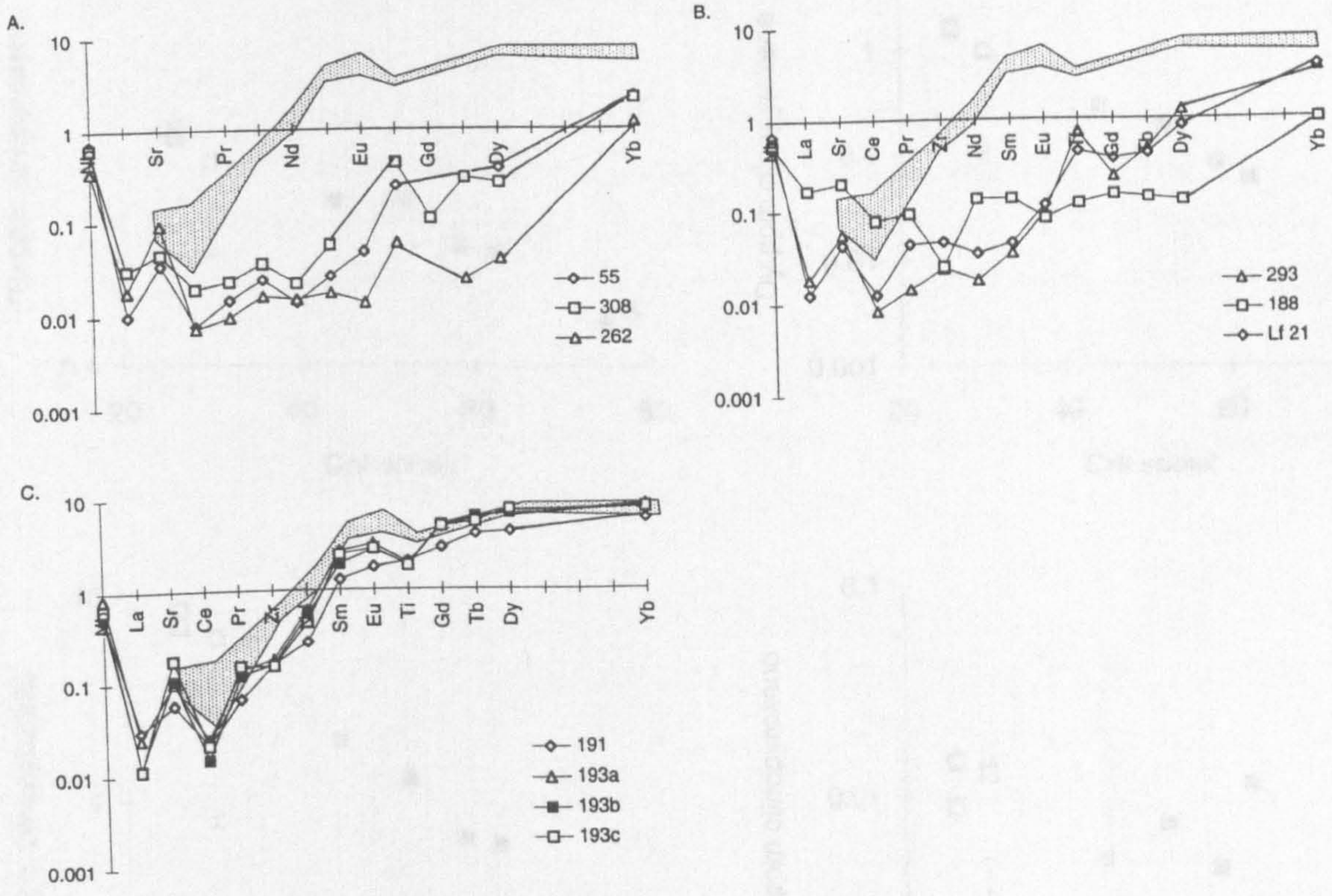

Figure 4.24 Extended chondrite-normalised REE plots for clinopyroxenes from the Troodos and Limassol Forest peridotites. Shaded areas indicate values in abyssal peridotite clinopyroxene, data from Johnson *et al.*, 1990.

4.10.2.1 MELTING MODELS FOR THE TROODOS HARZBURGITES

In order to examine the nature and extent of the partial melting process which produced the Troodos harzburgites, it is necessary to establish which elements have not been redistributed by other processes. Figure 4.25 illustrates the covariation of selected REE and other trace elements in clinopyroxene with $Cr\#_{spn}$. The HREE and Y concentrations display strong negative correlations with $Cr\#_{spn}$ in all the harzburgites analysed. This correlation suggests that their abundance is predominantly controlled by partial melting. As on the electron probe graphs (e.g. Figure 4.3), the serpentinite diapir samples define the least depleted end of the compositional variation. The LREE, Sr and Nb display a similar negative correlation with $Cr\#_{spn}$ at $Cr\#_{spn} < 50$. However, at $Cr\#_{spn} > 50$ there is no systematic correlation. A first order interpretation of these data is that partial melting is the main process controlling LREE, Sr and Nb distribution in the fertile peridotites, but in the more depleted harzburgites some other process affects their distribution.

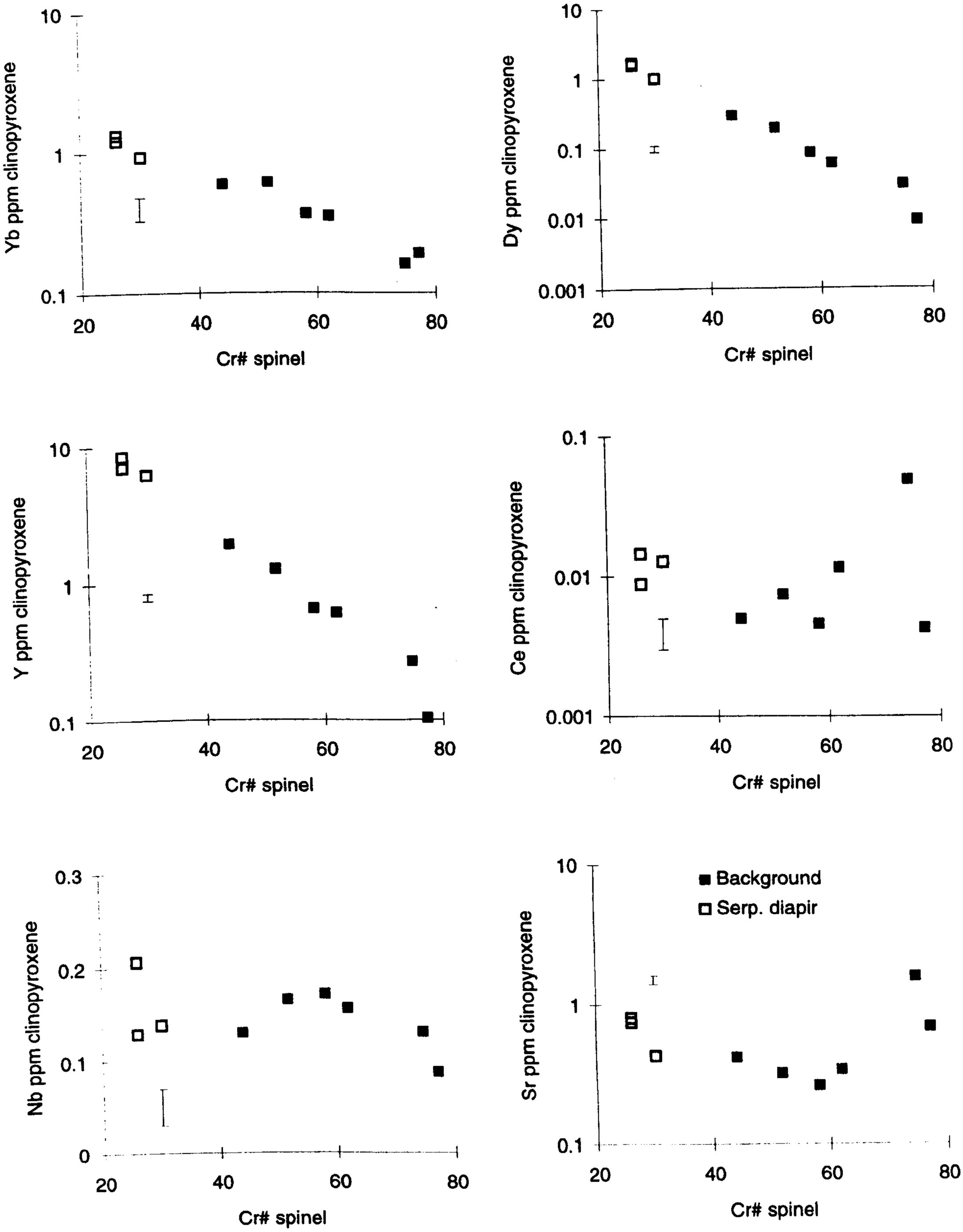

Figure 4.25 Plots illustrating the covariation of selected REE (in ppm) in clinopyroxenes with $Cr\#_{spn}$.

These relationships with $Cr\#_{spn}$ suggest that the HREE, and geochemically similar elements (i.e. Y), will give the most useful information about partial melting processes. Figure 4.26 shows the variation of Dy and Y with Yb. Also shown on these plots are the calculated batch and fractional melting trajectories for melting of a fertile mantle source. The starting composition, distribution coefficients, modal mineralogy and melting mode were taken from Pearce and Parkinson (1993), and references therein, and are summarised in Table 4.9. The starting composition used is defined as fertile MORB mantle (FMM) by Pearce and Parkinson (1993) and represents the global convecting reservoir from which N-MORB is extracted. The melting equations used were taken from Johnson *et al.* (1990) and are reproduced in Appendix C. Yb and Dy data (Y was not analysed in these samples) for abyssal (Johnson *et al.*, 1990) and forearc peridotites (Parkinson *et al.*, 1992) are plotted for comparison.

	Distribution coefficients				Starting composition
	Olivine	Orthopyroxene	Clinopyroxene	Spinel	
Nb	0.0001	0.001	0.015	0.1	0.2
Sr	0.01	0.04	0.06	0.0006	4.32
La	0.00001	0.0025	0.05	0.0006	0.31
Ce	0.00001	0.005	0.13	0.0006	0.96
Nd	0.00007	0.01	0.25	0.0006	0.96
Sm	0.0007	0.02	0.35	0.0006	0.39
Eu	0.001	0.003	0.45	0.0006	0.147
Gd	0.001	0.04	0.5	0.0006	0.518
Dy	0.004	0.05	0.51	0.0015	0.644
Er	0.009	0.07	0.52	0.003	0.42
Yb	0.023	0.11	0.52	0.0045	0.418
Zr	0.007	0.04	0.12	0.07	9.2
Ti	0.015	0.15	0.3	0.07	1050
Y	0.006	0.06	0.51	0.002	3.9
V	0.03	0.4	0.8	0.3	78
Ga	0.004	0.3	0.3	0.09	4
Sc	0.25	1	2	0.3	15.5
Start mode	0.58	0.25	0.15	0.02	
Melt mode	0.1	0.28	0.6	0.02	

Table 4.9 Summary of the data used for melt modelling, reproduced from Pearce and Parkinson (1993) and references therein, element concentrations in ppm.

On both graphs, the batch melting model cannot reproduce the range of natural peridotite compositions and therefore, does not realistically describe the melting process. Although there is no consensus on how, or at what degree of melting, partial melt will separate from a source peridotite, recent theories (McKenzie, 1984; Van Bargan and Waff, 1988; Kostopoulos, 1991) suggest that peridotites are permeable at low degrees of melting. The fact that the Troodos data cannot be modelled by a batch melting process supports these theories.

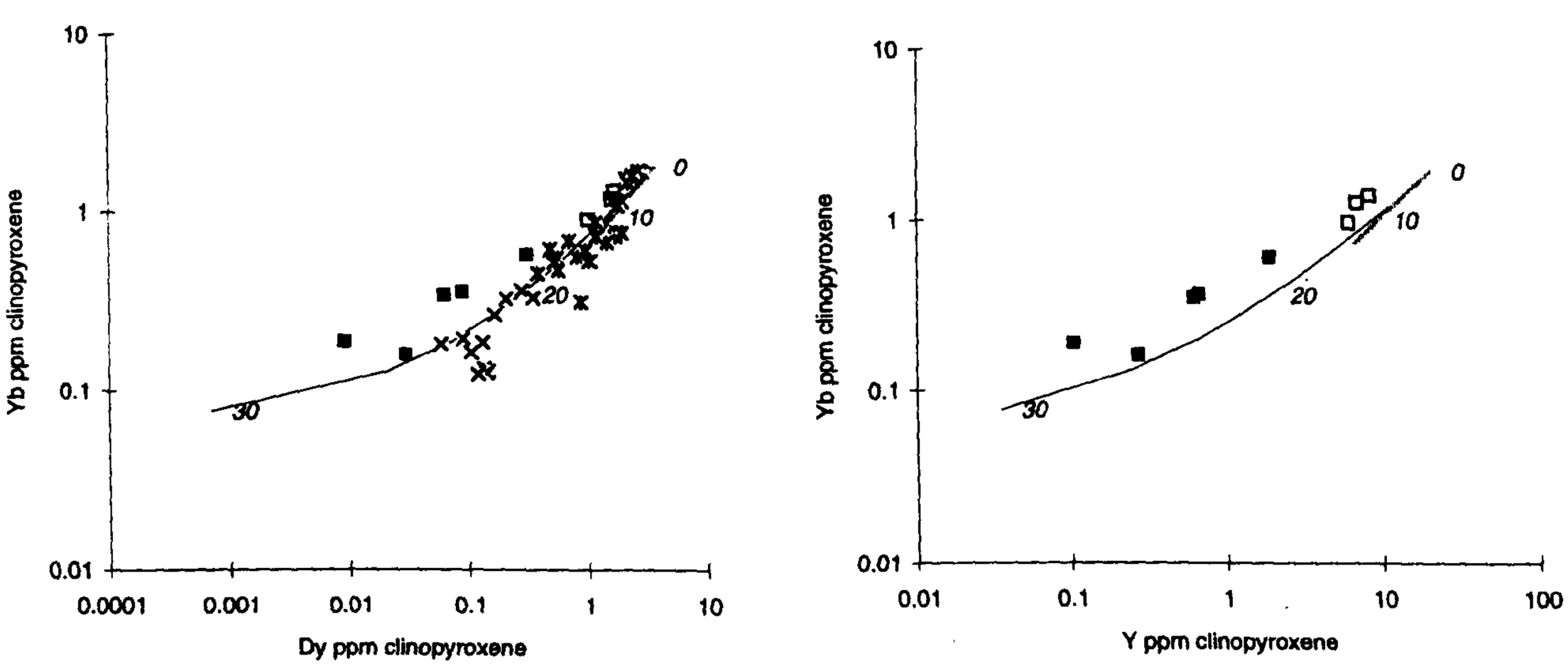

Figure 4.26 Graphs illustrating the variation of Dy and Y with Yb in clinopyroxene and modelled fractional melting trends from a fertile MORB source. Fore-arc peridotite data from Parkinson *et al.*, 1992; abyssal peridotite data from Johnson *et al.*, 1990; figures adjacent to calculated melting trajectories indicate percentage of melting.

However, the fractional melting model does produce a wide range of trace element concentrations, similar to those observed in the peridotites. This would suggest that a fractional melting process is more applicable. Johnson *et al.* (1990) also suggested that a fractional melting process was responsible for the trace element abundances in abyssal peridotite clinopyroxene. A model of incremental melting, which is conceptually intermediate between the batch and fractional melting end-members, could also produce the wide range of trace element concentrations seen in the Troodos data, as long as the extracted melt fraction was small.

For the parameters used in the fractional melt modelling, the HREE abundances in the serpentinite diapir samples would require 5 to 15% fractional melting and the *background* harzburgites 20 to 30% fractional melting. These estimates are consistent with the melting estimates obtained from the major element compositions of the Troodos harzburgite minerals in Section 4.6. For the incremental melting model, the melting percentage estimates would be slightly higher.

Figure 4.27 shows modelled REE patterns for 0, 10, 20 and 25% fractional melting and, for comparison, the REE patterns for various *background* harzburgites. The graph shows that while fractional melting can describe the variation in the HREE (i.e. Figure 4.26), this melting process depletes the LREE in the residues too rapidly to explain the full Troodos *background* harzburgite REE patterns. There are several possible explanations for this.

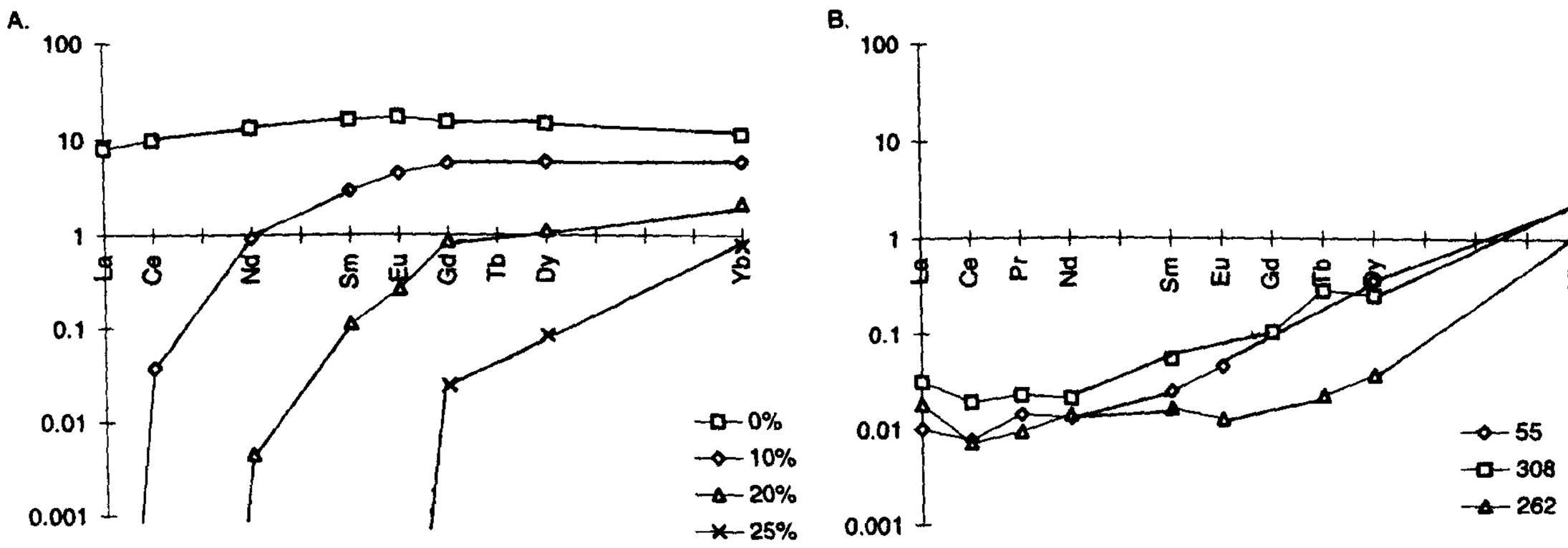

Figure 4.27 Graphs comparing the REE profiles of clinopyroxene in the Troodos *background* harzburgites (b) with those modelled for a fractional melting process (a).

Firstly, the fractional melting model might be an over simplified or inaccurate model of the real melting process. An alternative melting model that has been proposed to explain relatively high LREE contents in peridotites is the sequential disequilibrium model of Prinzhofer and Allègre (1985). In this model minerals melt out with their own composition and the initial stages of fusion take place in the garnet facies. Because garnet melts-out with its own composition, which is markedly HREE enriched, the source becomes depleted in the HREE. Further melting gradually reduces the MREE and LREE concentrations by melting-out of clinopyroxene, which results in the most depleted lithologies having a markedly U-shaped pattern. Prinzhofer and Allègres' original REE

cartoons comparing disequilibrium melting with batch and fractional melting models for whole-rock REE patterns are reproduced in Figure 4.28 to illustrate this process.

Bédard (1989) has suggested that, under melting conditions which favour slow melt extraction by pervasive melt percolation, equilibrium processes such as fractional melting will operate. He contrasts this with conditions where high melt extraction rates exist, such as during melt extraction in dykes, when disequilibrium processes will be more likely. In the Troodos sequence there is evidence for both melt transport in dykes and petrographic evidence (see Microstructure Chapter) for the presence of interstitial melt. However, the fact that in a disequilibrium model minerals melt-out with their own composition is difficult to reconcile with the LREE-enriched clinopyroxene patterns, in which the starting composition of the clinopyroxene is slightly LREE-depleted (e.g. Johnson *et al.*, 1990; Johnson and Dick, 1992). Furthermore, as Johnson *et al.* (1990) point out, there is a clear relationship between the modal proportion of clinopyroxene in abyssal peridotites and its composition. This relationship is also difficult to reconcile with a disequilibrium melting model. Therefore, while a disequilibrium process might be able to explain bulk rock trace element patterns, it is difficult to see how it would produce the REE patterns found in the Troodos clinopyroxene.

Johnson and Dick (1992) have suggested that perfect separation of melt from the residue required by the fractional melting model is unlikely to occur in real melting zones, and a more realistic scenario would be that a small fraction of melt is always present in the source. In the Johnson and Dick (1992) model, partial melting is viewed as an open system process with the source at any point consisting of a solid residue plus transient, rather than trapped, melt. The transient melt is derived from melting lower in the melting column and has the effect of slowing down the depletion of the highly incompatible elements in the residue.

Unfortunately, the algorithm used by Johnson and Dick (1992) has not been published, so it has not been possible to model precisely complete REE profiles for the Troodos peridotites using this process. However, the (Nd/Yb)n - Ti/Zr plot used by Johnson and Dick (1992) is reproduced in Figure 4.29a, with the Troodos data, a calculated fractional melting trajectory and Johnson and Dicks' modelled transient melt field sketched approximately into position. It should be noted that the parameters used for the melt modelling in this thesis are different from those used by Johnson and Dick (1992). The modelled field sketched on Figure 4.29 is, therefore, only a crude approximation of the values that would be expected for this process.

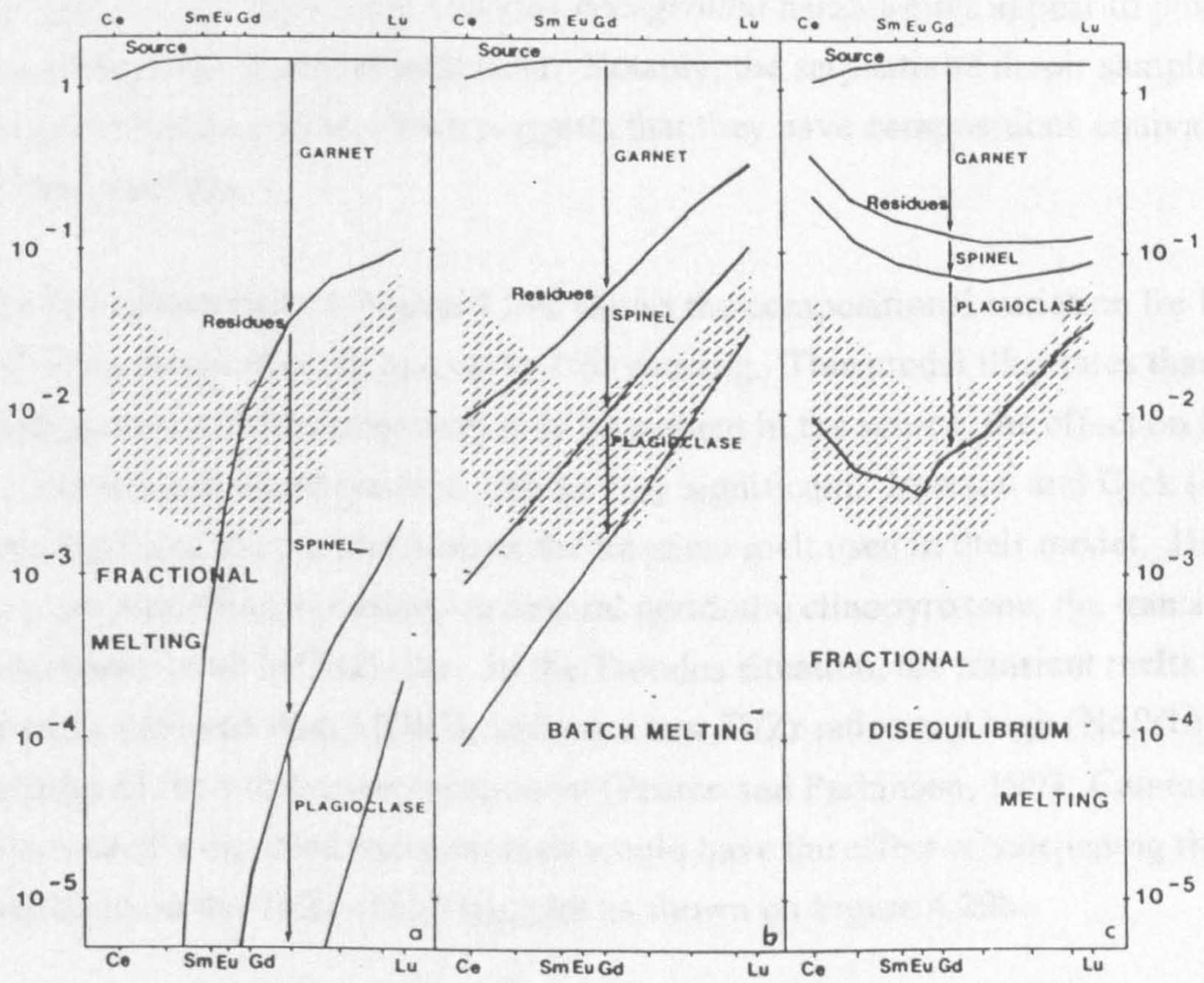

Figure 4.28 Graphs comparing fractional melting, batch melting and the fractional disequilibrium melting model according to Prinzhofer and Allègre (1985).

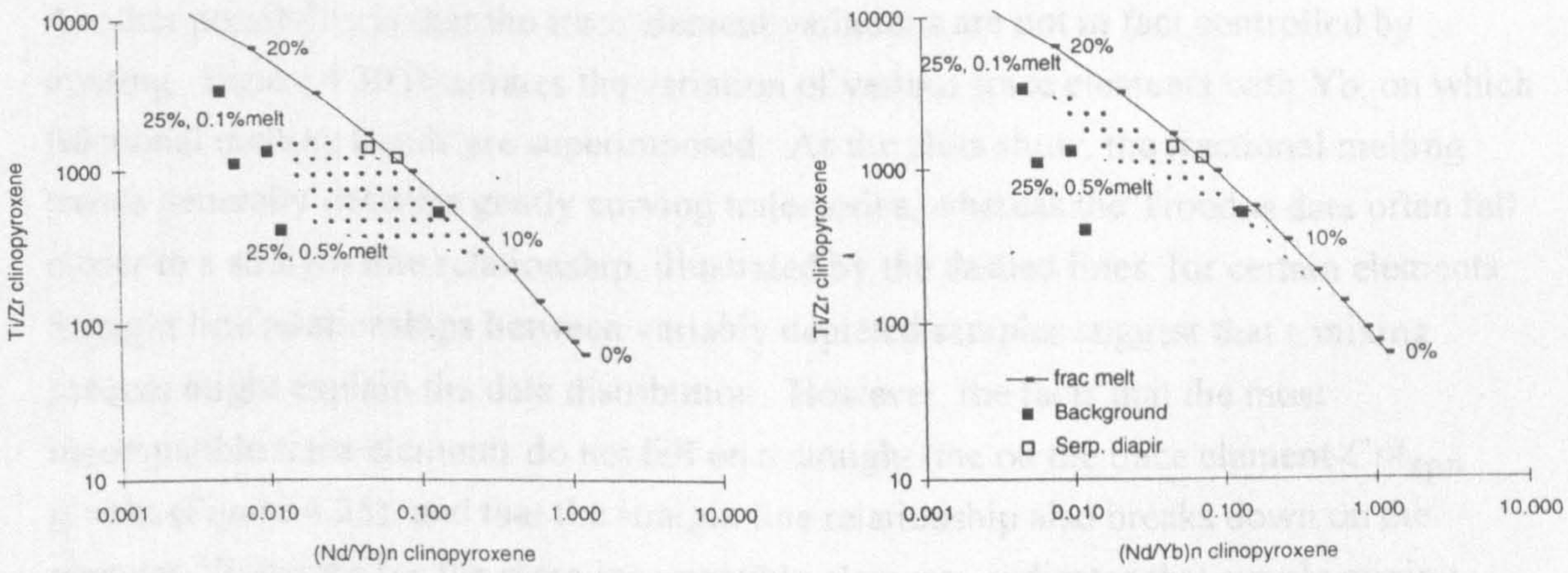

Figure 4.29 Variation of Ti/Zr with $(Nd/Yb)_n$ for the Troodos clinopyroxenes. Shaded areas indicate the variation produced by transient melts modelled according to Johnson and Dick (1992): a) modelled field for a MORB-like transient melt; b) modelled field for a more depleted transient melt. Both fields show the variation for 0.1 to 0.5% transient melt and up to 25% partial melting.

As Figure 4.29a shows, the Troodos *background* harzburgites appear to plot on an extension of the transient melt field. Notably, the serpentinite diapir samples plot on the fractional melting trend which suggests that they have compositions equivalent to simple melting residues.

The field illustrated on Figure 4.29a shows the compositional variation for between 0.1 and 0.5% transient melt, and up to 25% melting. This model illustrates that although only small amounts of transient melt may be present in the source, the effect on the incompatible element contents can be very significant. Johnson and Dick (1992) do not give details of the composition of the transient melt used in their model. However, since they are modelling variations in abyssal peridotite clinopyroxene, the transient melt is most likely to be MORB-like. In the Troodos situation, the transient melts are likely to be more depleted than MORB, and have low Ti/Zr ratios and high $(Nd/Yb)_n$ ratios because of the subduction component (Pearce and Parkinson, 1993; Cameron, 1985). The presence of a depleted transient melt would have the effect of steepening the transient melt field on the Ti/Zr-$(Nd/Yb)_n$ plot as shown on Figure 4.29b.

Despite the fact that the Johnson and Dick (1992) open system melting process cannot be modelled accurately for the Troodos data without their algorithm, Figure 4.29 suggests that at least some of the variation in the *background* harzburgites could be explained by this process.

Another possibility is that the trace element variations are not in fact controlled by melting. Figure 4.30 illustrates the variation of various trace elements with Yb, on which fractional melting trends are superimposed. As the plots show, the fractional melting trends generally describe gently curving trajectories, whereas the Troodos data often fall closer to a straight line relationship, illustrated by the dashed lines, for certain elements. Straight line relationships between variably depleted samples suggest that a mixing process might explain the data distribution. However, the facts that the most incompatible trace elements do not fall on a straight line on the trace element-$Cr\#_{spn}$ graphs (Figure 4.25), and that the straight line relationship also breaks down on the element-Yb graphs for the more incompatible elements, indicates that simple mixing might not be an applicable explanation for all the variation in the Troodos samples.

Considering the possible alternatives discussed above, the following model is proposed to explain the trace element abundances in the Troodos harzburgite clinopyroxene. The primary control on element abundances is partial melting, which the HREE data suggest was probably nearly fractional in nature. The melting conditions can be further

constrained by considering the distribution of V. As explained in Section 4.6.2, the compatibility of V during melting will be largely controlled by fO_2. Under conditions of low fO_2, V is in the 3+ state and therefore more compatible with clinopyroxene than under high fO_2, when it will be present predominantly in the 4+ or 5+ state. As pointed out by Parkinson (1993), the Izu-Bonin forearc peridotites plot on a vector towards lower V contents than the abyssal peridotite array. This deviation from the abyssal data was attributed to melting in the forearc occurring under high fO_2, hydrous conditions. The V-Yb variation for the Troodos, forearc and abyssal data is shown in Figure 4.31. The Troodos data plot along the same vector of decreasing V concentration with increasing depletion as the forearc harzburgites, which suggests that the Troodos mantle also experienced partial melting under high fO_2, possibly hydrous, conditions.

However, the most incompatible elements have concentrations which are too high to be adequately described solely by the fractional melting model. The electron probe data discussed above suggest that at various locations in the sequence, reaction between residual peridotites and melts produced enrichments in mineral parameters such as Ti_{spn} and Na_{cpx}. A similar model is proposed for the more widespread LREE enrichment in the Troodos sequence and is discussed in detail in the next section. Essentially, this model is similar to the Johnson and Dick (1992) open system model, because the presence of transient melts are required in order to increase the incompatible element content of the residue. The model for the Troodos harzburgites views the transient melt simply as a phase that is added to the harzburgites during or after the melting event. The variations in incompatible element contents between the harzburgites is a function of different amounts of added melt. This allows the composition of the added melt to be calculated as described below.

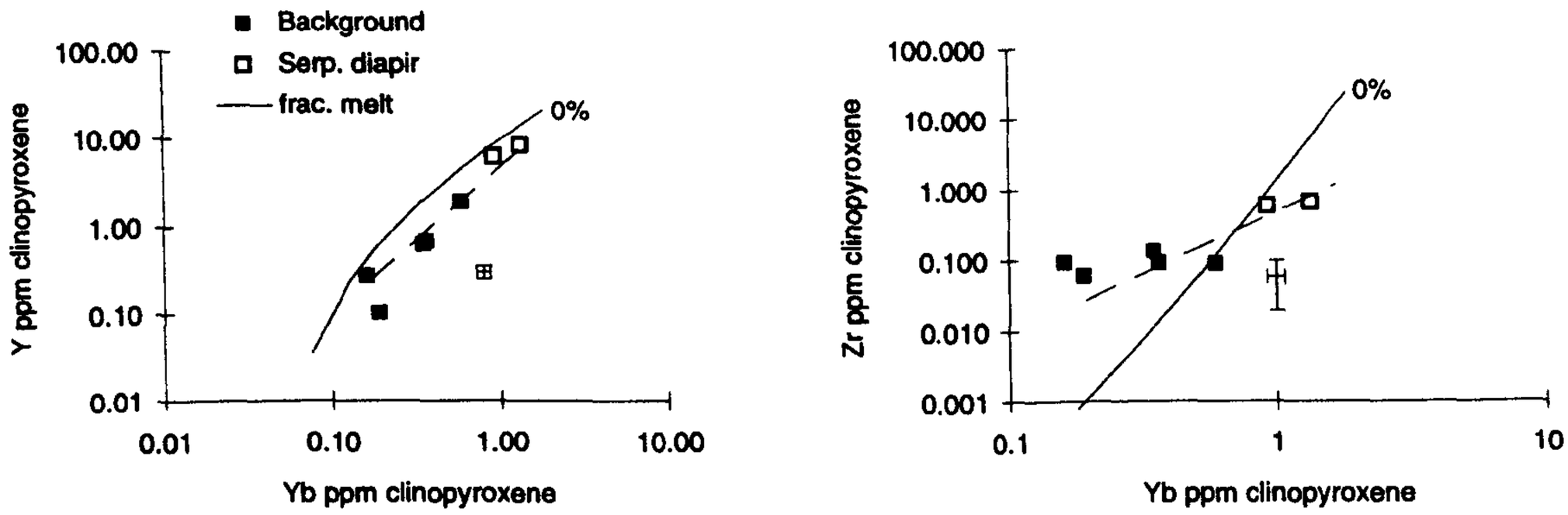

Figure 4.30 Plots illustrating the covariation of selected trace elements with Yb; dashed lines show possible mixing trends between fertile and depleted end-members.

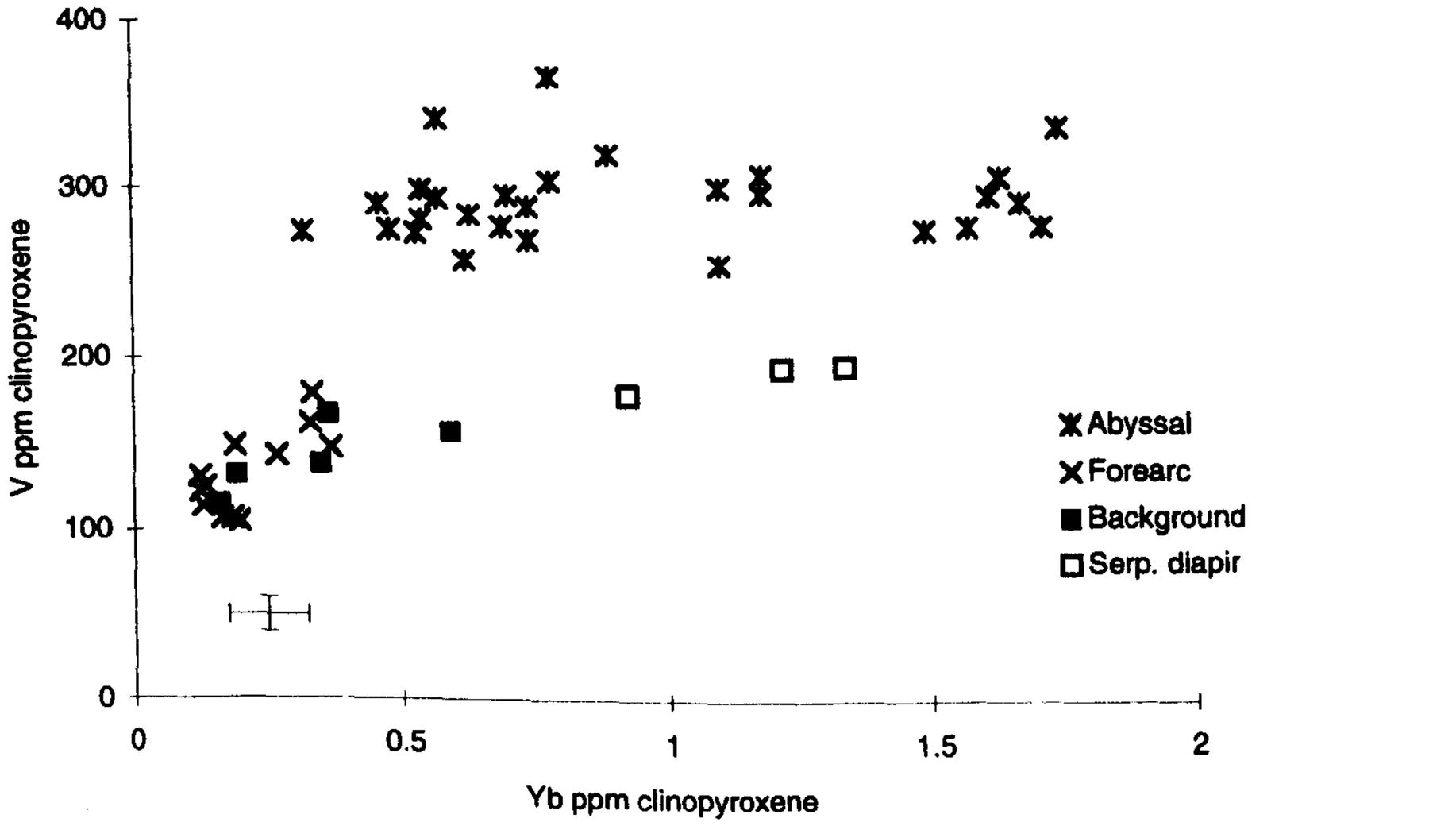

Figure 4.31 Graph illustrating the variation of V with Yb in clinopyroxene with data from forearc and abyssal peridotites for comparison. Abyssal peridotite data from Johnson *et al.*,, 1990; forearc data from Parkinson et al., 1992.

4.10.2.2 EVIDENCE FOR MANTLE-MELT INTERACTION IN THE *BACKGROUND* HARZBURGITES

As the data discussed in the previous section show, not all the trace element variation in the Troodos clinopyroxenes can be explained by a simple fractional partial melting model alone. In particular, the LREE, Sr and Nb do not have a coherent correlation with melting indices (i.e. $Cr\#_{spn}$) in the most depleted harzburgites. Furthermore, the extended chondrite-normalised plots (Figure 4.24) demonstrate that Sr, Zr and Ti are enriched relative to the adjacent REE in the *background* harzburgites. Figure 4.32 illustrates the variation of these and other trace elements with Yb, the distribution of which is thought to be primarily controlled by fractional partial melting. Also shown are the data for abyssal peridotites (Johnson *et al.*, 1990), forearc peridotites (Parkinson *et al.*, 1992; no La data are available for these samples) and fractional melting trajectories calculated using the parameters described above.

These graphs provide further evidence that simple fractional melting depletes the incompatible elements in residues too rapidly to explain the distribution of the LREE, Sr, Zr and Nb in the Troodos samples. These graphs also show that as the degree of depletion increases (i.e. lower Yb values), the *background* harzburgites plot further from the predicted partial melting abundances. This agrees with the conclusions reached in numerous other geochemical studies, that the most depleted peridotites are usually those which have the most enriched incompatible element chemistries (e.g. Keleman *et al*, 1992 and references therein). Furthermore, for many of the elements plotted in Figure 4.32 the Troodos *background* harzburgite samples have a similar distribution to the forearc peridotites and the serpentinite diapir samples have abundances similar to those in the abyssal peridotites.

This distribution matches that described above for the major element compositions of the Troodos minerals. These facts suggest that the serpentinite diapir samples might have had a similar source and melting/reaction history as abyssal peridotites, and the *background* harzburgites a similar melting/reaction history as forearc peridotites.

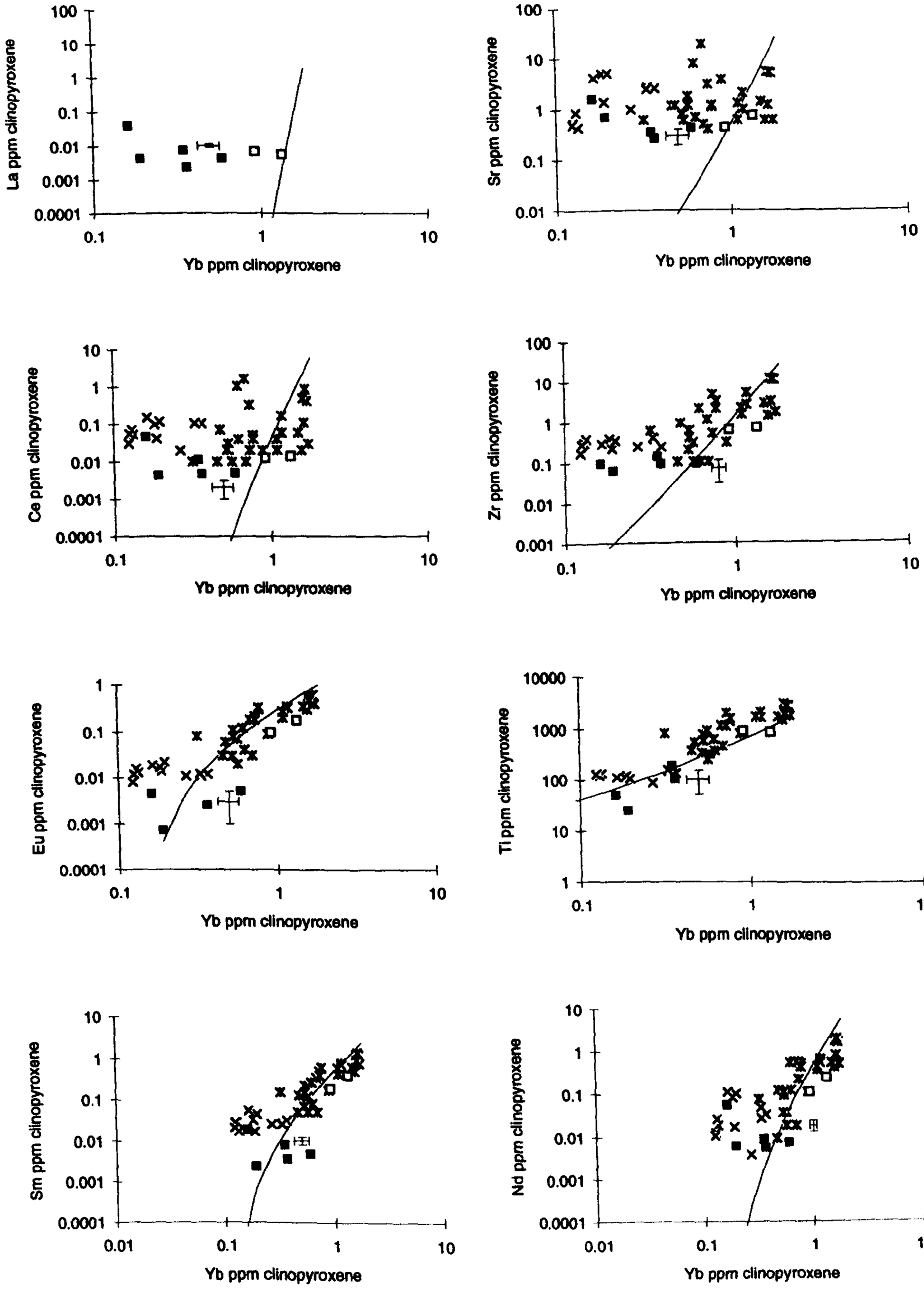

Figure 4.32 Plots illustrating the variation of selected trace elements with Yb in clinopyroxene and modelled fractional melting lines. Also shown for comparison are data from abyssal (Johnson *et al.*, 1990) and forearc peridotites (Parkinson *et al.*, 1992)

On the element-Yb graphs, enrichments are indicated by the sample plotting at higher incompatible element (i.e. those elements plotted on the y-axes) abundances than predicted by the melting trend defined by the abyssal peridotites and the model fractional melting trajectories. The plots show that clinopyroxenes from *background* harzburgites are enriched in La, Sr, and Ce in all the samples analysed, and also in Zr, Sm and Nd in some samples. Notably, the samples which are enriched in Zr, Sm and Nd are also those with the lowest Yb concentrations. The relative amounts by which each of these elements has been enriched can be estimated qualitatively from the displacement of a sample from the fractional melting trajectory. The forearc peridotites are also displaced from the melting trends for these elements, and are displaced further from the fractional melting line than the Troodos harzburgites. This suggests that the Troodos harzburgites might have under gone enrichment processes similar to those experienced by the modern forearc peridotites, and that the degree of interaction in the Troodos subduction zone was less than that in the present day Izu-Bonin arc.

Notably, the Ti-Yb graph on Figure 4.32 shows that the Troodos samples lie on the partial melting trend, despite the fact that the clinopyroxenes show positive Ti anomalies on the extended REE plots (Figure 4.24). Moreover, the Ti_{spn} cross-sections (Section 4.5) suggest that Ti has been added to the mantle sequence during mantle-melt interaction. As Suhr and Robinson (1994) pointed out, the mineral-mineral distribution coefficients for Ti change as partial melting progresses, with Ti residing in pyroxenes in fertile peridotites but partitioning more into spinel as $Cr\#_{spn}$ increases. This might explain why the Troodos spinels show evidence for Ti enrichment, yet clinopyroxene compositions lie on the partial melting trend. The apparent Ti anomalies on the extended REE plots might be a reflection of the fact that the plotting order of the elements is based on experimental derived $D^{cpx/melt}$ values, which have been determined on comparatively fertile compositions. Parkinson *et al.* (1992) and Suhr and Robinson (1994) have also shown that $D^{mineral/mineral}$ change as melting progresses and it may be that $D^{cpx/melt}$ also varies with the degree of depletion. If this is the case, the Ti anomalies on the extended REE plots could be false and a result of the wrong element ordering being used on these plots.

The element-Yb variation diagrams also place constraints on the relative timing of the partial melting and enrichment events. As the graphs show, the enriched elements plot at a wide range of Yb values, which are themselves modelled by 20 to 30% fractional melting. Because fractional melting efficiently depletes the source in the LREE, the enrichment event cannot have taken place before the melting event. The timing of the enrichment is therefore constrained to being at the very end of, or after, the partial

melting event. Furthermore, the fact that the Troodos samples plot on an extension of the abyssal peridotite melting array for more compatible trace elements (Ti, Y and the HREE) implies that prior to melting and enrichment events the Troodos mantle was similar in composition to a MORB mantle source.

4.10.2.3 COMPOSITION OF THE ENRICHING COMPONENT

As the graphs described above show, the chemistry of the Troodos clinopyroxene can be explained by a melting event followed by selective re-enrichment of certain elements. This agrees with the conclusions drawn from the mineral major element data in the first part of this chapter. Major element mineral compositions of samples which had interacted with melts were found to lie on straight line mixing trends between depleted melting residues and the composition of the reacting melt. As discussed above, straight line trends do not describe the distribution of all the trace element data in the Troodos clinopyroxenes (e.g. Figure 4.32). However, the distribution of the most incompatible elements on the element-Yb plots (Figure 4.33) can be described in terms of two straight line vectors, one equivalent to a partial melting trend (labelled PM on Figure 4.33) and one equivalent to a melt reaction trend (labelled IT on Figure 4.33).

In the examples illustrated in Figure 4.33, the interaction trend (IT) has been shown as a simple vector. However, two possible end-members can be envisaged for the interaction process. These two possible models are illustrated in Figure 4.34. In one case (Figure 4.34a) the residual component has a variable composition and the interacting melt a fixed composition. Alternatively, the residue could have a fixed composition and the melt component a variable composition (Figure 4.34b). A realistic scenario would probably be a combination of both end-members because, as the electron probe data show, the residual compositions vary with depth in the sequence and, as the differing mineral compositions of the *Anomaly 1* and *2* harzburgites suggests, possibly more than one melt was percolating through the sequence.

The composition of the enriching component can be calculated by mass balance (Ayers, 1993) if the pre-enrichment composition of the sample is known. Because there are no Troodos samples which unequivocally represent simple melting residues, the pre-enriched element concentrations have been obtained by matching the Yb value of the sample (which is assumed to be determined solely by melting) with calculated Yb values for fractional melting. The pre-enrichment composition for the other elements is then taken as their fractional melting modelled concentrations at that Yb value. Details of the equation used are given in Appendix C and the modelled enriching components (for the

assumption that it forms 1% of the final peridotite) for the *background* harzburgites are illustrated in Figure 4.35.

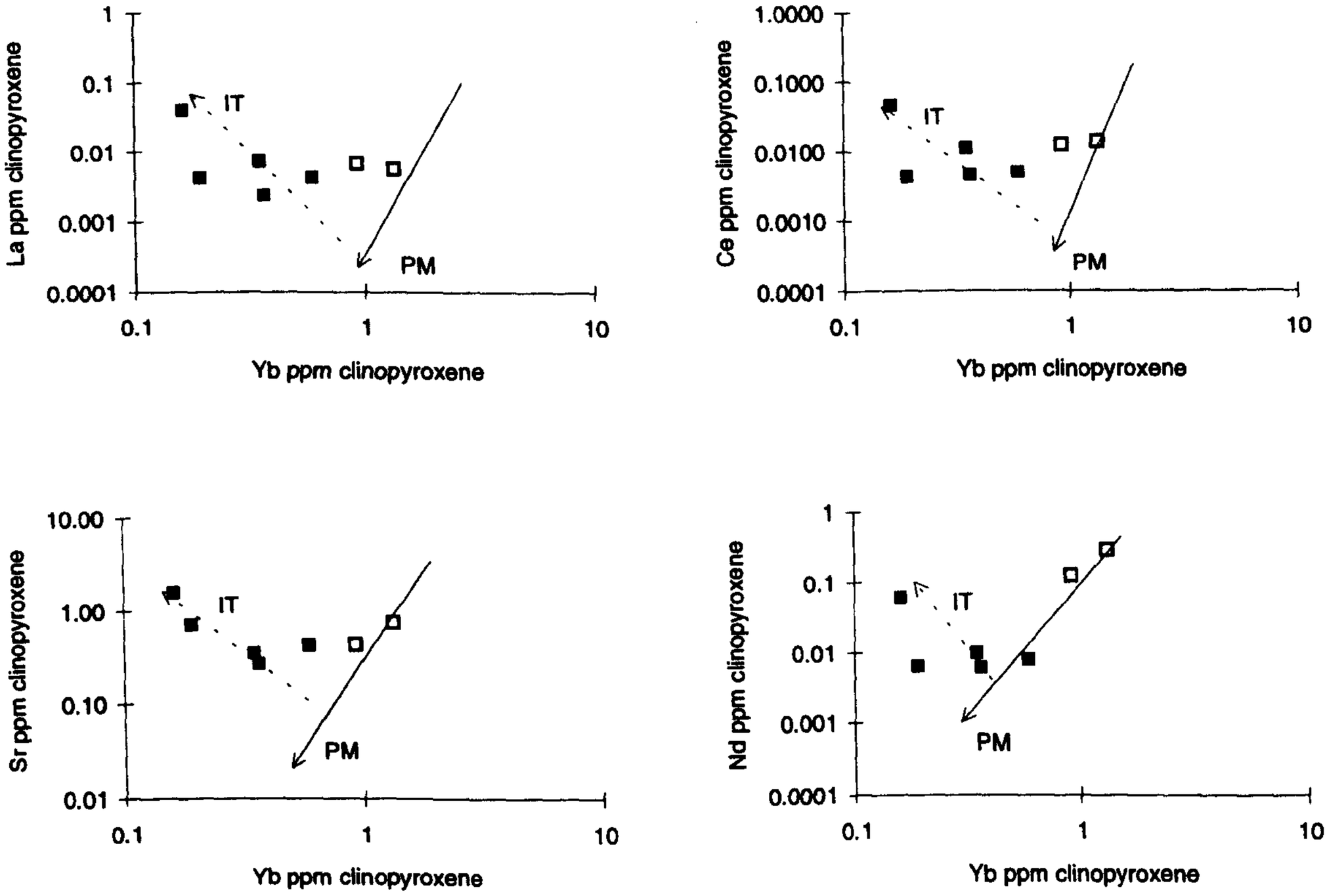

Figure 4.33 Graphs illustrating the variation of La, Ce, Sr and Nd with Yb; partial melting vectors are simplified from Figure 4.32 to simple straight line vectors marked PM and possible interaction vectors (dashed lines marked IT) describe the variation in the *background* harzburgites.

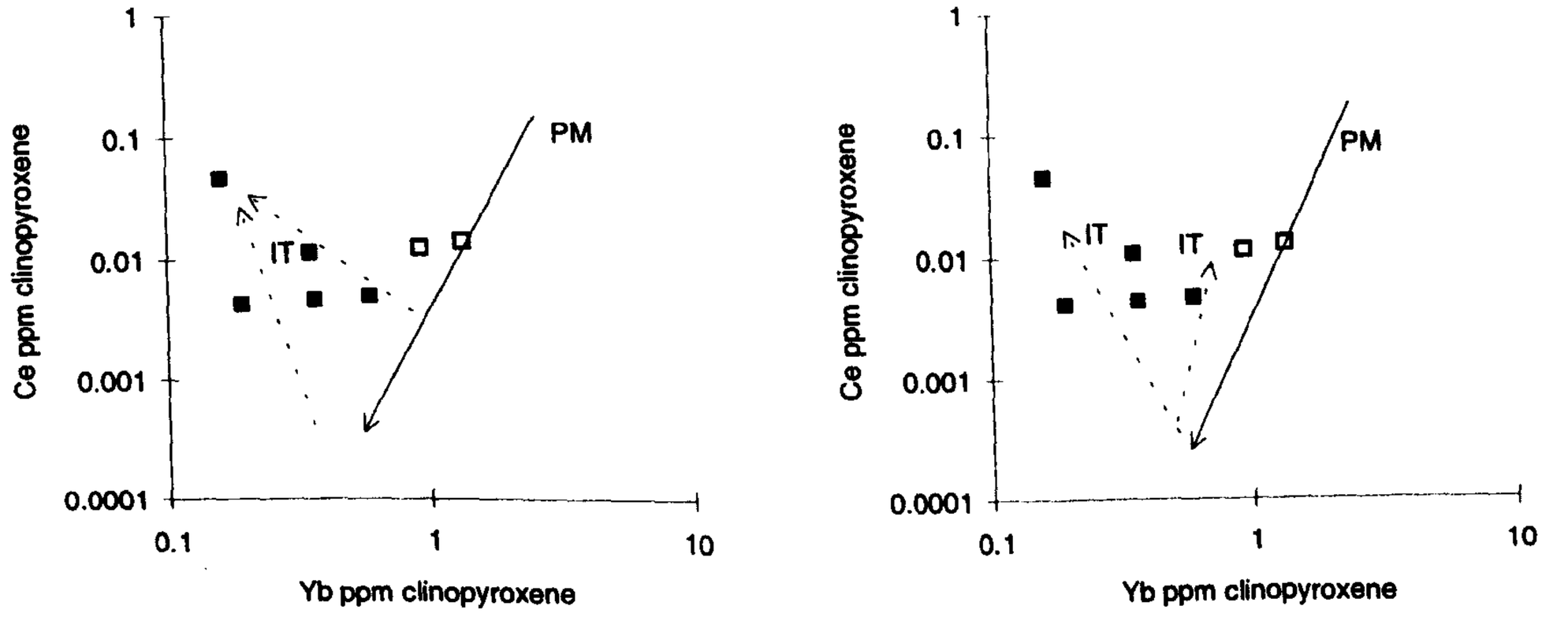

Figure 4.34 Plots illustrating possible end-members of the interaction process; a) fixed melt composition and variable harzburgite composition; b) fixed harzburgite composition and variable melt composition.

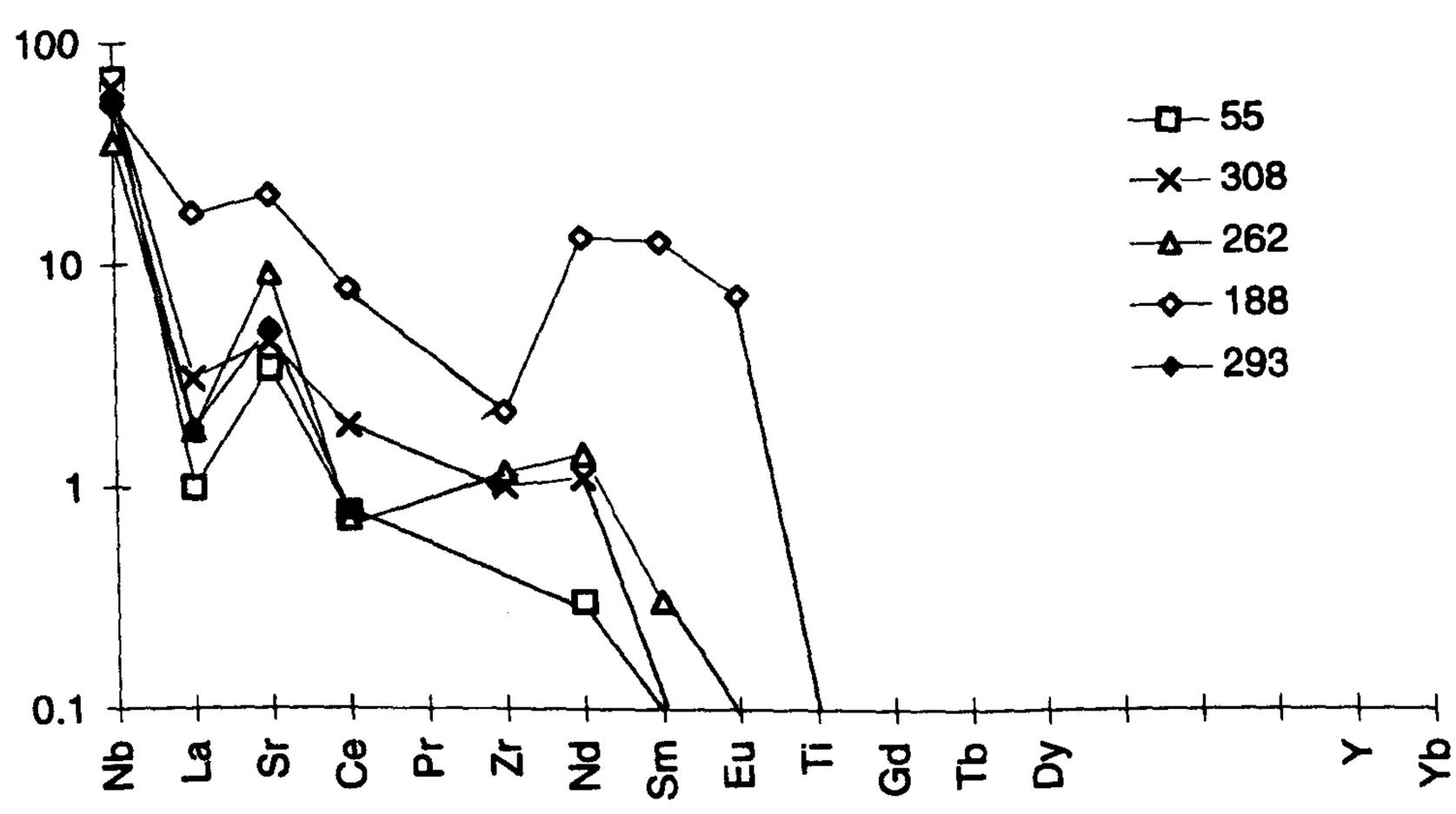

Figure 4.35 Extended chondrite -normalised trace element plot illustrating the composition of the enriching component calculated from the clinopyroxene trace element data.

As would be expected from the extended REE plots, the modelled enriching component is Nb, Sr, Zr and LREE-rich. Notably, the modelled component has negligible Ti which confirms the evidence from the Ti-Yb plot that Ti has not been added to the *background* harzburgite clinopyroxene, and supports the hypothesis that the Ti anomalies on the extended REE plots are false.

In general terms, two types of enriching component have been proposed to explain enriched trace element abundances in mantle peridotites: aqueous fluids or melts. Eggler (1987) and You *et al.* (1996) have described possible compositions of enriching fluids. Theoretical and experimental constraints suggest that fluids would be capable of transporting the LREE and the LIL elements, but that Zr would be immobile. Therefore, because Zr is enriched in the Troodos clinopyroxene it is likely that the enriching component must have contained a melt.

4.10.3 TRACE ELEMENT COMPOSITION OF TROODOS PYROXENITES

REE patterns and extended REE plots for various pyroxenite bodies are presented in Figures 4.36.

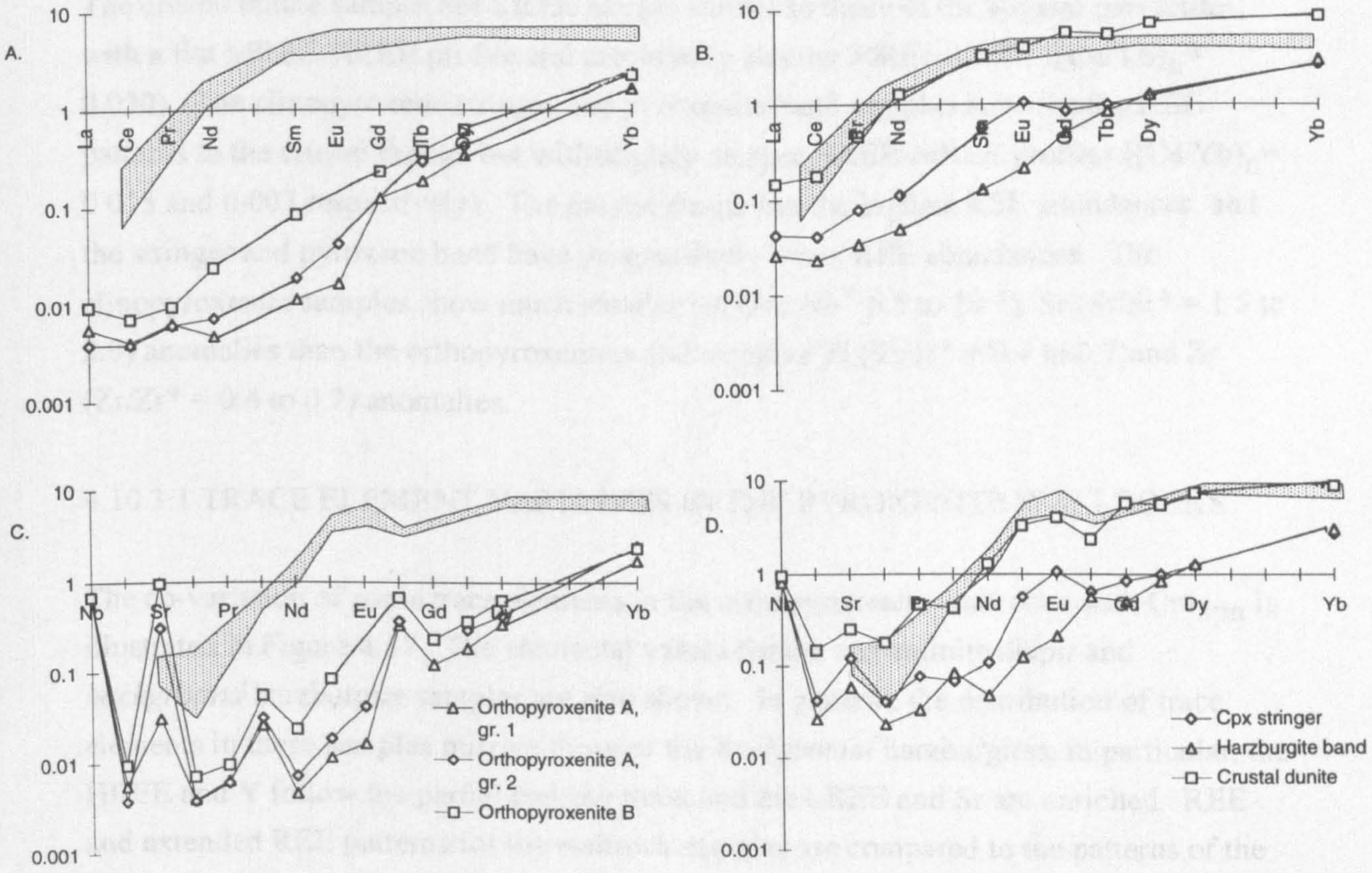

Figure 4.36 REE and extended REE plots illustrating the compositions of orthopyroxenite bodies (plots a and c) and clinopyroxenites (plots b and d) in the Troodos sequence. Figures 4.36 a and c illustrate the patterns for *orthopyroxenites A* and *B* (both of which plot on the Type II trend defined in section 4.8), and Figures 4.36 b and d illustrate the patterns for interstitial clinopyroxene in a crustal dunite, a clinopyroxenite stringer and a harzburgite pyroxene band. Shaded area illustrates the variation in abyssal peridotites (data from Johnson *et al.*, 1990)

Both orthopyroxenites have similar, uniformly-sloping REE patterns ($(Ce/Yb)_n$= 0.002 to 0.003) with minor La inflections. Two grains were analysed from the *orthopyroxenite A* sample and, like the serpentinite diapir sample, they show similar patterns which again

suggests that equilibrium is reached on a thin-section scale. The high field strength and transition element contents of the orthopyroxenites is higher than the *background* harzburgites but lower than the serpentinite diapir samples. The extended patterns show that the orthopyroxenites have large positive Nb (Nb/Nb^* = 71 to 177) and Sr (Sr/Sr^* = 6.4 to 114.4) anomalies, and smaller positive Ti (Ti/Ti^* = 4.7 to 17.4) and Zr (Zr/Zr^* = 3.4 to 4.7) anomalies.

The crustal dunite sample has a REE pattern similar to those of the abyssal peridotites, with a flat MREE-HREE profile and moderately sloping MREE-LREE ($(Ce/Yb)_n$= 0.020). The clinopyroxene stringer and pyroxenite band samples have similar REE patterns to the crustal dunite, but with slightly steeper HREE-MREE profiles ($(Ce/Yb)_n$= 0.015 and 0.003 respectively). The crustal dunite has the highest REE abundances, and the stringer and pyroxene band have progressively lower REE abundances. The clinopyroxenite samples show much smaller Nb (Nb/Nb^* 6.5 to 19.5), Sr (Sr/Sr^* = 1.5 to 2.9) anomalies than the orthopyroxenites and negative Ti (Ti/Ti^* = 0.4 to 0.7)and Zr (Zr/Zr^* = 0.4 to 0.7) anomalies.

4.10.3.1 TRACE ELEMENT VARIATION IN THE PYROXENITE WALLROCKS

The co-variation of some trace elements in the orthopyroxenite wallrocks with $Cr\#_{spn}$ is illustrated in Figure 4.37. The elemental values for the serpentinite diapir and *background* harzburgite samples are also shown. In general, the distribution of trace elements in these samples mirrors those of the *background* harzburgites; in particular, the HREE and Y follow the partial melting trend and the LREE and Sr are enriched. REE and extended REE patterns for the wallrock samples are compared to the patterns of the adjacent orthopyroxenite in Figure 4.38. Both orthopyroxenites illustrated lie on the Type II pyroxenite trend, defined by a trend of Al-Mg enrichment in spinel, as described earlier.

The *orthopyroxenite A* wallrock harzburgites have REE patterns which are parallel and at similar abundances to those in the adjacent orthopyroxenite. *Orthopyroxenite B* wallrocks also have REE patterns which are sub-parallel to the adjacent orthopyroxenite, but with more variable REE abundances. The extended plots show that both wallrock types have large positive Nb (Nb/Nb^* = 5.9 to 185.0), Sr (Sr/Sr^* = 1.1 to 8.2), Ti (Ti/Ti^* = 3.6 to 7.5)and Zr (Zr/Zr^* = 0.6 to 6.4) anomalies which are, in general, smaller than those in the adjacent orthopyroxenites.

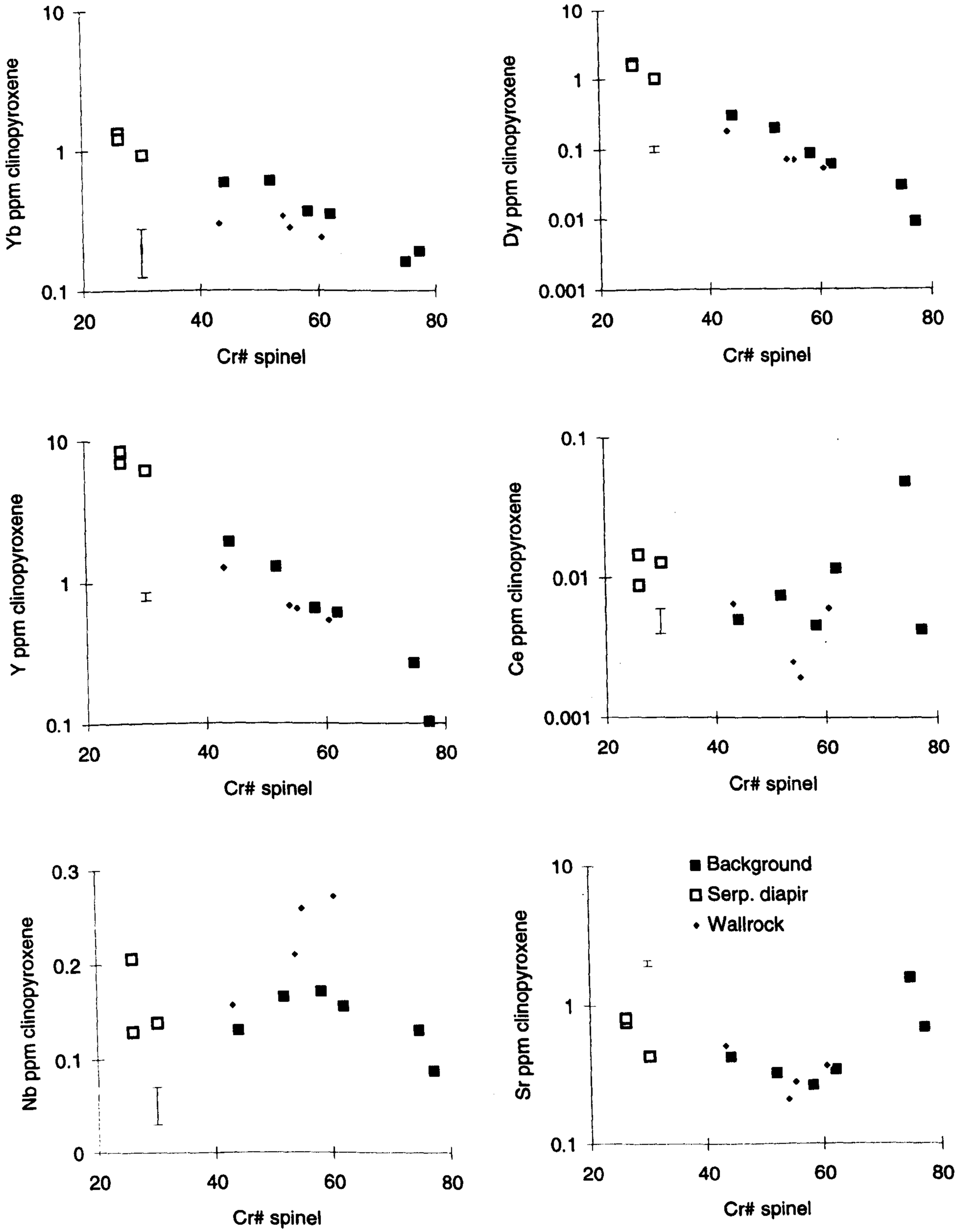

Figure 4.37 graphs illustrating the variation of selected trace elements in clinopyroxene with $Cr\#_{spn}$ for the pyroxenite wallrocks. Also illustrated for comparison are the data from the *background* harzburgites and serpentinite diapir samples.

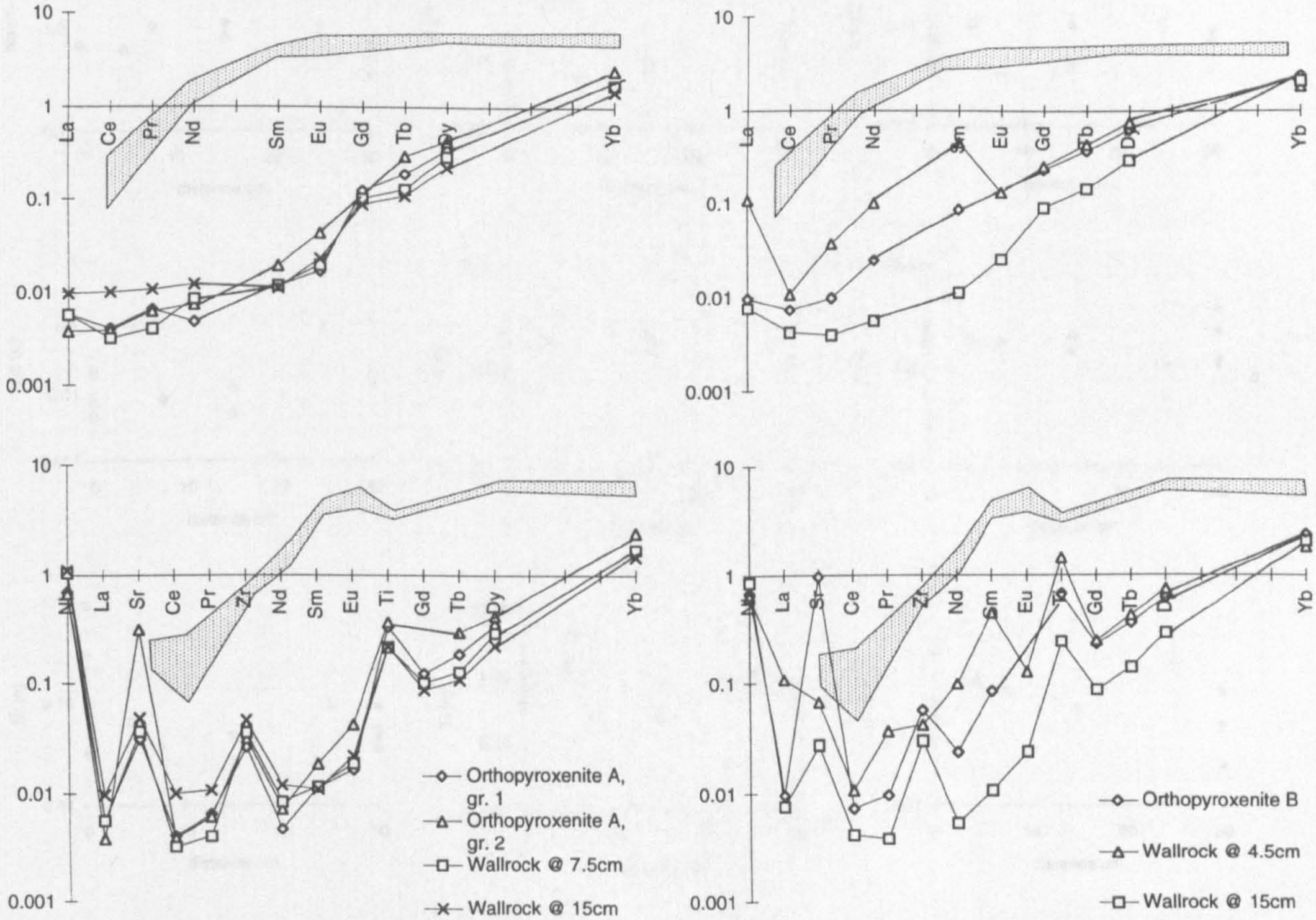

Figure 4.38 REE and extended REE plots illustrating the variation in: a) *orthopyroxenite A* intrusions and their wallrocks, b) *orthopyroxenite B* intrusions and their wallrocks. Shaded area illustrates the variation in abyssal peridotites (data from Johnson *et al.*, 1990)

The variation in trace element abundances with distance from the orthopyroxenites is illustrated in Figure 4.39, along with the variation displayed in the *background* harzburgites and electron-probe data from spinels. The wallrocks sampled nearest to the orthopyroxenites were always sampled at the dunite-harzburgite contact. The elemental variation in the wallrocks is in all cases smaller than that displayed by the *background* harzburgites. The HREE and Y show the least variation as the contact with the pyroxenite is approached, whereas the LREE generally show the largest wallrock variations. The variations in the elemental abundances in the wallrocks are summarised in Table 4.10.

	Orthopyroxenite A wallrock	Ortho-pyroxenite A	Orthopyroxenite B wallrock	Ortho-pyroxenite B
LREE	no change	> adj. wallrock	incs towards opxB	< adj. wallrock
HREE	no change	= to wallrock	no change	= to wallrock
Nb (n)	no change	< adj. wallrock	no change	= to wallrock
Ti (n)	no change	> adj. wallrock	incs towards opxB	< adj. wallrock
Zr (n)	no change	< adj. wallrock	no change	> adj. wallrock
(Ce/Yb)n	decs towards opxA	> adj. wallrock	incs towards opxB	< adj. wallrock
Zr/Y	no change	< adj. wallrock	no change	= adj. wallrock
Sr/Sr*	incs towards opxA	> adj. wallrock	decs towards opxB	> adj. wallrock
Ti/Ti*	no change	> adj. wallrock	no change	= adj. wallrock
Zr/Zr*	no change	= adj. wallrock	decs towards opxB	> adj. wallrock
Cr# spn	decs towards opxA	= adj. wallrock	decs towards opxB	> adj. wallrock
Ti spn	no change	= adj. wallrock	incs towards opxB	< adj. wallrock

Table 4.10 Summary of elemental variations in clinopyroxene in orthopyroxenite A and B bodies and surrounding wallrocks; incs = increases, decs = decreases, adj. = adjacent.

As discussed in Section 4.8.1, the electron probe data show that the pyroxenite wallrocks are displaced away from the main *background* harzburgite trend along the same vectors as the adjacent orthopyroxenite. The traverses presented in Figure 4.40 also show that $Cr\#_{spn}$ decreases towards the pyroxenites. The trace element data show that gradients exist in some of the incompatible element contents of the wallrocks. In general, incompatible elements in the *orthopyroxenite A* wallrocks do not show a significant variation compared to the analytical precision. Whereas, in the *orthopyroxenite B* wallrocks incompatible elements increase towards the pyroxenite. Furthermore, most elements and elemental ratios in the *orthopyroxenite B* bodies plot on an extension of the wallrock trend. Whereas, the *orthopyroxenite A* bodies show a sharp decrease from the adjacent wallrock trend.

4.10.3.2 IMPLICATIONS FOR THE ORIGIN OF PYROXENITES

The field evidence shows that both *orthopyroxenite A* and *B* bodies are associated with a marginal dunite facies which is in sharp contact with the enclosing harzburgite. The electron probe data define two trends, one of Cr-Fe-Ti enrichment in spinels (Type I trend) and one of Al-Mg enrichment in spinels (Type II trend). Orthopyroxenites of both trends have marginal dunites. The clinopyroxene trace element data suggest that there are

local-scale gradients in the incompatible elements in the wallrock harzburgites, although the variations are less than the total variation in the *background* harzburgites.

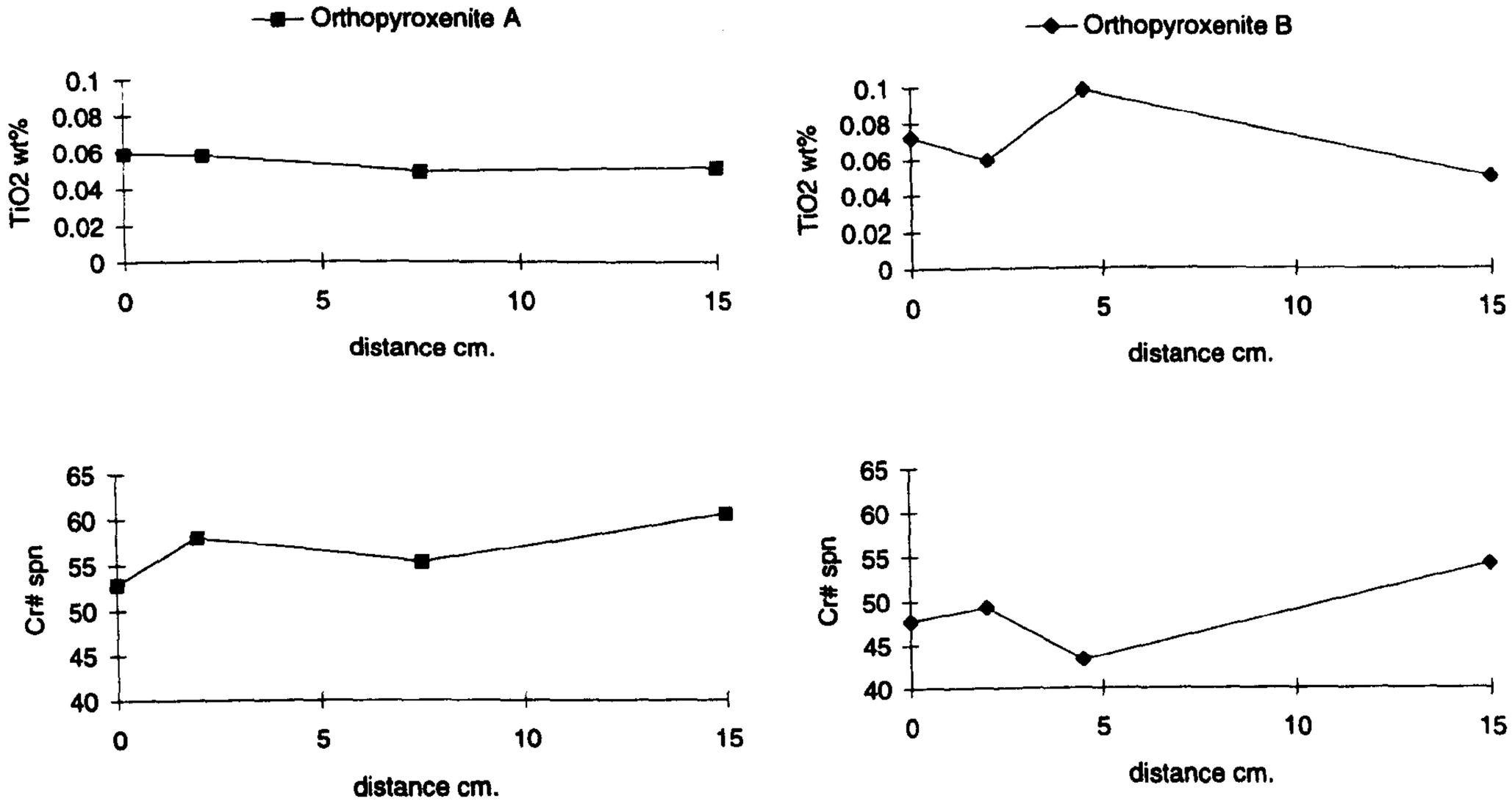

Figure 4.40 Graphs illustrating the variation in spinel chemistries in traverses away from *orthopyroxenite A* and *B* bodies.

Two end-member processes have been proposed to explain the formation of symmetrical pyroxenite-dunite bodies in other ophiolites. Keleman *et al.* (1992), through a study of the Trinity Ophiolite, suggested that the complexes represent zones of melt intrusion and reaction with the enclosing peridotites. In contrast, Takahashi (1992) studying the Horoman peridotite, has suggested the pyroxenite-dunite bodies mark zones of melt removal from the surrounding peridotites. In both cases, the outcrop patterns consist of concentric zones of plagioclase lherzolite, lherzolite and harzburgite around a central dunite, which may or may not be associated with a wehrlite, pyroxenite or gabbro-norite. These zones were developed on a sub-metre scale in single exposures and were also inferred to explain the distribution of lithological units on a map scale. Unfortunately, each theory is based on a slightly different data set, which makes them difficult to compare both with each other and the Troodos data. In general, the Horoman data shows an increase in compatible elements towards the central dunite, with a sudden change towards cumulate chemistries (high Ti_{spn}, low Fo_{ol} and $Cr\#_{spn}$) in the dunite. The Trinity data are based on clinopyroxene compositions which show an increase in the LREE/HREE ratio towards the central dunite. Table 4.11 summaries the main points of

the Keleman (1992) and Takahashi (1992) models; the direction of increase or decrease in the parameters is always considered towards the central dunite-pyroxenite.

	Horoman	Trinity	Troodos
Cpx modal %	gradual decrease	gradual decrease	little change
Fo olivine	increases with sudden decrease at harz-dunite contact	Monotonous inc or dec with no sudden change at contact	not analysed
Cr# spinel	increases with sudden decrease at harz-dunite contact	Monotonous inc or dec with no sudden change at contact	decreases with sudden inc at contact (see below)
HREE + major elements	little change	-	little change
Ti spinel in dunite	higher than wallrock	-	lower than wallrock in opxB, little change in opxA
compatible elements	increase	-	decrease

Table 4.11 Summary of mineral composition variations in the Trinity (Keleman *et al.*, 1992), Horoman (Takahashi, 1992) and Troodos (this study) ophiolites.

Both theories account for the sharp dunite-harzburgite contact. In the Keleman *et al.* (1992) model, it is explained by phase saturation in the mantle-melt system switching off orthopyroxene crystallisation. Takahashi (1992) suggests that high melt migration velocities towards the centre of the body prevent a gradational contact from developing.

The fact that the incompatible elements in the *orthopyroxenite A* wallrocks show little or no variation towards the pyroxenite, whereas incompatible elements increase in the *orthopyroxenite B* wallrocks towards the pyroxenite, suggests that the two types of pyroxenite have different modes of formation. A decrease in incompatible element contents is consistent with an increase in the degree of melting, and an increase in incompatible elements of the wallrocks would be consistent with increasing interaction with a LREE-enriched melt. However, the lack of variation in the HREE suggests that any variations in the degree of melting must have been small. As the partial melt modelling illustrates (see Section 4.10.2.1), only small variations in the amount of fractional melting are required to produce large variations in the LREE abundances. Furthermore, most elements and elemental ratios in the *orthopyroxenite B* bodies plot on

an extension of the wallrock trend. In contrast, the *orthopyroxenite A* bodies show a sharp decrease from the adjacent wallrock concentrations. This suggests that equilibrium was reached in the *orthopyroxenite B* wallrock but not the *orthopyroxenite A* wallrock.

However, the fact that the $Cr\#_{spn}$ data shows that the spinels in the wallrocks become more aluminous towards the contact with the pyroxenite is inconsistent with a simple model of increased melting producing the incompatible element variations. As pointed out by Varfalvy *et al.* (1996), harzburgites surrounding pyroxenites in the Bay of Islands Ophiolite experienced a complex series of mineral dissolution and crystallisation processes. The wide variation in mineral chemistry displayed by the Troodos pyroxenite wallrocks suggests that similar processes might have operated in the Troodos mantle section. The formation of the orthopyroxenites is discussed in more detail in the Conclusions Chapter after the major element data have been presented.

4.11 SUMMARY

Previous chapters in this thesis have presented field data and microstructural evidence for the evolution of the Troodos mantle sequence. In the Field Relations Chapter the variety of minor intrusions in the mantle sequence and their preferential location towards the top of the sequence was noted. In the Microstructure Chapter more detailed evidence for modal and textural variations in the *background* harzburgites was presented. In particular, an increase in the modal abundance and textural variety of clinopyroxene in the background harzburgites with increasing depth in the mantle sequence was described. Furthermore, distinctive clinopyroxene and spinel textures were noted in the *Anomaly 1* and *2* harzburgites. Clinopyroxene crystals often display growth twins and poikilitic habits in these harzburgites, suggesting that they crystallised from a melt, and spinel has both euhedral and intergrown morphologies which were also interpreted as reflecting the presence of melt. Spinel was also found to be a useful petrographic indicator in dunites. In the interdigitating dunites spinel morphologies are similar to those in the adjacent harzburgites suggesting that they are xenocrysts and the dunite formed by melt-harzburgite interaction. In the other dunite types fine-grained euhedral spinel is common suggesting that crystallisation from a melt was an important process in their formation. Pyroxenite textures include consertal contacts, poikilitic habits and growth twins in clinopyroxene, again indicting that a melt phase was present during their formation.

This chapter has described the major and trace element chemistry of the Troodos and Limassol Forest peridotites. The variations in mineral chemistry can be ascribed to two main processes: partial melting and interaction between melts/fluids and peridotites.

Partial melting depletes the peridotites in the magmaphile elements and the percentage of partial melting decreases with depth in the sequence. This trend of decreasing degrees of partial melting with depth is consistent with the increase in modal proportion of clinopyroxene with depth in the mantle sequence noted in Chapter 3. The amount of partial melting can be estimated by comparing the mineral compositions with the products of experimental melting studies or calculated melting trends. The experimental results suggest that the serpentinite diapir peridotites result from 10 to 20% melting and the Troodos harzburgites from 20 to 30% melting. Numerical modelling of the data shows that the HREE variations in clinopyroxene from the *background* harzburgites can be best explained by a fractional melting process. From a fertile MORB mantle (FMM) starting composition the serpentinite diapir samples are modelled by 5 to 15% fractional melting and the *background* harzburgites by 20 to 30% fractional melting. The fact that on major and trace element variation diagrams the Troodos data plot on extensions of the abyssal peridotite trends towards more depleted compositions, suggests that the assumption of a FMM starting composition is valid.

Three lines of evidence suggest that interaction between melts or fluids and the mantle sequence has occurred: elemental enrichments in minerals from certain parts of the sequence (e.g. *Anomaly 1* and *2* harzburgites), the occurrence of pyroxenitic and dunitic bodies which have wallrock harzburgites whose chemistry varies according to the nature of the adjacent intrusive, and REE patterns in clinopyroxenes which are incompatible with an origin as simple fractional melting residues.

The *Anomaly 1* and *2* harzburgites are thought to be the products of melt addition to the mantle sequence. The two areas exhibit different enrichment trends on element variation diagrams which suggests that at least two different melt compositions were responsible. The pyroxenites can also be divided into two sub-types on the basis of element variations. Type I pyroxenites display trends of Cr-Fe-Ti enrichment in spinel and Type II pyroxenites display trends of Al-Mg enrichment in spinel. These trends parallel those in the *Anomaly 1* and *2* harzburgites, the Type I trend matches that of the *Anomaly 1* harzburgites and the Type II trend matches that of the *Anomaly 2* harzburgites. These facts suggest that the melt's which crystallised the pyroxenites were also responsible for the elemental enrichments in the harzburgites. The fact that the *Anomaly 1* and *2* harzburgites have distinctive mineral chemistries, interpreted here as a result of melt interaction, supports the evidence presented in the Microstuctures Chapter for the presence of melt crystallised clinopyroxene and spinel in these harzburgites.

The mineral chemistry variations in the pyroxenite wallrocks show that on a local scale, the formation of these bodies affected the chemistry of the surrounding harzburgites. The fact that the orthopyroxenites are separated by a marginal dunitic facies from the enclosing harzburgites suggests that formation of the orthopyroxenites was a disequilibrium process. The fact that dunite was formed suggests that initially, the reaction involved consumption of the pyroxenes and crystallisation of olivine and spinel. The sharp contacts between the dunite and the enclosing harzburgite are consistent with crystallisation being controlled by phase saturation in the melt-mantle reaction system.

The trace element patterns measured in clinopyroxene from the harzburgites suggest that these mineral were enriched in Sr, Nb, and the LREE, and to a lesser extent Zr and Ti. The fact that these elements are incompatible during partial melting suggests that the enrichment event must have occurred at the end of, or after, the partial melting event. The clinopyroxene in pyroxenites is also enriched in these elements and to a greater degree than the clinopyroxene from *background* harzburgites. These intrusives might therefore, also be the origin of the wide-scale incompatible element enrichment of the *background* harzburgites.

CHAPTER 5
WHOLE-ROCK GEOCHEMISTRY

5.1 INTRODUCTION

This chapter describes the major and trace element whole-rock geochemistry of peridotites and pyroxenites from the Troodos Massif. In the first part of the chapter, the whole-rock data are used to establish whether serpentinisation has mobilised any elements. The elements thought to be least mobile during alteration are then used to further characterise the partial melting history and melt interaction events in the Troodos sequence.

The subdivisions of the *background* harzburgites established in Chapter 4 are retained in this chapter, with *Anomaly 1* and *top-of-the-sequence* samples described separately from the other *background* harzburgites. Unfortunately, only chip samples were taken from the *Anomaly 2* harzburgites, so no whole-rock data have been obtained for them.

5.1.1 PREVIOUS WORK

Despite the fact that the geochemistry of the lavas exposed in the Troodos Massif has been comprehensively studied (Pearce, 1975; Rautenschlein *et al.*, 1985; Cameron, 1985; Bendarz and Schmincke, 1994), there have been comparatively few analyses made of the peridotites. Menzies and Allen (1974) present several analyses of Troodos harzburgites. The samples were found to be refractory with high Mg# (90.6 to 91.1), CaO and Al_2O_3 both < 1%, total alkali contents of < 1000 ppm and extremely low Ti, S and P. These features were interpreted as a result of extensive partial melting and basalt extraction, leaving the harzburgites as a depleted residue. Only a single REE analysis for a Troodos harzburgite has been published (Kay and Senechal, 1976). The REE contents were found to be very low (0.05 to 0.08 chondrite), with a shallow dipping HREE to LREE profile and positive Eu anomaly. This pattern was also interpreted as characteristic of a mantle residue.

5.1.2 ANALYTICAL TECHNIQUES

Two analytical techniques were used to obtain whole-rock geochemical data from the peridotites: XRF and ICP-MS. Major elements were analysed by XRF on glass fusion discs. Trace elements were analysed by XRF on powder pellets for the elements Ni, Cr,

Co, V, Ti, and Sc and by ICP-MS for the elements Ga, Ba, Rb, Sr, Zr, Y, Nb, La, Ce, Nd and Yb. Details of the sample preparation procedures and the instrument configuration are given in Appendix A. To assist with the interpretation of the data in this chapter, the graphs are annotated with 2σ error bars and, where appropriate, the detection limit of the technique used is indicted by a dashed line labelled dl on the graph. For several parameters the analytical errors are smaller in size than the points on the graph. In these cases, the error bars have been omitted for clarity, and the error can be assumed to be less than the size of the points on the graph.

5.2 SERPENTINISATION AND WHOLE-ROCK GEOCHEMISTRY

As described in the previous chapter, the Troodos and Limassol Forest peridotites are serpentinised to varying degrees: between 10 and 60% in the *background* harzburgites, up to 80% in the serpentinite diapir and 90 to 100% in the Limassol Forest. Before the primary geochemical variations in the peridotites can be discussed, it is necessary to determine whether serpentinisation has affected the whole-rock geochemistry of the samples.

Three approaches are used to assess the effects of serpentinisation. Firstly, the data are examined for relationships between loss on ignition (LOI), as a measure of serpentinisation, and elemental abundances expressed on an anhydrous basis. Secondly, variably serpentinised samples collected around a heavily serpentinised harzburgite layer are compared, to see whether any elements are mobile within the serpentinised layer. These results are compared with bivariate plots of the Troodos harzburgite whole-rock data, to see if the inferred serpentinisation trends match any of the trends shown by the harzburgite data. Finally, these data are compared with the results of published experimental serpentinisation studies of peridotites and analyses of vein serpentines from the Troodos Massif.

The correlation of major and trace elements with LOI for the harzburgites analysed is illustrated in Figures 5.1 and 5.2. The basis for using LOI as an index of alteration is the work done on Turkish peridotites by Engin and Hirst (1970). This study demonstrated that the LOI of a sample is directly proportional to the modal serpentinite content and, therefore, that the LOI can be used as an alteration index. It should be noted however, that the LOI is only a measure of the amount of water absorbed by a sample and as an alteration index it fails to take into account the composition of the serpentinising fluid. The possible chemistry of the serpentinising fluid in the Troodos Massif is discussed in more detail below.

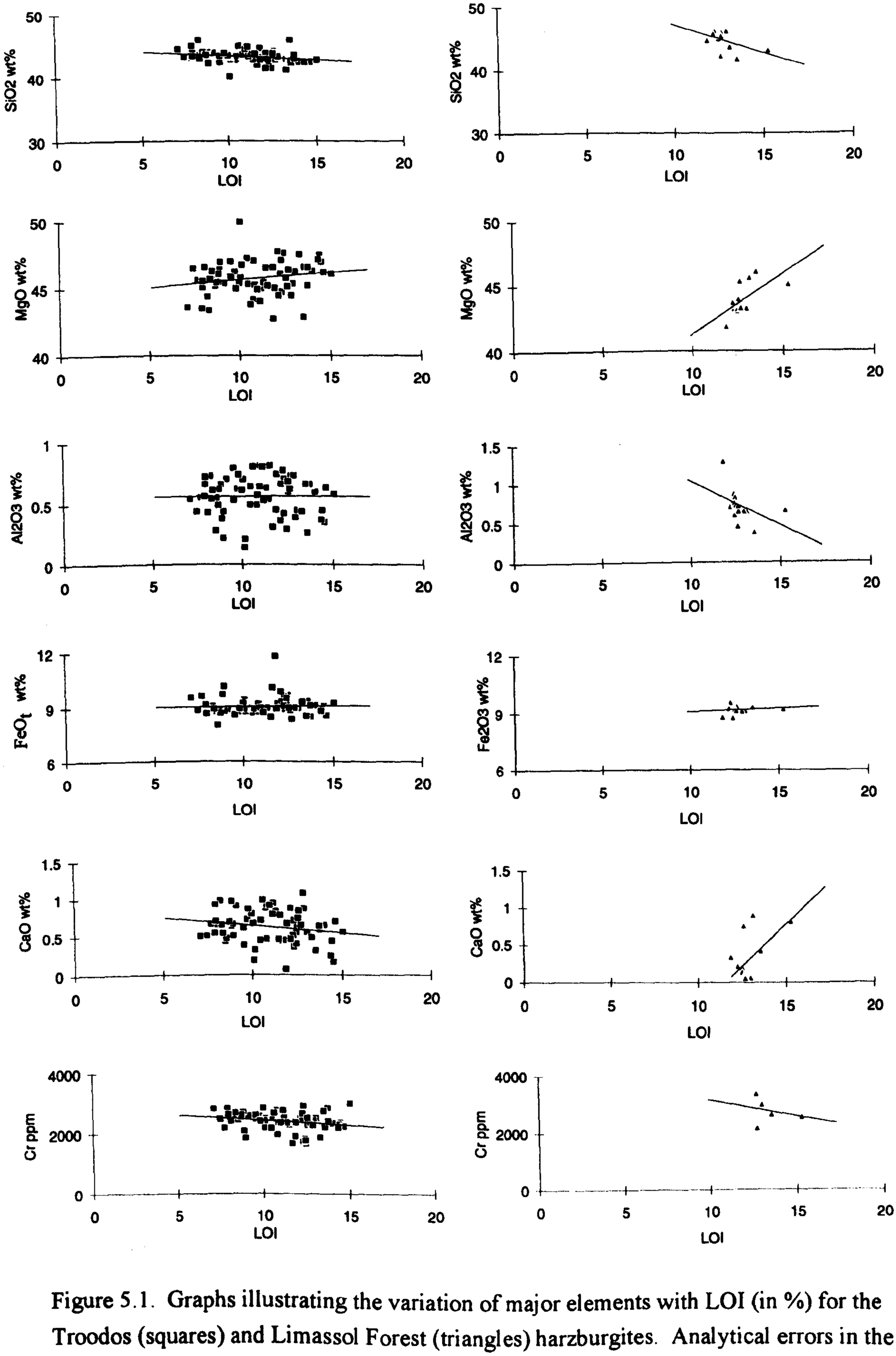

Figure 5.1. Graphs illustrating the variation of major elements with LOI (in %) for the Troodos (squares) and Limassol Forest (triangles) harzburgites. Analytical errors in the illustrated data are all smaller than the size of the points. This Figure continues overleaf.

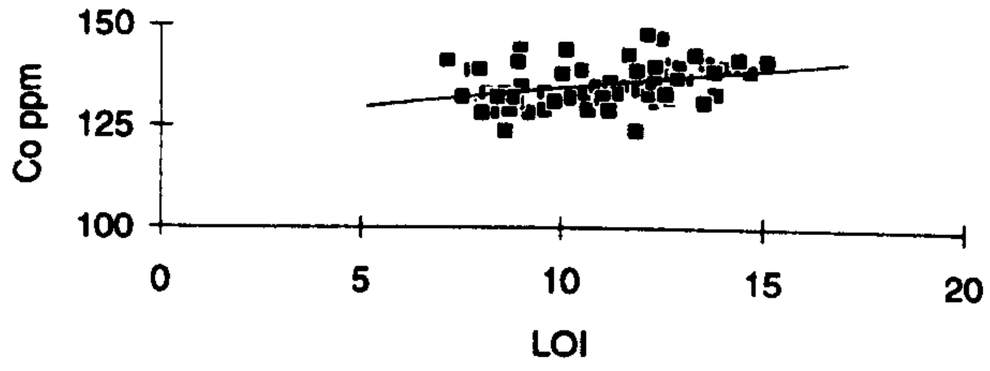

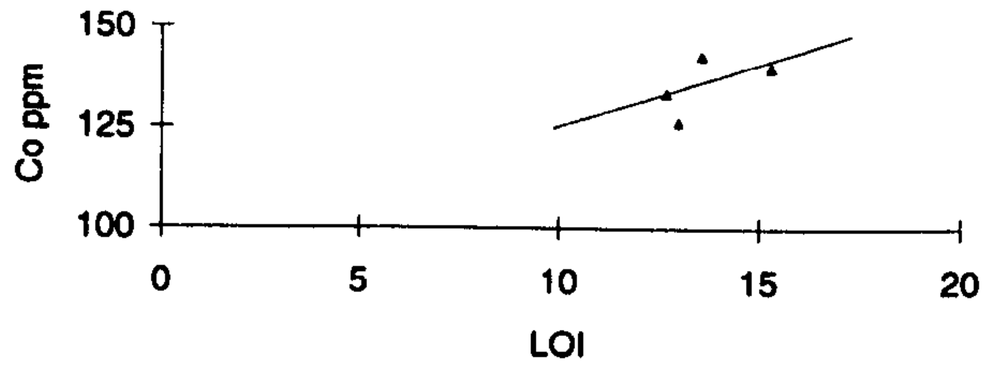

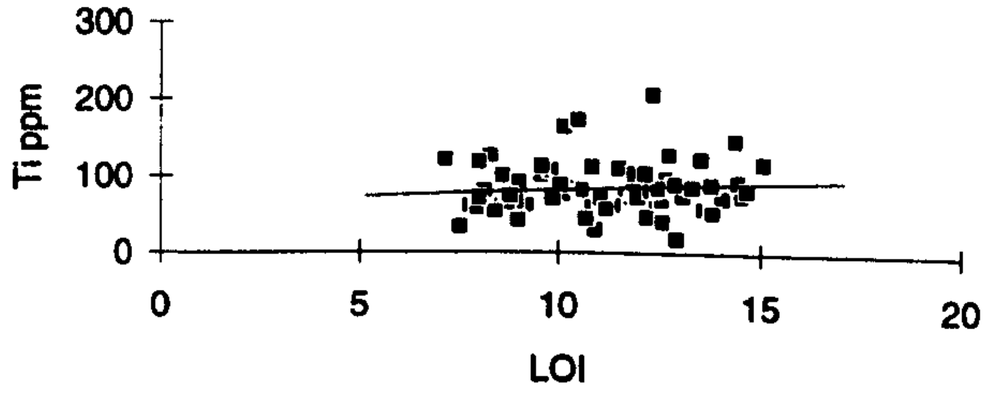

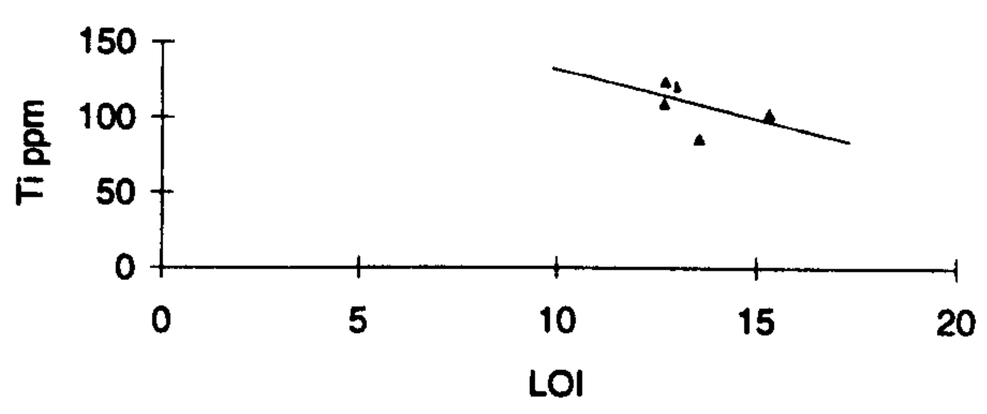

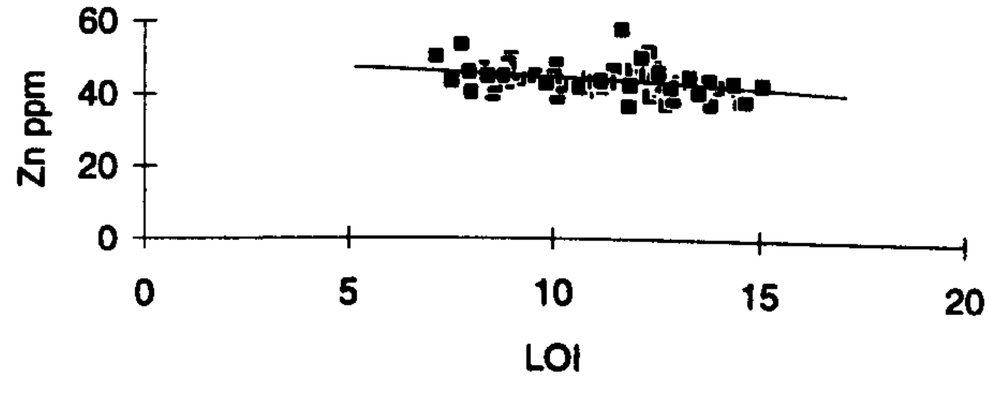

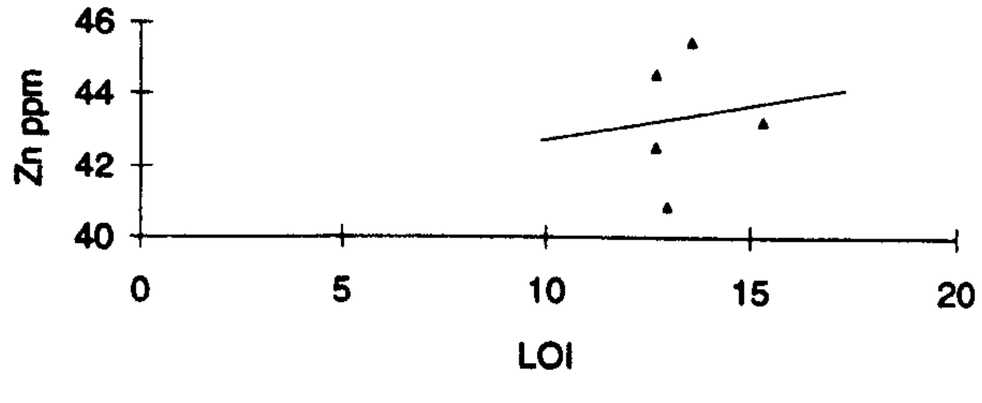

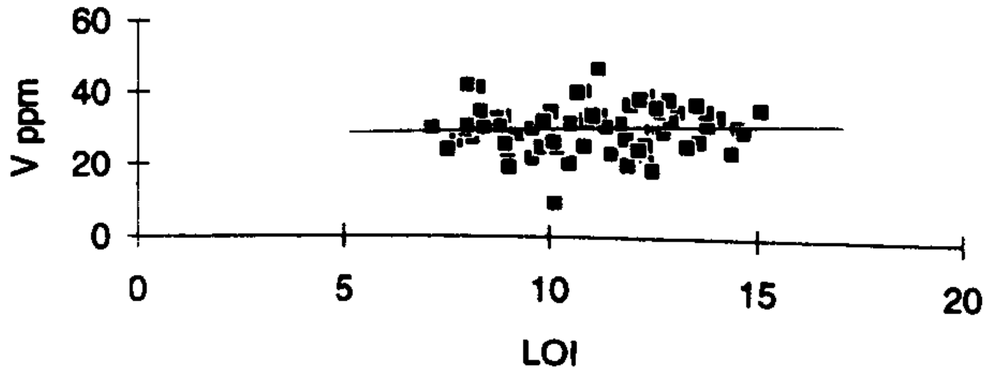

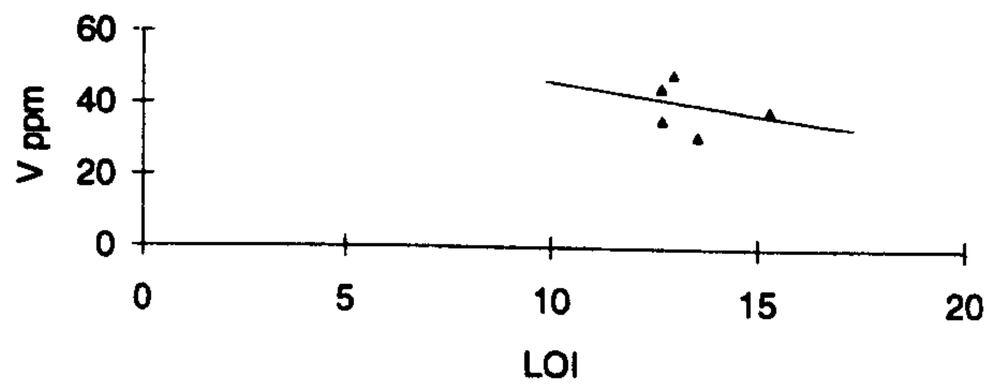

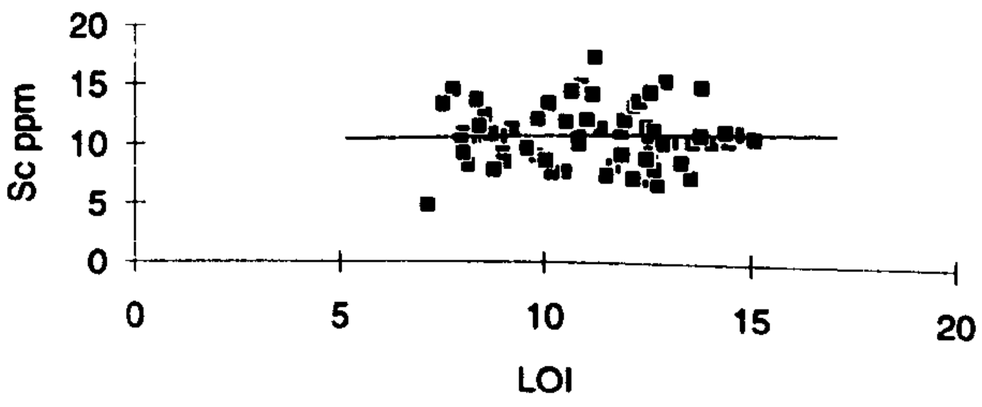

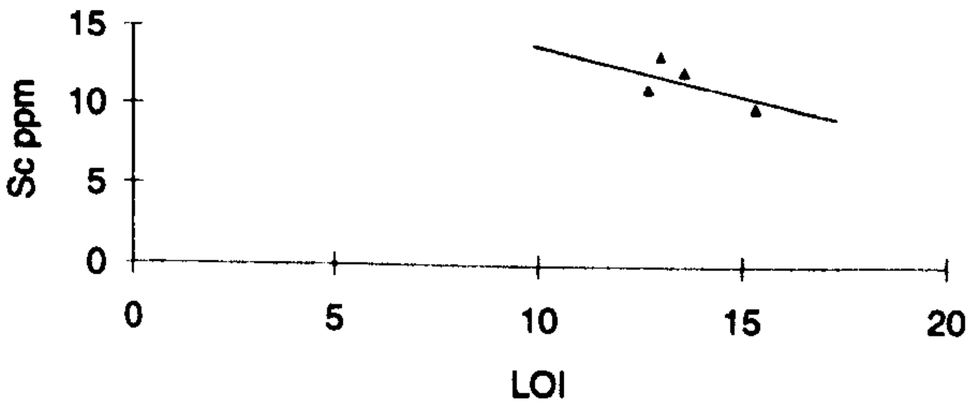

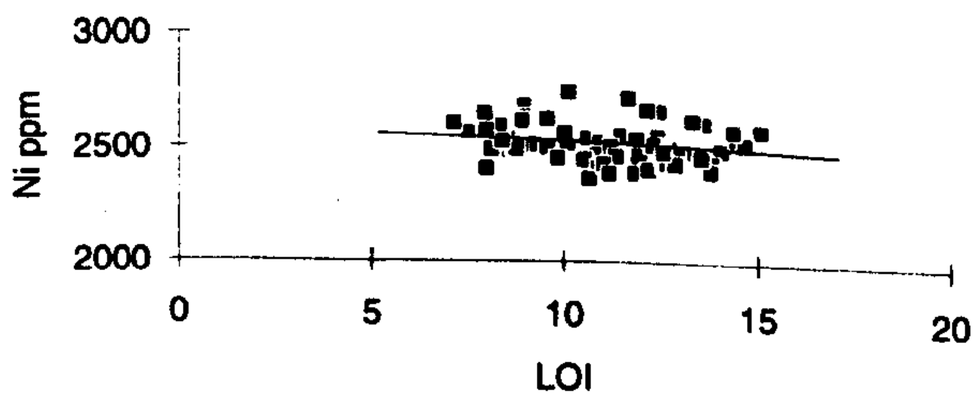

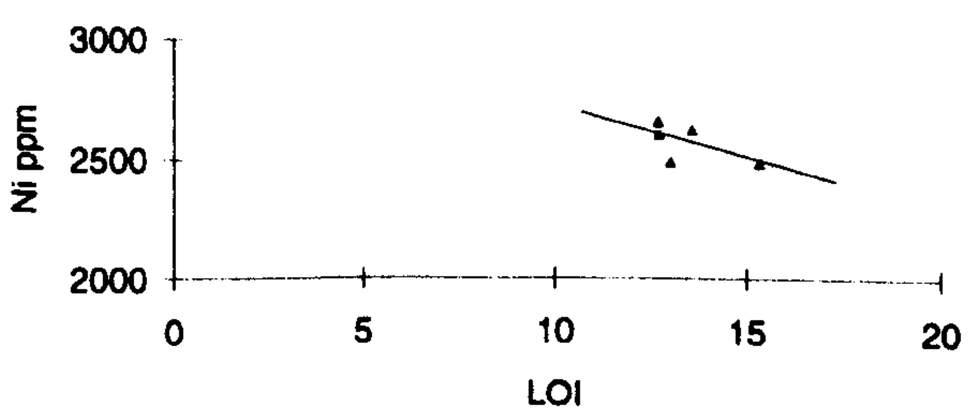

Figure 5.1 continued. Graphs illustrating the variation of trace elements with LOI (in %) for the Troodos and Limassol Forest harzburgites.

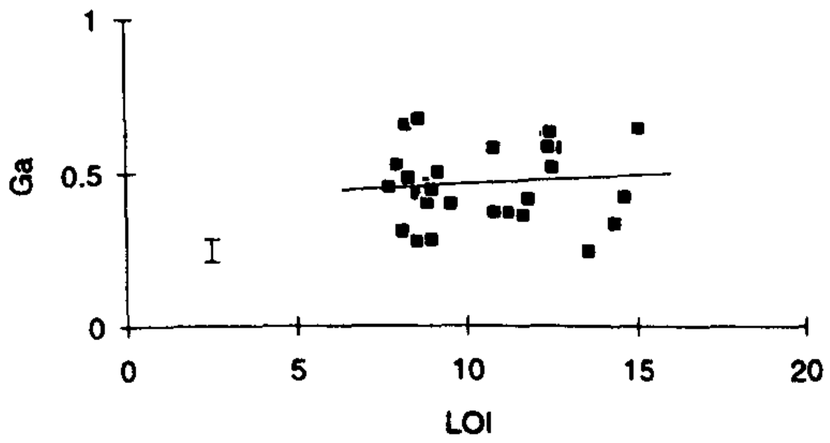

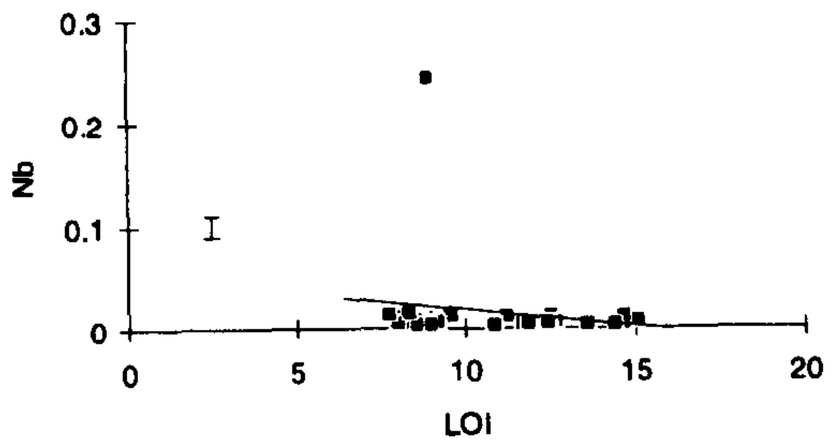

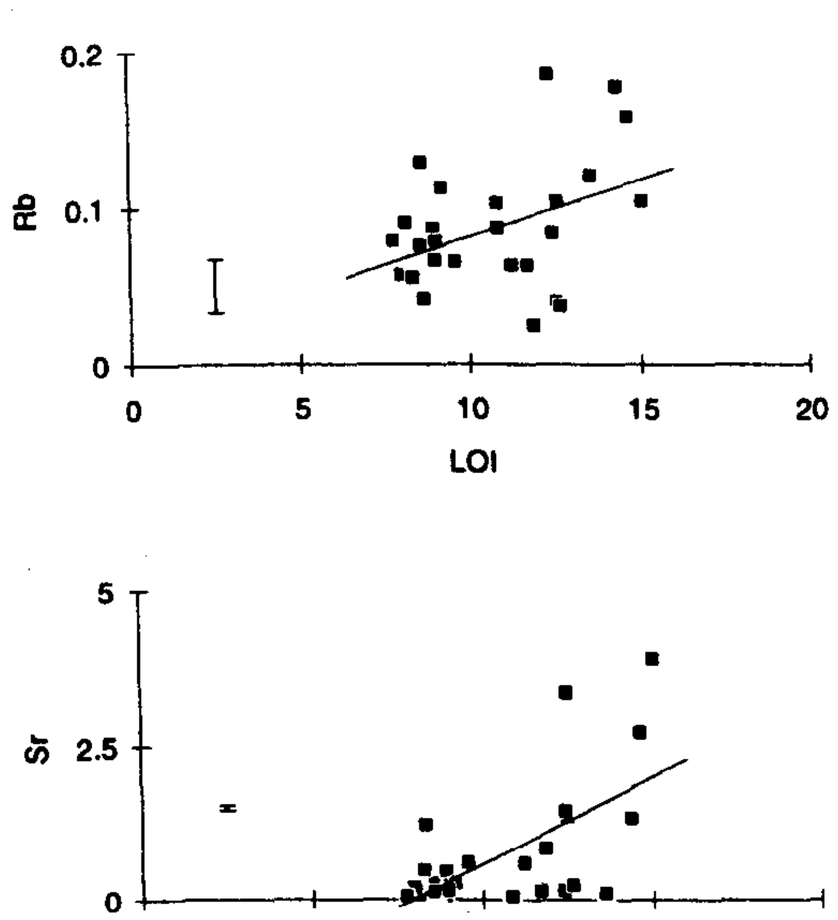

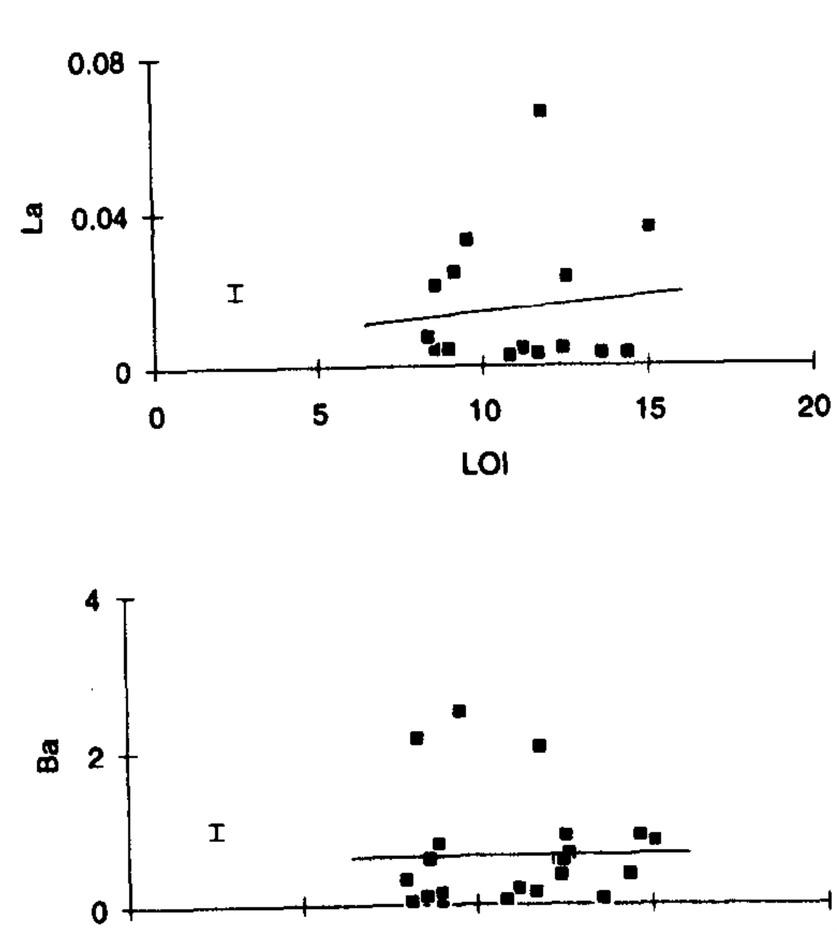

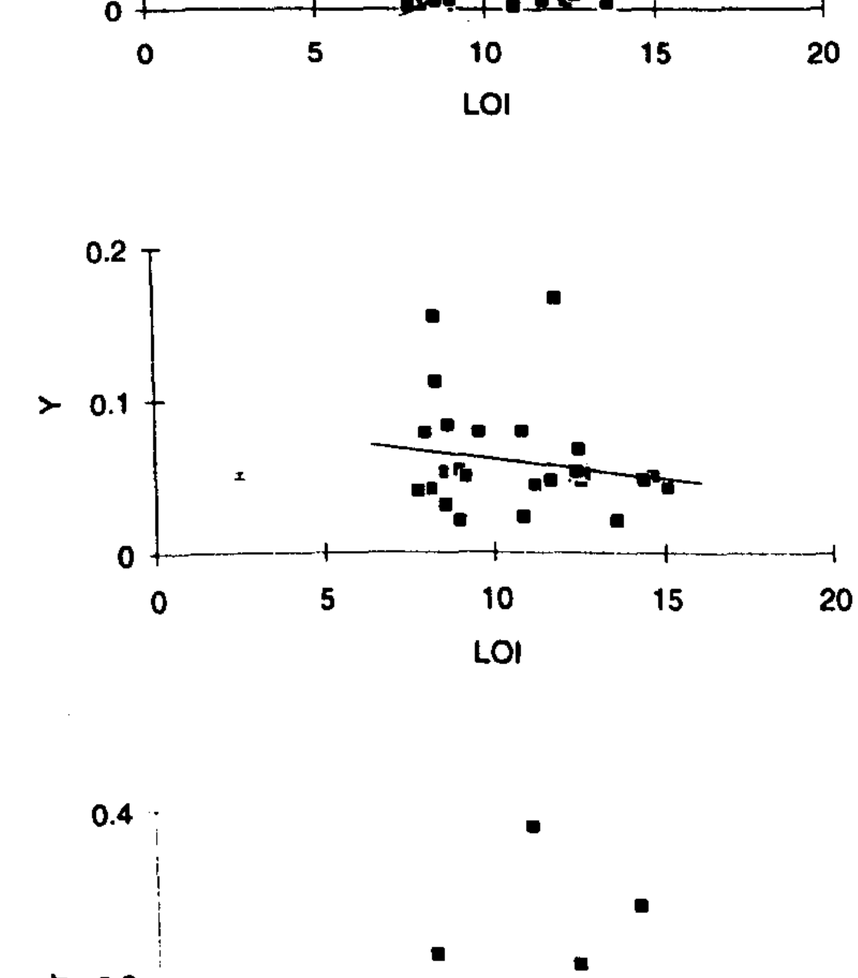

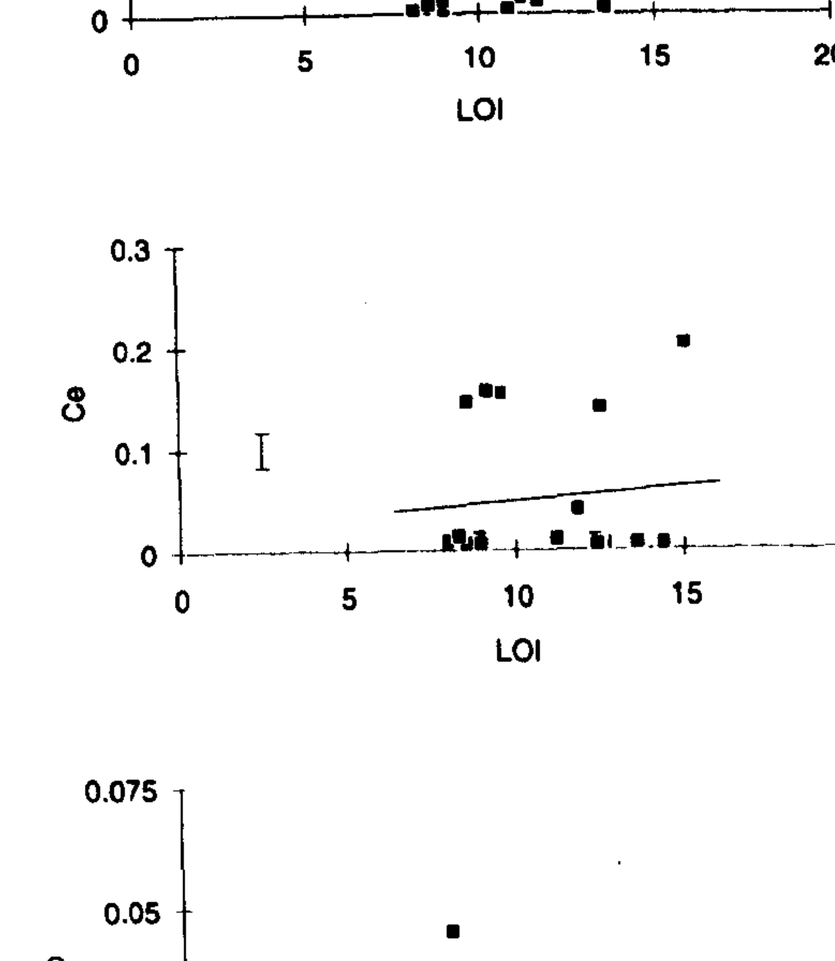

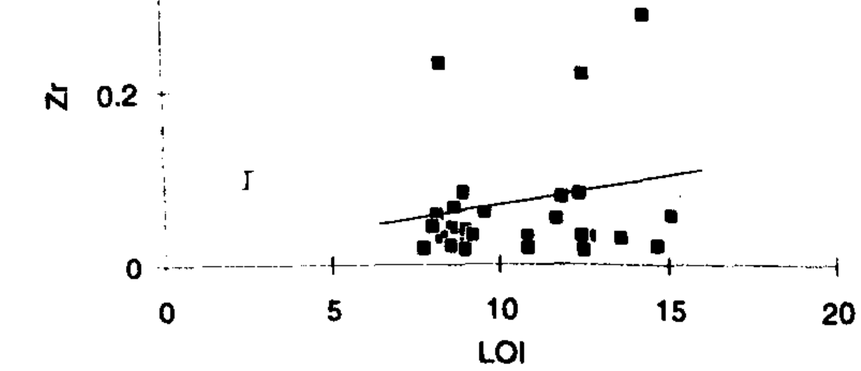

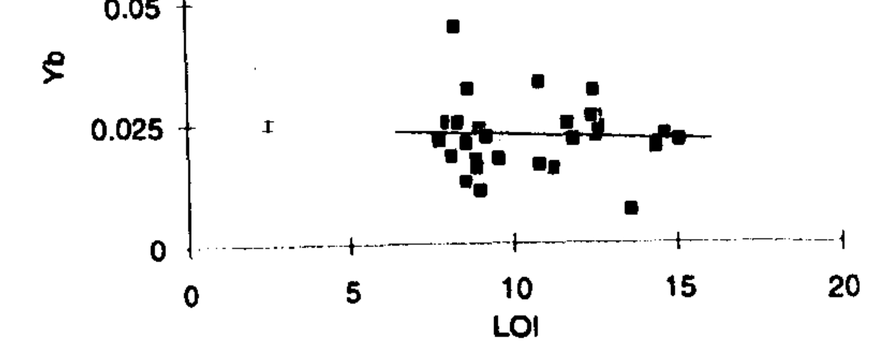

Figure 5.2. Graphs illustrating the variation of trace elements with LOI (in %) for the Troodos harzburgites. All trace element data in ppm

Only the data from harzburgite samples have been plotted in Figures 5.1 and 5.2 . This approach was taken so that the samples being compared at different degrees of serpentinisation (i.e. different LOI values) have similar mineralogies. This is important because, as illustrated in Chapter 3, the constituent minerals of the peridotites respond differently to serpentinisation. Therefore, the geochemical response of a sample to serpentinisation will, to an extent, depend on the proportion of minerals resistant to alteration it contains. By restricting this study to the harzburgite samples the aim was to reduce the effects of variable modal proportions on the data set.

Furthermore, the Troodos and Limassol data are plotted separately on Figure 5.1, so that the effects of almost total serpentinisation in the Limassol Forest can be compared with the lower degrees of serpentinisation (i.e. lower modal serpentine content) in the Troodos sequence. The most important difference between the peridotites from these two locations is that the orthopyroxene in the Troodos samples is only partly altered to serpentine and talc, whereas in the Limassol Forest orthopyroxene crystals are completely altered (for petrographic descriptions refer to Chapter 3). The variation of the large ion lithophile, high field strength and rare earth elements with LOI is illustrated in Figure 5.2. Only data for the Troodos harzburgites are shown, because too few Limassol Forest harzburgites were analysed for these elements for the data to be statistically significant. Least squares best fit lines have been drawn on the graphs to indicate the general trend of each element with LOI.

Figure 5.1 shows that the Limassol Forest samples generally display more extreme elemental variation with LOI than the Troodos samples, although the number of Limassol Forest samples analysed is relatively small and restricted to a narrower range of LOI than the Troodos samples, which may have biased the results. In order to assess the significance of these trends, the correlation coefficient (r) and t-value for each element with LOI has been calculated and these are presented in Tables 5.1 and 5.2, with the critical t-values for the 95% significance level. For the data presented in these tables, the null hypothesis is retained at the 95% confidence interval if the calculated t value is less than the critical t value, and there is no statistically significant correlation between the element and LOI.

The data in the tables shows that for the Troodos samples SiO_2, Zn and Co are significantly correlated with LOI at the 95% confidence level. SiO_2 and Zn both decrease with increasing LOI and Co increases. Sr and Rb are also significantly correlated with LOI at the 95% confidence interval, and increase with increasing serpentinisation. This evidence suggests that the whole-rock SiO_2, Zn, Co, Rb and Sr

data should treated with caution. In contrast the REE are not significantly correlated with LOI and, therefore, would appear to be immobile during serpentinisation. In the Limassol Forest samples, only FeO_t, Zn, Cr and V are not significantly correlated with LOI at the 95% confidence level. This suggests that element mobility was much higher under the serpentinising conditions which affected the Limassol Forest peridotites, compared to the Troodos sequence.

	Troodos			Limassol Forest		
	r value	t value	critical t	r value	t value	critical t
SiO_2	-0.238	2.031	1.96	-0.513	4.96	2.13
Al_2O_3	0.004	0.03	1.96	-0.451	4.19	2.13
MgO	0.187	1.58	1.96	0.64	7	2.13
FeO_t	0.030	0.247	1.96	0.133	1.12	2.13
CaO	-0.187	1.58	1.96	0.59	6.07	2.13
MnO	-0.220	1.87	1.96	0.51	4.86	2.13
Cr	-0.213	1.81	1.96	-0.271	2.34	3.18
Ni	-0.160	1.344	1.96	-0.596	6.16	3.18
V	0.094	0.785	1.96	-0.271	2.34	3.18
Sc	0.055	0.454	1.96	-0.525	5.12	3.18
Co	0.395	3.568	1.96	0.537	5.29	3.18
Ti	0.119	0.993	1.96	-0.467	4.39	3.18
Zn	-0.289	2.51	1.96	0.116	0.968	3.18
Cu	0.135	1.135	1.96	-0.594	6.13	3.18

Table 5.1. Summary of calculated correlation coefficients (r) and t values for the harzburgites with respect to LOI.

As a test of these correlations, a heavily serpentinised layer of harzburgite located in the top of the Troodos mantle section was sampled. The layer consists of a 10 cm thick, shallowly dipping, planar unit of heavily serpentinised harzburgite, which contains a few thin, discontinuous chrysotile veins. On fresh surfaces, the heavily serpentinised harzburgite is grey-brown in colour, rather than the usual green-black, and the layer is in gradational contact with the enclosing, less serpentinised, harzburgites. In thin section, the heavily serpentinised harzburgite (LOI = 11.85%) is similar in appearance to the Limassol Forest harzburgites, consisting of a 100% serpentinised matrix with irregular, discontinuous veinlets of chrysotile. The layer is interpreted as a fossil fluid pathway. The less serpentinised harzburgite (LOI = 8.33%) immediately adjacent to the

serpentinised layer was also sampled, and the whole-rock data for the two samples are compared in Figure 5.3. There are no dunite or pyroxenite bodies in the surrounding outcrops which might have introduced primary geochemical variations between the two samples, so any differences in geochemistry between the samples is assumed to be the result of serpentinisation. In Figure 5.3, the heavily serpentinised sample is normalised to the less serpentinised sample so that values greater than 1 indicate that the elemental abundance has increased during serpentinisation. By contrast, values less than 1 suggest that the element was removed during serpentinisation.

	r value	t value	critical t value		r value	t value	critical t value
Ga	0.106	0.553	2.09	Ba	0.014	0.072	2.14
Rb	0.418	2.388	2.09	La	0.109	0.569	2.23
Sr	0.630	4.214	2.09	Ce	0.088	0.458	2.18
Y	-0.157	0.828	2.09	Nd	0.290	1.573	2.26
Zr	0.171	0.903	2.09	Yb	-0.064	0.333	2.09
Nb	-0.163	0.857	2.09				

Table 5.2. Summary of calculated correlation coefficients (r) and t values for the Troodos harzburgites with respect to LOI.

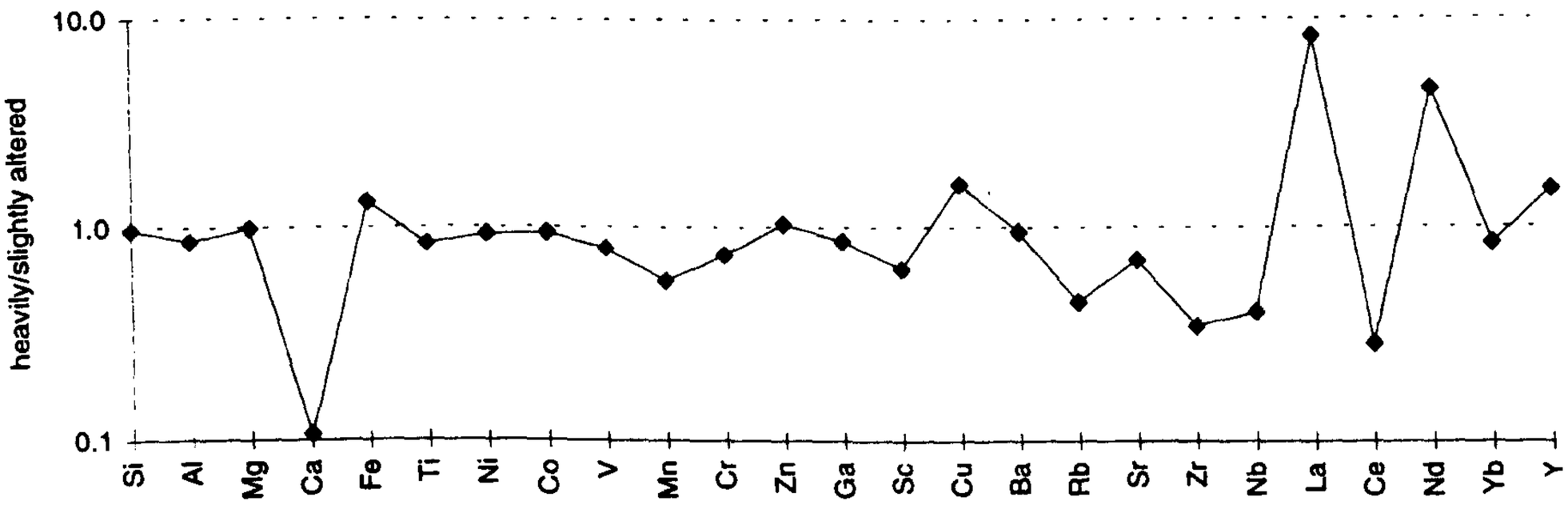

Figure 5.3. Plot illustrating the elemental variations between the heavily serpentinised layer and the surrounding less serpentinised harzburgite.

The data in Figure 5.3 suggests that Nb, Zr, MnO, Sc, CaO, Ce and Rb were removed from the serpentinised layer, whereas Nd and La were added during the serpentinisation process. It is notable that the serpentinite layer has a LOI value of 11.85% and is 100%

serpentinised, whereas the adjacent harzburgite has an LOI of 8.33% and in thin section has approximately 20% modal serpentine. Compared to the other Troodos sequence harzburgites, the serpentinite layer has a much higher modal serpentine content but a LOI value similar to an average *background* harzburgite (the *background* harzburgites range from 7.25 to 14.04% LOI, average 11.47%). For these reasons, and the similarity in petrographies, the data from these samples is thought to be more applicable to the serpentinisation reactions which occurred in the Limassol Forest harzburgites (which have LOI values between 11.87 and 15.3%, average 12.73%, and like the serpentinised layer are 100% serpentinised) rather than the *background* harzburgites. The fact that in the Figure 5.1 CaO appears to be added during serpentinisation of the Limassol Forest harzburgites, whereas Figure 5.3 suggests CaO is removed during serpentinisation, shows how difficult it is to draw any firm conclusions about element mobilities at high degrees of serpentinisation.

Selected whole-rock data for the Troodos sequence and the Limassol Forest peridotites are presented in Figure 5.4. These graphs show that the *background* harzburgite and serpentinite diapir samples form a coherent trend which, later in this Chapter, will be shown to be controlled predominantly by partial melting. Notably, Limassol Forest samples are displaced away from the partial melting trend defined by the *background* harzburgite and serpentinite diapir samples. However, the mineral chemistry presented in Chapter 4 suggested that the Limassol Forest samples were similar in composition to the *background* harzburgites. The differences between the whole-rock data for the Limassol Forest and *background* harzburgite samples could, therefore, be interpreted as the result of serpentinisation. Inferred serpentinisation trends between the *background* harzburgites and the Limassol Forest samples are shown by arrows marked SP on Figure 5.4. The fact that the SP vectors are oriented at an angle to the presumed melting trend (labelled PM on Figure 5.4, see below for further discussion of this), which connects the serpentinite diapir and *background* harzburgite compositions, confirms that the SP trends are unlikely to be a result of partial melting processes. Furthermore, the fact that the SP vectors do not trend in the direction of more fertile compositions (i.e. higher Ti and Ca) indicates that they are unlikely to be a result of mantle-melt interaction.

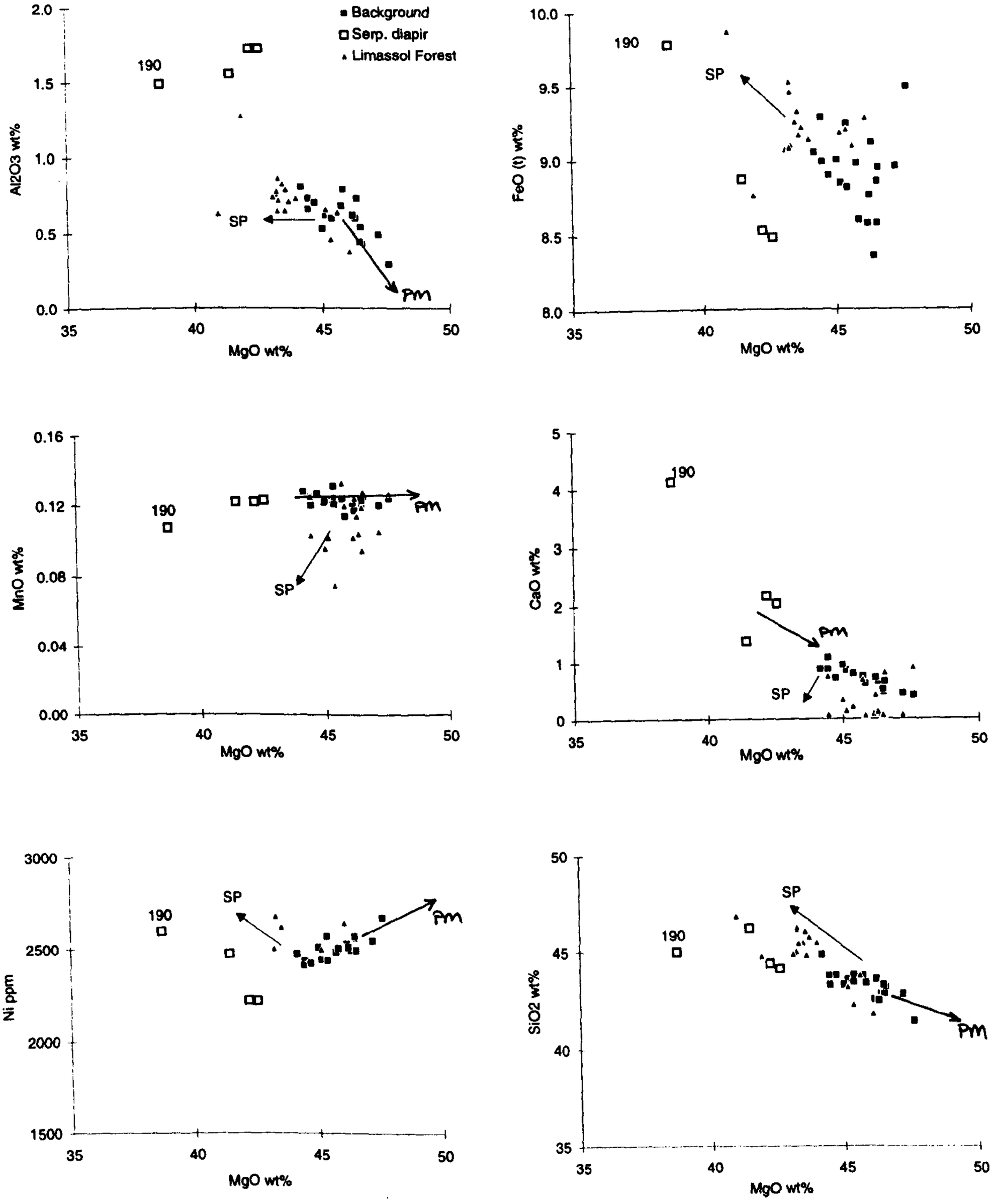

Figure 5.4. Graphs illustrating the variation of selected elements with MgO in the *background* harzburgites, serpentinite diapir lherzolites and Limassol Forest harzburgites. Solid arrows labelled SP show the inferred serpentinisation trends, arrows labelled PM show partial melting trends.

Also annotated on Figure 5.4 is sample 190 from the serpentinite diapir. This sample is unusually heavily altered compared to the other serpentinite diapir samples, with the primary minerals being 100% serpentinised. The sample also contains minor picrolite veins. This sample is displaced from the main group of serpentinite diapir samples along vectors parallel to the SP trend for Al_2O_3, FeO_t, MnO and Ni. The parallelism of the trends supports the suggestion that they represent serpentinisation vectors because, in the case of the serpentinite diapir samples, the vector connects samples which are known to have experienced different amounts of serpentinisation.

As noted above, the main difference in petrography between the *background* harzburgites and the Limassol harzburgites, is that orthopyroxene is completely altered in the Limassol Forest samples. The data presented in Figure 5.4 could, therefore, be interpreted as showing that the major elements are generally immobile provided orthopyroxene is not significantly serpentinised. When orthopyroxene is altered (i.e. the Limassol Forest, the serpentinised layer and sample number 190), MgO, CaO and Mn are leached by the serpentinising fluid and FeO_t, SiO_2 and Ni increase in the solid. However, Al_2O_3 appears to be immobile. The fact that the Troodos harzburgites show little or no tendency to plot away from the inferred serpentinisation trends could be interpreted as indicating that these elements were immobile during the alteration of the *background* harzburgites.

The question of major element mobility during serpentinisation was also addressed by Coleman and Keith (1971). In their study of the Burro Mountain dunites and harzburgites they found that SiO_2, MgO, FeO_t, Al_2O_3, Cr_2O_3 and NiO behaved conservatively during serpentinisation whereas CaO was lost. Notably, the Burro Mountain harzburgites analysed were considerably less altered (less than 5% serpentine) than the Troodos harzburgites and contained relics of fresh pyroxenes. The data from Burro Mountain would, therefore, support the conclusions drawn above that most major elements behave conservatively during serpentinisation until the orthopyroxene is altered.

Another approach that has been taken to try and establish mobility of elements during serpentinisation is to experimentally react peridotites with seawater (Seyfried and Dibble, 1980; Menzies *et al.*, 1993). Seyfried and Dibble (1980) found that Fe, Mn, and Zn increased in the serpentinising fluid and Mg, Ca and Sr decreased, during the experiment. In contrast, Menzies *et al.* (1993) found that the major elements behaved conservatively during serpentinisation. Menzies *et al.* (1993) also reported that the REE behaved conservatively in clinopyroxene-bearing peridotites, and that, in clinopyroxene-free samples, the LREE increased during the serpentinisation process due to LREE uptake from the reacting fluid by newly precipitated phases. Sr also increased in the

serpentinised peridotites. These experiments were run at moderate temperatures and pressures (300°C, 500 bars). Isotopic evidence (Magaritz and Taylor, 1974) suggests that the Troodos serpentinites formed at lower temperatures, between 75 and 100°C, in near surface conditions, where element solubility in the serpentinising fluid would probably have been even lower. Therefore, any transport of elements in or out of the alteration system by serpentinising fluids in the Troodos case is likely to have been less than in the experimental system of Menzies *et al.* (1993).

The possibility that the LREE could be added during serpentinisation has important implications for arc peridotites which typically have LREE-enriched chemistries. However, other studies have suggested that the LREE are in fact leached during serpentinisation. Ottonello *et al.* (1979) demonstrated that Alpine lherzolites had LREE depleted profiles accompanied by negative Ce anomalies which were too large to be explained by melting processes. They interpreted these patterns as a product of water-rock interaction. Unfortunately, the LREE are generally present in concentrations below the detection limit of the ICP-MS in the Troodos *background* harzburgites, so no whole-rock REE profiles can be plotted. The fact that Ce is usually the only REE present in measurable concentrations in the Troodos *background* harzburgites and, as will be shown later in this chapter (see section 5.4.1), is present in concentrations higher than those which would be expected from partial melting processes alone, suggest that a negative Ce anomaly would not be present in the Troodos *background* harzburgites. This evidence indicates that Ce was not leached during serpentinisation contrary to the conclusions of Ottonello *et al.* (1979).

The fact that LOI is an imperfect alteration index, because it does not consider the chemistry of the serpentinising fluid, has been mentioned above. In order to assess the chemistry of the serpentinising fluid in the Troodos Massif, samples of chrysotile and picrolite veins from the serpentinite diapir area were analysed for their trace element content by ICP-MS. The results are presented in Table 5.3.

Magaritz and Taylor (1974) used the isotopic composition of vein samples and the matrix serpentinite, to show that they were probably precipitated by the same fluid. Therefore, any element which is significantly enriched in the vein serpentine is also likely to be have been enriched in the host harzburgites. To give an indication of whether the fluids that precipitated the veins were significantly enriched in any trace elements relative to the harzburgites and, therefore, capable of increasing elemental abundances during serpentinisation, the vein data have been normalised against an average *background* harzburgite in Figure 5.5. The Figure shows that Ba is the only element which is

enriched in both vein types compared to the average *background* harzburgite. Notably, the veins have lower Rb and Sr concentrations than the harzburgite, despite the fact that the whole-rock data discussed above imply that these elements are enriched by serpentinisation.

	Picrolite Vein	Chrysotile Vein		Picrolite Vein	Chrysotile Vein
Sc	bd	bd	Sr	0.286	0.673
TiO_2	5.65	3.86	Y	0.164	0.018
V	9.11	26.28	Zr	0.182	0.047
MnO	0.053	0.095	Nb	0.011	0.007
Co	21.0	44.0	Ba	0.493	4.522
Cu	12.97	0.63	La	0.050	0.009
Zn	9.05	7.79	Ce	0.149	0.017
Ga	0.753	0.150	Nd	0.057	0.009
Rb	0.029	0.014	Yb	0.011	0.002

Table 5.3. Summary of vein serpentinite trace element analyses, all data in ppm except TiO_2 and MnO in wt%, bd = below detection limit.

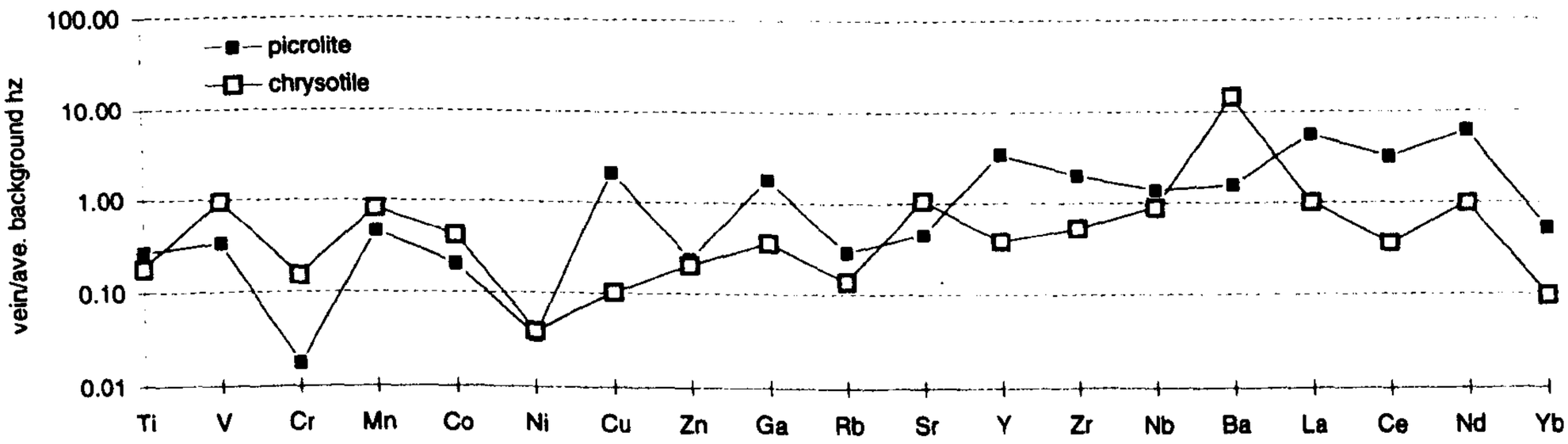

Figure 5.5. Plot illustrating the variation in chemistry of the vein serpentines normalised against an averaged *background* harzburgite value.

The data discussed above illustrate how difficult it is to constrain element mobilites during serpentinisation. In terms of major elements there is a clear distinction in the Troodos data between those samples which still contain relic orthopyroxene and those in which the serpentinisation process has destroyed this phase. Until the degree of serpentinisation at which orthopyroxene is broken-down is reached, the major elements behave conservatively. At greater degrees of serpentinisation the process is non-

isochemical for most major elements with the possible exception of Al_2O_3. MgO, CaO and MnO are leached from the harzburgite whereas FeO_t, SiO_2 and NiO increase in the solid. Because orthopyroxene is only slightly altered in the *background* harzburgites and serpentinite diapir lherzolites it is concluded that serpentinisation has been isochemical for the major elements in these samples. The conservative behaviour of Al_2O_3 during serpentinisation has also been noted by Ottonello *et al.* (1979) who suggest that it reflects the fact that Al can be more easily accommodated in the serpentine mineral lattice than the other major elements.

The behaviour of trace elements in the Troodos peridotites during serpentinisation is more ambiguous. In terms of their variation with LOI (see Figures 5.1 and 5.2) in the *background* harzburgites only Rb and Sr have statistically significant correlations (see Table 5.2); both increasing with increasing LOI. However, the data from the serpentinised harzburgite layer (see Figure 5.3) shows that Rb and Sr are leached during serpentinisation. It is probable that this variation is another reflection of the fact that the pyroxenes are not altered in the *background* harzburgites but are in the serpentinised harzburgite layer. However, the data from the vein serpentines (see Figure 5.5) shows that they are not significantly enriched or depleted in Rb and Sr compared to the average *background* harzburgite, which suggests that Rb and Sr are not being transported by the serpentinising fluid. Because the Troodos data does not allow tight constraints to be placed on the behaviour of Rb and Sr during serpentinisation they have not been used in the following petrogenetic discussions.

The behaviour of the REE, particularly the LREE, is also ambiguous. In terms of the variation in REE concentrations with LOI (see Figure 5.2, Table 5.2) there are no statistically significant correlations in the *background* harzburgites. In the more altered serpentinised harzburgite layer (see Figure 5.3), La and Nd are enriched by serpentinisation, whereas Ce is leached. This limited evidence would suggest that REE mobility during serpentinisation mirrors that of the major elements, and the serpentinisation process is largely isochemical until the point at which pyroxenes are altered. Considering the fact that clinopyroxene is the major repository of the REE in the harzburgites this conclusion is reasonable. Several lines of evidence from other studies also suggest that the REE are immobile in partially serpentinised peridotites: serpentinised peridotites with LREE-depleted chemistries anomaly have been found (Frey *et al.*, 1991); natural peridotites do not show any correlation between REE abundance and modal percentage of serpentine (Menzies *et al.*, 1993); clinopyroxene is the main REE bearing phase in peridotites and usually the least altered phase (this study and Menzies *et al.*, 1993 and references therein).

The data discussed above suggest that the main effect of serpentinisation in the Troodos *background* harzburgite and serpentinite diapir samples is probably that of dilution. Therefore, the data in this chapter will be presented on an anhydrous basis. Because of the possibility of Mg mobilisation (i.e. Figure 5.4), and the apparent immobility of Al under the range of serpentinisation conditions experienced by the Troodos peridotites, Al_2O_3, rather than MgO, will be used as an index of depletion in the following discussions. The fact that whole-rock Al_2O_3 contents are well correlated with mineral chemistry parameters (see Figure 5.6) supports this use of Al_2O_3.

The Limassol Forest data show statistically significant correlations between LOI and the concentrations of most elements, and also plot on proposed serpentinisation vectors on the bivariate plots presented in Figure 5.4. The serpentinisation process in the Limassol Forest would, therefore, appear to have been non-isochemical and the compositions of these samples are likely to have been significantly affected by alteration. Because of this, the whole-rock data for the Limassol Forest samples have not been examined in detail. The petrographic differences between the Limassol and Troodos harzburgites, suggests that the serpentinisation of orthopyroxene is largely responsible for the increased element mobility in the Limassol Forest samples.

The question of whether the serpentinisation process is isovolumetric has also been raised by several studies (e.g. Coleman and Keith, 1971; S. Edwards pers. comm.) The fact that the Troodos Massif currently forms the highest topographic point on the island of Cyprus and that the uplift of the massif is centred on the serpentinite diapir (Malpas *et al.*, 1990 and references therein) suggests that topography of the island is developing due to the presence of the low density serpentinite. If this is the case, it would require the serpentinisation process to be non-isovolumetric and involve a volume expansion. The microstructure of the harzburgites support this hypothesis as orthopyroxene (e.g. Plate 3.8b, Chapter 3) and spinel both develop expansion cracks which are filled by serpentine minerals in the early stages of alteration.

5.3 WHOLE-ROCK GEOCHEMISTRY

This section gives an overview of the whole-rock geochemistry of the samples analysed. Representative analyses are presented in Table 5.4. In this chapter the same sample naming conventions that were adopted in the Mineral Chemistry Chapter are followed.

5.3.1 HARZBURGITE AND LHERZOLITE GEOCHEMISTRY

The peridotites analysed are refractory, the whole-rock Mg# varying from 90.8 to 92.2 in the Troodos harzburgites and from 90.7 to 91.3 in the lherzolitic samples from the serpentinite diapir. CaO and Al_2O_3 contents are low, generally < 1wt% in the Troodos harzburgites but up to 3 wt% and 1.7 wt%, respectively, in the serpentinite diapir. K_2O, P_2O_5 and Na_2O are close to, or below, the detection limit of the XRF in most samples. Ti and V contents are around 100 ppm and 40 ppm, respectively, in the Troodos harzburgites, whereas the serpentinite diapir samples have contents of around 250 ppm Ti and 50 ppm V.

Anomaly 1 harzburgites have relatively high Al_2O_3 (average 0.79 wt%), CaO (average 0.87 wt%) and Ti (average 103 ppm) contents compared to the *background* harzburgites. However, the *top-of-the-sequence* harzburgites have compositions within the range defined by the *background* harzburgites.

5.3.2 DUNITE GEOCHEMISTRY

Dunites have Mg# in the range 88.0 and 92.0, with the crustal dunites having the lowest values. CaO, Al_2O_3 and Ti are also highest in the crustal dunites (averages of 0.95 wt%, 0.62 wt% and 153 ppm, respectively), reflecting the presence of interstitial clinopyroxene. Dunites have the highest Cr concentrations of all the lithologies analysed, with values up to 1 wt% in the most spinel-rich samples.

5.3.3 PYROXENITE GEOCHEMISTRY

The clinopyroxenites are the least refractory samples analysed with Mg# ranging from 86.9 to 90.5 and Al_2O_3 between 0.9 and 2.5 wt%. Orthopyroxenites have Mg# between 91.3 and 91.9 and Al_2O_3 between 1.1 and 2.2 wt%. TiO_2 contents vary between 113 and 230 ppm and CaO between 1.27 and 2.08 wt% in the orthopyroxenites.

Sample	195	180	173	371	294	111	323	191	257	344	105
Lithology	dunite	dunite	dunite	harz	harz	harz	harz	harz	opx A	opx B	cpxite
Location	crustal	II fol	x fol	adj dun	bckgrd	anomaly 1	between bands	serp diapir			
MnO	0.126	0.123	0.127	0.117	0.128	0.125	0.126	0.122	0.123	0.129	0.136
TiO2	0.020	0.008	0.014	0.014	0.014	0.016	0.011	0.039	0.017	0.023	0.067
Fe2O3	9.39	10.02	9.43	8.68	9.05	8.94	9.37	8.53	8.51	7.68	4.85
CaO	0.43	0.15	0.41	0.39	0.88	0.82	0.56	2.16	1.07	1.27	18.08
SiO2	39.80	40.44	40.41	42.42	44.86	43.26	43.75	44.41	45.38	47.74	51.99
Al2O3	0.57	0.08	0.63	0.53	0.81	0.79	0.62	1.73	1.07	2.39	1.58
MgO	48.95	49.44	47.41	46.96	44.15	44.10	45.92	42.19	43.07	39.41	22.27
Na2O	bd	bd	bd	bd	bd	bd	bd	bd	bd	bd	bd
TOTAL	99.87	100.92	99.12	99.69	100.48	99.01	100.83	99.73	99.85	99.68	98.99
LOI	11.88	14.40	9.32	9.58	10.82	8.66	12.48	12.64	8.20	8.34	1.00
Mg#	91.57	91.14	91.29	91.85	91.05	91.28	91.06	91.16	91.34	91.45	90.55
XRF data											
Zn	40.70	53.20	45.40	45.00	40.90	42.83	47.54	42.40	41.46	47.51	24.80
Cu	8.10	7.90	12.90	1.17	11.34	bd	3.23	13.10	4.91	18.06	6.94
Ni	1864	2970	2710	2625	2471	2517	2470	2222	2278	1619	370
Co	145.0	151.0	139.0	133.3	129.0	132.6	140.2	124.0	124.0	93.9	26.8
Cr	3306	580	4885	2482	2773	2562	1664	2929	3975	13066	2784
V	18.00	6.80	24.10	21.81	40.71	35.31	30.90	59.40	41.68	102.80	121.86
Ti	174.0	116.0	159.0	102.3	112.3	82.1	88.7	253.0	112.8	229.9	431.7
Sc	8.10	5.30	3.90	9.60	11.45	11.40	11.60	17.80	14.08	21.13	37.86
ICP-MS data											
Ga	0.398	0.578	0.675	0.629	1.490	0.843	2.290				
Rb	0.065	0.087	0.042	0.084	1.391	0.208	1.073				
Sr	0.618	0.114	0.084	1.367	3.136	3.746	5.578				
Y	0.079	0.080	0.084	0.068	0.957	0.083	0.145				
Zr	0.061	0.033	0.067	0.017	0.067	0.022	0.078				
Nb	0.012	0.005	0.008	0.006	0.008	0.004	0.020				
Ba	2.504	0.067	0.609	0.558	40.703	0.933	3.765				
La	0.032	0.003		0.005							
Ce	0.154		0.009	0.005							
Nd	0.016	0.012	0.010								
Yb	0.018	0.033	0.032	0.032	0.136	0.036	0.060				

Table 5.4. Representative whole-rock analyses.

Abbreviations: II fol = parallel to foliation, x fol = cross-cutting foliation, harz = harzburgite, adj dun = adjacent to dunite, opx A = *orthopyroxenite A*, opx B = *orthopyroxenite B*, cpxite = clinopyroxenite, serp diapir = serpentinite diapir. Major element data in wt% oxide, trace element data in ppm.

5.4 HARZBURGITE PETROGENESIS

A hypothesis that partial melting and reaction with melts has controlled the geochemistry of the Troodos harzburgite samples was made from the mineral chemistry data presented in Chapter 4. The variations of major elements and mineral chemistry parameters with Al_2O_3 in the *background* and serpentinite diapir samples are illustrated in Figure 5.6. SiO_2 and CaO are positively correlated with Al_2O_3, whereas MgO is inversely correlated. Compared with the other major elements, FeO_t is poorly correlated with Al_2O_3. The implications of this variation are discussed in detail below. Both mineral chemistry parameters, $Cr\#_{spn}$ and $Mg\#_{ol}$, are inversely correlated with whole-rock Al_2O_3.

The trends illustrated in Figure 5.6 correspond to the trends defined by upper mantle xenoliths (Maaløe and Aoki, 1977), Alpine peridotites (Frey *et al.*, 1985; Bodinier *et al.*, 1988) and other ophiolites (e.g. Roberts, 1992). These correlations between major element abundances and between major element concentrations and mineral chemistry parameters are also characteristic of residues formed in experimental studies of peridotite melting (Mysen and Kushiro, 1977; Jaques and Green, 1980). A first order interpretation of the major element data would be, therefore, that the degree of partial melting increases from the serpentinite diapir lherzolites to the *background* harzburgites. This supports the conclusions drawn from the mineral chemistry data described in Chapter 4. Furthermore, the correlation between the major element abundances and the mineral chemistry parameters suggests that the variation from more fertile harzburgites at the base of the *background* harzburgite sequence to depleted harzburgites at the top of the mantle section, is mirrored by variations in whole-rock chemistry.

Some authors have pointed out that linear major element data correlations can also be produced by progressive trapping of melt (Obata and Nagahara, 1987; Frey *et al.*, 1991). In this model, based on analyses of rhythmic layering in the Horoman peridotite, the most fertile peridotites have the highest trapped melt component. This model is not a preferred explanation for the Troodos *background* harzburgites, because the petrological variations produced by melt trapping typically produce rhythmic layering on a 100 m scale, rather than on the massif scale as shown by the Troodos data. Also, in a melt trapping model, the most fertile lithologies should be found at the top of the sequence where the melt flow and opportunities for melt trapping are highest. However, the *background* harzburgites become progressively more depleted upwards through the sequence.

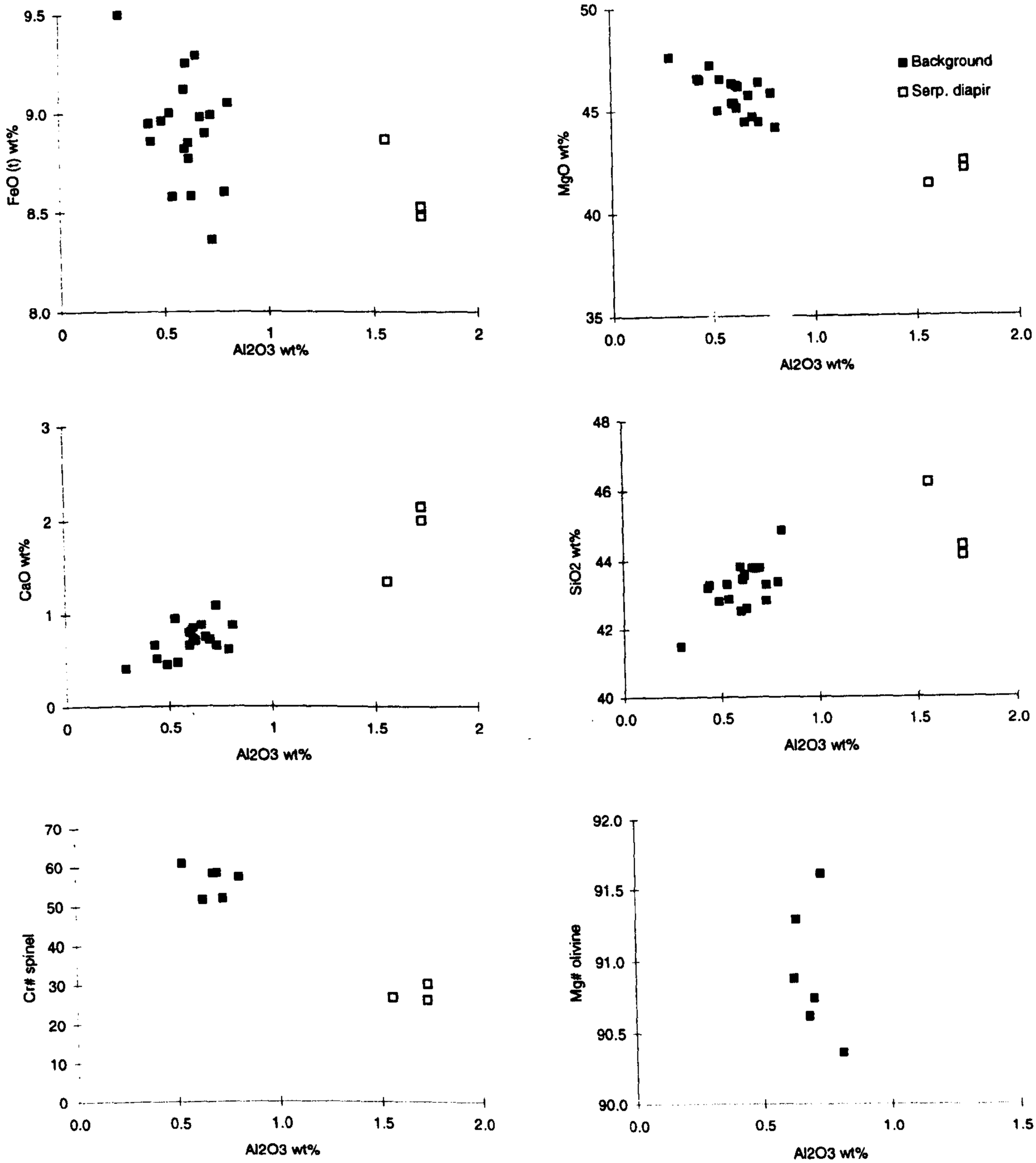

Figure 5.6. Variations of selected major elements and mineral chemistry parameters with Al_2O_3 for the *background* harzburgites and serpentinite diapir samples.

The variation of Ni, Co and Cr, elements thought to be compatible during partial melting, are illustrated in Figure 5.7. Ni and Co both display a negative correlation with Al_2O_3; the expected trend if their distribution is primarily controlled by partial melting. Cr however, shows a bimodal distribution. Between 1.75 and 0.75 wt% Al_2O_3, Cr shows relatively little change in concentration, suggesting that the distribution coefficient between residue and melt is close to unity. However, at Al_2O_3 concentrations less than 0.75 wt%, the concentration of Cr decreases rapidly, suggesting that Cr is behaving incompatibly. There is no consensus in the literature about the value of the Cr distribution coefficient during mantle melting. Many authors (e.g. Frey *et al.*, 1985) assume that Cr is compatible, despite the fact that good correlations with melting indices are rarely shown. The absence of a correlation is usually attributed to the heterogeneous distribution of spinel compared to the size of the sample analysed (Frey *et al.*, 1985). The data from mantle xenoliths is equivocal, Maaløe and Aoki (1977) found little variation of Cr with MgO and suggested a distribution coefficient close to 1, whereas Kurat *et al.* (1980) found a negative correlation, suggesting that Cr is incompatible. The Troodos data suggest that the distribution coefficient changes as the residue becomes more depleted, changing from a distribution coefficient of about 1 to <1 at approximately 0.75 wt% Al_2O_3. This change probably reflects a change in the composition of the main aluminous phase, from clinopyroxene in the more fertile peridotites to spinel in the depleted ones. The fact that Cr is incompatible at high degrees of partial melting means that the derived magmas will have high Cr concentrations, and will be capable of precipitating the chromite deposits found in the uppermost parts of the Troodos mantle section. A similar conclusion was reached by Roberts (1992) to explain the origin of chromitites in the Vourinos Ophiolite.

5.4.1 PARTIAL MELTING

Melt modelling of the mineral chemistry data (Chapter 4) showed that fractional melting was the most appropriate model to explain the distribution of the elements least affected by other processes (e.g. the HREE). Figure 5.8 shows the variation of the major elements with Al_2O_3 and fractional melting trends (details of the calculation are given in Appendix C). Ni and Cr are also illustrated on this figure because together they account of > 1 wt% of the total. The same starting composition, modal mineralogy and melting mode that were used for the modelling of the mineral chemistry data were used for the whole-rock data. The additional distribution coefficients and initial abundances for the major elements which were not given in Table 4.9 (Chapter 4) are presented here in Table 5.5.

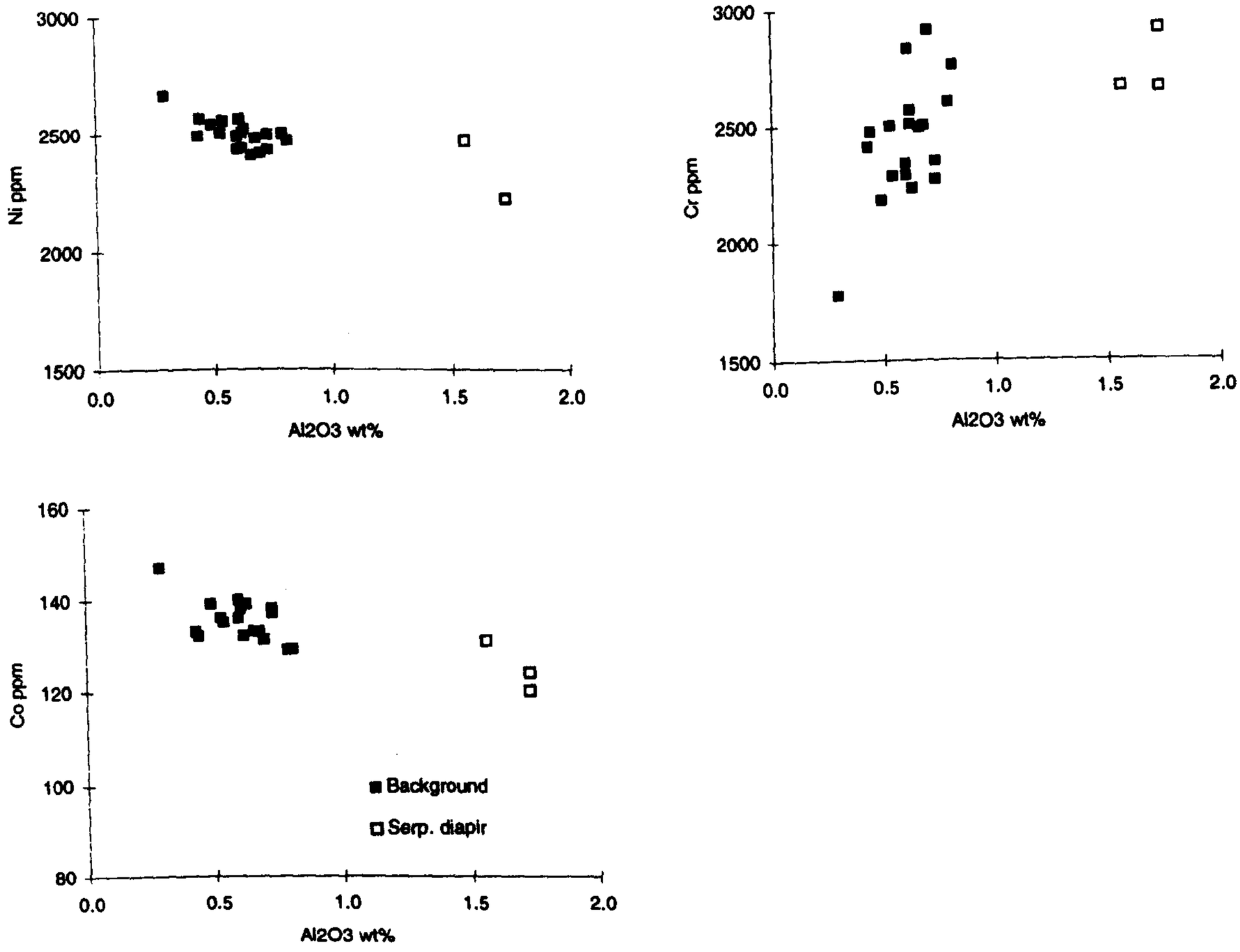

Figure 5.7. Plots showing the variation of Ni, Cr and Co with Al_2O_3 in the *background* harzburgites and serpentinite diapir lherzolites.

	Distribution Coefficients				Starting composition
	Olivine	Orthopyroxene	Clinopyroxene	Spinel	
Mg	4.2	3.2	2.1	3.5	38.4
Fe	1.2	1.1	0.8	1.7	8.8
Ca	0.03	0.19	1.2	0.03	3.25
Al	0.004	0.3	0.3	0.09	3.75
Ni	15	4.5	2.5	12	2020
Cr	1.5	7.0	10	200	2500
Mn	1.1	1.2	1.2	1.0	0.13
Co	4.0	2.0	1.0	4.5	106

Table 5.5. Summary of the data used for melt modelling (Pearce and Parkinson (1993) and references therein).

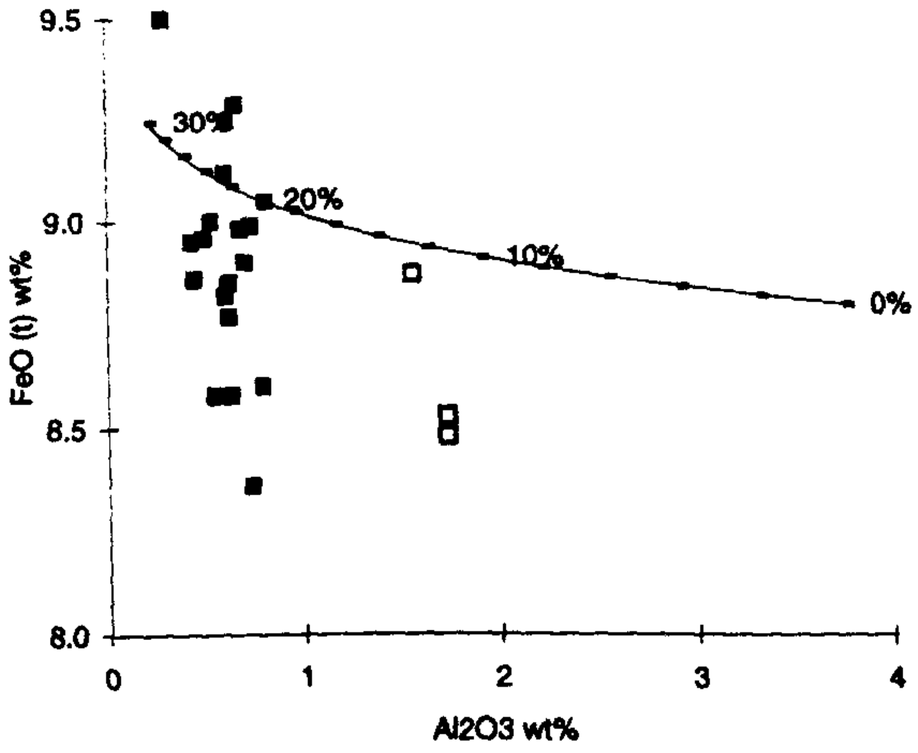

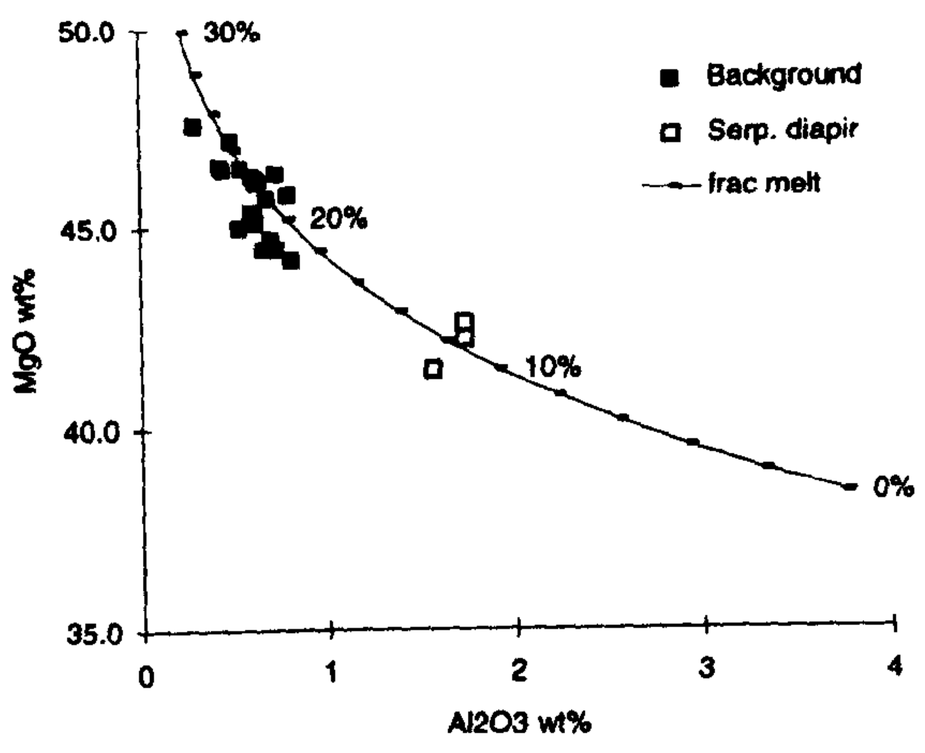

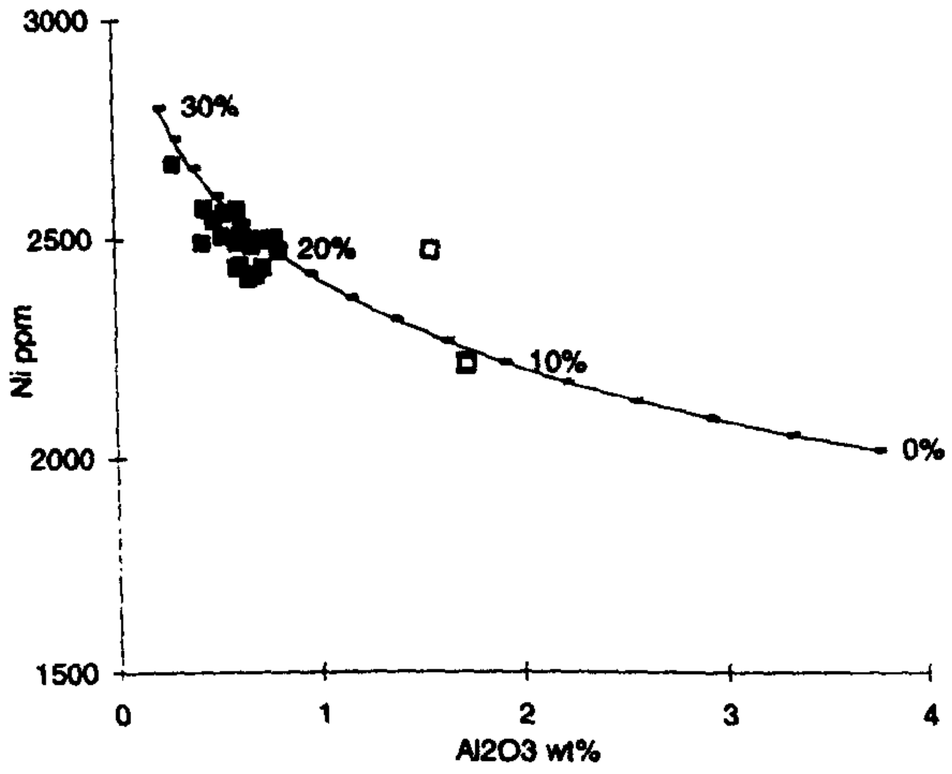

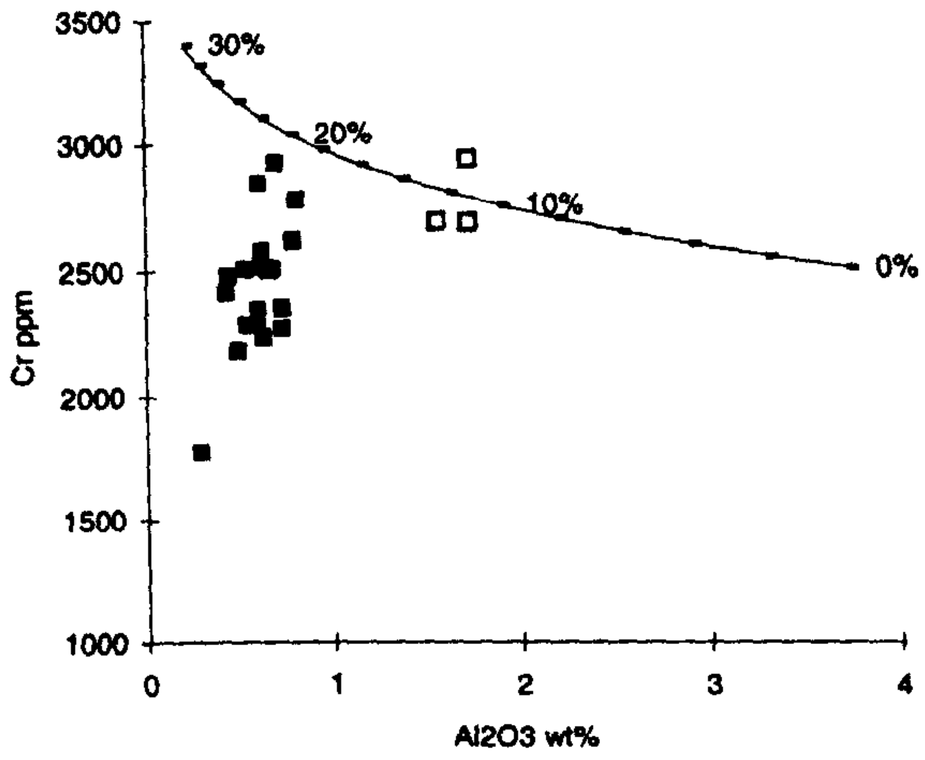

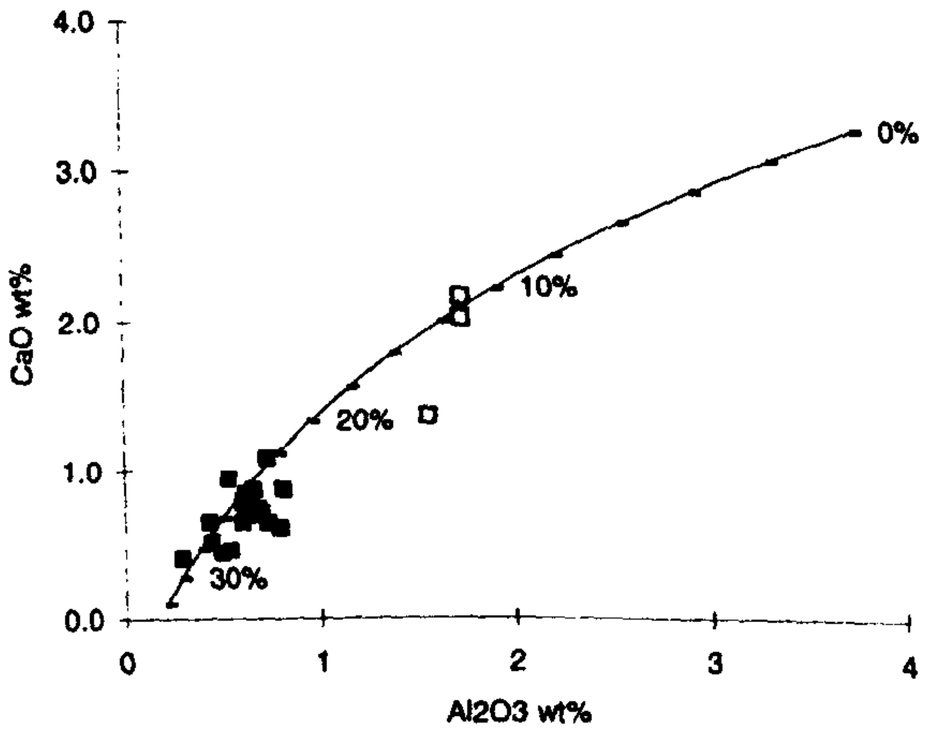

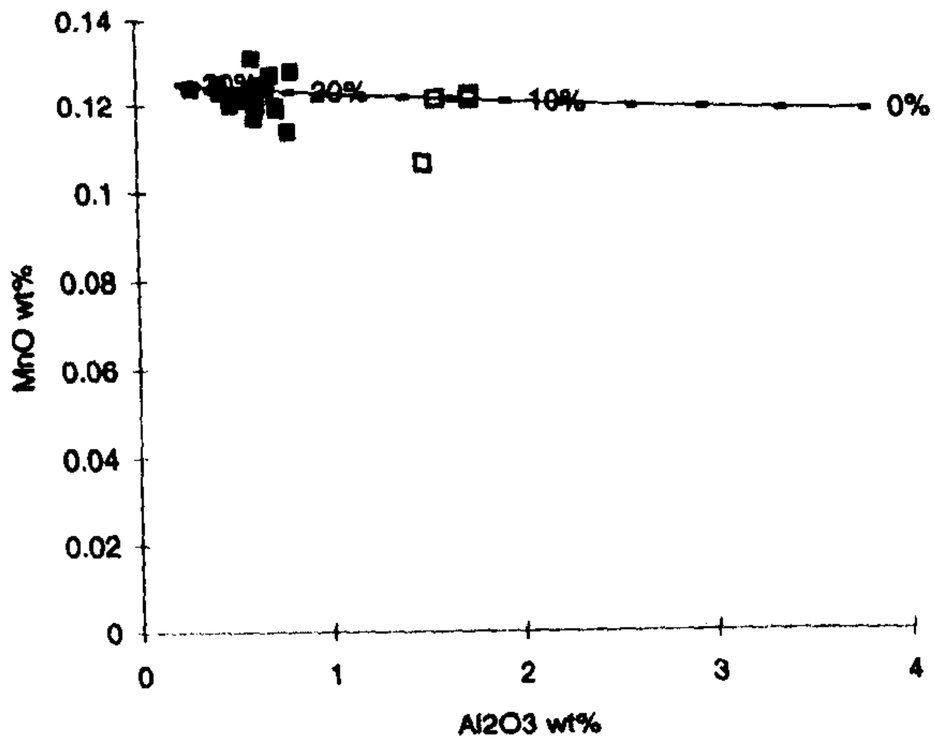

Figure 5.8. Graphs illustrating the variation of selected elements with Al_2O_3 and calculated fractional melting trends; tick marks on the fractional melting trajectories are at 2% melting intervals.

In general, the fractional melting trends match the whole-rock data reasonably well and produce estimates of the amount of melting of between 10 and 15% for the serpentinite diapir samples and 20 to 30% for the *background* harzburgites. These are similar to the results obtained from modelling the mineral chemistry data. As mentioned above, the behaviour of Cr in the harzburgites appears to change at an Al_2O_3 content of 0.75 wt%. The model fractional melting data presented on Figure 5.8 suggests that this would be equivalent to approximately 20% melting. According to the melting model of Kostopoulos (1991), this would correspond to a transition from a lherzolitic residue to a harzburgitic one. This agrees with the petrological evidence from the Troodos sequence because the serpentinite diapir samples are lherzolitic, whereas the *background* samples are harzburgites (see Chapter 3).

The FeO_t data are also poorly modelled by the fractional melting process. The scatter in the data parallel to the FeO_t axis could be partly a result of serpentinisation (see above). Another factor could be the strong control that pressure, temperature and fO_2 exert on the bulk distribution coefficient of Fe (Roeder and Emslie, 1970; Hanson and Langmuir, 1978; Elliot *et al.*, 1991). In general, the bulk distribution coefficient of Fe increases with falling temperature and pressure. Therefore, the Fe content of residues produced by shallow level melting will increase with the degree of melting. This variation in the distribution coefficient with P,T and fO_2 means that the simple fractional melting model, with a fixed distribution coefficient, is unlikely to match the real data. The fact that the Troodos *background* harzburgite data show a negative correlation between FeO_t and Al_2O_3 suggests that the melting event which produced these variations might have occurred at a shallow depth.

Figure 5.9 illustrates the variation of selected trace elements with Al_2O_3 and calculated fractional melting trends. Like the clinopyroxene trace element data, the whole-rock Y and Yb abundances are reasonably well modelled by the fractional melting model. In contrast, the Zr and Ti contents of the *background* harzburgites are higher than the model would predict. The variation of Ba and the LREE with Al_2O_3 is illustrated in Figure 5.10, along with calculated fractional melting trends. Unfortunately, the LREE are below the detection limit of the ICP-MS for most of the samples analysed, so it is difficult to draw any firm conclusions about their abundances from the small number of samples available. However, the limited data set shows that the whole-rock LREE abundances are higher than the simple fractional melting model predicts. This is the same as the clinopyroxene trace element analyses. Notably, the Ba concentrations in the serpentinite diapir samples are much higher than the fractional melting model starting composition. This suggests that Ba has been enriched by a post-melting process. The data from the

serpentine vein analyses shows that the serpentinising fluids had comparatively high Ba concentrations which would support serpentinisation as the process responsible for the Ba enrichments.

As previously discussed in Chapter 4, some authors (e.g. Johnson and Dick, 1992) have suggested that mantle melting might be better modelled as an open system process. In this model, the source consists of residual minerals plus transient melt derived from melting lower in the melting column. This process has the effect of reducing the rate at which the incompatible trace elements are depleted. Pearce and Parkinson (1993) have also suggested that retention of melt in the source during partial melting might be an important process. In this model, the melt is a trapped fraction of the magma produced in the previous melting increment. This process can be modelled by simply treating the trapped melt as a phase with a distribution coefficient of 1 in the standard fractional melting equation (Pearce and Parkinson, 1993). Selected Troodos trace element data have been modelled for this process and the variations produced are illustrated in Figure 5.11. Modelled melting trajectories for simple fractional melting, fractional melting with 1% trapped melt and fractional melting with 5% trapped melt are shown.

As Figure 5.11 shows, most of variation in the Zr and Ti data for the *background* harzburgites can be modelled with between 1 and 5% trapped melt. In contrast, the Nb and Ce concentrations in the *background* harzburgites are higher than the modelled values for 5% trapped melt. These facts suggest that the melt trapping model might be a possible explanation for some of the Zr and Ti variation in the *background* harzburgites. However, it should be noted that the modelled trajectories for 5% trapped melt are likely to represent absolute maximum values for this process, because the range of trace element variation in the Troodos clinopyroxenes require the melting process to be nearly fractional. The fact that in Figure 5.11a, the whole-rock Al_2O_3 data plot at lower values than those achieved by 30% fractional melting with 5% trapped melt, supports this suggestion. Therefore, if melt trapping has occurred in the Troodos Massif it can only have been a minor process, and some additional process is required in order to explain the variation in the whole-rock incompatible element concentrations.

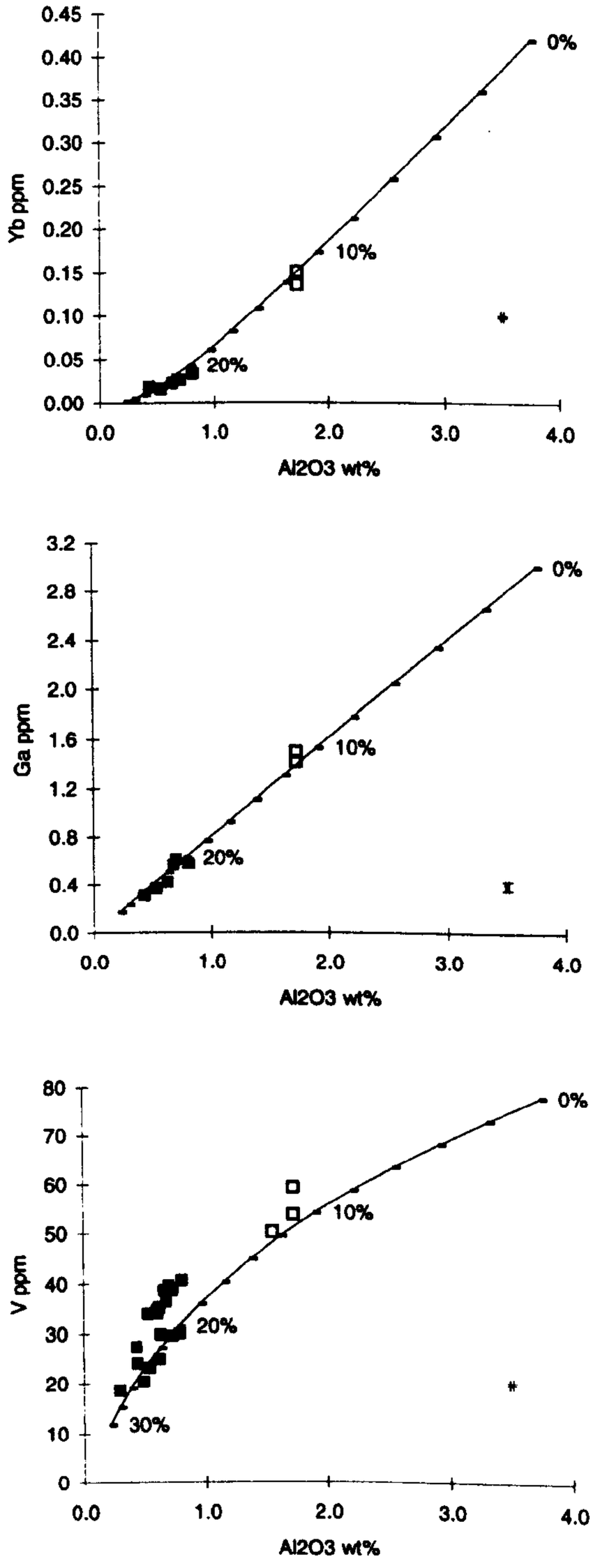

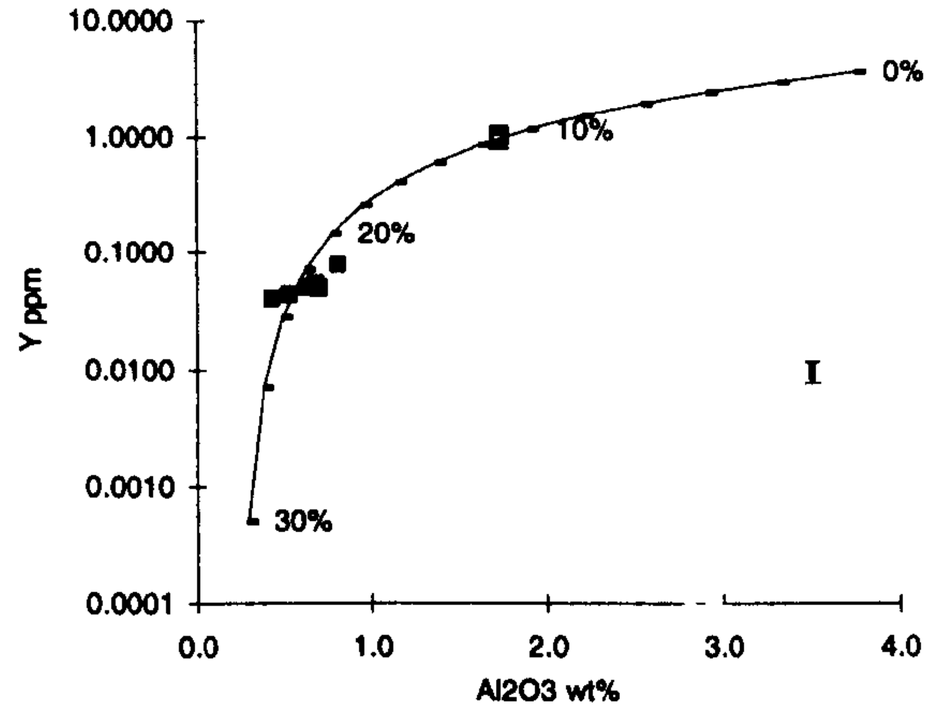

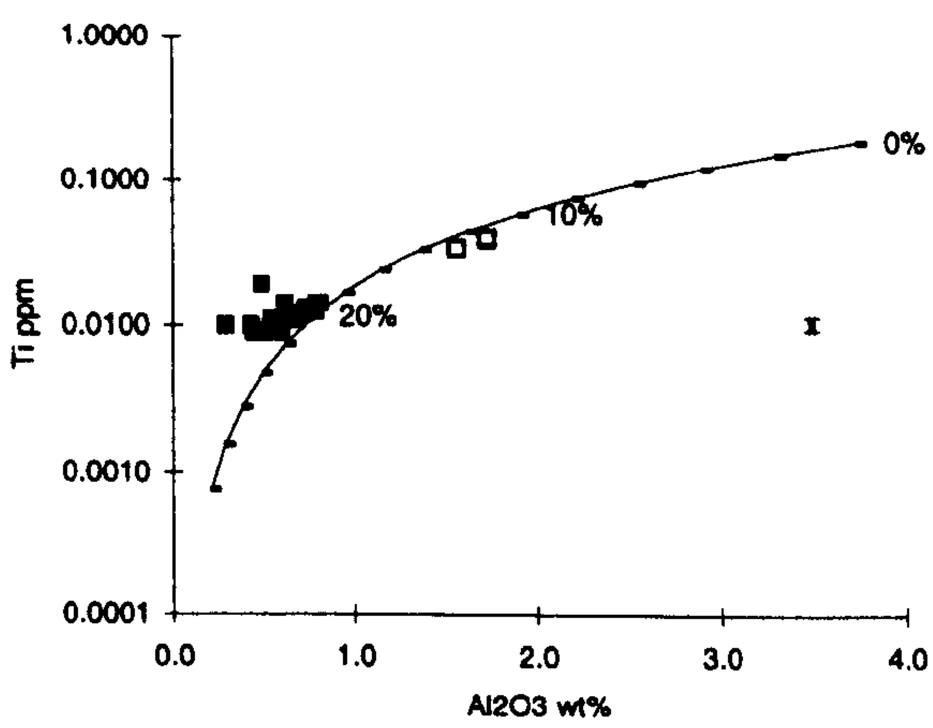

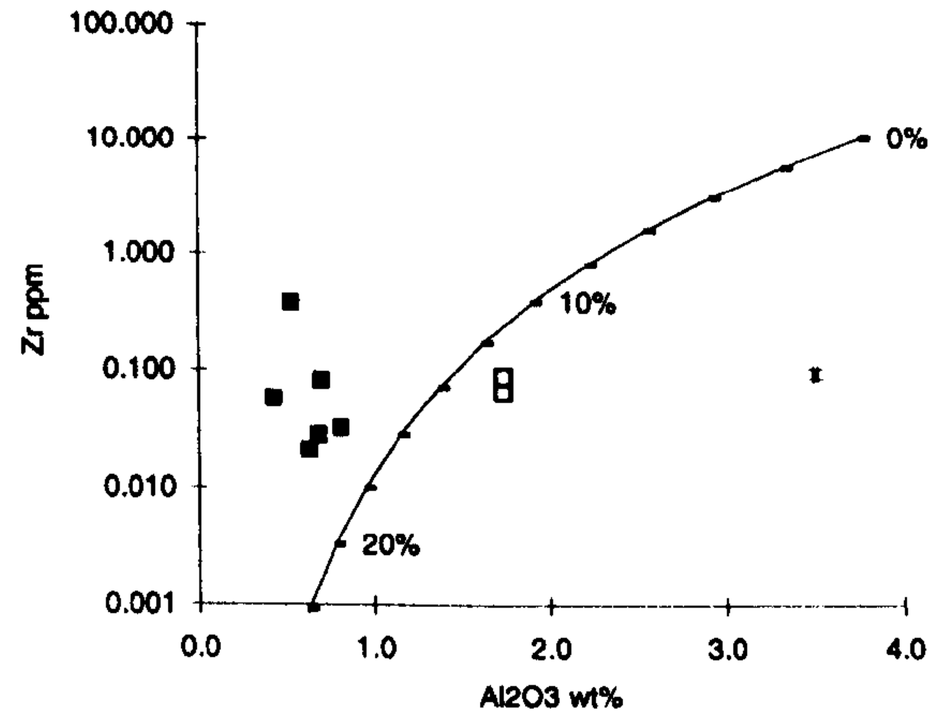

Figure 5.9. Graphs illustrating the variation of selected trace elements with Al_2O_3 and calculated fractional melting trends; tick marks on the fractional melting trajectories are at 2% melting intervals.

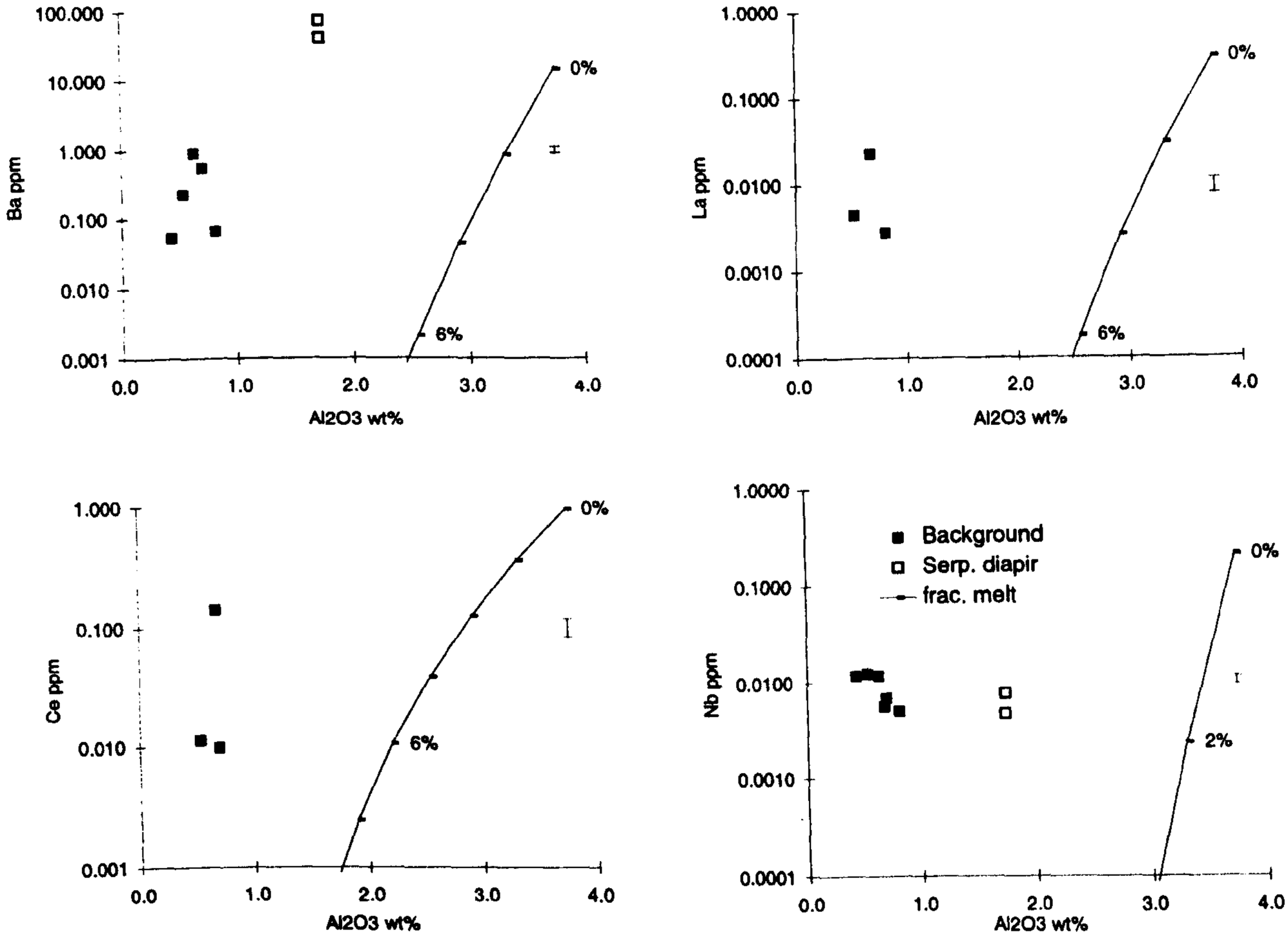

Figure 5.10. Plots illustrating the variation of Ba, La, Ce and Nb with Al_2O_3 and calculated fractional melting trends, tick marks on the fractional melting trajectories are at 2% melting intervals.

As noted in Chapter 4, the Johnson and Dick (1992) model accounts for LREE enrichment in clinopyroxenes by adding fertile melts, from deeper in the melting column, to the source. The melts could be variable in composition if the mantle at depth is heterogeneous. The evidence for addition of incompatible elements to the Troodos harzburgites by metasomatic melts/fluids is discussed in more detail below.

The fact that the Troodos data for Y and the HREE are reasonably modelled by fractional melting in the spinel facies suggests that melting was not initiated in the higher pressure garnet facies. To test this, the Yb-Al_2O_3 data are also modelled for fractional melting in the garnet facies (the garnet distribution coefficients used were Yb = 4.03 and Al = 1.5, Pearce and Parkinson, 1993). In this case, the depletion of the HREE in the source should be much slower than in the spinel facies model, because garnet strongly partitions the HREE. The results of the modelling are compared with the spinel facies data and Troodos harzburgite data in Figure 5.12.

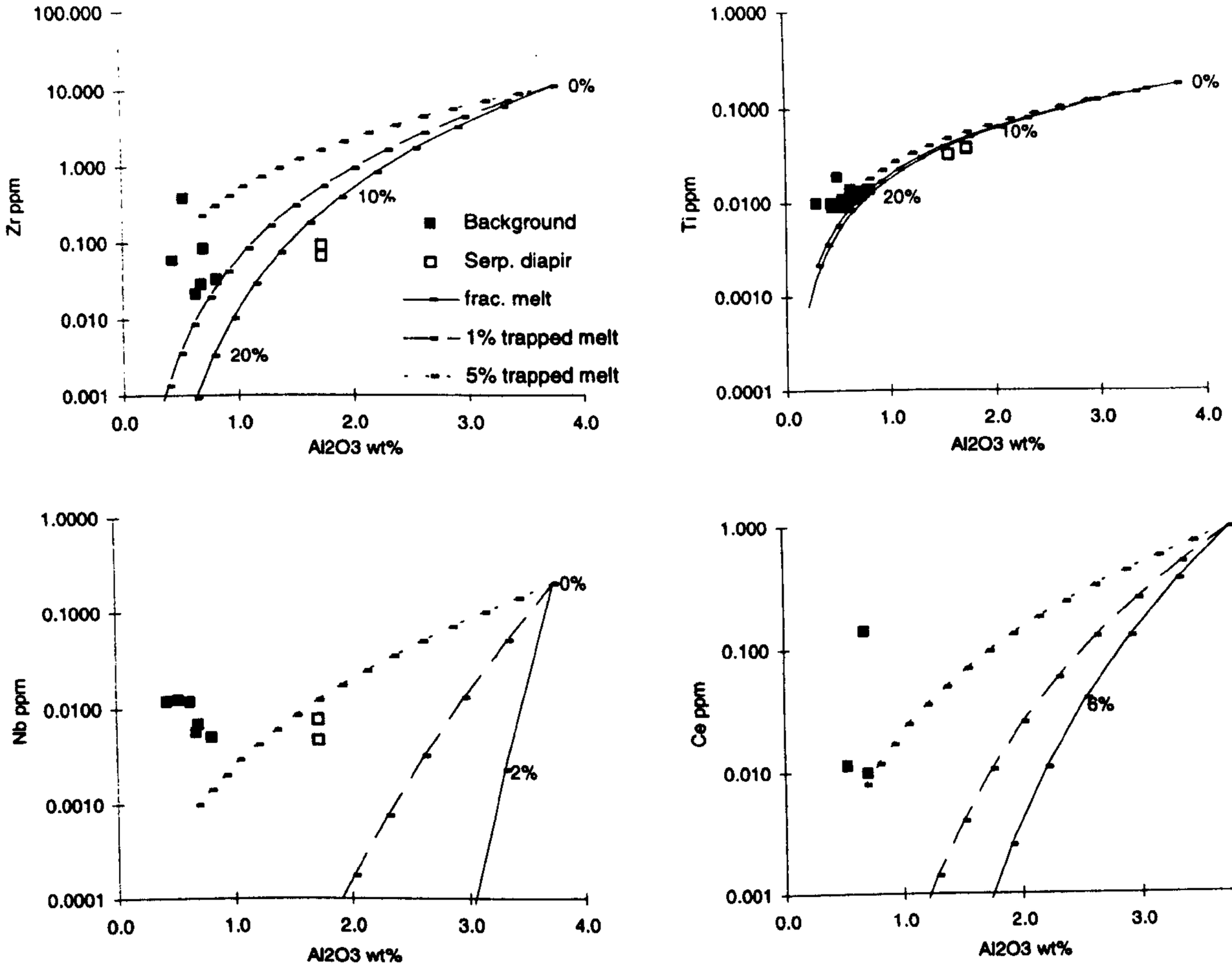

Figure 5.11. Graphs illustrating the variation of selected elements with Al_2O_3 and calculated fractional melting trends. Solid line = simple fractional melting, long dashed line = fractional melting with 1% trapped melt and short dashed line = fractional melting with 5% trapped melt. Tick marks on the melting trajectories are at 2% melting intervals.

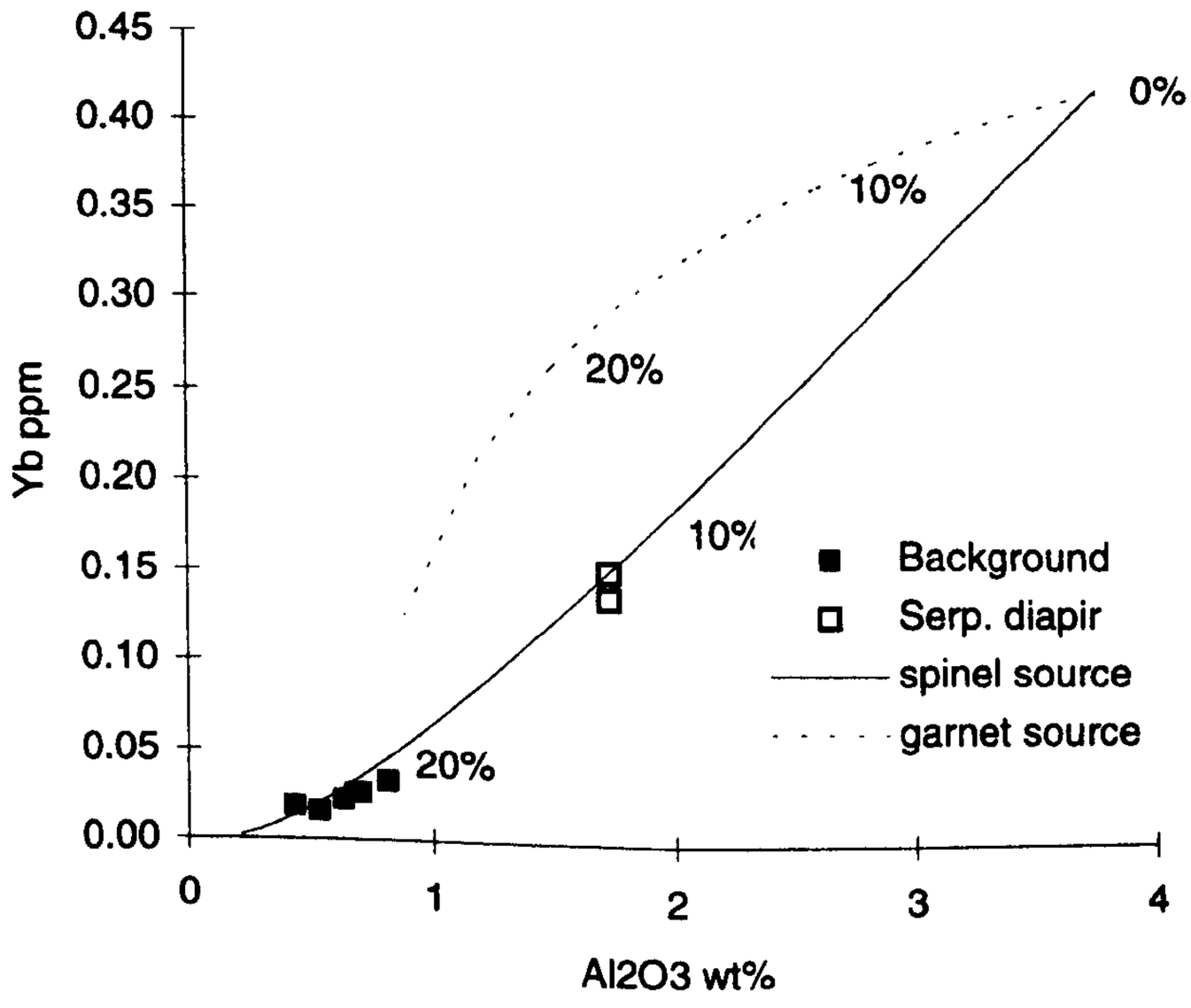

Figure 5.12. Graph comparing the different fractional melting trajectories produced by melting in the spinel (solid line) and garnet (dashed line) stability fields.

As the graph shows, the spinel fractional melting trajectory models the Troodos data much better than the garnet model. This data agrees with the conclusion reached by Pearce and Parkinson (1993) that melting in present-day volcanic arcs takes place in the spinel lherzolite facies.

5.4.1.1 COMPOSITION OF THE EXTRACTED MELTS

The composition of pooled melts produced by fractional partial melting can be calculated using a mass balance approach (Frey *et al.*, 1985). The full details of the calculation are given in Appendix C and only the salient points are outlined here. The calculation assumes that the harzburgites are simple residues without any trapped melt, and requires a source composition to be assumed. For the calculation, the same source used for the fractional melt modelling was used, namely the fertile MORB mantle of Pearce and Parkinson (1993). The calculation also requires the FeO and MgO contents of olivines in the residue to be known. Analytical data were available for these parameters in the *background* harzburgites but not for the serpentinite diapir samples. Therefore, olivine compositions for the serpentinite diapir samples had to be estimated. The values were obtained by matching the whole-rock Al_2O_3 contents for the serpentinite diapir samples with the same parameter in spinel facies Ronda peridotites (Frey *et al.*, 1985), which have been interpreted as melt residues. The appropriate olivine composition from the matching Ronda sample was then used in the calculation.

The errors inherent in this calculation are likely to be quite large because the melting process, or the chosen source composition, may be inaccurate, and because of the range of distribution coefficients that could be used. The calculated melt composition is therefore, given as a bracketed range of values, which delimit the minimum and maximum possible values of the melt chemistry. The calculated melt chemistries for melts in equilibrium with the *background* harzburgites and the serpentinite diapir samples are summarised in Table 5.6.

As the data show, the melts in equilibrium with the *background* harzburgites are highly magnesian and have high Ti and Cr contents. The Mg# values calculated in Table 5.6 fall within the range of melt Mg# values calculated from the olivine data (see Chapter 4, Section 4.6.4), and supports the conclusion that melts in equilibrium with the Troodos harzburgites would have had major element chemistries similar to island-arc basalts.

	Background	Diapir		*Background*	Diapir
SiO_2	45.6-51.8	48.1-49.1	CaO	9.8-14.0	8.9-9.0
TiO_2	0.59-0.91	0.16-0.17	Co	8-24	12-40
Al_2O_3	11.4-17.2	13.2-14.3	Cr	868-3247	266-1663
FeO_t	7.7-9.9	10.2-10.3	V	200-230	174-191
MnO	0.14-0.16	0.16-0.17	Sc	19-42	3-21
MgO	12.1-18.2	18.6-18.9	Ni	436-809	968-1089
Mg#	76.6-78.6	79.1-79.2			

Table 5.6. Summary of calculated melt compositions; oxides in wt% and trace elements in ppm. Melts calculated for 6 *background* harzburgite samples and 2 serpentinite diapir samples.

The serpentinite diapir melts have higher Mg# values than the *background* harzburgites, a result which is surprising considering their more fertile mineralogy and whole-rock chemistry. Serpentinite diapir melts also have higher Al_2O_3, FeO_t, Ni and lower TiO_2 and Sc contents than the *background* harzburgite melts. Notably the MgO contents of the two modelled melts are similar, therefore, the difference in Mg# between the *background* harzburgites and serpentinite diapir modelled melts must reflect the variation in the calculated FeO_t contents of the melts. As discussed in Section 5.4.1 in relation to the FeO_t - Al_2O_3 graph in Figure 5.8, the partition coefficient of Fe is unlikely to be a fixed value throughout the melting interval due to the effects of P,T and fO_2. The anomalously high Mg# of the serpentinite diapir melts compared to the *background* harzburgite melts is, therefore, interpreted as an artefact of the modelling process, and reflects the imprecision inherent in modelling analytical data without tightly constrained partition coefficients.

5.4.2 REACTION WITH MELTS

The fact that the abundances of several incompatible trace elements (e.g. Ti, Zr and the LREE) are difficult to reconcile with a fractional melting model has been mentioned above. The same conclusion was reached in Chapter 4 regarding the Ti_{spn}, Na_{cpx} and Ni_{ol} values in samples from the *Anomaly 1* harzburgites, the *top-of-the-sequence* harzburgites and the harzburgite *xenoliths* in the crustal dunite. In this section, the whole-rock data from these samples is examined to see whether the mineral chemistry variations are matched by whole-rock trace element variations.

The data presented so far in this chapter, and the evidence from the trace element variations in the Troodos clinopyroxenes, suggests that the elements best able to track partial melting variations are Y and the HREE, whereas Zr and the LREE have abundances controlled by some other process. The variations of the LREE and Zr in the Troodos sequence harzburgites are illustrated in Figure 5.13. In Figure 5.13, the element ratios are arranged with the more compatible element as the denominator. Partial melting will therefore cause the ratios to decrease, whereas processes which preferentially enrich the incompatible elements will increase the ratios. Calculated fractional partial melting vectors are also illustrated in Figure 5.13.

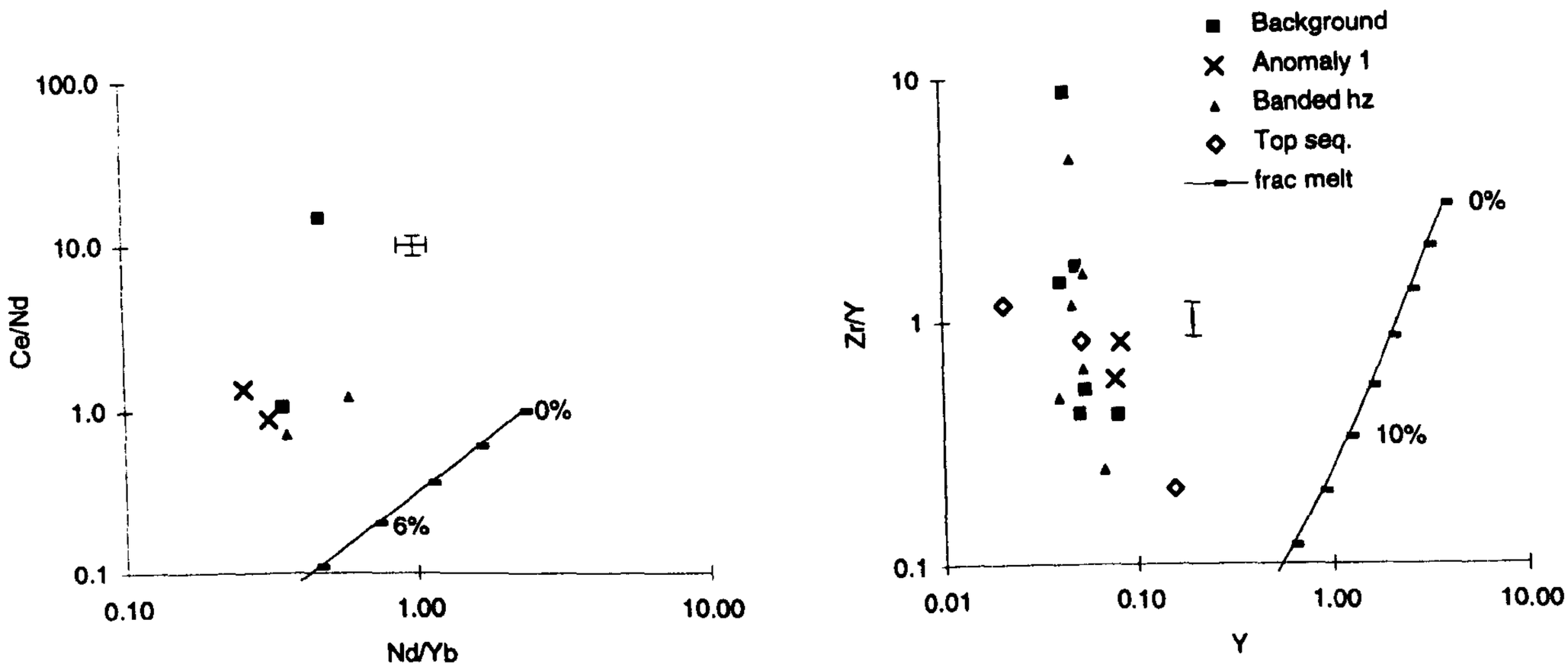

Figure 5.13. Plots illustrating the variation between Ce/Nd - Nd/Yb and Zr/Y - Y for the Troodos harzburgites.

Figure 5.13 shows that the incompatible/compatible ratios are higher than those which could be generated by fractional partial melting alone, which agrees with the evidence from the trace element-Al_2O_3 graphs (Figure 5.10). The distribution of the different harzburgite sub-types on the graphs also suggests that, unlike the mineral parameters mentioned above, the whole-rock enrichments are pervasive and not restricted to any particular locations in the sequence.

Numerous studies of peridotite geochemistry have shown that peridotites with depleted major element chemistries also have enriched trace element abundances. This characteristic is usually attributed to a two stage process involving a partial melting event followed by selected re-enrichment of the trace elements by transient melts or fluids. Eggler (1987) has shown that the HFSE are much more soluble in melts than fluids. It should therefore be possible to distinguish between melt metasomatism and fluid

metasomatism on the basis of HFSE abundances. To test whether the metasomatic agent in the Troodos sequence can be further characterised, the whole-rock Zr/Y and Ce/Y ratios for harzburgites have been plotted in Figure 5.14.

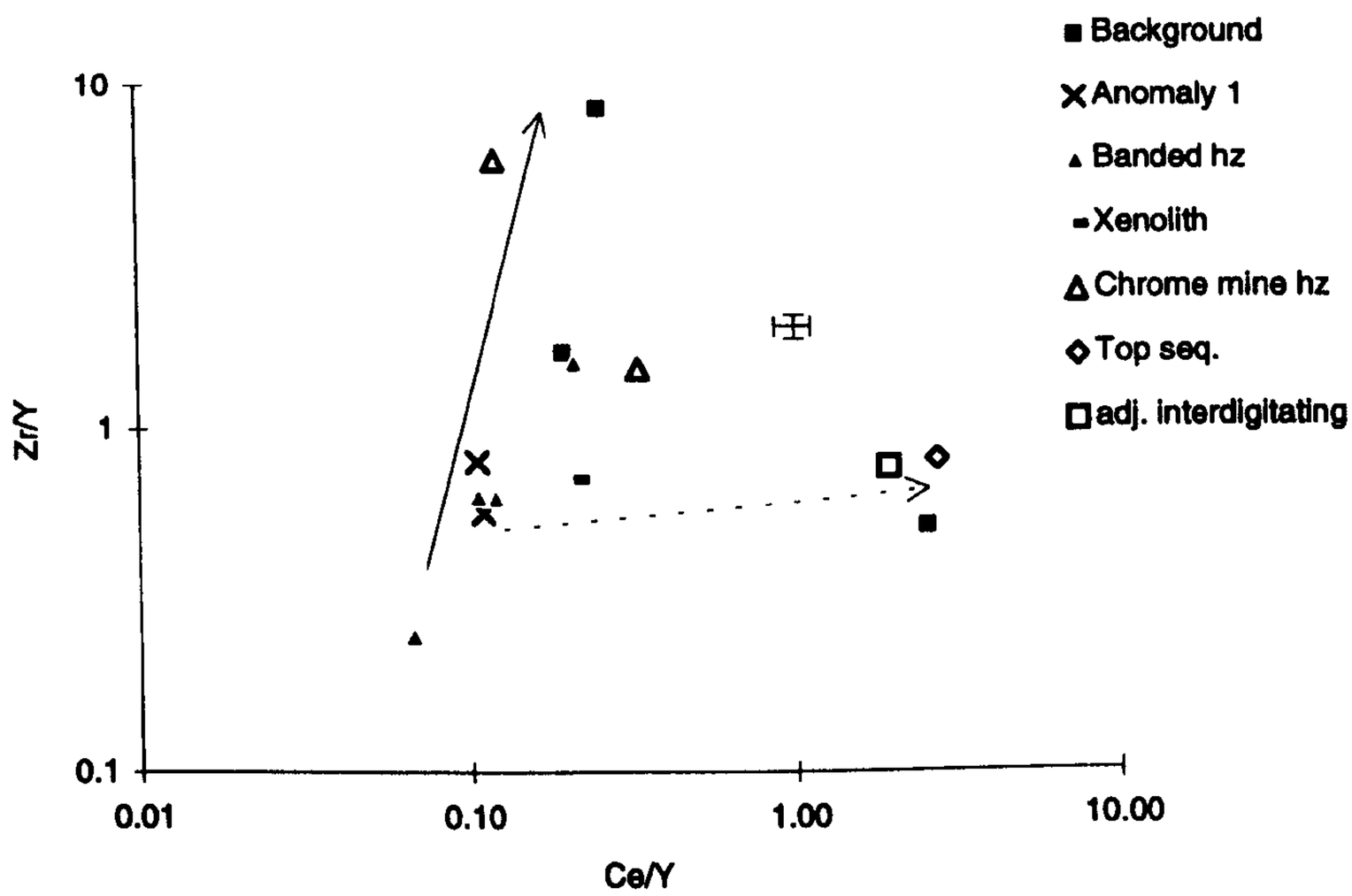

Figure 5.14. Graph illustrating the variation of Zr/Y - Ce/Y in the Troodos harzburgites.

The graph shows that two enrichment trends can be distinguished: one trend to high Zr/Y values at reasonably constant Ce/Y values; and a second trend towards higher Ce/Y values for constant Zr/Y. On the basis of the data presented by Eggler (1987), these trends would be broadly consistent with two different metasomatic agents: a melt which would be capable of producing higher Zr/Y ratios; and a fluid which would be capable of producing higher Ce/Y ratios but not Zr/Y ratios. However, as pointed out in recent papers (e.g. Zinnrebe and Foley, 1994), no consensus has yet been reached about the trace element characteristics of different metasomatic agents. Therefore, the conclusions drawn from the Troodos data should be regarded as speculative in the absence of other supporting data, such as isotopic evidence.

5.5 THE ORIGIN OF DUNITES

In Chapter 4, two main processes were proposed to explain the formation of dunites in the mantle sequence: reaction between melts and harzburgite, and crystallisation from melts. In this section, the dunite whole-rock data is examined in the light of these processes. The data are sub-divided on the basis of structural attitude of the dunite in the same way as in Chapter 4.

Frey *et al.* (1985) suggest that the Ni content of mantle lithologies is a good discriminant between melting and crystallisation processes. During mantle melting, Ni values will increase slowly in the residue because the melt-mantle distribution coefficient is >1, and the resulting lithologies will have a small range of Ni contents. The variation in the Ni content of the Troodos *background* harzburgites (see Figure 5.8) supports this conclusion. However, in cumulate lithologies, the Ni content will decrease rapidly because olivine, which is a liquidus phase in primitive melts, strongly partitions Ni. The resulting lithologies will therefore have a large range of Ni values. The variation of Ni in the Troodos dunites is illustrated in Figure 5.15. Data for the *background* harzburgites is also shown on the graph.

In a similar way, the Cr contents of partial melting residues will have a limited variation as spinel is consumed relatively slowly during melting. However, lithologies crystallised from melts will have a large range of Cr values because spinel is also a liquidus phase in primitive melts, as evidenced by the large number of chromitite occurrences in the Troodos mantle section. The variation in Cr content of the dunites is also illustrated in Figure 5.15.

Figure 5.15a shows that only the crustal dunites trend unequivocally towards lower Ni values, consistent with a melt crystallisation origin. In contrast, most of the dunites in the mantle sequence plot towards higher Ni and lower Al_2O_3 values than the *background* harzburgites. These characteristics would be consistent with an origin as residues of extreme partial melting. However, the Cr data (Figure 5.15b) suggest that many of the cross-foliation and parallel-to-foliation dunites are too Cr-rich to have an origin as residues.

An alternative possible process for dunite formation is reaction between melts and mantle lithologies (Quick, 1981a; Keleman *et al.*, 1992; Edwards and Malpas, 1996). In this process, pyroxenes are dissolved and a greater mass of olivine and spinel may be crystallised. The removal of a low-Ni phase (pyroxene) and crystallisation of a high-Ni phase (olivine), will result in the final lithology having a higher Ni content than the starting composition. Furthermore, the whole-rock Al_2O_3 content will decrease because the main aluminous phase (pyroxene) is removed by the melt. The high-Ni and low-Al contents in the mantle dunites could therefore be indicative of a reaction process between melts and the host harzburgites. These trends are also equivalent to those expected to result from partial melting . The high-Ni, low-Al dunites could, therefore, be interpreted as residues from greater degrees of melting than those recorded by the harzburgites. As

pointed out in Chapter 4, Ti is a sensitive indicator of melt interaction. Residual lithologies are expected to have low-Ti contents, whereas melts have high-Ti concentrations. The Ti-Al_2O_3 variation is illustrated in Figure 5.15c. As the figure shows, the dunites generally have much higher whole-rock Ti contents than would be anticipated if they had formed by extensive partial melting. The high Ti contents are, however, consistent with melt involvement, and support a process of melt-mantle interaction for the formation of the Troodos dunites.

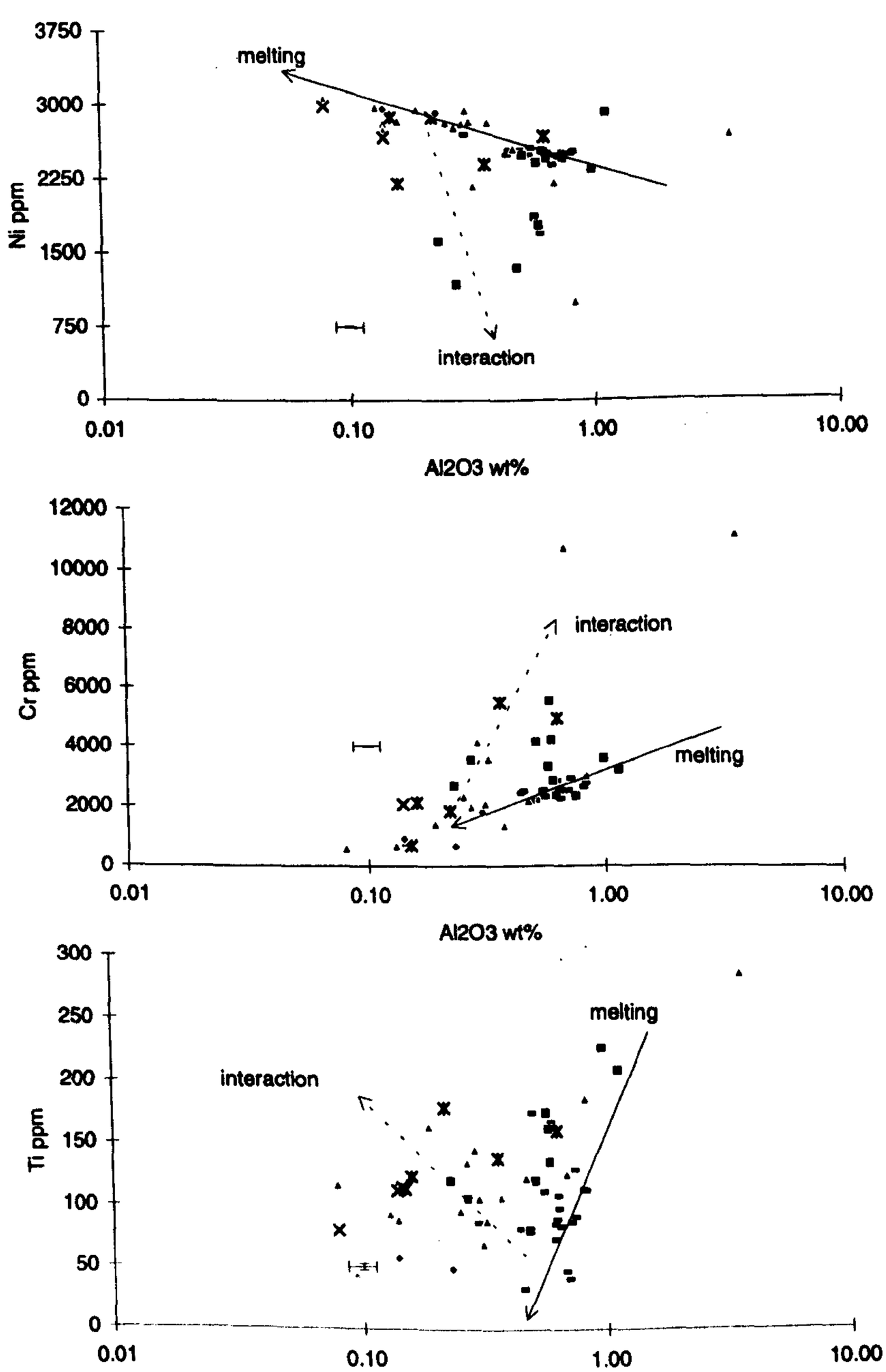

Figure 5.15. Plots illustrating the variation in whole-rock chemistries displayed by the Troodos dunites.

5.5.1 THE EFFECTS OF DUNITE FORMATION ON HARZBURGITE CHEMISTRY

The chemistry of harzburgites sampled adjacent to dunite bodies is illustrated in Figure 5.16 in terms of Ni-Al_2O_3 and Ti-Al_2O_3 variation. The harzburgites are not differentiated in terms of the structural attitude of the adjacent dunite, except for those adjacent to interdigitating dunites which have the best field evidence for dunite-harzburgite reaction (see Chapter 2).

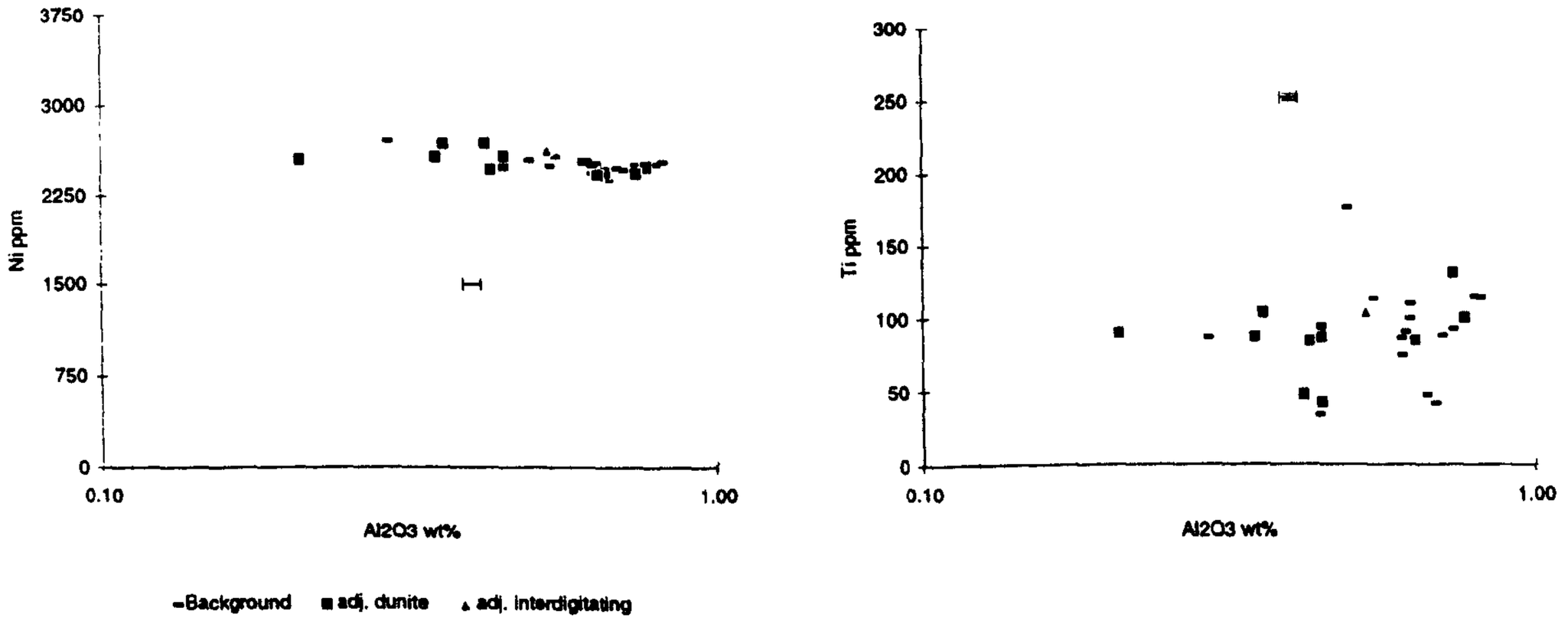

Figure 5.16. Plots illustrating the whole-rock chemistry of the harzburgites sampled adjacent to dunites compared to *background* harzburgite compositions.

Figure 5.16 shows that the harzburgites sampled adjacent to dunites generally have Ni and Ti contents similar to those of the adjacent dunite. This variation is similar to that shown by the mineral chemistry data (see Chapter 4), and suggests that dunite formation influences the chemistry of the enclosing harzburgite. Notably, despite the interdigitating dunites showing the best field evidence for dunite-harzburgite reaction, the harzburgite sampled adjacent to these dunites is not significantly different in composition to the other wallrock harzburgites. This may be because the compositions of the wallrock harzburgites is buffered by the greater mass of the surrounding harzburgite, compared to the mass of the reacting melt, and this may limit the amount of geochemical variation that develops in the wallrock harzburgites.

5.6 THE ORIGIN OF PYROXENITES

The chemistry of the *orthopyroxenite A* and *B*, clinopyroxenites and olivine-clinopyroxenites is illustrated in Figure 5.17. Unfortunately, only a few analyses of the pyroxenites were made because of the difficulty of obtaining representative samples from the deeply weathered exposures.

Two separate trends can be distinguished on the graphs in Figure 5.17; one towards the composition of the olivine-clinopyroxenite analysed and the second towards the composition of the *orthopyroxenite B* sample. As pointed out in the Mineral Chemistry Chapter, the variation of spinel compositions in the pyroxenites can be subdivided into two trends. The Type I trend was one of Cr-Fe-Ti enrichment in spinels and the end-member composition was that of the olivine-clinopyroxenities. The Type II trend was one of Al-Mg enrichment in spinel and was typical of the variation shown by the *orthopyroxenite B* bodies.

The fact that the trends in the whole-rock data shown in Figure 5.17 have the olivine-clinopyroxenite and the *orthopyroxenite B* as their end-members, suggests that they are the equivalent of the trends defined by the variations in spinel chemistry. The trends on Figure 5.17 have therefore been labelled I and II, where the Type I trend is towards the composition of the olivine-clinopyroxenite and the Type II trend is towards the composition of the *orthopyroxenite B*. Of the limited number of samples analysed, the *orthopyroxenite A* sample lies on the Type II trend and the clinopyroxenites on the Type I trend.

In Chapter 4, the mineral chemistry trends in the Type I pyroxenites were shown to be equivalent to the fractional crystallisation trends in the Troodos cumulates. The variations in the whole-rock incompatible element contents (increase with increasing Al_2O_3) and compatible elements (decreasing with increasing Al_2O_3), are consistent with these pyroxenites being related by fractional crystallisation. The Type II melts are distinguished from the Type I pyroxenites by lower abundances of the HREE, which suggests that they were derived from a more depleted source.

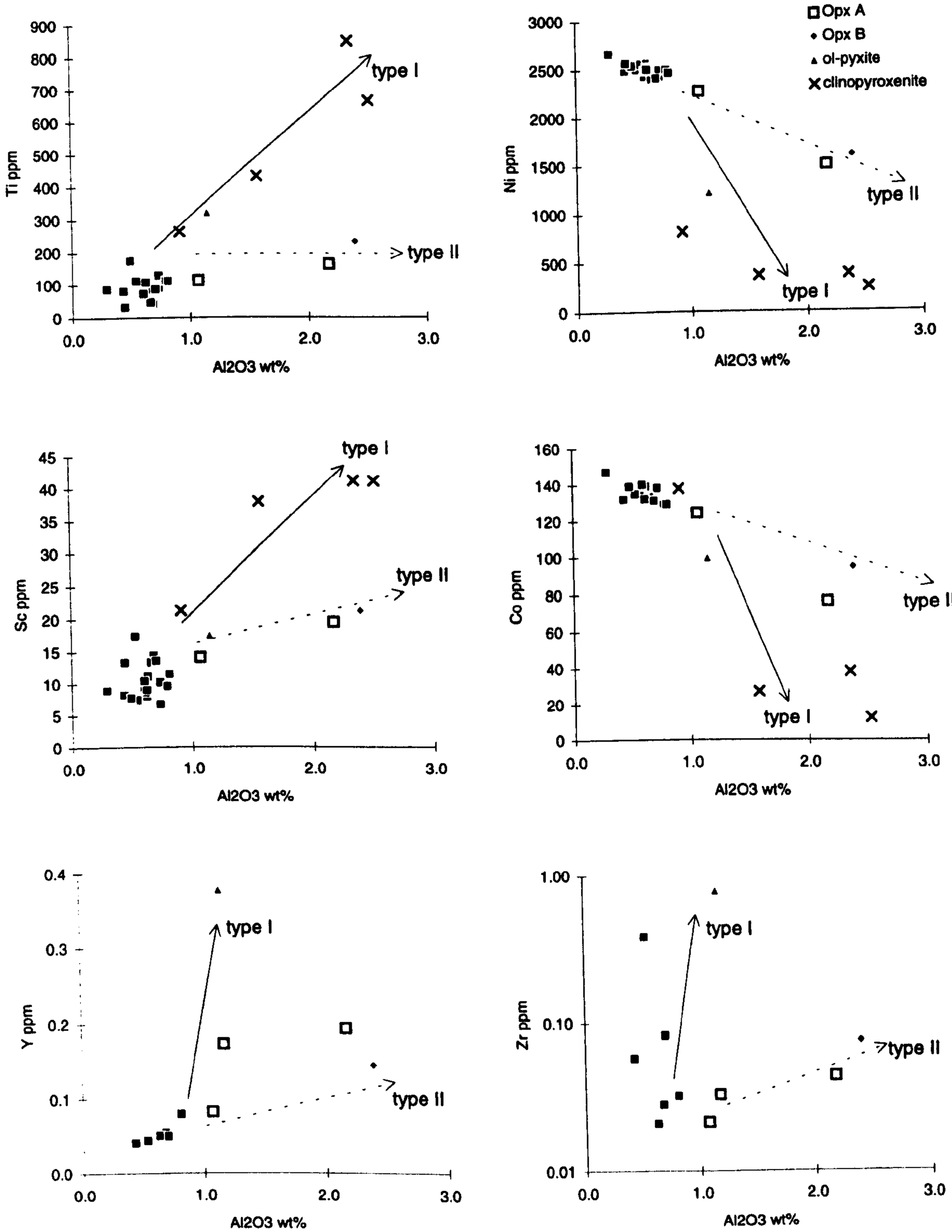

Figure 5.17. Graphs illustrating the variation in pyroxenite whole-rock chemistries with *background* harzburgite compositions shown for comparison. Analytical errors are all less than the size of the points on these graphs. Opx A = *Orthopyroxenite A* intrusion, Opx B = *Orthopyroxenite B* intrusion, ol-pyxite = olivine-clinopyroxenite vein.

The whole-rock trends show that Type I pyroxenites are characterised by high Ti, Sc, Zr and Y contents, and low Co and Ni contents compared to the Type II trend. Notably, the Type II trend plots as an extension of the partial melting trend for Y, Ni and Co. This suggests that the melts which crystallised the Type II pyroxenites was genetically related to the *background* harzburgites whereas, the Type I melt is clearly distinguished in terms of higher Y and Zr concentrations.

Pearce *et al.* (1992) point out that Zr/Ti ratios are useful indicators of source composition. Zr/Ti ratios also clearly distinguish the source of the melt from which the Troodos pyroxenites crystallised. Type I pyroxenites (Zr/Ti = 23.3) have much higher Zr/Ti values than the Type II pyroxenites (Zr/Ti = 1.3-3.4). High Zr/Ti ratios have been interpreted as characteristics of enriched end-member sources (e.g. the subducting slab) in subduction zones (e.g. Pearce *et al.*, 1992), and would be involved in the petrogenesis of boninites. The fact that the Type I melts have high ratios suggests that these might contain a greater subduction component than the Type II melts. The significance of this hypothesis is discussed in more detail in the following chapter.

5.6.1 THE EFFECTS OF PYROXENITE FORMATION ON HARZBURGITE CHEMISTRY

Figure 5.18 illustrates the geochemical variation in the harzburgites collected adjacent to various pyroxenites. Also shown are the compositions of harzburgite samples collected between the pyroxene bands (labelled banded harzburgite) in the harzburgite. Whole-rock values were not obtained from the pyroxene bands themselves because of the problem of adequately separating them from the enclosing harzburgite.

The graphs in Figure 5.18 show that the wall-rock compositions are not clearly distinguishable from the compositions of the *background* harzburgites, and do not plot along the trends defined by the adjacent pyroxenite. This is contrary to the evidence from the mineral chemistry data for spinel and clinopyroxene (Chapter 4), which show that wallrock harzburgite spinel and clinopyroxene have compositions which are intermediate between those of the *background* harzburgites and the pyroxenites. This suggests that reaction between melts and mantle harzburgites is best traced by the chemistry of minor phases. Whole-rock compositions, however, are dominated by the chemistry of the most abundant minerals (olivine and orthopyroxene), which are themselves buffered towards the composition of the surrounding harzburgite by virtue of its greater mass compared to the mass of the reacting melt.

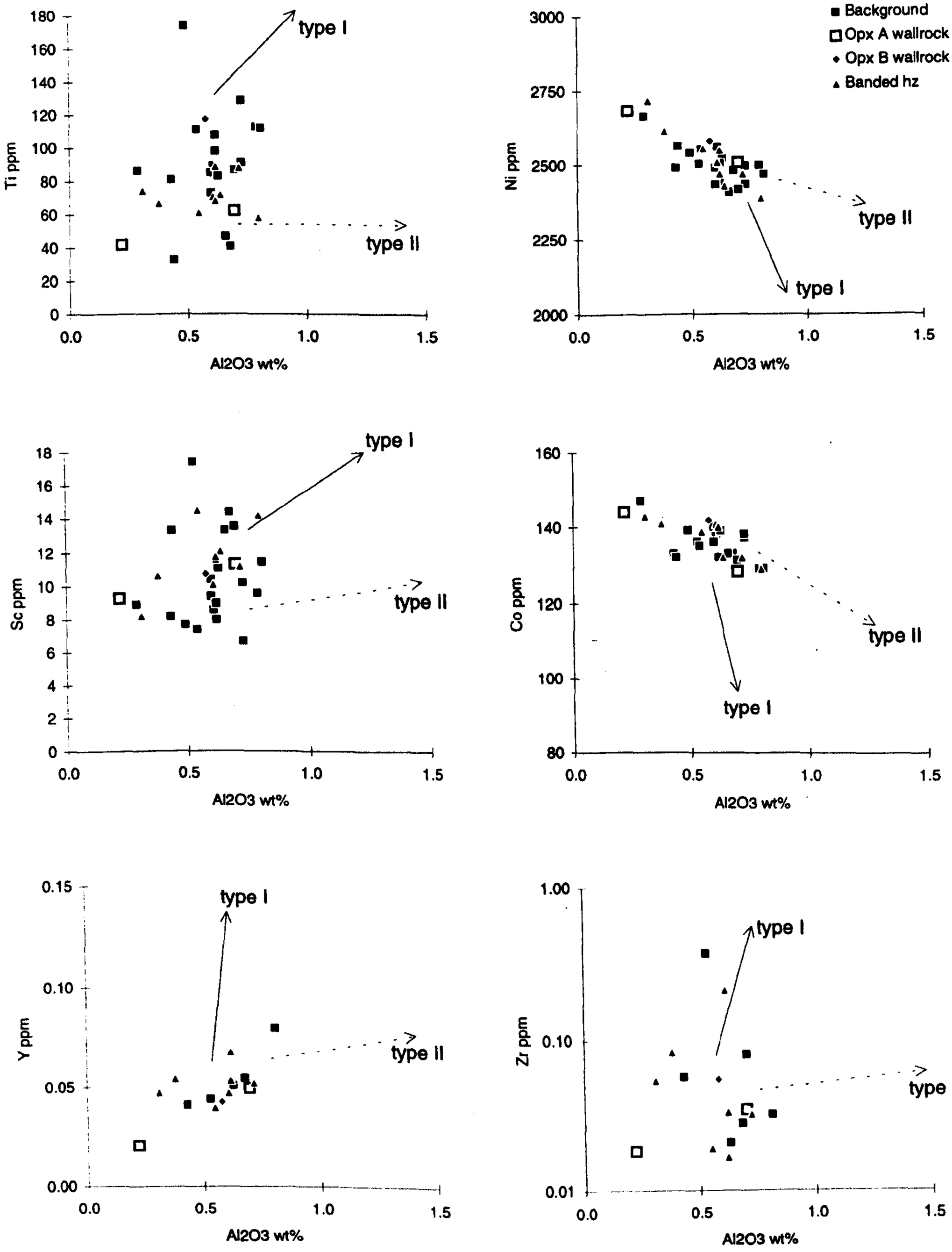

Figure 5.18. Graphs illustrating the chemistry of harzburgites sampled adjacent to pyroxenites, with the *background* harzburgite values shown for comparison; type I and type II vectors redrawn from Figure 5.17.

5.7 SUMMARY

The previous chapters of this thesis have described the field relations, microstructure and mineral chemistry of the mantle sequence exposed in the Troodos Massif. The microstructure and mineral chemistry data both demonstrated that the mantle sequence varied in fertility from the base to the top of the sequence and that this variation was primarily controlled by partial melting processes. Field relations, microstructure and mineral chemistry data also indicate that interaction between the depleted mantle and transient melts has been instrumental in producing a variety of pyroxenitic and dunitic bodies in the uppermost harzburgites and crystallising clinopyroxene and spinel, which are associated with enriched mineral chemistries, at specific locations in the mantle sequence.

In this chapter the major and trace element concentrations in the Troodos peridotites were presented. Variations of elemental abundances with LOI, compositions of vein serpentines and whole-rock data from variably serpentinised *background* harzburgites suggest that, under the serpentinising conditions experienced by the Troodos sequence peridotites, the serpentinisation process in the Troodos samples was largely isochemical. However, Ba, Rb and Sr do appear to be mobile during alteration and these elements were not used in the petrogenetic modelling. Element mobility in the Limassol Forest harzburgites appears to be much higher than in the Troodos sequence harzburgites. The petrographic differences between the harzburgites from the two areas suggests that the greater mobility may be due to the alteration of orthopyroxene in the Limassol Forest harzburgites.

Variations of major and trace elements with Al_2O_3 in the *background* harzburgites are consistent with the peridotites being the residues from extensive partial melting. This agrees with the conclusions drawn from the mineral chemistry data in Chapter 4. Modelling of the data suggests that the melting process was nearly fractional. The *background* harzburgites are modelled by 20 to 30% fractional melting of a FMM source and the serpentinite diapir peridotites by 10 and 15% fractional melting. These partial melting estimates are similar to those obtained from the mineral chemistry data.

Fractional melting trends fail to model the variation in the incompatible element contents of the *background* harzburgites. An open system melting process, involving the trapping of a fraction of the partial melt in the peridotite as melting proceeds, could explain some of the variation in the Zr data. However, to account for the entire Zr variation in the *background* harzburgites by a melt trapping model would require an unrealistically high

percentage of trapped melt, and the melting model would then not be able to reproduce the low Al_2O_3 contents of the Troodos harzburgites. Furthermore, the trapped melt model does not result in sufficiently high Nb and LREE values to explain the variations of these elements in the *background* harzburgites. These facts suggest that if trapping of melt produced *in situ* did occur, it could only have been a relatively minor factor in producing the elevated incompatible element contents of the Troodos harzburgites. Instead a model of widespread melt/fluid interaction is preferred. This model agrees with that proposed to explain the variation in clinopyroxene trace element chemistries.

The harzburgites identified as having the most enriched mineral chemistries (the *Anomaly 1* and *2* harzburgites, *top-of-the-sequence* harzburgites and the harzburgite *xenoliths*), also have whole-rock enrichments in Zr and the LREE. The variations in the Zr/Y and Ce/Y ratios define two trends. One of increasing Zr/Y for constant Ce/Y, and a second of increasing Ce/Y for constant Zr/Y. These trends may reflect interaction between the peridotites and melts, and peridotites and fluids/melts, respectively.

The variations in dunite and pyroxenite whole-rock chemistry match those identified in the mineral chemistries. Dunites were probably formed by a combination of direct crystallisation from picritic melts and reaction between melts and peridotites. The Type I pyroxenites (Cr-Fe-Ti_{spn} enriched) are characterised by whole-rock trends of Ti, Sc, Zr and Y enrichment and Ni, Co depletion. These variations are consistent with a fractional crystallisation relationship. The Type II pyroxenites (Mg-Al_{spn} enrichment) plot on an extension of the *background* harzburgite trend. This suggests that they might have crystallised from melts extracted from the Troodos harzburgites during the partial melting event. Variations in Zr/Ti ratios between the two types of pyroxenites suggest that the parental melts were probably derived from different sources.

CHAPTER 6
CONCLUSIONS

6.1 INTRODUCTION

This chapter contains an overview and discussion of the data presented in this thesis, and summarises the principal conclusions of the thesis. The two main themes of the thesis, partial melting processes and melt-mantle interaction in the Troodos Massif, are discussed with reference to the recent theoretical and experimental literature on these subjects. The melting history of the mantle is examined in the light of subduction zone melting models, and the evidence for melt interaction in the mantle sequence is used to evaluate the interaction models of Keleman *et al.* (1992) and Navon and Stolper (1987). The relationship between the geochemistry of the mantle sequence and the overlying crustal lithologies is also discussed.

6.2 THE GEOTECTONIC SETTING OF THE TROODOS MASSIF

The Troodos sequence harzburgites are characterised by high Cr# spinels, high Mg# silicates, high whole-rock Mg# values and very low incompatible trace element contents. The mineral chemistry data presented in Chapter 4 indicated that the *background* harzburgite minerals were similar in composition to forearc peridotites sampled by ODP Leg 125 (Ishii *et al.*, 1992). These forearc peridotites also have high whole-rock Mg# values and low incompatible trace element contents (Parkinson *et al.*, 1992), which supports the hypothesis that these peridotites are recent analogues for the Troodos harzburgites. The fact that the Mg# are high, and incompatible element contents are so low, suggests that the harzburgites are residues from large degrees of partial melting. This is in agreement with melting models which suggest that the degree of melting will be greater in subduction zones than at mid-ocean ridges (e.g. Pearce and Parkinson, 1993).

The fact that the mantle sequence has affinities with subduction zone peridotites agrees with the conclusions reached from the study of Troodos lava chemistries, namely that the erupted magmas have similarities to arc volcanics (Miyashiro, 1973; Pearce, 1975; Cameron, 1985; Rautenschlein *et al.*, 1985; Taylor and Nesbitt, 1988; Bednarz and Schmincke, 1994), and confirms the consensus view that the Troodos Massif has a supra-subduction zone origin. This places constraints on the nature and extent of the partial melting process, and possible source compositions available for magma genesis.

6.3 PARTIAL MELTING IN SUBDUCTION ZONES AND THE TROODOS MASSIF

Numerous studies have examined the nature of the melting process and variety of available source compositions in subduction zones using lava geochemistries. A consensus model would be as follows (Plank and Langmuir, 1988; McCulloch and Gamble, 1991; Davies and Stevenson, 1992; Pearce and Parkinson, 1993). Subduction of sediment and altered oceanic crust releases water into the overlying mantle wedge via a series of dehydration reactions of the hydrous phases. The main mineral involved is likely to be amphibole whose subsolidus stability is pressure-sensitive, and will break down at depths of approximately 100 km. At this depth, the main addition of a water-rich fluid to the overlying mantle will occur. The introduction of volatiles lowers the solidus of the peridotites, initiating melting. The less dense, partially molten mantle will then rise, undergoing more melting as a result of pressure release. The maximum degree of melting that can occur will be limited by composition of the mantle wedge and the length of the melting column. Depleted mantle wedges will have solidi displaced to higher temperatures than fertile wedges and will, therefore, produce less melt. The length of the melting column will be mainly controlled by the thickness of the lithospheric cap, which defines the upper limit to which the diapir can ascend. Thin lithospheric caps will allow longer melting columns and, therefore, greater degrees of melting than thick lithospheric caps. Compared with other geotectonic environments the combination of fluid addition to the mantle wedge and decompression melting results in high degrees of melting in subduction zones. These principles are summarised in Figure 6.1.

It can be seen from the above description that there will be three components involved in melt generation: the subducting slab, the fluid produced by dehydration reactions and the mantle wedge. The mantle wedge itself could have a range of compositions depending on the history of the mantle section prior to subduction; for example, the wedge could have a fertile MORB source composition, be enriched through mixing with a plume source or be depleted from an earlier melting event. Some authors have also proposed that the base of the lithospheric cap could also melt (Bednarz and Schmincke, 1994).

From the above discussion it is clear that subduction zone peridotites will record higher degrees of melting than peridotites from other geotectonic settings. Mineral chemistry and whole-rock parameters measured in the Troodos Massif both suggest that the *background* harzburgites are residues from 20 to 30% melting of a fertile MORB source. In contrast, the serpentinite diapir samples are less refractory and probably are residues from 10 to 15% melting of a fertile MORB source. These melting values compare with

melting estimates of between 20 and 33% for Leg 125 forearc peridotites (Parkinson *et al.*, 1992), and between 8-20% (Johnson and Dick, 1992) and 5-25% (Johnson *et al.*, 1990) for abyssal peridotites. Parkinson *et al.* (1992) suggest that the very depleted chemistries of the Leg 125 forearc peridotites was achieved by two melting stages; the first stage involving approximately 15% partial melting of a fertile MORB source at a spreading centre, and the second stage of 5 to 10% melting in a supra-subduction zone environment.

A.

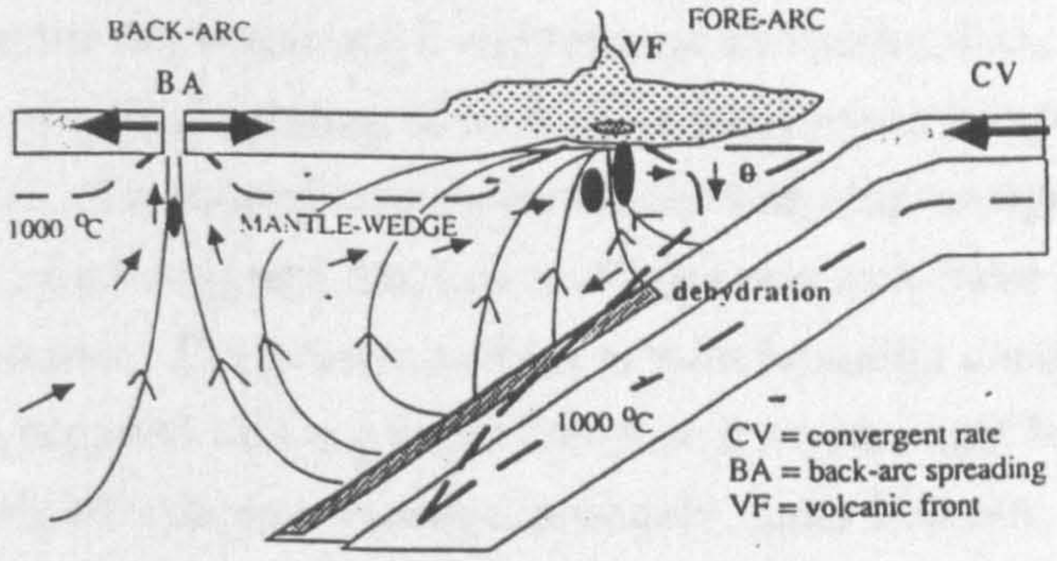

B.

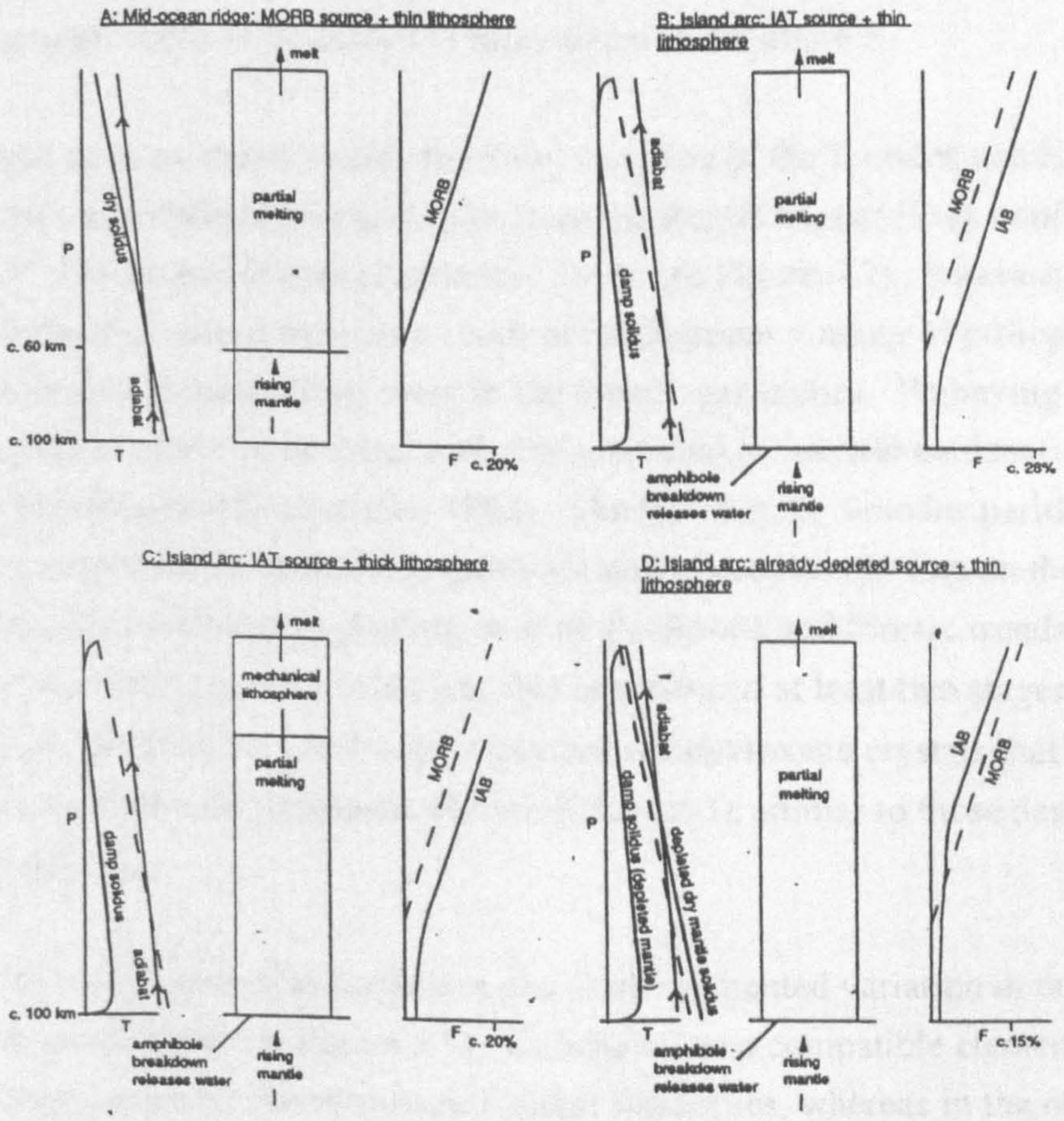

Figure 6.1. a) Sketch section of a typical subduction zone, redrawn from McCulloch and Gamble (1991). b) Figures illustrating the approximate amount of melting that can be produced for variable source composition and thickness of lithospheric cap (redrawn from Pearce and Parkinson, 1993).

The main geochemical division in the Troodos Massif is between the serpentinite diapir peridotites, which in terms of their mineral chemistry are similar to abyssal harzburgites, and the *background* harzburgites, which are mineralogically similar to forearc peridotites. If the Parkinson *et al.* (1992) two stage model is applicable to the Troodos peridotites, it is possible that the serpentinite diapir samples represent the residue from the first melting event and the *background* harzburgites the residue from the second stage of melting. The fact that the *background* harzburgites plot at the depleted end of the serpentinite diapir melting trend for the whole-rock and mineral chemistry data, indicates that they could be the products of partial melting of a source equivalent in composition to the serpentinite diapir samples. The chemical similarities between the *background* harzburgites and the forearc peridotites suggests that this melting event may have occurred in a subduction zone environment. The presence of lavas with boninitic chemistries in the upper pillow lavas (UPL) supports this argument, because the consensus for boninite genesis requires partial melting of a depleted source, probably under hydrous, but water-undersaturated, conditions. The relationship between the chemistry of the mantle peridotites and the overlying crustal rocks is discussed in more detail in Section 6.5.

As discussed in more detail below, the SiO_2 variation in the Troodos peridotites plots on a segmented trend defined by peridotites from the Ronda Massif (Frey *et al.*, 1985) and the Leg 125 forearc peridotites (Parkinson, 1993; see Figure 6.2). Parkinson (1993) interpreted the segmented trend as a result of incongruent melting of orthopyroxene during the second stage melting event in the forearc peridotites. Embaying of orthopyroxene crystals by neoblastic olivine was cited as textural evidence for this process (Girardeau and Lagabrielle, 1992). The fact that the Troodos peridotites show a similar segmented trend, with the serpentinite diapir samples plotting on the Ronda trend, and the Troodos harzburgites plotting on both the Ronda and forearc trends, supports the suggestion that the Troodos Massif has also experienced at least two stages of melting. Furthermore, the Troodos harzburgites contain orthopyroxene crystals that have embayed margins associated with neoblastic olivine (Chapter 3), similar to those described in the forearc peridotites.

The whole-rock Cr data also displays a distinctly segmented variation in the Troodos peridotites (see Chapter 5, Figure 5.7). Cr behaves as a compatible element in the fertile residues represented by the serpentinite diapir lherzolites, whereas in the more depleted *background* harzburgites Cr behaves incompatibly. As pointed out in Chapter 5, this is likely to be due to a change in the composition of the main aluminous phase as melting proceeds and would be consistent with a two stage melting history for the Troodos harzburgites.

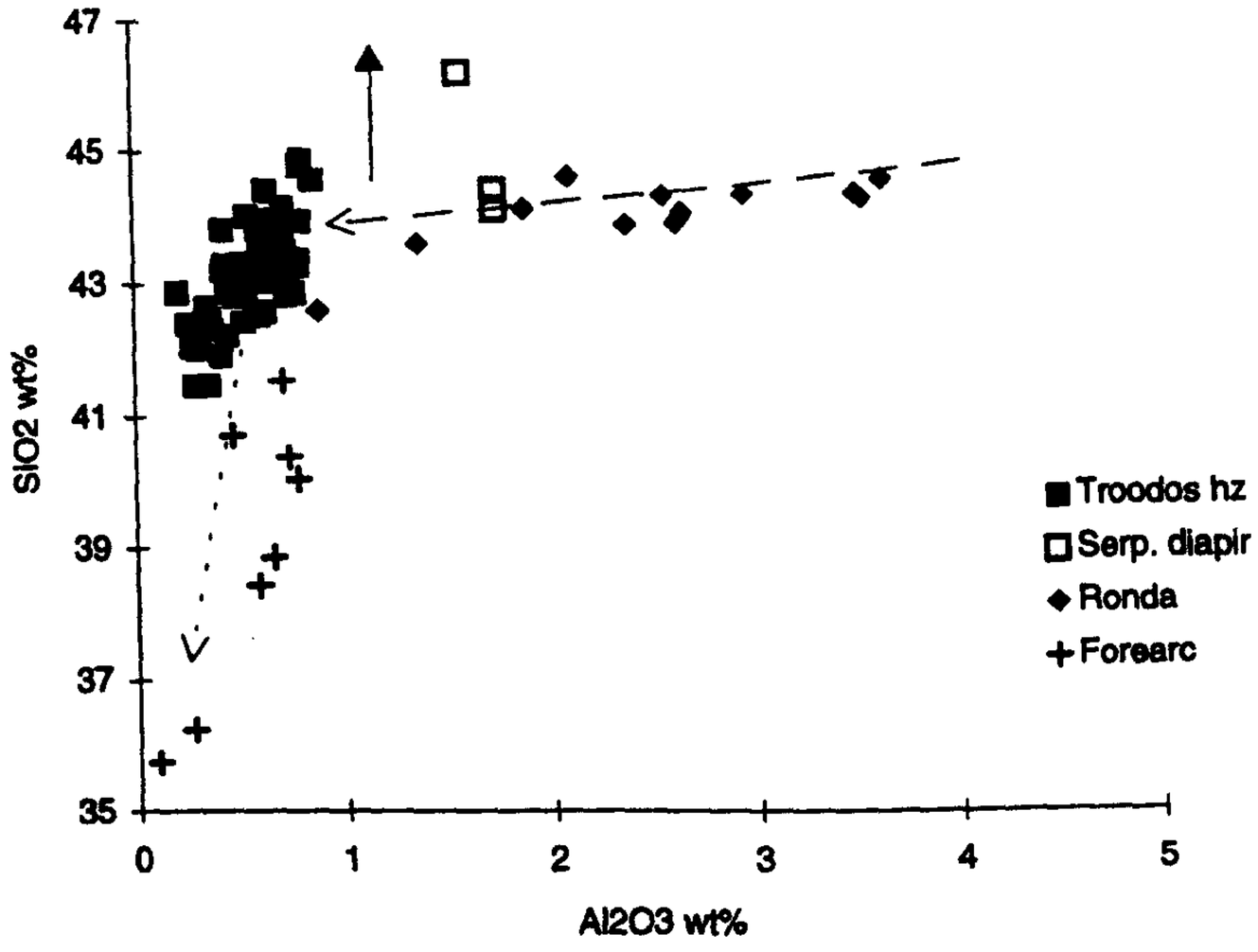

Figure 6.2. Graph illustrating the variation in whole-rock SiO_2-Al_2O_3 in the Troodos peridotites compared with the values in the Ronda (data from Parkinson 1993) and forearc peridotites (data from Parkinson 1993). Dashed lines indicate approximate melting trends, solid arrow shows the effect of serpentinisation.

Melt modelling of the mineral chemistry and whole-rock data suggested that fractional melting, or incremental melting with a very low increment, is the most applicable melting model to explain the geochemical variation in the Troodos peridotites. This agrees with the conclusions reached by Johnson *et al.* (1990) and Parkinson *et al.* (1992) for abyssal and forearc peridotites, respectively. This model implies that melt was efficiently extracted from the mantle and, therefore, that the mantle was permeable at low porosities.

The fact that the incompatible element contents of individual clinopyroxenes and the whole-rocks are higher than would be predicted for a simple fractional melting process was discussed in Chapters 4 and 5. Johnson and Dick (1992) have modelled LREE enriched patterns of abyssal peridotite clinopyroxene using an open system melting process. In this model, the incompatible element content of the source is re-enriched during the partial melting event by the influx of more fertile melts derived from deeper in the melting column. A similar model is envisaged to explain the LREE variation in the Troodos harzburgites and is discussed in Section 6.4.

The source composition used for the melt modelling was a fertile MORB mantle in the definition of Pearce and Parkinson (1993). This is equivalent to the global convecting reservoir from which N-MORB is extracted. The fact that the modelled melting trends produced from this source match the trends defined by the Troodos peridotite data, suggests that the Troodos mantle was not enriched by a plume component as proposed by Kostopoulos and Murton (1992). However, the large degrees of partial melting recorded by the peridotites might mask any signatures of primary source enrichment.

The mineralogy of the source used in the melt modelling for both the clinopyroxene trace element data and whole-rock data was that of a spinel lherzolite. The fact that the HREE distribution was consistent with a spinel-bearing residual lithology, rather than a garnet-bearing residuum, was discussed in Chapter 5. This suggests that melting took place at depths of < 75 km (Wilson, 1989). However, as pointed out above, because the Troodos samples are residua of high degrees of melting, incompatible element evidence for processes occurring during the early stages of melting may be obscured or removed by the later melting events. The fact that no evidence for a garnet bearing residue has been found in the Troodos harzburgites is consistent with data from modern island arc basalts, which also suggests that garnet is not stable in the source (Pearce and Parkinson, 1993).

The oxygen fugacity conditions prevailing during partial melting were discussed in Chapter 4, in relation to the ferric iron content of spinel and the V content of clinopyroxene. The V_{cpx} data show that the serpentinite diapir and *background* harzburgite samples plot on a vector towards lower V_{cpx} values than abyssal peridotites. The *background* harzburgites have similar V_{cpx} contents to forearc peridotites, which are interpreted as the residues of a hydrous, but water-undersaturated, melting event (Parkinson, 1993). These facts suggest that high fO_2 conditions prevailed throughout the melting event. This agrees with volatile contents of 2.1 to 2.3% H_2O in primitive glasses from the Troodos pillow lava sequence (Muenow *et al.*, 1990; see below), which are high compared to MORB (MORB peridotites have primary water contents of up to 0.75 wt% with an average of approximately 0.25 wt%, Johnson *et al.*, 1994).

The fact that both the serpentinite diapir and Troodos sequence peridotites record high fO_2 conditions is significant, because water is incompatible during mantle melting. This means that, in a model of progressive melting from the serpentinite diapir to the Troodos sequence peridotites, the peridotites and melts formed by later melting events should record lower fO_2 and H_2O values. The harzburgites should, therefore, record lower fO_2 values than the serpentinite diapir lherzolites. The fact that the *background* harzburgites

record high fO_2 conditions is most easily explained in the context of the proposed supra-subduction zone setting of the massif by continuous addition of volatiles to the melting zone from a subducting slab. This hypothesis is supported by the data from the pillow lavas (see below - Section 6.5.1) which shows that the youngest lavas originate from a depleted source which had a high H_2O content.

6.4 MELT AND FLUID INTERACTION PROCESSES IN THE TROODOS MASSIF

There are at least three lines of evidence that suggest that melt and/or fluid has interacted with the Troodos mantle sequence: i) pyroxenitic and dunitic bodies have wallrock harzburgites whose composition varies according to the nature of the adjacent intrusive; ii) minerals from certain parts of the sequence (e.g. the *Anomaly 1* and *2* harzburgites) are enriched in incompatible elements and iii) REE patterns in clinopyroxenes are incompatible with an origin via simple fractional melting.

Numerous geochemical studies have shown that depleted peridotites often have enriched incompatible element values (e.g. Menzies and Hawkesworth, 1987, and references therein). These values have conventionally been explained by a two stage process: depletion of the major elements by partial melting followed by selected re-enrichment of the incompatible elements by some metasomatic agent. Early studies were mostly based on mantle xenoliths which do not preserve the original field relationships between enriched and non-enriched samples. More recent studies have attempted to explain the formation of peridotites with depleted major element and enriched trace element signatures by a single process involving reaction between mantle peridotite and transient melts. Mantle-melt interaction theories are usually based on the study of reaction zones in peridotite massifs (e.g. Keleman *et al.*, 1992; Takahashi, 1992), which consist of concentric zones of dunite, harzburgite, lherzolite and plagioclase lherzolite often symmetrically arranged around a central pyroxenite or gabbro. Other studies (e.g. Navon and Stolper, 1987; Bodinier *et al.*, 1990; Godard *et al.*, 1995) have emphasised the role of chromatographic fractionation in developing trace element enrichments.

In this section, the Troodos data are examined to see whether the reaction model (termed 'Keleman-type' reactions in the following text) or the chromatographic fractionation model can explain the geochemical variation in the Troodos peridotites. In the second part of this section, a model is proposed to explain the origin and evolution of the pyroxenite and dunite intrusions and their wallrock harzburgites, the enriched mineral chemistries of the *Anomaly 1* and *2* harzburgites and the clinopyroxene REE patterns.

6.4.1 "KELEMAN" PROCESSES

Keleman *et al.* (1992) have suggested that mantle peridotites are too SiO_2-rich and have ratios of LREE/HREE which are too high to be the residues of partial melting processes. Instead, they propose that the major and trace element variation in mantle peridotites can be accounted for by a single interaction process between the peridotite and a basaltic melt, with or without previous partial melting of the peridotite reactant. The reaction process involves dissolution of clinopyroxene and crystallisation of orthopyroxene (resulting in elevated whole-rock SiO_2 values) and olivine. The symmetrical nature of pyroxenite-dunite-harzburgite-lherzolite reaction zones and the presence of trains of spinel grains through harzburgites and dunites (produced by dissolution of Cr-rich pyroxene) were cited as field evidence for this process. Chemically, the progress of the reaction is characterised by increasing whole-rock SiO_2 and decreasing $(Nd)_n$, $(Nd/Yb)_n$ and Ti/REE in clinopyroxenes.

There are two main ways of testing for this reaction process in the Troodos Massif. Firstly, the *orthopyroxenites A* and *B* analysed in this study conform to the symmetrical arrangement of reaction zones proposed by Keleman *et al.* (1992), and might therefore, mark the sites of 'Keleman-type' reactions The fact that orthopyroxenites crystallise in the centre of these zones would be explained by the Keleman process via enrichment and eventually saturation of the reacting melt in pyroxene, due to dissolution of the pyroxenes in the dunitic part of the reaction zone. The variation in the whole-rock and mineral chemistry of the orthopyroxenite wallrocks has been described in Chapters 4 and 5. The critical clinopyroxene data cited by Keleman as evidence for mantle-melt reaction are reproduced here in Figure 6.3. The Ti/REE ratio has been calculated using the same formula as Keleman, namely $Ti/REE = 4Ti_n / (3Dy_n + Sm_n)$, and the expected trends for 'Keleman-type' reactions are shown as dashed lines.

The *orthopyroxenite A* wallrocks show variations in $(Nd)_n$, $(Nd/Yb)_n$ and Ti/REE which consistently trend in the direction predicted by the Keleman *et al.* (1992) model. However, the variation in the *orthopyroxenite A* wallrocks is very small and always close to the analytical precision. Moreover, the variation in the *orthopyroxenite A* wallrocks is always much less than the total variation found in the *background* harzburgites. Therefore, the operation of Keleman-type processes cannot be proved in the *orthopyroxenite A* wallrocks. These data also indicate that any reaction process that has occurred around the *orthopyroxenite A* intrusions has had a much less significant impact on harzburgite geochemistry than partial melting processes. The *orthopyroxenite B* wallrocks show much greater variation in $(Nd)_n$, $(Nd/Yb)_n$ and Ti/REE than the *orthopyroxenite A* wallrocks. In most cases the variation in the wallrocks is as large as

the total variation found in the *background* harzburgites. However, as illustrated in Figure 6.3, the trends in the *orthopyroxenite B* wallrocks are all opposite to those expected to be produced by Keleman-type reactions. Therefore, the variation in the *orthopyroxenite B* wallrocks does not support the existence of Keleman-type reactions.

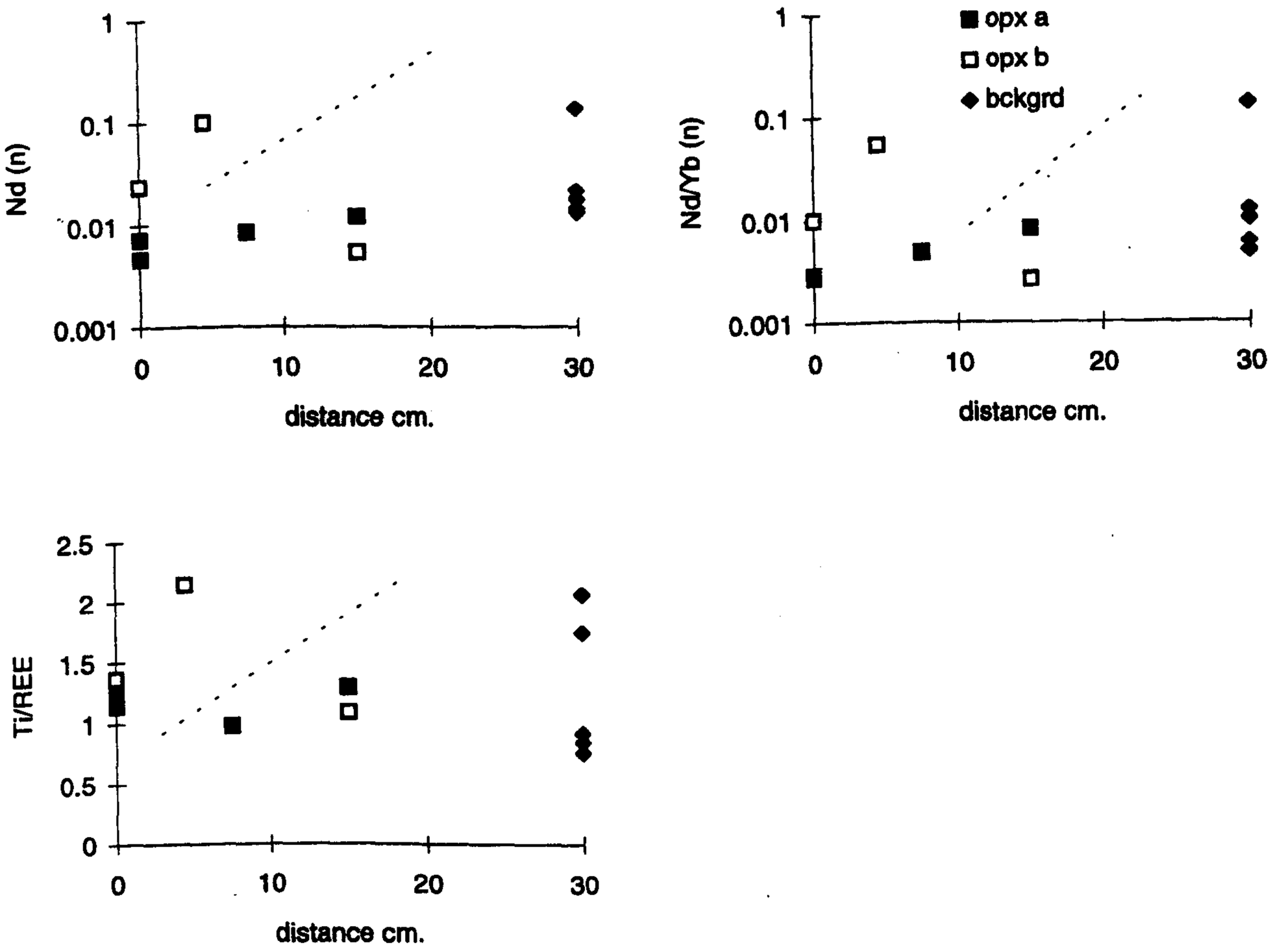

Figure 6.3. Plots illustrating the variation in the REE geochemistry of clinopyroxenes in wallrock peridotites surrounding *orthopyroxenite A* and *B* intrusions. Distances were measured from the centre of the orthopyroxenites; dashed lines show the trends which would be produced by 'Keleman-type' reactions.

A second way of testing for 'Keleman-type' reactions would be to see whether the whole-rock data show any enrichments in SiO_2. This enrichment should result from orthopyroxene crystallisation during mantle-melt interaction in the Keleman-type reaction. The variation of SiO_2 with Al_2O_3 for the Troodos harzburgites (including the

background harzburgites, banded harzburgites and wallrock harzburgites) is illustrated in Figure 6.2. Also shown for comparison are the compositions of peridotites from the Ronda Massif, which have been interpreted as residues from variable degrees of equilibrium melting of a MORB source (Frey *et al.*, 1985), and forearc peridotites, which have compositions that have been interpreted as the result of fractional melting and variable incompatible element enrichment without the effects of Keleman-type processes (Parkinson, 1993). Figure 6.2 shows that the SiO_2 variation in the peridotites from Troodos, Ronda and the Izu-Bonin forearc has a strongly segmented distribution; indicated on the plot by two dashed arrows. The Ronda peridotites, together with two of the serpentinite diapir samples, plot on a trend of slowly decreasing SiO_2. Whereas the Troodos harzburgites and forearc peridotites plot on a trend of sharply decreasing SiO_2. Parkinson (1993) has interpreted this segmentation as a result of Si being removed more rapidly from the forearc peridotites compared to the Ronda peridotites. The change in the behaviour of Si takes place as a result of incongruent melting of orthopyroxene. The fact that most of the Troodos samples plot on these trends suggests that the SiO_2 distribution is mainly controlled by partial melting. Notably, a few of the Troodos harzburgites and one of the serpentinite diapir samples plot to higher SiO_2 values than would be predicted by the partial melting trends. This is the expected variation for 'Keleman-type' reactions. However, as discussed in Chapter 5, serpentinisation reactions can also increase whole-rock SiO_2. The trend for SiO_2 - Al_2O_3 variation during serpentinisation is indicated on Figure 6.2 by a solid arrow. Clearly, the variation in these high SiO_2 could equally be explained by serpentinisation as by Keleman-type reactions.

These data suggest that the geochemical variations in the Troodos harzburgites are inconsistent with the operation of Keleman-type reactions. The geochemical variations around orthopyroxenite intrusions are either too weak to lend support to Keleman-type reactions (i.e. *orthopyroxenite A* wallrocks), or describe geochemical trends opposite to those expected to result from Keleman-type reactions (i.e. *orthopyroxenite B* wallrocks). Furthermore, the geochemical variations in the Massif as a whole do not show any evidence of the SiO_2 enrichment that should characterise Keleman-type processes. Therefore, Keleman-type reactions are discounted as significant influences on the geochemistry of the Troodos mantle sequence.

6.4.2 THE MANTLE AS A CHROMATOGRAPHIC COLUMN

Navon and Stolper (1987) proposed that the mantle might act in a similar way to a chromatographic column during two phase flow of peridotite and transient melt. In this model, transient melts which are out of equilibrium with the mantle in which they are moving react with the host peridotites. The effects of the reaction depend on the distribution coefficients of the elements involved. Compatible elements will be extracted from the melt at the base of the column, whereas incompatible elements are free to be transported along the column by the melt. This will have the effect of causing the incompatible elements to travel at a greater relative speed through the mantle section than the compatible elements and, in the simplest case, a series of concentration fronts will form in the column, controlled by the element distribution coefficients.

In a mantle situation, this process would result in 'far-field' clinopyroxenes (i.e. those located furthest from the base of the column) being enriched in the LREE over the HREE, because the HREE would be held back due to their greater compatibility with 'near-field' clinopyroxenes lower in the peridotite column. Over time, the reactive capability of a chromatographic column will be used up, and the entire column will be equilibrated towards the composition of the melt which is being introduced at the base of the column. Bodinier *et al.* (1990) have shown that this process can occur on a small scale around intrusive bodies. In the Bodinier *et al.* (1990) study, the REE patterns of the wallrocks changed with distance from the intrusion; far-field clinopyroxenes displayed LREE-enrichment because the HREE had been absorbed by the clinopyroxene closer to the intrusion (i.e. further down the chromatographic column).

In the Troodos Massif, an obvious situation in which to test this theory is around the pyroxenite bodies. The main mineral capable of fractionating the incompatible elements in the Troodos sequence is clinopyroxene. Therefore, in the chromatographic column model, clinopyroxene-melt distribution coefficients will, to a large extent, determine the relative speeds at which the incompatible elements are transported through the wallrock adjacent to the pyroxenites.

Chondrite-normalised trace element patterns for clinopyroxene in the pyroxenite wallrocks have been presented in Chapter 4 and are redrawn here in Figure 6.4. As Figure 6.4 shows, the *orthopyroxenite A* wallrocks are characterised by sub-parallel trace element patterns which show slight LREE enrichment over the HREE in the 'far-field' harzburgite (i.e. the wallrock sample at 15 cm from the pyroxenite, $Ce/Yb_n = 0.007$) compared to the wallrock immediately adjacent to the pyroxenite ($Ce/Yb_n = 0.002$). In

the context of the chromatographic model, the sub-parallel trends could be explained by exhaustion of the part of the chromatographic column which is adjacent to the pyroxenite. It may be that, if samples had been taken at progressively greater distances from the pyroxenite, clearer chromatographic trends might have been seen. However, the fact that *orthopyroxenite A* bodies are boudinaged and folded around the harzburgite foliation (Chapter 2), suggests that there was post-intrusion deformation, which will have physically disrupted any zonations produced by chromatographic processes.

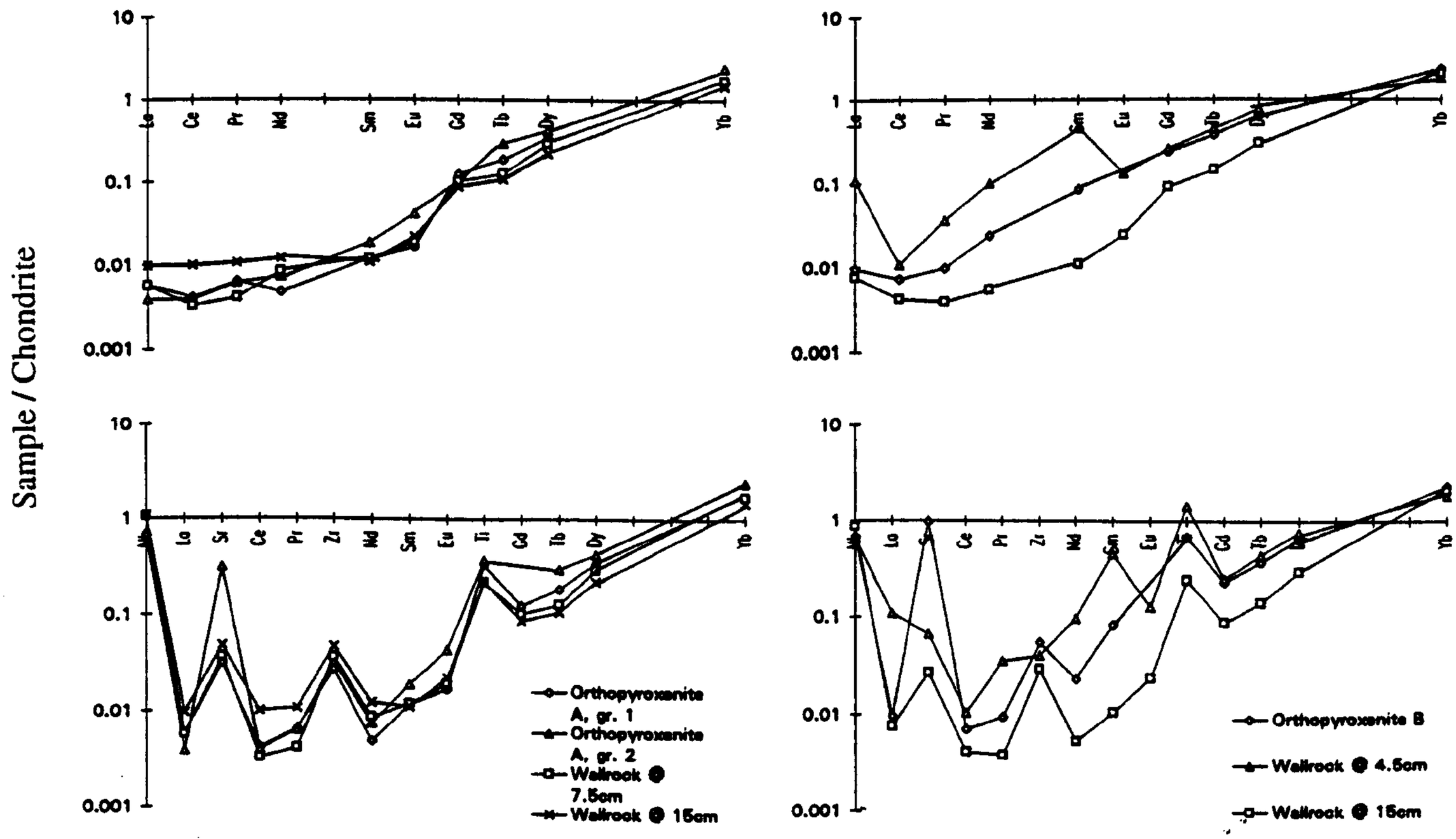

Figure 6.4. REE and extended REE plots showing the variation in geochemistry of clinopyroxenes at various distances from *orthopyroxenite A* and *B* intrusions.

The patterns for the *orthopyroxenite B* bodies are more complex, with the REE pattern showing greater enrichment of the LREE adjacent to the pyroxenite ($Ce/Yb_n = 0.006$) than in the 'far-field' peridotite ($Ce/Yb_n = 0.003$). The variation of $(Nd/Yb)_n$ in the pyroxenite wallrocks has been illustrated in Figure 6.3. The clinopyroxene-melt

distribution coefficient for Nd is less than that for Yb (see Table 4.9, Chapter 4) and, therefore, in a chromatographic column model, the $(Nd/Yb)_n$ ratio should increase with distance from the pyroxenite. As Figure 6.3 shows, the Troodos wallrocks do not show such a variation.

In their original work describing the chromatographic column concept, Navon and Stolper (1987) discussed the variation of the LREE with Sm in peridotite nodules from Algeria. The nodules displayed concave-downward trends between enriched and depleted compositions which were interpreted in terms of chromatographic fractionation during mantle-melt reaction. Unfortunately, Sm was not measured in the Troodos samples. However, a similar graph can be plotted using a more compatible element on the x-axis and an incompatible element on the y-axis. In this case, Ce and Nd were used. The variation in whole-rock Ce and Nd for the Troodos samples is illustrated in Figure 6.5.

As Figure 6.5 shows, the distribution does not fit a trend of concave-downward mixing trajectories between an enriched and a depleted end-member, which are expected for the chromatographic fractionation process (Navon and Stolper, 1987). A better explanation would be of selected LREE enrichment in the harzburgites adjacent to pyroxenites and at the top of the sequence.

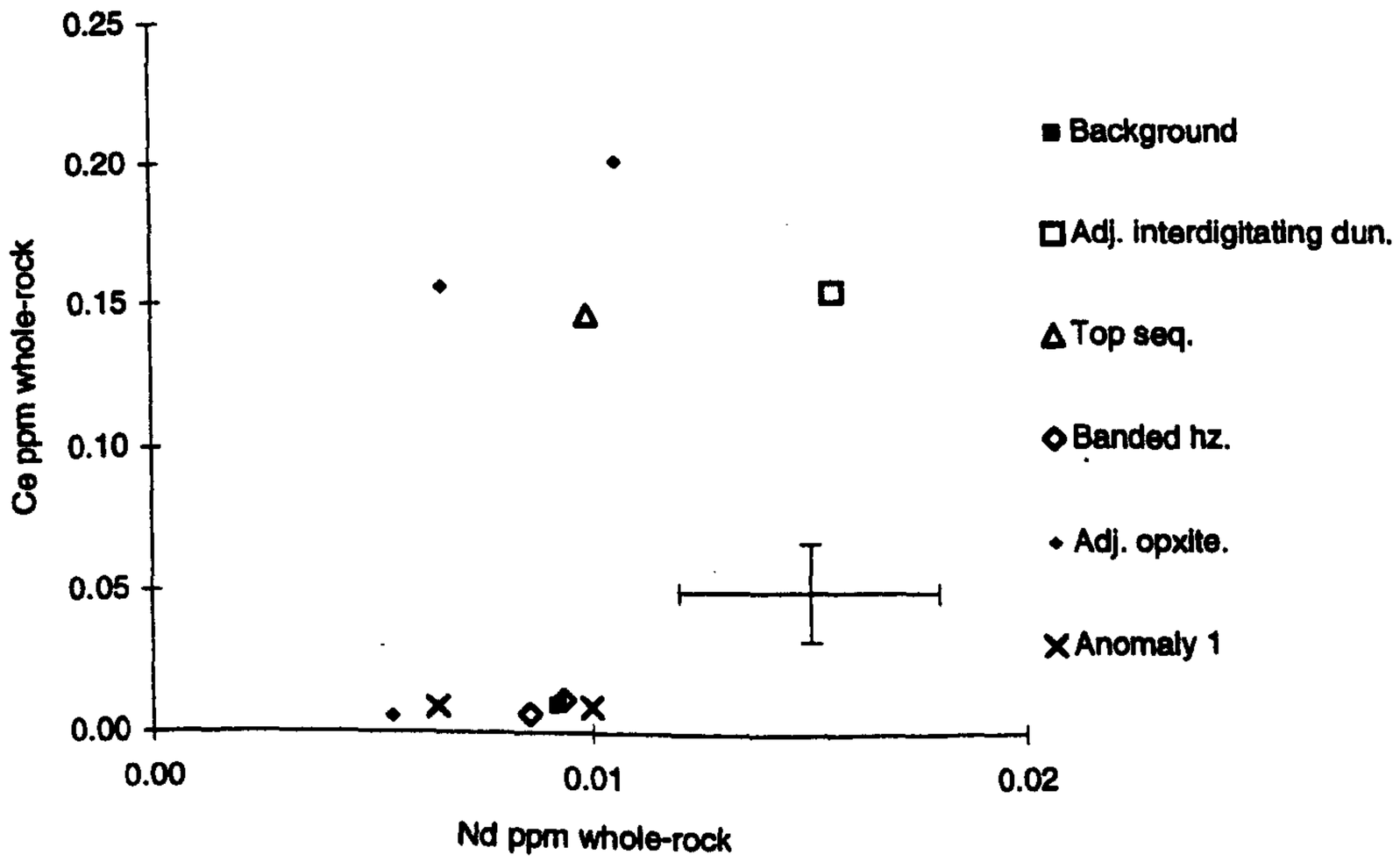

Figure 6.5. Graph illustrating the variation of Ce and Nd in clinopyroxene for various Troodos harzburgites.

These data provide some evidence for the operation of chromatographic processes around certain of the pyroxenite intrusions, but the trends are generally weak. There is little convincing evidence for chromatographic processes operating on a massif scale. While the theoretical model elegantly explains the geochemical variation around some intrusions (e.g. Bodinier *et al.*, 1990), the absence of convincing trends in the Troodos peridotites could be the result of post-chromatographic-zonation deformation or of exhaustion of the chromatographic column through complete re-equilibration with the transient melt. If the mantle had completely re-equilibrated with a transient melt, the peridotites should be characterised by trace element patterns that reflect the partitioning between melt and mantle. The fact that the Troodos peridotites preserve a range of chondrite-normalised trace element profiles (Chapters 4 and 5) suggests that either the mantle did not fully re-equilibrate with a transient melt, or that more than one melt composition was involved.

6.4.3 SUMMARY OF THE EVIDENCE AGAINST 'KELEMAN' AND CHROMATOGRAPHIC PROCESSES IN THE TROODOS MASSIF.

The previous two sections have analysed the Troodos data in the light of Keleman-type and chromatographic processes. Considering that the original authors (Navon and Stolper, 1987; Keleman *et al.* 1992) both implied that these reactions were universally applicable to mantle peridotites it is perhaps surprising that no evidence could be found to support them in the Troodos data. There are, however, several facts which should be considered before these processes are discounted as significant influences on harzburgite geochemistry.

Firstly, the Troodos harzburgites are extremely depleted compared to the composition of the lithologies in the type localities described by Keleman *et al.* (1992) and Navon and Stolper (1987). The reaction zones described by Keleman *et al.* (1992) and attributed to mantle-melt reaction are developed in a plagioclase lherzolite host and peridotite nodules described by Navon and Stolper (1987) are also lherzolitic. This has several implications. On a purely experimental basis, the very depleted chemistry of the Troodos harzburgites makes it difficult to extract quality analytical data from them. Some of the geochemical variation that could be attributable to the Keleman and chromatographic processes might, therefore, simply be obscured by the poor analytical precision for some elements. For example, the variation in the *orthopyroxenite A* wallrocks (see Figure 6.3) is not particularly significant because it is close to the analytical precision but, with future improvements in analytical techniques, the variation in these wallrocks may be

resolvable, and may lend some support to the Keleman-type reaction process. Also, studies of natural outcrops which support the operation of these processes have been from localities where the lithologies involved have strongly contrasting fertilities. For example, in the Bodinier *et al.* (1990) paper cited above, the intruding lithology is a LREE-enriched amphibole pyroxenite and the host a harzburgite. Clearly this provides a strong potential for exchange between the intrusion and its wallrocks. In contrast, in the Troodos Massif both the host harzburgite and the intruding pyroxenites have depleted chemistries which obviously restricts the potential for the development of cryptic geochemical variations.

Secondly, studies which have supported the existence of Keleman and chromatographic processes (e.g. Keleman *et al.*, 1992; Bodinier *et al.*, 1990) are always from tectonically-passive localities. This means that any geochemical variation produced by reaction are likely to be preserved. In contrast, the field evidence described in Chapter 2 shows that orthopyroxenites in the Troodos Massif intruded both prior to, and concurrent with, the mantle deformation. In this situation it is unlikely that the original field relationship between an intrusion and its wallrock will be preserved. It is notable that the *orthopyroxenite A* intrusions have much weaker geochemical variations in their wallrocks than the *orthopyroxenite B* intrusions, and are also the most heavily deformed. This evidence supports the argument that any geochemical halos produced by mantle-melt reaction were destroyed by the mantle deformation.

These facts suggest that the Troodos Massif is perhaps not the best location to study Keleman and chromatographic processes and that the data obtained during this study is not sufficient to discount the possibility of these processes operating in other harzburgite-type ophiolites.

6.4.4 A MODEL FOR PYROXENITE AND DUNITE FORMATION IN THE TROODOS MASSIF

Pyroxenitic and dunitic bodies in the mantle sequence of ophiolites are now widely believed to mark the sites of melt/fluid interaction with the host peridotites (Quick 1981b; Varfalvy *et al.*, 1996; Edwards, 1995; Quick and Gregory, 1995). In the Troodos mantle sequence, several lines of evidence suggest that a similar relationship exists:

The wallrocks of pyroxenite and dunite bodies have mineral and whole-rock chemistries which vary according to the chemistry of the adjacent pyroxenite or dunite.

Orthopyroxenites are typically separated from the host harzburgites by screens of dunite.

Some dunites contain resorbed xenolithic fragments of harzburgite, and orthopyroxene and spinel crystals which have textures that suggest that they are xenocrystic.

In Chapter 4, the Troodos pyroxenites were divided into two groups on the basis of spinel chemistry. Type I pyroxenites were defined as those with Cr-Fe-Ti-rich spinels and Type II pyroxenites were defined as those with Mg-Al-rich spinels. The variations in the chemistry of the Troodos pyroxenites are summarised in Table 6.1.

The most fertile end-members of the Type I trend are the clinopyroxene-bearing intrusions, namely the olivine-clinopyroxenites and the clinopyroxenite stringers. In Chapter 4 the mineral chemistry variation in the Type I pyroxenites was shown to match the trend of the Troodos plutonic cumulates. The whole-rock chemistry of the Type I pyroxenites shows that the incompatible elements increase, and the compatible elements decrease, with increasing Al_2O_3. This suggests that the Type I pyroxenites could be related by fractional crystallisation. The similarity in the mineral chemistries between the Troodos cumulates and Type I pyroxenites suggests that they crystallised from similar parental magmas. The fact that spinel chemistries are restricted to high Cr# and are Ti enriched, and silicates are Fe-rich, suggests that the parental melts were Fe-Ti-rich and Al-poor.

Type II pyroxenites generally have a much more restricted variation in both mineral and whole-rock chemistries. For both parameters, the Type II pyroxenites plot on an extension of the *background* harzburgite trend. The limited enrichment of the whole-rock incompatible element values suggests that fractional crystallisation was not a significant process in the evolution of the Type II melts. The fact that Type II spinels trend towards lower Cr# values and have limited Ti variation, that silicates are buffered to high Mg# and that the most evolved melts (i.e. highest whole-rock Al_2O_3 values) have low whole-rock Ti contents, suggest that the parental melts were refractory and were Mg-Al-rich and Ti-poor.

	Type I	Type II
Lithology	*orthopyroxenite A*, harzburgite pyroxene bands, olivine-clinopyroxenites	*orthopyroxenite A*, *orthopyroxenite B*
Spinel	Cr-Fe-Ti enriched	Mg-Al enriched
Olivine	Fe enriched, Ni depleted	Fe and Ni enriched
Orthopyroxene	Fe enriched, Al depleted	Al enriched
Clinopyroxene	Fe and Na enriched	Na enriched
Average equilibrium melt	Mg# 73.4±1.4	Mg# 74.0±1.2
Whole-rock	Trends to high Ti, Sc, Zr, Y and lower Ni, Co Zr/Ti = 23.3	Plot on an extension of the *background* harzburgite trend for Y, Ni, Co Zr/Ti = 1.3 - 2.3
Wallrocks	Ti enrichment in spinel, Fe enrichment in silicates	orthopyroxene and spinel Al enriched, all minerals buffered to high Mg#

Table 6.1. Summary of pyroxenite mineral chemistries and associated wallrocks.

The reaction systems in the wallrock harzburgites also allow inferences to be drawn about the melts. Type I wallrocks have high Ti_{spn} values and low Ni_{ol} values, orthopyroxene compositions trend towards low Al values, $Cr\#_{spn}$ is buffered at high values and all minerals trend towards more Fe-rich compositions. These data suggest that the melt was poor in Al and Ni, but comparatively rich in Fe and Ti. These characteristics suggest that the melts were tholeiitic in nature (Wilson, 1989). The Type II wallrocks have low Ti spinels, olivine compositions which trend towards high Ni values, all minerals buffered towards high Mg#, and orthopyroxene and spinel that trend towards more aluminous compositions. These data suggest that the reacting melt was poor in Ti but rich in Al and Ni. Mg-rich, low-Ti magmas would suggest that the melt had boninitic affinities (Wilson, 1989).

A similar division between units that crystallised from either tholeiitic or boninitic melts has been noted in the Troodos crustal section. The parental magmas of the sheeted dykes and lower pillow lavas (LPL) have been interpreted as tholeiitic (e.g. Robinson *et al.*, 1983), whereas the upper pillow lavas (UPL) have boninitic chemistries (e.g. Cameron, 1985). The fact that this first order subdivision can also be made between the two

pyroxenite types found in the mantle sequence suggests that there is a genetic relationship between the Type I pyroxenites and the sheeted dykes and LPL, and between the Type II pyroxenites and the UPL. The possible relationships between the Troodos crustal sequence and the mantle section are discussed in greater detail below (Section 6.5).

As mentioned above, both *orthopyroxenite A* and *B* bodies typically have a marginal dunite facies separating them from the host harzburgite. In agreement with studies in other ophiolites (e.g. Quick, 1981a), this arrangement is interpreted as evidence for reaction between the incoming melt and the wallrocks. To form dunite, this reaction must have consumed orthopyroxene and clinopyroxene from the harzburgites and crystallised olivine and spinel. Edwards and Malpas (1996) have proposed the following reaction to explain the breakdown of orthopyroxene:

$$\underset{\text{orthopyroxene}}{Mg_2Si_2O_6} + \text{melt} \Rightarrow \underset{\text{olivine}}{Mg_2SiO_4} + SiO_{2(\text{melt})}$$

A reaction hypothesis is also supported by the petrographic evidence from the orthopyroxenites (see Chapter 4), where wormy spinel separates embayed orthopyroxene crystals from olivine. Similar textures are found in the wallrock harzburgites adjacent to the orthopyroxenites, which supports the argument that reaction between the intruding melt and the peridotites has modified the composition of the wallrocks. A reaction which explains the formation of this texture might have the form:

$$\underset{\text{orthopyroxene}}{Mg_2Si_2O_6} + \underset{\text{olivine}}{(Mg,Fe)_2SiO_4} + 2Cr_{(\text{melt})} \Rightarrow \underset{\text{spinel}}{FeCr_2O_4} + \underset{\text{olivine}}{Mg_2SiO_4} + Mg,2Si,2O_{(\text{melt})}$$

Marginal dunites are features of orthopyroxenites that lie on both the Type I and II trends, although they are more common around Type II pyroxenites. This suggests that both Type I and II melts were undersaturated with respect to the pyroxenes. Dissolution of pyroxenes from the host harzburgites will enrich the melts in Ca, Al and Fe, and eventually lead to orthopyroxene saturation in the melt, resulting in crystallisation of orthopyroxene. The fact that dunite formed initially by melt-mantle reaction suggests that the primary melts involved were picritic. This is supported by the calculated Mg# of >70 for melts in equilibrium with the pyroxenites (see Table 6.1).

In thin section, the *orthopyroxenite A* bodies consist of orthopyroxene-rich areas intruded and embayed by olivine-rich areas. This texture suggests that orthopyroxene crystallised and was then resorbed by a melt crystallising olivine and, therefore, a simple model of

dunite formation followed by crystallisation of the orthopyroxenite may not be appropriate. Also, the *Orthopyroxenite B* intrusions often contain several orthopyroxene veins (see Chapter 2), which suggests that there were multiple episodes of pyroxene crystallisation during formation of these bodies. The crystallisation of orthopyroxene might have been switched on and off as a result of injections of fresh, primitive magma batches into the reacting system. This would move the melt away from the orthopyroxene phase field and back into the olivine phase field, resulting in more dunite crystallisation until further reaction led to renewed saturation of the melt with orthopyroxene.

Notably, the marginal dunites and adjacent harzburgites are always in sharp contact. This relationship is consistent with the theory of phase saturation in a melt-mantle reaction system as proposed by Keleman (1990). Keleman and Dick (1995) also point out that sharp contacts between dunites and harzburgites indicates that, at least on an outcrop scale, porous flow of reactive melt has been focused into specific conduits in the upper mantle. This is also likely to have been the case in the Troodos Massif. Furthermore, as pointed out in Chapters 2 and 4, the location of pyroxenites and enriched sections of mantle (i.e. the *Anomaly 1* and *2* harzburgites) in the Troodos mantle section suggests that on a massif scale, melt flow was focused predominantly into a zone approximately 300m wide rather than being a pervasive phenomenon across the massif.

Unfortunately, no cross-cutting relationships between the two pyroxenite types have been observed in the field area. However, a chronology of intrusion can be established on the basis of the amount of deformation a pyroxenite intrusion has suffered relative to the harzburgite deformation. As described in the Fieldwork Chapter, the *orthopyroxenite A* intrusions are the most deformed intrusions (oriented parallel to, folded around and boudinaged along the harzburgite foliation), and are, therefore, interpreted as the oldest intrusions. The *orthopyroxenite A* pyroxenites lie along the Type I and II trends. The *orthopyroxenite B* intrusions are also oriented parallel to the harzburgite foliation but do not show any evidence of boudinage or folding. These intrusions are, therefore, interpreted to be younger than the *orthopyroxenite A* intrusions. The *orthopyroxenite B* intrusions fall on the Type II pyroxenite trend. The olivine-clinopyroxenites are undeformed and cross-cut the harzburgite foliation and are, therefore, interpreted as the youngest intrusions. The olivine-clinopyroxenites form the fertile end-member of the Type I pyroxenite trend. These relationships show that, while the different lithological divisions of the pyroxenites can be placed into a relative chronological order, the geochemical divisions into the Type I and II pyroxenites do not fall into a simple chronological sequence. Rather, the evidence indicates that the Type I melt was present

for a considerable time period - from before the mantle deformation (i.e. boudinaged *orthopyroxenite A* intrusions) until post-mantle deformation (i.e. undeformed, cross-cutting olivine-clinopyroxenites). In contrast, the Type II melt was present for a shorter time, both before and during the mantle deformation. It would seem, therefore, that during the mantle deformation event, both Type I and II melts were present at the same time. Notably, in a detailed study of the Troodos cumulates, Malpas *et al.* (1990) found that both a high Ti (i.e. similar to Type I melts) magma type and a low Ti-high Mg (i.e. similar to the Type II melts) magma type were present at the same time, which corroborates the evidence found in this study.

Some authors have discussed the possibility that different pyroxenite types in ophiolite mantle sections may have genetic relationships. Varfalvy *et al.* (1996) proposed that melt-mantle reaction could enrich melts in the magmaphile elements, and might be responsible for derivation of Type II melts from Type I melts in the Bay of Islands ophiolite. Edwards and Malpas (1996) also noted two evolutionary trends in harzburgite spinel from Hess Deep peridotites. One trend of Fe-Ti enrichment is similar to the Troodos Type I trend, and the second trend of Al enrichment is similar to the Troodos Type II trend. The relationship between the two trends was interpreted as one of varying melt/peridotite ratios. In the Al enrichment trend, low melt/peridotite ratios allowed the of Mg# silicates to be buffered by the host harzburgite, while the melt produced enrichments in the incompatible elements. At high melt/peridotite ratios, orthopyroxene dissolves incongruently and clinopyroxene crystallises. In this case, the chemistries of the resulting minerals are controlled by the melts; the enrichments in Ti and Fe suggest that these melts were somewhat evolved.

As explained above, the rough chronology that can be established for the Troodos pyroxenites suggests that both Type I and II melts were present at the same time. The REE patterns presented in Chapter 4 (and reproduced here as Figure 6.6), show that the orthopyroxenites analysed (both Type II pyroxenites), have distinctly different trace element patterns to the clinopyroxenites (Type I pyroxenites). Type I pyroxenites have negative Ti anomalies and no Zr anomalies, whereas the Type I pyroxenites have positive Ti and Zr anomalies. The REE patterns of the Type I pyroxenites have flatter H-MREE profiles than the Type II pyroxenites, and higher REE abundances. These data suggest that it would be difficult to derive one pyroxenite type from the other and, therefore, two different source regions must have existed. This hypothesis is supported by the whole-rock data presented in Chapter 5, (and summarised above in Table 6.1), which demonstrated that the Type I pyroxenites have much higher Zr/Ti ratios than the Type II pyroxenites. Again this variation requires the pyroxenites to have 2 separate source

regions. The existence of two source regions is consistent with the hypothesis that the Type I melts were tholeiitic and the Type II melts boninitic, which would also require two different source regions and melting histories to produce such fundamentally different melts (Wilson, 1989).

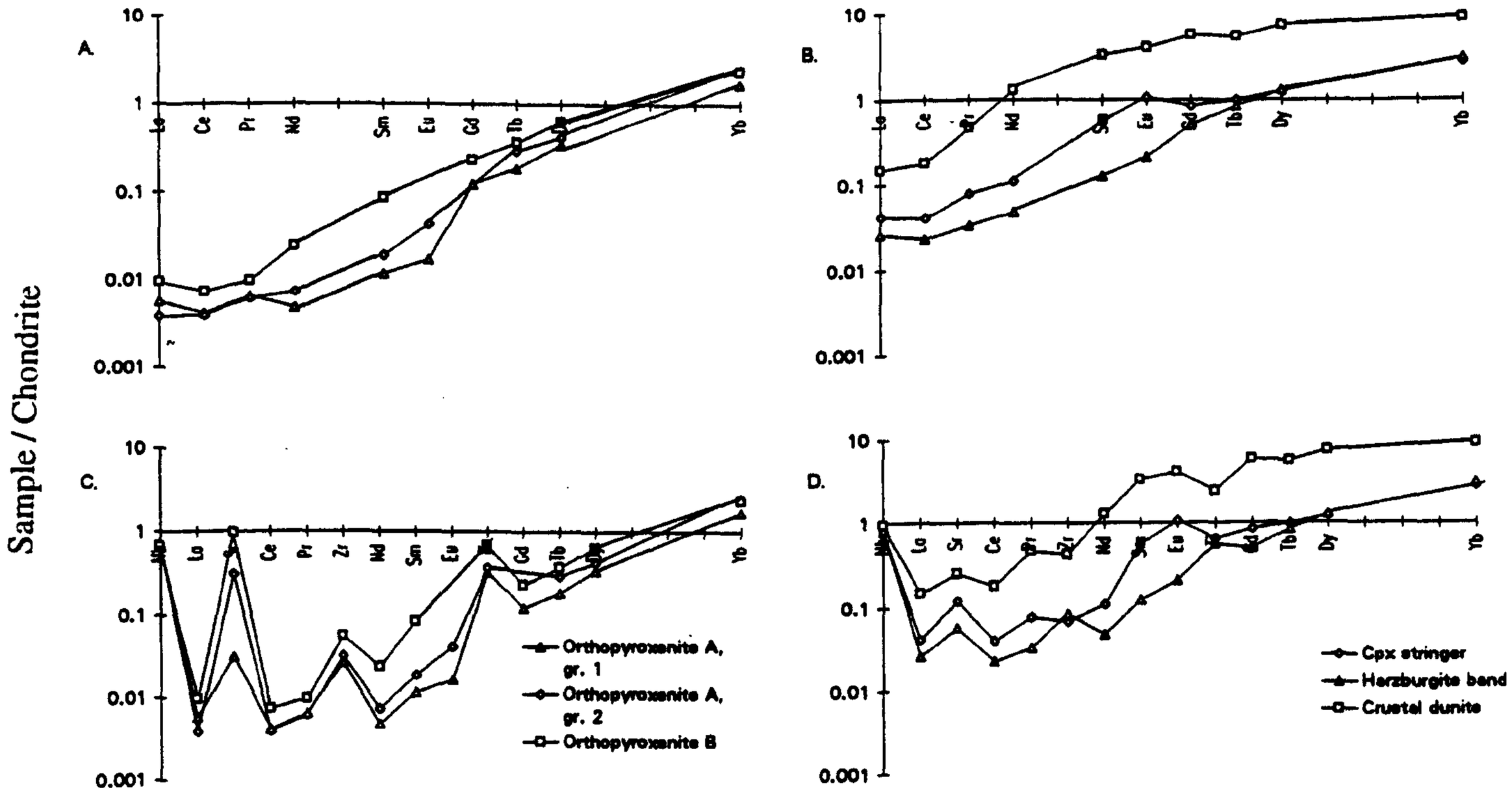

Figure 6.6. REE and extended REE patterns for the various pyroxenite bodies in the Troodos Massif.

The fact that the marginal dunites are formed adjacent to the pyroxenites suggests that melt-mantle reaction might be an important dunite-forming process in the Troodos Massif. The only dunites with good field, petrographic and mineral chemistry evidence for a reaction relationship with the enclosing harzburgites are the interdigitating dunites (Chapter 2). These dunites are characterised by their interpenetrating contacts with the adjacent harzburgites, the occurrence of xenocrystic orthopyroxene and spinel in the dunite, and the presence of resorbed harzburgite xenoliths. Petrographically, these dunites have bimodal spinel textures (Chapter 3). The fine-grained population of euhedral spinel is interpreted as having crystallised directly from the melt, and the coarse-grained fraction of resorbed porphyroclastic spinel is interpreted as xenocrystic material from the enclosing harzburgites. Notably, the coarse spinel forms a substrate on to which

clinopyroxene displaying growth twins has crystallised. This clinopyroxene supports the hypothesis of Edwards and Malpas (1996), that the first stage in reaction between a basaltic melt and peridotite is the dissolution of orthopyroxene and crystallisation of olivine, spinel and minor clinopyroxene.

The bimodal spinel population in the interdigitating dunites shows that these bodies are probably composite in nature, comprising both melt-mantle reaction products and being partly crystallisation from the melt. The mineral chemistry of the other dunites in the Troodos Massif (Chapter 4) suggests that their formation can also be explained by melt-mantle reaction and magmatic crystallisation. This supports the hypothesis of Quick (1981b) that dunites in the Trinity Peridotite are composite bodies consisting of reaction products at their contacts with the host peridotites and cumulates towards the centre of the dunites.

6.4.5 ORIGIN OF THE *ANOMALY 1* AND *2* HARZBURGITES

Mineral compositions that cannot be simply explained by partial melting processes characterise the *Anomaly 1* and *2* harzburgites as well as the areas around pyroxenites and dunites. The *Anomaly 1* harzburgites are located at the top of the mantle section and the *Anomaly 2* harzburgites are located stratigraphically below the *Anomaly 1* harzburgites, and form a layer of low $Cr\#_{spn}$ perched within a unit of higher $Cr\#_{spn}$ (Chapter 4). The variations in the mineral chemistries of the *Anomaly 1* and *2* harzburgites are summarised in Table 6.2.

	Anomaly 1	*Anomaly 2*
Cr# spn	low	low
Mg# ol	low	high
Ti spn	high	high
Na cpx	high	very high
Al_2O_3 opx	high	high
Spinel texture	coarse porphyroclastic, fine euhedral, intergrowths with clinopyroxene	vermicular intergrowths with silicates
Clinopyroxene texture	coarse poikilitic grains	intergrowths with spinel or associated with opx aggregates

Table 6.2. Summary of the mineral chemistries and textures of the *Anomaly 1* and *2* harzburgites.

As described in Chapter 4, the mineral chemistries of the *Anomaly 1* and *2* harzburgites are displaced away from the partial melting trends defined by the *background* harzburgites. These variations were interpreted as a result of interaction with transient melts which, because the *Anomaly 1* and *2* samples are *background* harzburgites sampled far from intrusive bodies, must have migrated through the mantle by pervasive porous flow. The location of the *Anomaly 1* harzburgites at the top of the sequence is not surprising considering that this is the area where melt supply from deeper in the sequence will be greatest. The *Anomaly 2* harzburgites are located at greater depth in the sequence. A method of introducing an enriched, melt related, component at this depth is by mechanical mixing of intrusive bodies during the asthenospheric deformation, as proposed by Edwards (1990) to explain the addition of an orthopyroxenite component to the Lewis Hill Massif harzburgites. The fact that the orthopyroxenites are all orientated parallel to, and in some cases deformed along, the harzburgite foliation in the Troodos mantle section would suggest that this process has also occurred in the Troodos Massif.

As noted in Chapter 4, the spinel in the *Anomaly 1* harzburgites defines an interaction trend a trend of constant Cr# for increasing Ti (labelled IT2 in Chapter 4). This trend matches that in the Type I pyroxenites. In contrast, the spinel in the *Anomaly 2* harzburgites defines an interaction trend (labelled IT1 in Chapter 4 and defining a trend of decreasing Cr# for gradually increasing Ti) which matches the variation in the Type II pyroxenites. The fact that the most fertile end-member of the Type I trend are the olivine-clinopyroxenites (which are only found in the uppermost parts of the sequence both within the *Anomaly 1* harzburgite outcrop and immediately below it) and that the *Anomaly 1* Cr_{spn}-Ti_{spn} trend matches the Type I trend support the hypothesis that the melts that enriched the *Anomaly 1* harzburgites were also those that crystallised the Type I pyroxenites. This hypothesis is also consistent with the fact that the clinopyroxenite bodies, found in the crustal dunites, are only located stratigraphically above the *Anomaly 1* harzburgites. The fact that the *Anomaly 1* harzburgites have low $Mg\#_{ol}$ indicates that they equilibrated with Fe-rich melts which supports the hypothesis that the Type I pyroxenite melts were tholeiitic in nature (see above). The geochemical similarities between the *Anomaly 1* harzburgites and the Type I pyroxenites are summarised in Table 6.3.

	Anomaly 1	Type I pyroxenites
Whole-rock	Trend of Zr enrichment	Trend towards high Ti, Sc, Zr, Y and low Ni, Co, Zr/Ti = 23.3
Olivine	Low Mg#, trend towards low Ni	Fe enriched, Ni depleted
Orthopyroxene	Al enriched	Fe enriched
Clinopyroxene	High Na, coarse poikilitic grains	Fertile end-member = clinopyroxene bearing
Spinel	Plot on interaction trend IT2 of increasing Cr# and Ti	Trend of Cr-Fe-Ti enrichment

Table 6.3. Summary of the geochemical variation in the *Anomaly 1* harzburgites and Type I pyroxenites.

The similarity between the *Anomaly 2* trends and the Type II pyroxenites also suggests that the melts were related. As discussed in the previous section, the Type II melts are thought to be boninitic because the Type II reaction system is characterised by the buffering of silicate Mg# to high values due to the magnesian chemistry of the melt. These facts agree with the presence of high $Mg\#_{ol}$ in the *Anomaly 2* harzburgites, which imply that these harzburgites equilibrated with an Mg-rich melt. The geochemical similarities between the *Anomaly 2* harzburgites and Type II pyroxenites are summarised in Table 6.4.

	Anomaly 2	Type II pyroxenites
Whole-rock	no data	Low Ti, plot on an extension of the *background* hz trend for Ni, Y, Co. Zr/Ti = 1.3 - 2.3
Olivine	High Mg# and Ni	Fe-Ni enriched
Orthopyroxene	High Al	High Mg# and Al
Clinopyroxene	Very high Na	High Mg# and Na
Spinel	Plot on interaction trend IT1 of decreasing Cr# and gradually increasing Ti	Mg-Al enrichment

Table 6.4. Summary of the geochemistry of the *Anomaly 2* harzburgites and the Type II pyroxenites.

Anomaly 1 harzburgites are characterised by high modal clinopyroxene contents. The clinopyroxene typically occurs as trains of undeformed, poikilitic crystals oriented parallel to the harzburgite foliation. The poikilitic nature of the grains, and their orientation, suggests that they crystallised from melts under conditions of directed stress. Spinel-silicate intergrowths have been identified as melt interaction textures in the *Anomaly 2* harzburgites, and the intergrowths are always located in the pressure shadows of orthopyroxene aggregates. These data suggest that the melts that interacted with the *Anomaly 1* and *2* harzburgites percolated through the mantle during the mantle deformation event. The contemporaneous presence of the two enriching melts in the mantle sequence supports the evidence discussed in the previous section for the co-existence of the Type I and II melts during the mantle deformation event. It also agrees with Malpas (1990) who suggested that several magma types were present in the mantle/crust system at approximately the same time.

6.4.6 REE PATTERNS IN TROODOS HARZBURGITE CLINOPYROXENE

The REE profiles in clinopyroxene grains from the Troodos harzburgites are characterised by steeply sloping HREE to MREE patterns, and flat MREE to LREE patterns. $(Ce/Yb)_n$ values are greater than those expected for residues from a simple fractional partial melting process. In the light of the theoretical interaction processes described above, and the interaction processes identified in the Troodos pyroxenites and *Anomaly 1* and *2* harzburgites, these REE profiles are interpreted as the result of a two stage process. Firstly, fairly high degrees of partial melting (>20%) deplete the clinopyroxenes in the REE, producing the steeply sloping H-MREE patterns. At this stage the clinopyroxenes will be very depleted in the LREE. Subsequently, the depleted peridotite interacts with an enriched melt/fluid, which increases the LREE contents of the clinopyroxenes, forming the gently sloping M-LREE patterns. Extended chondrite-normalised plots of the clinopyroxene trace element data suggest that the LREE enrichment was also accompanied by enrichments in Sr, Nb and Zr. The trace element patterns of the clinopyroxenes from the *background* harzburgites suggest that the enrichment of the Troodos harzburgites is a pervasive phenomenon on the coarse scale at which the *background* harzburgites were sampled. Notably, the harzburgite sample collected in the area of the Hadji Pavlou chromite mine which was analysed for its clinopyroxene trace element chemistry (No. 188), had the most enriched REE profile of all the *background* harzburgites analysed.

The trace element variations in the whole-rock data were described in Chapter 5. Two trends were identified in terms of the Zr/Y vs Ce/Y variation. One trend towards higher

Zr/Y for constant Ce/Y and a second trend towards higher Ce/Y values for constant Zr/Y. *Backgroumd* harzburgites plotted along both trends, whereas harzburgite samples collected in the area of the Hadji Pavlou chromite mine, *Anomaly 1* and banded harzburgite samples plotted on the high Zr/Y trend, and the *top-of-the-sequence* harzburgite and harzburgite collected adjacent to the interdigitating dunite plotted on the high Ce/Y trend. The graph illustrating these variations in Chapter 5 is reproduced here as Figure 6.7.

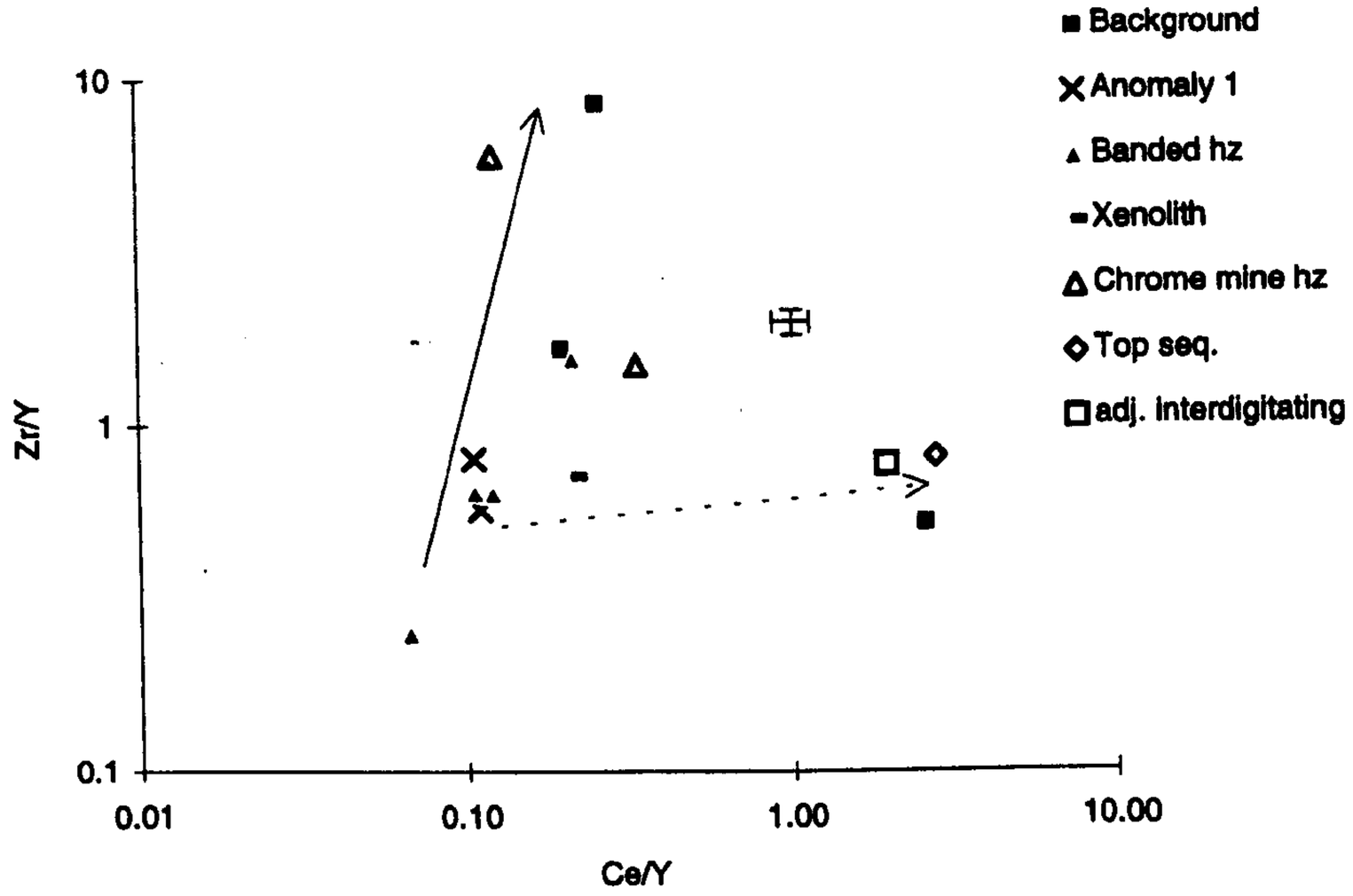

Figure 6.7. Graph illustrating the variation of Zr/Y and Ce/Y in the Troodos harzburgites.

As discussed in Chapter 5, these trends could be interpreted as the products of different chemistries of the enriching melt/fluid. Experimental evidence (Eggler, 1987) suggests that metasomatising fluids would be capable of transporting the LREE but not Zr. The trends on Figure 6.7 could therefore, be interpreted as evidence for two metasomatic agents in the Troodos Massif, a melt/fluid with high Ce/Y values and a melt with high Zr/Y values.

The clinopyroxene trace element data were used to calculate the trace element pattern of the enriching component in Chapter 4. The pattern of the calculated enriched component is reproduced here in Figure 6.8a. As would be expected from the extended clinopyroxene trace element patterns, the component has high concentration of the LREE, Nb, Sr and Zr. Unfortunately, there are insufficient data to compare the trace element pattern of the enriching component with the position of a sample on the Zr/Y vs Ce/Y graph.

In the previous section it was proposed that intrusion of the melts that crystallised the pyroxenites was responsible for some of the enrichments in the mineral major element chemistries observed in the Troodos harzburgites. The possibility exists that more widespread dispersion of these melts through the mantle sequence might have been the cause of the REE, Sr, Nb and Zr enrichments in the Troodos clinopyroxenes. The extended trace element patterns for the orthopyroxenites show that they are enriched in Nb and Sr, but have relatively low LREE abundances compared to the modelled enriching component. The clinopyroxene-bearing intrusives have higher LREE abundances than the orthopyroxenites but slightly lower Sr contents. The trace element profiles of melts in equilibrium with the pyroxenites, calculated using the distribution coefficient data presented in Chapter 4, are illustrated in Figure 6.8b. The calculation assumes that the pyroxenites are simply the products of melt crystallisation, and do not take into account any effects of melt/fluid - mantle reaction.

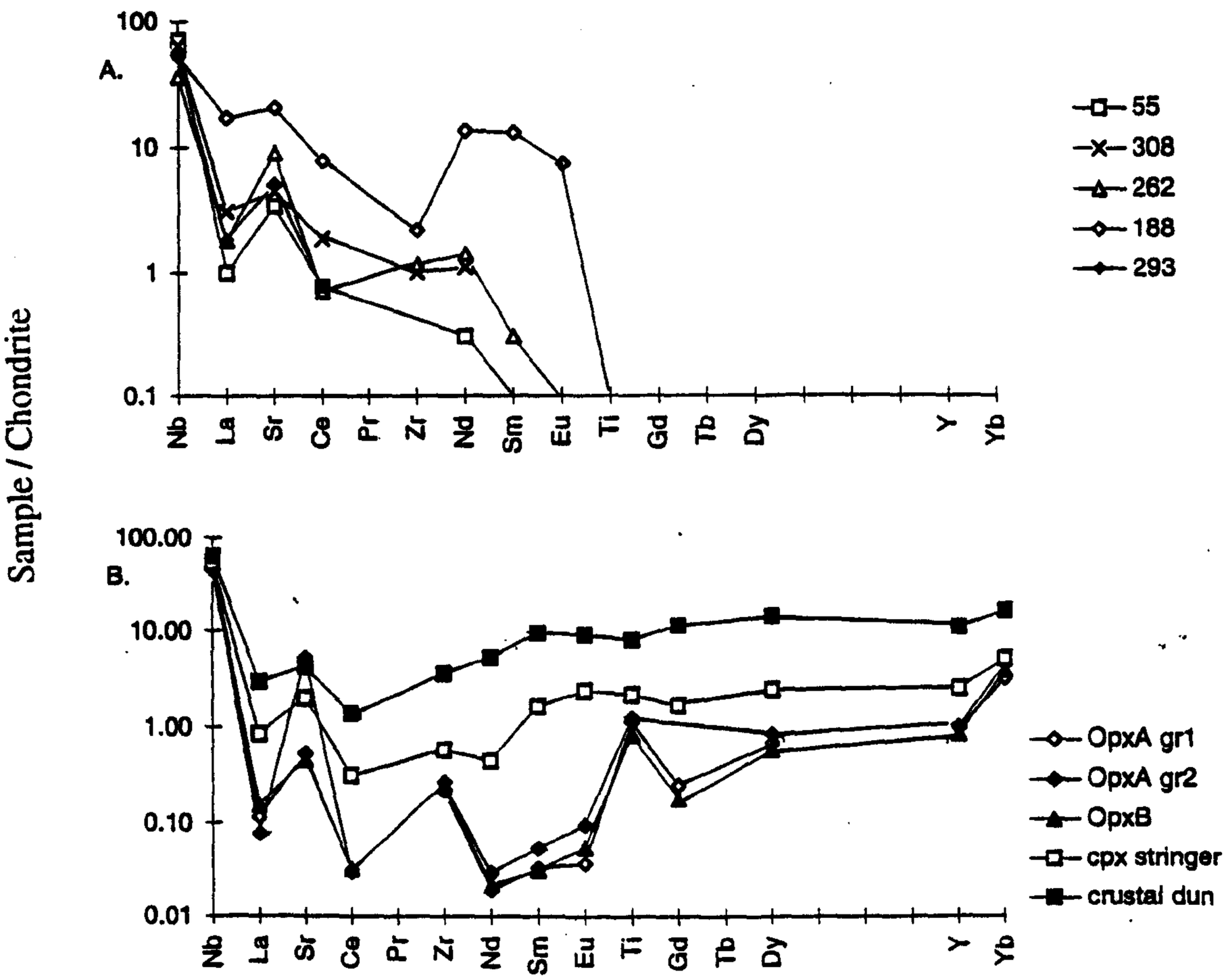

Figure 6.8. a) Trace element pattern of the enriching component calculated from the *background* harzburgite clinopyroxene data; b) Trace element patterns of melts in equilibrium with various Troodos pyroxenites calculated from the clinopyroxene trace element data presented in Chapter 4.

The pyroxenite equilibrium melt and enriched component profiles (Figure 6.8) are similar in the Nb-Ce part of the profile. Notably, the clinopyroxene bearing intrusions have Nb-Ce profiles similar to the enriched component for *background* harzburgite samples 188 and 293. Whereas, the orthopyroxenites have Nb-Ce profiles similar to the *background* harzburgite samples 55, 308 and 262. However, in both cases the calculated melts have significantly higher Ti and M-HREE abundances than the calculated enriched component.

These facts suggest that the LREE, Nb, Sr and Zr enrichment of the *background* harzburgites could be related to the intrusion of the pyroxenite melts into the mantle sequence. As noted in Chapter 4, the LREE enrichment of the clinopyroxenes must have occurred at the end of, or after, the melting event, because any post-enrichment partial melting event would rapidly deplete the LREE in the clinopyroxenes. The fact that the orthopyroxenites are parallel to the foliation, and are deformed, suggests that they were early intrusives and are, therefore, probably too old to explain the late incompatible element enrichment of the *background* harzburgite clinopyroxene. However, the olivine-clinopyroxenites are undeformed and cross-cut the harzburgite foliation and were, therefore, probably intruded after the main phase of mantle melting. This would suggest that the magma that crystallised the olivine-clinopyroxenites would be the one most likely candidate to have produced the LREE enrichment in the *background* harzburgites.

6.5 THE RELATIONSHIP BETWEEN THE TROODOS MANTLE SEQUENCE AND THE OVERLYING CRUST

In Sections 6.2 and 6.3 the very depleted nature of the Troodos harzburgites was emphasised, and related to their formation in a supra-subduction zone environment. In the first part of this section, the Troodos harzburgite data is compared to previously published geochemical data from the pillow lavas at the top of the Troodos ophiolite sequence to see whether it would have been possible to extract melts with compositions similar to the Troodos lavas from them. In the second part of this section further consideration is given to the relationship between the melts that crystallised the pyroxenites in the mantle sequence and the overlying Troodos lavas.

6.5.1 THE RELATIONSHIP BETWEEN THE TROODOS HARZBURGITES AND THE OVERLYING CRUST

The stratigraphy of the lavas was briefly described in Chapter 1 and consists of two main units, the lower pillow lavas (LPL) and the upper pillow lavas (UPL). The UPL have been further subdivided on the basis of their trace element contents into three groups, labelled I, II and III upwards through the section. The main geochemical features of each subdivision are summarised in Table 6.5 from the work of Cameron (1985) and Bednarz and Schmincke (1994).

	Sub-unit	TiO_2	Zr/Y	Ti/Zr	H_2O%	$(La/Yb)_n$	Zr/Rb
UPL		1.13-1.38	2.1	100	-	0.88	10.0
LPL	Group I	0.45-0.60	2.2	100	2.1	0.63-0.69	5.7
	Group II	0.30-0.40	2.0	100-120	2.3	0.56-0.61	4.0
	Group III	0.20-0.30	1.0	70-260	-	0.33-0.86	2.1

Table 6.5. Summary of the main geochemical characteristics of the Troodos Pillow lavas: LPL data from Bednarz and Schmincke (1994), UPL data from Cameron (1985) and primary H_2O data (H_2O%) from Muenow *et al.* (1990).

Summarising the work of Cameron (1985), Bednarz and Schmincke (1994) and Kostopoulos and Murton (1992), a model for the petrogenesis of the lavas would be as follows. The LPL and UPL Group I lavas are a series of island arc tholeiites produced by moderate to extensive melting of a fertile MORB-like source, and are the erupted equivalents of the magmas which crystallised the plutonic sequence. The UPL Group II lavas are transitional in chemistry between the UPL Group I lavas and the boninite series volcanics in the UPL Group III lavas. The relationship between the Group I, II and III UPL lavas is one of melting from a progressively depleted source, with increasingly significant additions of LILE, LREE and HFSE from fluids and/or melts derived from a subducted slab. The increasing degrees of melting required to produce each magma series is facilitated by the influx of volatiles from the slab. Chemical variations within the LPL and UPL groups I and II may be accounted for by fractional crystallisation process involving olivine, plagioclase, clinopyroxene, orthopyroxene and Fe-Ti oxides. Variations within the UPL Group III lavas are, in part, due to varying amounts of incompatible element enrichment of the source. The models presented by each author vary in detail; Bednarz and Schmincke (1994) appeal to the presence of Ti-rich phases in the lower crust to remove Ti, Ta and Nb from the UPL Group I lavas, whereas

Kostopoulos and Murton (1992) prefer to account for the incompatible enrichments in the UPL Group III lavas by the presence of an OIB component in the source.

The geochemical variations in the lavas are illustrated in Figures 6.9 and 6.10 together with that in the *background* harzburgites and the serpentinite diapir. Also shown are the compositions of melts in equilibrium with each of the peridotite samples, calculated using the mineral-melt distribution coefficients given in Chapter 4. These calculated melts give the composition of the last instantaneous fraction of melt that was extracted from the harzburgite sample and are, therefore, the most refractory melts that could be produced.

The Cr-Ti plot (Figure 6.9) shows that the melts which are in equilibrium with the serpentinite diapir samples have compositions that are similar to the UPL Group I lavas. This suggests that the serpentinite diapir lherzolites could be the residual lithologies from the melting event which produced the UPL Group I lavas and, by implication (Cameron, 1985; Bednarz and Schmincke 1994; Kostopoulos and Murton 1992), would represent the residual lithology after construction of the plutonic section and the LPL. The other plots on Figures 6.9 and 6.10 show that the serpentinite diapir melts are displaced from the UPL Group I lavas along a trend which is parallel to the one that describes the variation in the UPL Group III lavas, and has been interpreted by Cameron (1985) as a result of subduction zone enrichment processes. The Cr-TiO_2 plot (Figure 6.9) also shows that the melts in equilibrium with the Troodos *background* harzburgites have compositions similar to the UPL Group III lavas. On the plots involving elements thought to be added by subduction-related fluids/melts (Cameron, 1985; Bednarz and Schmincke 1994; Kostopoulos and Murton 1992), the equilibrium melts plot along the same enrichment vector as the UPL Group III lavas (e.g. the TiO_2/Zr - Zr plot). These relationships suggest that the *background* harzburgites are reasonable residual lithologies for the UPL Group III lavas and that the serpentinite diapir lherzolites are probable residues to the UPL Group I lavas.

The fact that the calculated equilibrium melts usually plot towards less enriched compositions than the UPL Group III lavas (e.g. the TiO_2/Zr - Zr plot), suggests that either the enrichment event preceded the main phase of melting or that the calculated melts do not accurately reflect the pooled melt compositions of the natural lavas. In the latter case, the melts calculated to be in equilibrium with the peridotites will give compositions of the most depleted melts that it would be possible to extract from the melting column, whereas natural melts will be pooled and mixed in magma chambers, and will therefore be less refractory.

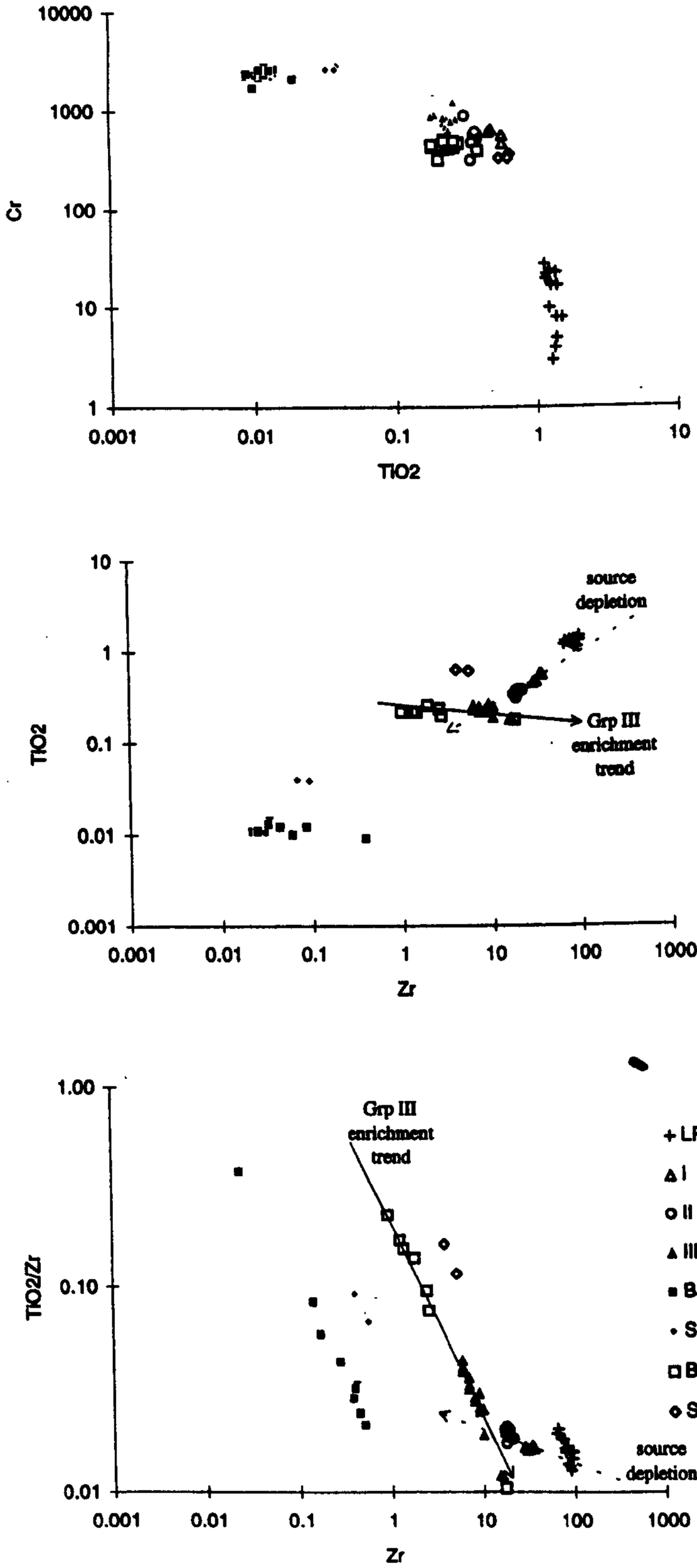

Figure 6.9. Graphs illustrating the Cr, Zr and Ti variation in the Troodos harzburgites and the pillow lavas; LPL data from Bednarz and Schmincke (1994), UPL data from Cameron (1985). Solid arrows show the vector of source enrichment proposed by Cameron (1985) to explain the variations in the chemistry of the Group III lavas; dashed arrow indicates vector of source depletion proposed by Cameron to explain the variations between the Group I and II lavas.

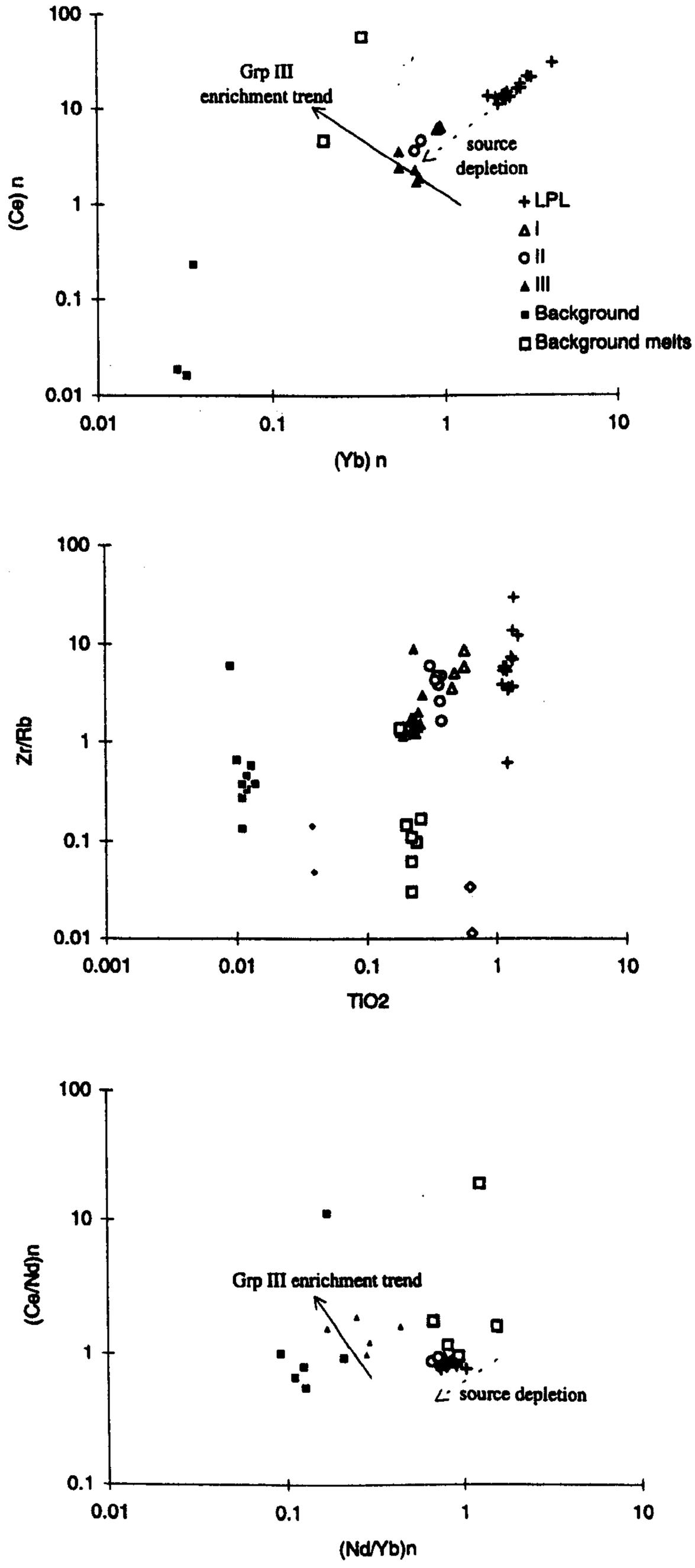

Figure 6.10. Graphs illustrating the Ce, Nd, Yb, Zr, Rb and Ti variation in the Troodos harzburgites and the pillow lavas; LPL data from Bednarz and Schmincke (1994), UPL data from Cameron (1985). The illustrated vectors are explained in Figure 6.9.

As noted above, several studies have appealed to the addition of a subduction component to describe the geochemical variation in the UPL Group III lavas. The composition of this enriching component can be calculated using the methodology of Pearce *et al.* (1992). To do this, the melt composition that would be expected to be produced in an un-enriched melting zone is calculated by assuming a source composition and melting history. The same source (fertile MORB mantle) used in the previous melting models was used, and a melting history of 15% fractional melting followed by pooling the melt of a further 5% fractional melting was assumed. An initial modal composition of olivine 65.90%, orthopyroxene 27.42%, clinopyroxene 5.90% and spinel 0.78%, for the second stage of melting, was taken from the modelled modes of Kostopoulos (1991). This melting history is similar to that proposed by Cameron (1985) from his study of the UPL and fits with the minimum melting estimates made from the harzburgite data in this thesis. This calculated, un-enriched, melt can then be subtracted from the natural melt composition to give the composition of the enriched component. The calculated enriched component is illustrated in Figure 6.11a.

The REE variation in clinopyroxene from the *background* harzburgites was described in Chapter 4 and the variation in L-MREE attributed to the addition of a L-MREE enriched component. The composition of this component was calculated in Chapter 4 and is presented here in Figure 6.11b in order to compare the presumed subduction component from the lava geochemistry to that modelled from the *background* harzburgite data.

Considering the number of assumptions that have to be made to produce the enriched component trace element profiles, and the fact that Cameron's (1985) Sr, Zr and Y data were determined by XRF and are therefore relatively imprecise, the two sets of patterns display a surprising number of similarities. Both graphs show that the enriched component had positive Sr anomalies, and no significant Zr anomalies, relative to the adjacent REEs. In both cases, the enriching component is LREE enriched and has no Ti. These data suggest that the enrichment event, linked by Cameron (1985) to an incompatible element enriched melt/fluid from a subducting slab, has been recorded by both the peridotites and the lavas. Because partial melting rapidly depletes the source in incompatible elements, this means that the influx of the subduction zone component must have continued after the melting event which produced the UPL Group III lavas.

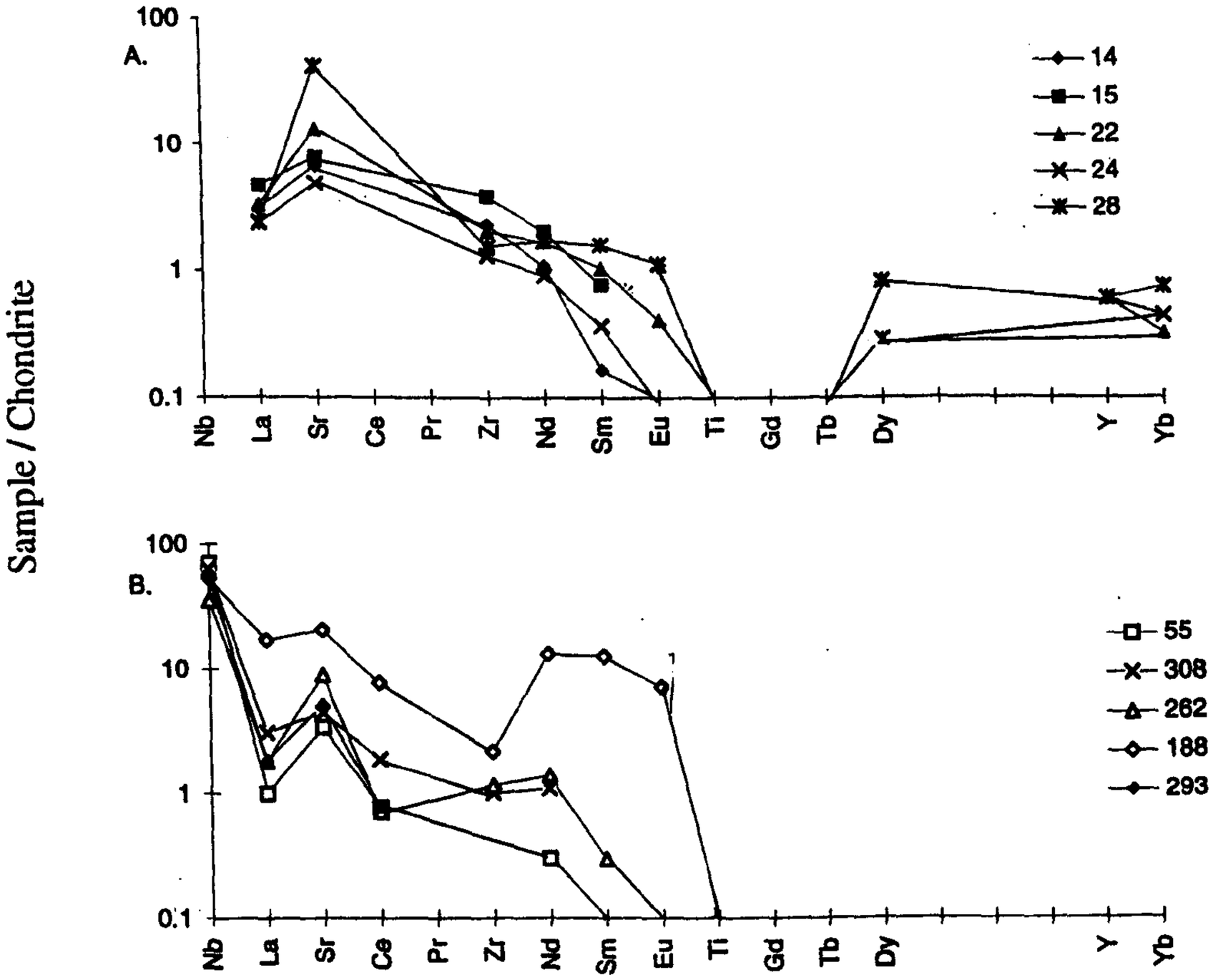

Figure 6.11. a) Enriched component calculated for the UPL lavas using the methodology of Pearce *et al.* (1992) and the lava geochemistry data from Cameron (1985); data labels refer to Camerons sample numbers. b) The enriched component calculated for the Troodos clinopyroxene trace element data in Chapter 4.

6.5.2 THE RELATIONSHIP BETWEEN THE PYROXENITES AND THE OVERLYING CRUST

The similarities between the geochemistry of the Type I pyroxenites and the LPL, and the Type II pyroxenites and UPL was noted in Section 6.4.4. A hypothesis was made that the geochemical division between the tholeiitic Type I pyroxenites and LPL, and the boninitic Type II pyroxenites and UPL, represented a fundamental genetic relationship between the lavas and pyroxenites. In Section 6.4.5, it was argued that the geochemical variation in the *Anomaly 1* harzburgites matched that in the Type I pyroxenites and the geochemical variation in the *Anomaly 2* harzburgites matched that in the Type II pyroxenites. Therefore, the element enrichments in the *Anomaly 1* harzburgites were attributed to interaction with a Type I pyroxenite melt and the element enrichments in the *Anomaly 1* harzburgites attributed to interaction with a Type II pyroxenite melt. The data presented in Sections 6.4.4 and 6.4.5 is complied here in Tables 6.6 and 6.7 to facilitate comparison between the chemistry of the pyroxenites, *Anomaly 1* and *2* harzburgites and the crustal sequence.

	Anomaly 1	Type I pyroxenites	Plutonic sequence/ LPL
Whole-rock	Trend of Zr enrichment	Trend towards high Ti, Sc, Zr, Y and low Ni, Co, Zr/Ti = 23.3	High Ti gabbros Average LPL Zr/Ti = 63.2
Olivine	Low Mg#, trend towards low Ni	Fe enriched (low Mg#), Ni depleted	Mineral chemistry trends plot on an extension of the Type I pyroxenite trends
Orthopyroxene	Al enriched	Fe enriched	
Clinopyroxene	High Na, coarse poikilitic grains	Fertile end-member = clinopyroxene bearing	
Spinel	Plot on interaction trend IT2 of increasing Cr# and Ti	Trend of Cr-Fe-Ti enrichment equivalent to IT2	

Table 6.6. Summary of the geochemical variation in the *Anomaly 1* harzburgites, Type I pyroxenites and the plutonic sequence. Plutonic sequence data from Malpas *et al*, 1990 and references therein.

As the data in Table 6.6 show, there are sufficient geochemical similarities between the *Anomaly 1* harzburgites, Type I pyroxenites and LPL to suggest a petrogenetic model in which the melts that eventually crystallised the high-Ti gabbros and LPL interacted with the mantle they traversed between the source region and eruption site. This interaction produced trace element enrichments in the host harzburgites (i.e. the *Anomaly 1* harzburgites) and the Type I pyroxenites. This model is supported by the following facts: i) the variation in the Type I pyroxenites is equivalent to that produced by fractional crystallisation - which is also the main process responsible for geochemical variation within the sheeted dykes and LPL (Malpas *et al.* 1990 and references therein); ii) the *Anomaly 1* harzburgites plot on an extension of the crustal dunite mineral chemistry trends on the mantle cross-sections presented in Chapter 4 (see Section 4.5); and iii) the olivine-clinopyroxenites (the most fertile end-member of the Type I pyroxenites) outcrop within and stratigraphically below the *Anomaly 1* harzburgites.

	Anomaly 2	Type II pyroxenites	UPL
Whole-rock	no data	Low Ti, plot on an extension of the *background* hz trend for Ni, Y, Co. Zr/Ti = 1.3 - 2.3	Low Ti, Zr/Ti decreases upwards through the sequence from 61.1 to 40.6
Olivine	High Mg# and Ni	Fe-Ni enriched	-
Orthopyroxene	High Al	High Mg# and Al	-
Clinopyroxene	Very high Na	High Mg# and Na	-
Spinel	Plot on interaction trend IT1 of decreasing Cr# and gradually increasing Ti	Mg-Al enrichment equivalent to IT 1	-

Table 6.7. Summary of the geochemistry of the *Anomaly 2* harzburgites, Type II pyroxenites and the UPL. UPL data from Cameron (1985) and references therein.

The data in Table 6.7 show that there are sufficient geochemical similarities between the *Anomaly 2* harzburgites, Type II pyroxenites and the UPL to suggest a model in which the melts that eventually crystallised the UPL also interacted with the mantle they traversed between the source region and eruption site. This interaction produced trace element enrichments in the host harzburgites (i.e. the *Anomaly 2* harzburgites) and the Type II pyroxenites.

The age relationships between the Type I and II pyroxenite melts have been discussed in Section 6.4.4. It is apparent from field evidence that the Type I pyroxenite melt was present in the mantle section for a considerable time period; from early in the mantle deformation event until after deformation had ceased. In contrast, the Type II melt was only intruded during the mantle deformation. Clearly there is a timing problem if the Type I and II melts are directly related to the LPL and UPL lavas respectively, as most studies of the lava sequence show a simple stratigraphy with the younger UPL lavas overlying the LPL (e.g. Cameron, 1985). The lava data would suggest therefore, that the Type II pyroxenites should be younger than the Type I pyroxenites if the proposed relationship with the pyroxenites is correct. However, recent studies of the lava sequence have found that there is considerable interlayering of the LPL and UPL and the simple stratigraphy proposed by earlier workers may not be correct (S. Edwards pers. comm.). This evidence is supported by studies of the plutonic section (Malpas, 1990) which show

that at least two distinct magma types were being supplied to the crust at the same time. The data from the pyroxenites support this hypothesis and it is clear that the main phase of pyroxenite intrusion occurred during deformation when both Type I and II melts were present. The 'timing problem' might, therefore, be a result of inadequate knowledge of the lava stratigraphy rather than a problem with the model relating the Type I pyroxenite-LPL and the Type II pyroxenite-UPL.

6.5.3 SUMMARY OF MANTLE-CRUST RELATIONSHIPS

It has been a concern of several authors who have worked on mantle harzburgites (e.g. Parkinson, 1993) that it is often difficult to show a simple correlation between the chemistry of residual harzburgites and the chemistry of the overlying, presumably genetically related, lavas. Because the Troodos Massif exposes a complete section of oceanic crust and high-quality analytical data are available for all the component units of the sequence it is an ideal location to examine the relationship between mantle and crust.

As discussed in the previous section, the serpentinite diapir lherzolites have compositions similar to residues that would have been produced during the melting event that formed the LPL. This is intuitively reasonable because the LPL are tholeiitic and evidence from dredged mid-ocean ridge basalts and peridotites indicates that tholeiitic melts will leave lherzolitic residues. Also, as discussed above, the Troodos harzburgites have compositions similar to the residues that would have been produced during the melting event that formed the boninitic UPL. Again this is intuitively reasonable because boninites should leave very depleted residues in their source regions. This thesis has shown that these two magma types can be recognised within the minor intrusions in the mantle sequence, despite the fact that the primary melts must have undergone significant reaction with the host harzburgites in order to crystallise the almost mono-mineralic pyroxenites.

Clearly, because most of the pyroxenite intrusion took place during the mantle deformation the original stratigraphic relationships between any individual pyroxenite and related lava will not be preserved. However, the fact that a correlation can be made between the magma types in the crust and mantle is testament to the longevity of magmatic processes in oceanic environments.

6.6 GEOCHEMICAL VARIATION IN THE TROODOS MANTLE SECTION AND ITS RELATIONSHIP TO OTHER HARZBURGITE-TYPE OPHIOLITES

This study has demonstrated that the Troodos Ophiolite consists of a harzburgitic mantle section that encloses a variety of pyroxenitic and dunitic bodies. The Troodos Massif is unusual in the context of harzburgite-type ophiolites in exposing a large mass of lherzolites - the serpentinite diapir. The original position of this lithology with respect to the exposed harzburgites is not known, although the $Cr\#_{spn}$ data (Chapter 4) indicates that they were once located approximately 5 km below the harzburgite-crustal dunite contact.

Where the Troodos Massif is unique is in its preservation, coupled with the fact that relationships between the harzburgites and lherzolites can be linked to the serpentinite diapir. In fragmentary ophiolites containing harzburgite and lherzolite this relationship is rarely preserved. Although few ophiolite mantle sequences have been subjected to a study as detailed as that presented here, similarities with other harzburgite-type mantle sequences are apparent, notably in: i) the relatively restricted, refractory major element geochemistry of silicate minerals and whole-rocks (e.g. Boudier and Coleman, 1981 - the Oman Ophiolite; Dick, 1977 - the Josephine Ophiolite); ii) limited variations in the modal proportions of the harzburgites (e.g. Jaques and Cappell, 1980 - the Papuan Ophiolites); iii) U-shaped REE patterns in the harzburgites (e.g. Pallister and Knight, 1981 - the Oman Ophiolite); iv) a decrease in the abundance of minor intrusions with increasing depth below the harzburgite-crustal dunite contact (e.g. Evans and Hawkins, 1989 - the Zambales Ophiolite; Boudier and Coleman, 1981 - the Oman Ophiolite); v) dunite comprises the most abundant lithology among the minor intrusions (e.g. Dick, 1977 - the Josephine Ophiolite); vi) the presence of chromitite bodies (e.g. Rassios and Pearce, 1995 - the Vourinos Ophiolite); vii) the presence of pyroxenitic dykes precipitated from transient melts and associated with reaction between the host harzburgites and the transient melts (e.g. Varvalvy *et al.*, 1996 and Edwards 1995 - the Bay of Islands Ophiolite; Boudier and Coleman, 1981 - the Oman Ophiolite; Piskin *et al.*, 1990 - the Hatay Ophiolite); and viii) the presence of irregular masses of clinopyroxenite in the base of the crustal dunites (e.g. Boudier and Coleman, 1981 - the Oman Ophiolite).

It is clear from this study, and those cited above, that harzburgite-type ophiolites record a complex history of partial melting and melt interaction events. In agreement with the numerous other studies of harzburgite-type ophiolites cited above, the depleted geochemistry of Troodos harzburgite mantle section was probably achieved via multiple melting events. The earliest phase of melting probably taking place at an oceanic-

spreading centre and the later partial melting events associated with the influx of volatiles produced by subduction processes. This influx of volatiles is extremely important because it lowers the solidus of the peridotite; allowing more melting to take place and, therefore, a greater range of melt compositions to be produced. The volatiles also introduce incompatible elements into the melting column which affects the chemistry of both the melts and the residues.

6.7 THE MAIN CONCLUSIONS OF THE THESIS

The Troodos Massif exposes an intact section of harzburgitic mantle from its contact with crustal lithologies, to a depth of approximately 3 km, where it is faulted against a mass of heavily fractured and serpentinised peridotites; the serpentinite diapir. The harzburgites are host to several generations of pyroxenitic and dunitic intrusives. Many of the intrusions have features suggestive of a reaction relationship with the enclosing harzburgites, such as resorbed harzburgite xenoliths and marginal dunites.

Mineral chemistry and whole-rock data suggest that the harzburgites in the Troodos sequence are residues from up to 30% fractional partial melting in the spinel stability field. The serpentinite diapir exposes lherzolitic lithologies which can be modelled by 10 to 15% fractional partial melting in the spinel stability field. In both cases, the starting composition for the melt modelling was a fertile MORB source, which suggests that, prior to the formation of the Massif, the mantle had a composition equivalent to the global convecting reservoir from which N-MORB was extracted. Whole-rock data are consistent with a two stage melting history to form the Troodos harzburgites. By analogy with the pillow lava sequence, the first of these probably occurred at a supra-subduction zone spreading centre and involved up to 20% melting. During this melting event the plutonic sequence and LPL were formed. The serpentinite diapir samples are possible equivalents to the residual lithologies which would have been formed during this event. The second stage of melting was possibly triggered by increased fluid influx from a subduction zone, and resulted in up to a further 10% melting. The UPL are the erupted melts produced by this melting event and the Troodos harzburgites have compositions similar to the expected residues.

Deviations from the compositions expected to result from simple fractional partial melting are found in several situations in the mantle section and suggest that melts/fluids interacted with the mantle during and after the partial melting event. Three main situations were identified; in specific parts of the *background* harzburgite section; around pyroxenites and in the clinopyroxene in the Troodos harzburgites. In the *background*

harzburgites, mineral chemistries were enriched at the top of the sequence (*Anomaly 1*) and in a layer towards the base of the sequence (*Anomaly 2*). Pyroxenites also enrich their wallrocks and two trends were identified on the basis of spinel compositions. The Type I trend is of Cr-Fe-Ti enrichment and is similar to the mineral chemistry variations in the *Anomaly 1* harzburgites. The melt involved is inferred to be tholeiitic in nature from the pattern of element variation in the Type I wallrocks. The Type II trend is of Mg-Al enrichment and is similar to the mineral chemistry variations in the *Anomaly 2* harzburgites. The melt involved is inferred to be boninitic in nature from the pattern of element variation in the Type II wallrocks. The fact that the LPL have tholeiitic chemistries and the UPL boninitic chemistries suggests a genetic link between the pyroxenite melts and the pillow lava sequence.

The clinopyroxene trace element patterns from the *background* harzburgites suggest that the LREE, Nd, Sr and Zr are enriched in these minerals compared to the expected values for fractional partial melting. The enriched component was modelled from the clinopyroxene data and is similar in trace element pattern to the enriched component in the UPL. This suggests that the addition of the subduction component proposed by Cameron (1985) to explain the UPL chemistries was probably added to the mantle both during and after the melting event which produced the UPL. The fact that most lavas in the Troodos pillow lava sequence have high primary H_2O contents (Muenow *et al.*, 1990) supports this hypothesis.

The Troodos data show that ophiolitic mantle sections can record a long history of melting and melt/fluid interaction. For some processes, such as partial melting and late stage fluid/melt interaction, the mantle peridotites provide a better record of events than the erupted lavas whose chemistry is complicated by pooling of melts and high level crystallisation processes. A flow chart summarising a possible geochemical evolution of the Troodos Massif is presented in Figure 6.12.

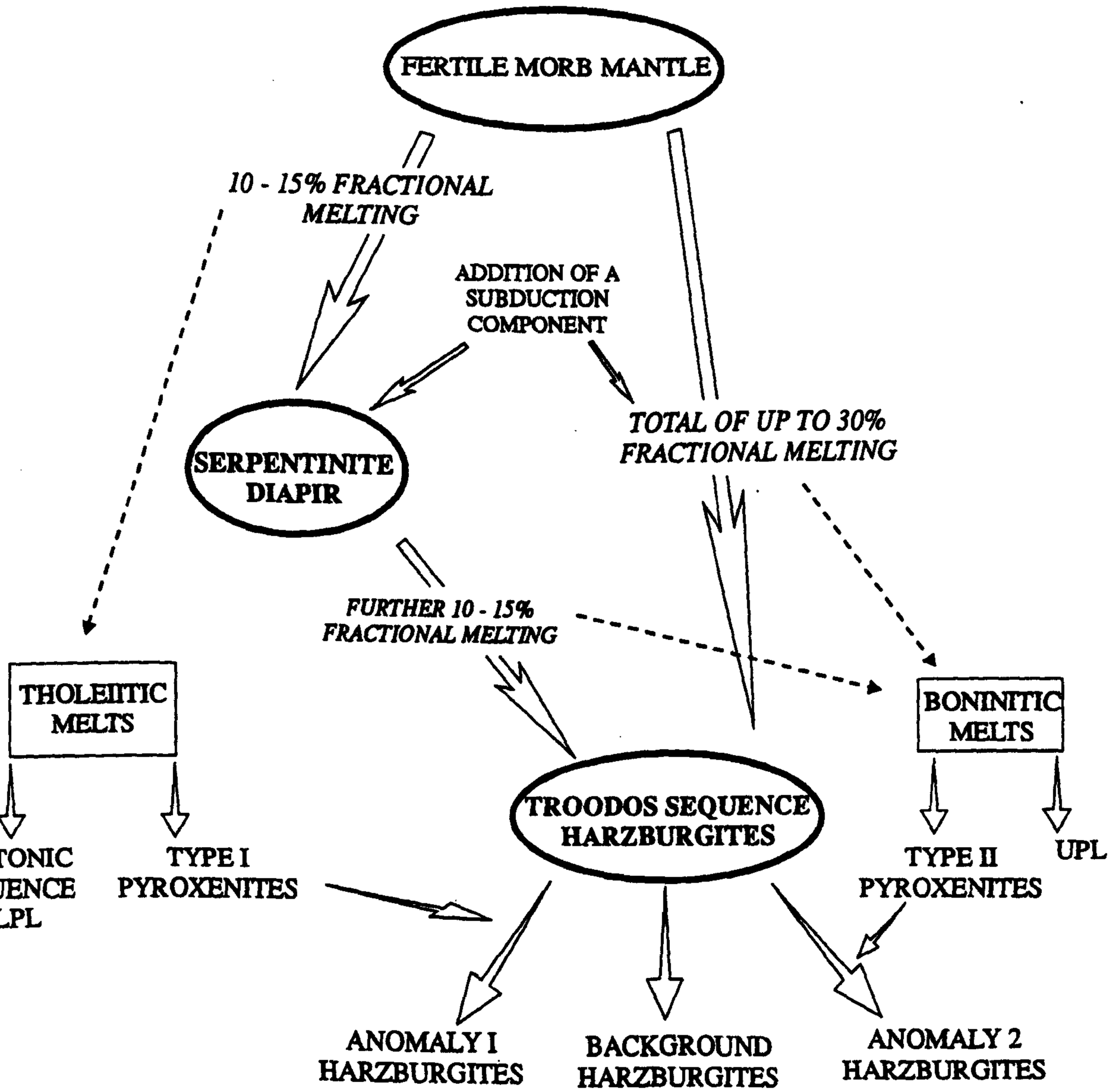

Figure 6.12. Flow diagram summarising the evolution of the Troodos Massif mantle section.

REFERENCES

Anders, E. and Gervesse, N., 1989. Abundances of the elements: Meteoritic and solar. *Geochemica et Cosmochimica Acta*, **53**, 197-214.

Anonymous, 1972. Penrose field conference on ophiolites. *Geotimes*, **17**, 24-25.

Arai, S., 1990. What kind of magmas could be equilibrated with ophiolitic peridotites? *In* Malpas, J., Moores, E.M., Panayiotou, A. and Xenophontos, C. (eds.). Troodos 1987. Ophiolites - Oceanic crustal analogues. 557-565.

Arai, S., 1994. Characteristics of spinel peridotites by olivine-spinel compositional relationships: review and interpretation. *Chemical Geology*, **113**, 191-204.

Augé, T. 1987. Chromite deposits in the northern Oman ophiolite: Mineralogical constraints. *Mineral. Deposita*, **22**, 1-10.

Ayers, J.C., 1993. Partitioning and mass-balance relations in lherzolites. *Chemical Geology*., **107**, 19-27.

Ballhaus, C., Berry, R.F. and Green, D.H., 1990. Oxygen fugacity controls in the Earth's upper mantle. *Nature*, **348**, 437-440.

Baragar, W.R.A., Lambert, M.B., Baglow, N. and Gibson, I.L., 1990. The sheeted dyke zone in the Troodos Ophiolite. *In* Malpas, J., Moores, E.M., Panayiotou, A. and Xenophontos, C. (eds.). Troodos 1987. Ophiolites - Oceanic crustal analogues. p. 37-52.

Bartholomew, I.D., 1993. The interaction of diapiric uprise centres along mid-ocean ridges - evidence from mantle fabric studies of ophiolite complexes. *From* Prichard, H.M., Alabaster, T., Harris, N.B.W. and Neary, C.R. (eds.), *Magmatic Processes and Plate Tectonics*, Geological Society Special Publication No. 76, 245-256.

Batanova, V.G., Sobolev, A.V. and Schmincke, H-U., 1994. Mantle lherzolites from Troodos Ophiolites: Mineralogy and ion probe chemistry of clinopyroxenes. *Min. Mag.*, **58A**, 57-58.

Bédard, J.H., 1989. Disequilibrium melting. *Earth. Planet. Sci. Lett.*, **91**, 359-366.

Bednarz, U. and Schmincke, H-U., 1994. Petrological and chemical evolution of the northeastern Troodos extrusive series, Cyprus. *J. Petrol.*, **35**, 489-523.

Bodinier, J.L., Vasseur, G., Vernieres, J., Dupuy, C., and Fabries, J., 1990. Mechanisms of mantle metasomatism: Geochemical evidence from the Lherz Orogenic Peridotite. *J. Petrol.*, **31**, 597-628.

Bodinier, J.L., Dupuy, C. and Dotcal, J., 1988. Geochemistry and petrogenesis of Eastern Pyrenean peridotites. *Geochemica et Cosmochimica Acta*, **52**, 2893-2907.

Bodinier, J.-L., Merlet, C., Bedini, R.M., Remaidi, M. and Garrido, C.J., 1996. Distribution of niobium, tantalum, and other highly incompatible trace elements in the lithospheric mantle: The spinel paradox. *Geochemica et Cosmochimica Acta*, **60**, 545-550.

Bonatti, E. and Michael, P.J., 1989. Mantle peridotites from continental rifts to ocean basins to subduction zones. *Earth. Planet. Sci. Lett.*, **91**, 297-311.

Bottinga, Y. and Allègre, C.J., 1978. Partial melting under spreading ridges. *Trans. R. Soc. Lond.*, **288**, 501-525.

Boudier, F. and Coleman, R.G., 1981. Cross section through the peridotite in the Samail Ophiolite, Southeastern Oman Mountains. *J. Geophys. Res.*, **86**, 2573-2592.

Brey, G.P. and Kohler, T., 1990. Geothermobarometry in four-phase lherzolites II. New thermobarometers and a practical assessment of existing thermobarometers. *J. Petrol.*, **31**, 1353-1378.

Browning, P., 1984. Cryptic variation within the Cumulate Sequence of the Oman ophiolite: magma chamber depth and petrological implications. *Geol. Soc. London Sp. Pub.*, **13**, 71-82.

Cameron, W.E., 1985. Petrology and origin of primitive lavas from the Troodos ophiolite, Cyprus. *Contrib. Mineral. Petrol.*, **89**, 239-255.

Cannat, M., Bideau, D. and Hébert, R., 1990. Plastic deformation and magmatic impregnation in serpentinized ultramafic rocks from the Garrett transform fault (East Pacific Rise). *Earth. Planet. Sci. Lett.*, **101**, 216-232.

Ceuleener, G. and Rabinowicz, M., 1992. Mantle flow and melt migration beneath oceanic ridges: Models derived from observations in ophiolites. *In* Phipps Morgan, J., Blackman, D.K. and Sinton, J.M. (eds.). Mantle flow and melt generation at mid-ocean ridges, *Geophysical Monograph*, **71**, 123-154.

Coleman, R.G. and Keith, T.E., 1971. A chemical study of serpentinisation - Burro Mountian, California. *J. Petrol.*, **12**, 311-328.

Conquéré, F. and Fabriès,J., 1984. Chemical disequlibrium and its thermal significance in spinel-peridotites from the Lherz and Freychinede ultramafic bodies (Ariege; French Pyrenees). *In* Kornprobst, J. (ed.), Kimberlites II: the mantle and crust-mantle relationships. Elsevier, 319-323.

Davies, J.H. and Stevenson, D.J., 1992. Physical model of source region of subduction zone volcanics. *J. Geophys. Res.*, **97**, 2037-2070.

Dick, H.J.B. and Natland, J.H., 1996. Late-stage melt evolution and transport in the shallow mantle beneath the East Pacific rise. *In* Mével, C., Gillis, K.M., Allan, J.F. and Meyer, P.S. (Eds.), *Proc. ODP, Sci. Results*, 147: College Station, TX (Ocean Drilling Program), 103-134.

Dick, H.J.B., 1989. Abyssal Peridotites, very slow spreading ridges and ocean ridge magmatism. *In* Saunders, A.D., and Norry, M.J., (eds.) *Magmatism in the Ocean Basins. Geol. Soc. London Sp. Pub.*, **42**, 71-105.

Dick, H.J.B., Fisher, R.L. and Bryan, W.B., 1984. Mineralogical variability of the uppermost mantle along mid-ocean ridges. *Earth. Planet. Sci. Lett.*, **69**, 88-106.

Dick, H.J.B., and Bullen, T., 1984. Chromian spinel as a petrogenetic indicator in abyssal and alpine-type peridotites and spatially associated lavas. *Contrib. Mineral. Petrol.*, **86**, 54-76.

Dick, H.J.B., 1977. Partial melting in the Josephine peridotite 1, The effect on mineral composition and its consequence for Geobarometry and Geothermometry. *Am. J. Sci.* **277**, 801-832.

Dick, H.J.B. and Sinton, F., 1979. Compositional layering in alpine peridotites: Evidence for pressure-solution creep in the mantle. *J. Geology*, **87**, 403-416.

Dungan, M.A. and Avé Lallement, H.G., 1977. Formation of small dunite bodies by metasomatic transformation of harzburgite in the Oregon Mountain Ophiolite, Northeast Oregon. *Oregon Dept. Geol. Mineral. Ind. Bull.*, **96**, 109-128.

Edwards, S.J., and Malpas, J., 1995. Multiple origins for mantle harzburgites: examples from the Lewis Hills, Bay of Islands ophiolite, Newfoundland. *Can. J. Earth Sci.*, **32**, 1046-1057.

Edwards, S.J., 1995. Boninitic and tholeiitic dykes in the Lewis Hills mantle section of the Bay of Islands ophiolite: implications for magmatism adjacent to a fracture zone in a back-arc spreading environment. *Can. J. Earth Sci.*, **32**, 2128-2146.

Edwards, S.J. and Malpas, J., 1996. Melt-peridotite interaction in shallow mantle at the East Pacific Rise: Evidence from ODP Site 895 (Hess Deep). *Min. Mag.*, **60**, 191-206.

Edwards, S.J., 1990. Harzburgites and refractory melts in the Lewis Hills Massif, Bay of Islands Ophiolite Complex: The base metals and precious metals story. *Can. Min.*, **28**, 537-552.

Eggler, D.H., 1987. Solubility of major and trace elements in mantle metasomatic fluids: Experimental constraints. *In* Menzies, M.A. and Hawkesworth, C.J., (eds) *Mantle Metasomatism*, Academic Press (London), 21-41.

Elliot, T.R., Hawkesworth, C.J. and Grönvold, K., 1991. Dynamic melting of the Iceland plume. *Nature*, **351**, 201-206.

Elthon, D.,1992. Chemical trends in abyssal peridotites: Refertilisation of depleted suboceanic mantle. *J. Geophys. Res.*, **97**, 9015-9025.

Engin, T. and Hirst, D.M., 1970. Serpentinisation of harzburgites from the alpine peridotite belt of southwest Turkey. *Chemical Geology*, **6**, 281-295.

Evans, C. and Hawkins, J.W., 1989. Compositional heterogeneities in upper mantle peridotites from the Zambales Range Ophiolite, Luzon, Philippines. *Tectonophysics*, **168**, 23-41.

Frey, F.A., Shimizu, N., Leinbach, A., Obata, M. and Takazawa, E., 1991. Compositional variations within the Lower Layered Zone of the Horoman Peridotite, Hokkaido, Japan: Constraints on models for melt-solid segregation. *In* Menzies, M.A., Dupuy, C. and Nicolas, A., (eds.) Orogenic lherzolites and mantle processes. *J. Petrol. Spec. Issue*, 211-227.

Frey, F.A., Suen, C.J. and Stockman, H.W., 1985. The Ronda high temperature peridotite: Geochemistry and petrogenesis. *Geochemica et Cosmochimica Acta*, **49**, 2469-2491.

Fryer, P., 1992. A synthesis of Leg 125 drilling of serpentinite seamounts on the Mariana and Izu-Bonin forearcs. *In* Fryer, P., Pearce, J.A., Stokking, L.B., *et al.*, *Proc. ODP, Sci. Results*, **125**, College Station, TX (Ocean Drilling Program), 539-614.

Fryer, P. and Pearce, J.P., 1992. Introduction to the scientific results of Leg 125. *In* Fryer, P., Pearce, J.A., Stokking, L.B., *et al.*, *Proc. ODP, Sci. Results*, **125**, College Station, TX (Ocean Drilling Program), 3-14.

Gass, I.G. and Smewing, J.D., 1973. Intrusion, extrusion and metamorphism at constructive margins: Evidence from the Troodos Massif, Cyprus. *Nature*, **242**, 26-29.

Gass, I.G., 1980. The Troodos Massif: Its role in the unravelling of the ophiolite problem and its significance in the understanding of constructive margin processes. *In* Panayiotou, A., ed., Ophiolites: Proceedings of the International Ophiolite Symposium, Cyprus, 1979: *Cyprus Geological Survey Department*, p. 23-35.

George, R.P., 1978. Structural petrology of the Olympus ultramafic complex in the Troodos ophiolite, Cyprus. *Geol. Soc. Am. Bull.*, **89**, 845-865.

Georgiou, E. and Xenophontos, C., 1980. Chromite occurrences and associated plutonic rocks in the Akapnou Forest. *In* Panayiotou, A., ed., Ophiolites: Proceedings of the International Ophiolite Symposium, Cyprus, 1979: *Cyprus Geological Survey Department*, p. 585-592.

Girardeau, J. and Lagabrielle, Y., 1992. Deformation history of peridotites from the Mariana forearc, Conical seamount, Leg 125. *In* Fryer, P., Pearce, J.A., Stokking, L.B., *et al.*, *Proc. ODP, Sci. Results*, **125**, College Station, TX (Ocean Drilling Program), 519-534.

Godard, M., Bodinier, J.L. and Vasseur, G., 1995. Effects of mineralogical reactions on trace element redistributions in mantle rocks during percolation processes: A chromatographic approach. *Earth. Planet. Sci. Lett.*, **133**, 8449-461.

Greenbaum, D., 1972. Magmatic processes at ocean ridges: Evidence from the Troodos massif, Cyprus. *Nature*, **238**, 18-21.

Greenbaum, D., 1977. The chromitiferous rocks of the Troodos Ophiolite Complex, Cyprus. *Economic Geology*, **72**, 1175-1194.

Hanson, G.N. and Langmuir, C.H., 1978. Modelling of major elements in mantle-melt systems using trace element approaches. *Geochemica et Cosmochimica Acta*, **42**, 725-741.

Hébert, R. and Laurent, R., 1990. Mineral chemistry of the plutonic section of the Troodos Ophiolite: New constraints for the genesis of arc-related ophiolites. Malpas, J., Moores, E.M., Panayiotou, A. and Xenophontos, C. (eds.). Troodos 1987. Ophiolites - Oceanic crustal analogues. p. 149-164.

Hinton, R.W., Davis, A.M., Scatena-Wachel, D.E., Grossman, L. and Draus, R.J., 1988. A chemical study of hibonite-rich refractory inclusions in primitive meteorites. *Geochemica et Cosmochimica Acta*, **52**, 2573-2598.

Ishii, T., Robinson, P.T., Maekawa, H. and Fiske, R., 1992. Petrological studies of peridotites from diapiric serpentinite seamounts in the Izu-Ogasawara-Mariana forearc, Leg 125. *In* Fryer, P., Pearce, J.A., Stokking, L.B., *et al.*, *Proc. ODP, Sci. Results*, **125**, College Station, TX (Ocean Drilling Program), 445-486.

Jaques, A.L. and Chappell, B.W., 1980. Petrology and trace element geochemistry of the Papuan Ultramafic Belt. *Contrib. Mineral. Petrol.*, **75**, 55-70.

Jaques, A.L. and Green, D.H., 1980. Anhydrous melting of peridotite at 0-15 kb pressure and the genesis of tholeiitic basalts. *Contrib. Mineral. Petrol.*, **73**, 287-310.

Johnson, M.C., Anderson, A.T. and Rutherford, M.J. 1994. Pre-eruptive volatile contents of magmas. *In* Carroll, M.R. and Holloway, J.R. (eds). *Volatiles in magmas*, Reviews in Mineralogy, **30**, 281-330.

Johnson, K.T. and Dick, H.J.B., 1992. Open system melting and temporal and spatial variation of peridotite and basalt at the Atlantis II fracture zone. *J. Geophys. Res.*, **97**, 9219-9241.

Johnson, K.T., Dick, H.J.B. and Shimizu, N., 1990. Melting in the upper mantle: An ion microprobe study of diopsides in abyssal peridotites. *J. Geophys. Res.*, **95**, 2661-2678.

Kay, R.W. and Senechal, R.G., 1976. The rare earth geochemistry of the Troodos Ophiolite Complex. *J. Geophys. Res.*, **81**, 964-970.

Keleman, P.B., 1990. Reaction between ultramafic rock and fractionating basaltic magma I. Phase relations, the origin of calc-alkaline magma series, and the formation of discordant dunite. *J. Petrol.*, **31**, 51-98.

Keleman, P.B., Joyce, D.B., Webster, J.D. and Holloway, J.R., 1990. Reaction between ultramafic rock and fractionating basaltic magma II. Experimental investigation of reaction between olivine tholeiite and harzburgite at 1150-1050°C and 5 kb. *J. Petrol.*, **31**, 99-134.

Keleman, P.B., Dick, H.J.B. and Quick, J.E., 1992. Formation of harzburgite by pervasive melt/rock reaction in the upper mantle. *Nature*, **358**, 635-641.

Keleman, P.B. and Dick, H.J.B., 1995. Focused melt flow and localised deformation in the upper mantle: juxtaposition of replacive dunite and ductile shear zones in the Josephine peridotite, S.W. Oregon. *J. Geophys. Res.*, **100**, 423-438.

Kimball, K.L., Spear, F.S. and Dick, H.J.B., 1985. High temperature alteration of abyssal ultramafics from the Islas Orcadas fracture zone, south Atlantic. *Contrib. Mineral. Petrol.*, **91**, 307-320.

Kimball, K.L., 1990. Effects of hydrothermal alteration on the compositions of chromian spinels. *Contrib. Mineral. Petrol.*, **105**, 337-346.

Kinzler, R.J., 1993. Major element constraints on the extent of re-equilibrium between melts and residues within melting regimes beneath ocean ridges. [abstr.] *in* AGU 1993 spring meeting, *Eos*, Transactions, American Geophysical Union, **74**, 283, May 1993.

Kostopoulos, D.K. and Murton, B.J., 1992. Origin and significance of components in boninite genesis: significance of the OIB component. *In* Parsons, L.M., Murton, B.J. and Browning, P. (eds), *Ophiolites and their modern oceanic analogues*. Geological Society Special Publication No. 60, pp. 153-154.

Kostopoulos, D.K., 1991. Melting of the shallow upper mantle: A new perspective. *J. Petrol.*, **32**, 671-699.

Kurat, G., Palme, H., Spettiel, B., Baddenhausen, H., Hofmeister, H., Palme, C. and Wänke, H., 1980. Geochemistry of ultramafic xenoliths from Kapfenstein, Austria: Evidence for a variety of upper mantle processes. *Geochemica et Cosmochimica Acta*, **44**, 45-60.

Laurent, R., 1990. Parental magma and crystal fractionation modelling of the CY-4 plutonic rocks, Troodos ophiolite, Cyprus. *In* Malpas, J., Moores, E.M., Panayiotou, A. and Xenophontos, C. (eds). Troodos 1987. Ophiolites - Oceanic crustal analogues. p. 139-148.

Lorand, J.-P. and Ceuleneer, G., 1989. Silicate and base-metal sulphide inclusions in chromites from the Masquad area (Oman Ophiolite, Gulf of Oman): A model for entrapment. *Lithos*, **22**, 173-190.

Maaløe, S. and Aoki, K., 1977. The major element composition of the upper mantle estimated from the composition of lherzolites. *Contrib. Mineral. Petrol.*, **63**, 161-173.

Maaløe, S., 1981. Magma accumulation in the ascending mantle. *J. Geol. Soc. Lond.*, **138**, 223-236.

MacLeod, C.J. 1990. Role of the Southern Troodos Transform Fault in the rotation of the Cyprus microplate: Evidence from the Eastern Limassol Forest Complex. *In* Malpas,

J., Moores, E.M., Panayiotou, A. and Xenophontos, C. (eds). Troodos 1987. Ophiolites - Oceanic crustal analogues. p. 75-86.

Magaritz, M. and Taylor, H.P., 1974. Oxygen and hydrogen isotope studies of serpentinisation in the Troodos Ophiolite Complex, Cyprus. *Earth. Planet. Sci. Lett.*, **23**, 8-14.

Malpas, J., 1990. Crustal accretionary processes in the Troodos Ophiolite, Cyprus: Evidence from field mapping and deep crustal drilling. *In* Malpas, J., Moores, E.M., Panayiotou, A. and Xenophontos, C. (eds). Troodos 1987. Ophiolites - Oceanic crustal analogues. p. 65-74.

Malpas, J., Moores, E.M., Panayiotou, A. and Xenophontos, C. (eds), 1990. Troodos 1987. Ophiolites - Oceanic crustal analogues. 733p.

Maltman, A.J., 1978. Serpentinite textures in Anglesey, North Wales, United Kingdom. *Geol. Soc. Am. Bull.*, **89**, 972-980.

Mattioli, G.S., Baker, M.B., Rutter, M.J. and Stolper, E.M., 1989. Upper mantle oxygen fugacity and its relationship to metasomatism. *J. Geology*, **97**, 521-536.

Mattioli, G.S. and Wood, B., 1986. Upper mantle oxygen fugacity recorded by spinel-lherzolites. *Nature*, **322**, 626-628.

Mattioli, G.S. and Wood, B., 1988. Magnetic activities across the $MgAl_2O_4$-Fe_3O_4 spinel joint, with applications to thermobarometric estimates of upper mantle oxygen fugacity. *Contrib. Mineral. Petrol.*, **98**, 148-162.

McCulloch, M.T. and Gamble, J.A., 1991. Geochemical and geodynamical constraints on subduction zone magmatism. *Earth. Planet. Sci. Lett.*, **102**, 358-374.

McDonough, W.F., Stosch, H.-G. and Ware, N.G., 1992. Distribution of titanium and the rare earth elements between peridotitic minerals. *Contrib. Mineral. Petrol.*, **110**, 321-328.

McElduff, B. and Stumpfl, E.F., 1991. The chromite deposits of the Troodos Complex, Cyprus: Evidence for the role of a fluid phase accompanying chromite formation. *Mineral. Deposita*, **2**, 307-318.

McElduff, B. and Stumpfl, E.F., 1990. Platinum-Group Minerals from the Troodos Ophiolite. *Mineral. Petrol.*, **42**, 211-232.

McKenzie, D.P., 1984. The generation and compaction of partially molten rock. *J. Petrol.*, **25**, 713-765.

Menzies, M.A. and Hawkesworth, C.J., 1987. (eds.) Mantle Metasomatism. Academic Press, (London).

Menzies, M.A., Long, A., Ingram, G., Tatnell, M. and Janecky, D., 1993. MORB peridotite-sea water interaction: Experimental constraints on the behaviour of trace elements, $^{87}Sr/^{86}Sr$ and $^{143}Nd/^{144}Nd$ ratios. *From* Prichard, H.M., Alabaster, T.,

Harris, N.B.W. and Neary, C.R. (eds.), *Magmatic Processes and Plate Tectonics*, Geological Society Special Publication No. **76**, 309-322.

Menzies, M. and Allen, C., 1974. Plagioclase lherzolite-residual mantle relationships within two eastern Mediterranean ophiolites. *Contrib. Mineral. Petrol.*, **45**, 197-213.

Mercier, J-C. C. and Nicolas, A., 1975. Textures and fabrics of upper-peridotites as illustrated by xenoliths from basalts. *J. Petrol.*, **16**, 454-487.

Michael, P.J. and Bonatti, E., 1985. Peridotite composition from the North Atlantic: Regional and tectonic variations and implications for partial melting. *Earth. Planet. Sci. Lett.*, **73**, 91-104.

Miyashiro, A., 1973. The Troodos Ophiolite complex was probably formed at an island arc. *Earth. Planet. Sci. Lett.*, **19**, 218-224.

Moores, E.M., Varga, R.J., Verosub, K.L. and Ramsden, T., 1990. Regional structure of the Troodos dyke complex. *In* Malpas, J., Moores, E.M., Panayiotou, A. and Xenophontos, C. (eds.). Troodos 1987. Ophiolites - Oceanic crustal analogues. p. 27-36.

Moores, E.M. and Vine, F.J., 1971. The Troodos massif, Cyprus and other ophiolites as oceanic crust: evaluation and implications. *Phil. Trans. Roy. Soc. Lond. A.* **268**, 443-466.

Mottl, M.J., 1992. Pore waters from serpentinite seamounts in the Mariana and Izu-Bonin forearcs, Leg 125: Evidence for volatiles from the subducting slab. *In* Fryer, P., Pearce, J.A., Stokking, L.B., *et al.*, *Proc. ODP, Sci. Results*, **125**, College Station, TX (Ocean Drilling Program), 373-386.

Muenow, D.W., Garcia, M.O., Aggrey, K.E., Bednarz, U. and Schminke, H.-U., 1990. Volatiles in submarine glasses as a discriminant of tectonic origin: Application to the Troodos Ophiolite. *Nature*, **343**, 159-161.

Murton, B.J. and Gass, I.G., 1986. Western Limassol Forest Complex, Cyprus. Part of an Upper Cretaceous leaky transform fault. *Geology*, **14**, 255-258.

Murton, B.J., 1986. Anomalous oceanic lithosphere formed in a leaky transform fault: Evidence from the western Limassol Forest complex, Cyprus. *J. Geol. Soc. London*, **143**, 845-854.

Mysen, B.O. and Kushiro, I., 1977. Compositional variations of coexisting phases with degree of melting of peridotite in the upper mantle. *Am. Mineral.*, **62**, 843-865.

Navon, O and Stolper, E., 1987. Geochemical consequences of melt percolation: The upper mantle as a chromatographic column. *J. Geology*, **95**, 285-307.

Nicolas, A., Boudier, F. and Bouchez, J.L., 1980. Interpretation of peridotite structures from ophiolitic and oceanic environments. *Amer. J. Sci.*, **280**,192-210.

Nicolas, A., 1986. A melt extraction model based on structural studies in mantle peridotites. *J. Petrol.*, **27**, 999-1022.

Nicolas, A., 1989. Structures of ophiolites and dynamics of oceanic lithosphere, Kluwer Academic Publishers, Netherlands, 367pp.

Nicolas, A. and Prinzhofer, A., 1983. Cumulative or residual origin for the transition zone in ophiolites: Structural evidence. *J. Petrol.*, **24**, 188-206.

O'Hara, M.J. and Matthews, R.E., 1981, Geochemical evolution in an advancing, periodically replenished, periodically tapped, continuously fractionated magma chamber. *J. Geol. Soc. London.*, **138**, 237-277.

Obata, M. and Nagahara, N., 1987. Layering of alpine-type peridotite and segregation of partial melt in the upper mantle. *J. Geophys. Res.*, **92**, 3467-3474.

Ottonello, G., Piccardo, G.B. and Ernst, W.G., 1979. Petrogenesis of some Ligurian peridotites - II. Rare earth element chemistry. *Geochemica et Cosmochimica Acta*, **43**, 1273-1284.

Ozawa, K., 1983. Evaluation of olivine-spinel geothermometry as an indicator of thermal history for peridotites. *Contrib. Mineral. Petrol.*, **82**, 52-65.

Ozawa, K., 1994. Melting and melt segregation in the mantle wedge above a subduction zone: Evidence from the chromite-bearing peridotites of the Miyamori ophiolite complex, northeastern Japan. *J. Petrol.*, **35**, 647-678.

Ozawa, K. and Takahashi, N., 1995. P-T history of a mantle diapir: the Horoman peridotite complex, Hokkaido, northern Japan. *Contrib. Mineral. Petrol.*, **120**, 223-248.

Pallister, J.S. and Knight, R.J., 1981. Rare-earth element geochemistry of the Samail Ophiolite near Ibra, Oman. *J. Geophys. Res.*, **86**, 2673-2697.

Parkinson, I.J. 1993. Geochemistry and petrogenesis of fore-arc peridotites, ODP Leg 125. Unpublished PhD thesis, University of Durham.

Parkinson, I.J., Pearce, J.A., Thirlwall, M.F., Johnson, K.T.M. and Ingram, G., 1992. Trace element geochemistry of peridotites from the Izu-Bonin-Mariana forearc, Leg 125. *In* Fryer, P., Pearce, J.A., Stokking, L.B., *et al.*, *Proc. ODP, Sci. Results*, **125**, College Station, TX (Ocean Drilling Program), 487-506.

Pearce, J.A., 1975. Basalt geochemistry used to investigate past tectonic environments on Cyprus. *Tectonophysics*, **25**, 41-67.

Pearce, J.A. and Parkinson, I.J., 1993. Trace element models for mantle melting: application to volcanic arc petrogenesis. *From* Prichard, H.M., Alabaster, T., Harris, N.B.W. and Neary, C.R. (eds), *Magmatic Processes and Plate Tectonics*, Geological Society Special Publication No. 76, 373-403.

Piskin, O., Delaloye, M., Moritz, R. and Wagner J.-J., 1990. Geochemistry and geothermometry of the Hatay Complex Turkey: Implications for the genesis of the ophiolite sequence. *In* Malpas, J., Moores, E.M., Panayiotou, A. and Xenophontos, C. (eds). Troodos 1987. Ophiolites - Oceanic crustal analogues. p. 329-338.

Plank, T. and Langmuir, C.H., 1988. An evaluation of the global variations in the major element chemistry of arc basalts. *Earth. Planet. Sci. Lett.*, **90**, 349-370.

Potts, P.J. 1987. A handbook of silicate rock analysis. Blackie, London.

Potts, P.J., Tindle, A.G. and Webb, P.C., 1992. Geochemical reference material compositions. Whittles Publishing, London.

Prinzhofer, A. and Allègre, C.J., 1985. Residual peridotites and the mechanisms of partial melting. *Earth. Planet. Sci. Lett.*, **74**, 251-265.

Quick, J.E., 1981a. Petrology and petrogenesis of the Trinity Peridotite, an upper mantle diapir in the Eastern Klamath Mountains, Northern California. *J. Geophys. Res.*, **86**,11837-11863.

Quick, J.E., 1981b. The origin and significance of large, tabular dunite bodies in the Trinity Peridotite, Northern California. *Contrib. Mineral. Petrol.*, **78**, 413-422.

Quick, J.E. and Gregory, R.T., 1995. Significance of melt-wallrock reaction: a comparative anatomy of three ophiolites. *Journal of Geology*, **103**, 187-198.

Rabinowicz, M., Ceuleneer, G. and Nicolas, A., 1986. Melt segregation and flow in mantle diapirs below spreading centers: Evidence from the Oman Ophiolite. *J. Geophys. Res.*, **92**, 3475-3486.

Rampone, E., Bottazzi, P. and Ottolini, L., 1991. Complementary Ti and Zr anomalies in orthopyroxene and clinopyroxene from mantle peridotites. *Nature*, **354**, 518-520.

Rassios, A. and Pearce, J.P., 1995. Advanced tectonic and geochemical methods for chromite exploration in ophiolites. Unpublished Final Technical Report, Commission of the European Communities under the Primary Raw Materials Programme.

Rautenschlein, M., Jenner, G.A., Hertogen, J., Hofmann, A.W., Kerrich, R., Schmincke, H.-U. and White, W.M., 1985. Isotopic and trace element composition of volcanic glasses from the Akaki Canyon, Cyprus: implications for the origin of the Troodos Ophiolite. *Earth. Planet. Sci. Lett.*, **75**, 369-383.

Roberts, S., 1992. Influence of partial melting regime on the formation of ophiolitic chromitite. *From* Parsons, L.M., Murton, B.J. and Browning, P.(eds.), *Ophiolites and their Modern Oceanic Analogues*. Geological Society Special Publications No.60. pp. 203-217.

Robinson, P.T., Melson, W.G., O'Hearn, T. and Schmincke, H.-U., 1983. Volcanic glass compositions of the Troodos Ophiolite, Cyprus. *Geology*, **11**, 400-404.

Roeder, P.L. and Emslie, R.F., 1970. Olivine-Liquid Equilibrium. *Contr. Mineral. and Petrol.*, **29**, 275-289.

Seyfried, W.E. and Dibble, W.E., 1980. Seawater-peridotite interaction at 300°C and 500 bars: Implications for the origin of oceanic serpentinites. *Geochemica et Cosmochimica Acta*, **44**, 309-321.

Shaw, D.M., 1970. Trace element fractionation during anatexis. *Geochemica et Cosmochimica Acta*, **34**, 237-242.

Smith, D., 1977. The origin and interpretation of spinel-pyroxene clusters in peridotite. *J. Geol.*, **85**, 476-482.

Suhr, G., 1993. Evaluation of upper mantle microstructures in the Table Mountain Massif, Bay of Islands Ophiolite. *J. Struc. Geol.*, **15**, 1273-1292.

Suhr, G. and Robinson, P.T., 1994. Origin of mineral chemical stratification in the mantle section of the Table Mountain massif (Bay of Islands ophiolite, Newfoundland, Canada). *Lithos*, **31**, 81-102.

Suzuki, K., 1987. Grain-boundary enrichment of incompatible elements in some mantle peridotites. *Chemical Geology*, **63**, 319-334.

Takahashi, N., 1992. Evidence for melt segregation towards fractures in the Horoman mantle peridotite complex. *Nature*, **359**, 52-65.

Taylor, R.N. and Nesbitt, R.W., 1988. Light rare-earth enrichment of supra subduction-zone mantle: Evidence from the Troodos Ophiolite, Cyprus. *Geology*, **16**, 448-451.

Varfalvy, V., Hébert, R. and Bédard, J.H., 1996. Interactions between melt and upper-mantle peridotites in the North Arm Mountain massif, Bay of Islands ophiolite, Newfoundland, Canada: Implications for the genesis of boninitic and related magmas. *Chemical Geology*, **129**, 71-90.

Wicks, F.J. and Whittaker, E.J.W., 1977. Serpentinite textures and serpentinisation. *Can. Min.*, **15**, 459-488.

Wilson, R.A.M., 1959. The geology of the Xeros-Troodos area: *Cyprus Geological Survey Memoir*, **No. 1**, 135p.

Wilson, M., 1989. Igneous Petrogenesis. Allen and Unwin (Australia), pp466.

Wood, B.J. and Virgo, D., 1989. Upper mantle oxidation state: Ferric iron contents of lherzolite spinels by ^{57}Fe Mössbauer spectroscopy and resultant oxygen fugacities. *Geochimica et Cosmochimica Acta*, **53**, 1277-1291.

Wood, B.J., Bryndzia, L.T. and Johnson, K.E., 1990. Mantle oxidation state and its relationship to tectonic environment and fluid speciation. *Science*, **248**, 337-345.

You, C.F., Castillo, P.R., Gieskes, J.M., Chan, L.H. and Spivack, A.J., 1996. Trace element behaviour in hydrothermal experiments: Implications for fluid processes at shallow depths in subduction zones. *Earth. Planet. Sci. Lett.*, **140**, 41-52.

Zhou, M., Robinson, P.T., Malpas, J. and Zijin, Li., 1996. Podiform chromitites in the Loubusa ophiolite (southern Tibet): Implications for melt-rock interaction in the upper mantle. *J. Petrol.*, **37**, 3-21.

Zinnrebe, E. and Foley, S., 1994. Metasomatism in two natural peridotites: Effects of low-$a$$SiO_2$ melts. *Min. Mag.*, **58a**, 1006-1007.

APPENDIX A
ANALYTICAL TECHNIQUES

A.1 SAMPLE PREPARATION

All the samples analysed in this study were prepared in the same way. Prior to sample preparation the samples were sorted into batches of similar lithological type. The samples were then processed in these batches, starting with the most depleted lithology first, in order to minimise cross-sample contamination. As a check of cross-sample contamination some samples were divided into three sub-samples prior to processing and then prepared at random intervals through each batch. The results of these analyses are presented in the relevant analytical method section.

Before the samples were crushed, they were brushed clean under running water and then washed in deionised water in an ultrasonic bath for 10 minutes to ensure that any surface contamination was removed. The samples were then dried in an oven.

Samples were crushed in a Pulverisette jaw crusher. Before crushing began the machine was stripped and scrupulously cleaned to avoid any contamination from previous users. The crusher was also thoroughly cleaned between each sample using a wire brush and absolute alcohol. The instillation of a dust extractor during this study helped to reduce the build up of dust within the machine considerably which speeded up the cleaning process.

Samples were then milled in an agate ball mill for 20 minutes. The mill was cleaned using sharp sand before use, at the end of each days work and between each sample batch. Between each sample the mill was cleaned under running water with a nylon brush.

A.2 X-RAY FLUORESCENCE ANALYSIS

All samples were analysed for major and selected trace elements by XRF at Durham. Major elements were analysed on fusion discs and trace elements on pressed pellets.

Before the fusion discs were prepared, the loss on ignition (LOI) for each sample was determined. Firstly, the powder was dried at 105°C to remove any surface water. Then a known amount of powder was heated at 900°C in porcelain crucibles for two hours to

derive the LOI. Fusion discs were prepared by thoroughly mixing 0.45g±0.001g of the LOI powder with 2.25g±0.001g of dried lithium metaborate/lithium tetraborate flux (Spectroflux 100B) using a pestle and mortar. It was found that careful mixing ensured good totals when the samples were analysed. The powder was then placed in a platinum crucible and heated in a furnace at 1050°C for 20 minutes. After removing the sample from the furnace, the molten mixture was homogenised by 'swirling' the crucible. The melt was then poured into moulds on a hot plate and quenched with a metal plunger. After the discs had cooled they were labelled, bagged and stored in a desiccator. Care was taken not to touch the analytical surface to avoid Na contamination but, even so, Na was generally below the detection limit of the XRF.

In some cases, samples with high modal spinel contents did not fuse completely and a residue of spinel grains could be seen in the fusion disc. An aliquot of these samples was then reground for 15 minutes in a small agate ball mill, which reduced the grain-size of the spinel further. Fusion of the finer-grained sample was generally successful. Despite taking this precaution, it was found that the precision for Cr was better from pressed pellets (see below). There are two possible explanation for this. Firstly, a larger sample size was used to produce the pressed pellets and therefore the sampling inhomogeneity introduced was less. Secondly, the pressed pellets were analysed on both sides and the results averaged which would tend to minimise the instrumental errors. The Cr pressed pellet data was used in the graphs presented in this thesis.

Pressed pellets were made by mixing approximately 10g of sample with 8 to 10 drops of Mowiol binder in a beaker using a glass rod. The amount of Mowiol used varied according to the properties of each sample and had to be judged from experience. The mix was pressed at 10 bars for approximately 30 seconds. The pellets were labelled then dried overnight at 110°C.

Fusion discs and pellets were analysed on a Philips PW 1500 spectrometer with a Rhodium tube. Count times were increased for elements close to the detection limits and are summarised in Table A.1. The machine was calibrated using international standards. Only standards with compositions close to those expected from the unknowns were used so that high concentration standards did not skew the calibration line at low levels. As a precaution, four in-house peridotite standard samples were run prior to the unknowns to check the calibration. During the analyses, a drift monitor was analysed every 6 samples. If the variation of the repeat analyses of the monitor had exceeded 1% for the major elements or 10% for the trace elements (Potts, 1987) the analytical run would have been

stopped and the XRF re-calibrated. In practise, the drift of the machine was very small as indicated by the precision values presented below.

Fusion discs, programme: harzburg				Pressed pellets, programme: jont			
	Count time		Count time		Count time		Count time
Mn	100	P	100	Rh3	40	Sc-	100
Mn+	80	P+	80	Ga	80	Sc	100
Ti-	20	Mg	100	Ga+	80	Fe	20
Ti	40	Mg+	80	Zn	100	Co	100
Fe-	20	Na	200	Zn+	100	Co+	100
Fe	40	Na+	200	Cu	100	V-	100
Ca-	20	Ni	100	Cu+	100	V	100
Ca	40	Ni+	100	Ni	40		
K	40	Cr	100	Ni+	40		
K+	20	Cr+	100	Cr	40		
Si	20	V	100	Cr+	40		
Si+	10	V-	100	Ti-	200		
Al-	20			Ti	200		
Al	40			Ca	20		

Table A.1. Summary of peak and background (labelled - or + in the table) count times (in seconds) used during the XRF analyses; programme names refer to the analytical programmes stored on the Durham XRF.

A.2.1 XRF ERROR CONTROL

Four main elements of error control were studied during the XRF analyses;
a) how accurate the calibration was in relation to the accepted values for the international standards,
b) the detection limit of the XRF,
c) the instrumental precision,
d) the sample preparation precision.

Accuracy: the accuracy of the calibration can be judged by comparing the values obtained for the analyses of international standards with the published accepted values. Because there are relatively few low level international standards with elemental abundances similar to the unknowns the international standards which were run as a check of

accuracy were the same as those used in the calibration. This means that the accuracy of the technique will be slightly over-estimated. The results of the analyses of the international standards are summarised in Table A.2.

	PCC1 (n=7)			BEN (n=4)			DTS1 (n=6)		
Discs	JF	Accpt.	RSD	JF	Accpt.	RSD	JF	Accpt.	RSD
MnO	0.12	0.125	2.8	0.21	0.21	0	0.12	0.21	30.3
TiO_2	0.01	0.014	10.1	2.70	2.70	0	0.01	0.01	0
Fe_2O_3	8.78	8.68	0.8	13.19	13.27	0.4	8.87	8.69	1.5
CaO	0.59	0.55	5.1	13.76	14.33	2.8	0.16	0.17	4.2
SiO_2	43.72	43.86	0.2	39.73	39.48	0.4	40.54	40.42	0.2
Al_2O_3	0.69	0.71	2.0	10.30	10.41	0.7	0.22	0.19	11.2
MgO	45.92	45.71	0.3	13.72	13.59	0.7	50.47	49.64	1.2
Ni	2502	2505	0.1	271	276	1.3	2387	2363	1.7
Cr	2248	2873	15.4	10	372	68.8	3508	3995	8.6
V	35.19	33.00	4.7	260	243	4.9	13	11	12.9
Pellets									
Zn	42.9	42	1.5	119.5	120	0.3	49.0	48	1.5
Cu	9.1	10	6.4	84.9	72	12.7	8.1	7.5	5.7
Ni	2397	2400	0.1	280	267	3.4	2453	2350	3.1
Co	121.5	110	7.4	60.2	61	0.9	139.4	139	0.2
Cr	2744	2730	0.4	363.8	360	0.7	4015	3920	1.1
V	30.3	30	0.7	248.8	235	4.2	10.4	12	9.4
Ti	122.2	140	9.0	3020	2610	11.1	140.9	-	-
Sc	8.3	8.5	1.7	20.7	22	4.2	6.1	3.5	52.5

Table A.2. Summary of international standard analyses for major elements analysed on fusion discs and trace elements on pressed pellets, n= number of repeat analyses, JF = analyses made during this study, accpt = accepted values for the international standards from Potts *et al.* (1992), RSD = relative standard deviation. Oxide data in wt%, elements in ppm.

Detection Limit: The detection limit at the 3σ level for the least abundant trace elements was calculated using the following equation;

$$\text{Limit of detection} = 3\sqrt{2R_b T_b} * \frac{c}{R_p T_p}$$

where R_p = the count rate on the peak,
R_b = the count rate on the background,
T_p = the time spent on the peak,
T_b = the time spent on the background,
c = concentration of the element in question.

The calculated limits of detection are summarised in Table A.3.

	Detection limit (ppm)		Detection limit (ppm)
Zn	0.4	Co	0.5
Cu	1.0	V	0.6
Sc	0.3		

Table A.3. Summary of the XRF detection limits for elements used in petrogenesis discussions in this thesis; values are the average of the count rate data from three standard samples.

Instrumental precision: the instrumental precision was determined by making repeat analysis of the same disc/pellet during the analytical run. The standard deviation of the analyses obtained is a measure of how reliably the XRF repeats each measurement (i.e. how well the crystals return to the same positions etc.). The results are summmarised in Table A.4.

Sample preparation precision: the sample preparation precision was also measured in order to check the standard of the disc/pellet making procedure, and as a check for cross-sample contamination in the crushing and disc/pellet making process. This precision measurement was achieved in two ways. Firstly, by sub-sampling a large sample into 3 separate samples immediately after collection (the precision value obtained will therefore, also give an indication of how representative the sample collection procedure was). These sub-samples were then processed separately, at random intervals during the sample preparation procedure, and each disc/pellet was analysed repeatedly during the analytical run. The results will therefore give a within sub-sample precision (i.e. a measure of the instrument precision) and a between sub-sample precision (i.e. a measure of the sample preparation precision). If the samples had been prepared carefully enough, the within sub-sample precision should be greater or equal to the between sub-sample precision. The results are summarised in Table A.4.

As a further check for cross-contamination, 12 samples were split into two prior to the crushing stage. These duplicate samples were then processed and analysed separately. The average relative standard deviation of the 12 duplicates is also given in Table A.4.

	Disc				Pellet		
	Instrument Precision	Sample Prep. Precision	Average Duplicate		Instrument Precision	Sample Prep. Precision	Average Duplicate
MnO	0.88	1.65	0.6	Zn	3.38	0.70	2.40
Fe_2O_3	0.35	0.24	0.31	Cu	0.99	0.79	0.77
CaO	0.53	0.17	0.38	Ni	0.09	0.53	0.73
SiO_2	0.26	0.30	0.35	Co	0.34	0.56	1.63
Al_2O_3	1.10	2.00	2.51	Cr	0.17	0.41	2.23
MgO	0.14	0.43	0.29	V	1.42	0.41	6.62
Ni	0.40	0.39	0.45	Ti	6.30	1.30	18.28
Cr	10.0	23.4	11.1	Sc	11.95	2.05	31.6
V	3.6	7.0	4.4				

Table A.4. Summary of relative standard deviations for instrumental, sample preparation and duplicate sample precision; all values in %.

A.3 ICP-MS ANALYSIS

Ga, Rb, Sr, Y, Zr, Nb, Ba, La, Ce, Nd and Yb were analysed by inductively coupled plasma mass spectrometry on a Perkin Elmer Sciex 6000 at Durham. Samples were prepared as follows.

All the equipment was scrupulously cleaned before the samples were dissolved. Funnels, volumetric flasks etc. were leached overnight with 5% nitric acid. The Savillex bombs were cleaned by heating overnight with approximately 5ml of 38% Romil Ultrapurity nitric acid. This process was repeated 3 times before the bombs were used for the first time, and then once between each batch of samples. While the peridotites were being prepared, the bombs were not used to prepare any other samples in order to avoid any cross-contamination. The samples were prepared in batches of 15, each batch included two blanks and one or two repeat samples.

Samples of 0.1 ± 0.001g were digested with 4ml of 48% hydrofluoric acid and 1 ml nitric acid in a Savillex bomb for at least 24 hours. The product was evaporated almost to

dryness and then taken up in 1 ml of nitric and again evaporated to near dryness. A further 1 ml of nitric acid was added and the product again evaporated to near dryness. The samples were redissolved with 2.5 ml nitric acid and approximately 20 ml of deionised water, and then boiled for 1 hour. The cooled solutions were spiked with 1.25 ml of a 2 ppm Rh, Re and Bi spike solution and made up accurately to 50 ml.

	DTS-1		PCC-1		X108	
Sc	**3.69+0.37**	3.5	**9.51+1.76**	8.5	**35.30+0.23**	33.9
Ti	**16.75+0.89**	-	**36.17+4.03**	83.8	**984+14**	839
V	**2.26+0.03**	12	**27.27+3.19**	30	**218+1**	218
Cr	**815+19**	3920	**2407+121**	2730	**497+24**	-
MnO	**0.125+0.002**	0.121	**0.122+0.008**	0.119	**0.144+0.010**	0.15
Co	**134+1.2**	139	**114+5.7**	110	**38.45+2.54**	38.3
Ni	**2490+21**	2350	**2512+120**	2400	**135+8**	117
Cu	**4.50+0.01**	7.5	**8.69+0.84**	10	**85.9+0.23**	86
Zn	**33.42+4.17**	48	**35.12+4.89**	42	**67.63+2.75**	66.1
Ga	**0.231+0.018**	0.15	**0.561+0.075**	0.7	**9.232+0.122**	4.26
Rb	**0.053+0.004**	0.058	**0.064+0.009**	0.066	**10.236+2.161**	13.0
Sr	**0.354+0.010**	0.33	**0.375+0.014**	0.40	**76.63+5.40**	85.5
Y	**0.043+0.001**	-	**0.092+0.001**	-	**4.349+0.198**	9.33
Zr	**0.216+0.006**	0.23	**0.338+0.098**	0.25	**25.54+1.82**	25.1
Nb	**0.021+0.004**	0.032	**0.023+0.004**	1.2	**0.505+0.087**	0.56
Ba	**0.485+0.026**	0.51	**0.957+0.235**	1.2	**40.05+12.78**	-
La	**0.021+0.004**	0.029	**0.041+0.026**	0.09	**0.943+0.019**	-
Ce	**0.052+0.031**	0.067	**0.080+0.027**	0.100	**2.716+1.977**	-
Nd	**0.015+0.004**	0.030	**0.025+0.009**	0.044	**1.018+0.075**	-
Yb	**0.010+0.001**	0.015	**0.023+0.002**	0.026	**0.680+0.001**	-

Table A.5 Comparison of accepted standard values for international standards (Potts *et al.*, 1992) and in-house standards (normal type), and values obtained during this study (bold type). Quoted standard deviations obtained from four separate measurements in 4 different analytical sessions. All values in ppm except MnO in wt%.

The samples were further diluted 1:10 with 5% nitric before running on the ICP-MS. The ICP-MS was configured to make 2 replicate analyses per sample with dwell times of 20 ms for all elements except Rb, Sr, Nb, Y, Zr and the REE when dwell times of 40 ms were used, and 50 scans were made across the mass range per replicate. Calibration lines

were constructed from analyses of international standards and in-house peridotite samples. The standard values and the values obtained during the analytical runs are compared in Table A.5.

A.3.1 ICP-MS DETECTION LIMITS

Because the machine had to operate close to the detection limit in order to obtain reliable data for the unknowns, it was important to have good blank data. Therefore two blanks per batch of samples were made. Before the samples were prepared, a range of possible preparation acids were tested for their trace element contents by preparing them in the same way as a normal blank. The results are shown in Table A.6. The lowest blanks were achieved with Aristar™ hydrofluoric acid and Romil™ Ultrapurity nitric acid. The same bottles of acid were then used for all the sample preparation.

Despite careful laboratory work, differences were still found between blanks made for each sample batch. Because the unknown concentrations were so low, the blank correction for each sample was made using the relevant blank from the sample batch, rather than calculating a bulk average blank. The detection limit was taken as 3 times the standard deviation of the blank, and typical values for several blanks are presented in Table A.7.

	Blank A	Blank B	Blank C		Blank A	Blank B	Blank C
Sc	0.024	0.111	0.138	Rb	0.006	0.006	0.003
Ti	0.066	0.09	0.099	Sr	0.006	0.009	0.009
V	0.006	0.009	0.105	Y	0.003	0.001	0.001
Cr	0.510	0.318	0.360	Zr	0.001	0.015	0.001
Mn	0.001	0.001	0.001	Nb	0.003	0.001	0.001
Co	0.027	0.001	0.015	Ba	0.075	0.102	0.009
Ni	0.093	0.03	0.348	La	0.003	0.001	0.001
Cu	0.201	0.132	0.066	Ce	0.003	0.003	0.001
Zn	0.225	0.966	0.213	Nd	0.001	0.003	0.003
Ga	0.018	0.009	0.001	Yb	0.001	0.003	0.001

Table A.7. Summary of detection limits at 3*s.d.of the blank for three different blank samples. Values in ppm.

ELEMENT	MILLIQ	Blank A	Blank B	Blank C	Blank D	1 ppb STD
45 Sc	59557±499	57902±882	55472±480	53877±501	52716±373	51187
49 Ti	163±49	331±45	262±38	316±36	311±81	
51 V	2200±33	2240±44	2162±27	2216±114	2372±294	
52 Cr	21621±103	22085±124	26275±4763	282850±257704	344259±472234	
53 Cr	1048±29	1075±24	1606±567	31706±30256	39180±55942	
55 Mn	3224±135	3324±15	4550±67	9501±4858	10542±8864	
59 Co	297±2	286±7	248±8	1739±1456	2049±2715	
60 Ni	2983±149	2935±465	2925±332	345499±337495	459223±617466	
63 Cu	1207±170	51821±87860	1211±223	1911±293	1666±697	
66 Zn	6769±9	7191±433	7354±227	7126±89	15745±7887	
71 Ga	173±17	172±7	158±12	200±40	435±210	
85 Rb	131±1	131±4	142±13	397±102	274±76	46526
88 Sr	611±115	682±71	570±54	995±89	4258±3958	60356
89 Y	50±5	61±1	67±13	100±19	160±63	70342
90 Zr	115±1	434±61	331±29	760±317	1945±667	33933
93 Nb	47±0	56±2	51±4	97±42	103±69	
133 Cs	50±0	46±5	50±6	45±4	53±1	
137 Ba	135±16	186±56	284±23	320±39	4629±2022	
139 La	63±17	67±10	62±7	84±11	174±85	
140 Ce	79±29	68±10	101±8	254±234	335±162	69595
141 Pr	37±1	39±2	37±5	46±4	64±20	83280
143 Nd	47±1	44±5	48±7	50±4	55±9	10090
147 Sm	41±13	35±6	38±1	36±5	38±2	12417
149 Sm	44±0	39±2	34±2	36±3	43±3	11496
151 Eu	31±2	35±5	34±3	34±0	41±4	39710
153 Eu	32±0	35±4	34±2	34±4	44±6	44487
157 Gd	36±2	33±7	36±1	30±5	38±12	14490
159 Tb	36±2	37±1	37±0	36±3	36±2	82837
161 Dy	33±1	33±1	30±3	33±2	34±1	14260
163 Dy	37±8	37±2	38±3	40±2	42±4	18835
165 Ho	36±1	37±2	32±3	34±3	39±1	79002
166 Er	35±1	38±5	38±3	36±3	39±5	27701
167 Er	43±11	43±5	41±4	45±6	37±2	19230
169 Tm	38±1	39±2	40±2	38±2	41±1	86224
172 Yb	36±4	38±6	37±6	36±6	38±7	17931
174 Yb	39±3	33±4	35±4	32±2	44±1	26340
175 Lu	37±1	37±2	33±1	35±2	38±3	80955
177 Hf	34±2	37±1	42±5	43±2	60±15	
178 Hf	35±8	36±4	39±8	50±7	74±16	
181 Ta	52±2	73±16	61±2	64±2	67±4	
182 W	52±4	76±3	62±6	1692±1549	1843±2805	
205 Tl	52±3	65±3	63±2	65±6	63±8	
206 Pb	865±49	908±94	916±122	1067±185	10309±7851	
207 Pb	716±24	796±101	823±49	896±156	8670±6555	
208 Pb	3353±33	3564±404	3626±342	4052±755	40341±30624	
208 Pb	1773±40	1861±213	1888±173	2088±415	21362±16218	
232 Th	39±5	42±4	40±2	44±1	69±10	69137
238 U	44±2	41±3	42±5	49±5	920±462	69146

Table A.6 Summary of data obtained during blank testing; all values are in counts per second and are the average measurement for three separate samples.

Blank A = Ultrapurity HNO_3 + Double distilled HF

Blank B = Ultrapurity HNO_3 + Aristar HF

Blank C = Superpurtiy HNO_3 + Aristar HF

Blank D = Analar HNO_3 + Aristar HF

Milliq = deionised water

A.3.2 ICP-MS PRECISION

Trying to estimate the precision of the technique for such low level analyses is difficult. Standard instrumental precision for the ICP-MS, measured by making repeat measurements of a sample throughout an analytical run, is high. The standard deviation and relative standard deviation of two international standards which were run 5 times during a single analytical session are shown in Table A.8. As the Table shows many elements have a precision of better than 1% and most better than 5%. Nd appears to have the worst instrumental precision at around 15%.

	PCC1	Sa32		PCC1	Sa32
Sc	2.8	3.6	Rb	5.5	0.9
Ti	1.8	1.3	Sr	1.7	1.3
V	0.8	0.1	Y	1.2	2.1
Cr	0.7	0.1	Zr	1.5	2.2
Mn	0.5	0.0	Nb	5.9	2.1
Co	0.7	0.9	Ba	3.5	2.1
Ni	0.4	0.6	La	3.1	2.8
Cu	0.8	2.8	Ce	2.0	2.5
Zn	1.7	1.6	Nd	14.1	16.2
Ga	2.9	1.1	Yb	3.8	5.8

Table A.8 Summary of relative standard deviations for the elements in standards PCC-1 and Sa32 based on 5 replicate analyses made in a single analytical session

However, these values are the best possible estimate of the precision because other factors can introduce significant errors into the data. Two of the most significant factors are likely to be;

a) differences in inter-run calibration lines - the samples were run over several days on the ICP-MS so a different calibration line had to be constructed for each days analyses. Because the unknowns were at such low concentrations, small differences in the slope of the calibration lines between runs produces significant differences in the calculated concentrations.

b) sampling inhomogeneity - this is a possible cause of error especially for elements concentrated in minor phases (e.g. Zr) and is exacerbated by the small sample size used in ICP-MS analysis (0.1g).

These factors will result in the 'method precision' being worse than the instrumental precision.

The errors introduced by differences in calibration line gradients and machine efficiencies during each daily run can be estimated from replicate analyses made of the calibration standards at the beginning of each days analyses. The relative standard deviation data calculated for three days analyses of the calibration standards are summarised in Table A.9.

	DTS1	PCC1	x108	Sa32	Average
Sc	7.0	15.7	0.8	27.7	12.8
Ti	8.4	9.2	1.3	2.6	5.4
V	6.2	9.6	0.4	2.9	4.8
Cr	3.6	4.2	4.8	2.0	3.7
Mn	2.4	5.5	5.5	4.2	4.4
Co	1.3	4.2	5.4	3.4	3.6
Ni	1.3	4.0	5.2	3.2	3.4
Cu	5.9	8.0	0.2	7.1	5.3
Zn	20.3	13.9	4.8	2.7	10.4
Ga	18.8	11.8	1.2	6.4	9.6
Rb	12.4	12.7	19.6	10.1	13.7
Sr	4.5	3.4	6.9	5.9	5.2
Y	8.0	3.4	3.9	3.7	4.7
Zr	14.9	26.2	7.4	8.7	14.3
Nb	22.6	21.9	14.7	13.7	18.2
Ba	24.9	20.4	26.0	17.4	22.2
La	20.7	56.2	1.8	24.1	25.7
Ce	38.5	37.8	68.8	31.3	44.1
Nd	25.5	30.5	7.0	39.9	25.7
Yb	6.1	7.7	0.0	9.4	5.8

Table A.9 Summary of relative standard deviations calculated for analyses of standard samples made at the beginning of each days analytical run; the same solution of each standard was used for each analysis.

As Table A.9 shows, the precision is much worse when the between run variation is taken into account. However, most elements still have a average precision of better than 5%,

although Ba and the LREE precision is considerably poorer at closer to an average of 25%.

To try to estimate the extent to which sampling inhomogeneity affects the precision, duplicate solutions were made for several samples. These were also run on different days, so the precision values obtained give a rough estimate of the 'method precision' value, which includes instrumental precision, sampling inhomogeneity and differences in inter-run machine performance and calibration. The results of these duplicate analyses are given in Table A.10.

	lf16	lf28	285	Average
Sc	67.2	48.5	47.6	54.4
Ti	4.2	3.2	6.5	4.6
V	4.6	2.8	4.6	4.0
Cr	4.8	6.1	4.6	5.2
Mn	9.0	7.6	7.7	8.1
Co	6.3	6.6	6.1	6.3
Ni	5.7	5.4	6.0	5.7
Cu	3.2	7.1	4.1	4.8
Zn	25.6	1.2	40.2	22.3
Ga	17.9	1.9	4.7	8.2
Rb	32.0		7.1	19.6
Sr	7.8	7.6	5.0	6.8
Y	2.3	1.3	3.5	2.4
Zr	6.1	11.2	4.0	7.1
Nb	17.6	18.4	16.7	17.6
Ba	39.4	20.4	58.4	39.4
La	35.4	6.7	20.0	21.1
Ce	38.6	38.6	8.3	28.5
Nd	84.9	56.6	53.0	64.8
Yb	10.1	4.4	4.3	6.3

Table A.10 Summary of relative standard deviations of duplicate analyses.

As the table shows, the precision values are slightly worse for most elements once the effects of sampling inhomogeneity have been taken into account and, in particular, considerably worse for Nd and Sc. Notably, the elements expected to be most affected by

sampling inhomogeneity, such as Zr, do not seem to show much variation in the duplicated solutions. However, analyses made of the international standard PCC1 over several years at Durham have shown particularly poor precision for Zr which has been attributed to the presence of heterogeneously distributed microscopic zircons (J. Pearce, pers comm.). The data presented in Table A.10 could mean that either: Zr is only present in a major mineral phase in the Troodos samples which is distributed homogeneously through the sample during crushing; that zircons were not sampled in the replicate solutions made of the Troodos samples; or that any zircons in the Troodos samples were crushed sufficiently to homogenise the sample powder.

The above discussion illustrates the difficulties inherent in trying to obtain reliable low level determinations of the trace elements in depleted peridotites. As a best estimate of the precision obtained during this study, the average relative standard deviation values calculated in Tables A.9 and A.10 were themselves averaged, and then converted to ppm by multiplying by an averaged *background* harzburgite value. The results obtained are presented in Table A.11 and are the basis upon which the error bars were drawn on graphs in which the ICP-MS data were presented. Future users of the ICP-MS would find in useful to carry out multiple analyses of replicate solutions before embarking on the analysis of their unknowns, in order to quantify and improve the method precision.

	S.D.		S.D.		S.D.		S.D.
Sc	2.819	Co	5.222	Rb	0.017	Ba	0.100
Ti	1.066	Ni	105	Sr	0.038	La	0.002
V	1.207	Cu	0.308	Y	0.002	Ce	0.017
Cr	88	Zn	6.267	Zr	0.010	Nd	0.004
Mn	0.007	Ga	0.037	Nb	0.001	Yb	0.001

Table A.11. Summary of the estimated standard deviation values for the ICP-MS analyses.

A.4 ELECTRON PROBE ANALYSIS

Major and selected trace elements in olivine, pyroxene and spinel were analysed on a Camebax wavelength-dispersive electron probe at the Electron Probe Unit, Edinburgh University. The probe was calibrated using natural and artificial standards, and peak count times of 30 seconds were used for all elements except Ti and V which were counted for 60 seconds. Background count times were half the peak count times and the

standard background offsets were used for all the elements analysed except V, when an offset of -750 was used. The data was corrected using the PAP programme.

The calibration was checked periodically during the analyses of the unknowns by analysing in-house natural standards. The standard values and results obtained during the analytical runs are compared in Table A.12.

	Andradite		Pyroxene		Olivine	
	Accepted	This study (n=27)	Accepted	This study (n=16)	Accepted	This study (n=23)
NaO_2	-	-	0.75	0.73	-	-
MgO	0.08	0.07	7.99	8.01	49.17	49.59
Al_2O_3	1.65	1.69	0.61	0.64	-	-
SiO_2	35.15	35.00	50.29	50.20	40.82	40.08
CaO	32.50	32.32	23.01	22.77	-	-
TiO_2	0.08	0.07	-	-	-	-
MnO	0.42	0.44	0.53	0.52	0.12	0.14
Fe_2O_3	27.15	27.25	16.45	16.21	9.55	9.73
NiO	-	-	-	-	0.36	0.32
ZnO	-	-	0.13	0.14	-	-
Total	97.03	96.84	99.76	99.21	100.02	99.85

Table A.12. Comparison of accepted standard values and the results obtained during this study; n= the number of repeat analyses for each standard and all values in weight%.

Detection limits were calculated using the equation:

$$D.L. = \frac{3}{m}\sqrt{\frac{R_b}{T_b}}$$

where: m = counts/second/wt% element,
R_b = background count rate,
T_b = count time on background,
and where R_b and T_b are taken from a typical analysis and m is taken from the relevant standard for the element in question. The calculated detection limits are summarised in Table A.13.

	Olivine	Orthopyroxene	Clinopyroxene	Spinel
Na_2O	0.03	0.02	0.02	0.03
MgO	0.01	0.01	0.01	0.01
Al_2O_3	0.01	0.01	0.01	0.01
SiO_2	0.01	0.01	0.01	0.01
CaO	0.01	0.01	0.02	0.01
TiO_2	0.01	0.01	0.01	0.01
Cr_2O_3	0.02	0.02	0.02	0.02
V_2O_3	0.02	0.02	0.02	0.02
MnO	0.02	0.02	0.02	0.02
Fe_2O_3	0.02	0.02	0.02	0.02
NiO	0.02	0.02	0.02	0.02
ZnO	0.02	0.2	0.03	0.02

Table A.13. Summary of detection limits in weight% for the four phases analysed by wavelength dispersive electron probe.

Electron probe precision was also calculated from counting statistics using the equation:

$$\text{Relative standard deviation} = \frac{100}{\sqrt{T} * \left(\sqrt{R_p} - \sqrt{R_b}\right)}$$

where T = count time on the peak.

R_p = count rate on the peak,

R_b = count rate on the background,

and where the count rate values were taken from a typical analysis.

The precision values in weight% were then obtained by multiplying the relative standard deviation value for each element in each mineral by the average concentration of each element in each mineral. The precision values are summarised in Table A.14.

	Olivine	Orthopyroxene	Clinopyroxene	Spinel
Na_2O	0.01	0.09	0.02	0.01
MgO	0.10	0.08	0.06	0.07
Al_2O_3	0.01	0.03	0.03	0.10
SiO_2	0.09	0.10	0.09	0.01
CaO	0.01	0.02	0.08	0.01
TiO_2	0.01	0.01	0.01	0.01
Cr_2O_3	0.02	0.02	0.03	0.08
V_2O_3	0.03	0.01	0.02	0.02
MnO	0.02	0.02	0.02	0.02
Fe_2O_3	0.07	0.06	0.04	0.09
NiO	0.02	0.02	0.02	0.02
ZnO	0.02	0.04	0.04	0.03

Table A.14. Summary of precision values in weight% oxide for each element for each mineral obtained by wavelength dispersive electron probe analysis.

A.5 ION PROBE ANALYSES

Trace elements were analysed in individual clinopyroxene grains on a Cameca IMS 4f ion probe at Edinburgh University. Gold-coated polished thin sections were bombarded with a primary beam of 10keV $^{16}O^-$ with a spot size of approximately 25μm. The primary beam was used to sputter secondary ions from the surface of the clinopyroxene grains. The elemental concentrations were determined by counting the higher energy secondary ions of individual isotopes. Because of the exceptionally low REE contents of the Troodos clinopyroxenes, long count times had to be used. For ease of analysis, two analytical programmes were used, one for the REE and one for the more abundant trace elements (Sc, Ti, V, Sr, Y, Zr, Nb and Ba). For the REE count times of 10 seconds per scan for 10 cycles were used, and for the other trace elements count times of 5 seconds and 10 cycles were used.

Interferences from molecular species were suppressed by applying an offset voltage to the secondary beam, for the REE analyses an offset of 40V was used, and 75V for the other trace elements. In order to circumvent daily variations in absolute ion yields, due to differences in primary ion bombardment and secondary ion tuning, ratios of count rates were measured and normalised to Si. The count rates were converted to concentrations using relative ion yields determined daily on an NBS610 silicate glass standard.

The background was measured at a mass of 130.5 where no ions are expected and was ≤ 1 count per analysis. Detection limits were estimated at 5 times the background using the equation shown below, and are summarised in Table A.15.

$$DetectionLimit = \frac{5}{cts} * wt$$

where cts = total number of counts of an element in a typical analysis,
wt = weight of the element in the typical analysis.

	Detection limit		Detection limit
Sc	2	Ce	1
Ti	45	Pr	1
V	6	Nd	10
Sr	10	Sm	10
Y	6	Eu	2
Zr	20	Gd	30
Nb	17	Tb	5
Ba	32	Dy	28
La	1	Yb	31

Table A.15. Summary of the ion probe detection limits in ppb.

The instrumental precision is estimated to be better than 15% for the REE and better than 10% for the other trace elements analysed (R. Hinton, *pers. comm.)*.

APPENDIX B
SECONDARY ION MASS SPECTROMETRY ANALYSIS OF SPINEL

During the course of this project an attempt was made to obtain trace element analyses from spinels using the ion probe at Edinburgh University. Because there are several outstanding problems with the data at the time of writing, it was not possible to present the figures as usable data in the main part of the thesis. Instead the data and description of the analytical set-up are presented in this appendix for the information of anyone wishing to attempt similar analyses in the future.

B.1 INSTRUMENT CONFIGURATION

The basic configuration of the ion probe for the spinel analyses was similar to that used for the clinopyroxene analyses, and the reader is referred to Appendix A for details of this configuration. An offset voltage of 75 volt was used and count times of 10 seconds per isotope for 5 cycles. The isotopes analysed were: 26Mg, 30Si, 40Ca, 42Ca, 45Sc, 48Ti, 51V, 53Cr, 54Fe, 55Mn, 60Ni, 64Zn, 66Zn, 71Ga, 89Y and 90Zr. Count rates were ratioed to Mg and were converted to concentrations using ion yields from the nbs silicate glass. Comparison of the (element counts per second/Mg counts per second) ratio from a spinel analysis with that from the NBS glass suggests that the ion yields from the silicate glass are accurate to within 20% of the values from a typical spinel analysis.

B.2 DATA REDUCTION

Correction factors were calculated for Ca, Fe and Mg to correct for the effects of mass fractionation (Hinton *et al.*, 1988). The equations used are as follows:

For calcium

$$\sum Ca_{40} = \frac{(40_{counts} - 42_{counts}) / 0.13938}{0.9698}$$

$$actualCa = \frac{\sum Ca_{40}}{mass.corr} * wt(ppm)$$

where ΣCa_{40} = total counts on Ca_{40},

40_{counts} = raw number of counts on isotope 40,

42_{counts} = raw number of counts on isotope 42,
mass.corr = mass correction factor calculated by the ion yield conversion programme,
wt(ppm) = weight of element calculated by the ion yield conversion programme,
actual Ca = the unknown.

For iron

$$\sum Fe = \frac{(Fe_{54} - Cr_{53}) * 0.2487}{0.057545}$$

$$actualFe = \frac{\sum Fe}{mass.corr} * wt(ppm)$$

where ∑Fe = total Fe counts,
Fe_{54} = raw number of counts on isotope 54,
Cr_{53} = raw number of counts on isotope 53,
mass.corr = mass correction factor calculated by the ion yield conversion programme,
wt(ppm) = weight of element calculated by the ion yield conversion programme,
actual Fe = the unknown.

For zinc

$$Zn_{cps} = \frac{64_{cps} - \left(\left[Ti_{cps} * 0.005\right] + \left[Ni_{cps} * 0.03471\right]\right)}{0.4863}$$

$$actualZn = \frac{Zn_{cps}}{mass.corr} * wt(ppm)$$

where Zn_{cps} = adjusted Zn counts per second,
64_{cps} = raw number of counts on isotope 64,
Ti_{cps} = raw number of counts on Ti isotope 48,
Ni_{cps} = raw number of counts on Ni isotope 60,
mass.corr = mass correction factor calculated by the ion yield conversion programme,

wt(ppm) = weight of element calculated by the ion yield conversion programme,
actual Zn = the unknown.

Mg values determined by electron probe were then used to convert the data from the standardised Mg value (60000) used in the count rate ratios.

B.3 CHROMITITE STANDARD

As a check and control on the ion yield conversion procedure it was necessary to produce an independent set of trace element values from a standard chromite sample. A typical sample of a Troodos chromitite from the Hadji Pavlou mine was chosen as the standard sample and the chromitite was prepared for analysis by ICP-MS as follows.

Firstly, the sample was crushed following the same procedure as the other samples and described in Appendix A. The sample contained approximately 5 to 10% modal serpentine minerals which had to be removed prior to sample dissolution. This was achieved in two ways. Firstly, the finely powdered sample was 'panned' in a glass beaker which allowed most of the low density serpentinite fraction to be washed off from the spinels. Then small aliquots of the sample (approximately 0.1g) were heated in HF for several hours, to ensure that any silicate grains which may have been attached to the surfaces of the spinel grains were dissolved. The sample was then washed repeatedly with HNO_3 to remove the HF.

The cleaned spinel powder was then fused in a flux developed by L.G.Sear at Camborne School of Mines. The flux was made by grinding 2.743g of $NaNO_3$ and 15.985g of H_3BO_3 into a homogeneous powder in an agate ball mill. This produces a flux with a formulation 10%Na_2O and 90% B_2O_3. An aliquot of the flux was heated at 1075°C for 5 minutes to determine the loss on ignition. For the batch of flux used in this study the LOI was 41.9%.

To fuse the chromitite sample a sample:flux ratio of 1:9 was used, with a sample weight of 0.1g. Enough flux to yield 0.9g on fusion was weighed into a platinum crucible and then fused for 5 minutes at 1075°C. A sample weight of 0.1$\pm$0.001g was then weighed out and transferred to a small glass bottle. 0.315g of Na_2O_2 was then weighed into the bottle and the sample and Na_2O_2 mixed thoroughly. This mixture was then transferred to the platinum crucible which was returned to the furnace at 500°C for 30 minutes, during which time the sample + Na_2O_2 sintered but did not melt. The temperature was then

increased to 1075°C and the sample fused for 30 minutes. After removing the crucible from the furnace the melt was allowed to cool and crystallise in the crucible, and was then removed by simply tapping the crucible up-side-down on a piece of weighing paper. The fact that no spinel grains were visible in the glass suggests that the fusion procedure achieved 100% dissolution of the chromitite. The glass was then finely powdered in a pestle and mortar, and a 0.1±0.001g aliquot dissolved in 10ml of 5% HNO_3 prior to introduction into the ICP-MS in the standard way.

In order to calibrate the ICP-MS for the chromite standard analysis, four international standards and one in-house standard were subjected to the same fusion preparation procedure. The values obtained for these samples, the method blank and the trace element values obtained from the chromitite standard are presented in Table B.1.

	NIM-P		BIR-1		BHVO-1		UBN		X108		Blk	Chrm std
Sc	**28.5**	27.3	**24.0**	44	**30.8**	31.8	**14.1**	13	**36.2**	33.9	**0.67**	**2.39±0.16**
Ti	**0.17**	0.2	**0.77**	0.96	**2.77**	2.71	**0.07**	0.11	**0.13**	0.14	**0.01**	**0.15±0.01**
V	**252**	230	**274**	313	**333**	317	**48.3**	75	**238**	218	**2.34**	**1233±113**
Mn	**0.23**	0.22	**0.16**	0.17	**0.20**	0.17	**0.10**	0.12	**0.15**	0.15	**0.01**	**0.19±0.02**
Co	**115**	110	**48.8**	51.4	**51.2**	45	**86.9**	100	**45.1**	38.3	**1.77**	**284±27**
Ni	**677**	555	**185**	166	**158**	121	**1925**	2000	**158**	117	**1.19**	**1397±139**
Cu	**bd**	18	**95.8**	126	**156**	136	**bd**	28	**107**	86	**16.2**	**bd**
Zn	**95.0**	100	**51.6**	71	**115**	105	**52.4**	85	**75.4**	66.1	**4.34**	**369±35**
Ga	**7.48**	8	**13.2**	16	**23.4**	21	**2.31**	3	**10.6**	4.26	**0.9**	**37.7±3.7**
Rb	**2.55**	4	**0.13**	0.27	**9.88**	11	**2.54**	6	**13.4**	13.0	**0.01**	**1.16±0.12**
Sr	**31.1**	32	**87.5**	108	**412**	403	**bd**	10	**97.6**	85.5	**5.15**	**3.62±3.36**
Y	**3.17**	5	**13.7**	16	**29.4**	27.6	**2.04**	2.5	**4.65**	9.33	**0.01**	**0.22±0.09**
Zr	**12.2**	15	**15.7**	22	**249**	179	**4.41**	8	**33.4**	25.1	**0.04**	**1.65±0.58**
Nb	**0.45**	-	**0.43**	2.0	**19.6**	19	**bd**	-	**0.58**	0.56	**0.06**	**0.86±0.19**

Table B.1. Summary of results from the fusion procedure used to prepare the chromite standard for ICP-MS analysis; bd = below detection limit, figures in bold are those obtained in Durham, figures in normal type are the accepted standard values from Potts *et al.*, (1992). X108 = in house boninite sample, Blk = blank values, Chrm std = values for the Hadji Pavlou chromitite standard. All data ppm except Mn, which is given in wt% MnO

B.4 COMPARISON OF ELECTRON PROBE AND ION PROBE RESULTS

The values obtained by ion probe for Ti, V, Cr, Mn, Ni and Zn are compared to the values determined by electron probe in Figure B.1. As the graphs show, there is a reasonably good correlation between the values obtained by each technique for most elements, which suggests that the ion yield correction procedure was reasonably good despite the fact it was based on a glass-silicate, rather than spinel, matrix. However, the ion probe generally over-estimates Ni values and the data are poorer for Zn, probably because of mass correction problems.

The V graph on Figure B.1 is of particular interest because of the trouble taken during this project to obtain good, low-level V determinations on spinels by electron probe. The fact that the graph shows a good fit between the two data sets suggests that the electron probe V analyses were successful.

B.5 OUTSTANDING PROBLEMS

The main purpose of producing the spinel standard was to correct the lowest abundance trace elements (Ga and Y), for which we had no other independent check on their abundances. When the Ga counting data was examined, the ion yield ratio of Ga/Mg for the standard chromite was found to be three times higher than would be predicted from the ion yields given by the nbs glass. One possible reason for this could be a MnO overlap on Ga_{71}. To test for this, the Ga_{cps} values were plotted against the Mn_{cps} values (Figure B.2). Figure B.2 shows the data from analyses made in two analytical sessions. Notably, all the analyses made in one session plot to the highest Ga_{cps} and Mn_{cps} values. This suggests that the instrument operating conditions varied between sessions and one possible reason for the highest Ga_{cps} and Mn_{cps} values occurring in the one session might be, that the vacuum conditions were poor and aluminium hydroxide species are overlapping on the measured Ga and Mn isotopes (R.Hinton pers comm.).

To date the Mn overlap problem has still not been resolved although it may be possible to resolve the Ga_{71} and MnO peaks by conducting detailed scans across this part of the mass spectrum and also collecting Ga data on the 69 isotope.

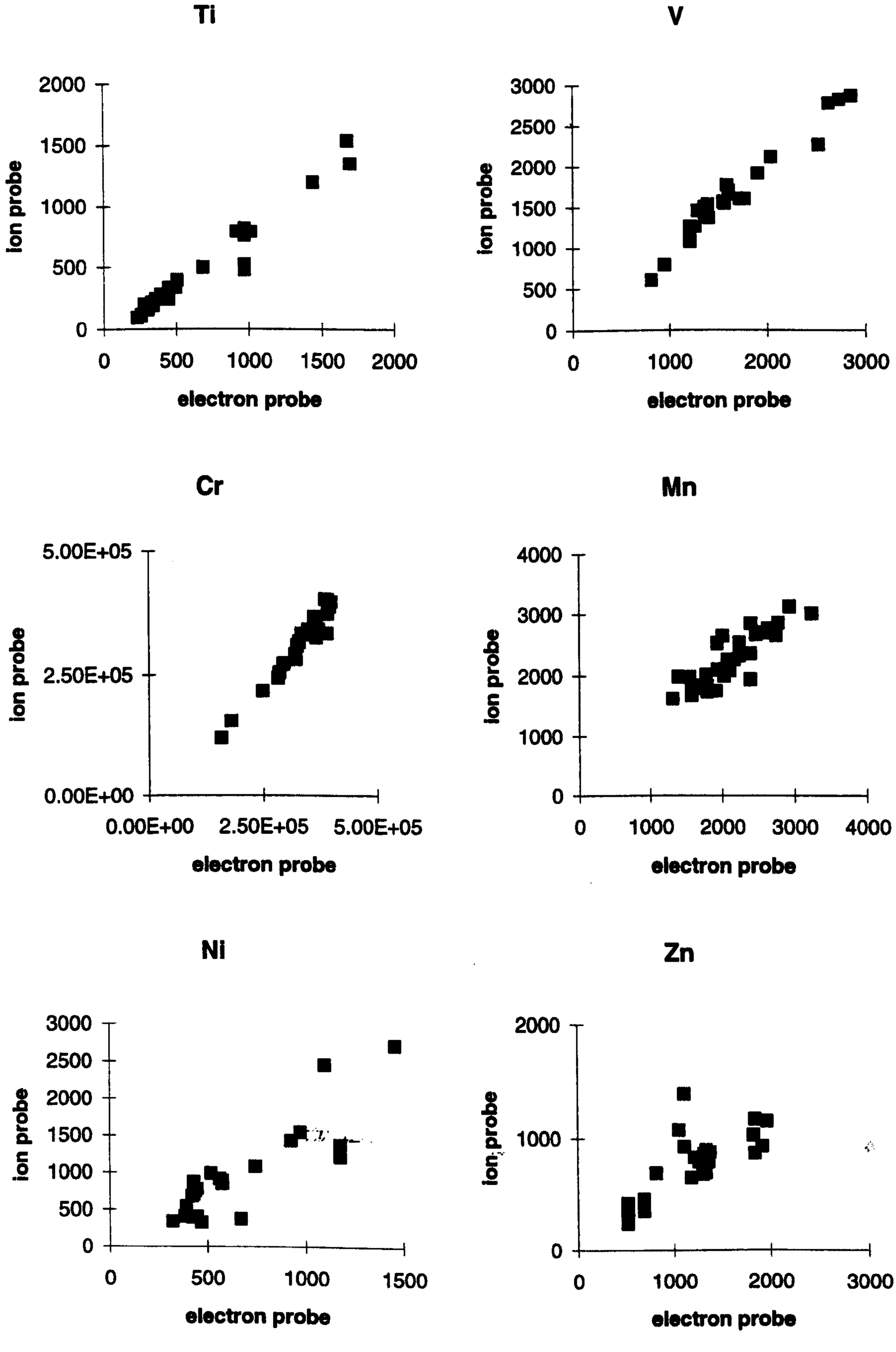

Figure B.1 Comparison of the data obtained for electron probe and ion probe spinel analyses, data in ppm.

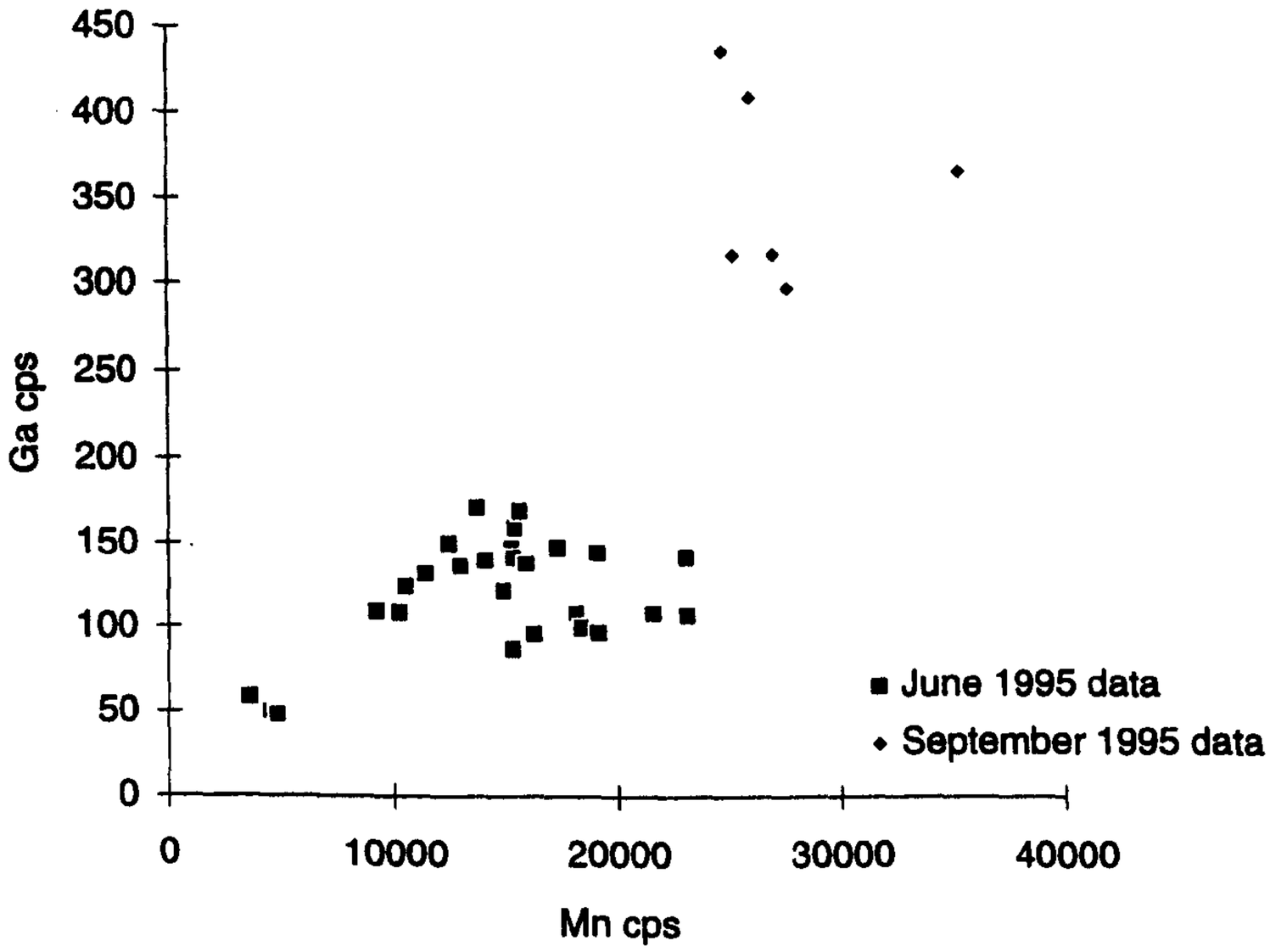

Figure B.2 Graph illustrating the variation in Ga and Mn in spinels, data in counts per second.

APPENDIX C
EQUATIONS

C.1 OXYGEN FUGACITY

Oxygen fugacities were calculated from the electron probe data using the following equations.

C.1.1 The Wood *et al.*, (1990) Method

$$\log(fO_2)_{P,T} = \log fO_2(FMQ)_{P,T} + \frac{220}{T} + 0.35 - \frac{0.0369P}{T} - 12\log X_{Fe}^{ol} - \frac{2620}{T} X_{Mg}^{ol\ 2} + 3\log(X_{Fe}^{M1} * X_{Fe}^{M2})^{opx} + 2\log a_{Fe3O4}^{spn}$$

where: X_{Fe}^{ol} and X_{Mg}^{ol} refer to the mole fractions of Fe and Mg end-members in olivine;

P is the pressure in bars;

T is absolute temperature;

X_{Fe}^{M1}, X_{Fe}^{M2} in orthopyroxene refer to the atomic fractions of Fe in the two orthopyroxene sites, these are calculated from the analysis with the assumption of equipartition of Mg and Fe after assignment of Al^{VI}, Cr and Ti to M1 and Mn to M2;

the last term is calculated from:

$$\log a_{Fe3O4}^{spn} = \log\left\{\frac{(Fe^{2+})*(Fe^{3+})^2}{4}\right\} + \frac{1}{T}\left[406(Al)^2 + 653(mg)(al) + 299(Cr)^2 + 199(Al)(Cr) + 346(Mg)(Cr)\right]$$

where the bracketed terms in parentheses refer to total Mg, Cr, Al, Fe^{3+} and Fe^{2+} cations in the spinel (spn) structure on a four oxygen basis.

C.1.2 The Ballhaus *et al.*, (1990) Method

$$\log(fO_2)_{P,T} = 0.27 + \frac{2505}{T} - 400\frac{P}{T} - 6\log(X_{Fe}^{ol}) - 3200\frac{(1-X_{Fe}^{ol})^2}{T} + 2\log(X_{Fe2+}^{spn}) + 4\log(X_{Fe3+}^{sp}) + 2603\frac{(X_{Al}^{sp})^2}{T}$$

where the terms are the same as in the Wood *et al.* equation except for:

P is in GPa;

X_{Fe3+}^{sp} and X_{Al}^{sp} are the $\frac{Fe^{3+}}{\sum R^{3+}}$ and $\frac{Al}{\sum R^{3+}}$ cation ratios in spinel ($\sum R^{3+}$ is the total content of trivalent cations).

C.2 GEOTHERMOMETRY - THE Ca IN ORTHOPYROXENE METHOD

Brey and Kohler (1990),

$$T_{Ca-in-opx}(K) = \frac{6425 + 26.4P}{-\ln Ca^{opx} + 1.843}$$

where P is the pressure in kb.

C.3 MELTING CALCULATIONS

C.3.1 FRACTIONAL MELTING

The following equation was used to calculate residual solid compositions from non-modal fractional melting (Shaw, 1970):

$$C_r = \left[\frac{C_o}{1-F}\right] * \left[1 - \frac{P_o F}{D_o}\right]^{\left(\frac{1}{P_o}\right)}$$

where: F = the degree of melting;

D_0 = the initial bulk solid partition coefficient of element i;

P_O = the initial bulk distribution coefficient of the solids entering the melt;

C_O = the initial concentration of an element in the solid;

C_r = the concentration of an element in the residue.

The following equation was used to calculate residual clinopyroxene compositions from non-modal fractional melting (Johnson *et al*, 1990):

$$C_i^{cpx} = C_i^o \left[1 - \frac{PF}{D_i^o}\right]^{\left(\frac{1}{P}\right)} * \left[\frac{D_i^{cpx/l}}{D_i^o - PF}\right]$$

where : F = the degree of melting;

D_i^o = the initial bulk solid partition coefficient of element i;

$D_i^{cpx/l}$ = distribution coefficient of element i between cpx and melt;

C_i^{cpx} = concentration of element i in clinopyroxene;

C_i^o = concentration of element i in the original bulk solid,

P = the weighted partition coefficient of the liquid;

C.3.2. BATCH MELTING

The following equation was used to calculate residual compositions from non-modal batch melting (Johnson *et al*, 1990):

$$C_i^{cpx} = C_i^o \left[\frac{D_i^{cpx/l}}{D_i^o + F(1-P)} \right]$$

where the terms have the same definitions as in the fractional melting equation and $D_i^{cpx/l}$ is the distribution coefficient for element i between clinopyroxene and melt.

C.3.3. FRACTIONAL MELTS

The equation was used to calculate the compositions of aggregated liquids produced by fractional melting (Shaw, 1970):

$$C_L = \frac{C_o}{D_o}\left[1 - \frac{P_o F}{D_o}\right]^{\left(\frac{1}{P}\right)}$$

where C_L = the composition of the aggregated liquid and the other symbols are as described above.

C.4 MASS BALANCE EQUATIONS

Mass balance equations have the following general form (Ayers, 1993):

$$C_a^T = X^\alpha C_a^\alpha + X^\beta C_a^\beta + \ldots\ldots + X^n C_a^n$$

where: C_a^T = total concentration of element a;

X^α, X^β and X^n = modal proportions of phases α, β and n;

C_a^α, C_a^β and C_a^n = concentration of element a in phases α, β and n.

For the modelling of the enriching component (Chapter 4) C_a^T was the abundance of the element in question (i.e. the value obtained by the ion probe), $X^\alpha C_a^\alpha$ was the contribution from the pre-enriched mantle where $X^\alpha = 0.99$ (i.e. 99%), C_a^α = the value obtained by fractional melt modelling and $X^\beta C_a^\beta$ was the contribution from the enriching melt where $X^\beta = 0.01$ (i.e. 1%) and C_a^β is the unknown.

APPENDIX D
GEOCHEMICAL DATA SET

This appendix contains a listing of all the geochemical data used in this thesis. The following abbreviations are used in the data tables:

II fol	dunite parallel to foliation;
interdig	dunite with interdigitating contacts against the harzburgites;
x fol	dunite cross-cutting the foliation;
harz	harzburgite;
anom 1	*Anomaly 1* harzburgite;
anom 2	*Anomaly 2* harzburgite;
bckgrd	*background* harzburgite;
chrm	peridotite sampled from the Hadji Pavlou chrome mine;
top seq	*top-of-the-sequence* harzburgite;
xeno	harzburgite *xenolith;*
wallrk a	harzburgite sampled adjacent to an *orthopyroxenite A;*
wallrk b	harzburgite sampled adjacent to an *orthopyroxenite B;*
ol-pyxite	olivine-clinopyroxenite;
Opx A	*orthopyroxenite A;*
Opx B	*orthopyroxenite B;*
pyxite band	pyroxenite banding in harzburgite;
chrmte	chromitite sample;
lim.for	sample from the Limassol Forest area;
serp. diapir	samples from the serpentinite diapir.

The data in this appendix is quoted in wt% oxide for the major elements and in ppm for the trace elements.

Sample	142 dunite crustal	81 dunite crustal	118 dunite crustal	195 dunite crustal	393 dunite crustal	223 dunite crustal	410 dunite folded	D93-4 dunite II fol	187 dunite II fol	D93-3 dunite II fol	180 dunite II fol	166 dunite II fol	170 dunite II fol	97 dunite II fol	354 dunite interdig	348 dunite interdig
MgO	49.53	49.41	49.19	50.02	50.22	49.20	49.98	50.06	49.88	49.80	49.03	49.49	49.10	49.44	49.56	49.45
Al2O3	bd	bd	0.01	0.01	0.01	0.02	0.01	bd	bd	0.02	bd	0.02	0.01	0.02	0.02	0.01
SiO2	40.10	40.32	39.91	40.27	40.31	40.63	40.11	40.38	40.07	40.42	40.57	39.85	40.30	39.97	40.27	40.03
CaO	0.15	0.05	0.12	0.13	0.09	0.08	0.04	0.06	0.11	0.06	0.07	0.14	0.04	0.07	0.07	0.06
TiO2	0.02	0.01	bd	0.02	bd	0.01	0.01	0.02	0.01	0.01	0.02	0.01	0.01	bd	0.02	bd
Cr2O3	0.03	0.03	0.03	0.02	bd	0.04	0.02	bd	0.04	bd	0.02	bd	bd	bd	0.02	0.02
V2O3	bd	bd	bd	bd	bd	bd	bd	bd	bd	bd	bd	bd	bd	bd	bd	bd
MnO	0.15	0.14	0.19	0.13	0.14	0.17	0.12	0.13	0.13	0.17	0.16	0.13	0.15	0.16	0.14	0.15
FeOt	9.23	9.02	9.45	8.46	8.05	9.84	8.52	8.55	8.38	8.64	9.83	9.21	9.52	8.92	8.81	8.88
NiO	0.13	0.20	0.09	0.25	0.29	0.04	0.41	0.16	0.15	0.17	0.08	0.23	0.25	0.12	0.28	0.39
ZnO	bd	bd	0.02	0.02	0.02	0.04	0.03	bd	0.03	bd	0.02	0.03	0.03	0.04	bd	bd
Total	99.37	99.22	99.04	99.34	99.16	100.08	99.27	99.42	98.84	99.32	99.82	99.19	99.45	98.77	99.21	99.02
MgO	1.820	1.815	1.816	1.833	1.840	1.797	1.835	1.832	1.836	1.825	1.796	1.824	1.805	1.825	1.821	1.822
Al2O3	-	-	0.000	0.000	0.000	0.000	0.000	-	-	0.000	-	0.001	0.000	0.001	0.001	0.000
SiO2	0.989	0.994	0.988	0.990	0.991	0.996	0.988	0.991	0.990	0.994	0.997	0.986	0.994	0.990	0.993	0.990
CaO	0.004	0.001	0.003	0.003	0.002	0.002	0.001	0.002	0.003	0.002	0.002	0.004	0.001	0.002	0.002	0.001
TiO2	0.000	0.000	-	0.000	-	0.000	0.000	0.000	0.000	0.000	0.000	0.000	0.000	-	0.000	-
Cr2O3	0.001	0.001	0.001	0.001	-	0.001	0.000	-	0.001	-	0.000	-	-	-	0.000	0.000
V2O3	-	-	-	-	-	-	-	-	-	-	-	-	-	-	-	-
MnO	0.003	0.003	0.004	0.003	0.003	0.003	0.003	0.003	0.003	0.004	0.003	0.003	0.003	0.003	0.003	0.003
FeOt	0.190	0.186	0.196	0.174	0.166	0.202	0.175	0.176	0.173	0.178	0.202	0.191	0.197	0.185	0.182	0.184
NiO	0.003	0.004	0.002	0.005	0.006	0.001	0.008	0.003	0.003	0.003	0.002	0.004	0.005	0.002	0.005	0.008
ZnO	-	-	0.001	0.001	0.000	0.001	0.001	-	0.001	-	0.001	0.000	0.001	0.001	-	-
Total	3.011	3.005	3.011	3.010	3.009	3.004	3.011	3.008	3.010	3.006	3.003	3.015	3.006	3.010	3.007	3.008
Mg#	90.53	90.72	90.27	91.33	91.74	89.91	91.29	91.26	91.37	91.13	89.89	90.54	90.18	90.80	90.93	90.83

Sample	370 dunite interdig	357 dunite interdig	396 dunite wall rk	130 dunite wallrk	224A dunite wallrk	363 dunite wallrk a	339 dunite wallrk b	326b1 dunite wallrk b	353 dunite wallrk b	345 dunite wallrk b	212A dunite x fol	411 dunite x fol	316 dunite x fol	400 dunite x fol	412 dunite x fol	212B dunite x fol
MgO	50.54	49.67	51.08	50.00	52.06	49.44	50.38	50.17	48.12	49.84	49.77	49.62	49.96	49.53	50.06	49.61
Al2O3	0.02	0.03	bd	0.02	0.02	bd	0.03	0.02	0.05	0.03	0.01	0.02	0.01	0.01	0.03	bd
SiO2	39.93	40.17	40.29	39.87	40.98	39.95	40.60	40.08	39.81	39.89	40.30	40.31	40.17	40.08	40.24	40.22
CaO	0.04	0.10	0.06	0.18	0.03	0.03	0.07	0.03	0.40	0.06	0.07	0.04	0.03	0.03	0.06	0.10
TiO2	0.01	0.01	0.01	bd	0.01	0.01	0.02	0.01	0.02	0.02	0.01	0.01	bd	bd	0.01	0.01
Cr2O3	0.02	0.04	bd	bd	bd	bd	bd	bd	0.02	bd	bd	bd	bd	bd	bd	0.02
V2O3	bd	bd	bd	bd	bd	bd	bd	bd	bd	bd	bd	bd	bd	bd	bd	bd
MnO	0.15	0.13	0.14	0.14	0.10	0.16	0.13	0.14	0.14	0.12	0.15	0.14	0.14	0.15	0.15	0.13
FeOt	8.33	8.74	8.22	8.32	5.95	9.76	8.83	9.34	10.32	8.80	8.75	8.81	8.95	9.41	8.97	8.80
NiO	0.30	0.30	0.29	0.22	0.10	0.34	0.29	0.41	0.27	0.28	0.18	0.40	0.40	0.40	0.30	0.11
ZnO	bd	0.04	0.02	bd	0.05	0.04	bd	bd	0.02	0.04	bd	bd	bd	bd	bd	0.02
Total	99.39	99.23	100.13	98.79	99.33	99.76	100.39	100.24	99.18	99.10	99.28	99.40	99.72	99.66	99.85	99.05
MgO	1.852	1.825	1.856	1.843	1.883	1.816	1.829	1.832	1.783	1.835	1.826	1.821	1.829	1.819	1.829	1.824
Al2O3	0.001	0.001	-	0.001	0.000	-	0.001	0.001	0.001	0.001	0.000	0.001	0.001	0.001	0.001	-
SiO2	0.982	0.990	0.982	0.986	0.994	0.985	0.989	0.982	0.990	0.985	0.992	0.993	0.987	0.987	0.987	0.992
CaO	0.001	0.003	0.002	0.005	0.001	0.001	0.002	0.001	0.011	0.002	0.002	0.001	0.001	0.001	0.002	0.003
TiO2	0.000	0.000	0.000	-	0.000	0.000	0.001	0.000	0.000	0.000	0.000	0.000	-	-	0.000	0.000
Cr2O3	0.000	0.001	-	-	-	-	-	-	0.001	-	-	-	-	-	-	0.001
V2O3	-	-	-	-	-	-	-	-	-	-	-	-	-	-	-	-
MnO	0.003	0.003	0.003	0.003	0.002	0.003	0.003	0.003	0.004	0.002	0.003	0.003	0.003	0.003	0.003	0.003
FeOt	0.171	0.180	0.168	0.172	0.121	0.201	0.180	0.192	0.215	0.182	0.180	0.182	0.184	0.194	0.184	0.182
NiO	0.006	0.006	0.006	0.005	0.002	0.007	0.006	0.008	0.006	0.006	0.004	0.008	0.008	0.008	0.006	0.002
ZnO	-	0.001	0.000	-	0.001	0.001	-	-	0.001	0.001	-	-	-	-	-	0.000
Total	3.018	3.009	3.017	3.014	3.005	3.014	3.010	3.018	3.009	3.014	3.008	3.008	3.013	3.012	3.013	3.008
Mg#	91.53	91.02	91.72	91.46	93.98	90.03	91.04	90.53	89.26	90.98	91.03	90.93	90.86	90.36	90.86	90.95

Olivine compositions

Sample	127 dunite x fol	173 dunite x fol	355 dunite x fol	209 dunite x fol	317 dunite x fol	410 harz adj dun	60 harz adj dun	154 harz adj dun	D93-5 harz adj dun	321 harz adj dun	169 harz adj dun	317 harz adj dun	185 harz adj dun	384 harz anom 1	111 harz anom 1	107 harz anom 1
MgO	48.82	49.47	49.95	48.82	49.89	50.18	49.28	49.99	49.28	49.04	48.88	49.95	49.93	50.19	49.74	49.14
Al2O3	bd	0.01	0.01	0.02	bd	bd	0.01	0.01	0.02	bd	0.13	0.02	bd	0.02	0.02	0.02
SiO2	40.07	40.35	40.13	39.93	40.36	39.94	39.91	40.32	40.02	40.06	40.06	40.56	40.45	40.33	40.43	40.09
CaO	0.16	0.08	0.07	0.07	0.04	0.02	0.03	0.03	0.04	0.02	0.12	0.03	0.05	0.06	0.05	0.04
TiO2	0.01	bd	0.01	bd	bd	0.01	0.01	0.01	bd	0.01	bd	0.01	0.01	0.01	bd	bd
Cr2O3	bd	bd	bd	bd	bd	bd	0.02	bd	bd	0.02	0.35	bd	bd	bd	0.02	0.03
V2O3	bd	bd	bd	bd	bd	bd	bd	bd	bd	bd	bd	bd	bd	bd	bd	bd
MnO	0.13	0.14	0.14	0.16	0.14	0.15	0.15	0.14	0.15	0.15	0.13	0.13	0.12	0.16	0.12	0.14
FeOt	9.41	8.90	8.61	9.02	8.85	8.58	9.08	8.66	9.02	9.22	9.14	8.81	8.95	9.10	8.90	9.51
NiO	0.15	0.08	0.40	0.17	0.39	0.40	0.17	0.41	0.11	0.46	0.13	0.40	0.42	0.30	0.44	0.11
ZnO	0.02	0.02	0.03	0.03	0.03	bd	bd	bd	bd	bd	0.02	0.04	0.05	bd	bd	0.03
Total	98.81	99.09	99.37	98.24	99.74	99.30	98.69	99.59	98.68	99.00	98.99	99.98	100.01	100.21	99.75	99.12
MgO	1.805	1.818	1.833	1.813	1.825	1.843	1.822	1.830	1.821	1.810	1.803	1.821	1.822	1.829	1.819	1.811
Al2O3	-	0.000	0.001	0.000	-	-	0.000	0.001	0.001	-	0.004	0.001	-	0.001	0.001	0.000
SiO2	0.994	0.995	0.988	0.994	0.990	0.984	0.990	0.990	0.992	0.992	0.991	0.992	0.991	0.986	0.992	0.991
CaO	0.005	0.002	0.002	0.002	0.001	0.001	0.001	0.001	0.001	0.000	0.003	0.001	0.001	0.002	0.001	0.001
TiO2	0.000	-	0.000	-	-	0.000	0.000	0.000	-	0.000	-	0.000	0.000	0.000	-	-
Cr2O3	-	-	-	-	-	-	0.000	-	-	0.000	0.007	-	-	-	0.000	0.001
V2O3	-	-	-	-	-	-	-	-	-	-	-	-	-	-	-	-
MnO	0.003	0.003	0.003	0.003	0.003	0.003	0.003	0.003	0.003	0.003	0.003	0.003	0.003	0.003	0.002	0.003
FeOt	0.195	0.184	0.177	0.188	0.181	0.177	0.188	0.178	0.187	0.191	0.189	0.180	0.184	0.186	0.183	0.197
NiO	0.003	0.002	0.008	0.003	0.008	0.008	0.004	0.008	0.002	0.009	0.003	0.008	0.008	0.006	0.009	0.002
ZnO	0.000	0.000	0.001	0.000	0.001	-	-	-	-	-	0.000	0.001	0.001	-	-	0.001
Total	3.005	3.005	3.012	3.005	1.505	3.016	3.010	3.010	3.008	3.005	3.003	3.007	3.010	3.014	3.007	3.008
Mg#	90.23	90.83	91.19	90.60	90.98	91.24	90.65	91.16	90.69	90.45	90.51	91.00	90.85	90.77	90.86	90.19

Olivine compositions

Sample	293 harz anom 2	295 harz anom 2	85 harz backgrd grd, mine area	80 harz	338 harz banded	333 harz banded	323 harz banded	325 harz banded	318 harz banded	319 harz banded	337 harz banded	55 harz bckgrd	304 harz bckgrd	297 harz bckgrd	287 harz bckgrd	294 harz bckgrd
MgO	50.34	50.45	49.65	50.27	50.27	49.77	49.83	50.35	49.98	50.24	50.20	49.33	49.51	49.35	49.11	49.26
Al2O3	0.01	bd	0.01	bd	0.03	0.02	0.06	0.03	0.02	0.30	0.02	0.02	0.02	bd	0.02	bd
SiO2	40.30	40.53	40.35	40.52	40.16	39.92	40.46	40.41	40.22	39.51	40.24	40.39	40.30	39.87	39.97	40.34
CaO	0.03	0.05	0.04	0.03	0.02	0.04	0.02	0.02	0.02	0.03	0.05	0.04	0.04	0.04	0.03	0.02
TiO2	bd	0.02	0.01	0.02	0.01	0.01	0.01	0.01	0.01	0.02	0.02	0.01	bd	0.01	0.03	0.02
Cr2O3	bd	bd	bd	bd	bd	bd	bd	0.03	bd	0.67	bd	bd	bd	bd	bd	bd
V2O3	bd	bd	bd	bd	bd	bd	bd	bd	bd	bd	bd	bd	bd	bd	bd	bd
MnO	0.14	0.15	0.13	0.13	0.14	0.14	0.14	0.12	0.14	0.12	0.15	0.14	0.14	0.13	0.12	0.14
FeOt	8.07	7.97	8.88	8.35	9.07	9.18	8.99	9.02	9.72	8.84	9.01	9.10	9.06	9.39	9.14	9.36
NiO	0.33	0.23	0.43	0.42	0.41	0.42	0.29	0.29	0.31	0.33	0.33	0.09	0.21	0.29	0.18	0.17
ZnO	0.03	0.04	bd	bd	bd	bd	bd	bd	bd	0.03	0.03	bd	bd	bd	bd	bd
Total	99.25	99.47	99.54	99.78	100.14	99.52	99.84	100.31	100.46	100.12	100.08	99.15	99.33	99.13	98.64	99.35
											:					
MgO	1.843	1.841	1.819	1.833	1.834	1.829	1.820	1.831	1.822	1.836	1.832	1.813	1.818	1.821	1.816	1.810
Al2O3	0.000	-	0.000	-	0.001	0.001	0.002	0.001	0.000	0.009	0.000	0.000	0.001	-	0.001	-
SiO2	0.990	0.992	0.992	0.991	0.983	0.984	0.992	0.986	0.984	0.969	0.985	0.996	0.993	0.987	0.992	0.995
CaO	0.001	0.002	0.001	0.001	0.001	0.001	0.001	0.001	0.001	0.001	0.001	0.001	0.001	0.001	0.001	0.001
TiO2	-	0.000	0.000	0.000	0.000	0.000	0.000	0.000	0.000	0.000	0.000	0.000	-	0.000	0.000	0.000
Cr2O3	-	-	-	-	-	-	-	0.001	-	0.013	-	-	-	-	-	-
V2O3	-	-	-	-	-	-	-	-	-	-	-	-	-	-	-	-
MnO	0.003	0.003	0.003	0.003	0.003	0.003	0.003	0.003	0.003	0.003	0.003	0.003	0.003	0.003	0.003	0.003
FeOt	0.166	0.163	0.183	0.171	0.186	0.189	0.185	0.184	0.199	0.181	0.184	0.188	0.187	0.194	0.190	0.193
NiO	0.006	0.004	0.009	0.008	0.008	0.008	0.006	0.006	0.006	0.006	0.007	0.002	0.004	0.006	0.004	0.004
ZnO	0.001	0.001	-	-	-	-	-	-	-	0.000	0.001	-	-	-	-	-
Total	3.010	3.008	3.008	3.008	3.017	3.014	3.008	3.013	3.016	3.020	3.015	3.004	3.007	3.013	3.008	3.005
Mg#	91.74	91.87	90.88	91.47	90.81	90.63	90.79	90.85	90.17	91.01	90.86	90.62	90.69	90.37	90.53	90.36

Olivine compositions

Sample	284 harz bckgrd	286 harz bckgrd	282 harz bckgrd	300 harz bckgrd	92 harz bckgrd	311 harz bckgrd	271 harz bckgrd	291 harz bckgrd	285 harz bckgrd	303 harz bckgrd	298 harz bckgrd	296 harz bckgrd	302 harz bckgrd	265 harz bckgrd	149 harz bckgrd	310 harz bckgrd
MgO	49.56	49.58	50.21	49.96	50.24	49.80	50.51	49.53	49.73	49.92	49.56	49.35	49.63	49.39	50.21	49.60
Al2O3	0.02	bd	bd	0.02	0.02	0.01	0.01	0.02	0.02	bd	0.01	0.03	0.02	0.02	bd	0.02
SiO2	39.96	40.40	40.18	40.43	40.48	40.40	40.18	40.16	40.45	40.09	40.20	40.25	40.19	40.36	40.56	40.33
CaO	0.03	0.04	0.04	0.04	0.04	0.03	0.03	0.04	0.02	0.03	0.05	0.01	0.05	0.04	0.04	0.04
TiO2	0.02	0.03	0.01	0.02	bd	bd	0.01	0.02	0.01	0.01	0.02	0.03	0.01	0.02	0.01	bd
Cr2O3	bd	bd	0.03	bd	bd	bd	bd	0.04	bd	0.02	0.02	0.03	bd	bd	0.02	bd
V2O3	bd	bd	bd	bd	bd	bd	0.14	bd	bd	bd	bd	bd	bd	bd	bd	bd
MnO	0.13	0.13	0.14	0.13	0.13	0.13	8.31	0.16	0.13	0.13	0.14	0.15	0.13	0.13	0.14	0.15
FeOt	8.48	8.99	8.93	8.73	8.19	8.99	0.43	9.01	9.02	8.72	9.00	9.06	8.67	8.96	8.53	8.72
NiO	0.23	0.15	0.44	0.24	0.43	0.43	bd	0.16	0.17	0.43	0.24	0.17	0.41	0.25	0.39	0.16
ZnO	bd	bd	bd	bd	bd	bd	bd	bd	0.02	0.02	0.02	0.02	0.03	0.03	0.03	0.03
Total	98.46	99.37	100.01	99.59	99.58	99.85	99.66	99.16	99.60	99.38	99.29	99.13	99.15	99.23	99.97	99.07
MgO	1.832	1.818	1.834	1.826	1.835	1.821	1.846	1.821	1.820	1.832	1.821	1.815	1.824	1.815	1.829	1.823
Al2O3	0.001	-	-	0.000	0.001	0.000	0.000	0.001	0.000	-	0.001	0.001	0.001	0.001	-	0.000
SiO2	0.991	0.994	0.984	0.992	0.992	0.991	0.985	0.991	0.993	0.988	0.991	0.993	0.992	0.995	0.992	0.994
CaO	0.001	0.001	0.001	0.001	0.001	0.001	0.001	0.001	0.001	0.001	0.001	0.000	0.001	0.001	0.001	0.001
TiO2	0.000	0.000	0.000	0.000	-	-	0.000	0.000	0.000	0.000	0.000	0.000	0.000	0.000	0.000	-
Cr2O3	-	-	0.001	-	-	-	-	0.001	-	0.001	0.000	0.001	-	-	0.001	-
V2O3	-	-	-	-	-	-	-	-	-	-	-	-	-	-	-	-
MnO	0.003	0.003	0.003	0.003	0.003	0.003	0.003	0.004	0.003	0.003	0.003	0.003	0.003	0.003	0.003	0.003
FeOt	0.176	0.185	0.183	0.179	0.168	0.185	0.170	0.186	0.186	0.180	0.186	0.187	0.179	0.185	0.175	0.180
NiO	0.005	0.003	0.009	0.005	0.009	0.008	0.009	0.003	0.003	0.009	0.005	0.003	0.008	0.005	0.008	0.003
ZnO	-	-	-	-	-	-	-	-	0.000	0.000	0.001	0.000	0.001	0.001	0.001	0.001
Total	3.008	3.006	3.016	3.008	3.008	3.009	3.015	3.008	3.007	3.012	3.009	3.005	3.008	3.005	3.009	3.006
Mg#	91.26	90.77	90.93	91.09	91.61	90.80	91.57	90.73	90.74	91.08	90.75	90.66	91.06	90.75	91.29	91.01

Sample	284 harz bckgrd	290 harz bckgrd	305 harz bckgrd	299 harz bckgrd	308 harz bckgrd	292 harz bckgrd	78 harz chrm	188 harz chrm	132 harz chrm	355 harz interdig	349 harz interdig	262 harz top seq	389 harz top seq	388 harz top seq	315 harz top seq	283 harz top seq
MgO	49.81	49.79	49.93	49.60	49.99	49.73	49.39	49.96	50.03	50.03	51.34	49.65	49.95	50.06	50.04	49.32
Al2O3	0.02	0.03	bd	0.01	bd	0.01	0.03	bd	0.01	bd	0.02	0.01	0.01	0.01	0.02	bd
SiO2	40.25	40.15	39.94	40.36	40.46	40.04	40.05	40.37	40.36	40.37	39.41	40.08	40.19	40.08	40.01	40.02
CaO	0.05	0.03	0.04	0.04	0.04	0.05	bd	0.03	0.05	0.04	0.05	0.03	0.06	0.07	0.04	0.04
TiO2	0.02	0.01	bd	0.01	bd	0.01	bd	0.01	0.01	0.01	0.01	0.01	bd	bd	bd	0.02
Cr2O3	bd	bd	bd	bd	bd	bd	0.07	0.03	0.02	bd	bd	bd	bd	0.02	0.02	bd
V2O3	bd	bd	bd	bd	bd	bd	bd	bd	bd	bd	bd	bd	bd	bd	bd	bd
MnO	0.12	0.15	0.14	0.14	0.12	0.12	0.13	0.16	0.13	0.14	0.13	0.14	0.15	0.12	0.14	0.14
FeOt	8.54	8.74	8.83	8.99	8.68	9.14	9.08	8.95	8.30	8.56	8.47	8.98	8.91	8.27	8.51	9.15
NiO	0.21	0.39	0.40	0.17	0.22	0.40	0.44	0.42	0.43	0.41	0.29	0.28	0.39	0.41	0.37	0.29
ZnO	0.03	0.03	0.04	0.04	0.05	0.05	bd	bd	0.03	bd	bd	bd	bd	bd	bd	bd
Total	99.08	99.33	99.36	99.39	99.60	99.59	99.24	99.96	99.41	99.56	99.76	99.24	99.72	99.06	99.18	99.04
MgO	1.830	1.828	1.835	1.819	1.827	1.826	1.819	1.824	1.831	1.830	1.879	1.826	1.829	1.839	1.839	1.819
Al2O3	0.001	0.001	-	0.000	-	0.000	0.001	-	0.000	-	0.001	0.001	0.000	0.001	0.001	-
SiO2	0.992	0.989	0.985	0.993	0.992	0.986	0.989	0.989	0.991	0.991	0.968	0.989	0.987	0.988	0.986	0.990
CaO	0.001	0.001	0.001	0.001	0.001	0.001	-	0.001	0.001	0.001	0.002	0.001	0.002	0.002	0.001	0.001
TiO2	0.000	0.000	-	0.000	-	0.000	-	0.000	0.000	0.000	0.000	0.000	-	-	-	0.000
Cr2O3	-	-	-	-	-	-	-	0.002	0.001	0.000	-	-	-	0.000	0.000	-
V2O3	-	-	-	-	-	-	-	-	-	-	-	-	0.001	-	-	-
MnO	0.003	0.003	0.003	0.003	0.003	0.003	0.003	0.004	0.003	0.003	0.003	0.003	0.003	0.003	0.003	0.003
FeOt	0.176	0.180	0.182	0.185	0.178	0.188	0.188	0.183	0.171	0.176	0.174	0.186	0.183	0.171	0.175	0.189
NiO	0.004	0.008	0.008	0.003	0.004	0.008	0.009	0.009	0.009	0.008	0.006	0.006	0.008	0.008	0.008	0.006
ZnO	0.001	0.001	0.001	0.001	0.001	0.001	-	-	0.001	-	-	-	-	-	-	-
Total	3.007	3.011	3.016	3.006	3.007	3.013	3.010	3.010	3.009	3.009	3.032	3.011	3.012	3.011	3.012	3.010
Mg#	91.24	91.04	90.98	90.77	91.12	90.66	90.65	90.87	91.48	91.23	91.52	90.78	90.90	91.52	91.31	90.59

Olivine compositions

Sample	309 harz top seq	216 harz top seq	314 harz top seq	257b harz wallrk a	346 harz wallrk b	390 harz xeno	278 harz xeno	392 harz xeno	356 harz xeno	351 harz xeno	387 harz xeno	364 pyxite hz band	327b pyxite hz band	326b1 pyxite hz band	361b pyxite opx a	399 pyxite opx a
MgO	49.66	49.79	49.60	49.86	49.69	48.45	49.54	51.13	51.19	50.21	50.46	50.17	49.64	49.42	49.06	49.88
Al2O3	0.02	0.01	0.01	0.02	0.02	0.04	0.02	0.03	0.02	0.03	0.02	0.01	0.02	bd	0.03	0.02
SiO2	40.15	40.21	40.44	40.04	40.42	39.71	40.14	39.14	39.91	40.14	40.03	38.98	39.92	40.26	39.70	40.22
CaO	0.05	0.06	0.05	0.04	0.05	0.07	0.05	0.05	0.03	0.04	0.08	0.02	0.03	0.04	0.05	0.02
TiO2	0.01	0.01	bd	bd	0.01	0.01	0.02	0.01	0.02	0.01	0.01	0.02	0.02	bd	bd	0.01
Cr2O3	bd	bd	bd	bd	bd	0.03	bd	bd	bd	bd	0.04	0.02	bd	bd	bd	0.03
V2O3	bd	bd	bd	0.03	bd	bd	bd	bd	bd	bd	bd	bd	bd	bd	bd	bd
MnO	0.14	0.15	0.14	0.13	0.13	0.18	0.14	0.15	0.13	0.14	0.14	0.14	0.14	0.14	0.14	0.13
FeOt	8.89	8.72	9.05	9.13	9.08	10.51	9.08	8.63	8.35	8.25	8.74	9.74	9.31	9.44	9.72	9.39
NiO	0.42	0.33	0.18	0.40	0.22	0.34	0.43	0.29	0.29	0.41	0.39	0.33	0.43	0.24	0.40	0.35
ZnO	0.02	0.03	0.03	bd	bd	bd	bd	bd	0.02	0.05	0.05	bd	0.03	0.03	bd	bd
Total	99.37	99.34	99.53	99.68	99.67	99.33	99.45	99.47	100.02	99.30	99.97	99.46	99.55	99.60	99.13	100.07
MgO	1.824	1.827	1.817	1.828	1.818	1.794	1.820	1.879	1.865	1.841	1.843	1.854	1.825	1.813	1.814	1.823
Al2O3	0.000	0.000	0.000	0.001	0.001	0.001	0.001	0.001	0.000	0.001	0.001	0.000	0.001	-	0.001	0.001
SiO2	0.989	0.990	0.994	0.985	0.992	0.986	0.989	0.965	0.976	0.987	0.981	0.967	0.985	0.991	0.985	0.986
CaO	0.004	0.001	0.001	0.001	0.001	0.002	0.001	0.001	0.001	0.001	0.002	0.001	0.001	0.001	0.001	0.000
TiO2	0.000	0.000	-	-	0.000	0.000	0.000	0.000	0.000	0.000	0.000	0.000	0.000	-	-	0.000
Cr2O3	-	-	-	-	-	0.001	-	-	-	-	0.001	0.001	-	-	-	0.001
V2O3	-	-	-	0.001	-	-	-	-	-	-	-	-	-	-	-	-
MnO	0.003	0.003	0.003	0.003	0.003	0.004	0.003	0.003	0.003	0.003	0.003	0.003	0.003	0.003	0.003	0.003
FeOt	0.183	0.180	0.186	0.188	0.186	0.218	0.187	0.178	0.171	0.170	0.179	0.202	0.192	0.194	0.202	0.193
NiO	0.008	0.007	0.004	0.008	0.004	0.007	0.009	0.006	0.006	0.009	0.008	0.007	0.009	0.005	0.009	0.007
ZnO	0.001	0.001	0.001	-	-	-	-	-	0.000	0.001	0.001	-	0.001	0.001	-	-
Total	3.012	3.010	3.006	3.015	3.007	3.013	3.009	3.035	3.024	3.013	3.019	3.034	3.015	3.009	3.015	3.014
Mg#	90.87	91.03	90.70	90.70	90.72	89.17	90.68	91.36	91.60	91.54	91.13	90.17	90.48	90.32	90.00	90.44

Olivine compositions

Sample	419 pyxite opx a	406 pyxite opx a	361a pyxite opx a	373 pyxite opx a	339 pyxite opx b	413 pyxite opx b	408 ol-pyxite	276 ol-pyxite	394 ol-pyxite
MgO	49.67	49.34	49.22	49.92	50.67	49.37	48.74	48.80	48.93
Al2O3	0.02	0.03	0.03	0.01	0.02	0.03	0.04	0.01	0.03
SiO2	39.90	39.82	39.91	40.24	40.70	39.93	39.81	40.15	39.88
CaO	0.03	0.03	0.05	0.04	0.01	0.10	0.05	0.03	0.05
TiO2	bd	0.02	0.02	0.01	bd	0.03	0.02	0.01	0.01
Cr2O3	bd	0.04	bd	0.02	bd	0.04	0.03	bd	bd
V2O3	bd	bd	bd	bd	bd	bd	bd	bd	bd
MnO	0.15	0.14	0.13	0.13	0.12	0.15	0.16	0.14	0.19
FeOt	9.01	9.59	9.77	8.65	8.80	9.52	10.00	10.35	11.03
NiO	0.50	0.48	0.41	0.46	0.27	0.31	0.27	0.34	0.32
ZnO	bd	0.02	0.03	0.03	0.03	0.03	bd	bd	bd
Total	99.32	99.52	99.59	99.53	100.66	99.54	99.16	99.88	100.46
MgO	1.828	1.817	1.812	1.829	1.834	1.816	1.803	1.794	1.796
Al2O3	0.001	0.001	0.001	0.001	0.001	0.001	0.002	0.001	0.001
SiO2	0.985	0.984	0.985	0.989	0.989	0.985	0.988	0.990	0.982
CaO	0.001	0.001	0.001	0.001	0.001	0.003	0.002	0.001	0.002
TiO2	-	0.000	0.000	0.000	-	0.001	0.001	0.000	0.000
Cr2O3	-	0.001	-	0.000	-	0.001	0.001	-	-
V2O3	-	-	-	-	-	-	-	-	-
MnO	0.003	0.003	0.003	0.003	0.003	0.003	0.003	0.003	0.004
FeOt	0.186	0.199	0.202	0.178	0.179	0.196	0.208	0.214	0.227
NiO	0.010	0.010	0.008	0.009	0.006	0.006	0.005	0.007	0.007
ZnO	-	0.001	0.001	0.001	0.001	0.000	-	-	-
Total	3.014	3.015	3.013	3.010	3.011	3.013	3.012	3.009	3.018
Mg#	90.76	90.15	89.97	91.13	91.11	90.24	89.68	89.36	88.78

Sample	186B Chrmte	183A Chrmte	224a Chrmte	065A Chrmte	079B Chrmte	148 Chrmte	130 Chrmte	228 dunite chr stringer	223 dunite crustal stringer	142 dunite crustal	118 dunite crustal	195 dunite crustal	393 dunite crustal	81 dunite crustal	410 dunite folded	D93-4 dunite II fol
MgO	14.54	13.73	13.10	13.75	14.55	12.79	12.35	15.27	8.79	9.74	11.22	12.87	8.57	9.54	12.16	10.36
Al2O3	18.46	15.59	12.33	11.76	17.29	16.74	17.74	20.99	9.81	12.71	14.22	23.31	10.92	13.55	22.42	13.02
SiO2	bd	0.02	0.04	0.03	0.03	0.03	0.04	0.03	0.04	0.05	0.03	0.03	0.04	0.05	0.06	0.02
TiO2	0.10	0.14	0.20	0.14	0.14	0.11	0.15	0.42	0.21	0.20	0.28	0.28	0.14	0.14	0.07	0.11
Cr2O3	52.33	56.23	57.31	57.67	51.44	52.62	50.52	49.58	59.02	53.19	50.93	41.42	56.41	53.41	44.76	56.47
V2O3	0.16	0.17	0.15	0.12	0.13	0.22	0.14	0.14	0.21	0.21	0.20	0.18	0.19	0.41	0.19	0.24
MnO	0.24	0.23	0.25	0.25	0.24	0.22	0.28	0.22	0.42	0.37	0.32	0.31	0.35	0.36	0.41	0.33
FeO	13.08	14.03	13.89	12.35	12.04	14.67	15.67	12.65	20.60	18.62	17.04	15.66	20.49	19.29	16.68	18.18
Fe2O3	2.89	2.08	3.02	2.89	3.28	1.81	2.92	2.48	3.35	4.23	6.17	5.32	3.38	3.57	3.71	2.02
NiO	0.02	0.04	bd	0.02	0.05	0.08	0.06	0.05	0.04	0.05	0.05	0.07	0.03	0.04	0.15	0.07
ZnO	bd	0.03	0.04	0.06	0.08	0.08	0.11	0.08	0.09	0.13	0.15	0.16	0.19	0.33	0.21	0.14
Total	101.83	102.32	100.36	99.06	99.32	99.40	99.99	101.96	102.59	99.52	100.65	99.63	100.74	100.74	100.87	101.02
MgO	5.287	5.057	4.991	5.288	5.431	4.831	4.641	5.468	3.421	3.822	4.294	4.725	3.382	3.695	4.457	3.988
Al2O3	5.309	4.539	3.716	3.578	5.101	5.002	5.271	5.941	3.019	3.942	4.302	6.772	3.405	4.151	6.499	3.964
SiO2	-	0.006	0.010	0.008	0.007	0.009	0.010	0.007	0.010	0.014	0.009	0.008	0.012	0.014	0.015	0.006
TiO2	0.019	0.025	0.038	0.028	0.027	0.021	0.029	0.076	0.041	0.040	0.054	0.052	0.027	0.027	0.013	0.022
Cr2O3	10.095	10.983	11.586	11.768	10.183	10.548	10.069	9.415	12.182	11.072	10.335	8.075	11.801	10.977	8.703	11.529
V2O3	0.030	0.034	0.031	0.024	0.026	0.045	0.029	0.028	0.043	0.045	0.043	0.035	0.041	0.086	0.038	0.051
MnO	0.049	0.049	0.055	0.055	0.052	0.048	0.060	0.045	0.092	0.083	0.070	0.065	0.078	0.080	0.084	0.072
FeO	2.669	2.899	2.971	2.666	2.522	3.110	3.304	2.541	4.498	4.100	3.659	3.233	4.534	4.192	3.430	3.926
Fe2O3	0.530	0.387	0.580	0.562	0.618	0.345	0.553	0.448	0.657	0.838	1.192	0.989	0.674	0.698	0.687	0.393
NiO	0.004	0.008	-	0.005	0.011	0.016	0.011	0.010	0.007	0.011	0.011	0.014	0.008	0.009	0.029	0.014
ZnO	-	0.005	0.008	0.012	0.014	0.015	0.020	0.015	0.018	0.025	0.028	0.029	0.038	0.062	0.039	0.028
Total	23.997	24.000	23.995	23.997	24.008	24.005	24.002	24.006	24.001	24.001	24.004	24.004	24.004	24.005	24.019	24.008
Cr# (Al)	65.54	70.76	75.71	76.68	66.63	67.83	65.64	61.31	80.14	73.75	70.61	54.40	77.61	72.56	57.25	74.42
Mg#	66.45	63.56	62.69	66.48	68.29	60.84	58.41	68.27	43.20	48.25	53.99	59.38	42.72	46.85	56.51	50.39
Fe2+/Fe3+	4.53	6.75	4.61	4.27	3.67	8.11	5.37	5.11	6.16	4.41	2.76	2.94	6.06	5.40	4.99	8.99

Sample	180 dunite II fol	97 dunite II fol	D93-3 dunite II fol	170 dunite II fol	166 dunite II fol	357 dunite interdig	348 dunite interdig	354 dunite interdig	370 dunite interdig	396 dunite wall rk	187 dunite wallrk	257a dunite wallrk a	363 dunite wallrk b	353 dunite wallrk b	339-spd dunite wallrk b	345 dunite wallrk b
MgO	10.15	13.71	10.53	10.01	10.70	13.41	11.97	10.91	11.62	13.08	9.93	11.66	9.22	12.60	14.03	13.46
Al2O3	10.66	24.00	13.05	14.49	22.55	21.97	18.32	16.17	21.33	22.57	11.02	21.89	14.02	27.28	28.74	26.93
SiO2	0.05	0.03	0.05	0.06	0.02	0.05	0.03	0.05	0.04	0.03	0.04	0.04	0.05	0.03	0.03	0.05
TiO2	0.21	0.13	0.09	0.16	0.07	0.09	0.17	0.12	0.10	0.26	0.17	0.06	0.15	0.23	0.12	0.11
Cr2O3	58.33	44.14	56.43	52.63	35.57	46.79	50.20	51.58	45.55	43.70	58.59	45.01	53.31	37.63	39.45	39.97
V2O3	0.23	0.21	0.27	0.25	0.40	0.18	0.21	0.20	0.23	0.27	0.23	0.23	0.23	0.20	0.21	0.26
MnO	0.33	0.24	0.31	0.34	0.27	0.27	0.43	0.34	0.30	0.24	0.38	0.41	0.49	0.27	0.25	0.27
FeO	18.57	14.34	17.84	18.58	18.16	14.75	16.26	17.70	17.10	15.56	18.57	17.21	19.84	16.75	15.00	15.31
Fe2O3	3.39	2.26	1.98	3.10	10.37	2.61	2.39	3.34	3.04	4.63	1.96	3.55	3.12	4.55	2.56	3.32
NiO	0.05	0.04	0.05	0.07	0.13	0.11	0.11	0.06	0.09	0.06	0.04	0.09	0.07	0.12	0.08	0.11
ZnO	0.12	0.13	0.16	0.18	0.29	0.14	0.14	0.18	0.29	0.13	0.18	0.24	0.17	0.17	0.20	0.21
Total	102.11	99.27	100.77	99.91	98.60	100.37	100.24	100.68	99.73	100.56	101.18	100.40	100.69	99.87	100.71	100.00
MgO	3.912	5.006	4.056	3.878	4.044	4.903	4.483	4.143	4.334	4.775	3.862	4.310	3.571	4.553	4.961	4.837
Al2O3	3.253	6.929	3.975	4.436	6.741	6.350	5.427	4.855	6.288	6.516	3.389	6.399	4.295	7.799	8.035	7.656
SiO2	0.014	0.008	0.012	0.015	0.006	0.012	0.008	0.013	0.010	0.008	0.011	0.010	0.013	0.008	0.007	0.011
TiO2	0.041	0.024	0.018	0.032	0.014	0.016	0.033	0.022	0.019	0.048	0.034	0.011	0.030	0.042	0.021	0.020
Cr2O3	11.938	8.548	11.529	10.811	7.135	9.073	9.989	10.389	9.014	8.466	12.083	8.837	10.958	7.217	7.398	7.622
V2O3	0.047	0.042	0.057	0.053	0.082	0.035	0.043	0.041	0.046	0.053	0.049	0.046	0.049	0.038	0.041	0.050
MnO	0.073	0.050	0.067	0.075	0.059	0.056	0.092	0.074	0.063	0.050	0.083	0.086	0.108	0.056	0.050	0.054
FeO	4.021	2.939	3.856	4.037	3.854	3.026	3.424	3.770	3.580	3.188	4.050	3.577	4.313	3.399	2.976	3.087
Fe2O3	0.659	0.417	0.385	0.606	1.981	0.481	0.451	0.641	0.574	0.853	0.385	0.665	0.611	0.830	0.458	0.602
NiO	0.012	0.009	0.010	0.014	0.027	0.022	0.021	0.012	0.019	0.013	0.009	0.017	0.016	0.024	0.016	0.021
ZnO	0.023	0.024	0.030	0.035	0.055	0.025	0.025	0.035	0.053	0.023	0.035	0.045	0.032	0.030	0.035	0.037
Total	24.003	24.004	23.998	24.003	24.017	24.002	24.002	24.006	24.012	24.003	24.007	24.010	24.002	24.012	24.011	24.006
Cr# (Al)	78.59	55.23	74.36	70.91	51.42	58.83	64.80	68.15	58.91	56.51	78.10	58.00	71.84	48.06	47.94	49.89
Mg#	49.31	63.01	51.26	49.00	51.20	61.84	56.70	52.36	54.77	59.96	48.81	54.65	45.29	57.26	62.51	61.04
Fe2+/Fe3+	5.48	6.34	9.03	6.00	1.75	5.66	6.81	5.30	5.62	3.36	9.47	5.38	6.35	3.69	5.85	4.61

Spinel Compositions

Sample	344 dunite wallrk b	212B dunite x fol	173 dunite x fol	168 dunite x fol	184 dunite x fol	412 dunite x fol	212A dunite x fol	209 dunite x fol	316 dunite x fol	411 dunite x fol	127 dunite x fol	317 dunite x fol	400 dunite x fol	D93-5 harz adj dun	409 harz adj dun	60 harz adj dun
MgO	12.16	14.06	13.05	9.07	8.37	12.45	12.51	12.57	11.56	11.79	13.05	9.75	12.73	11.48	10.92	12.19
Al2O3	26.93	21.74	21.62	11.48	9.41	22.85	22.10	24.88	20.28	21.09	24.43	17.90	25.79	13.76	17.24	22.10
SiO2	0.06	0.04	0.05	0.04	0.05	0.04	0.05	0.02	0.03	0.03	0.05	0.04	0.04	0.05	0.04	0.03
TiO2	0.06	0.16	0.13	0.16	0.10	0.10	0.14	0.06	0.05	0.10	0.07	0.06	0.06	0.06	0.10	0.07
Cr2O3	38.77	46.06	47.57	56.95	59.80	45.60	47.30	41.33	47.87	46.46	40.53	49.42	42.82	57.61	52.18	46.79
V2O3	0.31	0.18	0.19	0.24	0.26	0.23	0.18	0.27	0.26	0.19	0.36	0.28	0.27	0.30	0.23	0.26
MnO	0.28	0.23	0.27	0.40	0.34	0.28	0.26	0.27	0.43	0.40	0.26	0.43	0.38	0.28	0.45	0.26
FeO	16.94	13.43	15.40	19.92	20.67	16.46	16.38	16.23	17.21	17.01	15.19	19.61	16.21	16.83	17.69	16.75
Fe2O3	3.29	2.95	2.15	2.64	1.87	2.43	1.67	3.85	2.77	3.14	4.92	2.97	1.70	1.20	1.38	2.05
NiO	0.14	0.06	0.07	bd	0.07	0.10	0.08	0.09	0.09	0.10	0.04	0.07	0.10	0.05	0.06	0.05
ZnO	0.36	0.11	0.13	0.16	0.17	0.17	0.17	0.19	0.20	0.21	0.23	0.27	0.28	0.14	0.16	0.16
Total	99.33	99.04	100.68	101.10	101.14	100.76	100.87	99.80	100.76	100.54	99.16	100.83	100.41	101.78	100.48	100.73
MgO	4.429	5.178	4.775	3.544	3.313	4.548	4.576	4.592	4.294	4.366	4.787	3.700	4.601	4.340	4.132	4.474
Al2O3	7.758	6.332	6.255	3.546	2.946	6.602	6.394	7.183	5.956	6.178	7.085	5.372	7.367	4.114	5.158	6.416
SiO2	0.016	0.010	0.011	0.011	0.012	0.011	0.012	0.006	0.007	0.009	0.013	0.010	0.010	0.011	0.011	0.008
TiO2	0.011	0.031	0.025	0.033	0.021	0.018	0.026	0.012	0.009	0.019	0.013	0.012	0.011	0.011	0.019	0.013
Cr2O3	7.502	9.002	9.234	11.800	12.556	8.838	9.179	8.006	9.432	9.130	7.885	9.947	8.211	11.555	10.470	9.112
V2O3	0.062	0.036	0.037	0.051	0.055	0.045	0.036	0.053	0.052	0.038	0.070	0.057	0.053	0.062	0.047	0.051
MnO	0.058	0.049	0.056	0.090	0.077	0.058	0.055	0.056	0.091	0.084	0.055	0.093	0.077	0.060	0.096	0.055
FeO	3.467	2.775	3.162	4.365	4.591	3.374	3.363	3.325	3.586	3.535	3.125	4.175	3.288	3.571	3.756	3.450
Fe2O3	0.606	0.548	0.398	0.520	0.374	0.449	0.309	0.709	0.519	0.587	0.912	0.568	0.311	0.228	0.265	0.380
NiO	0.027	0.011	0.014	-	0.016	0.020	0.017	0.017	0.017	0.020	0.009	0.015	0.019	0.010	0.013	0.011
ZnO	0.064	0.019	0.024	0.031	0.033	0.031	0.031	0.034	0.037	0.038	0.041	0.051	0.051	0.027	0.029	0.029
Total	24.014	24.005	24.007	23.997	24.003	24.009	24.001	24.014	24.005	24.009	23.999	24.011	24.010	24.000	24.003	24.001
Cr# (Al)	49.16	58.71	59.62	76.89	80.99	57.24	58.94	52.71	61.29	59.64	52.67	64.93	52.71	73.74	67.00	58.68
Mg#	56.09	65.11	60.16	44.81	41.91	57.41	57.64	58.01	54.49	55.26	60.50	46.98	58.32	54.86	52.39	56.46
Fe2+/Fe3+	5.72	4.56	7.15	7.55	11.04	6.76	9.79	4.22	6.91	5.42	3.09	6.61	10.56	14.08	12.78	8.18

Sample	185 harz adj dun	87 harz adj dun	169 harz adj dun	410 harz adj dun	317 harz adj dun	154 harz adj dun	384 harz anom 1	107 harz anom 1	111 harz anom 1	293 harz anom 2	295 harz anom 2	338 harz banded	333 harz banded	337 harz banded	327b harz banded	319 harz banded
MgO	11.11	12.57	11.53	12.38	10.82	12.09	14.14	12.51	12.49	13.96	13.94	13.51	13.03	12.98	10.56	13.39
Al2O3	15.55	21.03	18.44	23.73	20.51	22.23	25.40	25.19	25.61	30.99	29.93	24.59	23.51	22.80	16.56	23.37
SiO2	0.08	0.05	0.05	0.04	0.04	0.04	0.03	0.04	0.03	0.03	0.02	0.05	0.04	0.02	0.03	0.04
TiO2	0.05	0.07	0.06	0.06	0.06	0.06	0.08	0.07	0.10	0.07	0.08	0.05	0.04	0.04	0.06	0.05
Cr2O3	54.35	48.58	51.91	44.68	47.56	46.63	42.16	43.24	42.63	36.50	37.53	45.42	45.81	46.93	52.23	45.39
V2O3	0.30	0.27	0.27	0.18	0.26	0.22	0.21	0.26	0.23	0.18	0.21	0.19	0.24	0.22	0.29	0.22
MnO	0.29	0.31	0.30	0.37	0.41	0.29	0.27	0.25	0.27	0.25	0.25	0.24	0.38	0.26	0.43	0.24
FeO	17.08	16.01	17.28	16.48	18.36	16.92	14.08	16.83	16.88	15.04	14.85	15.25	15.34	15.62	18.31	14.86
Fe2O3	0.97	1.82	1.07	2.14	2.23	2.12	3.53	2.36	2.33	2.13	2.15	1.56	1.46	1.50	2.46	2.10
NiO	0.05	0.10	0.04	0.09	0.08	0.08	0.14	0.06	0.11	0.07	0.06	0.09	0.11	0.11	0.09	0.09
ZnO	0.16	0.19	0.21	0.24	0.27	0.31	0.16	0.22	0.24	0.24	0.31	0.14	0.17	0.17	0.19	0.19
Total	100.03	101.02	101.21	100.46	100.62	101.05	100.22	101.06	100.92	99.52	99.37	101.12	100.16	100.66	101.24	99.97
MgO	4.243	4.611	4.295	4.520	4.037	4.429	5.084	4.514	4.506	4.940	4.961	4.854	4.753	4.729	3.993	4.882
Al2O3	4.694	6.100	5.433	6.852	6.053	6.438	7.222	7.188	7.306	8.673	8.424	6.982	6.780	6.571	4.949	6.739
SiO2	0.020	0.012	0.011	0.009	0.011	0.011	0.008	0.010	0.008	0.007	0.006	0.012	0.011	0.004	0.009	0.010
TiO2	0.010	0.013	0.012	0.012	0.012	0.011	0.014	0.014	0.018	0.012	0.015	0.009	0.008	0.008	0.011	0.009
Cr2O3	11.006	9.455	10.259	8.654	9.417	9.062	8.041	8.279	8.159	6.852	7.086	8.654	8.861	9.072	10.475	8.783
V2O3	0.062	0.052	0.055	0.036	0.053	0.044	0.041	0.051	0.045	0.034	0.039	0.037	0.047	0.042	0.059	0.043
MnO	0.062	0.064	0.063	0.077	0.086	0.061	0.056	0.052	0.056	0.050	0.051	0.049	0.079	0.053	0.093	0.051
FeO	3.658	3.296	3.613	3.376	3.845	3.479	2.840	3.409	3.418	2.987	2.967	3.073	3.138	3.193	3.884	3.040
Fe2O3	0.187	0.336	0.202	0.395	0.420	0.393	0.640	0.431	0.424	0.381	0.387	0.282	0.268	0.276	0.470	0.387
NiO	0.011	0.020	0.008	0.019	0.017	0.015	0.028	0.011	0.021	0.014	0.012	0.019	0.023	0.022	0.018	0.017
ZnO	0.031	0.034	0.040	0.043	0.050	0.057	0.028	0.039	0.042	0.043	0.055	0.025	0.030	0.030	0.036	0.035
Total	23.996	24.007	24.009	24.019	24.010	24.016	24.010	24.004	24.007	24.018	24.014	24.007	24.006	24.009	24.005	24.005
Cr# (Al)	70.10	60.78	65.38	55.81	60.87	58.47	52.68	53.53	52.76	44.14	45.69	55.35	56.65	57.99	67.92	56.58
Mg#	53.70	58.32	54.31	57.24	51.22	56.00	64.16	56.97	56.87	62.32	62.58	61.24	60.23	59.69	50.69	61.62
Fe2+/Fe3+	17.61	8.82	16.14	8.55	8.24	7.99	3.99	7.12	7.26	7.07	6.90	10.90	10.53	10.42	8.26	7.06

Sample	326b2 harz banded	325 harz banded	318 harz banded	323 harz banded	284 harz bckgrd	308 harz bckgrd	310 harz bckgrd	302 harz bckgrd	300 harz bckgrd	285 harz bckgrd	284 harz bckgrd	265 harz bckgrd	291 harz bckgrd	312 harz bckgrd	269 harz bckgrd	92 harz bckgrd
MgO	13.11	14.38	12.49	14.55	12.21	12.22	13.83	13.15	13.17	12.86	12.00	12.90	12.36	13.55	13.11	14.31
Al2O3	24.75	29.26	23.98	31.14	20.22	20.05	26.19	23.13	22.83	22.44	19.40	21.53	21.20	25.52	21.94	26.96
SiO2	0.05	0.03	0.03	0.04	0.03	0.04	0.04	0.03	0.06	0.06	0.03	0.04	0.05	0.04	0.17	0.03
TiO2	0.07	0.06	0.06	0.06	0.07	0.09	0.06	0.05	0.08	0.06	0.06	0.06	0.04	0.05	0.06	0.06
Cr2O3	43.66	39.44	44.25	37.46	48.83	48.83	43.03	45.74	46.78	46.78	49.83	47.35	47.93	43.29	46.76	43.60
V2O3	0.22	0.22	0.23	0.21	0.24	0.20	0.19	0.20	0.21	0.24	0.25	0.23	0.27	0.19	0.24	0.18
MnO	0.25	0.22	0.24	0.21	0.30	0.28	0.22	0.36	0.26	0.26	0.28	0.27	0.30	0.33	0.27	0.21
FeO	15.57	14.44	16.43	14.46	16.16	16.14	14.52	15.12	15.30	15.47	16.38	15.18	16.05	14.80	15.20	14.23
Fe2O3	2.19	2.03	2.25	1.87	1.72	1.87	1.10	2.02	1.52	1.39	1.59	1.76	1.60	1.67	2.59	0.52
NiO	0.07	0.08	0.08	0.10	0.03	0.05	0.07	0.10	0.06	0.04	0.03	0.07	0.05	0.12	0.04	0.08
ZnO	0.22	0.25	0.27	0.28	0.11	0.14	0.16	0.16	0.16	0.16	0.17	0.17	0.18	0.18	0.18	0.19
Total	100.18	100.43	100.34	100.40	99.94	99.94	99.45	100.07	100.47	99.79	100.06	99.58	100.03	99.76	100.59	100.40
MgO	4.755	5.072	4.559	5.093	4.545	4.552	4.993	4.803	4.797	4.727	4.483	4.769	4.575	4.902	4.790	5.093
Al2O3	7.098	8.163	6.920	8.618	5.950	5.906	7.476	6.682	6.576	6.523	5.731	6.295	6.202	7.298	6.337	7.588
SiO2	0.013	0.008	0.008	0.009	0.008	0.010	0.010	0.007	0.015	0.014	0.008	0.009	0.012	0.011	0.043	0.008
TiO2	0.013	0.011	0.012	0.011	0.013	0.016	0.011	0.009	0.015	0.011	0.013	0.011	0.007	0.010	0.011	0.010
Cr2O3	8.402	7.381	8.566	6.955	9.640	9.649	8.240	8.865	9.042	9.123	9.876	9.286	9.410	8.307	9.060	8.234
V2O3	0.044	0.042	0.046	0.039	0.048	0.040	0.036	0.039	0.041	0.049	0.050	0.047	0.053	0.038	0.048	0.034
MnO	0.052	0.044	0.050	0.041	0.063	0.060	0.046	0.074	0.054	0.055	0.060	0.057	0.062	0.068	0.056	0.043
FeO	3.170	2.858	3.364	2.840	3.376	3.374	2.940	3.100	3.128	3.192	3.435	3.149	3.332	3.005	3.114	2.842
Fe2O3	0.401	0.361	0.415	0.330	0.323	0.351	0.200	0.372	0.280	0.258	0.301	0.328	0.298	0.305	0.479	0.094
NiO	0.013	0.015	0.015	0.019	0.007	0.011	0.013	0.019	0.011	0.008	0.006	0.015	0.010	0.024	0.007	0.016
ZnO	0.040	0.043	0.048	0.049	0.020	0.026	0.029	0.029	0.029	0.030	0.031	0.031	0.032	0.032	0.032	0.033
Total	24.005	24.011	24.010	24.014	23.998	24.003	24.005	24.006	24.006	24.000	24.004	24.005	24.001	24.005	23.985	24.005
Cr# (Al)	54.21	47.48	55.31	44.66	61.83	62.03	52.43	57.02	57.89	58.31	63.28	59.60	60.27	53.23	58.84	52.04
Mg#	60.00	63.96	57.54	64.20	57.38	57.43	62.94	60.78	60.53	59.69	56.62	60.23	57.86	62.00	60.60	64.18
Fe2+/Fe3+	7.13	7.12	7.30	7.75	9.41	8.65	13.20	8.33	10.06	11.13	10.28	8.64	10.06	8.86	5.86	

Spinel Compositions

Sample	297 harz bckgrd	287 harz bckgrd	299 harz bckgrd	311 harz bckgrd	294 harz bckgrd	267 harz bckgrd	298 harz bckgrd	287 harz bckgrd	305 harz bckgrd	282 harz bckgrd	286 harz bckgrd	304 harz bckgrd	290 harz bckgrd	55 harz bckgrd	292 harz bckgrd	303 harz bckgrd
MgO	11.53	13.05	11.69	12.47	12.03	12.85	12.16	12.90	13.41	11.48	11.86	11.61	12.52	12.91	13.24	12.46
Al2O3	21.27	25.73	20.42	20.62	22.50	21.25	22.63	26.26	24.32	18.73	18.70	21.23	23.82	22.59	23.09	22.52
SiO2	0.04	0.03	0.04	0.07	0.03	0.04	0.02	0.03	0.03	0.05	0.26	0.02	0.04	0.03	0.03	0.03
TiO2	0.06	0.06	0.05	0.06	0.06	0.06	0.05	0.07	0.07	0.05	0.06	0.04	0.05	0.06	0.06	0.05
Cr2O3	45.80	42.15	47.76	48.66	45.14	48.73	45.01	41.38	44.24	50.24	49.78	46.36	44.82	46.96	46.18	46.12
V2O3	0.29	0.20	0.26	0.25	0.25	0.27	0.27	0.24	0.21	0.28	0.28	0.26	0.28	0.25	0.23	0.26
MnO	0.29	0.23	0.28	0.28	0.26	0.29	0.26	0.24	0.38	0.40	0.30	0.29	0.40	0.27	0.24	0.39
FeO	17.25	15.71	16.95	15.93	16.82	15.55	16.57	15.96	14.91	17.10	16.11	17.22	16.11	15.51	15.15	15.97
Fe2O3	3.02	2.34	2.27	1.77	2.69	1.40	2.67	2.23	2.25	2.08	1.63	2.80	1.74	1.28	1.74	1.82
NiO	0.08	0.06	0.05	0.09	0.06	0.05	0.09	0.07	0.12	0.09	0.03	0.05	0.10	0.06	0.11	0.07
ZnO	0.19	0.19	0.20	0.20	0.20	0.20	0.21	0.21	0.21	0.21	0.21	0.22	0.22	0.23	0.23	0.23
Total	99.83	99.77	100.00	100.44	100.07	100.72	99.97	99.62	100.19	100.72	99.27	100.12	100.13	100.18	100.33	99.96
MgO	4.298	4.735	4.362	4.607	4.439	4.712	4.486	4.679	4.865	4.293	4.471	4.317	4.579	4.729	4.824	4.589
Al2O3	6.271	7.379	6.025	6.024	6.566	6.161	6.599	7.531	6.975	5.539	5.574	6.241	6.886	6.543	6.655	6.557
SiO2	0.009	0.009	0.009	0.016	0.009	0.009	0.005	0.007	0.007	0.012	0.067	0.006	0.009	0.007	0.008	0.008
TiO2	0.010	0.011	0.009	0.011	0.012	0.011	0.010	0.013	0.013	0.009	0.010	0.008	0.008	0.010	0.010	0.009
Cr2O3	9.059	8.109	9.454	9.536	8.836	9.480	8.806	7.962	8.514	9.965	9.955	9.144	8.692	9.123	8.928	9.007
V2O3	0.058	0.040	0.053	0.050	0.049	0.054	0.054	0.048	0.042	0.056	0.056	0.052	0.055	0.050	0.044	0.053
MnO	0.062	0.047	0.060	0.058	0.054	0.061	0.055	0.048	0.078	0.085	0.064	0.061	0.083	0.057	0.050	0.082
FeO	3.610	3.198	3.549	3.302	3.482	3.200	3.430	3.249	3.036	3.588	3.407	3.593	3.305	3.187	3.098	3.298
Fe2O3	0.568	0.428	0.427	0.330	0.501	0.259	0.497	0.408	0.413	0.393	0.311	0.526	0.322	0.237	0.320	0.338
NiO	0.015	0.011	0.011	0.018	0.011	0.011	0.018	0.014	0.023	0.017	0.007	0.009	0.019	0.011	0.022	0.014
ZnO	0.035	0.035	0.036	0.036	0.037	0.037	0.038	0.038	0.038	0.039	0.040	0.041	0.041	0.041	0.041	0.043
Total	24.005	24.005	24.004	24.006	24.007	24.003	24.012	24.010	24.013	24.008	23.977	24.005	24.008	24.011	24.013	24.009
Cr# (Al)	59.09	52.36	61.07	61.28	57.37	60.61	57.17	51.39	54.97	64.27	64.11	59.43	55.80	58.23	57.29	57.87
Mg#	54.35	59.69	55.14	58.25	56.04	59.55	56.67	59.02	61.58	54.47	56.75	54.58	58.08	59.74	60.89	58.18
Fe2+/Fe3+	5.72	6.72	7.48	9.00	6.25	11.11	6.22	7.16	6.63	8.22	9.86	6.15	9.25	12.09	9.68	8.80

Sample	296 harz bckgrd	288 harz bckgrd	149 harz bckgrd	132 harz chrm	78 harz chrm	188 harz chrm	349 harz interdig	355 harz interdig	1f21 harz lim.for	28 harz lim.for	94-30 harz lim.for	30 harz lim.for	94-13 harz lim.for	29 harz lim.for	10 harz lim.for	24 harz lim.for
MgO	11.93	12.93	13.79	12.12	12.60	9.80	12.25	13.14	15.18	13.29	11.86	12.82	13.35	13.62	12.69	14.29
Al2O3	23.42	25.04	26.74	17.69	21.53	12.97	19.41	26.44	26.90	20.95	18.14	21.36	21.85	24.51	19.20	25.36
SiO2	0.03	0.03	0.04	0.03	0.05	0.05	0.06	0.03	0.06	0.03	0.03	0.03	0.05	0.03	0.06	0.04
TiO2	0.05	0.06	0.05	0.24	0.06	0.05	0.05	0.06	0.08	0.07	0.07	0.05	0.05	0.07	0.09	0.06
Cr2O3	44.26	42.92	42.69	50.49	47.61	57.38	49.53	41.89	43.27	48.07	50.70	46.36	47.98	43.32	48.63	41.77
V2O3	0.24	0.24	0.23	0.23	0.17	0.37	0.18	0.21	0.19	0.28	0.27	0.20	0.25	0.25	0.23	0.26
MnO	0.28	0.26	0.23	0.29	0.28	0.36	0.30	0.36	0.22	0.25	0.40	0.37	0.36	0.34	0.37	0.23
FeO	16.98	16.04	14.91	16.10	15.80	18.83	16.08	15.72	13.06	14.83	16.35	15.36	14.65	14.47	15.23	13.95
Fe2O3	2.25	2.92	1.36	2.70	1.69	0.68	2.32	2.16	1.77	2.58	2.29	3.39	1.46	2.69	3.41	4.34
NiO	0.05	0.05	0.10	0.06	0.11	0.09	0.07	0.10	0.12	0.10	0.11	0.13	0.12	0.15	0.13	0.12
ZnO	0.25	0.25	0.26	0.14	0.19	0.23	0.16	0.30	0.10	0.13	0.14	0.14	0.14	0.16	0.17	0.17
Total	99.79	100.78	100.45	100.11	100.12	100.81	100.45	100.46	100.97	100.61	100.39	100.23	100.27	99.63	100.21	100.61
MgO	4.400	4.688	4.932	4.555	4.648	3.792	4.555	4.726	5.354	4.871	4.448	4.722	4.886	4.952	4.720	5.120
Al2O3	6.827	6.254	7.560	5.261	6.280	3.969	5.708	7.517	7.500	6.073	5.379	6.222	6.323	7.048	5.648	7.182
SiO2	0.008	2.447	0.011	0.008	0.012	0.013	0.015	0.008	0.015	0.008	0.007	0.007	0.013	0.007	0.016	0.010
TiO2	0.010	0.008	0.010	0.046	0.011	0.009	0.009	0.011	0.014	0.012	0.014	0.009	0.008	0.012	0.017	0.010
Cr2O3	8.657	5.516	8.095	10.071	9.313	11.777	9.770	7.989	8.093	9.348	10.085	9.062	9.316	8.357	9.597	7.936
V2O3	0.047	2.739	0.044	0.047	0.034	0.077	0.036	0.040	0.036	0.056	0.054	0.040	0.050	0.049	0.047	0.050
MnO	0.058	0.041	0.047	0.062	0.059	0.079	0.063	0.075	0.043	0.052	0.086	0.078	0.075	0.071	0.078	0.047
FeO	3.513	2.170	2.992	3.395	3.270	4.088	3.356	3.171	2.584	3.051	3.442	3.176	3.009	2.952	3.179	2.804
Fe2O3	0.419	1.476	0.246	0.512	0.315	0.133	0.435	0.393	0.315	0.478	0.433	0.631	0.270	0.494	0.641	0.784
NiO	0.011	0.159	0.020	0.011	0.023	0.018	0.014	0.020	0.024	0.019	0.023	0.025	0.023	0.030	0.026	0.023
ZnO	0.045	0.031	0.046	0.026	0.034	0.044	0.029	0.054	0.018	0.024	0.026	0.026	0.026	0.029	0.031	0.030
Total	24.016	16.022	24.011	24.007	24.006	24.000	24.005	24.012	23.999	24.003	24.004	24.007	24.001	24.011	24.001	24.007
Cr# (Al)	55.91	46.87	51.71	65.69	59.72	74.79	63.12	51.52	51.90	60.62	65.21	59.29	59.57	54.25	62.95	52.49
Mg#	55.60	68.36	62.24	57.29	58.70	48.12	57.58	59.84	67.45	61.48	56.37	59.79	61.89	62.65	59.75	64.61
Fe2+/Fe3+	7.56	5.49	10.95	5.97	9.35	27.73	6.93	7.26	7.38	5.74	7.15	4.53	10.03	5.37	4.47	3.22

Sample	191 harz serp dp	194 harz serp dp	251 harz serp dp	255 harz serp diap	256 harz serp diap	193 harz serp diap	309 harz top seq	388 harz top seq	314 harz top seq	283 harz top seq	389 harz top seq	216 harz top seq	315 harz top seq	262 harz top seq	313 harz top seq	257c harz wallrk a
MgO	16.73	17.55	17.92	17.19	16.57	17.04	11.96	12.96	12.46	11.92	10.87	11.74	12.24	9.47	9.85	12.41
Al2O3	40.90	43.62	48.38	44.40	42.05	44.13	18.06	18.58	20.30	18.85	17.68	16.96	20.05	11.46	19.78	20.86
SiO2	0.03	0.03	0.02	0.04	0.03	0.03	0.03	0.04	0.03	0.05	0.04	0.03	0.06	0.04	0.04	0.08
TiO2	0.12	0.07	0.05	0.06	0.10	0.07	0.05	0.06	0.06	0.04	0.05	0.06	0.09	0.04	0.08	0.05
Cr2O3	26.43	23.79	19.72	22.91	25.19	23.28	50.30	50.53	47.86	49.47	50.24	52.14	48.12	57.91	46.00	47.75
V2O3	0.14	0.14	0.12	0.11	0.14	0.12	0.29	0.26	0.26	0.27	0.28	0.29	0.18	0.39	0.29	0.22
MnO	0.17	0.17	0.15	0.18	0.17	0.18	0.39	0.36	0.29	0.29	0.29	0.29	0.39	0.33	0.33	0.42
FeO	12.55	11.61	12.14	12.64	12.82	12.55	16.26	14.90	15.90	16.32	17.77	16.37	16.12	19.04	19.55	16.01
Fe2O3	2.26	2.10	1.66	2.73	1.75	1.96	3.06	2.83	3.03	2.50	2.54	1.98	2.89	1.64	3.64	2.62
NiO	0.19	0.11	0.25	0.23	0.19	0.14	0.10	0.12	0.07	0.07	0.09	0.11	0.10	0.05	0.05	0.11
ZnO	0.20	0.21	0.24	0.25	0.25	0.30	0.14	0.15	0.15	0.17	0.18	0.18	0.18	0.21	0.22	0.12
Total	99.74	99.42	100.69	100.77	99.29	99.85	100.67	100.83	100.42	99.97	100.05	100.20	100.45	100.65	99.86	100.65
MgO	5.600	5.800	5.758	5.623	5.547	5.623	4.475	4.800	4.612	4.472	4.123	4.436	4.539	3.704	3.737	4.574
Al2O3	10.825	11.399	12.289	11.483	11.129	11.510	5.343	5.442	5.942	5.589	5.303	5.065	5.882	3.544	5.931	6.080
SiO2	0.006	0.007	0.005	0.009	0.006	0.006	0.008	0.009	0.008	0.012	0.009	0.007	0.015	0.010	0.011	0.018
TiO2	0.019	0.012	0.008	0.011	0.018	0.013	0.009	0.012	0.010	0.008	0.009	0.011	0.016	0.008	0.015	0.010
Cr2O3	4.692	4.171	3.361	3.975	4.474	4.075	9.982	9.927	9.399	9.842	10.108	10.448	9.472	12.011	9.256	9.339
V2O3	0.025	0.024	0.021	0.020	0.025	0.021	0.058	0.052	0.052	0.054	0.058	0.059	0.037	0.083	0.059	0.043
MnO	0.033	0.031	0.029	0.032	0.032	0.034	0.083	0.077	0.061	0.061	0.062	0.063	0.083	0.073	0.072	0.088
FeO	2.356	2.153	2.189	2.321	2.407	2.324	3.412	3.097	3.302	3.436	3.782	3.470	3.358	4.178	4.162	3.312
Fe2O3	0.382	0.350	0.269	0.451	0.297	0.327	0.579	0.530	0.567	0.474	0.487	0.377	0.542	0.325	0.698	0.488
NiO	0.034	0.020	0.044	0.041	0.035	0.025	0.020	0.025	0.013	0.014	0.019	0.022	0.021	0.011	0.010	0.021
ZnO	0.033	0.035	0.039	0.041	0.042	0.049	0.026	0.027	0.027	0.032	0.034	0.034	0.035	0.042	0.041	0.022
Total	24.014	24.009	24.019	24.018	24.017	24.016	24.006	24.006	24.003	24.003	24.006	24.016	24.006	24.008	24.007	23.997
Cr# (Al)	30.24	26.79	21.47	25.72	28.67	26.15	65.14	64.59	61.26	63.78	65.59	67.35	61.69	77.21	60.95	60.57
Mg#	70.39	72.93	72.46	70.79	69.74	70.76	56.74	60.78	58.28	56.55	52.16	56.11	57.48	46.99	47.31	58.00
Fe2+/Fe3+	5.55	5.53	8.14	5.15	8.12	6.39	5.31	5.84	5.24	6.52	7.76	8.28	5.58	11.59	5.38	6.79

Sample	257b harz wallrk a	346 harz wallrk b	347a harz wallrk b	392 harz xeno	387 harz xeno	356 harz xeno	351 harz xeno	390 harz xeno	278 harz xeno	327b pyxite band	326b1 pyxite band	321 pyxite band	165b pyxite band	363 pyxite opx a	406 pyxite opx a	257a pyxite opx a
MgO	12.33	13.16	15.01	10.77	9.54	13.70	12.20	12.40	8.91	11.27	13.85	11.71	13.85	11.33	11.82	14.01
Al2O3	23.80	24.93	32.01	13.41	12.19	24.28	17.37	24.71	11.96	15.70	26.69	22.89	31.27	12.86	16.23	25.68
SiO2	0.04	0.03	0.05	0.04	0.05	0.06	0.02	0.04	0.05	0.02	0.03	0.03	0.07	0.03	0.07	0.08
TiO2	0.05	0.05	0.10	0.06	0.09	0.09	0.10	0.15	0.10	0.05	0.06	0.04	0.05	0.16	0.05	0.06
Cr2O3	43.84	43.65	36.28	54.98	56.23	44.79	52.71	42.04	56.41	53.55	42.72	44.48	36.91	56.76	52.44	42.97
V2O3	0.21	0.24	0.19	0.33	0.28	0.17	0.22	0.26	0.27	0.25	0.20	0.25	0.20	0.24	0.25	0.18
MnO	0.38	0.26	0.31	0.33	0.45	0.25	0.39	0.40	0.48	0.41	0.24	0.37	0.25	0.44	0.41	0.25
FeO	16.44	15.44	13.70	17.44	19.22	14.74	15.80	16.59	20.02	17.13	15.04	17.30	15.69	16.54	16.04	14.50
Fe2O3	2.69	1.93	1.98	3.16	2.96	2.15	1.33	3.38	2.43	2.57	1.92	2.91	2.35	2.24	2.71	2.71
NiO	0.10	0.07	0.14	0.07	0.08	0.08	0.08	0.14	0.08	0.09	0.11	0.11	0.13	0.10	0.14	0.10
ZnO	0.25	0.22	0.25	0.13	0.14	0.14	0.17	0.18	0.25	0.13	0.19	0.25	0.27	0.10	0.11	0.13
Total	100.18	100.00	100.06	100.72	101.25	100.48	100.45	100.32	100.99	101.19	101.07	100.37	101.08	100.79	100.29	100.68
MgO	4.513	4.775	5.234	4.137	3.696	4.948	4.577	4.514	3.481	4.256	4.927	4.315	4.841	4.344	4.473	5.014
Al2O3	6.890	7.154	8.822	4.075	3.737	6.933	5.153	7.116	3.696	4.689	7.507	6.666	8.640	3.898	4.855	7.265
SiO2	0.010	0.006	0.012	0.010	0.013	0.013	0.005	0.010	0.012	0.006	0.008	0.009	0.016	0.007	0.018	0.019
TiO2	0.009	0.009	0.017	0.011	0.018	0.016	0.020	0.028	0.020	0.010	0.011	0.008	0.010	0.030	0.009	0.011
Cr2O3	8.514	8.403	6.715	11.206	11.564	8.580	10.488	8.122	11.692	10.731	8.060	8.693	6.842	11.542	10.525	8.157
V2O3	0.042	0.047	0.035	0.068	0.058	0.033	0.044	0.051	0.058	0.051	0.039	0.050	0.038	0.049	0.050	0.035
MnO	0.078	0.055	0.062	0.071	0.099	0.051	0.084	0.082	0.106	0.088	0.047	0.077	0.050	0.096	0.088	0.051
FeO	3.377	3.144	2.681	3.761	4.182	2.985	3.325	3.390	4.388	3.632	3.002	3.575	3.077	3.558	3.406	2.912
Fe2O3	0.497	0.354	0.347	0.613	0.579	0.392	0.253	0.621	0.480	0.490	0.344	0.541	0.415	0.434	0.517	0.489
NiO	0.020	0.013	0.025	0.015	0.017	0.015	0.016	0.028	0.016	0.018	0.022	0.021	0.025	0.020	0.029	0.020
ZnO	0.046	0.039	0.044	0.024	0.027	0.026	0.032	0.032	0.048	0.024	0.034	0.045	0.046	0.018	0.020	0.023
Total	24.010	24.008	24.012	23.999	24.003	24.005	24.015	24.007	24.009	24.006	24.006	24.009	24.011	23.999	23.999	23.999
Cr# (Al)	55.27	54.01	43.22	73.34	75.58	55.31	67.06	53.30	75.98	69.59	51.78	56.60	44.19	74.75	68.43	52.89
Mg#	57.20	60.30	66.13	52.38	46.92	62.37	57.92	57.11	44.23	53.96	62.14	54.69	61.14	54.97	56.77	63.26
Fe2+/Fe3+	6.80	8.00	7.72	5.53	7.23	6.86	11.86	5.46	9.14	7.41	8.72	5.95	7.41	7.38	5.92	5.36

Spinel Compositions

Sample	361B pyxite opx a	361a pyxite opx a	364 pyxite opx a	419 pyxite opx a	399 pyxite opx a	373 pyxite opx a	339 pyxite opx b	344 pyxite opx b	413 pyxite opx b	276 ol-pyxite	408 ol-pyxite	394 ol-pyxite
MgO	11.39	12.73	10.33	11.24	11.44	13.41	14.43	14.31	14.96	9.91	11.40	7.56
Al2O3	18.62	22.86	17.62	17.22	19.76	27.86	28.16	29.28	36.94	12.29	17.16	14.50
SiO2	0.03	0.05	0.04	0.04	0.04	0.03	0.07	0.03	0.04	0.02	0.05	0.03
TiO2	0.05	0.08	0.16	0.09	0.05	0.05	0.09	0.07	0.08	0.20	0.18	0.20
Cr2O3	49.71	45.48	50.12	52.26	48.79	40.19	41.06	39.76	30.16	54.70	51.66	51.22
V2O3	0.24	0.22	0.23	0.31	0.24	0.22	0.22	0.20	0.22	0.30	0.23	0.33
MnO	0.42	0.39	0.30	0.44	0.27	0.34	0.24	0.20	0.22	0.31	0.29	0.43
FeO	17.08	15.80	18.79	17.12	17.42	15.41	14.30	14.34	14.53	18.58	17.03	22.71
Fe2O3	2.46	2.53	2.45	1.32	2.25	2.06	1.87	1.10	2.17	3.71	1.80	4.08
NiO	0.10	0.12	0.06	0.11	0.07	0.12	0.08	0.13	0.14	0.10	0.08	0.06
ZnO	0.16	0.17	0.19	0.19	0.23	0.29	0.13	0.13	0.30	0.11	0.11	0.29
Total	100.28	100.46	100.34	100.35	100.59	100.00	100.67	99.59	99.78	100.27	100.02	101.43
MgO	4.281	4.648	3.924	4.248	4.268	4.802	5.099	5.083	5.130	3.866	4.316	2.940
Al2O3	5.533	6.599	5.293	5.147	5.826	7.892	7.867	8.223	10.018	3.791	5.140	4.458
SiO2	0.009	0.011	0.009	0.011	0.011	0.007	0.016	0.008	0.008	0.006	0.012	0.009
TiO2	0.010	0.014	0.031	0.017	0.009	0.009	0.017	0.013	0.015	0.040	0.034	0.039
Cr2O3	9.909	8.830	10.100	10.478	9.652	7.639	7.697	7.490	5.496	11.320	10.378	10.564
V2O3	0.049	0.043	0.047	0.064	0.049	0.042	0.041	0.039	0.040	0.062	0.048	0.069
MnO	0.090	0.080	0.065	0.094	0.057	0.069	0.048	0.041	0.043	0.068	0.063	0.095
FeO	3.602	3.248	4.005	3.631	3.645	3.098	2.836	2.856	2.801	4.067	3.619	4.955
Fe2O3	0.466	0.468	0.471	0.251	0.423	0.373	0.334	0.198	0.377	0.731	0.344	0.802
NiO	0.020	0.024	0.012	0.023	0.015	0.023	0.016	0.024	0.026	0.021	0.017	0.012
ZnO	0.030	0.031	0.036	0.036	0.042	0.052	0.022	0.023	0.051	0.022	0.021	0.056
Total	24.005	24.007	24.015	24.003	24.008	24.013	23.996	24.009	24.013	24.006	24.002	24.007
Cr# (Al)	64.17	57.23	65.62	67.06	62.36	49.19	49.45	47.67	35.43	74.91	66.88	70.33
Mg#	54.30	58.87	49.49	53.91	53.93	60.79	64.26	64.02	64.68	48.73	54.39	37.24
Fe2+/Fe3+	6.96	6.93	7.66	13.02	7.75	8.31	7.63	14.45	6.71	5.56	9.48	6.18

sample	97	339	326B1	212a	173	412	400	D93-5	154	321	317	60	111	384	107	293
	dunite	dunite	dunite	dunite	dunite	dunite	dunite	harz	harz	harz	harz	harz	harz	harz	harz	harz
	II fol	wallrk b	wallrk b	x fol	x fol	x fol	x fol	adj dun	adj dun	adj dun	adj dun	adj dun	anom 1	anom 1	anom 1	anom 2
Na2O	bd	bd	bd	0.03	0.02	0.05	bd	0.02	bd	bd	bd	bd	bd	bd	bd	0.03
MgO	33.38	34.15	33.40	33.35	33.60	33.63	32.93	33.72	33.56	33.21	33.75	33.65	33.40	33.55	33.34	33.22
Al2O3	1.94	2.58	2.43	1.79	1.72	1.93	2.36	1.14	1.78	1.87	1.51	1.91	2.15	2.17	2.03	2.63
SiO2	55.92	55.76	55.37	55.92	56.17	55.78	55.34	56.77	56.20	55.46	56.22	55.91	55.75	55.73	55.77	55.19
CaO	1.26	1.44	2.42	1.66	1.36	1.52	1.78	1.43	1.61	1.31	1.18	1.04	1.47	1.77	1.49	1.73
TiO2	0.04	0.04	0.03	0.06	0.06	0.04	0.03	0.02	0.03	0.03	0.02	0.02	0.04	0.03	0.04	0.05
MnO	0.14	0.12	0.14	0.14	0.16	0.14	0.15	0.19	0.14	0.16	0.15	0.15	0.13	0.16	0.15	0.12
Cr2O3	0.65	0.73	0.80	0.69	0.74	0.70	0.75	0.52	0.67	0.78	0.64	0.70	0.66	0.73	0.65	0.95
V2O3	bd	bd	0.02	bd	bd	bd	bd	0.03	bd	bd	bd	0.02	bd	bd	bd	bd
FeOt	5.75	5.71	5.75	5.65	5.64	5.75	5.93	5.74	5.60	5.86	5.55	5.96	5.70	5.79	6.03	5.15
NiO	0.04	0.07	0.11	0.05	0.02	0.08	0.11	0.03	0.10	0.11	0.09	0.02	0.12	0.07	0.03	0.08
ZnO	bd	bd	bd	bd	bd	0.02	0.04	bd	bd	bd	bd	0.02	bd	bd	0.03	0.02
Total	99.14	100.64	100.49	99.37	99.52	99.67	99.45	99.64	99.74	98.81	99.14	99.42	99.42	100.06	99.58	99.20
Na2O	-	-	-	0.001	0.001	0.002	-	0.001	-	-	-	-	-	-	-	0.001
MgO	1.740	1.729	1.695	1.722	1.780	1.728	1.708	1.699	1.734	1.771	1.748	1.718	1.747	1.716	1.751	1.746
Al2O3	0.075	0.071	0.082	0.078	0.037	0.097	0.107	0.077	0.080	0.081	0.037	0.149	0.064	0.089	0.062	0.043
SiO2	1.948	1.945	1.947	1.937	1.963	1.920	1.925	1.945	1.949	1.926	1.969	1.903	1.946	1.939	1.957	1.959
CaO	0.043	0.066	0.084	0.081	0.049	0.075	0.071	0.093	0.047	0.063	0.062	0.039	0.046	0.069	0.044	0.058
TiO2	0.001	0.000	0.001	0.001	0.001	0.001	0.001	0.001	0.001	0.001	0.000	0.002	0.001	0.001	0.001	0.001
MnO	0.004	0.004	0.004	0.004	0.004	0.004	0.004	0.005	0.004	0.004	0.004	0.005	0.005	0.004	0.004	0.005
Cr2O3	0.016	0.021	0.021	0.021	0.014	0.022	0.026	0.021	0.018	0.018	0.014	0.019	0.017	0.020	0.017	0.015
V2O3	-	-	0.001	-	-	-	-	0.001	-	-	-	0.000	-	-	-	-
FeOt	0.176	0.170	0.163	0.165	0.163	0.169	0.162	0.161	0.168	0.155	0.165	0.173	0.183	0.165	0.162	0.180
NiO	0.001	0.001	0.001	0.002	0.003	0.003	0.002	0.002	0.001	0.002	0.002	0.003	0.003	0.004	0.003	0.003
ZnO	-	-	-	-	-	0.000	0.000	-	-	-	-	0.000	-	-	0.000	0.000
Total	4.006	4.010	4.000	4.013	4.014	4.021	4.007	4.006	4.001	4.025	4.006	4.011	4.013	4.006	4.002	4.011
Mg#	90.80	91.05	91.25	91.26	91.61	91.09	91.35	91.33	91.19	91.95	91.36	90.85	90.50	91.25	91.55	90.65
En	88.79	87.99	87.29	87.52	89.38	87.63	88.03	86.97	88.99	89.04	88.49	89.04	88.39	88.04	89.47	88.03
Fs	9.00	8.65	8.37	8.38	8.19	8.57	8.33	8.26	8.60	7.79	8.37	8.97	9.27	8.44	8.26	9.07
Wo	2.21	3.36	4.34	4.10	2.44	3.80	3.64	4.78	2.41	3.17	3.14	2.00	2.34	3.52	2.27	2.90

Orthopyroxene compositions

sample	295 harz anom 2	80 harz chrm	338 harz banded	319 harz banded	318 harz banded	337 harz banded	257 harz banded	323 harz banded	325 harz banded	85 harz backgrd	92 harz bckgrd	285 harz bckgrd	291 harz bckgrd	286 harz bckgrd	292 harz bckgrd	298 harz bckgrd
Na2O	0.02	bd	bd	bd	bd	bd	0.02	bd	bd	bd	bd	bd	bd	0.03	bd	bd
MgO	34.11	32.96	33.79	33.62	33.64	33.28	33.98	33.07	33.68	33.66	33.50	33.20	33.15	33.24	33.68	33.28
Al2O3	2.30	2.15	2.09	2.07	2.05	1.92	2.11	2.90	2.74	1.76	2.24	1.97	1.80	1.72	2.04	1.84
SiO2	55.81	55.59	55.64	55.49	55.48	55.78	55.56	55.21	55.27	56.18	55.65	55.74	55.92	55.71	55.53	55.92
CaO	0.90	2.33	1.75	1.95	1.60	2.17	1.44	1.79	1.32	1.48	1.56	1.72	1.78	1.76	1.62	1.62
TiO2	0.05	0.04	0.03	0.03	0.03	0.03	0.02	0.03	0.05	0.02	0.03	0.04	0.02	bd	0.03	0.03
MnO	0.13	0.14	0.14	0.16	0.14	0.14	0.14	0.15	0.17	0.14	0.13	0.13	0.15	0.14	0.01	0.17
Cr2O3	0.67	0.82	0.77	0.76	0.71	0.75	0.72	0.87	0.83	0.69	0.77	0.78	0.75	0.75	0.79	0.70
V2O3	bd	bd	bd	bd	bd	bd	bd	bd	bd	bd	0.03	bd	bd	bd	0.14	bd
FeOt	5.23	5.18	5.80	5.41	6.12	5.68	5.70	5.79	5.70	5.61	5.22	5.73	5.68	5.83	5.77	5.67
NiO	0.06	0.12	0.10	0.10	0.06	0.08	0.08	0.09	0.07	0.09	0.09	0.06	0.06	0.05	0.12	0.03
ZnO	0.03	bd	bd	bd	bd	bd	bd	bd	0.02	bd	bd	bd	bd	bd	bd	bd
Total	99.34	99.36	100.13	99.64	99.87	99.87	99.80	99.94	99.88	99.67	99.24	99.37	99.35	99.25	99.74	99.30
Na2O	0.001	-	-	-	-	-	0.001	-	-	-	-	-	-	0.004	-	-
MgO	1.738	1.745	1.745	1.699	1.731	1.726	1.742	1.776	1.724	1.752	1.782	1.732	1.736	1.742	1.744	1.791
Al2O3	0.092	0.078	0.085	0.179	0.073	0.108	0.047	0.054	0.081	0.078	0.037	0.078	0.072	0.079	0.083	0.072
SiO2	1.937	1.945	1.927	1.875	1.947	1.923	1.968	1.930	1.942	1.945	1.963	1.943	1.949	1.938	1.929	1.923
CaO	0.059	0.039	0.065	0.062	0.062	0.065	0.053	0.064	0.065	0.041	0.041	0.056	0.058	0.056	0.060	0.059
TiO2	0.001	0.001	0.001	0.002	0.001	0.001	0.001	0.001	0.001	0.001	0.001	0.001	0.001	-	0.001	0.001
MnO	0.004	0.005	0.004	0.004	0.004	0.003	0.005	0.005	0.004	0.004	0.005	0.004	0.004	0.004	0.000	0.004
Cr2O3	0.021	0.019	0.021	0.021	0.019	0.026	0.014	0.018	0.022	0.017	0.015	0.021	0.020	0.019	0.022	0.019
V2O3	-	-	-	-	-	-	-	-	-	-	0.000	-	-	-	0.004	-
FeOt	0.152	0.173	0.168	0.175	0.165	0.150	0.167	0.185	0.167	0.168	0.166	0.168	0.163	0.167	0.170	0.156
NiO	0.003	0.001	0.003	0.003	0.001	0.002	0.001	0.002	0.002	0.003	0.003	0.001	0.003	0.002	0.003	0.002
ZnO	0.000	-	-	-	-	-	-	-	0.000	-	-	-	-	-	-	-
Total	4.006	4.006	4.019	4.023	4.006	4.009	4.001	4.034	4.006	4.008	4.012	4.007	4.005	4.013	4.018	4.030
Mg#	91.96	90.97	91.22	90.66	91.32	91.99	91.27	90.59	91.17	91.27	91.50	91.14	91.41	91.23	91.12	91.99
En	89.20	89.16	88.22	87.76	88.43	88.92	88.79	87.75	88.16	89.38	89.61	88.52	88.73	88.62	88.35	89.27
Fs	7.80	8.86	8.50	9.04	8.41	7.75	8.49	9.12	8.54	8.55	8.32	8.60	8.33	8.51	8.61	7.77
Wo	3.00	1.98	3.29	3.20	3.16	3.33	2.72	3.14	3.30	2.08	2.06	2.88	2.94	2.87	3.04	2.96

Orthopyroxene compositions

sample	299 harz bckgrd	300 harz bckgrd	149 harz bckgrd	294 harz bckgrd	308 harz bckgrd	304 harz bckgrd	55 harz bckgrd	287 harz bckgrd	311 harz bckgrd	284 harz bckgrd	265 harz bckgrd	297 harz bckgrd	188 harz chrm	78 harz chrm	132 harz chrm	349 harz interdig
Na2O	bd	0.03	bd	bd	bd	bd	bd	0.02	bd	bd	bd	bd	bd	bd	bd	bd
MgO	33.48	33.53	33.09	33.47	33.73	33.35	32.66	34.02	33.98	33.13	32.56	33.04	34.31	32.81	33.93	34.53
Al2O3	1.75	1.96	2.35	1.82	1.70	1.89	2.00	1.90	1.67	2.00	1.86	1.90	0.89	1.90	1.43	1.75
SiO2	56.17	56.16	55.48	55.84	56.09	55.79	55.93	55.94	56.24	56.02	55.55	55.49	56.80	55.75	56.80	55.25
CaO	1.56	1.88	1.98	1.16	1.48	1.51	2.26	0.70	1.09	2.17	2.48	1.84	1.23	2.30	1.64	1.60
TiO2	0.01	0.02	0.03	0.03	0.03	0.02	0.02	0.03	0.02	0.02	0.03	0.03	0.02	0.02	0.08	0.03
MnO	0.16	0.14	0.13	0.14	0.14	0.14	0.15	0.15	0.16	0.11	0.16	0.15	0.16	0.15	0.13	0.15
Cr2O3	0.71	0.79	0.87	0.58	0.71	0.77	0.76	0.56	0.63	0.75	0.76	0.74	0.52	0.78	0.68	0.71
V2O3	bd	bd	bd	bd	bd	bd	bd	0.02	bd	bd	bd	bd	bd	bd	bd	bd
FeOt	5.70	5.42	5.33	6.04	5.42	5.77	5.59	5.82	5.80	5.32	5.50	5.82	5.69	5.83	5.39	5.35
NiO	0.04	0.07	0.11	0.05	0.06	0.04	0.02	0.05	0.08	0.05	0.06	0.06	0.09	0.12	0.13	0.07
ZnO	bd	bd	bd	bd	bd	bd	bd	bd	0.02	0.02	0.03	0.03	bd	bd	0.04	bd
Total	99.62	100.04	99.40	99.17	99.40	99.35	99.44	99.25	99.72	99.63	99.02	99.13	99.75	99.71	100.28	99.49
Na2O	-	0.001	-	-	-	-	-	0.001	-	-	-	-	-	-	-	-
MgO	1.742	1.719	1.710	1.737	1.728	1.734	1.763	1.724	1.742	1.729	1.751	1.738	1.737	1.763	1.682	1.721
Al2O3	0.084	0.162	0.153	0.069	0.076	0.073	0.094	0.104	0.058	0.083	0.105	0.056	0.095	0.108	0.093	0.074
SiO2	1.928	1.884	1.895	1.950	1.948	1.949	1.936	1.929	1.957	1.940	1.918	1.951	1.930	1.915	1.932	1.948
CaO	0.060	0.060	0.047	0.058	0.061	0.060	0.034	0.057	0.061	0.055	0.053	0.058	0.049	0.038	0.094	0.067
TiO2	0.001	0.002	0.001	0.001	0.001	0.001	0.001	0.001	0.002	0.001	0.001	0.001	0.001	0.001	0.001	0.001
MnO	0.004	0.004	0.005	0.005	0.005	0.004	0.004	0.005	0.004	0.005	0.003	0.005	0.005	0.004	0.005	0.004
Cr2O3	0.020	0.022	0.023	0.017	0.019	0.019	0.018	0.024	0.019	0.018	0.020	0.015	0.022	0.022	0.024	0.021
V2O3	-	-	-	-	-	-	-	0.000	-	-	-	-	-	-	-	-
FeOt	0.178	0.167	0.178	0.169	0.165	0.162	0.152	0.162	0.155	0.175	0.164	0.183	0.169	0.168	0.172	0.165
NiO	0.002	0.003	0.003	0.002	0.001	0.003	0.001	0.003	0.004	0.001	0.002	0.002	0.003	0.003	0.002	0.002
ZnO	-	-	-	-	-	-	-	-	0.001	0.001	0.001	0.000	-	-	0.000	-
Total	4.019	4.023	4.015	4.007	4.004	4.005	4.007	4.009	4.003	4.009	4.019	4.012	4.012	4.022	4.008	4.004
Mg#	90.75	91.17	90.59	91.13	91.28	91.46	92.08	91.41	91.83	90.79	91.44	90.46	91.15	91.30	90.71	91.24
En	88.01	88.38	88.39	88.46	88.45	88.65	90.49	88.73	88.97	88.23	88.97	87.80	88.86	89.54	86.33	88.12
Fs	8.97	8.56	9.18	8.61	8.45	8.28	7.78	8.34	7.92	8.95	8.33	9.26	8.62	8.53	8.84	8.46
Wo	3.01	3.06	2.43	2.94	3.10	3.07	1.73	2.93	3.12	2.82	2.69	2.94	2.51	1.93	4.82	3.41

Orthopyroxene compositions

sample	lf21	28	191	256	255	193	251	314	283	389	262	216	257C	347A	346	356
	harz	harz	harz	harz	harz	harz	harz	harz	harz	harz	harz	harz	harz	harz	harz	harz
	lim for	lim for	serp diap	serp diap	serp diap	serp diap	serp diap	top seq	top seq	top seq	top seq	top seq	wallrk a	wallrk b	wallrk b	xeno
Na2O	0.03	bd	bd	0.03	bd	bd	0.03	bd	bd	bd	0.02	bd	bd	bd	bd	0.04
MgO	33.16	34.14	33.00	32.94	33.34	32.95	32.89	33.55	33.00	33.84	33.60	33.42	33.33	33.60	32.67	34.31
Al2O3	2.34	1.61	3.61	3.63	3.97	4.39	4.40	1.68	1.55	1.39	0.89	1.35	1.89	2.61	2.17	1.98
SiO2	54.90	56.19	54.51	54.69	54.47	54.21	54.11	56.14	55.65	56.14	56.40	56.30	55.37	55.32	55.51	55.62
CaO	2.01	1.64	1.02	1.23	1.61	0.89	1.67	1.55	1.93	1.78	1.66	1.80	1.85	1.39	2.21	1.69
TiO2	0.03	0.02	0.09	0.07	0.07	0.07	0.07	0.02	0.02	0.02	0.01	0.03	0.03	0.06	0.03	0.03
MnO	0.15	0.14	0.16	0.01	0.14	0.16	0.14	0.16	0.17	0.02	0.15	0.13	0.15	0.14	0.14	0.13
Cr2O3	0.79	0.62	0.68	0.78	0.80	0.86	0.77	0.61	0.66	0.60	0.52	0.65	0.70	0.79	0.80	0.67
V2O3	bd	bd	bd	0.14	bd	0.03	bd	bd	bd	0.15	bd	bd	bd	bd	bd	bd
FeOt	5.77	5.81	5.92	5.85	5.77	5.84	6.05	5.83	5.74	5.58	5.66	5.54	5.72	5.65	5.67	5.36
NiO	0.10	0.05	0.09	0.09	0.10	0.08	0.11	0.06	0.08	0.10	0.08	0.09	0.11	0.12	0.06	0.08
ZnO	bd	0.02	bd	bd	bd	bd	0.02	bd	bd	bd	0.03	0.04	bd	bd	0.02	bd
Total	99.31	100.27	99.12	99.46	100.31	99.51	100.25	99.62	98.85	99.66	99.04	99.39	99.15	99.73	99.31	99.94
Na2O	0.001	-	-	0.002	-	-	0.001	-	-	-	0.001	-	-	-	-	0.000
MgO	1.147	1.708	1.739	1.709	1.745	1.739	1.739	1.758	1.747	1.752	1.757	1.760	1.700	1.706	1.732	1.712
Al2O3	0.035	0.180	0.074	0.149	0.072	0.071	0.107	0.066	0.070	0.057	0.087	0.036	0.089	0.084	0.089	0.098
SiO2	1.297	1.886	1.944	1.904	1.948	1.950	1.920	1.941	1.949	1.950	1.927	1.971	1.938	1.937	1.930	1.930
CaO	0.070	0.033	0.050	0.046	0.053	0.051	0.052	0.061	0.055	0.067	0.054	0.051	0.083	0.088	0.066	0.067
TiO2	0.000	0.002	0.001	0.002	0.001	0.002	0.002	0.000	0.001	0.001	0.000	0.001	0.000	0.001	0.001	0.001
MnO	0.003	0.005	0.004	0.000	0.005	0.005	0.004	0.004	0.004	0.001	0.004	0.004	0.004	0.005	0.005	0.005
Cr2O3	0.010	0.024	0.018	0.022	0.019	0.021	0.022	0.017	0.019	0.017	0.020	0.014	0.022	0.023	0.020	0.021
V2O3	-	-	-	0.004	-	0.001	-	-	-	0.005	-	-	-	-	-	-
FeOt	0.115	0.170	0.176	0.171	0.163	0.164	0.164	0.168	0.157	0.162	0.165	0.164	0.165	0.165	0.168	0.173
NiO	0.002	0.002	0.002	0.003	0.003	0.001	0.003	0.001	0.001	0.003	0.002	0.003	0.002	0.002	0.002	0.003
ZnO	-	0.001	-	-	-	-	0.000	-	-	-	0.000	0.000	-	-	0.000	-
Total	2.681	4.011	4.010	4.009	4.006	4.003	4.015	4.018	4.006	4.014	4.019	4.004	4.005	4.009	4.015	4.010
Mg#	90.89	90.95	90.79	90.93	91.48	91.40	91.38	91.29	91.74	91.54	91.40	91.48	91.13	91.20	91.18	90.85
En	86.11	89.38	88.47	88.78	89.03	89.04	88.97	88.50	89.15	88.46	88.92	89.14	87.27	87.13	88.13	87.75
Fs	8.63	8.90	8.97	8.86	8.29	8.37	8.39	8.44	8.03	8.18	8.37	8.31	8.49	8.40	8.53	8.84
Wo	5.26	1.73	2.56	2.36	2.68	2.59	2.64	3.05	2.82	3.36	2.72	2.56	4.24	4.47	3.34	3.41

Orthopyroxene compositions

sample	387 harz xeno	165B pyxite band	326b2 pyxite band	364 pyxite opx a	373 pyxite opx a	363 pyxite opx a	257a pyxite opx a	419 pyxite opx a	406 pyxite opx a	399 pyxite opx a	361A pyxite opx a	413 pyxite opx b	344 pyxite opx b	408 ol-pyxite	276 ol-pyxite	394 ol-pyxite
Na2O	bd	bd	bd	bd	bd	bd	0.02	bd	bd	bd	bd	bd	0.02	0.02	bd	bd
MgO	34.35	34.38	32.33	34.11	33.11	33.48	33.98	32.90	33.40	33.51	32.82	32.83	32.97	33.34	32.84	33.75
Al2O3	0.89	2.66	2.27	1.30	2.51	1.04	2.11	1.35	1.32	1.65	1.89	3.71	2.64	1.47	0.93	1.01
SiO2	56.48	55.66	55.37	55.22	55.23	56.00	55.56	55.58	55.97	55.80	55.37	54.24	55.07	55.76	56.49	56.32
CaO	1.29	1.03	2.51	1.69	1.52	1.54	1.44	2.75	2.25	1.85	2.03	1.25	1.52	1.24	1.91	1.57
TiO2	0.02	0.04	0.03	0.05	0.03	0.04	0.02	0.03	0.02	0.02	0.03	0.05	0.04	0.05	0.03	0.05
MnO	0.14	0.14	0.17	0.15	0.16	0.15	0.14	0.16	0.15	0.12	0.16	0.17	0.03	0.16	0.00	0.20
Cr2O3	0.49	0.79	0.87	0.66	0.86	0.54	0.72	0.66	0.59	0.70	0.74	0.85	0.78	0.60	0.47	0.41
V2O3	bd	bd	0.02	bd	bd	bd	bd	bd	0.02	bd	bd	bd	0.13	0.03	0.20	bd
FeOt	5.61	5.83	5.91	6.31	5.55	6.14	5.70	5.49	5.98	6.02	6.16	6.07	5.73	6.63	6.64	6.94
NiO	0.10	0.10	0.07	0.08	0.11	0.11	0.08	0.11	0.12	0.09	0.12	0.10	0.13	0.06	0.11	0.10
ZnO	0.02	bd	bd	bd	bd	bd	bd	bd	bd	bd	0.02	bd	bd	bd	bd	bd
Total	99.42	100.68	99.58	99.59	99.10	99.08	99.80	99.05	99.84	99.79	99.34	99.31	99.07	99.39	99.65	100.37
Na2O	-	-	-	-	-	-	0.001	-	-	-	-	-	0.002	0.001	-	-
MgO	1.737	1.714	1.702	1.710	1.734	1.722	1.757	1.710	1.733	1.728	1.712	1.712	1.718	1.717	1.707	1.737
Al2O3	0.068	0.082	0.078	0.119	0.055	0.099	0.087	0.078	0.075	0.080	0.089	0.078	0.109	0.096	0.038	0.078
SiO2	1.940	1.944	1.941	1.916	1.959	1.915	1.927	1.945	1.940	1.942	1.937	1.937	1.925	1.931	1.970	1.936
CaO	0.069	0.081	0.086	0.066	0.067	0.090	0.054	0.076	0.073	0.069	0.087	0.076	0.057	0.074	0.071	0.070
TiO2	0.001	0.001	0.000	0.001	0.001	0.001	0.000	0.002	0.001	0.001	0.001	0.001	0.001	0.001	0.001	0.001
MnO	0.003	0.003	0.004	0.005	0.004	0.004	0.004	0.004	0.005	0.004	0.004	0.005	0.001	0.004	0.000	0.005
Cr2O3	0.019	0.021	0.022	0.024	0.018	0.022	0.020	0.022	0.020	0.022	0.023	0.021	0.021	0.024	0.013	0.020
V2O3	-	-	0.001	-	-	-	-	-	0.001	-	-	-	0.004	0.001	0.006	-
FeOt	0.175	0.154	0.170	0.168	0.161	0.167	0.165	0.163	0.163	0.157	0.151	0.180	0.168	0.155	0.194	0.168
NiO	0.002	0.002	0.003	0.003	0.002	0.003	0.002	0.001	0.003	0.002	0.004	0.004	0.004	0.003	0.003	0.003
ZnO	0.000	-	-	-	-	-	-	-	-	-	0.000	-	-	-	-	-
Total	4.016	4.004	4.009	4.012	4.004	4.023	4.019	4.006	4.013	4.007	4.007	4.014	4.010	4.007	4.004	4.016
Mg#	90.83	91.74	90.94	91.05	91.49	91.18	91.40	91.30	91.42	91.67	91.92	90.48	91.09	91.71	89.79	91.21
En	87.67	87.94	86.96	87.95	88.36	87.06	88.92	87.74	88.04	88.42	87.81	86.99	88.42	88.23	86.56	87.99
Fs	8.85	7.92	8.67	8.64	8.22	8.42	8.37	8.36	8.27	8.03	7.72	9.15	8.65	7.98	9.84	8.49
Wo	3.48	4.14	4.38	3.41	3.41	4.53	2.72	3.90	3.69	3.55	4.46	3.86	2.93	3.78	3.60	3.52

Orthopyroxene compositions

Sample	142	118	195	166	355	173	400	d93-5	321	154	384	111	293	295	323	319
	dunite	dunite	dunite	dunite	dunite	dunite	dunite	harz	harz	harz	harz	harz	harz	harz	harz	harz
	crustal	crustal	crustal	II fol	x fol	x fol	x fol	adj dun	adj dun	adj dun	anom 1	anom 1	anom 2	anom 2	banded	banded
Na2O	0.08	0.11	0.16	0.03	0.05	0.26	0.04	0.03	bd	0.07	0.05	0.03	0.11	0.21	0.02	0.02
MgO	17.28	17.16	17.28	16.24	16.09	17.12	18.13	17.34	16.85	17.28	17.53	17.57	17.09	17.14	17.49	17.73
Al2O3	0.94	1.00	3.01	2.41	2.82	2.21	2.85	1.28	2.45	2.25	2.86	2.44	2.38	2.53	2.78	2.45
SiO2	53.86	54.01	51.43	51.80	51.72	52.71	51.62	53.46	52.08	52.83	52.14	52.66	52.67	52.32	51.69	52.54
CaO	24.87	25.03	23.29	25.52	25.32	23.69	21.29	24.52	23.64	23.53	22.62	23.20	23.56	22.90	23.04	23.22
TiO2	0.05	0.09	0.23	0.07	0.07	0.08	0.05	0.03	0.03	0.03	0.06	0.06	0.08	0.09	0.07	0.02
MnO	0.05	0.06	0.08	0.05	0.06	0.10	0.11	0.08	0.10	0.11	0.11	0.08	0.08	0.08	0.10	0.10
Cr2O3	0.64	0.54	1.27	0.99	1.19	1.11	1.18	0.82	1.27	1.00	1.12	0.93	0.90	0.98	0.95	1.08
V2O3	bd	bd	0.03	0.04	bd	bd	0.04	bd	0.03	bd	0.05	bd	0.03	0.03	0.04	0.03
FeOt	1.65	1.96	2.25	1.90	1.80	2.19	2.82	1.95	2.27	2.16	2.56	2.45	1.97	2.06	2.31	2.29
NiO	0.03	bd	0.03	0.04	0.06	bd	0.05	0.04	0.07	0.07	0.05	0.07	0.04	0.04	0.03	0.06
ZnO	bd	bd	bd	bd	bd	bd	0.04	bd	bd	0.06	bd	bd	bd	bd	bd	bd
Total	99.46	100.00	99.08	99.11	99.18	99.49	98.23	99.60	98.82	99.39	99.18	99.55	98.93	98.39	98.52	99.56
Na2O	0.006	0.008	0.011	0.002	0.003	0.018	0.003	0.002	-	0.006	0.004	0.002	0.008	0.015	0.002	0.002
MgO	0.941	0.931	0.949	0.894	0.885	0.935	1.000	0.840	0.927	0.943	0.959	0.958	0.936	0.943	0.963	0.966
Al2O3	0.040	0.043	0.131	0.105	0.122	0.096	0.124	0.049	0.107	0.098	0.124	0.106	0.103	0.110	0.121	0.106
SiO2	1.968	1.967	1.895	1.913	1.907	1.931	1.909	1.737	1.922	1.934	1.913	1.925	1.935	1.931	1.910	1.920
CaO	0.974	0.977	0.919	1.010	1.001	0.930	0.844	0.853	0.935	0.923	0.889	0.909	0.927	0.906	0.912	0.910
TiO2	0.002	0.002	0.007	0.002	0.002	0.002	0.002	0.001	0.001	0.001	0.002	0.002	0.002	0.003	0.002	0.001
MnO	0.001	0.002	0.002	0.002	0.002	0.003	0.003	0.002	0.004	0.004	0.004	0.003	0.003	0.003	0.003	0.003
Cr2O3	0.019	0.016	0.037	0.029	0.035	0.033	0.035	0.021	0.038	0.029	0.032	0.027	0.026	0.029	0.028	0.031
V2O3	-	-	0.001	0.001	-	-	0.001	-	0.001	-	0.001	-	0.001	0.001	0.001	0.001
FeOt	0.051	0.060	0.070	0.059	0.056	0.068	0.088	0.053	0.070	0.066	0.079	0.075	0.061	0.064	0.071	0.070
NiO	0.001	-	0.001	0.001	0.002	-	0.002	0.001	0.002	0.002	0.001	0.002	0.001	0.001	0.001	0.002
ZnO	-	-	-	-	-	-	0.001	-	-	0.002	-	-	-	-	-	-
Total	4.003	4.006	4.021	4.018	4.015	4.013	4.010	3.561	4.007	4.005	4.008	4.008	4.002	4.004	4.014	4.011
Mg#	94.89	93.99	93.17	93.84	94.05	93.26	91.95	94.03	92.98	93.46	92.42	92.78	93.93	93.69	93.13	93.24
En	47.89	47.33	48.97	45.54	45.57	48.38	51.76	48.09	47.98	48.80	49.77	49.34	48.65	49.31	49.49	49.65
Fs	2.58	3.02	3.59	2.99	2.88	3.49	4.53	3.05	3.62	3.42	4.08	3.84	3.15	3.32	3.65	3.60
Wo	49.53	49.64	47.44	51.47	51.54	48.12	43.71	48.85	48.40	47.79	46.15	46.82	48.21	47.37	46.87	46.75

Sample	318 harz banded	327B harz banded	337 harz banded	338 harz banded	80 harz bckgrd	305 harz bckgrd	308 harz bckgrd	303 harz bckgrd	297 harz bckgrd	287 harz bckgrd	149 harz bckgrd	300 harz bckgrd	304 harz bckgrd	290 harz bckgrd	286 harz bckgrd	285 harz bckgrd
Na2O	0.01	0.02	0.03	0.03	0.06	0.02	0.05	0.02	0.03	0.02	0.03	0.13	0.05	0.02	0.02	0.02
MgO	18.35	18.20	18.02	17.70	16.87	17.01	17.94	18.43	17.12	16.80	17.02	17.81	17.15	16.93	17.32	17.09
Al2O3	2.49	1.79	2.34	2.75	2.59	2.46	2.04	2.08	1.95	2.31	2.37	2.01	2.03	2.36	1.83	2.38
SiO2	52.84	52.88	52.63	51.37	52.36	52.02	53.13	52.87	52.45	52.34	52.63	53.31	52.71	52.11	52.60	52.73
CaO	22.30	22.49	22.64	22.82	24.26	24.09	22.77	22.31	23.09	23.90	24.31	22.89	23.82	24.16	23.66	23.88
TiO2	0.03	0.03	0.03	0.04	0.03	0.05	0.04	0.03	0.03	0.05	0.05	0.04	0.04	0.03	0.03	0.04
MnO	0.09	0.11	0.09	0.08	0.08	0.07	0.05	0.10	0.10	0.08	0.08	0.08	0.08	0.10	0.09	0.11
Cr2O3	1.02	1.06	1.06	1.23	1.16	1.06	1.01	0.90	0.85	0.95	1.07	0.92	0.95	1.13	0.92	1.11
V2O3	0.02	0.02	0.03	0.04	0.03	bd	0.05	bd	0.03	0.02	0.03	bd	0.03	bd	0.03	0.03
FeOt	2.66	2.72	2.39	2.58	1.95	2.09	2.21	2.54	2.35	2.04	1.99	2.31	2.10	1.94	1.98	2.16
NiO	0.03	0.08	0.05	0.07	0.04	0.06	0.06	0.06	0.05	0.03	0.03	0.03	0.03	0.07	0.03	bd
ZnO	bd	bd	bd	0.03	bd	bd	bd	bd	bd	bd	bd	bd	bd	bd	bd	bd
Total	99.88	99.39	99.35	98.73	99.46	98.94	99.35	99.36	98.07	98.55	99.62	99.55	99.00	98.87	98.54	99.56
Na2O	0.001	0.001	0.002	0.002	0.005	0.001	0.004	0.002	0.002	0.002	0.003	0.010	0.003	0.001	0.002	0.001
MgO	0.995	0.993	0.982	0.975	0.922	0.935	0.976	1.004	0.946	0.925	0.928	0.968	0.940	0.931	0.953	0.932
Al2O3	0.107	0.077	0.101	0.120	0.112	0.107	0.088	0.090	0.085	0.101	0.102	0.087	0.088	0.102	0.080	0.102
SiO2	1.922	1.936	1.925	1.899	1.919	1.918	1.940	1.932	1.945	1.933	1.925	1.944	1.938	1.922	1.941	1.928
CaO	0.869	0.882	0.887	0.904	0.953	0.951	0.891	0.874	0.918	0.946	0.953	0.894	0.938	0.955	0.936	0.936
TiO2	0.001	0.001	0.001	0.001	0.001	0.001	0.001	0.001	0.001	0.001	0.001	0.001	0.001	0.001	0.001	0.001
MnO	0.003	0.003	0.003	0.003	0.003	0.002	0.002	0.003	0.004	0.003	0.003	0.003	0.002	0.003	0.003	0.003
Cr2O3	0.030	0.030	0.030	0.036	0.034	0.031	0.029	0.026	0.025	0.028	0.031	0.027	0.028	0.033	0.027	0.032
V2O3	0.001	0.001	0.001	0.001	0.001	-	0.001	-	0.001	0.001	0.001	-	0.001	-	0.001	0.001
FeOt	0.081	0.083	0.073	0.080	0.060	0.064	0.068	0.078	0.073	0.063	0.061	0.071	0.065	0.060	0.062	0.066
NiO	0.001	0.002	0.001	0.002	0.001	0.002	0.002	0.002	0.002	0.001	0.001	0.001	0.001	0.002	0.001	-
ZnO	-	-	-	0.001	-	-	-	-	-	-	-	-	-	-	-	-
Total	4.009	4.010	4.008	4.024	4.009	4.012	4.002	4.011	4.000	4.002	4.008	4.003	4.004	4.011	4.005	4.003
Mg#	92.50	92.26	93.08	92.42	93.89	93.59	93.51	92.83	92.84	93.64	93.83	93.21	93.56	93.95	93.93	93.39
En	51.17	50.71	50.57	49.77	47.65	47.95	50.45	51.34	48.85	47.83	47.80	50.08	48.38	47.84	48.85	48.19
Fs	4.15	4.26	3.76	4.08	3.10	3.28	3.50	3.97	3.77	3.25	3.14	3.65	3.33	3.08	3.15	3.41
Wo	44.69	45.04	45.67	46.15	49.25	48.77	46.05	44.69	47.38	48.93	49.06	46.27	48.29	49.08	48.00	48.40

Clinopyroxene compositions

Sample	92 harz bckgrd	298 harz bckgrd	55 harz bckgrd	299 harz bckgrd	292 harz bckgrd	310 harz bckgrd	85 harz bckgrd	294 harz bckgrd	291 harz bckgrd	296 harz bckgrd	188 harz chrm	349 harz interdig	24 harz lim.for	1f21 harz lim.for	28 harz lim.for	255 harz serp dp
Na2O	0.06	0.02	0.01	0.02	0.01	0.05	0.01	0.02	0.02	0.02	0.10	0.05	0.04	0.03	0.01	0.20
MgO	16.96	17.13	17.28	17.37	17.48	17.07	17.35	17.05	17.12	16.94	18.28	18.43	18.02	17.91	17.59	17.63
Al2O3	2.67	2.09	2.04	1.31	2.03	2.93	1.79	2.10	2.33	2.44	0.96	2.03	2.78	3.03	1.95	3.22
SiO2	52.25	52.75	52.66	53.04	52.99	52.23	52.89	52.84	52.28	52.19	53.98	51.73	52.00	52.05	52.67	52.07
CaO	24.09	23.69	23.97	24.21	23.86	23.59	24.37	23.83	23.22	23.86	23.32	22.77	22.19	22.06	23.34	23.18
TiO2	0.06	0.04	0.04	0.05	0.04	0.05	0.04	0.04	0.03	0.03	0.02	0.03	0.04	0.06	0.05	0.14
MnO	0.09	0.10	0.44	0.08	0.04	0.08	0.09	0.09	0.11	0.10	0.10	0.10	0.11	0.10	0.09	0.09
Cr2O3	1.17	1.04	0.47	0.61	0.84	1.17	0.87	0.89	1.14	1.12	0.69	0.96	1.10	1.23	0.87	0.67
V2O3	0.03	0.04	0.10	0.05	0.09	0.03	0.02	0.02	0.03	0.03	0.03	0.02	0.03	bd	0.03	bd
FeOt	1.97	2.23	2.12	1.75	2.09	2.13	2.11	2.24	2.28	2.19	2.19	2.32	2.55	2.65	2.37	2.32
NiO	0.05	0.05	0.04	0.03	0.06	0.04	0.05	0.03	0.04	0.04	0.05	0.05	0.06	0.05	0.06	0.05
ZnO	bd	bd	bd	bd	bd	bd	0.03	0.03	0.04	0.05	bd	bd	bd	bd	bd	bd
Total	99.42	99.20	99.19	98.53	99.58	99.40	99.63	99.20	98.64	99.01	99.72	98.50	98.93	99.20	99.03	99.59
Na2O	0.005	0.002	0.001	0.001	0.001	0.004	0.001	0.002	0.001	0.001	0.007	0.004	0.003	0.002	0.000	0.015
MgO	0.927	0.937	0.946	0.955	0.952	0.932	0.946	0.933	0.942	0.930	0.992	1.016	0.987	0.978	0.964	0.960
Al2O3	0.115	0.091	0.089	0.057	0.088	0.127	0.077	0.091	0.101	0.106	0.041	0.088	0.121	0.131	0.084	0.139
SiO2	1.916	1.936	1.934	1.957	1.936	1.913	1.936	1.939	1.929	1.922	1.965	1.913	1.911	1.908	1.936	1.903
CaO	0.947	0.932	0.943	0.957	0.934	0.926	0.956	0.937	0.918	0.942	0.910	0.902	0.874	0.866	0.919	0.908
TiO2	0.002	0.001	0.001	0.001	0.001	0.002	0.001	0.001	0.001	0.001	0.001	0.001	0.001	0.002	0.001	0.004
MnO	0.003	0.004	0.013	0.002	0.002	0.003	0.003	0.003	0.003	0.003	0.003	0.003	0.003	0.003	0.003	0.003
Cr2O3	0.034	0.031	0.014	0.018	0.025	0.034	0.025	0.026	0.033	0.033	0.020	0.028	0.032	0.035	0.025	0.020
V2O3	0.001	0.001	0.003	0.002	0.003	0.001	0.001	0.001	0.001	0.001	0.001	0.001	0.001	-	0.001	-
FeOt	0.061	0.069	0.065	0.054	0.064	0.065	0.065	0.069	0.070	0.067	0.067	0.071	0.078	0.081	0.073	0.071
NiO	0.002	0.002	0.001	0.001	0.002	0.001	0.002	0.001	0.001	0.001	0.002	0.002	0.002	0.001	0.002	0.002
ZnO	-	-	-	-	-	-	0.001	0.001	0.001	0.001	-	-	-	-	-	-
Total	4.011	4.003	4.010	4.004	4.008	4.007	4.013	4.003	4.003	4.008	4.008	4.029	4.013	4.008	4.005	4.022
Mg#	93.87	93.19	93.57	94.65	93.70	93.48	93.62	93.11	93.08	93.28	93.67	93.44	92.68	92.35	92.96	93.11
En	47.93	48.37	48.41	48.58	48.82	48.48	48.12	48.10	48.80	47.96	50.39	51.07	50.90	50.82	49.28	49.52
Fs	3.13	3.54	3.33	2.75	3.28	3.38	3.28	3.56	3.63	3.46	3.40	3.59	4.02	4.21	3.73	3.66
Wo	48.94	48.09	48.26	48.68	47.90	48.14	48.60	48.34	47.57	48.58	46.20	45.34	45.07	44.97	46.98	46.81

Clinopyroxene compositions

Sample	256 harz serp dp	193 harz serp dp	191 harz serp dp	251 harz serp dp	314 harz top seq	216 harz top seq	262 harz top seq	283 harz top seq	257B harz wallrk a	257C harz wallrk a	326b2 harz wallrk b	347A harz wallrk b	346 harz wallrk b	390 harz xeno	326B1 pyxite band	165B pyxite band
Na2O	0.34	0.35	0.29	0.20	0.02	0.05	0.02	0.02	0.01	0.03	0.04	0.17	0.07	0.16	0.02	0.04
MgO	16.35	16.04	16.76	16.49	17.99	17.72	17.83	17.34	17.70	17.22	16.86	17.96	17.10	17.25	17.59	17.78
Al2O3	4.53	4.63	4.03	4.72	2.09	1.63	0.88	1.95	2.25	2.45	2.34	2.85	2.71	2.45	2.42	2.78
SiO2	51.19	51.44	51.66	51.20	52.99	53.04	53.49	52.73	52.65	52.24	52.49	52.88	52.41	52.38	52.17	52.39
CaO	22.49	23.11	23.20	23.36	22.54	22.67	23.41	22.89	23.28	23.59	24.03	22.87	23.09	22.78	23.74	23.29
TiO2	0.20	0.18	0.21	0.15	0.03	0.03	0.02	0.03	0.03	0.04	0.06	0.15	0.04	0.10	0.04	0.06
MnO	0.04	0.10	0.09	0.08	0.11	0.09	0.09	0.12	0.02	0.11	0.10	0.08	0.09	0.10	0.10	0.08
Cr2O3	1.17	1.16	1.07	1.04	0.99	0.89	0.62	1.15	0.91	1.19	1.03	1.03	1.13	1.00	0.96	1.07
V2O3	0.11	0.02	bd	0.03	bd	0.03	0.03	bd	0.10	0.03	0.02	0.02	0.03	bd	0.02	0.03
FeOt	2.39	2.25	2.32	2.45	2.62	2.42	2.06	2.35	2.44	2.44	2.08	2.32	2.25	2.53	2.13	2.24
NiO	0.05	0.04	0.06	0.06	0.06	0.06	0.05	0.06	0.06	0.06	0.04	0.06	0.04	0.06	0.06	0.07
ZnO	bd	bd	bd	0.06	bd	bd	bd	bd	bd	bd	bd	bd	0.06	0.08	bd	bd
Total	98.86	99.33	99.72	99.83	99.47	98.64	98.50	98.66	99.46	99.42	99.08	100.41	99.02	98.91	99.27	99.83
Na2O	0.024	0.025	0.021	0.014	0.001	0.004	0.001	0.002	0.001	0.003	0.003	0.012	0.005	0.011	0.001	0.003
MgO	0.897	0.876	0.913	0.898	0.979	0.972	0.979	0.953	0.966	0.942	0.924	0.969	0.936	0.946	0.962	0.966
Al2O3	0.197	0.200	0.173	0.203	0.090	0.070	0.038	0.085	0.097	0.106	0.102	0.122	0.117	0.106	0.105	0.119
SiO2	1.884	1.885	1.888	1.871	1.936	1.952	1.971	1.943	1.927	1.917	1.930	1.914	1.925	1.928	1.915	1.910
CaO	0.887	0.908	0.909	0.914	0.882	0.894	0.924	0.904	0.913	0.928	0.947	0.887	0.909	0.898	0.934	0.910
TiO2	0.006	0.005	0.006	0.004	0.001	0.001	0.001	0.001	0.001	0.001	0.002	0.004	0.001	0.003	0.001	0.002
MnO	0.001	0.003	0.003	0.003	0.003	0.003	0.003	0.004	0.001	0.004	0.003	0.002	0.003	0.003	0.003	0.003
Cr2O3	0.034	0.034	0.031	0.030	0.029	0.026	0.018	0.034	0.027	0.035	0.030	0.029	0.033	0.029	0.028	0.031
V2O3	0.004	0.001	-	0.001	-	0.001	0.001	-	0.003	0.001	0.001	0.001	0.001	-	0.001	0.001
FeOt	0.074	0.069	0.071	0.075	0.080	0.075	0.063	0.073	0.075	0.075	0.064	0.070	0.069	0.078	0.066	0.068
NiO	0.001	0.001	0.002	0.002	0.002	0.002	0.002	0.002	0.002	0.002	0.001	0.002	0.001	0.002	0.002	0.002
ZnO	-	-	-	0.002	-	-	-	-	-	-	-	-	0.002	0.002	-	-
Total	4.007	4.005	4.015	4.014	4.005	4.000	4.000	3.998	4.011	4.012	4.004	4.012	4.001	4.006	4.018	4.014
Mg#	92.43	92.73	92.83	92.29	92.45	92.84	94.06	92.93	92.84	92.67	93.52	93.23	93.13	92.38	93.61	93.41
En	48.29	47.29	48.24	47.57	50.44	50.08	49.78	49.39	49.45	48.46	47.75	50.30	48.91	49.22	49.05	49.69
Fs	3.96	3.71	3.73	3.98	4.12	3.86	3.14	3.76	3.82	3.83	3.31	3.65	3.61	4.06	3.35	3.51
Wo	47.75	49.00	48.03	48.45	45.44	46.06	47.07	46.85	46.73	47.71	48.94	46.05	47.48	46.72	47.60	46.80

Clinopyroxene compositions

Sample	105 pyxite crustal	257a pyroxenite opx a	406 pyxite opx a	399 pyxite opx a	361B pyxite opx a	361A pyxite opx a	344 pyxite opx b	381 pyxite stringer	102 ol pyxite vein
Na2O	0.07	0.03	0.03	0.02	0.04	0.05	0.12	0.08	0.10
MgO	18.73	18.14	17.12	17.24	17.60	20.68	17.06	17.72	18.32
Al2O3	1.78	2.82	1.85	2.23	2.02	3.05	2.85	2.26	2.02
SiO2	52.49	52.12	52.38	52.58	52.32	52.47	52.42	52.48	52.92
CaO	21.84	22.41	24.02	23.49	23.11	18.45	23.40	22.66	22.19
TiO2	0.08	0.05	0.03	0.03	0.04	0.07	0.06	0.07	0.10
MnO	0.13	0.07	0.07	0.08	0.12	0.11	0.04	0.04	0.12
Cr2O3	0.49	1.23	1.10	1.10	1.02	1.23	1.04	1.07	0.92
V2O3	0.02	bd	0.02	0.03	bd	0.04	0.08	0.11	bd
FeOt	3.58	2.50	2.31	2.33	2.62	3.91	2.18	2.60	3.04
NiO	0.03	0.07	0.08	0.04	0.05	0.08	0.07	0.06	0.05
ZnO	0.04	bd	bd	bd	bd	bd	bd	bd	bd
Total	99.27	99.48	99.02	99.18	98.94	100.14	99.33	99.15	99.83
Na2O	0.005	0.002	0.003	0.002	0.003	0.004	0.008	0.006	0.007
MgO	1.025	0.988	0.941	0.943	0.966	1.114	0.931	0.970	0.996
Al2O3	0.078	0.122	0.081	0.096	0.088	0.130	0.123	0.098	0.087
SiO2	1.928	1.906	1.931	1.930	1.928	1.896	1.920	1.927	1.930
CaO	0.859	0.878	0.949	0.924	0.912	0.715	0.918	0.891	0.867
TiO2	0.003	0.001	0.001	0.001	0.001	0.002	0.002	0.002	0.003
MnO	0.004	0.002	0.002	0.003	0.004	0.003	0.001	0.001	0.004
Cr2O3	0.015	0.036	0.032	0.032	0.030	0.035	0.030	0.031	0.026
V2O3	0.001	-	0.001	0.001	-	0.001	0.002	0.004	-
FeOt	0.110	0.077	0.071	0.072	0.081	0.118	0.067	0.080	0.093
NiO	0.001	0.002	0.003	0.001	0.002	0.002	0.002	0.002	0.001
ZnO	0.001	-	-	-	-	-	-	-	-
Total	4.027	4.015	4.014	4.005	4.015	4.021	4.004	4.010	4.015
Mg#	90.31	92.81	92.98	92.91	92.26	90.42	93.29	92.38	91.49
En	51.40	50.86	47.99	48.63	49.31	57.21	48.59	49.96	50.94
Fs	5.52	3.94	3.62	3.71	4.13	6.06	3.50	4.12	4.74
Wo	43.08	45.20	48.39	47.65	46.55	36.73	47.91	45.92	44.32

Clinopyroxene compositions

	195 dunite crustal	55 harz bckgrd	293 harz bckgrd	308 harz bckgrd	188 harz chrm	262 harz bckgrd	lt21 harz lim.lor	191 harz serp diapir	193a harz serp diapir	193b harz serp diapir	193c harz serp diapir	257A, gr1 opx A	257A, gr2 opx A	257B harz wallrk A	257C harz wallrk opx A	381 cpxite stringer	165B pyxite band	344 opx B	347A hz wallrk B	346 harz wallrk opx B
Sc	68.7	65.7	55.3	54.8	70.0	46.0	59.4	62.2	56.1	57.2	53.8	55.7	60.7	66.6	61.3	65.4	56.6	72.5	72.7	66.0
Ti	1042.1	103.3	312.8	184.9	50.3	24.7	191.1	871.8	832.8	788.8	786.5	144.8	160.3	94.1	94.9	282.2	248.9	294.4	628.8	106.8
V	174.9	167.3	157.3	138.8	115.2	132.3	186.6	178.0	195.9	194.7	196.0	144.8	160.3	150.9	147.7	169.6	199.8	200.6	205.4	189.2
Sr	1.969	0.270	0.433	0.352	1.599	0.708	0.330	0.438	0.760	0.814	1.347	0.244	2.420	0.284	0.373	0.934	0.453	7.482	0.521	0.211
Zr	1.687	0.093	0.092	0.139	0.095	0.062	0.175	0.611	0.688	0.613	0.583	0.104	0.125	0.141	0.180	0.272	0.334	0.222	0.163	0.117
Nb	0.235	0.172	0.131	0.156	0.131	0.088	0.166	0.139	0.206	0.130	0.158	0.170	0.166	0.258	0.271	0.201	0.201	0.167	0.157	0.210
Y	9.101	0.663	1.904	0.616	0.271	0.103	1.277	6.173	8.415	7.008	6.774	0.787	0.825	0.652	0.541	2.066	2.101	1.210	1.247	0.685
Ba	0.682	0.073	0.022	0.026	0.288	0.091	0.076	3.398	0.640	0.928	2.587	bd	0.096	0.011	0.005	0.317	0.034	1.599	0.112	0.021
La	0.035	0.002	0.004	0.007	0.040	0.004	0.003	0.007	0.006	0.003	0.003	bd	bd	bd	0.002	0.010	0.006	0.002	0.025	0.002
Ce	0.108	0.005	0.005	0.011	0.047	0.004	0.007	0.013	0.014	0.009	0.012	0.002	0.002	0.002	0.006	0.025	0.014	0.004	0.006	0.003
Pr	0.042	0.001	0.001	0.002	0.008	0.001	0.004	0.006	0.012	0.010	0.013	0.001	0.001	bd	0.001	0.007	0.003	0.001	0.003	0.000
Nd	0.586	0.006	0.008	0.010	0.060	0.006	0.015	0.121	0.273	0.239	0.199	0.002	0.003	0.004	0.005	0.050	0.022	0.011	0.045	0.002
Sm	0.486	0.004	0.005	0.008	0.019	0.002	0.006	0.189	0.388	0.278	0.351	0.002	0.003	0.002	0.002	0.084	0.019	0.012	0.066	0.002
Eu	0.226	0.003	0.005	bd	0.004	0.001	0.006	0.098	0.176	0.153	0.156	0.001	0.002	0.001	0.001	0.060	0.012	bd	0.007	0.001
Gd	1.128	bd	0.046	0.020	0.029	bd	0.071	0.560	0.935	0.972	0.932	0.024	bd	0.020	0.017	0.166	0.100	0.046	0.049	0.017
Tb	0.201	bd	0.017	0.011	0.005	0.001	0.015	0.142	0.208	0.223	0.192	0.007	0.011	0.005	0.004	0.036	0.031	0.013	0.016	0.005
Dy	1.795	0.089	0.306	0.062	0.030	0.009	0.203	1.009	1.673	1.582	1.776	0.063	0.103	0.071	0.054	0.302	0.312	0.153	0.182	0.072
Yb	1.440	0.364	0.590	0.349	0.161	0.191	0.609	0.925	1.335	1.216	1.243	0.277	0.398	0.278	0.240	0.443	0.494	0.382	0.297	0.338

	195 dunite crustal	55 harz bckgrd	293 harz bckgrd	308 harz bckgrd	188 harz chrm	262 harz bckgrd	lf21 harz lim.for	191 harz serp diapir	193a harz serp diapir	193b harz serp diapir	193c harz serp diapir	257A, gr1 opx A	257A, gr2 opx A	257B harz wallrk A	257C harz wallrk opx A	381 cpxite stringer	165B pyxite band	344 opx B	347A hz wallrk B	346 harz wallrk opx B
Sc	68.7	65.7	55.3	54.8	70.0	46.0	59.4	62.2	56.1	57.2	53.8	55.7	60.7	66.6	61.3	65.4	56.6	72.5	72.7	66.0
Ti	1042.1	103.3	312.8	184.9	50.3	24.7	191.1	871.8	832.8	788.8	786.5	144.8	160.3	94.1	94.9	282.2	248.9	294.4	628.8	106.8
V	174.9	167.3	157.3	138.8	115.2	132.3	186.6	178.0	195.9	194.7	196.0	144.8	160.3	150.9	147.7	169.6	199.8	200.6	205.4	189.2
Sr	1.969	0.270	0.433	0.352	1.599	0.708	0.330	0.438	0.760	0.814	1.347	0.244	2.420	0.284	0.373	0.934	0.453	7.482	0.521	0.211
Zr	1.687	0.093	0.092	0.139	0.095	0.062	0.175	0.611	0.688	0.613	0.583	0.104	0.125	0.141	0.180	0.272	0.334	0.222	0.163	0.117
Nb	0.235	0.172	0.131	0.156	0.131	0.088	0.166	0.139	0.206	0.130	0.158	0.170	0.166	0.258	0.271	0.201	0.201	0.167	0.157	0.210
Y	9.101	0.663	1.904	0.616	0.271	0.103	1.277	6.173	8.415	7.008	6.774	0.787	0.825	0.652	0.541	2.066	2.101	1.210	1.247	0.685
Ba	0.682	0.073	0.022	0.026	0.288	0.091	0.076	3.396	0.640	0.928	2.587	bd	0.096	0.011	0.005	0.317	0.034	1.589	0.112	0.021
La	0.035	0.002	0.004	0.007	0.040	0.004	0.003	0.007	0.006	0.003	0.003	bd	bd	bd	0.002	0.010	0.006	0.002	0.025	0.002
Ce	0.108	0.005	0.005	0.011	0.047	0.004	0.007	0.013	0.014	0.009	0.012	0.002	0.002	0.002	0.006	0.025	0.014	0.004	0.006	0.003
Pr	0.042	0.001	0.001	0.002	0.008	0.001	0.004	0.006	0.012	0.010	0.013	0.001	0.001	bd	0.001	0.007	0.003	0.001	0.003	0.000
Nd	0.586	0.006	0.008	0.010	0.060	0.006	0.015	0.121	0.273	0.239	0.199	0.002	0.003	0.004	0.005	0.050	0.022	0.011	0.045	0.002
Sm	0.486	0.004	0.005	0.008	0.019	0.002	0.006	0.189	0.386	0.278	0.351	0.002	0.003	0.002	0.002	0.084	0.019	0.012	0.066	0.002
Eu	0.226	0.003	0.005	bd	0.004	0.001	0.006	0.098	0.176	0.153	0.156	0.001	0.002	0.001	0.001	0.060	0.012	bd	0.007	0.001
Gd	1.128	bd	0.046	0.020	0.029	bd	0.071	0.560	0.935	0.972	0.932	0.024	bd	0.020	0.017	0.166	0.100	0.046	0.049	0.017
Tb	0.201	bd	0.017	0.011	0.005	0.001	0.015	0.142	0.208	0.223	0.192	0.007	0.011	0.005	0.004	0.036	0.031	0.013	0.016	0.005
Dy	1.795	0.089	0.306	0.062	0.030	0.009	0.203	1.009	1.673	1.582	1.776	0.083	0.103	0.071	0.054	0.302	0.312	0.153	0.182	0.072
Yb	1.440	0.364	0.590	0.349	0.161	0.191	0.609	0.925	1.335	1.216	1.243	0.277	0.398	0.278	0.240	0.443	0.494	0.382	0.297	0.338

sample	370	257DUN	118	119	121	142	172	195	197	200	231	233	D93-004	66	97	166	180	170
lithology	dunite interdig	dunite wallrk a	dunite crustal	dunite crustal	dunite crustal	dunite crustal	dunite crustal	dunite crustal	dunite crustal	dunite crustal	dunite crustal	dunite crustal	dunite II fol	dunite II fol	dunite II fol	dunite II fol	dunite II fol	dunite II fol
XRF data																		
MnO	0.12	0.13	0.14	0.11	0.17	0.13	0.14	0.13	0.12	0.15	0.12	0.12	0.12	0.12	0.13	0.12	0.12	0.13
TiO2	0.01	0.01	0.01	0.02	0.02	0.01	0.01	0.02	0.02	0.02	0.02	0.02	0.01	0.01	0.01	0.01	0.01	0.01
Fe2O3	9.12	9.64	10.37	10.01	12.56	10.10	10.73	9.39	9.07	10.50	8.79	9.08	9.59	9.00	9.25	10.04	10.02	10.43
CaO	0.17	0.36	0.46	0.09	1.73	0.54	0.28	0.43	0.33	1.72	0.62	0.91	0.34	0.31	0.68	0.32	0.15	0.40
SiO2	40.68	41.45	39.93	42.13	40.87	40.00	39.30	39.80	39.68	40.61	39.98	40.40	39.74	40.21	42.63	39.89	40.44	39.36
Al2O3	0.14	0.23	0.23	0.60	0.48	0.27	0.51	0.57	0.58	0.59	0.99	1.14	0.29	0.27	0.47	0.13	0.08	0.32
MgO	49.99	48.61	48.16	46.25	44.31	48.58	48.12	48.95	49.00	45.33	47.91	47.29	48.93	49.97	46.63	48.80	49.44	48.09
TOTAL	100.67	100.80	99.85	99.70	100.64	100.13	99.86	99.87	99.81	99.59	99.07	99.67	100.33	100.55	100.41	99.96	100.92	99.41
LOI	10.11	9.87	11.77	14.96	5.23	10.99	12.72	11.88	13.33	8.16	11.09	11.54	15.93	15.39	9.32	10.86	14.40	16.06
Zn	43	46	48	56	50	42	49	41	41	44	36	41	52	39	45	50	53	36
Cu		1	8	8	13	9	9	8	8	12	9	10	9	8	9	8	8	9
Ni	2867	2853	1637	1863	1350	1145	2523	1864	2471	1800	2410	2972	2823	2679	2543	2954	2970	2192
Co	143	145	146	150	156	154	155	145	142	141	145	141	151	153	135	153	151	157
Cr	887	650	2670	2828	2165	3522	4129	3306	5505	4189	3561	3177	4140	1971	2161	664	580	3546
V	12	14	12	16	26	21	22	18	24	28	22	24	20	11	23	10	7	20
Ti	57	49	120	165	80	106	120	174	161	135	225	207	145	135	122	93	116	88
Sc	7	9	8	7	14	8	8	8	7	11	4	8	3	5	7	7	5	10
ICP-MS data																		
Ga	0.202	0.219						0.610										
Rb	0.047	0.036						0.058										
Sr	0.137	0.304						1.863										
Y	0.021	0.022						0.242										
Zr	0.051	0.106						0.144										
Nb	0.010	0.004						0.087										
Ba	0.353	0.000						1.269										
La		0.044						0.014										
Ce		0.294						0.032										
Nd	0.008	0.017						0.019										
Yb	0.008	0.011						0.044										

sample	D93-003	69	74	99	114	131	151	152		167	178	396	187	168	173	184	127	153	D93-005
lithology	dunite ll fol	dunite ll fol	dunite ll fol	dunite ll fol	dunite ll fol	dunite ll fol	dunite ll fol	dunite ll fol	dunite ll fol	dunite ll fol	dunite ll fol	dunite wall rk	dunite wallrk	dunite x fol	dunite x fol	dunite x fol	dunite x fol	dunite x fol	harz adj. dun
XRF data																			
MnO	0.12	0.12	0.12	0.12	0.12	0.12	0.14	0.13	0.16	0.12	0.14	0.11	0.13	0.12	0.13	0.12	0.12	0.11	0.12
TiO2	0.01	0.01	0.01	0.01	0.01	0.01	0.01	0.01	0.04	0.01	0.03	0.01	0.01	0.01	0.01	0.01	0.01	0.01	0.01
Fe2O3	9.42	9.88	10.34	10.18	9.26	9.26	10.19	10.34	9.76	10.32	10.40	8.62	9.35	10.00	9.43	10.24	10.25	9.02	8.90
CaO	0.36	0.32	0.35	0.32	0.17	0.23	0.23	0.28	3.35	0.21	0.24	0.32	0.15	0.38	0.41	0.07	0.30	0.26	0.58
SiO2	40.09	40.05	39.71	40.14	40.05	40.11	38.46	39.84	47.67	39.89	36.23	40.55	39.76	39.00	40.41	40.89	40.05	39.65	43.81
Al2O3	0.16	0.14	0.37	0.30	0.14	0.19	0.69	0.31	0.83	0.25	3.66	0.08	0.14	0.36	0.63	0.16	0.15	0.22	0.43
MgO	49.31	49.42	48.67	49.79	49.55	49.50	47.90	48.66	36.53	48.84	45.94	50.03	49.62	48.10	47.41	47.81	48.85	49.55	45.45
TOTAL	100.13	100.60	100.22	101.81	99.93	100.21	99.33	100.19	98.86	100.27	97.88	100.10	99.82	98.96	99.12	99.84	100.15	99.50	99.89
LOI	16.54	15.93	16.04	11.46	11.72	15.45	13.06	14.01	3.34	11.89	13.20	16.33	15.98	16.11	9.32	17.46	14.06	14.92	13.16
Zn	44	46	51	50	40	39	52	43	53	47	63	31	41	38	45	43	49	40	46
Cu	9	9	9	8	8	8	8	8	15	8	9		8	9	13	8	9	8	9
Ni	2806	2709	2766	2862	2680	2846	2340	2852	1044	2832	2929	2922	2639	2530	2710	2146	2784	2848	2444
Co	156	155	157	150	147	151	146	156	111	150	141	142	159	153	139	167	160	151	133
Cr	2261	797	1353	1879	2028	1406	10669	2063	3003	2310	11054		2056	5461	4885	2099	666	1831	2472
V	18	11	11	12	10	12	39	13	60	13	55	9	7	26	24	13	9	10	34
Ti	126	88	107	106	118	163	125	69	185	96	284	79	112	138	159	123	113	178	71
Sc	4	8	9	8	5	1	9	10	20	7	4	8	7	5	4	5	5	-1	11
ICP-MS da																			
Ga												0.145							
Rb												0.067							
Sr												4.663							
Y												0.032							
Zr												0.037							
Nb												0.004							
Ba												2.049							
La																			
Ce																			
Nd												0.017							
Yb												0.014							

Whole-rock data

sample	60	169	185	67	70	75	113	128	171	181	154	371	55	62	84	85	87
lithology	harz adj. dun	harz adj. dun	harz adj. dun	harz adj. dun	harz adj. dun	harz adj. dun	harz adj. dun	harz adj. dun	harz adj. dun	harz adj. dun	harz adj. dun	harz adj. dun	harz bckgrd	harz bckgrd	harz bckgrd	harz bckgrd	harz bckgrd
XRF data																	
MnO	0.13	0.12	0.12	0.11	0.12	0.12	0.13	0.12	0.12	0.12	0.12	0.12	0.12	0.12	0.12	0.12	0.12
TiO2	0.01	0.01	0.01	0.01	0.02	0.01	0.01	0.01	0.01	0.02	0.01	0.01	0.01	0.01	0.01	0.01	0.01
Fe2O3	9.87	8.96	9.06	8.93	9.08	9.10	8.78	9.19	8.94	9.61	8.71	8.68	8.98	9.50	8.99	8.85	9.00
CaO	0.47	0.56	0.17	0.45	0.52	0.65	0.33	0.68	0.45	0.37	0.72	0.39	0.75	0.41	1.09	0.85	0.95
SiO2	41.46	42.94	42.64	42.88	42.86	43.53	42.86	43.17	42.22	41.91	43.32	42.42	43.76	41.46	43.29	43.56	43.30
Al2O3	0.36	0.45	0.35	0.45	0.77	0.66	0.21	0.74	0.45	0.42	0.64	0.53	0.68	0.29	0.73	0.62	0.53
MgO	47.70	46.19	46.92	46.53	46.03	45.18	46.73	44.98	47.47	47.04	45.26	46.96	45.72	47.59	44.45	45.13	44.99
TOTAL	100.36	99.76	99.80	99.86	99.87	99.74	99.61	99.34	100.26	100.02	99.31	99.69	100.59	99.94	99.15	99.64	99.49
LOI	12.14	13.07	14.53	11.88	12.29	13.77	10.18	11.95	14.44	12.33	10.53	9.58	12.57	12.46	12.87	12.65	11.22
Zn	50	44	38	43	46	44	42	47	42	52	43	45	46	45	42	43	42
Cu	9	9	8	8	9	9	8	10	8	9	9	1	9	9	10	10	9
Ni	2670	2484	2533	2540	2515	2403	2528	2466	2542	2670	2447	2625	2482	2667	2434	2439	2505
Co	148	137	140	139	136	139	132	134	140	140	133	133	133	147	137	132	136
Cr		2502	2362	2367	2659	2854	2484	2374	2298	1738	2534	2482	2508	1777	2272	2515	2505
V	24	35	31	20	26	35	25	37	24	23	32	22	36	19	39	35	34
Ti	104	76	77	104	83	90	85	74	94	208	83	102	41	86	91	98	
Sc	7	10	10	9	14	11	8	12	11	7	12	10	14	9	10	8	17
ICP-MS da																	
Ga												0.398	0.569				0.370
Rb												0.065	0.105				0.063
Sr												0.618					0.612
Y												0.079	0.055				0.044
Zr												0.061	0.029				0.380
Nb												0.012	0.006				0.012
Ba												2.504					0.223
La												0.032	0.023				0.005
Ce												0.154	0.140				0.011
Nd												0.016					
Yb												0.018	0.026				0.016

sample	91	92	93	94	149	182	208	211	214	217	219	221	285	294	388	389	391	107	107
lithology	harz bckgrd	harz bckgrd	harz bckgrd	harz bckgrd	harz bckgrd	harz bckgrd	harz bckgrd	harz bckgrd	harz bckgrd	harz bckgrd	harz bckgrd	harz bckgrd	harz bckgrd	harz bckgrd	harz top seq	harz top seq	harz top seq	harz anom 1	harz anom 1
XRF data																			
MnO	0.13	0.12	0.12	0.13	0.12	0.12	0.12	0.11	0.12	0.13	0.12	0.12	0.13	0.13	0.12	0.13	0.13	0.13	0.13
TiO2	0.01	0.01	0.01	0.01	0.01	0.01	0.01	0.01	0.01	0.01	0.02	0.01	0.01	0.01	0.01	0.01	0.01	0.02	0.02
Fe2O3	9.25	8.36	8.82	9.29	8.58	8.58	9.12	8.60	8.77	8.95	8.96	8.86	8.90	9.05	8.05	8.82	8.94	9.11	9.10
CaO	0.81	0.66	0.80	0.88	0.71	0.47	0.66	0.62	0.73	0.66	0.45	0.52	0.72	0.88	0.48	0.64	0.98	0.87	0.85
SiO2	43.44	42.82	43.81	43.78	42.58	42.86	42.51	43.37	43.58	43.19	42.81	43.27	43.78	44.86	44.01	43.96	43.50	43.94	44.56
Al2O3	0.61	0.73	0.60	0.66	0.63	0.54	0.60	0.79	0.62	0.43	0.49	0.44	0.70	0.81	0.55	0.66	0.73	0.80	0.86
MgO	45.35	46.36	45.37	44.43	46.14	46.49	46.29	45.82	46.20	46.54	47.19	46.47	44.70	44.15	45.60	45.38	44.38	43.47	43.89
TOTAL	100.13	99.68	100.06	99.70	99.33	99.48	99.86	99.83	100.46	100.41	100.41	100.28	99.54	100.48	99.38	100.15	99.27	98.86	100.00
LOI	10.04	12.74	12.57	12.18	14.66	11.49	14.04	9.58	9.81	8.13	10.48	7.51	12.35	10.82	8.60	8.88	8.28	7.25	7.25
Zn	45	37	42	47	39	47	43	45	45	45	43	44	40	41	42	43	47	47	46
Cu	10	9	10	10	9	9	10	9	9	9	8	9	6	11	5	7	15	11	14
Ni	2563	2498	2434	2408	2523	2556	2491	2501	2506	2491	2541	2566	2417	2471	2484	2504	2481	2496	2474
Co	138	138	136	133	139	135	140	129	132	133	139	132	131	129	124	131	128	132	128
Cr	2840	2354	2292	2499	2234	2286	2344	2613	2574	2415	2183	2479	2920	2773	2456	2709	2700	2672	2790
V	35	30	35	39	30	23	34	30	25	27	21	24	40	41	34	33	41	42	45
Ti	89	129	85	47	83	111	73	113	108	81	174	33	87	112	101	72	127	123	134
Sc	9	7	9	13	11	7	10	10	9	8	8	13	14	11	10	10	11	9	12
ICP-MS da																			
Ga					0.420					0.311			0.614	0.578	0.432	0.403	0.655		
Rb					0.159					0.091			0.186	0.087	0.130	0.065	0.056		
Sr					2.714					0.089			0.153	0.114	0.293	0.067	0.494		
Y					0.051					0.041			0.050	0.080	0.053	0.021	0.155		
Zr					0.021					0.058			0.084	0.033	0.043	0.024	0.032		
Nb					0.012					0.012			0.007	0.005	0.004	0.011	0.004		
Ba					0.909					0.054			0.549	0.067		0.070			
La														0.003	0.021				
Ce													0.010		0.146				
Nd													0.009	0.012	0.010				
Yb					0.022					0.018			0.026	0.033	0.021	0.018	0.045		

sample	111	384	111	56	68	318	319	323	328	337	362	418	80	132	188	188	78
lithology	harz anom 1	harz anom 1	harz anom 1	harz banded	harz banded	harz banded	harz banded	harz banded	harz banded	harz banded	harz banded	harz banded	harz chr mine	harz chr mine	harz chr mine	harz chr mine	harz chr mine
XRF data																	
MnO	0.13	0.13	0.13	0.12	0.13	0.13	0.12	0.13	0.13	0.13	0.12	0.13	0.12	0.11	0.12	0.13	0.13
TiO2	0.02	0.02	0.01	0.01	0.01	0.01	0.01	0.01	0.01	0.01	0.01	0.01	0.01	0.02	0.01	0.01	0.01
Fe2O3	8.94	9.13	8.89	8.73	8.97	9.68	8.77	9.37	9.73	9.14	9.66	10.11	8.49	8.82	9.28	9.33	8.91
CaO	0.82	0.93	0.77	0.80	0.92	0.64	0.71	0.56	0.97	0.57	0.67	0.44	0.60	0.26	0.33	0.32	0.99
SiO2	43.26	43.84	43.02	44.77	44.40	43.47	44.14	43.75	42.31	43.20	43.04	42.01	43.03	42.48	42.06	42.40	44.94
Al2O3	0.79	0.72	0.73	0.80	0.64	0.61	0.72	0.62	0.38	0.62	0.55	0.31	0.65	0.37	0.28	0.26	0.80
MgO	44.10	45.05	44.66	44.04	44.89	45.54	45.18	45.92	46.03	45.95	45.57	46.49	46.53	47.11	46.54	46.53	43.78
TOTAL	99.01	100.45	98.65	99.78	100.41	100.57	100.25	100.83	100.07	100.07	100.06	99.91	99.93	99.74	99.26	99.58	100.08
LOI	8.66	8.00	8.66	11.17	11.03	12.54	12.64	12.48	8.92	12.42	7.75	11.68	13.80	14.37	13.59	13.59	10.66
Zn	43	45	44	44	44	46	41	48	48	48	54	58	38	44	45	42	42
Cu		11	9	9		2	6	3	6	1	3		9	8	8	3	10
Ni	2517	2407	2515	2390	2429	2510	2470	2470	2618	2551	2557	2720	2437	2577	2624	2610	2366
Co	133	129	131	129	132	141	132	140	141	140	139	143	133	142	145	141	129
Cr	2562	2869	2555	2774	2367	2232	2479	1664	2085	1834	2190	1675	2417	2195	2301	2221	2682
V	35	42	31	47	34	36	30	31	26	30	26	32	32	24	23	27	40
Ti	82	118	107	58	72	71	88	89	67	68	61	74	54	148	88	59	45
Sc	11	11	8	14	12	10	11	12	11	12	15	8	15	11	9	10	14
ICP-MS da																	
Ga	0.675	0.523				0.516	0.577	0.629	0.463	0.580	0.454	0.361		0.335		0.246	
Rb	0.042	0.057				0.040	0.038	0.084	0.087	0.084	0.079	0.063		0.179		0.122	
Sr	0.084	0.207				3.349	0.240	1.367	0.477	1.452	0.064	0.161		1.351		0.122	
Y	0.084	0.078				0.047	0.052	0.068	0.054	0.054	0.040	0.047		0.048		0.021	
Zr	0.067	0.045				0.221	0.033	0.017	0.085	0.034	0.019	0.055		0.290		0.032	
Nb	0.008	0.006				0.013	0.007	0.006	0.244	0.006	0.014	0.005		0.005		0.005	
Ba	0.609	0.342				0.903	0.666	0.558	0.805	0.397		0.170		0.406		0.080	
La								0.005		0.005		0.004		0.004		0.004	
Ce	0.009	0.009					0.006	0.005	0.012	0.006				0.006		0.007	
Nd	0.010	0.006					0.009		0.009			0.010					
Yb	0.032	0.025				0.022	0.024	0.032	0.016	0.026	0.022	0.025		0.020		0.007	

sample	349	LF94-13	LF94-16	LF94-21	LF94-28	LF94-31	191	193	194	356	392	96	175	176	257	374
lithology	harz	harz lim.for	harz lim.for	harz lim.for	harz lim.for	harz lim.for	harz serp diapir	harz serp diapir	harz serp diapir	harz xeno	harz xeno	harz	harz serp shear	harz serp shear	harz wallrk a	harz wallrk a
XRF data																
MnO	0.12	0.12	0.12	0.13	0.11	0.10	0.12	0.12	0.12	0.12	0.13	0.12	0.07	0.13	0.13	0.13
TiO2	0.01	0.01	0.01	0.01	0.02	0.01	0.04	0.04	0.03	0.01	0.01	0.02	0.01	0.01	0.01	0.01
Fe2O3	8.74	9.10	9.29	9.19	9.33	9.08	8.53	8.48	8.87	8.80	8.78	8.91	11.79	9.08	8.88	10.19
CaO	0.47	0.06	0.43	0.82	0.08	0.07	2.16	2.02	1.37	0.52	0.44	0.68	0.07	0.66	0.91	0.67
SiO2	44.03	45.45	41.87	43.21	46.06	46.27	44.41	44.13	46.20	42.44	43.71	43.21	44.61	45.89	43.85	42.09
Al2O3	0.49	0.72	0.38	0.66	0.65	0.65	1.73	1.73	1.56	0.44	0.28	0.70	0.46	0.54	0.70	0.22
MgO	47.00	43.29	46.07	45.12	43.54	43.24	42.19	42.56	41.43	46.90	46.25	45.74	42.69	43.36	45.34	46.56
TOTAL	101.36	99.36	98.90	99.66	100.28	99.98	99.73	99.53	100.12	99.79	100.14	99.94	100.09	100.26	100.37	100.37
LOI	10.83	12.67	13.56	15.30	12.69	12.98	12.64	12.97	13.22	9.01	8.55	10.10	11.85	8.33	9.20	8.98
Zn	44	43	45	43	45	41	42	38	40	45	40	48	37	44	44	50
Cu	1	11	6	3	5	14	13	12	12	5	3	9	9	9		
Ni	2524	2674	2639	2496	2619	2502	2222	2218	2472	2635	2539	2517	2392	2595	2510	2686
Co	129	134	144	140	136	127	124	120	131	135	133	138	124	132	128	144
Cr	1974	3427	2685	2594	2217	3027	2929	2678	2682	1866	2437	2423	1915	2592	2579	1921
V	25	45	31	39	36	49	59	54	50	19	29	26	27	35	28	23
Ti	62	111	88	104	126	122	253	275	281	92	62	78	82	53	62	42
Sc	10	11	12	10	11	13	18	14	10	8	12	13	11	14	11	9
ICP-MS da																
Ga	0.371	0.643	0.434		0.795	0.803	1.490	1.416		0.444	0.277		0.415	0.483	0.502	0.283
Rb	0.103	0.045	0.062		0.037	0.030	1.391	0.643		0.079	0.076		0.025	0.056	0.113	0.066
Sr	0.063	1.995	1.694		2.110	1.383	3.136	9.570		0.243	0.138		0.864	1.232	0.278	0.164
Y	0.023	0.056	0.036		0.129	0.091	0.957	1.081		0.055	0.031		0.167	0.112	0.050	0.021
Zr	0.020	0.062	0.094		0.130	0.040	0.067	0.092		0.041	0.022		0.080	0.233	0.035	0.019
Nb	0.003	0.008	0.008		0.013	0.007	0.008	0.005		0.005	0.004		0.006	0.015	0.007	0.004
Ba		1.338	0.497		1.386	0.474	40.703	73.849		0.056	0.124		2.050	2.161		0.164
La					0.012					0.005	0.004		0.066	0.008	0.024	0.004
Ce		0.014	0.019		0.019						0.007		0.040	0.014	0.156	0.005
Nd		0.006	0.009		0.011					0.011			0.032	0.007	0.007	0.005
Yb	0.017	0.027	0.016		0.036	0.033	0.136	0.151		0.024	0.013		0.021	0.025	0.022	0.011

sample	346	408	105	116	227	234	373	419	257PX	344PYX
lithology	harz wallrk b	ol-pyxite	cpxite	cpxite	cpxite	cpxite	Opx A	Opx A	Opx A	Opx B
XRF data										
MnO	0.13	0.15	0.14	0.17	0.14	0.14	0.13	0.13	0.12	0.13
TiO2	0.01	0.03	0.07	0.04	0.13	0.10	0.02	0.02	0.02	0.02
Fe2O3	9.25	8.08	4.85	10.98	5.47	4.35	6.90	7.18	8.51	7.68
CaO	0.57	1.50	18.08	7.68	16.83	19.88	1.21	2.08	1.07	1.27
SiO2	42.84	51.46	51.99	44.36	50.11	53.00	52.12	51.43	45.38	47.74
Al2O3	0.58	1.15	1.58	0.92	2.35	2.52	2.17	1.17	1.07	2.39
MgO	46.04	37.09	22.27	34.98	23.42	19.11	37.70	36.53	43.07	39.41
TOTAL	99.95	100.02	98.99	99.31	98.87	99.43	100.74	99.18	99.85	99.68
LOI	15.08	5.71	1.00	3.86	2.03	0.71	3.48	3.74	8.20	8.34
Zn	43	40	25	45	23	19	32		41	48
Cu	17	10	7	3	5	7	6		5	18
Ni	2582	1218	370	815	385	250	1514		2278	1619
Co	142	99	27	137	38	12	76		124	94
Cr	3010	4866	2784	1462	5854	3931	6874		3975	13066
V	36	64	122	58	140	174	94		42	103
Ti	117	320	432	261	849	666	161		113	230
Sc	11	18	38	21	41	41	19		14	21
ICP-MS d										
Ga	0.641	1.159					2.195	1.205	0.843	2.290
Rb	0.105	0.371					1.816	0.311	0.208	1.073
Sr	3.868	2.234					2.288	0.995	3.746	5.578
Y	0.042	0.377					0.194	0.173	0.083	0.145
Zr	0.057	0.796					0.045	0.034	0.022	0.078
Nb	0.007	0.016					0.011	0.017	0.004	0.020
Ba	0.837	3.780					1.745	1.671	0.933	3.765
La	0.035	0.000					0.004			
Ce	0.202	0.008					0.006			
Nd	0.011	0.008					0.006			
Yb	0.021	0.082					0.059	0.066	0.036	0.060